



UCTEA Turkish Chamber of Civil Engineers

# Teknik Dergi

*Technical Journal*

Volume 33    Issue 4    July 2022

## **TEKNİK DERGİ PUBLICATION PRINCIPLES**

Teknik Dergi is a scientific and technical journal indexed by the Science Citation Index Expanded. Annually six issues are published, three in Turkish in the months of January, May and September, three in English in March, July and November. Its main principles of publication are summarized below:

1. Articles reporting original scientific research and those reflecting interesting engineering applications are accepted for publication. To be classified as original, the work should either produce new scientific knowledge or add a genuinely new dimension to the existing knowledge or develop a totally new method or substantially improve an existing method.
2. Articles reporting preliminary results of scientific studies and those which do not qualify as full articles but provide useful information for the reader can be considered for publication as technical notes.
3. Discussions received from the readers of the published articles within three months from publication are reviewed by the Editorial Board and then published together with the closing remarks of the author.
4. Manuscripts submitted for publication are evaluated by two or three reviewers unknown to the authors. In the light of their reports, final decision to accept or decline is taken by the Editorial Board. General policy of the Board is to get the insufficient manuscripts improved in line with the reviewers' proposals. Articles that fail to reach the desired level are declined. Reasons behind decisions are not declared.
5. A signed statement is taken from the authors, declaring that the article has not been published as a "journal article or book chapter". In case the Editorial Board is in the opinion that the article has already been published elsewhere with minor changes or suspects plagiarism or a similar violation of ethics, then not only that article, but none of the articles of the same authors are published.
6. Papers reporting works presented as conference papers and developed further may be considered for publication. The conference it was presented to is given as a footnote in the first page.
7. Additionally, a document signed by all authors, transferring the copyright to UCTEA Chamber of Civil Engineers is submitted together with the manuscript.



UCTEA Turkish Chamber of Civil Engineers

# Teknik Dergi

*Technical Journal*

Volume 33    Issue 4    July 2022



**UCTEA (TMMOB)**

**Turkish Chamber of Civil Engineers (*İnşaat Mühendisleri Odası*)**

Necatibey St. No: 57, Kızılay 06440 Ankara, Turkey

Tel: +90.312.294 30 00 - Faks: +90.312.294 30 88

E-mail: imo@imo.org.tr - www.imo.org.tr

**Publisher (*Sahibi*):**

Taner YÜZGEÇ

On behalf of UCTEA Turkish Chamber of Civil Engineers

**Administrative Officer (*Yazı İşleri Müdürü*):**

Özer AKKUŞ

Volume 33 - Issue 4 - July 2022 (*Cilt 33 - Sayı 4 - Temmuz 2022*)

Published bi-monthly. Local periodical. (*İki ayda bir yayınlanır, yerel süreli yayın*)

Date of Print: July 1, 2022 (*Baskı Tarihi: 1 Temmuz 2022*)

Number of copies: 1.000 (*1.000 adet basılmıştır*)

Quotations require written approval of the Editorial Board.

(*Yayın Kurulunun yazılı onayı olmaksızın alıntı yapılamaz.*)

**ISSN: 1300-3453**

Teknik Dergi is indexed by

- Science Citation Index Expanded
- Scopus
- Journal Citation Reports / Science Edition
- Engineering Index
- Concrete Abstracts (American Concrete Institute)
- National Technical Information Service (US NTIS)
- CITIS
- Ulrich's International Periodical's Directory
- TR Index

Teknik Dergi is a peer reviewed open access periodical publishing papers of original research and interesting practice cases. It addresses both the research community and the practicing engineers.

Teknik Dergi ekidir.

---

UCTEA Turkish Chamber of Civil Engineers

# Teknik Dergi

## Editor in Chief:

Alper İLKİ

## Co-Editors:

İsmail AYDIN

Özer ÇİNİCİOĞLU

Metin GER

Gürkan Emre GÜRCANLI

Kutay ORAKÇAL

İsmail ŞAHİN

Özkan ŞENGÜL

Tuğrul TANKUT

Emine Beyhan YEĞEN

## Secretary:

Cemal ÇİMEN

## Advisory Board:

Prof. M. Aral, USA

Prof. D. Arditi, USA

Prof. A. Aydilek, USA

Prof. K. Beyler, Switzerland

Prof. N. Çatbaş, USA

Prof. M. Çetin, USA

Prof. M. Dewoolkar, USA

Prof. T. Edil, USA

Prof. K. Elwood, New Zealand

Prof. M. Fardis, Greece

Prof. G. Gazetas, Greece

Prof. P. Gülkan, Türkiye

Prof. J. Han, USA

Prof. I. Hansen, Netherlands

Prof. T. Hartmann, Germany

Prof. F. Imamura, Japan

Prof. T. Kang, Korea

Prof. K. Kusunoki, Japan

Prof. S. Lacasse, Norway

Prof. R. Al-Mahaidi, Australia

Prof. K. Özbay, USA

Prof. H. Özer, USA

Prof. G. Özmen, Türkiye

Prof. S. Pampanin, Italy

Prof. A. J. Puppala, USA

Prof. M. Saatçioğlu, Canada

Prof. C. Santamarina, Saudi Arabia

Prof. S. Sheikh, Canada

Prof. E. C. Shin, South Korea

Prof. J. Smallwood, South Africa

Prof. M. Sümer, Türkiye

Dr. H. A. Şentürk, Türkiye

Dr. S. S. Torisu, Japan

Prof. E. Tutumluer, USA

Prof. M. Tümay, USA

## Reviewers:

This list is renewed each year and includes reviewers who served in the last two years of publication.

|                          |                            |                           |                      |                        |
|--------------------------|----------------------------|---------------------------|----------------------|------------------------|
| Şükran AÇIKEL            | Halil İbrahim BURGAN       | Fazlı Erol GÜLER          | Umut OKKAN           | Serhan TANYEL          |
| Merve AÇIKGENÇ           | Erdem CANBAY               | İlgin GÜLER               | Derviş Volkan OKUR   | Yüksel TAŞDEMİR        |
| ULAŞ                     | Zekai CELEP                | Hamza GÜLLÜ               | Mehmet Hakkı OMURTAG | Kerem TAŞTAN           |
| Stüleyman ADANUR         | Cihan CENGİZ               | Gürkan GÜNAY              | Engin ORAKDÖĞEN      | Gökmen TAYFUR          |
| Ali Mardani              | Halim CEYLAN               | Taylan GÜNAY              | Şeref ORUÇ           | Beytullah TEMEL        |
| AGHABAGLOU               | Hüseyin CEYLAN             | Murat GÜNAYDIN            | Akin ÖNALP           | Rasim TEMÜR            |
| Perviz AHMEDZADE         | Ömer CİVALEK               | Samet GÜNER               | Halil ÖNDER          | Egemen TEOMETE         |
| Bülent AKBAŞ             | Ayşe COŞKUN BEYAN          | Ülker GÜNER BACANLI       | Jülide ÖNER          | Serdal TERZİ           |
| Ragıp AKBAŞ              | Melih ÇALAMAK              | Oğuz GÜNEŞ                | Bihart ÖNÖZ          | Berrak TEYMUR          |
| Samir Oğuzhan AKBAŞ      | Gülben ÇALIŞ               | Mehmet Şükrü GÜNEY        | Ali Hakan ÖREN       | Hüseyin Onur TEZCAN    |
| Şeref Doğuşcan AKBAŞ     | Süheyla Pelin ÇALIŞKANELLİ | Tuba GÜRBÜZ               | Mustafa ÖZAKÇA       | Mesut TİĞDEMİR         |
| Rıfat AKBIYIKLI          | Dilay ÇELEBI               | Melike GÜREL              | Ceyhan ÖZÇELİK       | Şahnaz TİĞREK          |
| Özge AKBOĞA KALE         | Tevfik Kutay ÇELEBİOĞLU    | İbrahim GÜRER             | Yiğit ÖZÇELİK        | Salih TİLEYLİOĞLU      |
| Hüseyin AKBULUT          | Ahmet Ozan ÇELİK           | Aslı Pelin GÜRGÜN         | Gökhan ÖZDEMİR       | Vedat TOĞAN            |
| Sarven AKCELYAN          | Oğuz Cem ÇELİK             | İman HAJİRASOULİHA        | Osman Nuri ÖZDEMİR   | Onur Behzat TOKDEMİR   |
| Burcu AKÇAY              | Semet ÇELİK                | Soner HALDENBİLEN         | Halit ÖZEN           | İrem Dikmen TOKER      |
| ALDANMAZ                 | Hilmi Berk ÇELİKOĞLU       | Mustafa HATİPOĞLU         | Murat ÖZEN           | Cengiz TOKLU           |
| Cihan Taylan AKDAĞ       | Mahmut ÇETİN               | Bo-Tao HUANG              | Pelin ÖZENER         | Ali TOPAL              |
| Cem AKGÜNER              | Mecit ÇETİN                | Zeynep İŞİK               | Cem ÖZER             | İlker Bekir TOPÇU      |
| Muhammet Vefa AKPINAR    | Gökhan ÇEVİKBİLEN          | Hande İŞİK ÖZTÜRK         | Hasan ÖZER           | Cem TOPKAYA            |
| Atakan AKSOY             | Erdal ÇOKÇA                | Sabriye Banu İKİZLER      | Serkan ÖZGEN         | Kamile TOSUN           |
| Hafızullah AKSOY         | İsa ÇÖMEZ                  | Ragıp İNCE                | Eren Arman ÖZGÜVEN   | ÇELEKOĞLU              |
| Hakan AKSU               | İsmail DABANLI             | Recep İYİSAN              | Hakkı Oral ÖZHAN     | Gökçe TÖNÜK            |
| Tülay AKSU ÖZKUL         | Ömer DABANLI               | Nihat KABAY               | M. Hulusi ÖZKUL      | Ülgen Mert TUĞSAL      |
| Büşra AKTÜRK             | Atilla DAMCI               | Mehmet Sedat KABDAŞLI     | Zeynep Huri ÖZKUL    | Gürşen TURAN           |
| Zuhal AKYÜREK            | Yakup DARAMA               | Mehmet Rifat KAHYAOĞLU    | BİRGÖREN             | Ö. Tuğrul TURAN        |
| Uğurhan AKYÜZ            | Osama M.F. DAWOUD          | Özkan KALE                | Gülen ÖZKULA         | Cüneyt TÜZÜN           |
| Sadık ALASHAN            | Tayfun DEDE                | Volkan KALPAKÇI           | Ahmet ÖZTOPAL        | Eren UÇKAN             |
| Cenk ALHAN               | Özgür DEĞERTEKİN           | Murat KARACASU            | Sadık ÖZTOPRAK       | Ergin ULUTAŞ           |
| Ayşe Burcu ALTAN SAKARYA | Abdullah DEMİR             | Halil KARAHAN             | Turan ÖZTURAN        | Berna UNUTMAZ          |
| Sinan ALTIN              | Cem DEMİR                  | Cenk KARAKURT             | Hasan Tahsin ÖZTÜRK  | Tayfun UYGUNOĞLU       |
| Adlen ALTUNBAŞ           | Emre DEMİR                 | Mustafa KARASAĞIN         | Mustafa ÖZUYAL       | Volkan Emre UZ         |
| Ahmet Can ALTUNBAŞ       | Munise Didem DEMİRBAŞ      | Zülküf KAYA               | Ahmet Onur PEHLİVAN  | Nihal UZCAN ERATLI     |
| Ahmet Can ALTUNİŞİK      | Ender DEMİREL              | Hasan Ahmed KAZMEE        | Onur PEKCAN          | İbrahim Mert UZUN      |
| Yalçın ALVER             | Mehmet Cüneyd DEMİREL      | Mustafa Kubilay KELEŞOĞLU | Seval PINARBAŞI      | Deniz ÜLGEN            |
| Bahadır ALYAVUZ          | Fatih DİKBAŞ               | Elçin KENTEL              | ÇUHADAROĞLU          | Mehmet ÜLKER           |
| Özgür ANIL               | Seyyit Ümit DİKMEN         | Havvanur KILIÇ            | Elişan Filiz PİROĞLU | Mehmet Barış Can ÜLKER |
| Necati ARAS              | Ali Ersin DİNÇER           | Young Hoon KIM            | Selim PUL            | Yurdanur ÜNAL          |
| Yalçın ARISOY            | İsmail DURANYILDIZ         | Ufuk KIRBAŞ               | Selçuk SAATÇİ        | Cüneyt VATANSEVER      |
| Musa Hakan ARSLAN        | Selim DÜNDAR               | Veysel Şadan Özgür KIRCA  | Selman SAĞLAM        | Syed Tanvir WASTI      |
| Deniz ARTAN İLTER        | Nurhan ECEMİŞ ZEREN        | Cem KIRLANGIÇOĞLU         | Mehmet SALTAN        | Ahmet YAKUT            |
| Şenay ATABAY             | Volkan Ş. EDİGER           | Güven KIYMAZ              | İlyas SARIBAŞ        | Mehmet Cem YALÇIN      |
| Ali Osman ATAHAHAN       | Muhammet Emin EMİROĞLU     | Gökhan KIRKİL             | Metin SARIGÖL        | Aslı YALÇIN            |
| Hakan Nuri ATAHAHAN      | Murat Altuğ ERBERİK        | Kasım KOÇAK               | Afşin SARITAŞ        | DAYIOĞLU               |
| Bekir Özer AY            | Ali ERCAN                  | Salih KOÇAK               | Altuğ SAYGILI        | Ahmet Cevdet YALÇINER  |
| Ersin AYDIN              | Hakan ERDEM                | Niyazi Uğur KOÇKAL        | Serdar SELAMET       | İsmail Özgür YAMAN     |
| Gökçe AYDIN              | Sinan Turhan ERDOĞAN       | Mehmet Melih KOŞUCU       | Senem SEYİS          | Alper SEZER            |
| Hakan AYGÖREN            | Ramazan Cüneyt ERENOĞLU    | Baha Vural KÖK            | Osman SİVRİKAYA      | Osman SİVRİKAYA        |
| Mustafa Tamer AYVAZ      | Esin ERGEN PEHLEVAN        | Mete KÖKEN                | Behzad SOLTANBEIGI   | Behzad SOLTANBEIGI     |
| İhsan Engin BAL          | Gökmen ERGÜN               | Şerife Yurdağül KUMCU     | Celal SOYARSLAN      | Celal SOYARSLAN        |
| Selim BARADAN            | Bülent ERKMEN              | Murat KURUOĞLU            | Serdar SOYÖZ         | Serdar SOYÖZ           |
| Eray BARAN               | Barış ERKUŞ                | Akif KUTLU                | Rifat SÖNMEZ         | Rifat SÖNMEZ           |
| Türkay BARAN             | Tuğba ESKİŞAR TEFÇİ        | Abdullah KÜRKCÜ           | Tayfun Altuğ SÖYLEV  | Tayfun Altuğ SÖYLEV    |
| Bekir Oğuz BARTIN        | Burak FELEKOĞLU            | Hilmi LUŞ                 | Erol ŞADOĞLU         | Erol ŞADOĞLU           |
| Eyüp Ensar BAŞAKIN       | Okan FISTIKOĞLU            | Kasım MERMERTAŞ           | Güvenç ŞAHİN         | Güvenç ŞAHİN           |
| Özgür BAŞKAN             | Abdullah GEDİKLİ           | Mehmet Murat MONKUL       | Ömer Lütfi ŞEN       | Ömer Lütfi ŞEN         |
| Niyazi Özgür BEZGİN      | Ergun GEDİZLİOĞLU          | Hamid MORTEZAEİ           | Burak ŞENGÖZ         | Burak ŞENGÖZ           |
| Senem BİLİR              | Ömer GİRAN                 | Yetiş Şazi MURAT          | Özkan ŞENGÜL         | Özkan ŞENGÜL           |
| MAHÇİÇEK                 | Zehra Canan GİRGIN         | Sepanta NAİMİ             | Aynur ŞENSOY         | Aynur ŞENSOY           |
| Gökçen BOMBAR            | İlknur BOZBEY              | Öcal NECMİOĞLU            | ŞORMAN               | ŞORMAN                 |
| Burak BOYACI             | Zafer BOZKUŞ               | Sinan Melih NİĞDELİ       | Karin ŞEŞETAYAN      | Karin ŞEŞETAYAN        |
| Atıl BULU                | İlgin GÖKAŞAR              | Elif OĞUZ                 | Okan ŞİRİN           | Okan ŞİRİN             |
| Burcu BURAK BAKIR        | Serdar GÖKTEPE             | Fuad OKAY                 | Ali Ünal ŞORMAN      | Ali Ünal ŞORMAN        |
|                          |                            |                           | Gülüm TANIRCAN       | Gülüm TANIRCAN         |
|                          |                            |                           |                      | Abdullah Can ZÜLFİKAR  |

## CONTENTS

### Foreword by the Retiring Editor

New and Promising Editor for Teknik Dergi

### Foreword

Thanks to Our Founding Editor, Milestones and Future Targets of Teknik Dergi

Critical Inclination of Failure Surface and Seismic Active Earth Thrust for a Broken Slope Backfill..... 12027

**Umit CALIK**

Investigations of Exterior Wind Flow and Aerodynamic Coefficient around Y-Plan Shape Tall Building..... 12045

**Vigneshwaran RAJENDRAN, Prabavathy SHANMUGASUNDARAM**

Entropy Based Regional Precipitation Prediction in the Case of Gediz River Basin..... 12067

**Özgür BOZOĞLU, Türkay BARAN, Filiz BARBAROS**

Rainfall Intensity-Duration-Frequency Analysis in Turkey, with the Emphasis of Eastern Black Sea Basin..... 12087

**Ömer YÜKSEK, Tuğçe ANILAN, Fatih SAKA, Emrah ÖRGÜN**

Effect of Sub-Contractor Selection on Construction Project Success in Turkey..... 12105

**Ali Erkan KARAMAN, Koray SANDAL**

Multi Agent System Based Risk Allocation Model for Public-Private-Partnership Type Projects (RAMP3)..... 12119

**Hande ALADAG, Zeynep ISIK**

The High Temperature Performance Evaluation of Polymer/Nanocomposite Modified Asphalt Cement..... 12143

**Mustafa ALAS, Ali Shaban ALBRKA ISMAEL, Hüseyin GÖKÇEKUŞ**

Experimental Study of Hydrodynamic Pressures Acting on a Submerged Gate..... 12163

**Sochheat SMOK, Mehmet Anil KIZILASLAN, Adnan Tolga KURUMUS, Ender DEMİREL**

Evaluation of Stripping Problem in Terms of Additive Types and Ratios in Asphalt Pavements..... 12183

**Celeleddin Ensar ŞENGÜL, Atakan AKSOY, Erol İSKENDER**

Influence of Gravity Framing on the Collapse Probability of Steel Buildings with Special Moment Frames..... 12203

**Adem KARASU, Cüneyt VATANSEVER**

|  |       |
|--|-------|
| Meteorological Drought Analysis for Helmand River Basin, Afghanistan.....  | 12223 |
| <b>Mohammad Musa ALAMI, Gokmen TAYFUR</b>  |       |
| The Effect of Hydrated Lime Mixing Forms and Ratios on Performance in<br>Asphalt Pavements.....                  | 12243 |
| <b>Celaleddin Ensar ŞENGÜL, Dünder AYYILDIZ, Erol İSKENDER,<br/>Atakan AKSOY</b>                                 |       |
| Fully Implicit Form of Differential Quadrature Method for Multi-Species<br>Solute Transport in Porous Media..... | 12265 |
| <b>Amin GHAREHBAGHI</b>  |       |
| An Investigation on Force Modification Factors in Cold-Formed Steel<br>Structures.....                           | 12283 |
| <b>Macit YURTSEVER, Serdar SOYÖZ</b>   |       |
| Determination of Finite Element Modelling Errors for Box Culverts Using<br>Field Load Tests.....                 | 12309 |
| <b>Tuna ULGER</b>  |       |
| <b>TECHNICAL NOTE</b>  |       |
| Sliding and Rollover on Highways - Subtleties to Note .....  | 12329 |
| <b>Banihan GÜNAY</b>   |       |
| Evaluation of Field Shear Wave Velocity in Deep Soil Mixing Based on<br>Laboratory Studies .....                 | 12335 |
| <b>Mojtaba ASLMAND, Mehmet Cemal GENES</b>   |       |

## Foreword by the Retiring Editor

# NEW AND PROMISING EDITOR FOR TEKNİK DERGİ

When I expressed my desire to give up my duty as the Editor of Teknik Dergi, I was politely invited to propose a name as my successor. Based on our twenty years of acquaintance and five years of collaboration, I considered Professor Alper İlki as the most appropriate candidate.

Before making my proposal, I asked for his consent and he kindly agreed. I am pleased to see that the Executive Board of the Chamber of Civil Engineers has approved my proposal.

\* \* \*

I started my brief talk by sharing my sentiments:

*“When a young man sought the father’s consent (in the good old days) for his beloved daughter’s hand of marriage, the father would feel the urge to make a speech of the following kind:*

*‘Look young man, she is the apple of my eye. I brought her up my heart full of love and affection. She is so tender and fragile that I demand you to promise to handle her with utmost care and attention. Otherwise...’*

Alper interrupted with a smile:

*‘I very well understand what you mean. I indeed have a daughter approaching that age. I promise to treat your beloved journal with utmost care and attention.’*

I am fully contented. I know without a doubt that Professor İlki will perform the duty better than I did, vis-à-vis the changing principles of international journal publication and the developing procedures and technologies. I wholeheartedly wish him good luck.

\* \* \*

I would like to take this opportunity to express my gratitude to the present and past members of the Editorial Board for their valuable efforts to sustain and improve Teknik Dergi.

I am also grateful to the present and past Executive Boards of the Chamber of Civil Engineers for their continuous support during our long-lasting collaboration.

Last but certainly not least, I would like to mention my dear old friends Professor Metin Ger and the late Mr. Ender Arkun who have been my most dependable consultants from the very beginning, from the brain storming meetings in 1989 to the present. Professor Ger agreed to stay on the Editorial Board despite his strong desire to retire. Thank you Metin, for all your support and advice and for staying on with me.

My best wishes.

Professor Tuğrul Tankut



## Foreword

# THANKS TO OUR FOUNDING EDITOR MILESTONES AND FUTURE TARGETS OF TEKNIK DERGI

Dear Readers and Authors,

Since its establishment in 1990, Teknik Dergi has become an increasingly recognized and prestigious journal due to dedicated efforts of a number of individuals, such as members of the current and previous editorial boards, reviewers, advisory board members, contributing authors, and the continuous strong support of the executive board of Turkish Chamber of Civil Engineers. Among all these respected contributors, one name requires a special mention; Professor Tuğrul Tankut of Middle East Technical University, who has been serving for the establishment and development of Teknik Dergi since 1989. Over the course of 34 years; his leadership, wisdom, enthusiasm, discipline and diligence have been the major constituents of the success of Teknik Dergi.

This issue of Teknik Dergi, in its 33rd year, marks a smooth change in the editorship of Teknik Dergi, from the first generation to the next generation. It is a great honor and a huge responsibility to be the successor of our founding editor Professor Tuğrul Tankut. While the name of the editor will be changed from this issue on, the previous editorial board will continue to work following the strong and well-established principles of Teknik Dergi without sacrificing from its high-quality standards. It is also an honor for us that we will still have Professor Tankut in the board to support and guide us now and in future. In addition to him, Professor Metin Ger, who has also been contributing to Teknik Dergi since its establishment will continue his service in the editorial board.

On this occasion, a summary of the milestones for Teknik Dergi is summarized below:

*1990 January; publication of the first issue of Teknik Dergi*

*2004 January; free online access to all issues of Teknik Dergi*

*2008 July; inclusion in Web of Science Core Collection-Science Citation Index Expanded (SCIE)*

*2017 January; online submission, communication, review and decision procedure adapted*

*2017 January; online publication and DOI assignment upon acceptance*

*2018 January; bilingual Teknik Dergi with 3 issues in Turkish and 3 issues in English per year*

*2019 January; towards sustainability targets; online publication and distribution (with limited printed volumes)*

*2021 February; establishment of advisory board composed of eminent individuals from all over the world*

*2022 January; two issues in Turkish and four issues in English per year*

*2023 January; change of journal title to “Turkish Journal of Civil Engineering”*

*2023 January; all issues in English (with few papers in Turkish)*

The targets we set in 2023 for Teknik Dergi, the first and unique journal in Turkey in the field of civil engineering, indexed by Web of Science Core Collection and Scopus; are faster evaluation of the submitted manuscripts, further internationalization, wider recognition and further improvement in terms of journal rankings. It should also be mentioned here that open access nature of the journal with no cost to the authors will continue as was the case since 1990. We are also proud about this unique feature of Teknik Dergi. We are eagerly looking forward to receive high quality contributions from all around the world to this unique and advancing journal, which consistently follows its ethical and well-established principles by adapting itself to the developing technology and recent advances.

Alper İlki

On behalf of the Editorial Board

# **Critical Inclination of Failure Surface and Seismic Active Earth Thrust for a Broken Slope Backfill**

Umit CALIK<sup>1</sup>

## **ABSTRACT**

This paper presents an analytical approach, based on the limit-equilibrium state, to determine the critical inclination of failure surface and active earth thrust for a cohesive-frictional backfill with a broken slope and a surcharge load at a constant distance from a retaining wall under the seismic condition. A combined analysis using Mononobe-Okabe's and Culmann's methods within a trial and error procedure is performed in this study. The influences of several parameters such as wall height, surcharge magnitude, cohesion, and internal friction angle of the backfill, adhesion between the wall-backfill interface, tension cracks, horizontal and vertical seismic acceleration coefficients have been investigated on the critical inclination of failure surface and the active earth thrust. Additionally, the performance of the proposed approach is explored by geotechnical software (Geo5) and two available methods in the literature. All of the results and the detailed comparisons are given in tabular and graphical forms.

**Keywords:** Critical inclination of failure surface, Seismic active earth thrust, Cohesive-frictional broken backfill, Adhesion, Tension cracks, Trial and error procedure.

## **1. INTRODUCTION**

In seismic regions, the static and seismic forces act on retaining walls and simultaneously lead to failure. So, they should be taken into account together during the design of retaining structures. Okabe [1] and Mononobe and Matsuo [2] developed a method, the so-called Mononobe-Okabe method, to evaluate lateral earth pressure for cohesionless soils under dynamic conditions. This method was a seismic version of Coulomb's static earth pressure analysis. The earthquake-induced forces on the failure mass are applied by the pseudo-static method using seismic acceleration coefficients in the Mononobe-Okabe method.

The researchers have presented several solutions using the Mononobe-Okabe method, based on the limit-equilibrium of the different failure planes. Düzgün and Bozdağ [3], Ghosh and Sharma [4], and Shao-jun et al. [5] extended the Mononobe-Okabe method to consider the effect of the dynamic behavior of earthquakes with a single critical soil wedge and a planar

---

Note:

- This paper has been received on February 5, 2020 and accepted for publication by the Editorial Board on January 18, 2021.
- Discussions on this paper will be accepted by September 30, 2022.

• <https://doi.org/10.18400/tekderg.684834>

1 Dept. of Civil Engineering, Faculty of Technology, Karadeniz Technical University, Trabzon, Turkey - [calik@ktu.edu.tr](mailto:calik@ktu.edu.tr) - <https://orcid.org/0000-0002-7321-1998>

failure surface. In the recent past, the analytical formulations were given in explicit forms to calculate the seismic active earth pressure and the critical angle of the critical failure surface behind retaining walls. Das and Puri [6], Saran and Gupta [7] and Ghosh et al. [8] developed the expressions to cohesive-frictional ( $c, \phi$ ) backfills to calculate the static or dynamic active earth pressure. Shukla [9] and Shukla and Bathurst [10] presented the analytical formulations to estimate the dynamic active force and the critical inclination of the failure plane considering the effects of tension cracks, adhesion, and surcharge load. Ghosh and Sengupta [11], Iskander et al. [12], Shukla [13], Lin et al. [14], Zhou et al. [15], Tang and Chen [16], Gupta and Sawant [17], Gupta et al. [18] and Peng and Zhu [19] developed the mathematical expressions taking into account wall height, inclination of the back face of the wall, tension cracks, adhesion, cohesion, internal friction angle of the backfill and surcharge with an infinite sloping surface.

Caltabiano et al. ([20], [21], and [22]) studied the critical angle of failure surface considering the presence of a uniform surcharge at different distances from the retaining wall. Aminpour et al. [23] investigated the effects of intensity, width, height, and location of surcharge related to the edge of the slope as well as the soil properties. Hou and Shu [24] improved the existing trial wedge method to calculate the earth pressure regardless of the irregularity of surcharges at a constant distance from the wall. Arda and Çinicioğlu [25] studied the influences of mean grain size, particle shape, and surcharge on the geometry of the active failure surface.

There is a limited number of studies in the literature regarding the irregular shape of the backfill surface. Yazdani et al. [26] formulated their solution to estimate the seismic active earth pressure for the noncontinuous backfill geometries. Greco [27] derived a formula for the general backfill profile subjected to line and strip surcharges considering soil friction angle, soil unit weight, and friction angle between soil and wall. Afterward, Greco [28] extended his solution to take account of seismic forces using the Mononobe-Okabe method.

Kim et al. [29] solved the problem of determining the critical inclination of the failure plane by considering a trial and error method. However, Greco [30] criticized Kim et al. [29]'s solution for the limitation of the trial and error method. Lu and Yuan [31] constructed a new method using the trial and error method and Culmann's [32] graphical solution with consideration of the inclination of the back face of the wall, the cohesive and adhesive forces in the problem under the static condition.

In the published literature, the common concept for determining critical failure surface and seismic active earth pressure is to accept the soil backfill surface as horizontal or continuously sloping at an angle with the horizontal plane. However, in-situ conditions may generally prevent the construction of backfill like this form. That's why an attempt is made to solve the problem for a retaining wall supporting a broken backfill (in the case of broken terrain). Besides, the chosen specific geometry and the input parameters of the problem in this paper are more realistic and practical to use in the geotechnical analysis of retaining structures. Here, a combined framework which has consisted of Culmann [32]'s graphical solution and Mononobe-Okabe's method is also designed to estimate the critical inclination of failure surface and the active earth thrust by resorting to a trial and error procedure. A script with MATLAB programming language is written to overcome the complex and time-consuming repetitive steps in the calculations. The algorithm of the script is constructed to include all effects of wall height, surcharge magnitude and location, cohesion and internal friction angle of the backfill, horizontal and vertical seismic acceleration coefficients, adhesion between

the wall-soil interface, and tension cracks for a cohesive-frictional backfill with the irregular surface profile. Briefly, this study strives to develop an analytical approach, to derive mathematical formulations, and to write its MATLAB code considering all of the mentioned geotechnical methods within the influences of soil, loads, and the surface geometry for the determination of the critical inclination of failure surface and the active earth thrust. Moreover, the proposed approach herein is verified by powerful geotechnical software (Geo5) and two available methods by Shukla [13] and Motta [33]. All of the results and the comparisons are presented in tabular and graphical forms.

## 2. METHOD OF ANALYSIS

In the development of the analytical approach, the following assumptions have been made:

- (a) The backfill is homogeneous, dry, frictional, and cohesive. As known, there is always no access to a cohesionless backfill due to economic aspects. The cohesive-frictional backfills are commonly encountered in the real field applications. The deriving expressions for such a backfill are usable and practicable to estimate the critical inclination of failure surface and the active earth thrust.
- (b) The failure surface in the backfill is assumed to be planar to simplify the calculations. The failure surface that develops in the backfill is a plane if  $\delta=0$ . But the failure surface is curved for a rough wall ( $\delta \neq 0$ ). However, the planar failure surface is still used in the practice of Coulomb's theory. It is known to provide acceptable results in the active state (Paik and Salgado [34]).
- (c) The retaining wall yields away from the backfill. The displacement of the wall is sufficient enough to cause an active earth pressure condition.
- (d) The uniform surcharge load that acts on the backfill at a distance from the wall is long enough to intersect the failure plane.

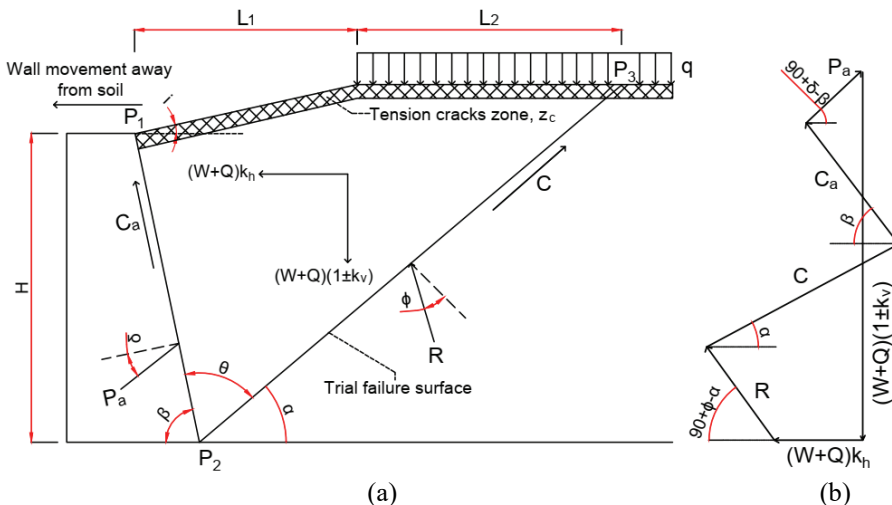


Figure 1 – Geometry of the trial failure wedge and its force polygon

Figure 1(a) shows a general schematic diagram of the cross-section geometry and the forces acting on a trial failure wedge behind the retaining wall for the cohesive-frictional backfill with the broken slope and the uniformly distributed surcharge load at the constant distance in the active state. Also, the force polygon of this trial failure wedge can be seen in Figure 1(b).

Shukla et al. [35] reported that the active earth pressure with tension cracks in the cohesive backfill could increase up to 20%-40% over the case without cracks. Therefore, the effect of tension cracks is taken into consideration. Nian and Han [36] calculated the depth ( $z_c$ ) of tension cracks zone in seismic condition by using Equation (1). This equation takes the seismic inertial forces and the inclination of backfill into consideration while calculating  $z_c$ . Besides, it is assumed that the (unit) cohesion and the (unit) adhesion decrease linearly from their initial values to zero at the surface of the backfill in the tension cracks zone.

$$z_c = \frac{2H\left(\frac{c}{\gamma H}\right)}{\left[(1+\tan \psi \tan i)^2 + \frac{4\tan^2 \psi}{\cos^2 \varphi}\right](1 \mp k_v) \cos \varphi} \left[ \sin \varphi (1 + \tan \psi \tan i) + \sqrt{(1 + \tan \psi \tan i)^2 + 4 \tan^2 \psi} \right] \quad (1)$$

All of the calculated forces on the trial failure wedge in Figure 1(a) are  $R$ ,  $C$ ,  $C_a$ ,  $W$  and  $Q$ . Equations (1) and (2) can be written considering the equilibrium of these forces in Figure 1(b) which is drawn in the horizontal [ $\rightarrow +$  and  $\leftarrow -$ ] and the vertical [ $\uparrow +$  and  $\downarrow -$ ] directions of the force polygon, respectively:

$$P_a \cos(90-\beta+\delta) - C_a \cos \beta + C \cos \alpha - R \cos(90+\phi-\alpha) - (W+Q)k_h = 0 \quad (2)$$

$$P_a \sin(90-\beta+\delta) + C_a \sin \beta + C \sin \alpha + R \sin(90+\phi-\alpha) - (W+Q)(1 \pm k_v) = 0 \quad (3)$$

From Equation (2),  $R$  is obtained as,

$$R = \frac{P_a \cos(90-\beta+\delta) - C_a \cos \beta + C \cos \alpha - (W+Q)k_h}{\cos(90+\phi-\alpha)} \quad (4)$$

Substituting the  $R$  from Equation (4) into Equation (3), the following equation can be derived for the active earth thrust ( $P_a$ ):

$$P_a = \frac{(W+Q)(1 \mp k_v + mk_h) + C_a(m \cos \beta - \sin \beta) - C(m \cos \alpha + \sin \alpha)}{m \cos(90-\beta+\delta) + \sin(90-\beta+\delta)} \quad (5)$$

$$\text{where } m = \tan(90+\phi-\alpha). \quad (6)$$

The trial failure wedge is taken as an example in Figure 1(a). It is assumed that a downward failure movement of this trial wedge in the backfill occurs along a surface  $P_2P_3$ . The failure surface passes through the heel of the wall. It is inclined at an angle ( $\theta$ ) to the back face of the retaining wall.

The magnitude of  $P_a$  is calculated from Equations (5) and (6) for the trial wedge. The calculation is repeated many times for the other potential failure surfaces to obtain the maximum magnitude of  $P_a$  with resorting to a trial and error procedure. The failure surface that gives the maximum value of  $P_a$  is the critical failure plane; the corresponding  $P_a$  and  $\theta$

are the active earth thrust and the critical inclination of the failure surface ( $\theta_{cr}$ ) of the problem. An algorithm in MATLAB programming language is built and a script is coded to estimate  $P_a$  and  $\theta_{cr}$  because of the several input parameters in the problem, the complex and repetitive steps in the calculations. The flowchart of the algorithm in the script is given in Figure 2.

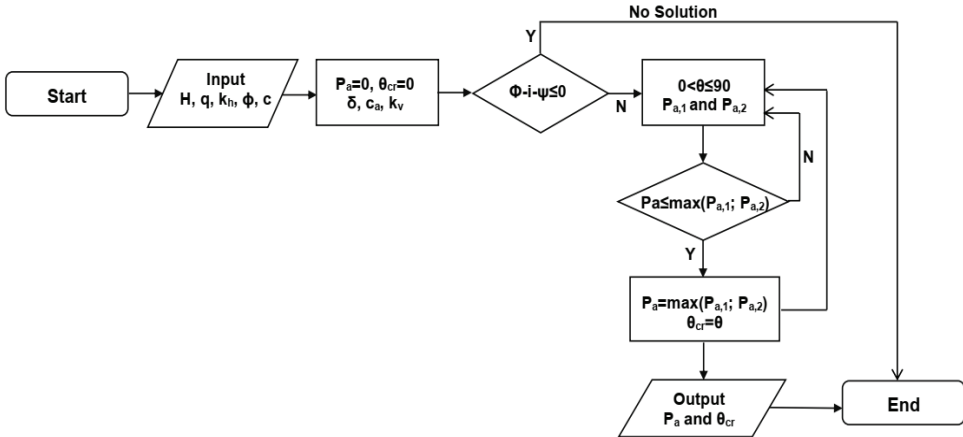


Figure 2 - Flowchart of the algorithm in the script

### 3. PARAMETRIC STUDY

The parametric study aims to explore the effects of the input parameters on the critical inclination of failure surface with the vertical plane and the active earth thrust in the static and seismic conditions. The details of the input parameters are shown in Table 1.

Table 1 - Details of the input parameters

| Input parameter        | Values         |
|------------------------|----------------|
| H (m)                  | 6, 8 and 10    |
| q (kN/m <sup>2</sup> ) | 15, 30 and 45  |
| c (kN/m <sup>2</sup> ) | 0, 10 and 20   |
| φ (°)                  | 25, 30 and 35  |
| k <sub>h</sub>         | 0, 0.1 and 0.2 |

The three parameters in the study are correlated with the parameters in Table 1 (e.g.,  $\delta = (2/3)\phi$ ,  $c_a = (2/3)c$  and  $k_v = (2/3)k_h$ ). The four parameters are kept constant (e.g.,  $\gamma = 18 \text{ kN/m}^3$ ,  $i = 15^\circ$ ,  $\beta = 90^\circ$  and  $L_1 = 5 \text{ m}$ ) during the problem-solving process for simplicity.

### 3.1. Effects of the Parameters on the Critical Inclination of Failure Surface

The first step of the parametric study is to determine the critical inclinations of the failure surface with the vertical plane. The coded MATLAB script is run through all of the analyses for  $\theta_{cr}$ . The calculated values of  $\theta_{cr}$  are shown in Figures 3, 4, and 5. Mononobe-Okabe's method has no result when  $\phi - i - \psi \leq 0$ . Therefore, the approach in this study does not apply to the problem at  $\phi = 25^\circ$  and  $k_h = 0.2$  in Figure 5.

In the static condition, the critical inclination decreases with the increase in the values of wall height, cohesion, and internal friction angle. On the other hand, the surcharge load increases the critical inclination. In the seismic condition, the critical inclination has a decreasing tendency with increasing the wall height, the cohesion, and the internal friction angle. The critical inclination shows an increment due to the horizontal seismic acceleration coefficient and the surcharge load. There are the same trends with the parameters, such as the internal friction angle and the seismic acceleration coefficient, in the papers which are studied by Shukla et al. [35], Ghosh and Sengupta [11], and Ghosh and Sharma [37].

The shear strength parameters ( $c$  and  $\phi$ ) of the backfill soil lead to an increase in the resisting forces along the potential failure surface. Also, increasing the height of the wall geometrically occurs the longer surface  $P_2P_3$  in Figure 1(a) where  $c$  and  $\phi$  make the soil-wall system safer against the shear failure. As a result of this, the lower inclinations of failure surface with the vertical plane are more critical. In other words, the wall-soil system is vulnerable to failure at the smaller  $\theta$  under both static and seismic loads.

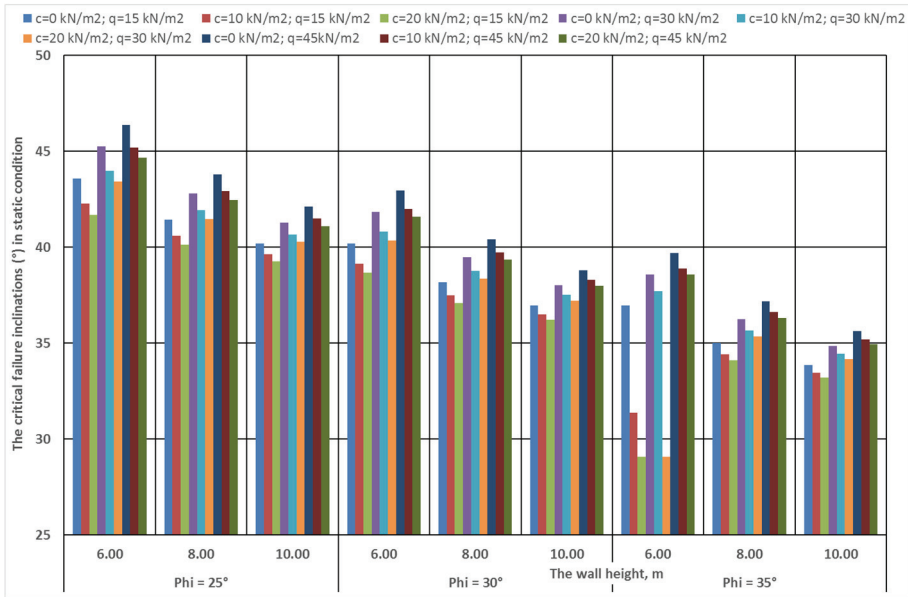


Figure 3 - The critical inclinations in the static condition

The parameters  $q$  and  $k_h$  contribute  $P_a$  to exceed the shear strength of the backfill soil after a certain cross-sectional area of the trial failure wedge. Thus, increasing the critical inclination

provides a large enough area to increase the effects of  $q$  and  $k_h$  on the soil-wall system. As expected, the critical inclinations under the earthquake-induced loads are higher than those under the static loads. According to Figures 3, 4, and 5, the seismic loads increase the critical inclination up to 4-5 degrees each 0.1g increment of  $k_h$ .

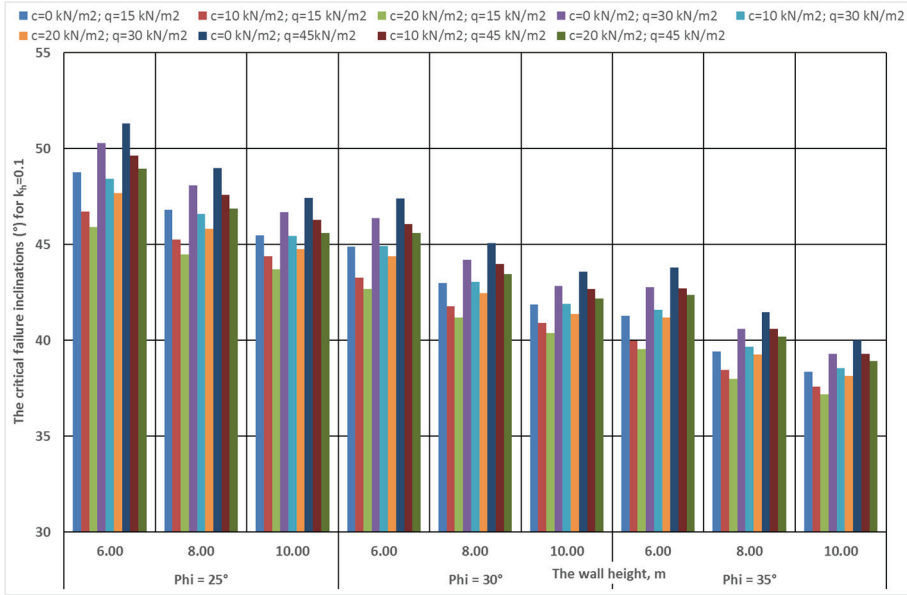


Figure 4 - The critical inclinations in the seismic condition, for  $k_h = 0.1$

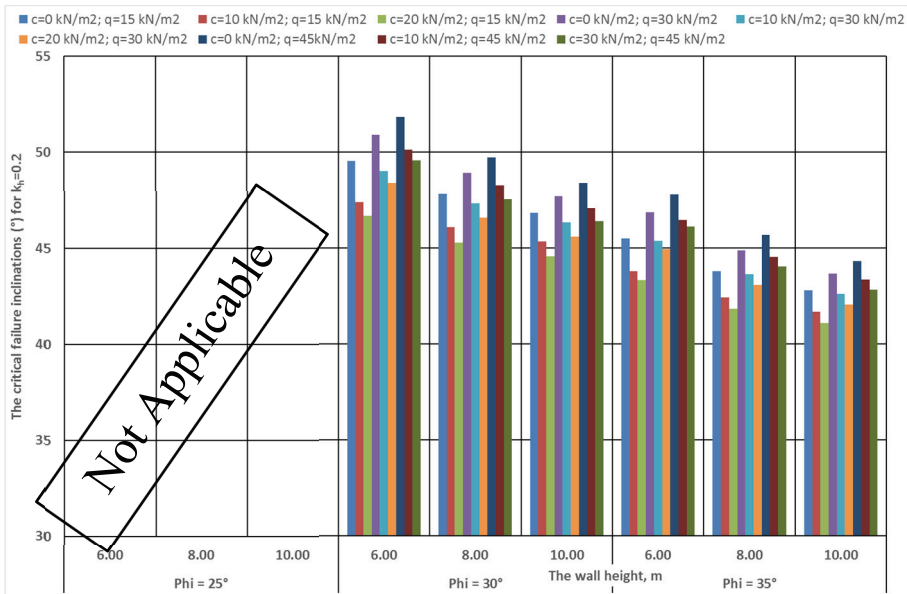


Figure 5 - The critical inclinations in the seismic condition, for  $k_h = 0.2$

### 3.2. Effects of the Parameters on the Active Earth Thrusts

The second step of the parametric study is to estimate the active earth thrusts obtained from Equations (5) and (6) in the state of failure. The computed results of active earth thrust are listed in Figures 6, 7, and 8. At  $\phi = 25^\circ$  and  $k_h = 0.2$ , the proposed approach has still no solution in Figure 8 since  $\phi - i - \psi \leq 0$ .

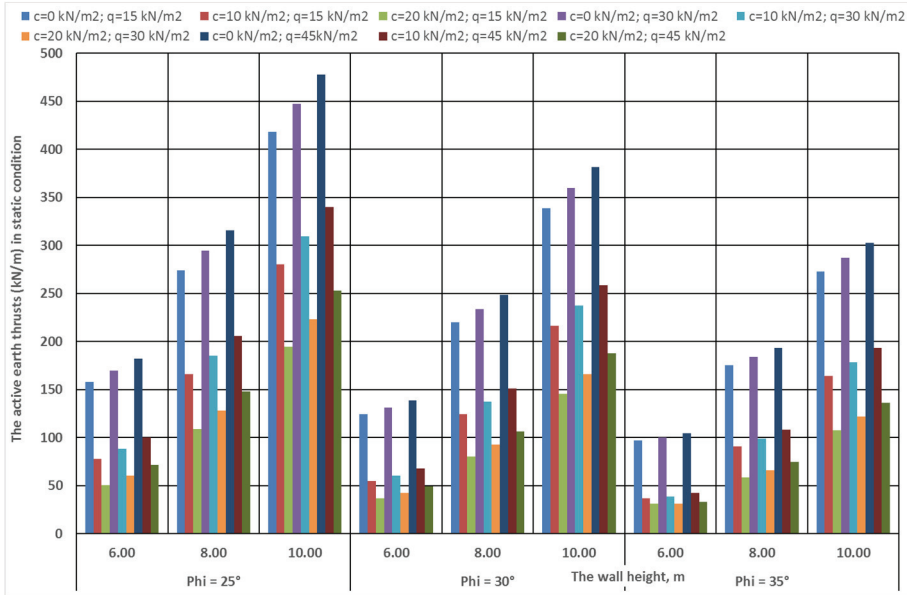


Figure 6 - The active earth thrusts in the static condition

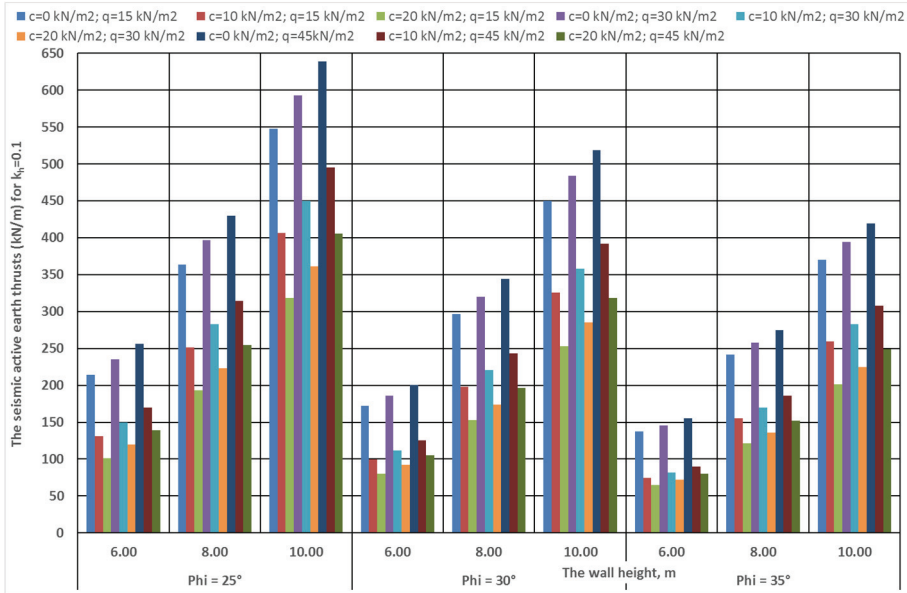


Figure 7 - The active earth thrusts in the seismic condition, for  $k_h = 0.1$

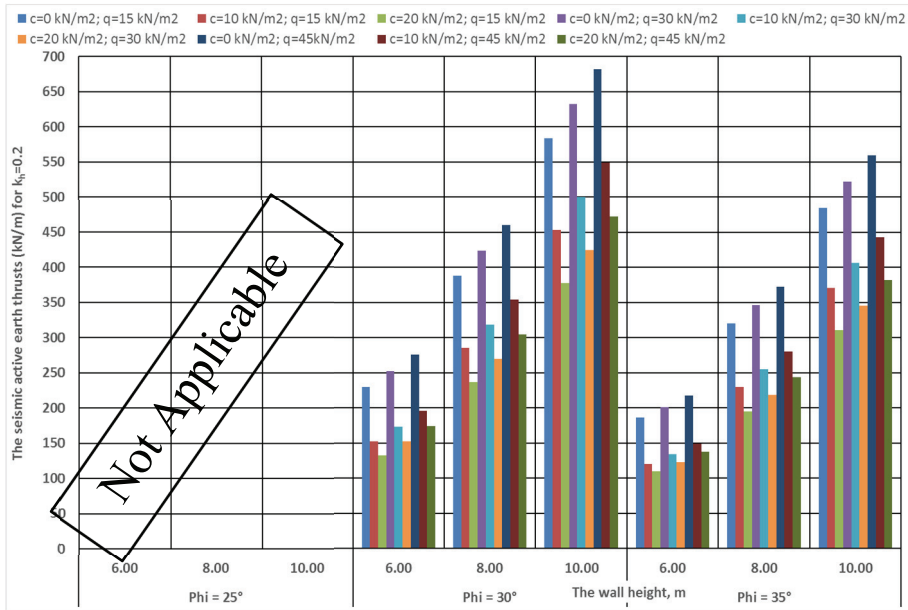


Figure 8 - The seismic active earth thrusts in the seismic condition, for  $k_h = 0.2$

In the static condition, the active earth thrust shows a notable decreasing behavior when the cohesion and the internal friction angle of the backfill increase. On the contrary, the wall height and the surcharge load increase the active earth thrust. Herein, the wall height is more dominant to get a higher active earth thrust. In the seismic condition, the active earth thrust indicates a decreasing trend with the cohesion and the internal friction angle of the backfill, and an increasing trend with the height of the wall, the horizontal seismic acceleration coefficient, and the surcharge load. The similar tendency of the seismic active earth thrusts is reported by Shukla et al. [35], Ghosh and Sengupta [11], and Ghosh and Sharma [37].

As shear strength parameters ( $c$  and  $\phi$ ) increase (i.e. the backfill soil becomes stronger), Coulomb’s active pressure coefficient decreases. Therefore, these two parameters reduce the magnitude of the active earth thrust.

An increase in the height of the wall geometrically induces the higher values of the horizontal surcharge load distance ( $L_2$ ) and the weight of the failure wedge ( $W$ ). These new geometrical cases maximize the influences of static and seismic loads (via  $q$  and  $k_h$ ) on the soil-wall system. Hence, the higher loads apply the additional lateral forces along the back of the retaining wall. In other words, the retaining wall is subjected to higher values of the active earth thrust. As seen in Figures 6, 7, and 8, the seismic forces considerably increase  $P_a$  up to 300% according to the values under the static condition. It is worthy to note here that  $H$  shows a more significant effect on  $P_a$  in comparison to the effects of  $q$  and  $k_h$ .

### 3.3. Comparison of the Results of Active Earth Thrusts

The performance of the proposed approach is deeply investigated by using geotechnical software (Geo5) and the two previously published studies for the cohesive-frictional backfills.

Firstly, the analysis in this study is verified by the geotechnical software Geo5. Geo5 does not explicitly indicate the critical inclination of the failure surface. That's why the study only compares its computed values of  $P_a$  to the results of Geo5. Figure 9 shows this comparison attempt for the case  $k_h = 0.2$ ,  $k_v = (2/3)k_h$ ,  $\delta = (2/3)\phi$ ,  $c_a = (2/3)c$ ,  $\gamma = 18 \text{ kN/m}^3$ ,  $i = 15^\circ$ ,  $\beta = 90^\circ$  and  $L_1 = 5 \text{ m}$ .

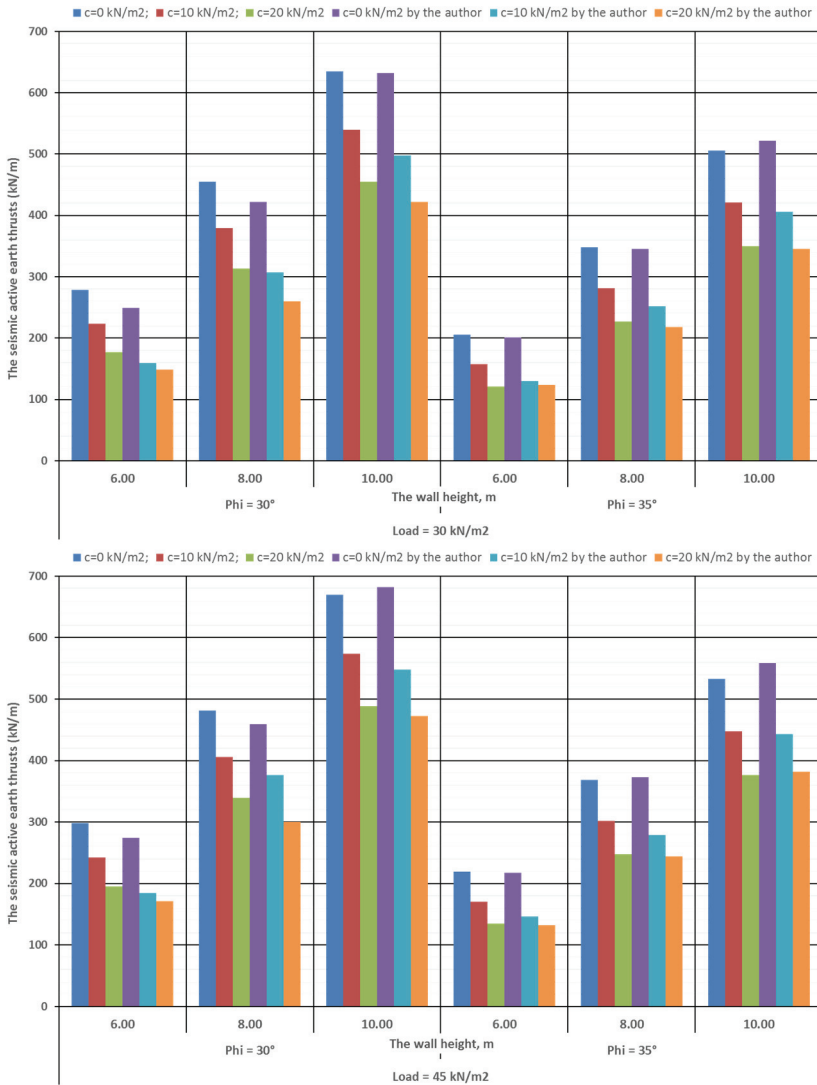


Figure 9 - The seismic active earth thrusts calculated by Geo5 and the study

As seen in Figure 9, the differences in  $P_a$  range from 1.1% to 28.6%. The results of the study mostly diverge from the values given by Geo5 at  $H = 6$  m and  $c = 10$  kN/m<sup>2</sup> for  $q = 30$  kN/m<sup>2</sup> and 45 kN/m<sup>2</sup>. Furthermore, the comparison of the values of  $P_a$  with Geo5 reveals that this study underestimates  $P_a$ . At this point, it can be stated the most important reason for the discrepancy in the values that the different computation approaches and equations are used by the study and Geo5 to consider the effects of the soil mass, tension cracks zone, and (static and seismic) loads. On the other hand, the results in Figure 9 depict a convergence with the increase in the values of input parameters.

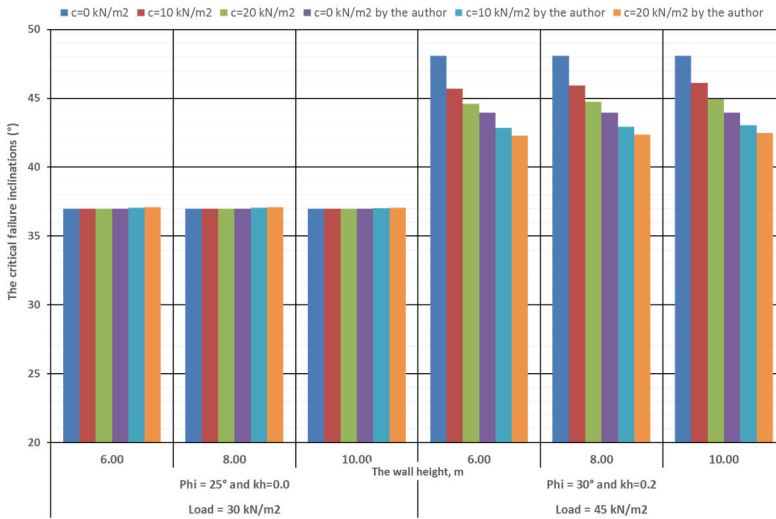


Figure 10 - The critical failure inclinations calculated by Shukla [13] and the study

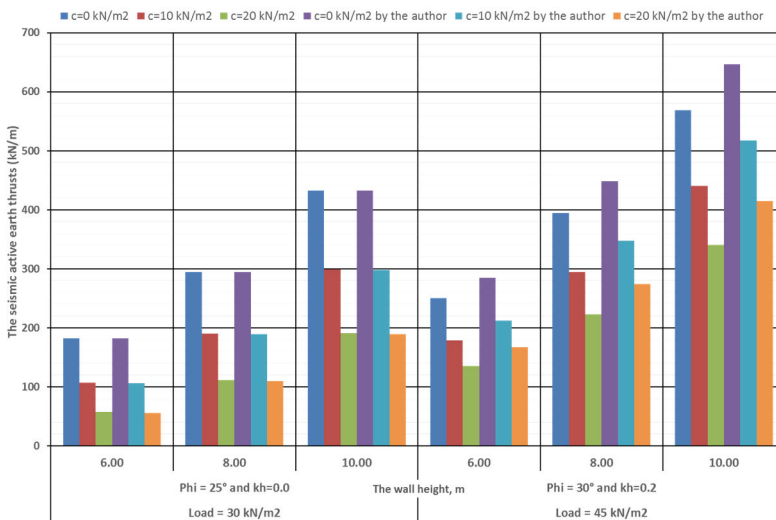


Figure 11 - The seismic active earth thrusts calculated by Shukla [13] and the study

Secondly, the study also performs another comparison of the seismic active earth thrusts and the critical failure inclinations with the results calculated by Shukla [13] for the case  $k_v = (2/3)k_h$ ,  $\delta = (2/3)\phi$ ,  $c_a = (2/3)c$ ,  $\gamma = 18 \text{ kN/m}^3$ ,  $\beta = 90^\circ$ .  $L_1$  and  $i$  are equal to 0 to ignore the geometry differences between the two studies. The bar graphs of  $\theta_{cr}$  and  $P_a$  are shown in Figures 10 and 11, respectively.

The two studies approximately give the same results of  $\theta_{cr}$  and  $P_a$  for cohesionless and cohesive backfill soils in the static condition. The established minor difference between the values of  $\theta_{cr}$  and  $P_a$  barely increases up to 1.8% with increasing cohesion. Hence, it could be concluded that  $\theta_{cr}$  and  $P_a$  are calculated in quite a proximity in these two studies.

The differences in  $\theta_{cr}$  and  $P_a$  given by these two studies are noticed in all cases of the soil-wall system subjected to the earthquake loads in addition to the static surcharge load. Under the seismic condition, the proposed approach in this study slightly underestimates the angles of  $\theta_{cr}$  and significantly overestimates the values of  $P_a$  in comparison to Shukla [13].

The computed values of  $\theta_{cr}$  by the two studies just show a few degrees of variation (max 4 degrees) in the case of cohesionless soils. However, the increasing cohesion decreases the difference in the values of  $\theta_{cr}$  to 1 degree. Therefore, Shukla [13]’s study confirms the present  $\theta_{cr}$  findings of this study.

A similar convergence does not exist when the values of  $P_a$ , calculated by this study, are compared with the results given by Shukla [13]. The proposed approach estimates higher values of  $P_a$  (from 13.7% to 23.7%) with increasing cohesion. Herein, the problem is solved by Geo5 once again to investigate the accuracy of the two studies at  $k_h = 0.2$ ,  $q = 45 \text{ kN/m}^2$ ,  $\phi = 30^\circ$ , and  $c = 20 \text{ kN/m}^2$  for  $H = 6 \text{ m}$ ,  $8 \text{ m}$ , and  $10 \text{ m}$ . The results of  $P_a$  calculated by Geo5, this study, and Shukla [13] are summarized in Table 2.

Table 2 -  $P_a$  (kN/m) calculated by Geo5, this study, and Shukla [13]

|                                | The software Geo5 | This study  | Shukla [13] |
|--------------------------------|-------------------|-------------|-------------|
| H = 6 m                        | 195.732           | 177.407     | 135.410     |
| Normalized $P_a$ by this study | <b>1.10</b>       | <b>1.00</b> | <b>0.76</b> |
| H = 8 m                        | 319.483           | 289.085     | 223.000     |
| Normalized $P_a$ by this study | <b>1.11</b>       | <b>1.00</b> | <b>0.77</b> |
| H = 10 m                       | 488.218           | 435.871     | 340.755     |
| Normalized $P_a$ by this study | <b>1.12</b>       | <b>1.00</b> | <b>0.78</b> |

In light of the results of  $P_a$  in Table 2, this study gives 23% more values than Shukla [13]’s results but 11% fewer values than the results of Geo5. The proposed approach in this study shows a better convergence to the values of the substantial commercial software Geo5 which is currently available to use for geotechnical engineers. It can be said from this viewpoint that this study is appropriate to estimate the values of  $P_a$  in geotechnics.

The two approaches, presented by this paper and Shukla [13], have not considered the total adhesive force between the wall and the backfill, the total cohesive force along the failure

plane, the depth of tension crack zone, and the loads (especially seismic forces) in a similar way throughout the process of developing their expressions and the calculations. Moreover, Shukla [13] presented his generalized expression in terms of dynamic active earth pressure coefficients without a trial and error procedure. Therefore, more or less variation exists between the given values by the two studies.

Thirdly, the examples, presented by Motta [33] to determine the values of  $\theta_{cr}$  and  $P_a$ , are calculated again for a cohesionless backfill with a uniform surcharge load at a constant distance from the wall under the static and seismic conditions. The results are shown in Table 3 for  $H = 4$  m,  $\gamma = 20$  kN/m<sup>3</sup>,  $c = 0$  kN/m<sup>2</sup> and  $\beta = 90^\circ$ .

Table 3 -  $P_a$  and  $\theta_{cr}$  calculated by Motta [32] and this study, respectively

| q                         | 40 kN/m <sup>2</sup>                          | 20 kN/m <sup>2</sup>                            |
|---------------------------|---|---|
| $\phi$                    | 30°   | 35°   |
| $\delta$                  | 0°  | 17.5°   |
| i                         | 0°  | 15°   |
| $L_1$                     | 1 m   | 2 m   |
|                           | $P_a$ (kN/m) for $k_h = 0$ and $k_v = 0$      | $P_a$ (kN/m) for $k_h = 0.1$ and $k_v = 0$      |
| $c = 0$ kN/m <sup>2</sup> | 85.83 and 85.83                               | 79.36 and 70.46                                 |
| $\Delta$ , %              | <b>0.0</b>                                    | <b>-12.6</b>                                    |
|                           | $\theta_{cr}$ (°) for $k_h = 0$ and $k_v = 0$ | $\theta_{cr}$ (°) for $k_h = 0.1$ and $k_v = 0$ |
| $c = 0$ kN/m <sup>2</sup> | 34.85 and 34.85                               | 43.31 and 39.69                                 |
| $\Delta$ , %              | <b>0.0</b>                                    | <b>-9.1</b>                                     |

The values of  $\theta_{cr}$  and  $P_a$  computed by Motta [33] and this study are the same in the first example for the case of static analysis. About 10% variation is observed in the second example for the case of dynamic analysis. Motta [33] considered that the backfill was continuously sloping at an angle (i) with the horizontal plane. However, this study solves the second example for the case of the broken slope of the backfill. The difference between the slope geometries in the studies causes the different results of  $P_a$  and  $\theta_{cr}$ .

#### 4. CONCLUSIONS

This paper firstly presents an analytical approach, based on Culmann's and Mononobe-Okabe's methods within a trial and error procedure, to calculate the critical inclination of failure surface and the active earth thrust for a cohesive-frictional backfill with a broken slope and a surcharge load at a constant distance under seismic conditions. Then, a parametric attempt, using its derived equations and coded MATLAB script, is made to explore the effects of the major field parameters in the design of a retaining structure, such as wall height, surcharge magnitude, cohesion, and internal friction angle of the backfill, horizontal and vertical seismic acceleration coefficients, adhesion between wall-soil interface and tension

cracks. Finally, the results of the proposed approach are verified by the comparison with Geo5 and previously published two studies.

By the parametric attempt in this study, it is found that the critical inclination of the failure surface increases with an increase in the surcharge load and the horizontal seismic acceleration coefficient, while it decreases with the wall height, the cohesion, and the internal friction angle. The critical inclination of the failure surface is highly sensitive to the horizontal seismic acceleration coefficient according to the effects of the other parameters.

The present work shows that the active earth thrust increases with increasing the wall height, the surcharge magnitude, and the horizontal seismic acceleration coefficient. Herein, it is worth noting that wall height has a greater influence on the active earth thrust. The cohesion and the internal friction angle of the backfill soil decrease the values of active earth thrust.

Under the static condition, the results of the critical inclination and the active earth thrust given by this work are the same for the cohesionless backfill when compared to the values of Shukla [13]'s and Motta [32]'s studies. However, the study shows significant differences in the results of the active earth thrust with increasing the cohesion and the horizontal seismic acceleration coefficient. It overestimates the seismic active earth thrust compared to Shukla [13]'s study but underestimates compared to Motta [32]'s study and Geo5. Besides, the study still results in fairly close to the critical inclinations of the failure surface estimated by Shukla [13] and Motta [32] under the seismic condition.

The approach presented by this paper about deriving the equations and the algorithm of the coded MATLAB script herein can be employed by engineers in any geotechnical problems associated with a critical inclination of failure surface and an active earth thrust for a cohesive-frictional backfill with a broken slope and a surcharge load at a constant distance under seismic conditions.

## **Symbols**

- $c$  : the (unit) cohesion of the backfill
- $c_a$  : the (unit) adhesion between the retaining wall and the backfill
- $C$  : the total cohesion along the failure plane
- $C_a$  : the total adhesion along the back face of the wall
- $H$  : the height of the retaining wall
- $i$  : the inclination of the backfill surface
- $k_h$  : the horizontal seismic acceleration coefficient
- $k_v$  : the vertical seismic acceleration coefficient
- $m$  : a dimensionless factor in Equation (5)
- $L_1$  : the horizontal distance from the wall to the surcharge load
- $L_2$  : the horizontal surcharge load distance on the failure wedge
- $P_a$  : the active earth thrust

- $P_{a,1}$  : the calculated active earth thrusts from Equation (5) considering positive (downward) vertical seismic acceleration coefficient
- $P_{a,2}$  : the calculated active earth thrusts from Equation (6), considering negative (upward) vertical seismic acceleration coefficient
- $q$  : the magnitude of the surcharge load
- $Q$  : the resultant force of the surcharge load on the trial failure wedge ( $= qL_2$ )
- $R$  : the soil reaction on the failure plane
- $W$  : the weight of the trial failure wedge ( $= \gamma \text{Area}_{\text{wedge}}$ )
- $z_c$  : the depth of tension cracks zone
- $\beta$  : the obliquity of the back face of the retaining wall
- $\theta$  : the angle between the back face of the retaining wall and the failure surface
- $\theta_{cr}$  : the critical inclination of failure surface
- $\Delta$  :  $(P_{a, \text{by the study}} - P_{a, \text{by Motta}}) / P_{a, \text{by the study}}$  ;  $(\theta_{cr, \text{by the study}} - \theta_{cr, \text{by Motta}}) / \theta_{cr, \text{by the study}}$
- $\alpha$  : the inclination of the failure plane with the horizontal
- $\delta$  : the friction angle between the retaining wall and the backfill
- $\gamma$  : the unit weight of the backfill
- $\phi$  : the internal friction angle of the backfill
- $\psi$  : the seismic inertia angle which is defined as  $\arctan(k_h/(1 \pm k_v))$

### References

- [1] Okabe, S., General theory of earth pressure and laboratory testings on seismic stability of retaining walls. Journal of the Japanese Society of Civil Engineers, 12, 1, 123-134, 1926.
- [2] Mononobe, N., Matsuo, H., On the determination of earth pressure during earthquakes. Proceedings of the World Engineering Congress Vol 9, Tokyo-Japan, 177-185, 1929.
- [3] Düzgün, M., Bozdağ, Ö., İstinat duvarlarına etkiyen sismik zemin basıncının dağılımı için geliştirilen yeni bir yöntem. Teknik Dergi, 14, 66, 2819-2834, 2003.
- [4] Ghosh, S., Sharma, R.P., Pseudo-dynamic response of non-vertical retaining wall supporting  $c-\phi$  soil backfill. Geotechnical and Geological Engineering, 28, 5, 633-641, 2010.
- [5] Shao-jun, M., Kui-hua, W., Wen-bing, W., Pseudo-dynamic active earth pressure behind retaining wall for cohesive soil backfill. Journal of Central South University of Technology, 19, 3298-3304, 2012.
- [6] Das, B.M., Puri, V.K., Static and dynamic active earth pressure. Geotechnical and Geological Engineering, 14, 4, 353-366, 1996.

- [7] Saran, S., Gupta, R.P., Seismic earth pressures behind walls. *Indian Geotechnical Journal*, 33, 3, 195-213, 2003.
- [8] Ghosh, S., Dey, G.N., Datta, B., Pseudo-static analysis of rigid retaining wall for dynamic active earth pressure. 12th International Conference of International Association for Computer Methods and Advances in Geomechanics (IACMAG) 1-6 October, Goa-India, 4122-4131, 2008.
- [9] Shukla, S.K., Dynamic active thrust from  $c-\phi$  soil backfills. *Dynamic Earthquake Engineering*, 31, 3, 526-529, 2011.
- [10] Shukla, S.K., Bathurst, R. J., An analytical expression for the dynamic active thrust from  $c-\phi$  soil backfill on retaining walls with wall friction and adhesion. *Geomechanics and Engineering*, 4, 3, 209-218, 2012.
- [11] Ghosh, S., Sengupta, S., Extension of Mononobe-Okabe theory to evaluate seismic active earth pressure supporting  $c-\phi$  soil backfill, *Electronic Journal of Geotechnical Engineering*, 17(D), 495-504, 2012.
- [12] Iskander, M., Chen, Z., Omidvar, M., Guzman, I., Rankine pseudo-static earth pressure for  $c-\phi$  soils. *Mechanics Research Communications*, 51, 51-55, 2013.
- [13] Shukla, S.K., Generalized analytical expression for dynamic active thrust from  $c-\phi$  soil backfills. *International Journal of Geotechnical Engineering*, 9, 4, 416-421, 2015.
- [14] Lin, Y., Leng, W., Yang, G., Zhao, L., Li, L., Yang, J., Seismic active earth pressure of cohesive-frictional soil on retaining wall based on a slice analysis method. *Soil Dynamics and Earthquake Engineering*, 70, 133-143, 2015.
- [15] Zhou, Y., Chen, F., Wang, X., Seismic active earth pressure for inclined rigid retaining walls considering rotation of the principal stresses with pseudo-dynamic method. *International Journal of Geomechanics*, 18, 7: 04018083, 1-9, 2018.
- [16] Tang, Y., Chen, J., A computational method of active earth pressure from finite soil body. *Mathematical Problems in Engineering*, Vol. 2018: 9892376, 1-7, 2018.
- [17] Gupta, A., Sawant, V.A., Effect of soil amplification on seismic earth pressure using pseudo-dynamic approach. *International Journal of Geotechnical Engineering*, 4, 2, 1-12, 2018.
- [18] Gupta, A., Yadav, V., Sawant, V.A., Agarwal R., Development of design charts considering the effect of backfill inclination and wall inclination on the seismic active pressure for  $c-\phi$  soil. *International Journal of Mathematical, Engineering and Management Sciences*, 4, 2, 409-419, 2019.
- [19] Peng, J., Zhu, Y., Derivation of Shukla's generalized expression for dynamic active thrust by inclined slice element method. *Soil Mechanics and Foundation Engineering*, 56, 2, 77-81, 2019.
- [20] Caltabiano, S., Cascone, E., Maugeri, M., Seismic stability of retaining walls with surcharge. *Soil Dynamics and Earthquake Engineering*, 20, 469-476, 2000.
- [21] Caltabiano, S., Cascone, E., Maugeri, M., A procedure for seismic design of retaining walls, seismic prevention of damage: A case study in a mediterranean city. *WIT Trans. State Art Sci. Eng.*, 8, 263-277, 2005.

- [22] Caltabiano, S., Cascone, E., Maugeri, M., Static and seismic limit equilibrium analysis of sliding retaining walls under different surcharge conditions. *Soil Dynamics and Earthquake Engineering*, 37, 38-55, 2012.
- [23] Aminpour, M.M., Maleki, M., Ghanbari, A., Investigation of the effect of surcharge on behavior of soil slopes, *Geomechanics and Engineering*, 13, 4, 653-669, 2017.
- [24] Hou, G., Shu, S., Trial wedge approach to determine lateral earth pressures. *International Journal of Geomechanics*, 19, 1: 06018035, 1-16, 2019.
- [25] Arda, Ç., Çinicioğlu, Ö., Kohezyonsuz zeminlerin tane dağılım ve şekil özelliklerinin aktif göçme yüzeyi geometrisine etkileri. *Teknik Dergi*, 30, 5, 9399-9420, 2019.
- [26] Yazdani, M., Azad A., Farshi, A.H., Talatahari, S., Extended ‘Mononobe-Okabe’ method for seismic design of retaining walls. *Journal of Applied Mathematics*, Vol. 2013, 1-10, 2013.
- [27] Greco, V.R., An algorithm for the evaluation of active thrust for backfill with irregular profile. *Geotechnique Letters*, 5, 2, 1-6, 2015a.
- [28] Greco, V.R., Seismic active thrust due to backfill of general topographic profile. *Soil Dynamics and Earthquake Engineering*, 79, 66-70, 2015b.
- [29] Kim, W.C., Park, D., Kim, B. Development of a generalized formula for dynamic active earth thrust. *Geotechnique*, 60, 9, 721-727, 2010.
- [30] Greco, V.R., Discussion of ‘Development of a generalized formula for dynamic active earth thrust by Kim, W.C., Park, D. and Kim, B.’. *Geotechnique*, 62, 4, 365-366, 2012.
- [31] Lu, H., Yuan, B., Calculation of passive earth pressure of cohesive soil based on Culmann’s method. *Water Science and Engineering*, 4, 1, 101-109, 2011.
- [32] Culmann, K., *Die graphische statik*, Meyer&Zeller, Zurich, 1866.
- [33] Motta, E., Generalized coulomb active-earth pressure for distanced surcharge. *Journal of Geotechnical Engineering*, 120, 6, 1072-1079, 1994.
- [34] Paik, K.H., Salgado, R., Estimation of active earth pressure against rigid retaining walls considering arching effects. *Geotechnique*, 53, 7, 643-653, 2003.
- [35] Shukla, S.K., Gupta, S.K., Sivakugan, N., Active earth pressure on retaining wall for  $c-\phi$  soil backfill under seismic loading condition. *Journal of Geotechnical and Geoenvironmental Engineering*, 135, 5, 690-696, 2009.
- [36] Nian, T., Han, J., Analytical solution for Rankine’s seismic active earth pressure in  $c-\phi$  soil with infinite slope. *Journal of Geotechnical and Geoenvironmental Engineering*, 1399, 1611-1616, 2013.
- [37] Ghosh, S., Sharma, R.P., Seismic active earth pressure on the back of battered retaining wall supporting inclined backfill. *International Journal of Geomechanics*, 12, 1, 54-63, 2012.



# Investigations of Exterior Wind Flow and Aerodynamic Coefficient around Y-Plan Shape Tall Building

Vigneshwaran RAJENDRAN<sup>1</sup>  
Prabavathy SHANMUGASUNDARAM<sup>2</sup>

## ABSTRACT

In recent years, the construction of skyscrapers is emerging in many countries and the study on the behaviour of wind around the building receives an additional interest among structural engineers and architects. Mostly, tall skyscrapers are planned in the shape of 'Y' in order to have a maximum exterior view and to support the central core of the structure. In the current scenario, it is important to study the actual wind load for irregular plan shape building. This paper presents the numerical wind flow simulation around 'Y' plan shape tall building using ANSYS Fluent software and validation is done using wind tunnel testing. The building model and wind velocity are scaled to the ratio 1:300 and 1:5 respectively. A wind velocity of 10 m/s is applied both for wind tunnel testing and for the numerical simulation. Error analysis is carried out in order to check the accuracy of the results obtained between wind tunnel and CFD. From the test results the mean  $C_p$  is investigated for various faces of the building for the wind angle  $0^\circ$ ,  $45^\circ$  and  $90^\circ$  from both using CFD and wind tunnel. The investigation of drag and lift coefficient is made on Y-plan shape building and it is observed that the maximum drag occurs at  $45^\circ$  wind angle, because of the less projected area when compared with the other wind angles  $0^\circ$  and  $90^\circ$  respectively. Further, this paper continues with the physics of wind flow behaviour around Y-plan shape building and flow character such as vortex formation, streamlines and identification of wake region for different wind angles.

**Keywords:** Aerodynamic forces, Computational Fluid Dynamics (CFD), wind tunnel, tall buildings.

## 1. INTRODUCTION

Today, 55% of the world population are living in cities and the percentage might increase in the upcoming years due to the availability of opportunities in cities. The rise in the urban population leads to the demand for land area and vertical constructions are increasing. These

---

Note:

- This paper has been received on March 6, 2020 and accepted for publication by the Editorial Board on December 11, 2020.
  - Discussions on this paper will be accepted by September 30, 2022.
- <https://doi.org/10.18400/tekderg.699861>

1 Department of Civil Engineering, Mepco Schlenk Engineering College, Sivakasi, India - vignesh.rajn.93@gmail.com - <https://orcid.org/0000-0003-2405-3898>

2 Department of Civil Engineering, Mepco Schlenk Engineering College, Sivakasi, India - spraba@mepcoeng.ac.in - <https://orcid.org/0000-0001-6110-5912>

high-rise structures are subject to predominate lateral forces, mainly the wind force. For the past two decades, many researchers explored the wind effect on tall buildings and their response. It is possible to study the wind effects on tall buildings with both numerical and experimental methods. The following earlier researchers Yasushi Uematsu et al and G.M. Richardson et al [1,2] adopted the wind tunnel tests to investigate the dynamic behaviour wind loads on engineering structures such as single-layer latticed dome, siloes structures using wind tunnel tests. In this regard, the investigation of aerodynamic coefficient such as drag and lift coefficient for a rectangular tall building with  $0^\circ$  and  $90^\circ$  wind angles are investigated by the author Chitra ganapathi et al [3]. The test is carried out for different terrain conditions namely suburban, open, and uniform terrain conditions. From the results, it is well known that the terrain condition has a greater influence in the pressure coefficient ( $C_p$ ) at different faces of the building.

In addition to the experimental studies and with the recent development of supercomputer and turbulence model in 20<sup>th</sup> century makes it possible to predict the wind flow behaviour around the tall buildings and to have a comparative study on wind pressure distribution around the building with both numerical and experimental methods. The numerical prediction of wind flow around a rectangular plan shape building is done successfully by Ben Mou et al [4] using RNG k- $\epsilon$  turbulent model and the distribution of the pressure around the building is investigated. The obtained result is compared with the Commonwealth Advisory Aeronautical Research Council (CAARC) standard models. The simulation of atmospheric boundary conditions is very much important for the wind flow around the building. Gu M and Quan Y [5] investigated the cross-wind load for fifteen typical tall buildings with different aspect ratios. The test is conducted in a high-frequency force balancing test. New formula for crosswind power spectra is investigated and compared with the previous result. Zhao Liu et al [6] performed a twisted wind flow on a square mega tall building using wind tunnel test and the results of pressure distribution are studied. In order to reduce the wind load on structure, many major and minor modifications are made on buildings with different shapes and is performed by the researcher Ashutosh Sharma et al and Kim Y., Kanda J [7, 8]. Further, the researchers continued with the detailed review of shape modifications in buildings such as curve corners and major modifications such as altering the building shape and elevation. These modifications lead to a decrease in wind loads by 30 to 60% and the wind flow pattern changes with the building shape and height. Further investigation is done on 'E' plan shape building by the author Biswarup Bhattacharyya and Sujit Kumar Dalui [9] using Wind tunnel and validated using Computational Fluid Dynamics (CFD) software for wind angles  $0^\circ$ ,  $30^\circ$ ,  $60^\circ$ ,  $90^\circ$ ,  $120^\circ$ ,  $150^\circ$  and  $180^\circ$ . The scaling of building models is done using a 1:300 ratio. Rajdip Paul and Sujit Kumar Dalui [10] performed a wind pressure distribution around 'Z' plan shape building for wind angles  $0^\circ$ ,  $30^\circ$ ,  $60^\circ$ ,  $90^\circ$ ,  $120^\circ$  and  $150^\circ$ .

The investigation of wind force and wind pressure acting on a tall building with unconventional configuration is carried out in the present study because most of the Wind Engineering (WE) codes are silent in providing the mean  $C_p$  for irregular and complex geometry. Even in the revised code of Indian Wind Engineering Code (IWEC) IS875 (2015), there is a lack of mean  $C_p$  for irregular plan shape building. Therefore, in the present scenario it is important to investigate wind flow around an irregular plan geometry using a wind tunnel testing and CFD analysis.

This paper investigates the wind behaviour around Y-plan shape tall building. The reason for the selection of Y-plan shape building is that many existing tall skyscrapers such as Burj Khalifa of the height 828 meters and upcoming skyscrapers such as Kingdom/Jeddah Tower of height more than 1000 m are designed in the form of Y-plan shape. The investigation of Y-plan shape building is performed with both the wind tunnel testing and with the numerical simulation using CFD for the wind angles  $0^\circ$ ,  $45^\circ$ ,  $90^\circ$  respectively. The test is performed for a constant wind velocity 10 m/s and turbulence model realizable k- $\epsilon$  is used for the CFD simulation.

## 2. EXPERIMENT SETUP

The experiment is conducted using a subsonic wind tunnel, which is available in Kumaraguru College of Technology (KCT), Coimbatore, India. Figure 1 shows the schematic representation of a wind tunnel. The building models are tested in the wind tunnel of test section of size 0.6 m x 0.6 m and the length of the tunnel is 40 m. Figure 2 shows a pictorial representation of a test section of a subsonic wind tunnel. The experiment flow is simulated similar to terrain category – I as per IS 875 (Part-3) 2015. The value of ground roughness  $Z_0$  as per code is 0.002 is used for both wind tunnel and CFD in this study. The building models scaled in the ratio of 1:300 and the wind tunnel is operated at a wind speed of 10 m/s. Since the blockage ratio lies between 9 to 11%, necessary blockage correction is done for calculating the pressure coefficient ( $C_p$ ) from the building model. The power-law index ( $\alpha$ ) for the tunnel is 0.133. The pressure measurements are taken with the help of a pressure tube which is connected to the manometers.

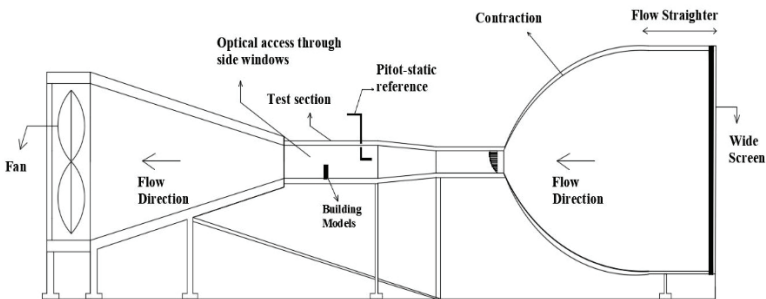


Figure 1 - Schematic representation of Wind Tunnel

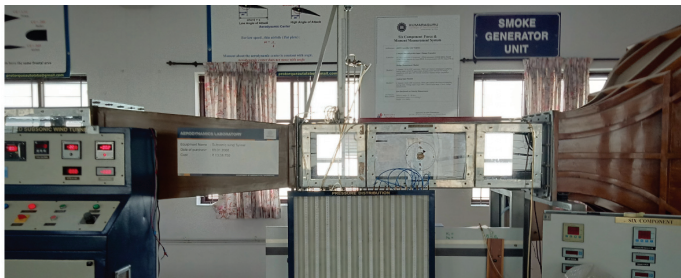


Figure 2 - Sub-sonic Wind tunnel test section 0.6 m x 0.6 m at Kumaraguru College of Technology (KCT) – Coimbatore

### 2.1. Details of the Model

The building models were made-up with the help of transparent perspex sheet (acrylic sheets) having a thickness of about 0.003 m. The acrylic sheet is chosen because it is easy to fabricate to the desired shape and for drilling holes to connect the pressure tubes. The base of the building is made of a thick sheet plywood to hold the building model in a fixed position. The actual building dimension for the study is 90 m and the building are scaled in the ratio 1:300. Pressure measurements are made at three different levels, Level-1 ( $h/6$ ), Level-2 ( $h/2$ ), Level-3 ( $4.15h/5$ ), where ‘h’ represents the height of the building model; in total 27 pressure taps are made. Pressure taps are placed at three different heights 50 mm ( $h/6$ ), 150 mm ( $h/2$ ) and 250 mm ( $4.15h/5$ ) from the base. On each face of the building model, three pressure taps are made. The building modes are tested for a three-wind incidence direction of about  $0^\circ$ ,  $45^\circ$ , and  $90^\circ$  respectively. Figure 3 (a) display the fabricated model of Y-plan shape building, Figure 3 (b) shows the solid work model for Y-plan shape building, Figure 3(c) represents the wind direction for Y-plan shape building. Figures 3 (d) and (e) shows the plan and elevation for Y shape building with pressure taps location.

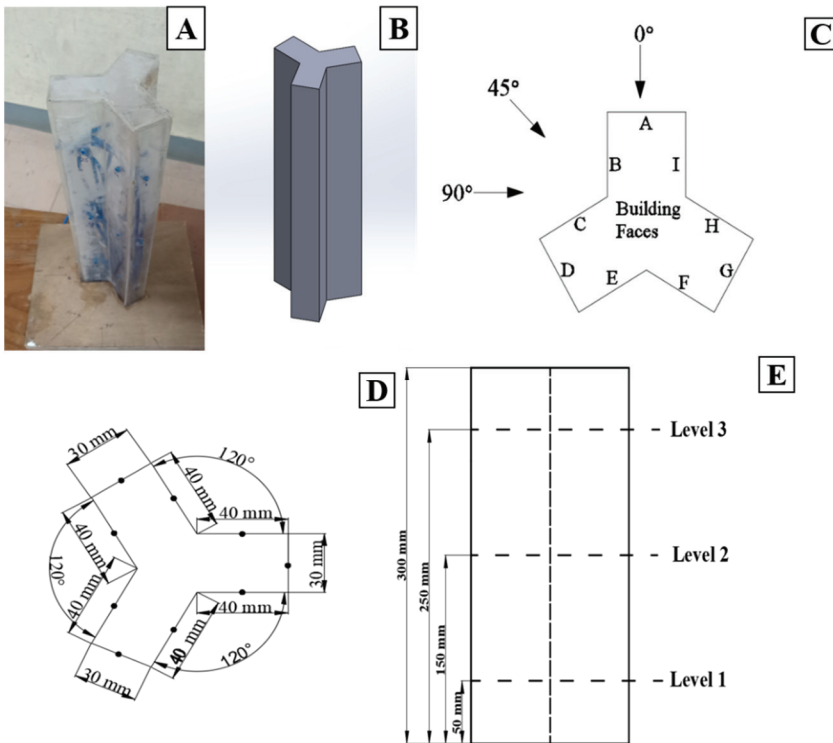


Figure 3 - Represents Y-plan shape building (a) Fabricated building model using acrylic sheet (b)Modelling using Solid works (c) Different wind direction angles (d) Plan dimension and location of pressure taps on building model (e) Elevation dimension

### 3. NUMERICAL STUDY

The numerical study is performed using a turbulence model using realizable k-ε available in ANSYS Fluent 19.2 software package. The transport equation involved is momentum (k) and turbulence energy dissipation rate (ε) are given the equations 1 and 2

$$\frac{\partial(\rho k)}{\partial t} + \frac{\partial}{\partial x_j}(\rho U_j k) = \frac{\partial}{\partial x_j} \left[ \left( \mu + \frac{\mu_t}{\sigma_k} \right) \frac{\partial \epsilon}{\partial x_j} \right] + P_k - \rho \epsilon + P_{kb} \quad (1)$$

$$\frac{\partial(\rho \epsilon)}{\partial t} + \frac{\partial}{\partial x_j}(\rho U_j \epsilon) = \frac{\partial}{\partial x_j} \left[ \left( \mu + \frac{\mu_t}{\sigma_\epsilon} \right) \frac{\partial \epsilon}{\partial x_j} \right] + C_1 \frac{\epsilon}{k} (P_k + C_3 P_b) - C_2 \rho \frac{\epsilon^2}{k} + S_\epsilon \quad (2)$$

Where  $P_k$  is the production due to mean velocity shear,  $P_b$  is the production due to buoyancy,  $S_k$  is a user-defined source. The present study uses a turbulence constants values as stated by the previous authors Jones and Launder [11] and the values are  $\sigma_k$  is 1,  $\sigma_\epsilon$  is 1.3,  $C_1$  is 1.55,  $C_2$  is 2.0,  $C_\mu$  is 0.09 respectively. For high Reynolds number, the energy dissipation  $\epsilon$  may be assumed to  $\rho k^{1.5}/l$ .

$$\mu_t = \frac{C_\mu \rho l k^2}{\epsilon} \quad (3)$$

Where,  $\mu_t$  and  $k$  is nonzero,  $\rho$  is the fluid density,  $C_\mu$  is a constant of value 0.09,  $l$  is turbulence length scale.

#### 3.1. Boundary Condition

The similar boundary condition is adopted for both wind tunnel testing and numerical simulation. The inlet is based on power-law coefficient ( $\alpha$ ) taken as 0.133

$$\frac{U}{U_0} = \left( \frac{Z}{Z_0} \right)^\alpha \quad (4)$$

Where  $U_0$  is the basic wind speed taken as 10 m/s,  $U$  is the velocity at a particular height ( $Z$ ) and  $Z_0$  is the boundary layer height. Turbulence model realizable k-ε is used for external flow simulation. The parameters including turbulent kinetic energy ( $k$ ) and turbulent dissipation rate ( $\epsilon$ ) are considered. Turbulent kinetic energy ( $k$ ) is closely related to turbulent intensity ( $I$ ) and wind speed ( $U$ ) [4].

The typical default profile law for setting the Atmospheric Boundary Layer (ABL) may not be suitable for most of the cases. For the present study, ABL is interpreted in the ANSYS Fluent in the form of user-defined coding script as suggested by the authors D.M Hargreaves and N.G Wright [12] for turbulence model k-ε. For creating an open terrain profile in CFD, the wall distance  $\Delta_x$  should be greater than the roughness height ( $\Delta_x > K_s$ ). The wall function  $y^+$  is the empirical function, for the current study  $y^+$  is 30, which falls in the log layer and the first cell height distance is 0.002 m.

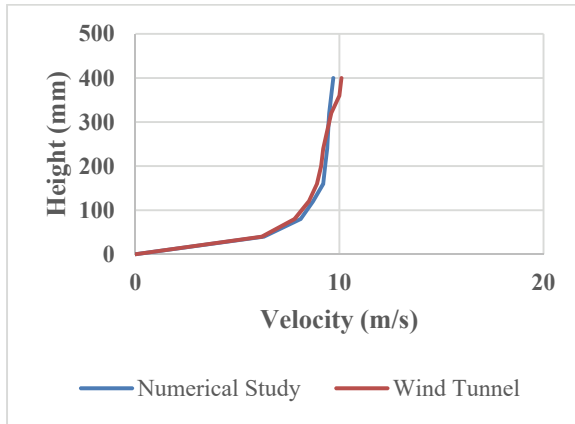


Figure 4 - Velocity profiles

### 3.2. Computational Domain Size and Meshing

The size of the domain is fixed based on the flow simulation. The domain size reference is taken from a recommendation given by Franke et al and Tominaga et al [13,14]. The dimension of the domain is 5 H on the upstream side of the building, 15 H in the downstream of the building, and 5 H is considered on the side face of the building, where ‘H’ represents the height of the building inside the computational domain. Figure 5(a) shows the plan view of the computation domain and 5(b) shows the side view of the computation domain. The adopted domain size is very much enough for the generation of a vortex and backflow because of wind. For the present study the inlet boundary condition is 10 m/s and is given as per the Equation 4, the outlet boundary condition is  $\frac{\partial}{\partial x}(u, v, w, k, \epsilon) = 0$ , No-slip is considered on the floor of the computational domain ensuring that no velocity had occurred between the wall and the moving fluids,  $u = v = w = 0$  and the free slip is considered in the top and sidewall of the computational domain  $\frac{\partial}{\partial x}(u, v, w, k, \epsilon) = 0$ .

Finite element tetrahedral mesh element is used throughout the domain. Grid quality and quantity determine computation time and cost. Mesh in the building is made to be fine when compared to the computational domain [19]. Grid independency test is performed namely coarse grid, basic grid and fine grid and the results are displayed in table 1. Figure 6(a) shows the grid generation over the entire domain, Figure 6(b) shows the grid generation closer to Y-plan shape building.

Table 1 - Grid sensitivity study and grid size

| Name        | $\Delta_x$ (m) | No of Node | No. of Elements |
|-------------|----------------|------------|-----------------|
| Course grid | 0.0025         | 530314     | 2832920         |
| Basic       | 0.0020         | 736719     | 3392253         |
| Fine        | 0.0020         | 2509599    | 8067948         |

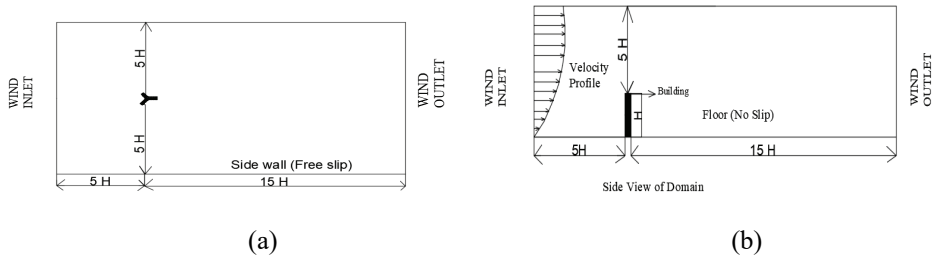


Figure 5 - Computational domain size (a) Plan view of Computational domain (b) Side view of the Computational domain

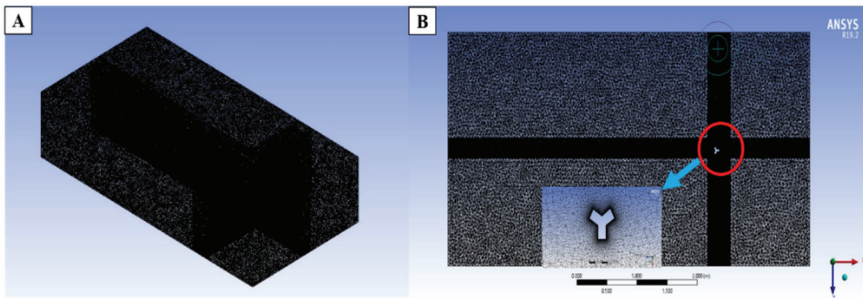


Figure 6 - Grid generation (a) Overall grid distribution over the entire domain (b) Grid generation closer to Y-plan shape building surface.

### 3.3. Solver Settings

The numerical simulation is performed using ANSYS Fluent 19.2 commercial software package. The simulation is solved using steady-state, 3-D Reynolds Averaged Navier-Stokes Equation (RANS) equation is incorporated in ANSYS Fluent software. Since the flow over a building model is an incompressible flow, the Mach number is less than three ( $M < 3$ ). Pressure based velocity coupling solver is used and turbulence model reliable  $k-\epsilon$  is used for the present study. Many previous studies prove that reliable turbulence model  $k-\epsilon$  is good to capture the flow involving rotations, flow separation and recirculation. The Semi-Implicit Method for Pressure Linked Equations (SIMPLE) algorithm is used for coupling pressure and velocity. Second-order discretization schemes are used for solving the governing equation involving convection and viscous terms. The simulation is performed using Intel 9<sup>th</sup> Generation Core i5, running at 1.9 GHz with 8 G.B internal memory. The iterations were performed when the convergence of the variable momentums in X, Y and Z direction, continuity,  $k$  and  $\epsilon$  are archived when the residual reaches a value of  $1 \times 10^{-4}$ .

## 4. RESULTS AND DISCUSSIONS

### 4.1. Pressure Distribution around the Buildings

Knowledge of external pressure distribution is very much important to evaluate the wind loads on various structural components. Pressure distribution around the building at various faces is investigated for the wind angles 0°, 45° and 90° respectively. The wind flow pattern depends on ground roughness, velocity profiles, computational domain, grid spacing, etc. Previous researchers conducted [4] a numerical simulation and investigated the pressure distribution around rectangular buildings with varying dimensions and validation is done with the CAARC building model to check the accuracy of CFD results. Validation of CFD results with the experimental studies is very much important for all computational studies [24]. Validation gives us a high degree of accuracy to represent all real-world problems. The investigation of CFD results in this paper is compared with the experimental wind pressure values and are checked for its accuracy. The mean pressure coefficient ( $C_p$ ) is a non-dimensional parameter and calculated using equation 5.

$$C_{p, \text{mean}} = \frac{p - p_0}{\frac{1}{2} \rho U_H^2} \tag{5}$$

Where  $p$  is the pressure value from the point needed,  $p_0$  is the pressure at reference height,  $\rho$  is the density of air of value 1.225 kg/m<sup>3</sup>,  $U_H^2$  is the mean wind velocity.

### 4.2. Blockage Correction

Blockage correction is introduced by Maskell in the year 1958 [15], to reduce the overestimated flow obtained from wind tunnel. Since the blockage ratio is more than 5% for the present study, the necessary blockage corrections are made using the equation 6.

$$C_{p, \text{Corrected}} = \frac{C_{p,m}}{n} + \frac{(n-1)}{n} \tag{6}$$

Where  $n$  is the blockage correction factor. Table 3 shows the blockage correction for C plan shape building for wind angles 0°, 45° and 90° respectively.

Table 2 - Blockage correction ( $n$ ) for C-plan shape building with different wind angles

| Wind angles | Blockage value (%) | Blockage correction ( $n$ ) |
|-------------|--------------------|-----------------------------|
| 0°          | 11.383             | 1.0638                      |
| 45°         | 10.925             | 1.5925                      |
| 90°         | 10.067             | 1.5067                      |

### 4.3. Pressure Distribution on Building Faces

For the design of tall building one of the most important parameters to be considered in wind load is the pressure coefficient ( $C_p$ ) [17]. Usually, windward faces of the building experience positive  $C_p$  and leeward and side faces experience negative  $C_p$ . The mean  $C_p$  on various faces of the Y-plan shape building model is investigated using wind tunnel and CFD. Figure 7 shows the comparison of mean  $C_p$  for the wind angles  $0^\circ$ ,  $45^\circ$  and  $90^\circ$  obtained from wind tunnel testing. Figure 8 shows the comparison of mean  $C_p$  for the wind angles  $0^\circ$ ,  $45^\circ$  and  $90^\circ$  obtained using realizable k- $\epsilon$  turbulence model using CFD.

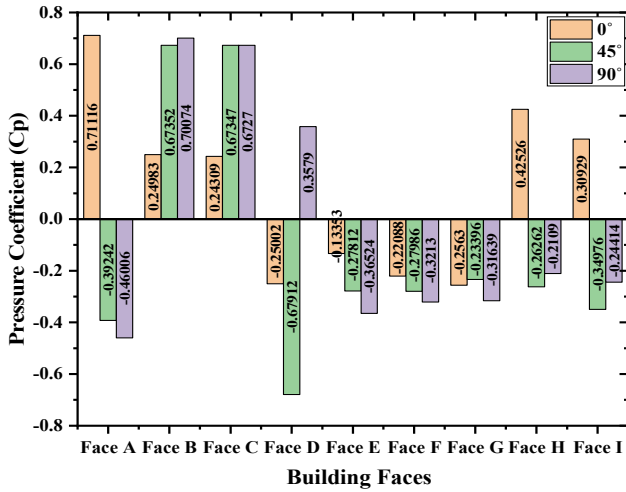


Figure 7 - Comparison of face pressure coefficient for different angles  $0^\circ$ ,  $45^\circ$  and  $90^\circ$  from Wind tunnel testing

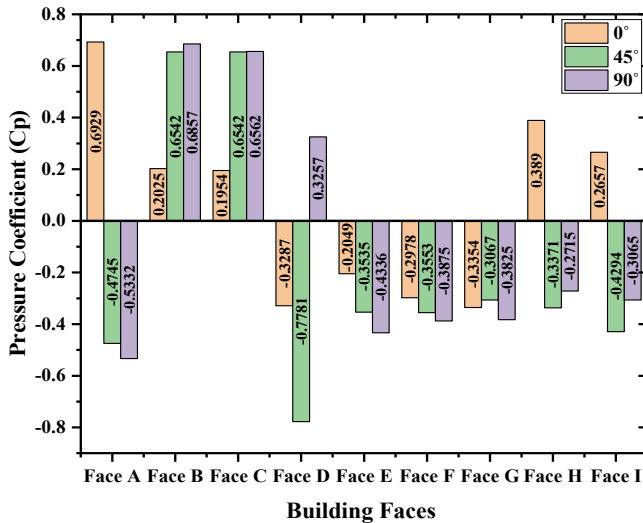


Figure 8 - Comparison of face pressure coefficient for different angles  $0^\circ$ ,  $45^\circ$  and  $90^\circ$  from CFD results

**4.2. Angle of Incidence - 0°**

For 0° Angle of Incidence (AoI), building faces A, B, C, H, and I experience positive pressure coefficient ( $C_p$ ), whereas faces D, E, F, and G experience a negative pressure coefficient ( $C_p$ ). It is noticeable that high positive  $C_p$  is observed in the face A of about 0.6929 in CFD and 0.7116 from the wind tunnel test. On the other hand, very low negative pressure coefficient ( $C_p$ ) is observed in face D of about -0.3287 in CFD and -0.2500 in wind tunnel test. Table 3 shows the comparison of mean  $C_p$  with turbulence model realizable k-ε in CFD and wind tunnel test for 0° wind angle.

The pressure coefficient contour for the building faces A, B, C, D, E, F, G, H, and I for 0° wind angle are displayed in figure 9. The pressure contour on different faces provides very useful information regarding the distribution of the pressure on the various heights of the building. Most of the present Wind Engineering Code (WEC) provides a single mean  $C_p$  for the entire face of a regular plan geometry; but in the actual condition the value of  $C_p$  varies along with the height of the building. Further positive  $C_p$  decreases along the edges due to dispersion of flow in the windward face and negative  $C_p$  increases along the edge as noticed by the author [18] K. Suresh Kumar. For the present study in the distribution of the pressure on each face of the building as representing in figure 9, face A experiences high positive  $C_p$  and the pressure decreases along the top and side edges in face A of the building due to the windward direction. However, for the faces D, E, F, G undergoes negative  $C_p$  because of leeward direction and the negative  $C_p$  increases along the edges for the leeward building faces due to convergence of flow from the top. Figure 10 shows the  $C_p$  that is measured around the perimeter of the building with different heights  $h/6$ ,  $h/2$ ,  $4.15h/5$  for 0° wind angle. The  $C_p$  on windward sides experience equal  $C_p$  on all the three height ( $h/6$ ,  $h/2$ ,  $4.15h/5$ ) along the perimeter from 0 to 15 m, whereas the pressure in the leeward sides experience a high negative  $C_p$  at the height of  $4.15h/5$ . This proves that the negative pressure is high in the leeward face top of the building.

Table 3 - Comparison of mean pressure coefficient on different faces for 0° wind angle

| Location | Mean $C_p$ |             | Remarks   |
|----------|------------|-------------|---|
|          | k-ε        | Wind tunnel |   |
| Face A   | 0.6929     | 0.7111      | <b>All results are within the acceptable limits</b> |
| Face B   | 0.2025     | 0.2498      |   |
| Face C   | 0.1954     | 0.2500      |   |
| Face D   | -0.3287    | -0.2500     |   |
| Face E   | -0.2049    | 0.2500      |   |
| Face F   | -0.2978    | 0.1335      |   |
| Face G   | -0.3354    | -0.2208     |   |
| Face H   | 0.3890     | 0.4252      |   |
| Face I   | 0.2657     | 0.3092      |   |

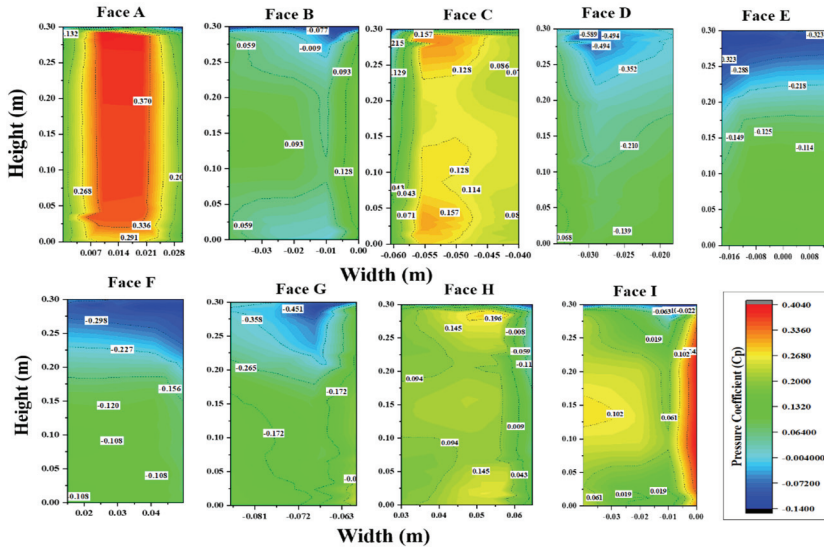


Figure 9 - Represents the pressure coefficient ( $C_p$ ) contour on various faces for  $0^\circ$  wind angle

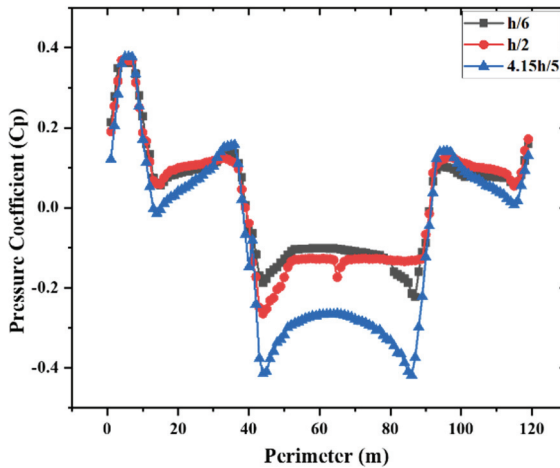


Figure 10 - Pressure coefficient ( $C_p$ ) along the perimeter of Y-plan shape building for  $0^\circ$  wind angle

### 4.3. Angle of Incidence - $45^\circ$

For  $45^\circ$  AoI building faces B and C experience positive coefficient ( $C_p$ ), whereas faces A, D, E, F, G, H, and I experience negative pressure coefficient ( $C_p$ ). Obviously, high positive pressure coefficient ( $C_p$ ) is experienced in windward faces of the building B and C of about 0.6542 from CFD and 0.6735 from the wind tunnel. Further, very low negative pressure

coefficient ( $C_p$ ) is experienced in the face G of about -0.3067 from CFD and -0.2339 from the wind tunnel testing. Table 4 shows the comparison of surface pressure coefficient with CFD and wind Tunnel testing for 45° wind angle.

Table 4 - Comparison of mean surface pressure coefficient on different faces for 45° wind angle

| Location | Mean $C_p$ |             | Remarks                                      |
|----------|------------|-------------|--|
|          | k-ε        | Wind tunnel |  |
| Face A   | -0.4745    | -0.3924     | All results are within the acceptable limits |
| Face B   | 0.6542     | 0.6735      |  |
| Face C   | 0.6542     | 0.6732      |  |
| Face D   | -0.7781    | -0.6791     |  |
| Face E   | -0.3535    | -0.2781     |  |
| Face F   | -0.3553    | -0.2798     |  |
| Face G   | -0.3067    | -0.2339     |  |
| Face H   | -0.3371    | -0.2626     |  |
| Face I   | -0.4294    | -0.3497     |  |

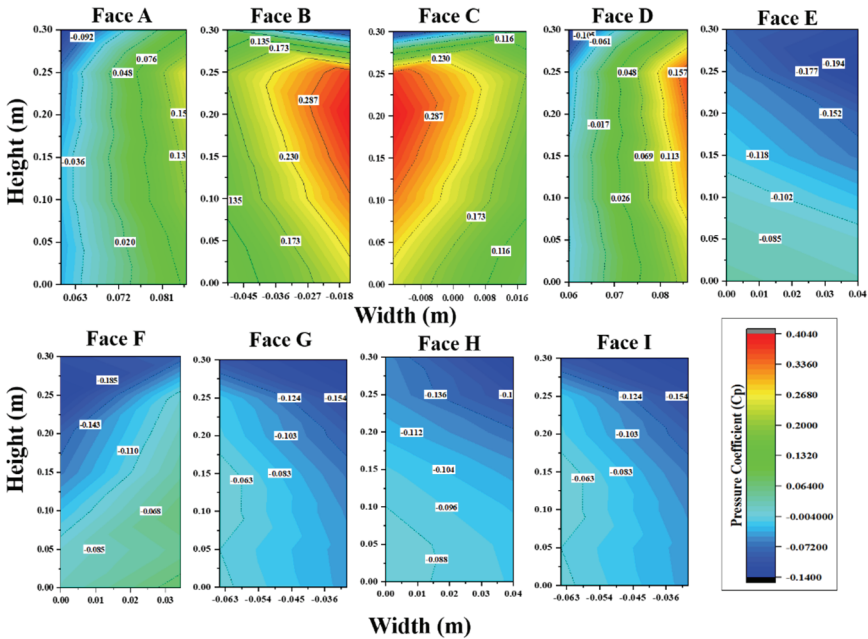


Figure 11 - Represents the pressure coefficient ( $C_p$ ) contour on various faces for 45° wind angle

Figure 11 shows the wind pressure distribution on Y-plan shaped building for  $45^\circ$  wind angle. High positive pressure contour is observed in the faces B and C, further the pressure contour decreases along the side faces of the building as represented in figure 11. Due to symmetrical flow of wind, faces B and C experiences similar mirror contour pressure, as shown in the figure 11. Whereas, 90% similar contour pressure is observed in the leeward faces E, F, G, H, and I of the building. High positive pressure decreases along the top edges of the building faces B and C, because of the dispersion of the flow along the top edges of the building.

The pressure measurement is measured along the perimeter of the building at different heights  $h/6$ ,  $h/2$ ,  $4.15h/5$  for  $45^\circ$  wind angle. Figure 12 indicates the pressure coefficient ( $C_p$ ) along the perimeter of the building at three different heights. Minor variation in pressure coefficient ( $C_p$ ) is observed in the positive faces at different levels. Similar negative pressure is observed in the leeward face for the heights  $h/6$ ,  $h/2$  and further major deviation in pressure coefficient ( $C_p$ ) has occurred at bottom level  $4.15h/5$ .

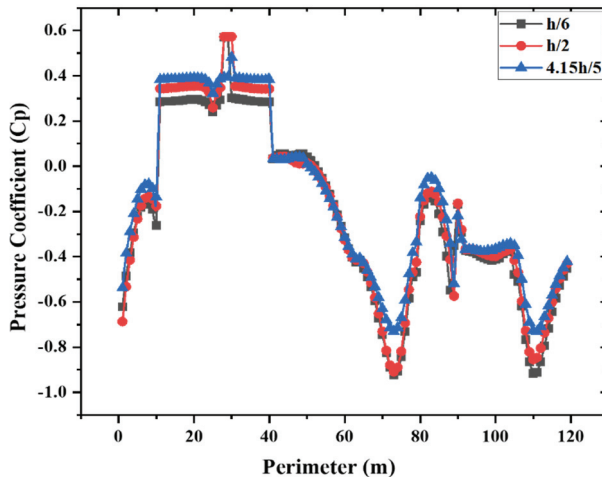


Figure 12 - Pressure coefficient ( $C_p$ ) along the perimeter of Y-plan shape building for  $45^\circ$  wind angle

#### 4.4. Angle of Incidence - $90^\circ$

For  $90^\circ$  AoI, building faces B, C, and D experience positive pressure coefficient ( $C_p$ ); whereas the faces A, E, F, G, H, and I experience negative pressure coefficient ( $C_p$ ). High positive pressure coefficient ( $C_p$ ) is observed in the face B of about 0.6857 from CFD and 0.7007 from wind tunnel testing and furthermore, very low negative pressure coefficient ( $C_p$ ) is observed in the face A of about -0.5484. Table 5 shows the comparison of the mean pressure coefficient for the  $90^\circ$  wind angle.

Figure 13 shows the wind pressure distribution contour on Y-plan shape building for  $90^\circ$  wind angle. As expected for all the wind angles, the middle position of the windward faces experience high positive wind pressure distributions along the perimeter of the buildings. The windward faces B, C and D experience positive pressure coefficient ( $C_p$ ), whereas in the faces

B the pressure gets reduces at the top faces due to the dispersion of flow at the top and for the faces C and D, the pressure reduces along the sides and the top faces of the building model. Moreover, 80% similar contour pressure distribution is observed in the leeward face the building A, G and H; 90% of the similar pressure is observed in the faces E and I. Negative pressure coefficient ( $C_p$ ) increase along with the top corners of the building due to the convergence of the flow.

Table 5 - Comparison of mean surface pressure coefficient on different faces for 90° wind angle

| Location | Mean $C_p$ |             | Remarks                                      |
|----------|------------|-------------|--|
|          | k-ε        | Wind tunnel |  |
| Face A   | -0.5332    | -0.4606     | All results are within the acceptable limits |
| Face B   | 0.6857     | 0.7007      |  |
| Face C   | 0.6562     | 0.6726      |  |
| Face D   | 0.3257     | 0.3578      |  |
| Face E   | -0.4336    | -0.3652     |  |
| Face F   | -0.3875    | -0.3213     |  |
| Face G   | -0.3825    | -0.3163     |  |
| Face H   | -0.2715    | -0.2109     |  |
| Face I   | -0.3065    | -0.2441     |  |

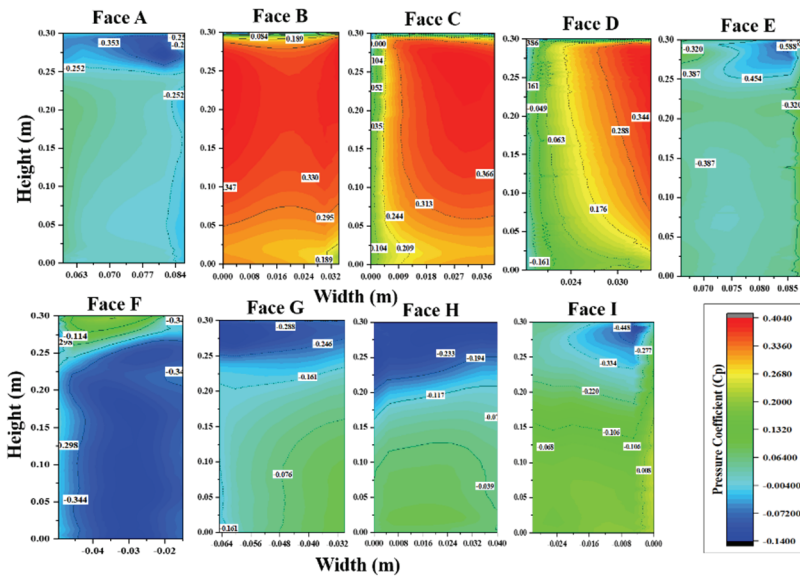


Figure 13 - Represents the pressure coefficient ( $C_p$ ) contour on various faces for 90° wind angle

Figure 14 shows the pressure measurement along the perimeter of the building at three different levels  $h/6$ ,  $h/2$ ,  $4.15h/5$ . Similar pressure coefficient ( $C_p$ ) is observed in the windward faces for the levels of height  $h/6$  and  $h/2$ , whereas a mild deviation is observed leeward faces for the levels  $h/6$  and  $h/2$  respectively. On the contrary, for the top height  $4.15h/5$  experiences a huge negative pressure coefficient ( $C_p$ ) for the faces G and H.

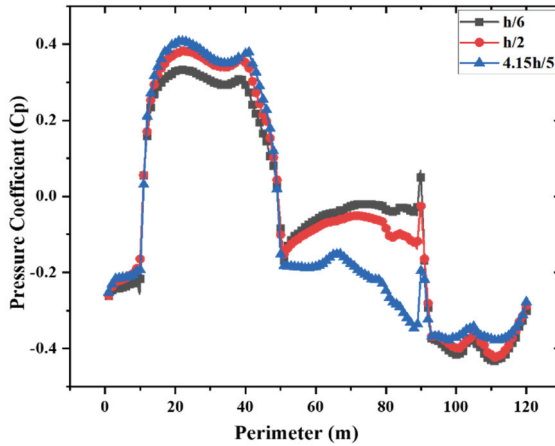


Figure 14 - Pressure coefficient ( $C_p$ ) along the perimeter of Y-plan shape building for  $90^\circ$  wind angle

#### 4.5. Error Analysis

Error analysis is performed using Coefficient of determination  $R^2$ , Mean percentage Error (ME), Root Mean Square Error (RMSE) and Mean Absolute Percentage Error (MAPE). Table 6 shows the error analysis for  $R^2$ , ME, RMSE and MAPE for all the predicted  $C_p$ . The value of  $R^2$ , ME, RMSE and MAPE is calculated using the equation 7, 8, 9 and 10 respectively.

$$\text{Coefficient of determination } R^2 = \frac{\sum(\hat{y}-\bar{y})^2}{\sum(y_i-\bar{y}_i)^2} \quad (7)$$

$\hat{y}$ = CFD value (actual),  $\bar{y}$ = Average of observed value,  $y_i$ = Wind Tunnel reading (observed Exp),  $\bar{y}_i$ = Average of all reading.

$$\text{Mean absolute error is calculated (MAE) from} = \frac{1}{n} \sum_{i=1}^n (x_i - x) \quad (8)$$

where,  $x_i$ = Exp Value,  $x$ = CFD value

$$\text{Root mean square error (RMSE)} = \sum_{i=1}^N \left[ \frac{(Z_{fi}-Z_{oi})^2}{N} \right]^{1/2} \quad (9)$$

Where,  $Z_{fi}$  = CFD value and  $Z_{oi}$  = Exp value and Mean absolute percentage error is

$$\text{calculated (MAPE) from} = \frac{1}{n} \sum_{i=1}^n \frac{|(Actual-Forecast)|}{Actual} \times 100 \quad (10)$$

Previous researcher [27] have carried out error analysis by comparing a wind tunnel and CFD results for the building of C-plan shape building and rectangular building with an opening. Table 6 displays the error analysis for the present study using  $R^2$ , ME, RMSE and MAPE. From the results the calculated value of  $R^2$  is 0.9, which shows a very good curve fitting and for  $RMSE > 0.5$  is a good result and other data MAE and MAPE are also within the permissible error limits for all the building faces.

*Table 6 - Error analysis of predicted  $C_p$  for the model*

| <b>Building Faces</b> | <b><math>R^2</math></b> | <b>MAE</b> | <b>RMSE</b> | <b>MAPE</b> |
|-----------------------|-------------------------|------------|-------------|-------------|
| A                     | 0.9                     | 0.0284     | 0.0306      | 2.7513      |
| B                     | 0.9                     | 0.0175     | 0.0194      | 3.3782      |
| C                     | 0.9                     | 0.0256     | 0.0283      | 8.6880      |
| D                     | 0.9                     | 0.0201     | 0.0221      | 1.7195      |
| E                     | 0.9                     | 0.0487     | 0.0509      | 17.8990     |
| F                     | 0.9                     | 0.0321     | 0.0342      | 8.9875      |
| G                     | 0.9                     | 0.0374     | 0.0401      | 11.0106     |

#### **4.6. Wake Regions**

Wake regions are created in the downstream of the building because of the low wind velocity and turbulence. Usually for a bluff body such as buildings, the region of wake formation is large and smaller wake are found in streamline bodies. For Y plan shape building, broad wakes are observed in the leeward face of the building for the wind angles  $0^\circ$ ,  $45^\circ$  and  $90^\circ$ . The size of the wake depends on the shape of the body and type of turbulence flow. Figures 15(a),(b) and (c) display the wake formation for the wind angles  $0^\circ$ ,  $45^\circ$  and  $90^\circ$ .

#### **4.7. Numerically Predicted Wind Flow**

In figures 16(a), (b) and (C) presents the numerically predicted velocity flow patterns for the wind angles  $0^\circ$ ,  $45^\circ$  and  $90^\circ$ . Prior researcher Rajasekarababu et al and Prasenjit Sanyal et al [16,25] observed the flow pattern for setback buildings for wind angles  $0^\circ$  and  $90^\circ$  respectively. For all the wind directions the wind passes sharply from the inlet and strikes the building. In addition, the flow separation occurs at the corners which leads to the formation of negative pressures. In the figures 16 (a to c) the numbering are made from 1 to 9 in order to study physics of the flow pattern behind Y-plan shape tall building, number 1 in the figures 16 (a), (b) and (c) indicate the separation point where the flow gets separated, Number 2 indicates the shear layer, Number 3 indicates the recirculation regions, Number 4 indicates flow above the building, Number 5 indicates oncoming flow, Number 6 indicates stagnation flow, Number 7 indicates corner streamlines, Number 8 indicates Recirculation cavity due to suction, Number 9 indicates the expansion of wake regions. When the wind flow hits the building surface the flow gets separated and results in the formation of the vortex on the downstream of the bluff bodies such as a building.

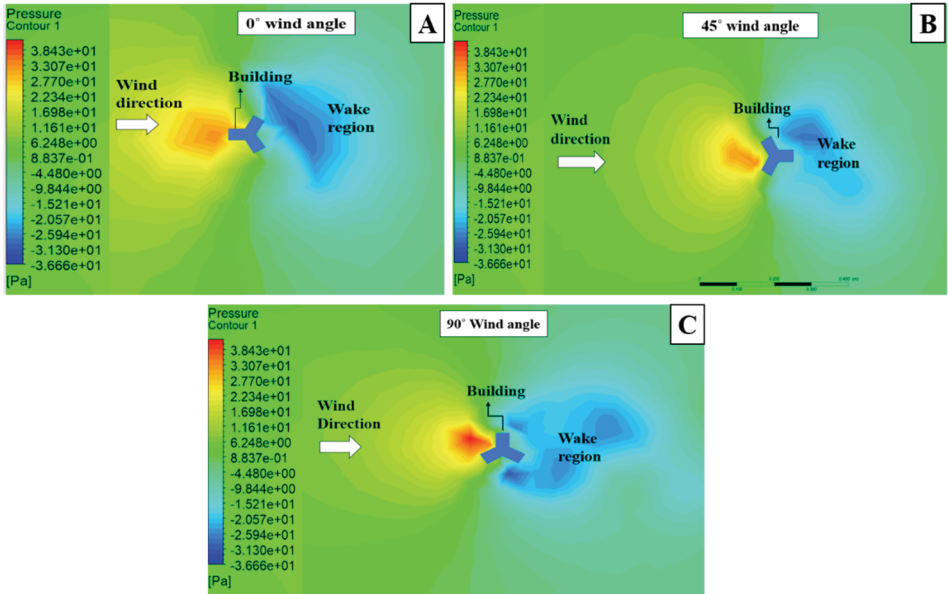


Figure 15 - Identification of wake regions (a) 0° wind angle (b) 45° wind angle (c) 90° wind angle

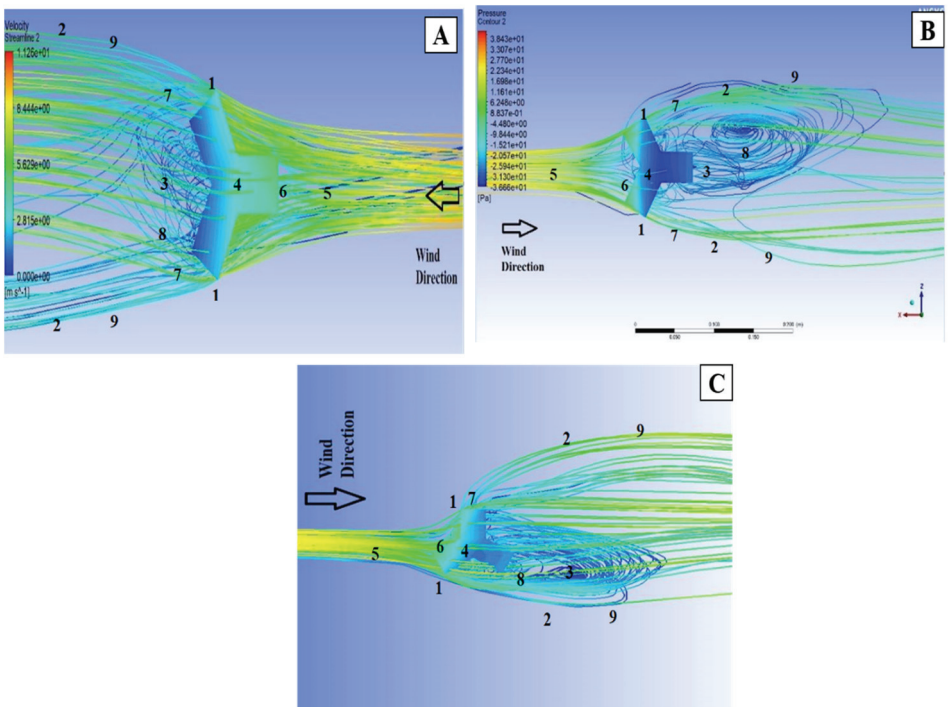


Figure 16 - Wind Flow pattern (a) 0° wind angle (b) 45° wind angle (c) 90° wind angle

### 4.8 Drag and lift coefficient

Cantilever structures such as buildings presented above the earth are subject to along wind, crosswind and torsional moment. Drag forces are caused due to along-wind force (i.e forces parallel to the body), lift forces are generated due to crosswind force (i.e perpendicular to along wind direction) and torsional moments are due to twisting of buildings [20]. The aerodynamic coefficients for buildings are found by using the following formula.

$$C_{D \text{ mean}} = \frac{F_D}{\frac{1}{2} \rho V_H^2 A} \tag{11}$$

$$C_{L \text{ mean}} = \frac{F_L}{\frac{1}{2} \rho V_H^2 A} \tag{12}$$

$C_{D \text{ mean}}$  and  $C_{L \text{ mean}}$  are the drag and lift coefficient respectively.  $F_D$  represents the drag force,  $F_L$  represents lift force,  $\rho$  represents the density of air,  $V$  represents a velocity of wind,  $A$  represents projected area.

The discussion about the drag and lift coefficient for the Y-plan shape building model for the particular wind velocity 10 m/s is made. The drag coefficient ( $C_D$ ) for 0° wind angle is 1.066 and the lift coefficient ( $C_L$ ) is 1.224. With regard to 45° wind angle, drag coefficient ( $C_D$ ) is 1.656 and lift coefficient ( $C_L$ ) is 1.662. Further with respect to 90° wind angle, drag coefficient ( $C_D$ ) is 1.648 and lift coefficient ( $C_L$ ) is 1.458. Maximum drag is found at 45° wind angle because it has less projected area when compared with all the other wind angles, followed by a 90° wind angle and 0° wind angle. The results of the drag force indicate that the drag force depends on the frontal area of the building i.e. façade or elevation. In order to reduce the drag force on buildings, modifications have to be done in elevations, building façade design. Many previous researchers [21,22 and 23] have worked on building modification in order to reduce the drag and lift coefficient on the buildings. Figure 17 shows the drag and lift coefficient for Y-plan shape building with wind angles 0°, 45° and 90°.

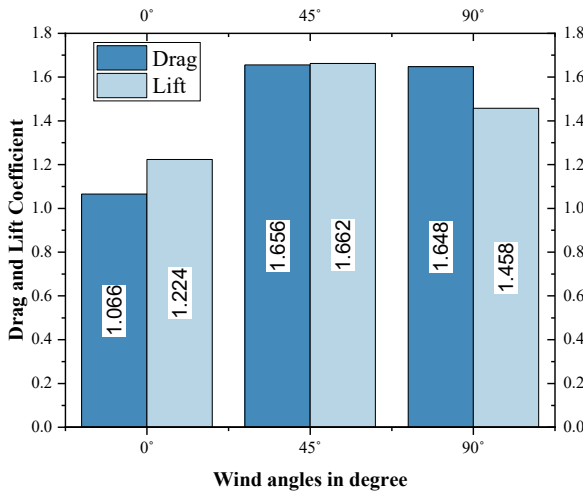


Figure 17 - shows the drag and lift coefficient for Y-plan shape buildings with wind angles 0°, 45° and 90°

## 5. CONCLUSIONS

Systematic wind pressure measurements are conducted to investigate the effect of wind flow around the Y-plan shape tall buildings. From the analysis of CFD and wind tunnel testing, it is possible to have an evident result in pressure distributions on various faces of the building at different wind angles. From the above study, the following conclusions are drawn.

- From the results of wind tunnel and CFD it is evident that high positive pressure coefficient ( $C_p$ ) is observed in face A, at  $0^\circ$  wind angle followed by faces B and C for  $45^\circ$  wind angle and further succeeded by the face B for  $90^\circ$  wind angle. Besides high negative pressure coefficient ( $C_p$ ) is observed in face G for  $0^\circ$  wind angle, followed by face D for  $45^\circ$  wind angle and further succeeded by face A for  $90^\circ$  wind angle.
- With regard to the pressure measurement along the perimeter of the building, a mild variation in the pressure at the top height  $4.15h/5$  is observed. For windward face the pressure reduces in the top height and in the leeward face the pressure increases. Whereas in the pressure distribution in the middle and lower height only a mild differences in pressure fluctuation occurs.
- With the support of turbulence model, realizable  $k-\varepsilon$  is very much useful for finding the external flow behaviour around the building such as stagnation flow, recirculation cavity, corner streamlines, etc. as represented in figure 16 and the identification of wake region is observed for the wind angle  $0^\circ$ ,  $45^\circ$  and  $90^\circ$ .
- The outcome of pressure coefficient ( $C_p$ ) obtained from CFD shows an equal agreement with the experimental values, and no substantial deviation occurs from the results obtained by performing of error analysis using  $R^2$ , MAE, RMSE and MAPE and the obtained values is within the allowable limits.
- The maximum drag coefficient is obtained in  $45^\circ$  wind angle is 55.34% higher than  $0^\circ$  wind angle drag coefficient and maximum lift coefficient is obtained at  $45^\circ$  wind angle is 35.7% higher than  $0^\circ$  wind angle lift coefficient.

The future scope of this work is to perform the wind flow around irregular plan shape building model under transient condition with different turbulence model and to study the dynamic behaviour of buildings subjected to wind loads.

## Acknowledgment

The author would like to thank Department of Civil Engineering in Mepco Schlenk Engineering College, India and Department of Aeronautical Engineering Kumaraguru Engineering College, India, for providing adequate Computation and Experimental facilities to carry out the research study and sincerer thanks to Institute of Engineers (India) IE(I) for its grateful financial support (Project ID: DR2020004) to complete the project work successfully.

## References

- [1] Yasushi Uematsu., Motohiko Yamada., Akira Inoue., Takeshi Hongo., Wind loads and wind-induced dynamic behavior of a single-layer latticed dome, *J. of Wind Eng and Industrial Aerodynamics.*, 66(3), 227-248, 1997
- [2] G, M, Richardson., R, P, Hoxey., A, P, Robertson., J, L, Short., The Silsoe Structures Building: Comparisons of pressures measured at full scale and in two wind tunnels, *J of Wind Eng and Industrial Aerodynamics.*, 72, 187-197, 1997
- [3] Chita Ganapathi, S., Harikrishna, P., Selvi Rajan, S., Effects of upstream terrain characteristics on aerodynamic coefficient of structures, *Archives of Civil and Mechanical Engineering.*, 17(4), 776-785, 2017
- [4] Ben Mou., Bao-Jie He., Dong-Xue Zhao., Kwok wing Chau., Numerical simulation of the effects of building dimensional variation on wind pressure distribution, *Engineering Application of Computational Fluid Mechanics.*, 11, 293-309, 2017
- [5] Gu, M., Quan, Y., Across-wind loads of typical tall buildings, *J of Wind Eng and Industrial Aerodynamics.*, 92, 1147-1165, 2004
- [6] Zhao Liu., Chaorong Zheng., Yue Wu., Richard G.J. Flay., Kan Zhang., Investigation on the effects of twisted wind flow on the wind loads on a square section megatall building, *J of Wind Eng and Industrial Aerodynamics.*, 191, 127-141, 2019
- [7] Ashutosh Sharma., Hemant Mittal., Ajay Gairola., Mitigation of wind load on tall building through aerodynamic modifications: Review, *J. of Building Eng.*, 18, 180-194, 2018
- [8] Kim Y., Kanda J., Characteristics of aerodynamic forces and pressures on square plan buildings with height variations, *J of Wind Eng and Industrial Aerodynamics.*, 98, 449-465, 2010
- [9] Biswarup Bhattacharyya., Sujit Kumar Dalui., Investigation of mean wind pressure on E plan shaped tall building. *Wind and structures.*, 26(2), 99-114, 2018
- [10] Rajdip Paul and Sujit Kumar Dalui, Wind effects on 'Z' plan-shaped tall building: a case study, *Int J Adv Struct Eng.*, 8, 319-335, 2016
- [11] W.P. Jones and B.E Launder, The prediction of laminarization with a two equation model of turbulence, *Int. Journal of Heat and Mass transfer.*, 15, 301-314, 1972
- [12] Hargreaves, D, M., Wright, N, G., On the use of the k- $\epsilon$  model in commercial CFD software to model the neutral atmospheric boundary layer, *J of Wind Eng. and Industrial Aerodynamics.*, 95, 355-369, 2007
- [13] Franke, J., Hellsten, A Schlunzen, K, H., Carissimo, B., The COST 732 Best practice Guidelines for CFD simulation of flow in urban Environment: A summary, *International J of Environment and Pollution.*, 44, 419-427, 2011
- [14] Tominaga, Y., Mochida, A., Yoshie, R., Kataoka, H., Nozu, T., Yoshikawa M., Shirasawa, T., AIJ guidelines for practical application of CFD to pedestrian wind environment around building, *J of Wind Eng. and Industrial Aerodynamics.*, 96 (10-11), 1749-176, 2008

- [15] Peter Sachs., Wind forces in Engineering, 2nd Edition., Pergamon Press., 1978
- [16] Rajasekarababu, K., Vinayagamurthy, B., Selvi Rajan. S., Experimental and Computational investigation of outdoor wind flow around a setback building, Building Simulation., 12, 891-904, 2019
- [17] Zhao, X., Ding, J.M., Sun, H., Structural Design of Shanghai Tower for wind Loads, Procedia Engineering., 14, 1759-1767, 2011
- [18] Suresh Kumar, K., Wind loading on tall buildings: Review of Indian Standards and recommended amendments, J of Wind Eng. and Industrial Aerodynamics., 204, 104240, 2020
- [19] Hellsten, A., Schunzen, K.H., Carissimo, B., (2007), Best Practice Guidelines for the CFD simulation of flow in the urban Environment, Brussels: COST office.
- [20] Y.C Kim, E.K Bandi, A.Yoshida, Y.Tamura, Response characteristics of super tall building – Effect of number of sides and helical angles, J of wind Eng. and Industrial Aerodynamics., 145, 252-262, 2015
- [21] Jiming Xie, Aerodynamic optimization of super tall buildings and its effectiveness assessment. J of wind Eng. and Industrial Aerodynamics., 130, 88-98, 2014
- [22] Eswara Kumar Bandi, Yukio Tamura, Akihito Yoshida, Yong Chul Kim, Qingshan Yang, Experimental investigation on aerodynamics characteristic of various triangular section high rise buildings., J of Wind Eng. and Industrial Aerodynamics, 122, 60-68, 2013
- [23] Hideyuki Tanaka, Yukio Tamura, Kazuo Ohtake, Masayoshi Nakai, Yong Chul Kim, Eswara Kumar Bandi, Aerodynamic and Flow Characteristics of Tall buildings with various Unconventional Configurations, International Journal of High-Rise buildings., 2(3), 213-228, 2013.
- [24] Souvik Chakraborty, Sujit Kumar Dalui, Ashok Kumar Ahuja, Wind load on irregular plan shaped tall building – a case study, Wind and Structures., 19 (1), pp. 59-73, 2014.
- [25] Prasenjit Sanyal, Sujit Kumar Dalui, Effect of courtyard and opening on a rectangular plan shaped tall building under wind load, International Journal of Advanced Structural Eng., 10, 169-188, 2018
- [26] Amin, J.A, Ahuja, A.K., Characteristic of wind forces and responses of rectangular tall buildings, International Journal of Advanced Structural Eng., 6(66), 2018
- [27] Monalisa Mallick, Abinash Mohanta, Awadhesh Kumar, Vivek Raj, Modelling of wind pressure coefficient in C-shaped building models, Modelling and simulation in Eng., 6524945, 2018



# Entropy Based Regional Precipitation Prediction in the Case of Gediz River Basin

Özgür BOZOĞLU<sup>1</sup>

Türkay BARAN<sup>2</sup>

Filiz BARBAROS<sup>3</sup>

## ABSTRACT

The Shannon's entropy concept is defined to measure the information content of hydrological processes in hydrology and water resources. Entropy concept has also provided an opportunity to solve several related topics in water resources engineering. The presented study aims to define the regional distribution of the expected long-term annual total precipitation, by using the entropy concept. For this purpose, the frequency analysis of the observed long-term total monthly precipitation data for each station is analyzed, and entropy values are calculated using the frequency histogram called "*Intensity Entropy – IE*". By using the IE values, it is possible to define the regional information of long-term expected precipitation even if the gauging stations have different observation periods without missing any information of available data. In addition, there is no need to complete the data of the missing observation years (months) to define the precipitation-elevation relations for producing an isometric map. In regional analysis, it is possible to create isoentropy map, by using the determined IE values for each gauging station. The IE method is performed and isoentropy map is created for Gediz Basin as a case study, and the a priori conditions of using IE method results for regional information are discussed in the paper.

**Keywords:** Gediz River Basin, water resources management, entropy, uncertainty, hydrological processes, intensity entropy.

## 1. INTRODUCTION

In water systems planning, using an objective criterion is essential to determine the information content of hydrological data. Hydrological processes must be measured in order to make optimal

---

Note:

- This paper has been received on April 28, 2020 and accepted for publication by the Editorial Board on January 18, 2021.
- Discussions on this paper will be accepted by September 30, 2022.

• <https://doi.org/10.18400/tekderg.724164>

1 Civil Engineering Department, Dokuz Eylul University, Izmir, Turkey - [zgr\\_tmz@hotmail.com](mailto:zgr_tmz@hotmail.com)  
<https://orcid.org/0000-0002-8991-8445>

2 Civil Engineering Department, Dokuz Eylul University, Izmir, Turkey - [turkay.baran@deu.edu.tr](mailto:turkay.baran@deu.edu.tr)  
<https://orcid.org/0000-0002-2325-2628>

3 Civil Engineering Department, Dokuz Eylul University, Izmir, Turkey - [filiz.barbaros@deu.edu.tr](mailto:filiz.barbaros@deu.edu.tr)  
<https://orcid.org/0000-0002-2697-911X>

decisions in the design and operation of water resources systems. However, in order to perform the measurement practice in an optimum way, the following questions must be answered: what, where, when and how often. In their studies, planners frequently use the concepts of expected information, available information, lack of information and increase in information and state that design parameters are based on the information brought by the measurements. However, there is no concrete definition of how information can be measured. Similarly, information cannot be defined directly like any statistical parameter; mostly variance, standard error or correlation coefficients are defined indirectly in terms of statistical magnitudes [1].

In order to demonstrate the measurability of the information content, the subject can be approached from another standpoint. Learning about any subject or event means learning about new situations that concern that subject or event. If previously known situations do not carry any innovation, they do not bring any new information. Therefore, if the degree of innovation of the situation in question can be measured, a criterion can be developed for the information it contains. Considering that, the simplest way to measure the degree of innovation in any situation is to determine the relative frequency of the situation therefore it can be concluded that information content can be defined by using the probability concept and probability rules [2].

Entropy is one of the methods to measure information content and has been used by researchers in wide range of disciplines, such as hydrology and water resources planning [3]. Entropy is a measure of the uncertainty or disorder of a variable. The probability mass function (p.m.f.) or probability density function (p.d.f.) of a random variable in a discrete or continuous form can be used to determine the entropy.

The entropy theory has been applied in hydrology and water resources for measuring the information content of random processes, evaluation of information transfer between hydrological processes, assessment of recharge systems for a river basin, evaluation of data acquisition systems, assessment of model performance, assessment of regional information on floods, and designing water quality monitoring network. Entropy concept is also an excellent tool for computing the information content of time series. The structure of the time series should be determined before the calculations are made. The comprehensive review of the application of entropy theory in hydrology and water resources is given by Singh [4, 5].

Determining the spatiotemporal variability of precipitation is essential in water resources research. For this reason, many researchers have contributed to this issue for years. One of them is Kawachi et al. [6], in which Shannon's informational theory is applied for determining the temporal variability of daily rainfall at 1107 stations in Japan to delineate water resources zones. Thus, the obtained entropy based climatic map presents the characteristics of nationwide rainfall of Japan.

Mishra et al. [7] analyzed monthly, seasonal and annual precipitation data sets by entropy method to assess the space-time variability of rainfall. The results indicate that the disorder in precipitation amount and the number of days with rain show a strong spatial gradient and could be related to significant historical drought periods.

Zhang et al. [8] used the optimal entropy model to analyze the spatiotemporal differences of monthly precipitation complexity in Heilongjiang, China. In this study, it has been demonstrated that agricultural production change is the main reason for the spatial difference of monthly precipitation complexity in the plain areas of the study.

Dey and Mujumdar [9] demonstrated that higher fraction of grid cells across the country shows an increasing trend in Relative Entropy (RE) which is measured as the degree of uniformity of rainfall. A significant increasing trend in RE affects the timing and amount of rainfall, which are crucial for sustainable planning and management of water in rainfed-agriculture practices.

Wang et al. [10] presented a multi-objective optimization technique based on information theory realized for a rainfall network design method in Wei basin, China. To design a multi-objective optimization technique, an integrated network design framework is developed for streamflow and precipitation networks. The results of the optimization method were further examined using an artificial neural network (ANN) model for streamflow simulation.

In information theory, uncertainty of a variable or the probability distribution of that variable (entropy) is the negative expected value of the logarithm of the probability density function of the variable. Entropy is also defined as the amount of *information gained*  $\equiv$  *reduction of uncertainty* through observations; in other words, the entropy criterion indirectly measures the information content. This concept is thought to be a measure of determining how much information can be gained from a measured parameter. Hence, Kawachi *et al.* [6] - *for daily precipitation* - and later Maruyama *et al* [11] - *for monthly precipitation* - used the apportionment entropy values to illustrate water resources zones and assessment of potential water resources availability.

The concept of entropy performs many roles in hydrology and water resources [12]:

- i) determines the uncertainty of hydrological processes in water resources engineering,
- ii) determines the probability distributions that will represent the process,
- iii) transfers the information between hydrological processes,
- iv) optimizes the measurement networks and defines optimal measurement intervals,
- v) defines the knowledge content of mathematical models,
- vi) performs the relations between processes and the operational performance of feeding systems and measurement networks, whereas providing the application of optimization and decision theory.

A review by Singh [13] discussed the frequency distributions, which have different origins based on different hypotheses and belong to different generating systems. This paper suggests various frequency distributions, which have been derived using different approaches, which include differential equations, distribution elasticity, genetic theory, generating functions, transformations, Bessel function, expansions, and entropy maximization. Each frequency distribution is used for several data analysis in hydrologic, hydraulic, environmental and water resources engineering.

These studies [6 - 11] have addressed the disorder (or uncertainty) in the intensity and occurrence of rainfall in time, which is the main constraint in water resources engineering. The most important information of developing a strategy for water use is to define the priorities, and make a decision for water allocation so as to define “water quantity”. The entropy concept, which is applicable to any distribution even if the probability distribution is unknown, is a convenient tool for defining disorder of rainfall.

On the other hand, if researchers aim to define regional information without missing any information from the available data with entropy concept, one of the fundamental steps of

determining entropy is to define validated regional class interval  $\Delta x$  for every single data set. Otherwise, the determined entropy values represent only the local information [12, 13] and the obtained regional information will be inaccurate. Another important problem for determining the regional information is the decay of data stationarity, which depends on climate change. To eliminate these problems, it is necessary to define validated regional class interval  $\Delta x$  and examine all of the data with trend analyses.

Hence, in the presented paper, an entropy method application on precipitation pattern is studied from a case area located in Turkey. Turkey is below the earth's average in terms of per capita water amount and among the water-stressed countries. A large number of reasons such as population growth, industrial wastes and adverse environmental conditions have affected water resources negatively. In Turkey, especially west and middle regions are in danger of drought. Among 25 river basins in Turkey, the Gediz River Basin, with its limited water resources, increasing population and industrial activities, was selected as a case study for water shortage conditions.

The objectives of this study are executing the degree of variability of the precipitation pattern using entropy theory in the Gediz River Basin and applying the intensity entropy (IE) method to monthly total precipitation series to discuss how and why entropy analysis can give reliable insights into multivariate hydrological processes. The study focused on increasingly obvious complexity evolution characteristics of the monthly precipitation series in Gediz River Basin, under the long-term influence of various natural factors and major agricultural developments. The approach in the presented study is to estimate the frequency analysis of precipitation records to define the region-wide water availability map.

The study will be significant for analyzing the variability of observed precipitation using the concept of entropy and forming a map by linking entropy and precipitation. In the following sections, applied method is presented in Section 2; available data and the study area are introduced in Section 3; the application and results are given in Section 4, and finally conclusions and future research suggestions are summarized in Section 5.

## 2. METHOD

Entropy is a value that can be determined by knowing or calculating the probability distribution function or probability density function of a random variable given in a discrete or continuous form using the information theory defined by Shannon [3]. Characteristically, increasing randomness or irregularity of the variable reduces the skewness of the probability distribution, thereby leading to an increase in entropy. Entropy takes the maximum value if the probability distribution is uniform without any deviation, whereas the occurrence of a specific value of the variable with a probability leads to the approach of entropy value to zero [13].

In this study, monthly rainfall intensities (monthly total rainfall) are considered as a random variable. The relationship between the probability of occurrence (frequency) of the variable at a selected time period and the monthly rainfall intensity is defined as entropy based expressions. Thus, the calculated entropy values are also called *Intensity Entropy* (IE).

An entropy value (H) for a set of probabilities  $P_1, P_2, \dots, P_n$  is defined by Shannon (1948) as;

$$H = - \sum_{i=1}^n p_i \log p_i \quad (\text{Eq. 1})$$

The negative sign ensures that the result is always positive or zero. If the monthly precipitation intensity (or sum) is considered as a random variable and the probability of occurrence in a precipitation series takes a value such as  $p_i$  then the intensity entropy ( $IE$ ) value at a station can be determined using equation (1). The  $p_i$  probabilities for a given station are defined for the discrete form by taking into account all available monthly precipitation values at this station and the probability of occurrence of these values.  $IE$  is calculated by following steps;

1. Complete years of monthly total precipitation series are collected for each station. Then, the monthly precipitation values are sorted in ascending order to form a dataset without any serial features (Hence, the total length of the series for the evaluated gauging stations will be reached,  $N = 12 \text{ months} * \text{Number of observation years}$ ).
2. The most important point in the frequency series is to determine what the class number will be or what the class range is. Various authors suggest various formulas about the class interval. Nevertheless, these formulas are only suggestive, they are not exact. The small number of classes leads to the loss of information provide in/by the series. It is recommended that due to the information loss, the number of classes should not be less than four. On the other hand, too many classes give difficulty in interpreting and operating the series, thus the number of classes should not be more than eight. One of the suggested rules is that the number of classes is chosen as the square root of number of observations [14]. In presented study, the observed monthly total rainfall values is divided into  $k$  equally spaced classes.
3. The class width is obtained by subtracting the smallest value from the largest value in the sequence and dividing this difference by the number of classes. However, in the proposed study, the smallest value in the sequence, that is, the smallest monthly total rainfall value is zero for each station. So that the class interval is obtained by dividing the largest monthly total precipitation value  $R_{max}$  in the ascending sorted series by the number of class expressed above ( $k$ ).

$$\Delta x = \frac{R_{max}}{k} \quad (\text{Eq. 2})$$

4. The frequency value for each class is calculated and a frequency distribution table is generated.
5. The relative frequency values in each range are calculated to obtain a discrete probability density function for all monthly precipitation values.
6.  $IE$  entropy value can be calculated using these relative frequencies and the formula is as follows.

$$IE = \sum_{i=1}^k \frac{f_i}{N} \ln \frac{f_i}{N} \quad (\text{Eq. 3})$$

$k$  in the Eq. 3 means the number of classes and the  $f_i$  is frequency value for each class. Since the logarithm is used at base  $e$ , the  $IE$  entropy value unit is “napier”.

The  $IE$  value, defined in the semi-infinite range  $0 \leq IE < \infty$ , is a measure used to express the irregularity of the monthly rainfall intensity. The less disordered intensity value is measured with a smaller  $IE$  value, thus indicating that the frequency distribution of the

monthly precipitation value is more skewed. On the other hand, definition of monthly precipitation with a wider range leads to much more irregular density values and larger *IE* values. However, the probability density function of the precipitation intensity is defined as a positive x-axis (horizontal axis), which always includes the zero origin due to the non-negative precipitation. The increase in *IE* value creates an expectation for an increase in the expected monthly rainfall value. In other words, there is a positive correlation between the *IE* value and the expected monthly rainfall. For this reason, the *IE* value is indicative of the total amount of rainfall [11]. It is considered that observations are random and so there is no autocorrelation between them [15].

On the other hand, it is known that the selection of  $\Delta x$  is a crucial problem, such that each specified class interval size gives a different reference level of zero uncertainty with respect to the computed entropies. While researchers approximate the discrete probabilities  $p_i$  by using  $f(x)\Delta x$ , where  $f(x)$  is the relative class frequency and  $\Delta x$ , the size of class intervals for continuous variables, various entropy measures become relative to the discretizing interval  $\Delta x$  and change in value as  $\Delta x$  changes [12, 16]. Hence, to define the regional information, same class intervals are used for all frequency analyses. If individual class ranges are selected for stations based on their own data and a specific figure is used for the whole basin stations, regional information can be obtained, as described in Fig. 1.

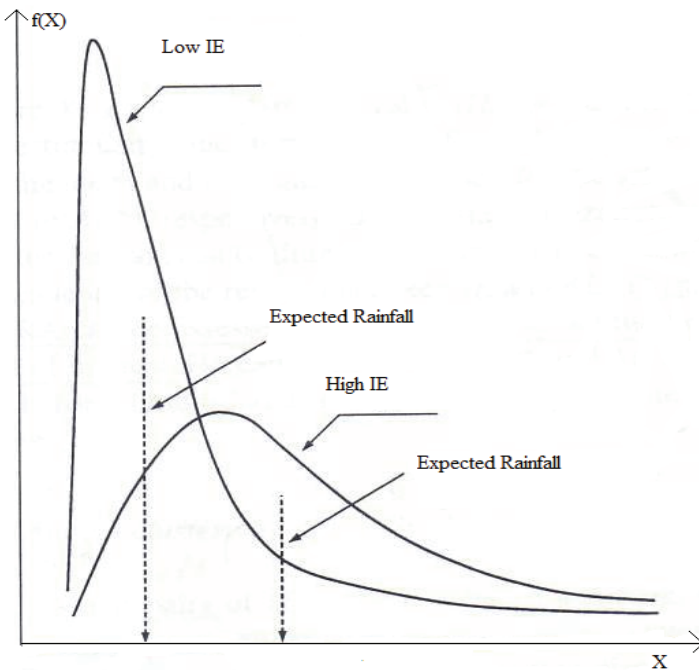


Figure 1 - Expected Precipitation with *IE*.

Expected rainfall values increase in the form given in Figure 1 with increasing *IE* results. This suggests that *IE* has a positive correlation with the expected precipitation and can therefore be an alternative to the prediction of total precipitation [11]. Thus *IE* values come from the

frequency analyses of data sets, *IE* can be used to define the regional information even if stations have different observation periods. Other advantages of this method are;

- i) there is no need to complete the missing observation data, since, no need to define mutual observation period for the basin,
- ii) no need to define elevation–precipitation relations and orographic maps for homogenizing the determined expected precipitation values, since *IE* value is indicative of the total amount of rainfall at observed site.

### 3. DATA AND STUDY AREA

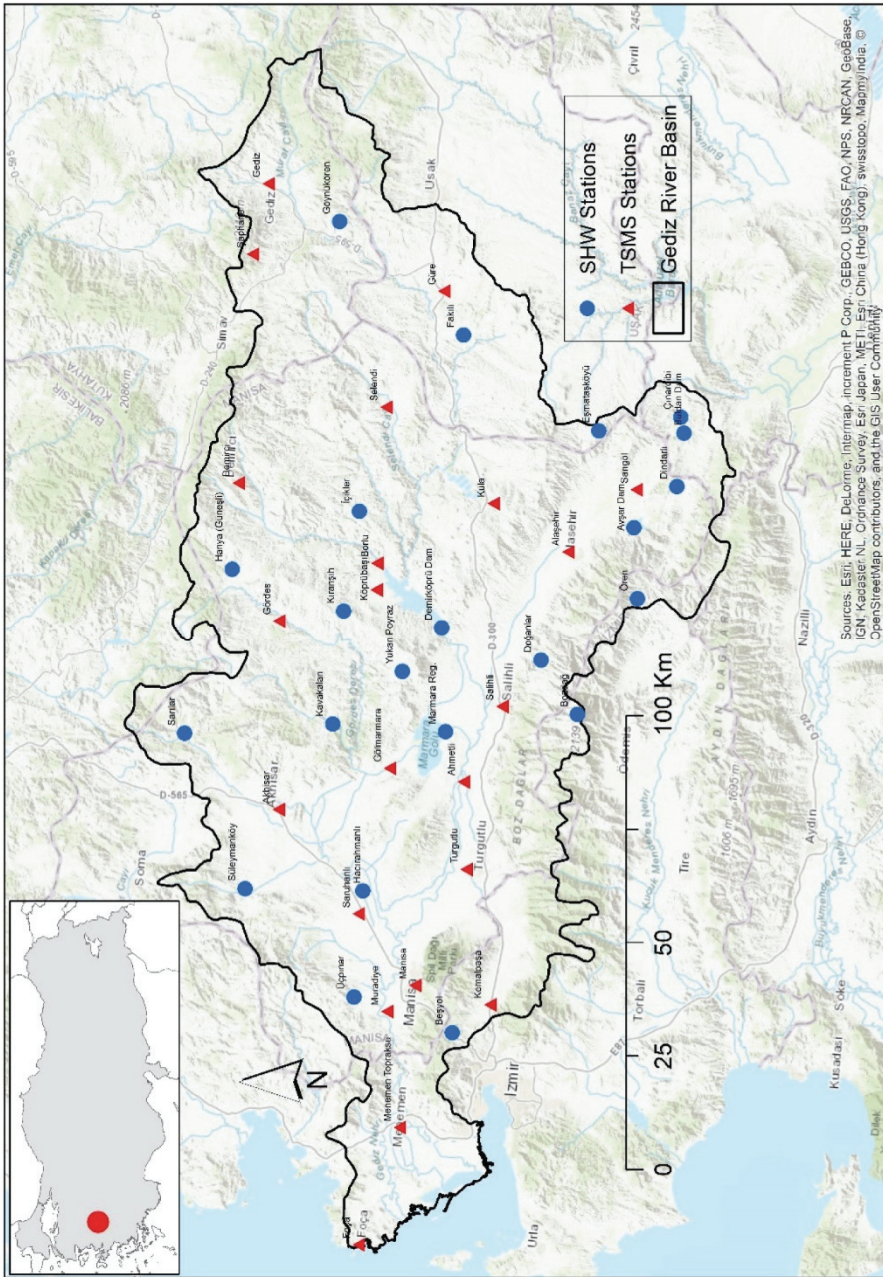
The presented study is carried out with the available precipitation data in the Gediz Basin, which is located in the western part of Turkey within the borders of the Aegean Region. The average annual precipitation in the Gediz Basin is approximately 635 mm. The Gediz basin is the 20<sup>th</sup> of Turkey's 25 major river basins, with a drainage area of 17,500 km<sup>2</sup> and the 21<sup>st</sup> with an annual surface water potential of 1.95 billion m<sup>3</sup>. These values are 2.2 % of the country's surface area and 1.7 % of the country's water potential [17].

The Gediz River Basin is one of the most important water basins located within İzmir Metropolitan Municipality boundaries. The Gediz River meets both agricultural and domestic water demand of Izmir city. The Gediz delta and wetlands (İzmir Bird Paradise provide habitat for 205 bird and 308 plant species) are conservation areas protected by law. It is also of particular importance that it is an area included in the Ramsar Convention in 1997 [17].

In Gediz Basin, monthly total precipitation data of 44 gauging stations, which have more than 19 years of observation (number of monthly data are greater than 228), are evaluated. The State Hydraulic Works (SHW) operates 22 of stations and the others 22 operates by the Turkish State Meteorological Service (TSMS). The locations of the stations are presented in Figure 2.

As it is mentioned before, to define the decay of data stationarity depends on the effects of climate change, the first step all of the data sets must examined with trend analyses. As given in Tables 1 and 2, the earliest historical observation throughout the region begins in 1927 and the latest data evaluated belongs to 2006. In trend analyses, the available data from SHW and TSMS stations were investigated for a priori trends; both for monthly and annual total precipitation values. The trend analyses are performed by parametric and non-parametric methods. The results showed that most of the monthly data have negative/positive trends but the annual data series do not have statistically significant trends. To test the trend parameters, Student-t and Mann-Kendall test statistics were used [18].

The results of trend analyses showed that the annual data can be acceptable first order stationary [18]. Hence, the monthly data, which verified that there is no trend in annual period of the earliest historical observation throughout the region from 1927 to 2006 are used for defining the regional information. The unbiased statistical parameters related to the observation values of the examined stations are presented in Tables 1 and 2, for annual total precipitation values.



Sources: Esri, HERE, DeLorme, Intermap, increment P Corp., GEBCO, USGS, FAO, NPS, NRCAN, GeoBase, IGN, Kadaster NL, Ordnance Survey, Esri, Japan, MEI, Swisstopo, Swisstopo, MapmyIndia, © OpenStreetMap contributors, and the GIS User Community

Figure 2 - Gediz Basin and the Station Locations of SHW and TSMS [18].

#### 4. APPLICATION

Although the stations have different observation durations, Intensity Entropy (*IE*) can be used in the definition of regional information since it defines the total monthly rainfall intensity obtained as a result of frequency analysis by defining validated regional class interval  $\Delta x$ . Therefore, it is possible to use the available data (except very short-term stations) in the basin. However, the reliability of the data should be investigated by analyzing the stations one by one before performing frequency analysis. If the data can be acceptable as first order stationary, than *IE* values can be calculated without any extension/completion for missing years from frequency analyses. There is no need to define mutual observation period for the basin and also no need to determine precipitation/evaluation relationship for the region.

*Table 1 - Observation period, Altitude and Main Statistical Parameters of Total Annual Precipitation Values of TSMS.*

| Station Name     | Observation Period | Altitude | Mean (mm)     | Std.Dev. (mm) | Skewness     | Variability (%) | Kurtosis     |
|------------------|--------------------|----------|---------------|---------------|--------------|-----------------|--------------|
| Ahmetli          | 1938 – 1988        | 100      | 485.65        | 125.12        | -1.204       | 25.76           | 2.600        |
| Akhisar          | 1929 -             | 93       | 588.76        | 132.87        | 0.464        | 22.56           | -0.198       |
| Alaşehir         | 1931 -             | 189      | 482.87        | 111.77        | 0.387        | 23.14           | -0.631       |
| Borlu            | 1964 – 1982        | 250      | 541.12        | 100.46        | 0.242        | 18.56           | -0.189       |
| Demirci          | 1929 -             | 851      | 646.55        | 143.30        | -0.014       | 22.16           | -0.708       |
| Foça             | 1957 – 1994        | 10       | 552.39        | 115.75        | 0.051        | 20.95           | 0.040        |
| Gediz            | 1934 -             | 825      | 602.37        | 119.54        | 0.202        | 19.84           | -0.531       |
| Gölmarmara       | 1939 – 1992        | 150      | 546.22        | 129.23        | 0.602        | 23.65           | -0.018       |
| Gördes           | 1929 – 1997        | 550      | 638.46        | 151.61        | 0.473        | 23.74           | 0.860        |
| Güre             | 1964 – 1995        | 650      | 452.26        | 78.89         | 0.105        | 17.44           | -1.282       |
| Kemalpaşa        | 1938 – 1997        | 200      | 1071.88       | 405.50        | 2.347        | 37.83           | 7.311        |
| Köprübaşı        | 1967 -             | 250      | 447.80        | 94.63         | 0.415        | 21.13           | 0.418        |
| Kula             | 1929 – 1991        | 675      | 590.44        | 142.36        | 0.578        | 24.11           | 0.033        |
| Manisa           | 1929 -             | 71       | 727.03        | 162.75        | 0.514        | 22.38           | -0.024       |
| Menemen Topraksu | 1929 – 1995        | 10       | 537.57        | 144.89        | 0.556        | 26.95           | 0.031        |
| Muradiye         | 1964 – 1987        | 25       | 648.65        | 160.36        | 0.196        | 24.72           | -0.388       |
| Salihli          | 1939 -             | 111      | 489.44        | 98.32         | 0.485        | 20.09           | 0.109        |
| Sarıgöl          | 1963 – 1986        | 225      | 486.71        | 99.40         | 0.250        | 20.42           | -1.204       |
| Saruhanlı        | 1959 – 1996        | 50       | 454.73        | 92.09         | 1.197        | 20.25           | 1.651        |
| Selendi          | 1955 – 1991        | 575      | 514.41        | 110.21        | 0.199        | 21.42           | -0.763       |
| Şaphane          | 1964 – 1990        | 925      | 677.84        | 112.28        | 0.272        | 16.56           | -0.874       |
| Turgutlu         | 1929 -             | 120      | 584.02        | 140.34        | 0.578        | 24.03           | -0.098       |
| <b>MEAN</b>      |                    |          | <b>580.33</b> | <b>135.08</b> | <b>0.404</b> | <b>22.62</b>    | <b>0.279</b> |

To define the regional information, the critical period of observations (number of years) is defined first; then raingauges which have less than the designated critical number of observation years are screened out and the selected stations which have enough data to be processed are determined significant statistical analysis were evaluated.

Table 2 - Observation period, Altitude and Main Statistical Parameters of Total Annual Precipitation Values of SHW.

| Station Name      | Observation Period | Altitude | Mean (mm)     | Std. Dev. (mm) | Skewness     | Variability (%) | Kurtosis     |
|-------------------|--------------------|----------|---------------|----------------|--------------|-----------------|--------------|
| Avşar Dam         | 1980 -             | 275      | 430.53        | 75.55          | -0.039       | 17.54           | -1.314       |
| Beşyol            | 1976 -             | 530      | 772.68        | 183.39         | 0.563        | 23.73           | -0.061       |
| Bozdağ            | 1961 -             | 1150     | 1258.62       | 338.44         | 1.014        | 26.88           | 1.600        |
| Buldan Dam        | 1967 -             | 470      | 468.34        | 95.07          | 0.486        | 20.30           | -0.625       |
| Çınardibi         | 1961 – 2002        | 705      | 932.89        | 215.89         | 0.486        | 23.14           | 0.520        |
| Demirköprü Dam    | 1962 – 1993        | 290      | 486.65        | 101.40         | 0.009        | 20.83           | -0.576       |
| Dindarlı          | 1962 -             | 685      | 455.36        | 96.10          | 0.298        | 21.10           | 0.045        |
| Doğanlar          | 1970 -             | 650      | 630.46        | 152.52         | 0.323        | 24.19           | 0.497        |
| Eşmataşköyü       | 1962 -             | 930      | 468.62        | 97.70          | 0.754        | 20.84           | 0.293        |
| Fakılı            | 1962 -             | 715      | 447.13        | 77.95          | 0.436        | 17.43           | -0.755       |
| Göynükören        | 1966 – 2003        | 1020     | 467.92        | 133.60         | -0.264       | 28.55           | -0.290       |
| Hacırahmanlı      | 1961 – 1997        | 45       | 483.33        | 108.81         | 0.778        | 22.51           | 1.084        |
| Hanya (Güneşli)   | 1961 – 1995        | 640      | 634.88        | 157.95         | 0.231        | 24.88           | -0.243       |
| İçikler           | 1961 -             | 710      | 568.13        | 131.65         | 0.253        | 23.17           | -0.742       |
| Kavakalan         | 1962 – 1998        | 460      | 625.48        | 145.26         | 0.579        | 23.22           | 1.019        |
| Kıranşih          | 1962 -             | 670      | 589.24        | 124.79         | 0.320        | 21.17           | -0.323       |
| Marmara Lake Reg. | 1961 – 2001        | 75       | 435.22        | 77.01          | 0.227        | 17.69           | -0.239       |
| Ören              | 1961 -             | 940      | 735.21        | 256.56         | -0.212       | 34.89           | 0.731        |
| Sarılar           | 1962 -             | 340      | 595.22        | 146.70         | 0.519        | 24.64           | 0.273        |
| Süleymanköy       | 1962 – 1997        | 240      | 472.56        | 99.52          | 0.231        | 21.06           | -0.708       |
| Üçpınar           | 1961 -             | 100      | 547.92        | 165.78         | 0.570        | 30.25           | 0.045        |
| Yukarı Poyraz     | 1962 - 2003        | 630      | 588.52        | 115.66         | 0.727        | 19.65           | 0.611        |
| <b>MEAN</b>       |                    |          | <b>595.22</b> | <b>140.79</b>  | <b>0.377</b> | <b>23.08</b>    | <b>0.038</b> |

Since the presented study is an example application of the methodology proposed for developing a map of water availability, trend analysis of monthly total precipitation data (up to 2006) are used to determine the *IE* values. In the case study of Gediz Basin, 44 precipitation-gauging stations with long-term data are evaluated for determining the *IE* values. The results show that the expected (mean) monthly total precipitation and the mean annual total precipitation values have strong statistical relations between the *IE* values ( $r = 0.996$  and  $r = 0.990$  respectively) on the Gediz catchment basis. Consequently, *IE* values can be used to define regional information for the expected value of annual total precipitation, which have the same meaning of potential water resources availability of the Gediz basin.

#### 4.1. Turkish State Meteorological Service (TSMS) Rainfall Observation Stations in the Basin

Throughout the twenty-three precipitation observation stations belonging to the Turkish State Meteorological Service (TSMS) in the Gediz Basin, Yarbasan was not suitable for use in entropy calculations due to its eight-year total monthly rainfall observation values. The same interval width (15 mm/month) was used at all stations for frequency analysis. The longest

observed observations (76 years \* 12 months) belong to Akhisar and Manisa; the shortest observations (19 years \* 12 months) belong to Borlu station.

Relative frequency histogram and frequency density functions were obtained and plotted for all stations used in the study. In the present study, only graphs belonging to Ahmetli station are presented as an example. The absolute frequency histogram  $\{f_i\}$  obtained for the total monthly rainfall and frequency density values calculated using relative frequency  $\{f_i/N\}$  at Ahmetli station are presented in Figure 3.

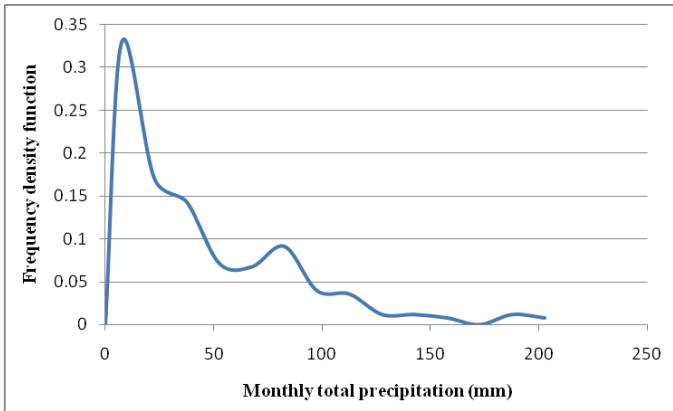


Figure 3 - Frequency Density Function of Ahmetli Station.

#### 4.2. State Hydraulic Works (SHW) Precipitation Observation Stations in the Basin

The longest evaluated observations belong to Kıransh (44 years \* 12 months), Bozdağ (44 years \* 12 months) and Üçpınar (44 years \* 12 months) stations, and the shortest observation period (25 years \* 12 months) belong to Avşar Dam station. Although there are no shortcomings in the observations of the six stations used in the study, some years of the observations of the remaining sixteen stations are missing due to some observational errors. However, in the calculation of  $IE$ , it is considered that there is no autocorrelation between years and each data is random. Therefore, the years with observational errors or deficiencies on a monthly basis were ignored. If any year or years are missing within the observation range, the present observations were studied as if there were no missing data in the series.

#### 4.3. Isometric Maps

The isometric map, which refers to the isometric lines of the mean annual total precipitation for observation period (Table 1 and 2) are drawn by using Surfer mapping tools by using linear interpolation approach and presented in Figure 4. Since the isohyetal maps need to define elevation–precipitation relations and use orographic maps for homogenizing of data, this map is diverged from standard isohyetal lines. Figure 4 was drawn by using determined long-term mean of the raw data for the whole observation periods.

In Figure 5, isoentropy maps are presented which are drawn by using same approach above. For isoentropy map, the determined  $IE$  values (Table 3) are used.





Table 3 - Total Annual Precipitation and Entropy Values of Stations.

| Station Name      | Altitude (m) | Annual Total Average RainFall | IE values |
|-------------------|--------------|-------------------------------|-----------|
| Ahmetli           | 100          | 485.66                        | 1.9667    |
| Akhisar           | 93           | 585.11                        | 2.1725    |
| Alaşehir          | 189          | 467.22                        | 1.9221    |
| Avşar Dam         | 275          | 430.54                        | 1.8622    |
| Beşyol            | 530          | 772.68                        | 2.3399    |
| Borlu             | 250          | 541.12                        | 2.0823    |
| Bozdağ            | 1150         | 1258.62                       | 2.8409    |
| Buldan Dam        | 470          | 468.34                        | 1.9572    |
| Çınardibi         | 705          | 932.89                        | 2.5249    |
| Demirci           | 851          | 581.42                        | 2.2826    |
| Demirköprü Dam    | 290          | 466.32                        | 2.0095    |
| Dindarlı          | 685          | 455.37                        | 1.9459    |
| Doğanlar          | 650          | 630.46                        | 2.2410    |
| Eşmataşköyü       | 930          | 468.63                        | 1.9653    |
| Fakılı            | 715          | 447.13                        | 1.9151    |
| Foça              | 10           | 555.24                        | 2.0808    |
| Gediz             | 825          | 569.79                        | 2.1322    |
| Gölmarmara        | 150          | 546.23                        | 2.1026    |
| Gördes            | 550          | 638.46                        | 2.2399    |
| Göynükören        | 1020         | 467.93                        | 1.9484    |
| Güre              | 650          | 452.27                        | 1.9066    |
| Hacırahmanlı      | 45           | 483.33                        | 1.9653    |
| Hanya (Güneşli)   | 640          | 634.88                        | 2.2409    |
| İçikler           | 710          | 568.13                        | 2.1477    |
| Kavakalan         | 460          | 625.49                        | 2.2097    |
| Kemalpaşa         | 200          | 1071.88                       | 2.6545    |
| Kıranşih          | 670          | 589.25                        | 2.1659    |
| Köprübaşı         | 250          | 447.80                        | 1.9166    |
| Kula              | 675          | 590.45                        | 2.1728    |
| Manisa            | 71           | 728.83                        | 2.3722    |
| Marmara Lake Reg. | 75           | 435.23                        | 1.8667    |
| Menemen Topraksu  | 10           | 537.57                        | 2.0571    |
| Muradiye          | 25           | 648.74                        | 2.2117    |
| Ören              | 940          | 735.21                        | 2.3539    |
| Salihli           | 111          | 490.15                        | 1.9979    |
| Sarıgöl           | 225          | 486.72                        | 2.0030    |
| Sarılar           | 340          | 595.23                        | 2.1563    |
| Saruhanlı         | 50           | 454.74                        | 1.9198    |
| Selendi           | 575          | 514.42                        | 2.0522    |
| Süleymanköy       | 240          | 472.56                        | 1.9604    |
| Şaphane           | 925          | 677.85                        | 2.3085    |
| Turgutlu          | 120          | 584.02                        | 2.1441    |
| Üçpınar           | 100          | 547.93                        | 2.0710    |
| Yukarı Poyraz     | 630          | 588.53                        | 2.1617    |

## 5. RESULTS

The entropy values of the precipitation gauging stations with long-term observations in the Gediz basin, define the expected values for the long-term average monthly precipitation. The mean annual total precipitation and the  $IE$  values, which were determined by using the monthly series (Table 3) are also performed for the mutual information. The result for the linear regression analysis between the  $IE$  values and mean monthly and annual total precipitation are presented in Figure 6 and 7 respectively.

At all stations evaluated both the mean monthly total precipitation (Figure 6) and mean annual total precipitation during the observation period (Figure 7) show that the results are quite consistent. The conversion correlations between intensity entropy and mean monthly/annual total precipitation show a high statistical dependence for logarithmic relationship ( $R^2 = 0.991 \rightarrow r = 0.996$  for monthly values and  $R^2 = 0.979 \rightarrow r = 0.990$ ).

The annual total precipitation values versus calculated  $IE$  values ( $r = 0.99$ ) are evaluated by graphical analysis and the relationship as given in Eq. 4 was obtained from the graph given in Figure 7.

$$P = 52,58. e^{1,12IE} \quad (\text{Eq. 4})$$

The determined  $IE$  values and the regional  $IE$  distribution of the Gediz basin are presented in Figure 8 and 9. The regional distribution was achieved through basin-wide interpolation of the  $IE$  values by the Spline algorithm, and are presented in Figure 9. By using Fig. 9 and Eq. 4, researchers can estimate total annual precipitation, which also means gross water potential in the long-term period.

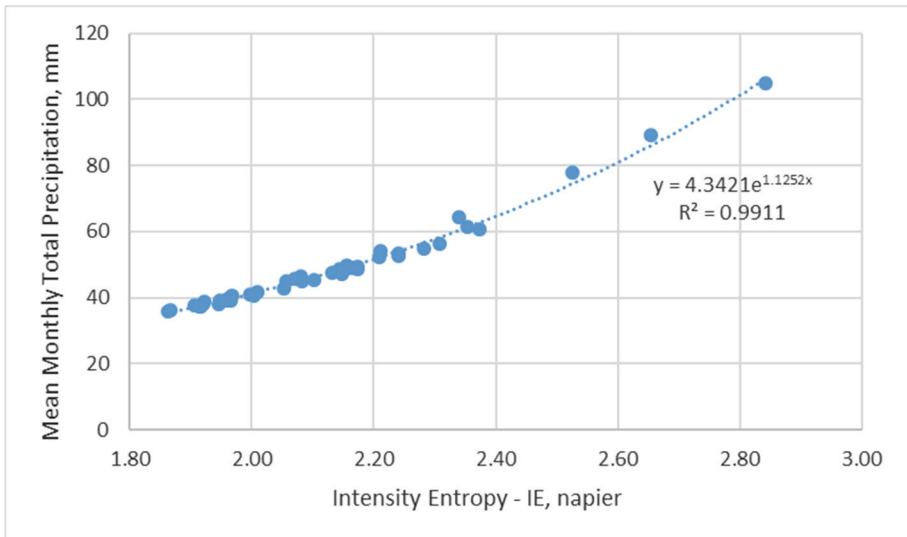


Figure 6 - The relationship between the Mean Monthly Total Precipitation and  $IE$  values in Gediz basin.

Entropy Based Regional Precipitation Prediction in the Case of Gediz River Basin

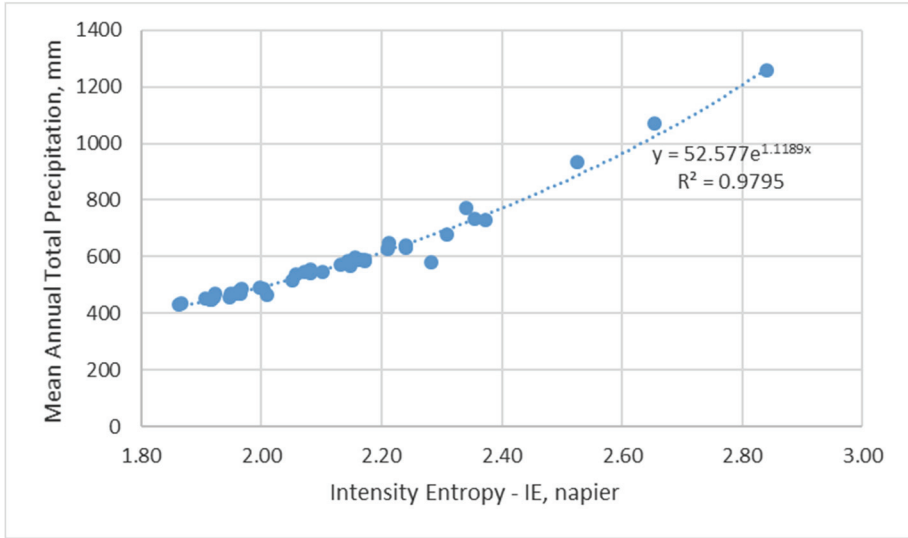


Figure 7 - The relationship between the Mean Annual Total Precipitation and IE values in Gediz basin.

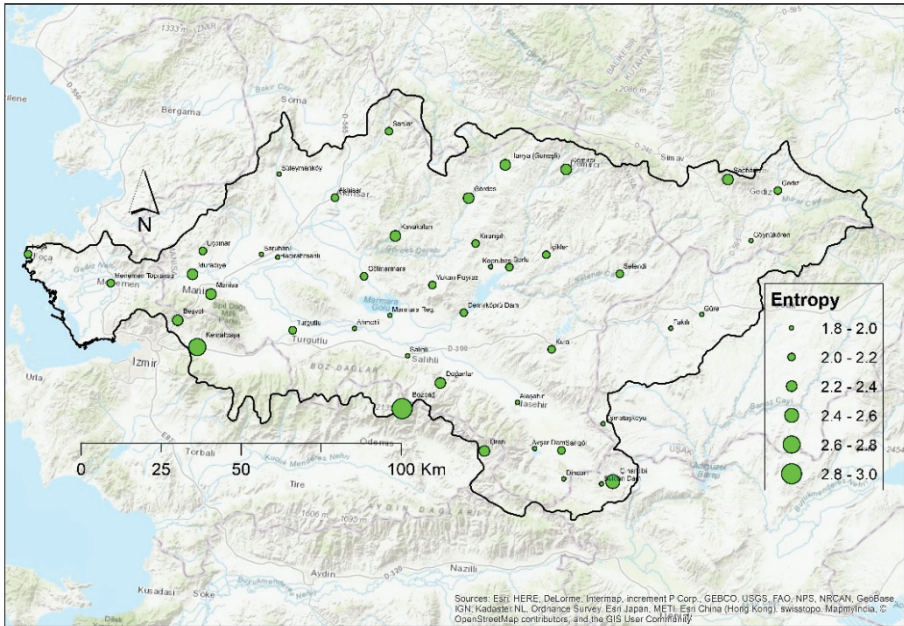


Figure 8 - The determined IE values in Gediz Basin.

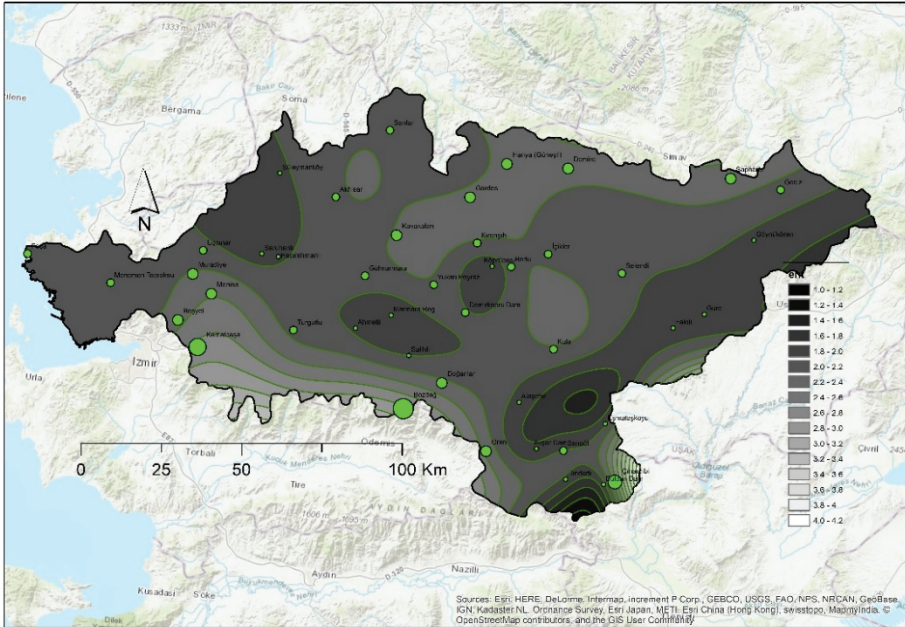


Figure 9 - Intensity Entropy -IE Distribution in Gediz Basin.

## 6. CONCLUSION

Employing intensity entropy method based on Shannon's informational entropy theory, a methodology is proposed for assessing potential water resources availability in terms of disorder of precipitation. Unlike traditional statistics such as mean, standard deviation, and variance, the entropy method focuses on the information content generated by variable monthly rainfall for the assessment of potential water resources availability.

Consequently, in the presented study, the expected value of long-term annual total precipitation is determined by entropy theory. The frequency analysis of the observed long-term total monthly precipitation is carried out and entropy values are determined by the histogram of frequency - "Intensity Entropy - IE".

Within the scope of this study, monthly rainfall intensities (monthly total rainfall precipitation) were considered as a random variable. The relationship between the probability of occurrence (frequency) of the variable at a selected time period and the monthly rainfall intensity is defined as entropy based expression. *IE* is used to define the regional information even if stations have different observation periods.

To avoid any effects of climate change, all available data were examined with trend analyses. To define regional information without missing any information from the available data and to obtain regional information accurately with entropy concept, a validated regional class interval  $\Delta x$  has been determined by using all available data.

The advantage of the proposed method is that it is possible for the researchers to use all the data sets from different periods in execution. In addition, a more simple-fast-reliable tool has been obtained as an alternative to similar methods.

The entropy-based methodology is applicable to any distribution whether the distribution is a priori known or unknown and although rain-gauges may not have the same number of observation years at every station.

The presented case study for the Gediz Basin offers a powerful tool to help detect water availability by relating the monthly total precipitation and intensity entropy. Local precipitation variations over the Gediz River Basin are reviewed by frequency analysis and consequently entropy concept.

### **Acknowledgement**

Authors would like to acknowledge to Assoc. Prof. Dr. Ali GÜL for his great contribution to the mapping process of the manuscript.

### **References**

- [1] Harmancioglu N. B., Singh V. P., An Information-Based Approach to Monitoring and Evaluation of Water Quality Data. Athens, ECOWARM, European Conference on Advances in Water Resources Technology, A.A. Balkema Publishers, pp. 377-386, 1991.
- [2] Cherry C., On Human Communication: A Review. A Survey and a criticism. Massachusetts, the Technology Press of Massachusetts Institute of Technology, 333 p, 1957.
- [3] Shannon C.E., Mathematical Theory of Information. In The Mathematical Theory of Information, the University of Illinois Press: Urbana, IL, USA, 27: 170–180, 1948.
- [4] Singh V. P., The Use of Entropy in Hydrology and Water Resources. Hydrological Processes, Hydrol. Process., 11: 587-626, DOI: 10.1002/(SICI)1099-1085(199705)11:6<587::AID-HYP479>3.0.CO;2-P, 1997.
- [5] Singh V.P., The Entropy Theory as a Tool for Modelling and Decisionmaking in Environmental and Water Resources. Water S.A. 26(1):1-10., 2000.
- [6] Kawachi T., Maruyama T., Singh V. P., Rainfall Entropy for Delineation of Water Resources Zones in Japan, Journal of Hydrology, 246: 36-44, DOI: 10.1016/S0022-1694(01)00355-9, 2001.
- [7] Mishra A.K., Ozger M., Singh V.P., An Entropy Based Investigation into the Variability of Precipitation, Journal of Hydrology, 370:139–54, DOI: 10.1016/j.jhydrol.2009.03.006, 2009.
- [8] Zhang L., Li H., Liu D., Fu Q., Li M., Faiz M., A., Khan M., I., Li T., Identification and application of the most suitable entropy model for precipitation complexity measurement. Atmospheric Research 221, 88-97, ISSN 0169-8095, DOI: 10.1016/j.atmosres.2019.02.002, 2019.

- [9] Dey P., Mujumdar P.P., On the uniformity of rainfall distribution over India, *Journal of Hydrology*, 578, 124017, ISSN 0022-1694, DOI: 10.1016/j.jhydrol.2019.124017, 2019.
- [10] Wang W., Wang D., Singh V.P., Wang Y., Wu J., Zhang J., Liu J., Zou Y., He R., Information theory-based multi-objective design of rainfall network for streamflow simulation. *Advances in Water Resources*. 135-103476, ISSN 0309-1708, DOI: 10.1016/j.advwatres.2019.103476, 2020.
- [11] Maruyama T., Kawachi T., Singh V.P., Entropy-based Assessment and Clustering of Potential Water Resources Availability. *Journal of Hydrology*, 309, 104-113, DOI: 10.1016/j.jhydrol.2004.11.020, 2005.
- [12] Baran T., Hidrolojik süreçlerin bilgi içeriğindeki değişim miktarı olarak entropi tanımı. Dokuz Eylül Üniversitesi, Fen Bilimleri Enstitüsü, İnşaat Mühendisliği Bölümü, Hidrolik-Hidroloji ve Su Kaynakları Doktora Tezi No: 10, 1993
- [13] Singh V.P., Systems of Frequency Distributions for Water and Environmental Engineering. *Physica A: Statistical Mechanics and its Applications*, 506: 50-74, ISSN 0378-4371, DOI: 10.1016/j.physa.2018.03.038, 2018.
- [14] Hines W.H., Montgomery D.C., Goldsman D.M., Borror C.M., *Probability and Statistics in Engineering*. John Wiley & Sons, 655 pp., ISBN 0-471-24087-7, 2003.
- [15] Temiz Ö., Baran T., Determination of Expected Value for Monthly Total Precipitation by Entropy Based Method Case Study: Gediz Basin. 10th International Congress on Advances in Civil Engineering, Paper No: 769, 10 p, 2012.
- [16] Baran T., Harmancioglu N.B., Cetinkaya C.P., Barbaros F., An Extension to the Revised Approach in the Assessment of Informational Entropy, *Entropy*, 19(12): 634, DOI: 10.3390/e19120634, 2017.
- [17] SHW, Environmental Master Plan of Gediz Basin, II. Directorate of State Hydraulic Works, Izmir, 2005.
- [18] Baran T., Temiz Ö., Gediz Havzası Yağışlarının Eğilim Analizi. IV. Ulusal Su Mühendisliği Sempozyumu, Bildiriler, s. 241 – 251, 2009.



# **Rainfall Intensity-Duration-Frequency Analysis in Turkey, with the Emphasis of Eastern Black Sea Basin**

**Ömer YÜKSEK<sup>1</sup>**  
**Tuğçe ANILAN<sup>2</sup>**  
**Fatih SAKA<sup>3</sup>**  
**Emrah ÖRGÜN<sup>4</sup>**

## **ABSTRACT**

In this study, regional intensity-duration-frequency (IDF) curves for Turkey were developed using the available maximum rainfall intensity values for various durations (D=5, 15 and 30 minutes, and 1, 3, 6, 12 and 24 hours). Multi-nonlinear regression analysis was carried out by using nine kinds of IDF formulas, which were taken by using various IDF formulae in the literature and newly generated formulae. In order to test the reliability of the functions, two criteria were used: the determination coefficient and the mean relative error. IDF analysis in the Eastern Black Sea Basin of Turkey, which is the most raining basin, is also emphasized and studied in detail. It has been concluded that the reliability of the results is high enough and that this paper will motivate and open new horizons to detailed studies on IDF analysis.

**Keywords:** Intensity-duration-frequency analysis, LPT3 distribution, rainfall, regression analysis, Turkey.

## **1. INTRODUCTION**

The rainfall intensity-duration-frequency (IDF) relationship is one of the most commonly used tools in water resources engineering, either for planning, designing and operating of water resource projects, or the protection of various engineering projects against floods

---

### Note:

- This paper has been received on April 27, 2020 and accepted for publication by the Editorial Board on November 9, 2020.
- Discussions on this paper will be accepted by September 30, 2022.

• <https://doi.org/10.18400/tekderg.727085>

1 Karadeniz Technical University, Department of Civil Engineering, Trabzon, Turkey - [yukse@ktu.edu.tr](mailto:yukse@ktu.edu.tr)  
<https://orcid.org/0000-0002-3425-1890>

2 Karadeniz Technical University, Dep. of Civil Engineering, Trabzon, Turkey - [kocugce@gmail.com](mailto:kocugce@gmail.com)  
<https://orcid.org/0000-0001-9571-4695>

3 Karabük University, Department of Civil Engineering, Karabük, Turkey - [sakafatih@karabuk.edu.tr](mailto:sakafatih@karabuk.edu.tr)  
<https://orcid.org/0000-0003-0956-8658>

4 Çaykur General Directorate, Project and Construction Dep., Rize, Turkey - [emrah8661@gmail.com](mailto:emrah8661@gmail.com)  
<https://orcid.org/0000-0003-2727-8056>

[1,2,3]. Civil infrastructure such as storm sewers, storm water management ponds, culverts and bridges are commonly designed using IDF curves, which assume that the occurrence of precipitation is in the form of rainfall and immediately available for the rainfall-runoff process [4]. The appropriately sized capacities of these civil infrastructure are so important to avoid overdesign which could lead to economic losses and/or increased property damage and possibly increased risk of loss of life. Thus, obtaining reliable estimates of IDF curves is essential [5].

The IDF relationship is a mathematical relationship between the rainfall intensity  $I$ , the duration  $D$ , and the exceedance frequency  $F$  ( $F=1/T$ ,  $T$  is return period). This relation is usually obtained as curves, and each curve shows the change of intensity of rainfall with respect to a return period. These curves are generally obtained by empirical and statistical approaches [6].

The establishment of IDF relationships goes back to the 1930s [7]. Since then, different forms of relationships have been constructed for several regions of the world up to today. A general IDF relationship formula, consistent with the theoretical probabilistic foundation of the rainfall data, was provided by Koutsoyiannis et al. [8] in Greece. Okonkwo and Mbajjorgu [9] analyzed rainfall data and characteristics for locations in seven states of Southeastern Nigeria and developed IDF curves for these locations using graphical and statistical methods. Also, an application to rainfall datasets from two Mediterranean climate locations (Spain and Chile) was set up by Ayuso-Munoz et al. [10]. The regional properties of IDF relationships have been also investigated in the recent studies and maps have been developed to provide the rainfall intensities or depths for various return periods and durations [11]. There are also several studies about IDF in Turkey. Karahan et al. [12], applied a solution algorithm that solves IDF relationship by using Genetic Algorithm (GA) optimization technique to four city centers in the Southeastern Anatolia Project (GAP) region. Their results showed that the developed solution algorithm that is alternatively proposed to determine IDF relationship gives accurate results for the cities located in the GAP region. Ghiaei et al. [13], analyzed rainfall intensity-duration-return period data in the Eastern Black Sea Region by using L-moments and artificial neural networks (ANN). Based on the distribution functions, they extracted the governing equations for calculation of intensities of 2, 5, 25, 50, 100, 250, and 500 years return periods ( $T$ ). Then,  $T$  values for different rainfall intensities were estimated using data quantifying maximum amount of rainfall at different times. Yavuz [14], calculated the parameters of five different potential analytical equations for the intensity-duration-return period (IDF) relationship of annual extreme rainfalls at each one of the seven geographical regions of Turkey. In the study, a single IDF equation was obtained using all the 22 stations, and by the same criteria, the most appropriate expression valid for all of Turkey has been determined.

IDF functions are used for quantifying the magnitude of rainfall events that are used in the design of a variety of civil infrastructure, especially in an urban environment. These relationships of extreme rainfall intensities are one of the most used tools in water resources engineering for planning, design, and operation of water resources projects [15]. IDF curves for a location are generally obtained by fitting a theoretical probability distribution, such as Gumbel (GM), Generalized Extreme Value (GEV), Log Pearson Type III (LPT3), Log Normal (LN), to the extreme rainfall data. These curves provide precipitation accumulation

depths for various return periods and different durations, usually, 5, 10, 15, 30 min, 1, 2, 6 and 24 h. Longer durations are also used, depending on the use of IDF curves [16].

Concisely, the typical procedure involves the following: steps (i) fitting a probability distribution to the annual maximum rainfall intensity values for several rainfall durations, (ii) estimating extreme rainfall quantiles for each rainfall duration for a number of return periods, and (iii) fitting a relationship between rainfall intensity and rainfall duration, for each return period, based on the rainfall intensity quantiles estimated for each rainfall duration. The resulting relationships between rainfall intensity and rainfall duration constitute the IDF curves for the given location [5].

In Turkey, IDF analyses have been developed only for local sites and analysis with the current data encompassing the whole country is needed. In this study, maximum rainfall intensity values for various durations observed in Turkey, were analyzed and the best fit distribution for these intensities was determined. Nonlinear regression analysis was carried out by using nine types of IDF formulae, which were a combination of existing IDF formulae in literature and newly generated formulae. Then the best formula for each meteorological station was determined. In the study, IDF functions for four stations located in the Eastern Black Sea Basin (EBSB), the most raining region in Turkey, were also calculated and presented both as equations and graphics. In this study, the IDF analysis has been made for whole Turkey which is the main novelty of the paper. It is believed that this paper will motivate and will open new horizons to detailed studies on IDF analysis of Turkey, which is an important issue to optimum design of various kinds of hydraulic structures.

## **2. STUDY AREA AND USED DATA**

In Turkey, there are significant differences in climatic conditions from one region to the other because of the existence of the mountains that run parallel to the coasts and the diverse nature of the landscape. The annual average rainfall depth of Turkey is 643 mm [17]. Due to geographical location, geology and hydrological properties, Turkey has a potential risk of mainly three different types of natural disasters related to gravity flows: floods, landslides and snow avalanches. Floods are the second important natural hazards after earthquakes and destructive flood events have occurred in various river basins of Turkey, especially in The Black Sea coast, which receives the greatest amount of rainfall [21].

In last 100 years 66 extremely severe floods took place and caused great life and economic losses [21, 22]. EBSB is also the only region of Turkey that receives rainfall throughout the year. Very major and destructive floods have occurred in the EBSB of Turkey. In this basin, 51 major floods have taken place since 1955, causing 258 deaths and nearly 500 000 000 US dollars of damage [17, 23]. Thus, EBSB, the most raining basin in Turkey, is presented in detail in this paper. Total basin area of EBSB is 24 077 km<sup>2</sup>, yielding 14.9 km<sup>3</sup> water, with an average 19.5 lt/sn-km<sup>2</sup> yield [18,19]. The annual average rainfall in the EBSB is 1 019 mm, reaching 2 300 mm near the Rize Province [17,20]. Turkey and the EBSB located on the northeastern coast of Turkey can be seen in Figure 1.

The data used in this paper are annual maximum precipitation depth values, measured at 242 meteorological stations (MS) in Turkey, which are equipped with pluviographs. Thus, by measuring precipitation depths for several time intervals it is possible to calculate rainfall

intensities. These values are measured and published by Turkish State Meteorological Service (MGM, in Turkish). The observation periods of the data were between 10 to 73 years. The data were published as tables for each year, including annual maximum precipitation depths for various standard rainfall durations from 5 minutes to 24 hours. In this study, only the data of eight standard durations ( $D=5, 15$  and  $30$  minutes, and  $1, 3, 6, 12$  and  $24$  hours) have been employed. The detailed information of whole Turkey data can be found in Örgün [24].

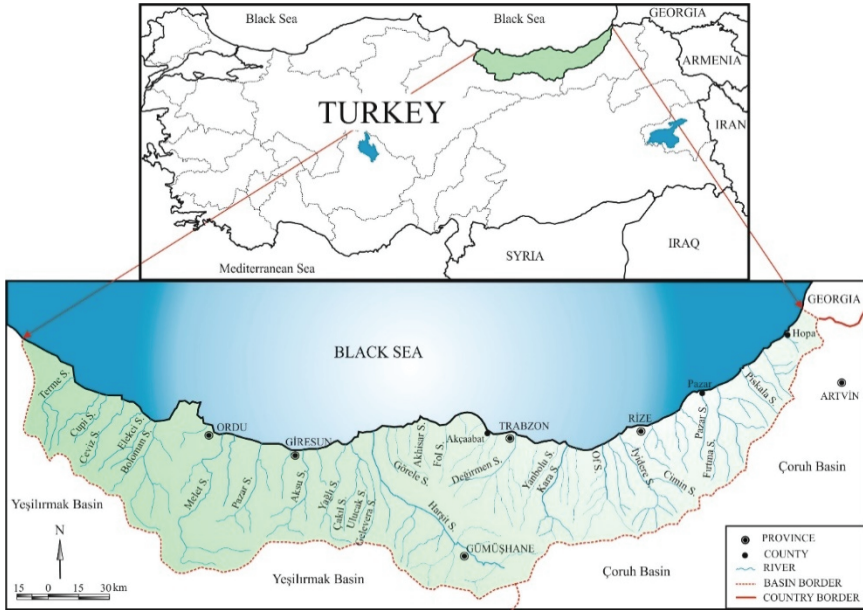


Figure 1 - Location map of the Eastern Black Sea Basin and Turkey (Ghiaei et al. 2018)

### 3. METHODOLOGY

#### 3.1. Obtaining IDF Values

To obtain IDF values, the best statistical distribution for the data must be determined and by using this distribution, an intensity-frequency analysis must be carried out for the selected standard rainfall durations. There are several statistical distributions that might be suitable for rainfall intensity-frequency (or return period,  $T=1/F$ ) analysis. One should select a few (say 3 to 5) distributions to test the best fit distribution. Various studies have favored the use of three suitable distributions for annual maximum precipitation (and also flood) data in Turkey: Log-Normal Distribution (LN2), Gumbel Distribution (GM) and Log-Pearson Type 3 Distribution (LPT3) [17,25]. Therefore, in this study, these three distributions were tested. In order to determine the best distribution, Chi-Square ( $\chi^2$ ) and Probability Plot Correlation Coefficient (PPCC) tests were applied to the data. Once the best distribution is determined, then the rainfall intensity which has a return period  $T=1/F$  is calculated as:

$$I(F) = I_{mean} + KI_{sd} \quad (1)$$

where,  $I_{mean}$  and  $I_{sd}$  are the mean and standard deviation of annual maximum intensities and  $K$  is a frequency factor, which depends both on  $T$  and the related distribution.

LN2 Distribution:

$$K_F = z = \frac{(1-F)^{0.135} - F^{0.135}}{0.1975} \quad (2)$$

GM Distribution:

$$K_F = \frac{-\ln\left[\ln\left(\frac{1/F}{1/F-1}\right)\right] - y_N}{S_N} \quad (3)$$

where  $Y_N$  and  $S_N$  are coefficients depending on number of data ( $N$ ) and given in statistical tables.

LPT3 Distribution:

$$K_F = \frac{2}{C_s} \left( 1 + \frac{zC_s}{6} - \frac{C_s^2}{36} \right)^3 - \frac{2}{C_s} \quad (4)$$

where  $z$  is calculated by Eq. (2) and  $C_s$  is skewness coefficient.

Since LN and LPT3 distributions are related the logarithmic values of data ( $y=\ln x$ ), for these distributions, the mean and standard deviations of logarithmic values are used, and the real intensity values are calculated by inverse logarithm as follows:

$$\ln[I(1/F)] = (\ln I)_{mean} + K(\ln I)_{sd} \quad (5)$$

$$I(1/F) = \text{Exp}[\ln I(1/F)] \quad (6)$$

where  $\text{Exp}(x)$  is the exponential function of  $x$ .

### 3.2. The Used IDF Functions

There are several formulae to determine IDF relationship. In general, return period is used instead of frequency. General structure of these formulae is as follows [24].:

$$I(D, F) = \frac{A(F)}{B(D)} \quad (7)$$

where  $I(D, F)$  is rainfall intensity (mm/hour) as a function of frequency ( $F=1/T$ , year<sup>-1</sup>) and rainfall duration ( $D$ , hour). Several functions have been given in the literature for the  $A(F)$  and  $B(D)$  functions [26, 27, 28, 29, 30]. A list of these is presented in Table 1. By combining these functions, nine IDF functions are obtained and they are given in Table 2. In Table 1 and 2;  $a, b, c$  and  $d$  are regression coefficients to be calculated by non-linear regression analysis. By using calculated  $I, D$  and  $F$  values, the related non-linear functions are transformed to linear ones by using appropriate transformations and then both the regression coefficients ( $a, b, c$ , and  $d$ ) and determination coefficients ( $R^2$ ) are calculated.

Table 1 - Functions for  $A(F)$  and  $B(D)$

| No   | Function                | References   |
|------|-------------------------|--|
| A(T) | 1 $a*(1/F)^b$           | Sherman, 1931; Koutsoyionnis et al.,1998                   |
|      | 2 $a + b*\ln(1/F)$      | Koutsoyionnis et al., 1998; Aşıkoğlu, 2005                 |
|      | 3 $a + b*\ln(\ln(1/F))$ | Minh Nhat et al, 2007                                      |
| B(D) | 4 $D^c$                 | Sherman, 1931; Bernard, 1932                               |
|      | 5 $D^c + d$             | Minh Nhat et al. 2006                                      |
|      | 6 $(D + d)^c$           | Koutsoyionnis et al., 1998; Benzeden and Hacısüleyman,2003 |

Table 2 - Used IDF Functions

| Combination | Funtion   | Equation no |
|-------------|---|-------------|
| 1 and 4     | $I(D, F) = \frac{a*(1/F)^b}{D^c}$               | 8           |
| 1 and 5     | $I(D, F) = \frac{a*(1/F)^b}{D^c + d}$           | 9           |
| 1 and 6     | $I(D, F) = \frac{a*(1/F)^b}{(D+d)^c}$           | 10          |
| 2 and 4     | $I(D, F) = \frac{a + b*\ln(1/F)}{D^c}$          | 11          |
| 2 and 5     | $I(D, F) = \frac{a + b*\ln(1/F)}{D^c + d}$      | 12          |
| 2 and 6     | $I(D, F) = \frac{a + b*\ln(1/F)}{(D+d)^c}$      | 13          |
| 3 and 4     | $I(D, F) = \frac{a + b*\ln(\ln(1/F))}{D^c}$     | 14          |
| 3 and 5     | $I(D, F) = \frac{a + b*\ln(\ln(1/F))}{D^c + d}$ | 15          |
| 3 and 6     | $I(D, F) = \frac{a + b*\ln(\ln(1/F))}{(D+d)^c}$ | 16          |

## 4. RESULTS

### 4.1. The Best Distribution

In the study, the data of 242 meteorological stations (MS), with eight different durations (D, hours) have been used, thus there are totally  $242 \times 8 = 1936$  models available. The results of the best distribution show that no data fit LN distribution. Totally 191 data (9.87%) fit GM and 1745 data (90.13%) fit LPT3. It is obvious that LPT3 is the best distribution. Especially, as the duration increases, the data tend to fit LPT3. Results of the analysis are given in Table 3, which shows the percentage of the best distribution depending on rainfall duration. After determining the best distribution, IDF values were found by using Eq. (1 and 3) for GM and Eq. (4, 5 and 6) for LPT3 distributions.

Table 3 - The Percentage of the Best Distribution

| Dist. | Overall | Rainfall Duration (Hours) |       |       |       |       |       |       |       |
|-------|---------|---------------------------|-------|-------|-------|-------|-------|-------|-------|
|       |         | 0.08                      | 0.25  | 0.5   | 1     | 3     | 6     | 12    | 24    |
| LPT3  | 90.13   | 78.93                     | 78.93 | 82.64 | 88.84 | 96.69 | 98.35 | 98.76 | 97.93 |
| GM    | 9.87    | 21.07                     | 21.07 | 17.36 | 11.16 | 3.31  | 1.65  | 1.24  | 2.07  |

### 4.2. IDF Functions

By using SPSS program, regression coefficients were calculated and IDF functions, with Eq. 8 to 16, were obtained for 242 MS. Then, in order to test the reliability of the functions, two criteria were used. The first criterion is the determination coefficient ( $R^2$ , square of correlation coefficient, R) and the second one is the mean relative error (RE, %) among the calculated IDF values both by the best distribution and by SPSS program. RE is calculated by:

$$RE = \frac{1}{N} \sum \left( \frac{IDF_1 - IDF_2}{IDF_1} \right) * 100 \quad (17)$$

where,  $IDF_1$  and  $IDF_2$  are calculated IDF values for the best distribution by SPSS program, and N is the number of data. RE value should be as low as possible. A summary of  $R^2$  and RE values for 242 MS are given in Table 4.

### 4.3. Success Rating of the Functions

Determination of the best IDF function is of importance and is also among the outcomes of this paper. Out of nine analyzed functions, the best is the one with greatest  $R^2$  and smallest RE. Considering these criteria and taking into account the data given in Table 4, it is obvious that Eqs. 12 and 13 have relatively high  $R^2$  and low RE values. Determination of success rating out of these two functions is not an easy task, due to fact that the average values of

both  $R^2$  and RE values are close to each other. However, Eq. 13 has minute greater average  $R^2$  and less RE. Moreover, both minimum  $R^2$  value is greater and maximum RE is less than those of Eq. 12. Therefore, Eq. 13 is chosen as the best and Eq. 12 is the second good IDF function. Similarly, Eqs. 9 and 10 exhibit closer results, however similar considerations lead that Eq. 9 is better than Eq. 10. Eqs. 15 and 16 also have both great  $R^2$  and small RE values and they are considered as sixth and fifth good functions, respectively. These six functions may be acceptable for IDF functions. The other three functions, Eqs. 8, 11 and 14 have smaller  $R^2$  and rather greater RE values, which means that they are not suitable for IDF functions. Finally, success rating of the functions (from 1, the best to 9, the worst) is given as the last column of Table 4.

Table 4 - Summary of  $R^2$ , RE and Success Ratings for the Equations

| Eq. No | $R^2$ |       |       | RE   |        |       | Success Rating |
|--------|-------|-------|-------|------|--------|-------|----------------|
|        | Min.  | Max.  | Mean  | Min. | Max.   | Mean  |                |
| 8      | 0.921 | 0.988 | 0.967 | 9.87 | 151.59 | 52.31 | 8              |
| 9      | 0.978 | 0.996 | 0.985 | 6.62 | 45.76  | 17.25 | 3              |
| 10     | 0.972 | 0.997 | 0.984 | 6.97 | 48.55  | 17.55 | 4              |
| 11     | 0.911 | 0.998 | 0.973 | 6.74 | 142.94 | 49.15 | 7              |
| 12     | 0.950 | 0.998 | 0.987 | 3.76 | 87.56  | 16.04 | 2              |
| 13     | 0.973 | 0.999 | 0.989 | 3.65 | 54.61  | 15.39 | 1              |
| 14     | 0.832 | 0.979 | 0.952 | 9.18 | 142.19 | 52.80 | 9              |
| 15     | 0.917 | 0.997 | 0.969 | 4.13 | 59.26  | 20.76 | 6              |
| 16     | 0.860 | 0.996 | 0.966 | 3.63 | 63.69  | 20.08 | 5              |

**4.4. Analysis of Numerators and Denominators of the Used Functions**

As was stated in Chapter 3.2., general structure of IDF functions is given in Eq. 7. By analyzing the success rating of the IDF functions, the following analysis has been made for the reliability of numerator A(F) and denominator B(D). Numerator A(F): Eqs. 12 and 13 are the best two functions. Both have numerator as  $A(F)=a+b*\ln(1/F)$ . This finding recommends and encourages the use of this function as a numerator. However, as can be seen in Table 4, Eq. 11, which has the same numerator but a different denominator, is not a good suggestion. The cause of this is the function of denominator  $B(D)=D^c$ , as will be emphasized in the following, it is not a good function. Eqs. 9 and 10, both of which numerator is  $A(F)=a*(1/F)^b$  have the 3rd and 4th ratings. Similarly, Eq.8, which has the same numerator but a different denominator,  $B(D)=D^c$  is the 8th good function. Comparison of Eq. 15 with 9 and 12, and Eq. 16 with 10 and 13, all of which have the same denominators, has yielded that the numerator of both Eqs. 15 and 16,  $A(F)=a+b*\ln(\ln(1/F))$  is not a good proposal. Mutual comparison of Equations (9 and 12) and (10 and 13) makes it clear that a numerator as

$A(F)=a+b*\ln(1/F)$  is a little better than  $A(F)=a*(1/F)^b$ . Denominator  $B(D)$ : For  $B(D)$ , two functions have resulted in similar findings:  $D^c+d$  and  $(D+d)^c$ . Mutual comparison of Equations (9 and 10), (12 and 13) and (15 and 16) has concluded that  $A(F)=a+b*\ln(1/F)$  is a little better than  $B(D)=D^c+d$ . A value of  $B(D)=D^c$  has resulted in both small  $R^2$  and great RE values, which means that this kind of a function is not appropriate.

By summarizing the above considerations, out of nine functions for IDF analysis, for the numerator, both  $A(F)=a+b*\ln(1/F)$  and  $A(F)=a*(1/F)^b$  may be used. A conclusion on which function is better depends greatly on the MS. The results of some MS have favored the use of one, some have favored use of the other one and there is no significant difference between their reliabilities. The use of a function of  $A(F)=a+b*\ln(\ln(1/F))$  is not recommended, due to both low  $R^2$  and high RE values. Similarly, for the denominator, both  $B(D)=(D+d)^c$  and  $B(D)=D^c+d$  may be used. A conclusion on which function is better depends greatly on the meteorological station. The results of some MS have favored the use of one, some have favored use of the other one and there is no significant difference between their reliabilities. The use of a function of  $B(D)=D^c$  is not recommended, due to both low  $R^2$  and high RE values.

#### **4.5. Reliability of the Functions**

As can be seen in Table 4, the calculated mean determination coefficients, for the best six functions (Eqs. 13, 12, 9, 10, 16 and 15) are between 0.966 and 0.989. Taking into consideration the fact that minimum number of the used data is 10 years, these  $R^2$  values are high enough and they can be used with reliability for prediction of IDF values. Yet, the calculated RE values, which are between 15.39 and 20.76, are relatively high and their reliability is questionable. However, these values are calculated as average values for all the MS. When these values are calculated for individual stations, RE values are lower and their reliabilities are higher.

#### **4.6. Results and Analysis of IDF Functions in the EBSB**

The  $R^2$  and RE values for IDF functions (equations), which were given in Table 2, of the meteorological stations in the EBSB are presented in Table 5. In this table, the best three equations are also given in parenthesis as (1, 2 and 3).

#### **4.7. Comparison of the Results of Turkey and EBSB**

By comparing the results given in Table 4 and 5, it is obvious that, they are similar. For example, Eq. 13 is the best one both for all of Turkey and EBSB. Although Eq. 12 is the second good one in Turkey, it is suitable only for Ordu MS. Eq. 9 is convenient for Giresun, Trabzon and Rize MS, and Eq. 10 is proper for Trabzon and Rize. Eq. 16, which has 5th success rating in Turkey, has also 5th rating in EBSB. The most surprising result is that Eq. 15, which is the 6th good one for Turkey, has yielded very unreliable estimations for EBSB. Of course, similar analyses should be made for various sub basins in Turkey. By making these analyses, general conclusions, about which kind of functions may be advisable in which kinds of basins and stations, may be attained. By obtaining these kind of conclusions, more practical decisions about IDF functions may be achieved.

Table 5 - Summary of IDF Functions in the EBSB

| Eq. No | Ordu           |           | Giresun        |           | Trabzon        |           | Rize           |           |
|--------|----------------|-----------|----------------|-----------|----------------|-----------|----------------|-----------|
|        | R <sup>2</sup> | RE        |
| 8      | 0.924          | 63.64     | 0.952          | 64.01     | 0.966          | 59.58     | 0.980          | 42.35     |
| 9      | 0.978          | 15.24     | 0.979          | 21.76 (3) | 0.986          | 12.22 (2) | 0.991          | 18.04 (2) |
| 10     | 0.978          | 14.81     | 0.977          | 22.10     | 0.986          | 12.77 (3) | 0.989          | 20.27 (3) |
| 11     | 0.932          | 60.53     | 0.959          | 60.51     | 0.971          | 55.67     | 0.983          | 40.28     |
| 12     | 0.986          | 12.71 (2) | 0.141          | 271.91    | 0.883          | 118.81    | 0.126          | 244.16    |
| 13     | 0.986          | 11.99 (1) | 0.994          | 19.10 (1) | 0.991          | 10.61(1)  | 0.993          | 17.79 (1) |
| 14     | 0.923          | 59.62     | 0.945          | 60.98     | 0.950          | 57.62     | 0.962          | 42.93     |
| 15     | 0.136          | 242.42    | 0.123          | 272.65    | 0.140          | 324.05    | 0.107          | 245.72    |
| 16     | 0.977          | 13.40 (3) | 0.970          | 20.56 (2) | 0.969          | 17.69     | 0.972          | 21.85     |

4.8. The Best Functions and Relative Errors

As was explained, Eq. 13 was the best function for all the four stations in the EBSB and they were presented as follows. Equations of 17, 18, 19, 20 are for Ordu, Giresun, Trabzon and Rize MS, respectively. In these equations, the dimensions were as: I (D, F): mm/minute, F: year<sup>-1</sup>, and D: minute. The results of these equations are presented in Tables 6, 7, 8 and 9 for the related stations. In these tables, the rainfall intensities calculated by best equations (17, 18, 19, 20) are given together with relative errors. In the last column of each row, mean RE values for each duration and in the last row mean RE values for each duration are also presented. As can be seen, mean RE values tend to increase as duration goes up. However, there is no significant relation between mean RE values and return period. The graphical presentation of the rainfall intensity values is given in Figs 2, 3, 4 and 5 as considered equation (EQ) values

$$I(D, F) = \frac{30.268 + 12.054 * \ln(1 / F)}{(D + 35.114)^{0.932}} \tag{17}$$

$$I(D, F) = \frac{12.349 + 5.620 * \ln(1 / F)}{(D + 19.229)^{0.737}} \tag{18}$$

$$I(D, F) = \frac{9.236 + 5.680 * \ln(1 / F)}{(D + 14.026)^{0.819}} \tag{19}$$

$$I(D, F) = \frac{6.459 + 12.948 * \ln(1 / F)}{(D + 7.377)^{0.606}} \tag{20}$$

Table 6 - Rainfall Intensity Values of Ordu MS Calculated by LPT3 Distribution and Equation 17

| t<br>(hour) | F = 1/2 year <sup>-1</sup> |      | F = 1/5 year <sup>-1</sup> |      | F = 1/10 year <sup>-1</sup> |      | F = 1/25 year <sup>-1</sup> |       | F = 1/50 year <sup>-1</sup> |      | F = 1/100 year <sup>-1</sup> |      | F = 1/500 year <sup>-1</sup> |      |      |      |      |      |      |      |      |      |
|-------------|----------------------------|------|----------------------------|------|-----------------------------|------|-----------------------------|-------|-----------------------------|------|------------------------------|------|------------------------------|------|------|------|------|------|------|------|------|------|
|             | I (mm/h)                   |      | I (mm/h)                   |      | I (mm/h)                    |      | I (mm/h)                    |       | I (mm/h)                    |      | I (mm/h)                     |      | I (mm/h)                     |      |      |      |      |      |      |      |      |      |
|             | LP                         | EQ   | LP                         | EQ   | LP                          | EQ   | LP                          | EQ    | LP                          | EQ   | LP                           | EQ   | LP                           | EQ   |      |      |      |      |      |      |      |      |
| 0.083       | 80.0                       | 74.2 | 7.3                        | 107  | 95.3                        | 11.2 | 123                         | 110.5 | 9.1                         | 139  | 133                          | 4.7  | 150                          | 149  | 0.7  | 159  | 165  | 3.6  | 177  | 202  | 14.4 | 7.3  |
| 0.250       | 52.3                       | 60.2 | 15.1                       | 77.2 | 77.5                        | 0.5  | 93.5                        | 90.5  | 3.2                         | 114  | 108                          | 5.5  | 129                          | 121  | 6.3  | 143  | 134  | 6.7  | 175  | 164  | 6.3  | 6.2  |
| 0.500       | 35.9                       | 47.2 | 31.6                       | 53.4 | 60.7                        | 13.7 | 65.3                        | 70.9  | 8.6                         | 80.5 | 84.4                         | 4.8  | 91.9                         | 94.6 | 3.0  | 103  | 105  | 1.7  | 128  | 129  | 0.1  | 9.1  |
| 1.000       | 22.9                       | 33.2 | 44.6                       | 35.3 | 42.7                        | 20.9 | 44.2                        | 49.8  | 12.5                        | 56.5 | 59.3                         | 5.0  | 66.0                         | 66.5 | 0.6  | 76.0 | 73.6 | 3.1  | 100  | 90.3 | 9.6  | 13.8 |
| 3.000       | 10.5                       | 15.5 | 47.4                       | 15.8 | 19.9                        | 26.5 | 19.7                        | 23.3  | 18.3                        | 25.1 | 27.7                         | 10.2 | 29.5                         | 31.1 | 5.1  | 34.2 | 34.4 | 0.6  | 45.9 | 42.2 | 8.1  | 16.6 |
| 6.000       | 6.42                       | 8.76 | 37.3                       | 9.30 | 11.3                        | 21.9 | 11.5                        | 13.2  | 14.5                        | 14.9 | 15.7                         | 5.8  | 17.7                         | 17.6 | 0.3  | 20.8 | 19.5 | 6.0  | 29.1 | 23.9 | 17.8 | 14.8 |
| 12.000      | 3.94                       | 4.80 | 22.2                       | 5.57 | 6.18                        | 10.8 | 6.84                        | 7.20  | 5.6                         | 8.64 | 8.58                         | 0.6  | 10.1                         | 9.66 | 5.1  | 29.1 | 11.9 | 17.8 | 16.1 | 13.1 | 18.6 | 11.5 |
| 24.000      | 2.66                       | 2.58 | 3.4                        | 3.68 | 3.30                        | 10.0 | 4.47                        | 3.84  | 13.5                        | 5.62 | 4.62                         | 18.1 | 6.60                         | 5.16 | 21.7 | 16.1 | 6.1  | 18.6 | 10.5 | 7.0  | 33.1 | 16.9 |
|             | MEAN RE: 26.1              |      | MEAN RE: 14.4              |      | MEAN RE: 10.7               |      | MEAN RE: 6.8                |       | MEAN RE: 5.4                |      | MEAN RE: 7.3                 |      | MEAN RE: 13.4                |      |      |      |      |      |      |      |      |      |

Table 7 - Rainfall Intensity Values of Giresun MS Calculated by LPT3 Distribution and Equation 18

| t<br>(hour) | F = 1/2 year <sup>-1</sup> |      | F = 1/5 year <sup>-1</sup> |      | F = 1/10 year <sup>-1</sup> |      | F = 1/25 year <sup>-1</sup> |      | F = 1/50 year <sup>-1</sup> |      | F = 1/100 year <sup>-1</sup> |      | F = 1/500 year <sup>-1</sup> |      |      |      |      |      |      |      |      |      |
|-------------|----------------------------|------|----------------------------|------|-----------------------------|------|-----------------------------|------|-----------------------------|------|------------------------------|------|------------------------------|------|------|------|------|------|------|------|------|------|
|             | I (mm/h)                   |      | I (mm/h)                   |      | I (mm/h)                    |      | I (mm/h)                    |      | I (mm/h)                    |      | I (mm/h)                     |      | I (mm/h)                     |      |      |      |      |      |      |      |      |      |
|             | LP                         | EQ   | LP                         | EQ   | LP                          | EQ   | LP                          | EQ   | LP                          | EQ   | LP                           | EQ   | LP                           | EQ   |      |      |      |      |      |      |      |      |
| 0.083       | 100                        | 92.9 | 7.5                        | 138  | 122                         | 11.3 | 161                         | 145  | 10.0                        | 187  | 174                          | 6.9  | 205                          | 196  | 4.3  | 222  | 219  | 1.5  | 256  | 270  | 5.6  | 6.7  |
| 0.250       | 62.6                       | 72.0 | 15.1                       | 87.0 | 94.9                        | 7.9  | 105                         | 112  | 7.2                         | 126  | 135                          | 7.5  | 141                          | 152  | 8.0  | 156  | 169  | 8.7  | 190  | 210  | 10.6 | 9.3  |
| 0.500       | 45.6                       | 55.1 | 20.9                       | 67.2 | 72.5                        | 7.9  | 82.7                        | 85.7 | 3.7                         | 103  | 103                          | 0.3  | 120                          | 116  | 2.8  | 136  | 130  | 5.0  | 176  | 160  | 9.2  | 7.1  |
| 1.000       | 30.0                       | 38.8 | 28.8                       | 45.5 | 51.1                        | 12.3 | 57.2                        | 60.4 | 5.5                         | 73.9 | 72.7                         | 1.7  | 87.7                         | 82.0 | 6.5  | 102  | 91.3 | 10.9 | 140  | 113  | 19.6 | 12.2 |
| 3.000       | 14.6                       | 19.6 | 34.6                       | 21.7 | 25.9                        | 18.9 | 27.3                        | 30.6 | 12.1                        | 35.2 | 36.8                         | 4.6  | 41.8                         | 41.5 | 0.6  | 48.9 | 46.3 | 5.4  | 67.4 | 57.2 | 15.1 | 13.0 |
| 6.000       | 8.48                       | 12.2 | 44.2                       | 12.3 | 16.1                        | 31.3 | 15.1                        | 19.0 | 26.1                        | 19.1 | 22.9                         | 20.1 | 22.3                         | 25.9 | 15.8 | 28.7 | 11.7 | 34.5 | 35.6 | 3.1  | 21.8 |      |
| 12.000      | 4.89                       | 7.50 | 52.9                       | 6.78 | 9.84                        | 45.1 | 8.21                        | 11.6 | 41.7                        | 10.2 | 14.0                         | 36.9 | 11.9                         | 15.8 | 32.8 | 13.7 | 17.6 | 28.6 | 18.3 | 21.7 | 19.0 | 36.7 |
| 24.000      | 2.99                       | 4.50 | 51.1                       | 3.93 | 5.94                        | 51.5 | 4.66                        | 7.02 | 51.3                        | 5.70 | 8.46                         | 48.8 | 6.56                         | 9.54 | 45.7 | 7.51 | 10.6 | 41.8 | 10.0 | 13.1 | 31.7 | 46.0 |
|             | MEAN RE: 31.9              |      | MEAN RE: 23.3              |      | MEAN RE: 19.7               |      | MEAN RE: 15.9               |      | MEAN RE: 14.6               |      | MEAN RE: 14.2                |      | MEAN RE: 14.2                |      |      |      |      |      |      |      |      |      |

Table 8 - Rainfall Intensity Values of Trabzon MS Calculated by LPT3 Distribution and Equation 19

| t<br>(hour) | F = 1/2 year <sup>-1</sup> |      |        | F = 1/5 year <sup>-1</sup> |      |        | F = 1/10 year <sup>-1</sup> |      |        | F = 1/25 year <sup>-1</sup> |      |        | F = 1/50 year <sup>-1</sup> |      |        | F = 1/100 year <sup>-1</sup> |      |        | F = 1/500 year <sup>-1</sup> |      |        |      |  |
|-------------|----------------------------|------|--------|----------------------------|------|--------|-----------------------------|------|--------|-----------------------------|------|--------|-----------------------------|------|--------|------------------------------|------|--------|------------------------------|------|--------|------|--|
|             | I (mm/h)                   |      | RE (%) | I (mm/h)                   |      | RE (%) | I (mm/h)                    |      | RE (%) | I (mm/h)                    |      | RE (%) | I (mm/h)                    |      | RE (%) | I (mm/h)                     |      | RE (%) | I (mm/h)                     |      | RE (%) |      |  |
|             | LP                         | EQ   |        | LP                         | EQ   |        | LP                          | EQ   |        | LP                          | EQ   |        | LP                          | EQ   |        | LP                           | EQ   |        | LP                           | EQ   |        |      |  |
| 0.083       | 79.1                       | 70.8 | 10.5   | 110                        | 98.8 | 10.3   | 130                         | 120  | 7.8    | 155                         | 148  | 4.3    | 172                         | 169  | 1.9    | 189                          | 190  | 0.5    | 227                          | 239  | 5.6    | 5.8  |  |
| 0.250       | 44.7                       | 50.1 | 12.1   | 64.4                       | 69.8 | 8.5    | 78.8                        | 84.8 | 7.7    | 98.4                        | 105  | 6.4    | 114                         | 120  | 5.0    | 130                          | 135  | 3.4    | 170                          | 169  | 0.5    | 6.2  |  |
| 0.500       | 29.3                       | 35.6 | 21.6   | 43.3                       | 49.7 | 14.6   | 54.3                        | 60.3 | 11.0   | 70.3                        | 74.3 | 5.7    | 83.8                        | 85.0 | 1.4    | 98.5                         | 95.6 | 3.0    | 138                          | 120  | 12.6   | 10.0 |  |
| 1.000       | 19.1                       | 23.3 | 21.9   | 27.8                       | 32.5 | 16.5   | 35.0                        | 39.4 | 12.6   | 45.8                        | 48.6 | 6.1    | 55.2                        | 55.6 | 0.5    | 65.9                         | 62.5 | 5.2    | 95.6                         | 78.6 | 17.8   | 11.5 |  |
| 3.000       | 9.00                       | 10.6 | 17.8   | 12.6                       | 14.8 | 17.4   | 15.4                        | 17.9 | 16.1   | 19.7                        | 22.1 | 12.1   | 23.3                        | 25.2 | 8.1    | 27.4                         | 28.4 | 3.5    | 38.6                         | 35.7 | 7.6    | 11.8 |  |
| 6.000       | 5.35                       | 6.18 | 15.2   | 7.18                       | 8.58 | 19.8   | 8.63                        | 10.4 | 21.0   | 10.8                        | 12.9 | 19.6   | 12.6                        | 14.8 | 16.8   | 14.6                         | 16.6 | 13.2   | 20.2                         | 20.9 | 3.5    | 15.6 |  |
| 12.00       | 3.36                       | 3.54 | 5.6    | 4.42                       | 4.98 | 12.0   | 5.21                        | 6.00 | 15.5   | 6.29                        | 7.44 | 17.9   | 7.17                        | 8.46 | 18.3   | 8.10                         | 9.54 | 17.8   | 10.5                         | 12.0 | 14.8   | 14.6 |  |
| 24.00       | 2.25                       | 2.04 | 9.9    | 2.85                       | 2.82 | 0.8    | 3.28                        | 3.42 | 4.7    | 3.86                        | 4.26 | 9.7    | 4.32                        | 4.86 | 12.2   | 4.80                         | 5.46 | 13.7   | 5.97                         | 6.84 | 14.9   | 9.4  |  |
|             | MEAN RE: 14.3              |      |        | MEAN RE: 12.5              |      |        | MEAN RE: 12.1               |      |        | MEAN RE: 10.2               |      |        | MEAN RE: 8.0                |      |        | MEAN RE: 7.5                 |      |        | MEAN RE: 9.7                 |      |        |      |  |

Table 9 - Rainfall Intensity Values of Rize MS Calculated by LPT3 Distribution and Equation 20

| t<br>(hour) | F = 1/2 year <sup>-1</sup> |      |        | F = 1/5 year <sup>-1</sup> |      |        | F = 1/10 year <sup>-1</sup> |      |        | F = 1/25 year <sup>-1</sup> |      |        | F = 1/50 year <sup>-1</sup> |      |        | F = 1/100 year <sup>-1</sup> |      |        | F = 1/500 year <sup>-1</sup> |      |        |      |  |
|-------------|----------------------------|------|--------|----------------------------|------|--------|-----------------------------|------|--------|-----------------------------|------|--------|-----------------------------|------|--------|------------------------------|------|--------|------------------------------|------|--------|------|--|
|             | I (mm/h)                   |      | RE (%) | I (mm/h)                   |      | RE (%) | I (mm/h)                    |      | RE (%) | I (mm/h)                    |      | RE (%) | I (mm/h)                    |      | RE (%) | I (mm/h)                     |      | RE (%) | I (mm/h)                     |      | RE (%) |      |  |
|             | LP                         | EQ   |        | LP                         | EQ   |        | LP                          | EQ   |        | LP                          | EQ   |        | LP                          | EQ   |        | LP                           | EQ   |        | LP                           | EQ   |        |      |  |
| 0.083       | 115                        | 111  | 3.6    | 151                        | 146  | 3.0    | 176                         | 173  | 1.7    | 210                         | 208  | 0.6    | 236                         | 235  | 0.4    | 263                          | 262  | 0.4    | 328                          | 324  | 1.4    | 1.6  |  |
| 0.250       | 75.3                       | 77.5 | 3.0    | 99.9                       | 102  | 2.3    | 116                         | 121  | 3.8    | 138                         | 145  | 5.6    | 154                         | 164  | 6.6    | 170                          | 183  | 7.4    | 207                          | 226  | 8.8    | 5.4  |  |
| 0.500       | 55.9                       | 56.8 | 1.6    | 76.2                       | 74.9 | 1.7    | 90.3                        | 88.5 | 2.0    | 109                         | 107  | 2.2    | 123                         | 120  | 2.5    | 138                          | 134  | 3.0    | 173                          | 166  | 4.3    | 2.5  |  |
| 1.000       | 38.7                       | 39.7 | 2.8    | 53.8                       | 52.4 | 2.7    | 64.8                        | 61.9 | 4.4    | 79.7                        | 74.6 | 6.5    | 91.6                        | 84.1 | 8.2    | 104                          | 93.7 | 9.9    | 135                          | 116  | 13.9   | 6.9  |  |
| 3.000       | 18.1                       | 21.4 | 17.8   | 25.4                       | 28.2 | 10.7   | 31.3                        | 33.3 | 6.6    | 39.9                        | 40.0 | 0.6    | 47.2                        | 45.2 | 4.2    | 55.4                         | 50.4 | 9.1    | 77.8                         | 62.3 | 19.9   | 9.8  |  |
| 6.000       | 11.7                       | 14.2 | 21.8   | 15.6                       | 18.7 | 20.1   | 18.5                        | 22.1 | 20.1   | 22.4                        | 26.6 | 19.1   | 25.5                        | 30.0 | 17.8   | 28.9                         | 33.5 | 16.1   | 37.2                         | 41.5 | 11.5   | 18.1 |  |
| 12.00       | 6.89                       | 9.42 | 36.2   | 8.98                       | 12.4 | 37.9   | 10.5                        | 14.6 | 39.6   | 12.6                        | 17.6 | 40.4   | 14.2                        | 19.9 | 40.0   | 15.9                         | 22.1 | 38.9   | 20.3                         | 27.4 | 35.0   | 38.3 |  |
| 24.00       | 4.36                       | 6.18 | 41.9   | 5.45                       | 8.16 | 49.8   | 6.19                        | 9.66 | 55.9   | 7.15                        | 11.6 | 62.4   | 7.89                        | 13.1 | 66.1   | 8.64                         | 14.6 | 68.9   | 10.4                         | 18.1 | 73.4   | 59.8 |  |
|             | MEAN RE: 16.1              |      |        | MEAN RE: 16.0              |      |        | MEAN RE: 16.8               |      |        | MEAN RE: 17.2               |      |        | MEAN RE: 18.1               |      |        | MEAN RE: 19.2                |      |        | MEAN RE: 21.0                |      |        |      |  |

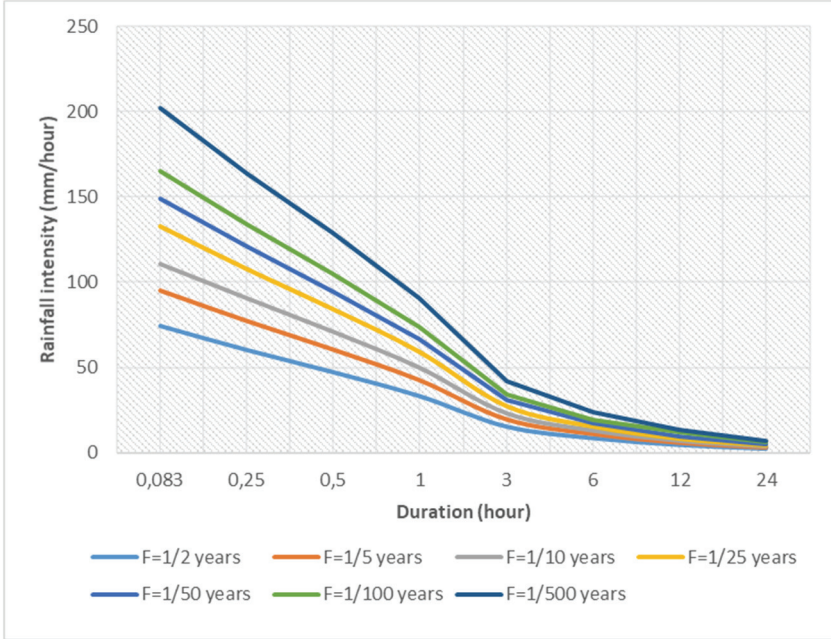


Figure 2 - IDF relationship for Ordu

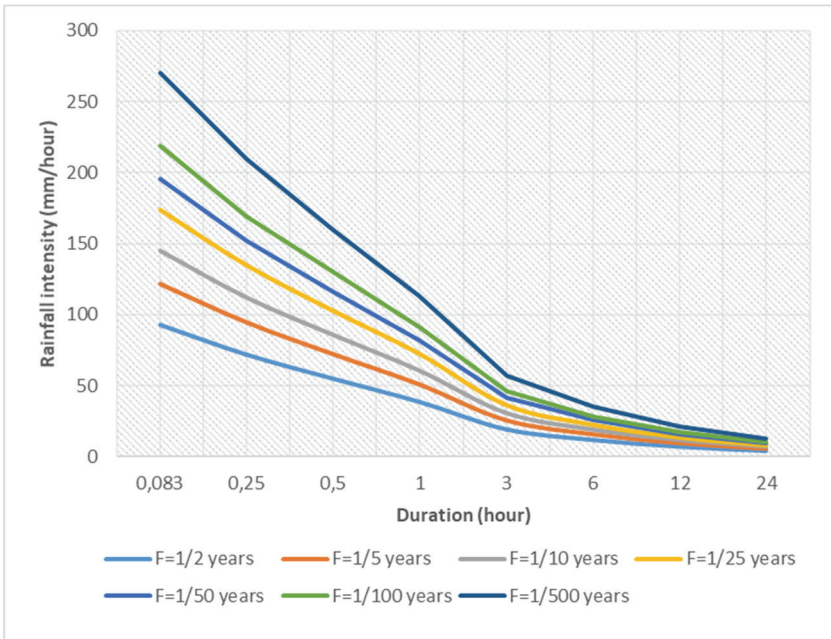


Figure 3 - IDF relationship for Giresun

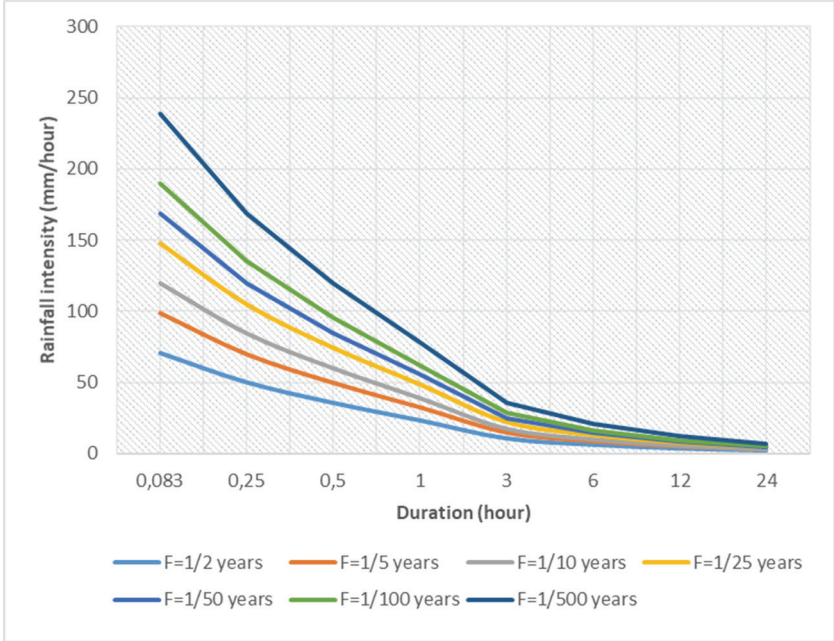


Figure 4 - IDF relationship for Trabzon

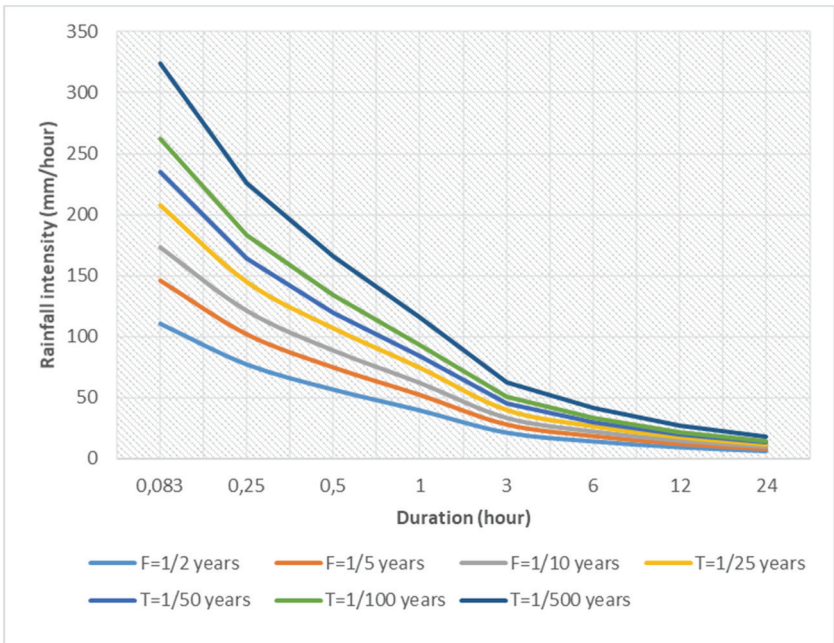


Figure 5 - IDF relationship for Rize

## 5. CONCLUSIONS

In this study, by using the annual maximum rainfall depth values in 242 MS in Turkey, maximum intensity values for various durations are calculated and analyzed, and the best fit distribution for these intensities are determined as LPT3, by employing Chi-Square and PPCC tests. Rainfall intensity (I) values are estimated for various rainfall duration (D) and frequency (F) values according to the LPT3 distribution. Multi-nonlinear regression analysis has been carried out by using nine kinds of IDF formulas and various regression coefficients are obtained. The best formula for each MS is determined depending on  $R^2$  and RE between intensity values, calculated by both the best statistical distribution and by multi non-linear regression. The best formula has been determined as one with maximum  $R^2$  and the minimum RE. The mean  $R^2$  and RE values have varied between 0.952 and 0.989 and between 15.39 and 52.80 %, respectively. The studied 9 functions are analyzed in detail. In this context, the numerator A(F) and denominator functions of Equation 7, have been evaluated in the context of their reliabilities in predicting rainfall intensities. A success rating list of nine functions is presented. Then, it has been determined that 6 functions, out of 9 proposed functions, to have great  $R^2$  and small RE values, are proposed as to be suitable to estimate IDF values in Turkey.

In the final phase of the study, IDF functions for four stations, located in the EBSB, the most raining region in Turkey, are presented both as equations and graphics. Also, the results of the whole Turkey and EBSB have been compared and similar trends about the best functions are detected. Although RE values are great for all of Turkey, they are relatively small when they have been calculated for each MS. Therefore, it has been concluded that the reliability of the results is high enough and that this paper will motivate and open new horizons to detailed studies on IDF analysis.

Most of the previous IDF analysis in Turkey are the local studies [12,13] Nevertheless, this study covers all Turkey. As for the EBSB, in their study Ghiaei et al. [13] applied homogeneity measure to the seven stations and they concluded the EBSB to be homogeneous according to the Hosking's discordancy and heterogeneity measures. In this study the homogeneity test was not applied to the data but there was no significant heterogeneity observed in the previous studies [13,14]. Nevertheless, homogeneity tests and other methods such as L-moments [13], GA optimization technique [12] etc. should be applied for whole Turkey in future studies.

## References

- [1] Chow, V. T., Maidment, D. R., Mays, L.W., Applied Hydrology, McGraw- Hill Book Company, New York, 1988.
- [2] Şengül, S., Can, İ., Stochastic Modelling of Mean Monthly Flows of Karasu River, in Turkey. Water and Environment Journal, 25(1): 31-39, 2011.
- [3] Can, İ., Tosunoğlu, F., Kahya, E., Daily Streamflow Modelling Using Autoregressive Moving Average and Artificial Neural Networks Models: Case Study of Çoruh Basin, Turkey. Water and Environment Journal, 26(4): 567-576., 2012.

- [4] Yan, H., Sun, N., Wigmosta, W., Leung, L. R., Hou, Z., Coleman, A., Skaggs R., Evaluating Next-Generation Intensity–Duration–Frequency Curves for Design Flood Estimates in the Snow-Dominated Western United States, *Hydrological Processes* 34.5: 1255-1268, 2020.
- [5] Burn, D. H., A Framework for Regional Estimation of Intensity–Duration–Frequency (IDF) Curves. *Hydrological Processes*. 28: 4209–4218, 2014.
- [6] Karahan, H., Ceylan, H., Ayvaz, T., Predicting Rainfall Intensity Using a Genetic Algorithm Approach. *Hydrological Processes*. 470–475, 2007.
- [7] Bernard, M. M., Formulas for Rainfall Intensities of Long Duration. *Transactions ASCE*, 96 (1801): 592-624, 1932.
- [8] Koutsoyiannis, D., Kozonis. D., Manetas, A., A Mathematical Framework for Studying Rainfall Intensity-Duration-Frequency Relationships. *Journal of Hydrology*, 206: 118-135, 1998.
- [9] Okonkwo, G. I., Mbajiorgu, C. C., Rainfall Intensity-Duration-Frequency Analysis for Southeastern Nigeria. *Agricultural Engineering International: CIGR Journal*, 12(1): 22 –30, 2010.
- [10] Ayuso-Munoz J. L., Garcia-Marin, A., Ayuso-Ruiz, P., Estevez, J., Pizarro-Tapia, R., Taguas, E. V., A More Efficient Rainfall Intensity-Duration-Frequency Relationship by Using an "At-Site" Regional Frequency Analysis: Application at Mediterranean Climate Locations. *Water Resources Management*, 29: 3243-3263, 2015.
- [11] El-Sayed, A. H., Generation of Rainfall Intensity Duration Frequency Curves for Ungauged Sites, Nile Basin. *Water Science and Engineering Journal* 4(1): 112-124, 2011.
- [12] Karahan, H., Ayvaz, T. M., Gürarslan G., Şiddet-Süre-Frekans Bağıntısının Genetik Algoritma ile Belirlenmesi: GAP Örneği, *İMO Teknik Dergi* 4393.4407: 290, 2008.
- [13] Ghiaei, F., Kankal, M., Anılan, T., Yüksek, O. (2018). Regional Intensity–Duration–Frequency Analysis in the Eastern Black Sea Basin, Turkey, by using L-moments and Regression Analysis., *Theoretical and Applied Climatology*, 131(1-2), 245-257.
- [14] Yavuz, K., Türkiye'deki Standart Süreli Yağışlar İçin Şiddet-Süre-Tekerrür Periyodu İlişkisinin Uygun Olasılık Dağılım Fonksiyonunun Belirlenmesi ve Formülüze Edilmesi, *Diss. Master Thesis Erciyes University, Kayseri*, 2018.
- [15] De Vyver, H. V., Bayesian Estimation of Rainfall Intensity–Duration–Frequency Relationships. *Journal of Hydrology*. 529: 1451–1463, 2015.
- [16] Srivastav, R. K., Schardong, A., Simonovic, S. P., Equidistance Quantile Matching Method for Updating IDF Curves Under Climate Change. *Water Resources Management*, 28: 2539–2562, 2014.
- [17] Yüksek, Ö., Kankal, M., Üçüncü, O., Assessment of Big Floods in the Eastern Black Sea Basin of Turkey, *Environmental Monitoring and Assessment*, 185:797–814, 2013.

- [18] Bayazıt, M., Avcı, I., Water Resources of Turkey: Potential, Planning, Development and Management. *International Journal of Water Resources Development*. 13:443-452, 1997.
- [19] Uzlu, E., Akpınar, A., Komurcu, M. I., Restructuring of Turkey's Electricity Market and the Share of Hydropower Energy: The case of Eastern Black Sea Basin. *Renewable Energy*, 36: 676–688, 2011.
- [20] DSİ, Annual Flood Reports, Ankara, Turkey, General Directorate of State Hydraulic Works, 1970-2005.
- [21] Anılan, T., Yüksek, Ö., Kankal, M., Doğu Karadeniz Havzası'nın L-Momentlere Dayalı Taşkın Frekans Analizi, *Teknik Dergi* 27.2: 7403-7427,2016.
- [22] Akçalı, E., Arman, H., Yağış Eşiği Bazlı Heyelan Erken Uyarı Sistem Önerisi: Trabzon İli Örneği, *Teknik Dergi* 24.116, 2013.
- [23] Anılan, T., Yüksek, Ö., Perception of Flood Risk and Mitigation: Survey Results from the Eastern Black Sea Basin, Turkey, *Natural Hazards Review* 18.2: 05016006, 2017
- [24] Örgün, E., Analysis of Rainfall Intensity-Duration-Return Period Relationship for Turkey. MSc Thesis, Karadeniz Technical University Institute of Natural Sciences, Civil Engineering Division (in Turkish), 2015.
- [25] Yüksek, Ö., Yüksel, İ., Ertaş, B., Rainfall Intensity-Duration-Return Period Analysis in the Eastern Black Sea Region, Turkey. 9th International Congress on Advances in Civil Engineering, September 27-30, Trabzon, Turkey, 2010.
- [26] Sherman, C. W., Frequency and Intensity of Excessive Rainfall at Boston, Massachusetts. *Transaction Paper*, 95: 951-960, 1931.
- [27] Benzeden, E., Hacısüleyman, H., Variation of Parameters in Rainfall Intensity-Duration-Return Period with Return Period. *Proceedings of 1st National Water Engineering Symposium*, İzmir, Turkey.1: 159-161 (in Turkish), 2003.
- [28] Minh, N. L., Tachikawa, Y., Sayama, T., Takara, K., Derivation of Rainfall Intensity-Duration-Frequency Relationships for Short-Duration Rainfall from Daily Data. *IHP Technical Documents in Hydrology*, 6: 89-96, 2006.
- [29] Minh, N. L., Tachikawa, Y., Sayama, T., Takara, K., A Simple Scaling Characteristic of Rainfall in Time and Space to Derive Intensity-Duration-Frequency Relationships. *Annual Journal of Hydraulic Engineering JSCE*, 51:73-78, 2007.
- [30] Asikoglu, O. L., Benzeden, E., Simple Generalization Approach for Intensity–Duration–Frequency Relationships. *Hydrological Processes*, 28(3):1114-1123., 2014.



# **Effect of Sub-Contractor Selection on Construction Project Success in Turkey**

**Ali Erkan KARAMAN<sup>1</sup>**

**Koray SANDAL<sup>2</sup>**

## **ABSTRACT**

The construction industry leads the national economy in developing countries. It involves industrial requirements, such as developing technologies, related expertise, demand variability, high production speed and progress. Firms in the industry use subcontractors to produce fast, effective solutions. Therefore, projects' success varies depending on subcontractors' rather than general contractors' performance. This study aimed to develop a model of selection criteria for subcontractors and measure their impact on project success. Construction firms using subcontractors were chosen as the target group. Data on the selection of subcontractors from 93 construction firms that employ subcontractors in their projects were collected through a survey. The impact of the subcontracting selection factor on projects' overall performance was presented with five hypotheses and modeled using a structural equation model. The weight of each selection factor in the subcontracting selection and the impact on the overall project were designated in the model by determining the standardized regression weights ( $\beta$ ). Four hypotheses were accepted and one rejected. This study may contribute to the prequalification conditions in the process of selecting subcontractors in the future.

**Keywords:** Subcontracting, subcontractor selection factors, subcontractor project performance.

## **1. INTRODUCTION**

Subcontracting is a popular term within the construction industry and Doloi et al.'s [1] model, which measures the impact of contractor selection on project success, was developed (by adding safety performance) and used to measure subcontractors' impact on project success[2]. General contractors tend to work with subcontractors for reasons such as cost, better management of time and quality and an opportunity to work with experts [3].

---

Note:

- This paper has been received on May 4, 2020 and accepted for publication by the Editorial Board on March 1, 2021.
- Discussions on this paper will be accepted by September 30, 2022.

• <https://doi.org/10.18400/tekderg.731728>

1 Balıkesir University, Department of Civil Engineering, Balıkesir, Turkey  
ekaraman@balikesir.edu.tr - <https://orcid.org/0000-0003-1958-9743>

2 Balıkesir Metropolitan Municipality Department of Science Affairs, Balıkesir, Turkey  
koraysandal@gmail.com - <https://orcid.org/0000-0001-9668-4352>

Subcontractors can generally be defined as parties that co-operate with general contractors based on their skills and competencies in the execution of construction projects. The construction industry has a hierarchical structure consisting of the general contractor contracting with the customer, subcontractors working with the general contractor and numerous members of staff working in both.

A construction project is awarded to a general contractor, who is an expert in its field and has completed prior projects, to conduct a specific project. The general contractor is responsible for the management process, such as executing agreements with the clients, project finance, supplying material and equipment and reviewing the progress of the project [4]. The main purpose of contractor selection is to reduce the project risk, maximize the quality and maintain a strong relationship between the project parties. The same concept is applied to the subcontractor selection process. According to Albino and Garavelli [5], the success of subcontractors is the key element of the performance of the general contractor. This is asserted by the study conducted by Mbachu [6] as well. According to some proprietors, the cost is the most fundamental criterion in the contractor selection process. However, following the research conducted, more consideration should be given to a selection process with multiple factors in contractor selection. Many general contractors and owners only deal with the lowest bidder and ignore other criteria in their consideration. A similar situation applies to the subcontractor selection process [7].

Subcontractors have a vital role in the construction industry and are specialized contractors hired to conduct specific tasks in a project. In many projects, especially building projects, the work carried out by subcontractors can amount to 80–90% of the total work. Hinze and Tracey [8] and Dainty et al. [9] stated that 57% of the gross amount of construction work (including small-scale maintenance repairs) consists of consumables and subcontracting services. The larger and the more complex a project becomes, the more subcontractors are needed [10]. Therefore, whenever a large construction project takes place, the number of subcontracts increases. Miller et al. [11] pointed out that material and service purchases from suppliers and subcontractors make up approximately 75–80% of the total cost. Kumaraswamy and Matthews [12] asserted that subcontractors can contribute up to 90% of the total construction project value. Subcontracting is a solution to uncertainty and complexity whereby trust, technical and financial risks are shared between the parties [13]. The subcontractor selection procedure varies according to conditions related to the necessities, environment and agreement. The more important the agreement is, the more attention should be paid to the selection and purchase processes [14].

The Turkish construction industry is one of the industrial sectors that uses subcontracting most comprehensively. Subcontracting services are considered as a fundamental and unchanging feature of construction-based organizations [15]. Subcontracting enables employment at the minimum and encourages expertise in construction projects [16]. Topcu [17], Ulubeyli et al. [18] and Polat et al. [19] conducted research related to the selection of subcontractors in Turkey. This study offers a different performance measurement model from others. The research objective is to measure the impact of subcontractor selection criteria on project success. In the literature section of this study, national and international studies related to subcontracting selection are examined. Hypotheses regarding this research are put forward. Finally, the findings and conclusions are presented.

## **2. LITERATURE RESEARCH**

Albino and Garavelli [5] explained the complexity of subcontractor selection among companies operating in the construction industry. According to Albino and Garavelli, this process is conducted following the intuition and experiences of the firm managers rather than depending on the data. Five measurement factors were defined, and each was measured with a single question and evaluated statistically. Hatush and Skitmore [20] identified a systematic multi-criteria decision analysis technique based on utility theory and evaluation according to the capacities of different subcontractors for proposal and selection in a construction project. Data on 24 measurement factors obtained from 5 contractors were evaluated. Okoroh and Torrance [21] and Abbasianjahromi et al. [22] used the fuzzy logic theory for subcontractor selection in repair projects. Dloi et al. [1] measured project success with (1) soundness of the business and workforce, (2) planning and control, (3) quality performance and (4) past performance. For this measurement, the effects of these factors on each other are included in the model. Piasny and Paslawski [23] researched the progress of quality by selecting the most appropriate subcontractor using survey data obtained from 8 construction projects. Bingöl and Polat [24] stated that general contractors' selection of subcontractors according to the lowest price results in them working with poor-quality subcontractors. They introduced a performance measurement system taking key performance indicators (KPI) as a model while mentioning the importance of performance assessment in the subcontractor selection process. Lew et al. [25] developed a structural equation model that evaluates the data obtained from 162 general contractor companies. Yu et al. [26] developed a model called PreCSAM for contractor selection. This model offers a three-stage evaluation with criteria such as the lowest offer and the best value.

In the doctoral study by Ulubeyli [15] on subcontractor selection in the Turkish construction industry, a fuzzy decision-making base model was developed and tested in a construction project. Graduate studies on the subcontractor selection process were carried out with the analytic hierarchy process (AHP) method [27] and the analytic network process (ANP) method [28]. Polat and Damci [29] determined the importance levels of the criteria used in the subcontractor selection of Turkish companies in international construction projects. Aydın et al. [30] solved the subcontractor selection problem through the TOPSIS and VIKOR methods. Ulubeyli et al. [18,31] examined the subcontractor selection of Turkish companies in international construction projects based on fuzzy importance weights. Erdoğan [32] used the TOPSIS methodology for risk-based subcontractor selection. The studies conducted mostly aimed to determine the importance level of subcontractor selection criteria, and no research has been conducted on the impact of these selection criteria on project success.

The analysis methods used in the literature research on subcontractor selection are generally based on AHP or first-generation statistical methods (such as regression analysis). Structural equation modeling, referred to as a second-generation data analysis technique [33], has been used in several studies (e.g. [1,25]). The structural equation model provides a systematic and comprehensive approach to a complex research problem in a single process by modeling the relationships between many dependent and independent variables [34]. In this study, a model was developed to measure the direct effects of expressions of subcontractor selection criteria on project success. The developed model is based on the model previously used by Dloi et al. [1]. In this model, the safety performance factor was included in addition to Dloi et al.'s measurement factors.

### **3. SUB-CONTRACTOR SELECTION IN CONSTRUCTION PROJECTS**

Many general contractors work in the construction area and hire subcontractors. A general contractor can deal with some parts of the work itself; however, it should work with expert subcontractors to complete most of the project successfully. While a good subcontractor contributes to the success of a project, a bad subcontractor can lead a project into trouble.

The selection of the right subcontractor increases the general contractor's success in construction projects [35]. Different models have been presented in the literature regarding the importance of subcontractor selection. Mbachu [6], in his study, examined the effective criteria to evaluate the ability of subcontractors to be invited to participate in the tender process. Subcontractors are listed according to the decision makers' opinions in line with the determined criteria. In the selection of the best candidate, their parameters are considered, including the weight of each decision maker, the weight of each criterion and the subcontractor scores. Wang et al. [36] applied fuzzy logic and genetic algorithms together to develop a fuzzy hybrid model in subcontractor selection. In their work, they divided projects into sub-projects via fuzzy logic and assigned the best subcontractor to each sub-project. Ng and Luu [3] collected the prior records of successful and unsuccessful subcontractors and submitted a model that they built on case-based reasoning. Hartmann and Carteling [37] searched for the criteria that general contractors give more importance. The results obtained showed that the price is the most important criterion for general contractors. Kozlovska and Strukova [38] stated that reliability performance should be added to the determining key factors for the selection of a contractor or subcontractor.

In this study, the fundamental factors that can be used for subcontractor selection by general contractor companies in construction projects were identified using an evaluation undertaken through literature research on similar studies (e.g. [1, 25, 29, 39, 40]) in the construction industry or in different organizations. On the other hand, as subcontractors are a kind of contractor, they make use of the factors formed for the selection of the general contractor. In this context, five selection factors that play a role in subcontractor performance were investigated in this study: (1) soundness of the business and workforce (SBW), (2) planning and control (PC), (3) quality performance (QP), (4) past performance (PP) and (5) safety performance (SP). The overall project success (OPS) was determined through the variables of duration, budget, quality and cost. Please find the measurement factors used in the study in Table 1.

*Table 1 - Measurement factors used in the research.*

| <b>Factors and indicators</b>  | <b>Source reference</b>             |
|--|-------------------------------------|
| <b>Soundness of business and workforce (SBW)</b> <ul style="list-style-type: none"><li>• Technical expertise (SBW1)</li><li>• Defects liability attitude (SBW2)</li><li>• Site safety records (SBW3)</li><li>• Successful past projects (SBW4)</li><li>• Yearly turnover (SBW5)</li><li>• Relevant work experience (SBW6)</li><li>• Working capital (SBW7)</li></ul> | Doloi et al. [1]<br>Lew et al. [25] |

Table 1 - Measurement factors used in the research. (Continue)

| Factors and indicators   | Source reference  |
|--|---|
| <b>Planning and control (PC)</b> <ul style="list-style-type: none"> <li>• Plant maintenance programs (PC1)</li> <li>• Work method statement (PC2)</li> <li>• Work's quality record (PC3)</li> <li>• Flexibility in the critical paths (PC4)</li> <li>• Failure to comply with quality specifications (PC5)</li> <li>• Failure in on-time delivery (PC6)</li> </ul> | <p>Doloi et al. [1]<br/>Lew et al. [25]</p>                                 |
| <b>Quality performance (QP)</b> <ul style="list-style-type: none"> <li>• Tender quality (QP1)</li> <li>• Tender timeliness (QP2)</li> <li>• Safety initiatives record (QP3)</li> <li>• Quality control and quality assurance programs (QP4)</li> <li>• Query response timeliness (QP5)</li> <li>• Failure to perform safety requirements (QP6)</li> </ul>          | <p>Doloi et al. [1]<br/>Lew et al. [25]<br/>Polat and Damci [29]</p>        |
| <b>Past performance (PP)</b> <ul style="list-style-type: none"> <li>• Length of relationships (PP1)</li> <li>• Regulation knowledge (PP2)</li> <li>• Turnover fluctuations (PP3)</li> <li>• Time in business (PP4)</li> <li>• Overall trade experience (PP5)</li> <li>• Past record of conflicts and disputes (PP6)</li> </ul>                                     | <p>Doloi et al. [1]<br/>Lew et al. [25]<br/>Polat and Damci [29]</p>        |
| <b>Safety performance (SP)</b> <ul style="list-style-type: none"> <li>• Safety control (SP1)</li> <li>• Investigation of causes of accidents (SP2)</li> <li>• Safety trainings (SP3)</li> <li>• High safety motivation (SP4)</li> </ul>  | <p>Subramaniam et al. [39]<br/>Lew et al. [25]<br/>Polat and Damci [29]</p> |
| <b>Overall project success (OPS)</b> <ul style="list-style-type: none"> <li>• On-time project delivery (OPS1)</li> <li>• On-budget project delivery (OPS2)</li> <li>• Desired quality outcomes (OPS3)</li> <li>• Cost savings (OPS4)</li> </ul>  | <p>Doloi et al. [1]<br/>Tam et al. [40]</p>                                 |

#### 4. RESEARCH METHODOLOGY

A survey was conducted to determine the effect of subcontractors on the success of construction projects. The survey form used in this study was prepared following principles determined using scientific research methods [41]. The survey questions were evaluated on a five-unit Likert scale from “totally agree to totally disagree.”

The sample of this study, which examined the impact of subcontractors on project success, was determined as construction projects hiring subcontractors. The judgment sampling method was used to identify the research sample due to the lack of a database showing

projects in which subcontractors were hired. The subcontractors that participated in the research consisted of technical staff and firm managers. For this reason, project managers, project supervisors, technical office managers, chefs and engineers in the construction area were determined as the target respondents of the research. Following the determination of the sample and target respondents, 150 construction companies, in conformity with the determined factor, were contacted in person, by telephone or by e-mail; 98 participants formed the scope of the study, and 5 survey forms were omitted from the assessment due to insufficient information. Therefore, the information obtained from 93 participants in the survey, which aimed to measure the impact of subcontractors on project success, was assessed following the guidance.

In this study, the structural equation model was used to analyze the data. Since the structural equation model involves adding the effect of each measurement indicator to the model, it has frequently been used in recent years [42,43,44]. The structural equation model was used to examine the hypotheses proposed above and presented in Figure 1. To increase the strength of the structural equation model [45,46,47], the width of the sample was upgraded with the bootstrap algorithm, and the value of the bootstrap was set as 500.

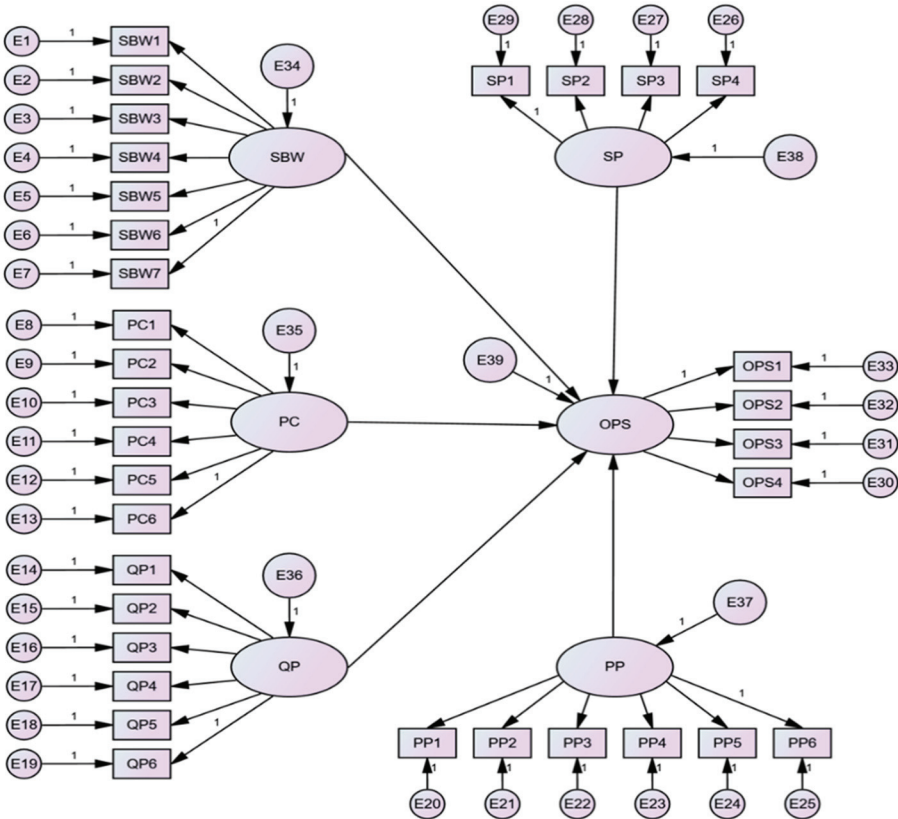


*Figure 1 - Hypothetical model of the relationship between subcontractor performance and overall project success.*

The studies mentioned above provided a theoretical base for the model created in this study and presented in Figure 1. Five research hypothesis were presented in this study to investigate the impact of five fundamental factors used in subcontractor selection (SBW, PC, QP, PP and SP) on the overall project success (OPS).

H1: The soundness of the business and workforce (SBW) has a positive and significant effect on the overall project success (OPS).

H2: Planning and control (PC) have a positive and significant effect on the overall project success (OPS).

H3: Quality performance (QP) has a positive and significant effect on the overall project success (OPS).

H4: Past performance (PP) has a positive and significant effect on the overall project success (OPS).

H5: Safety performance (SP) has a positive and significant effect on the overall project success (OPS).

## 5. RESEARCH FINDINGS

Information on the participants in the research is presented in Table 2. The table shows that 42% of the participants are in the age range of “30–40,” 29% are 30 years old or younger, 23% are in the age range of “40–50,” 5% are in the age range of “50–60” and 1% are aged 60 years or more. The distribution of project types found in the survey is 54% “general projects,” 27% “public projects,” 15% “road projects” and 4% “infrastructure projects.” Information regarding the subcontracting companies that had their contracts terminated during the project are also presented in Table 2: 70% of the participants responded “no,” 29% responded “yes” and the response of 1% was “unspecified”.

Table 2 - Information about the participants.

|   | Distribution           | Rate |
|---|------------------------|------|
| Age range of the participants                         | 30 and under           | 29%  |
|   | From 30 to 40          | 42%  |
|   | From 40 to 50          | 23%  |
|   | From 50 to 60          | 5%   |
|   | 60 and above           | 1%   |
| Project type  | Public project         | 27%  |
|   | Road project           | 15%  |
|   | Infrastructure project | 4%   |
|   | General project        | 54%  |
| Did you terminate the contract of any subcontractors? | Yes                    | 29%  |
|   | No                     | 70%  |
|   | Unspecified            | 1%   |

In the scope of the research, reliability analysis of the data to be used in the evaluation of the five subcontractor selection factors that have an impact on project success was performed by means of the SPSS program. Reliability analysis aims to determine the consistency of the questions among the measurement subjects. The Cronbach’s alpha ( $\alpha$ ) values obtained as a result of the reliability analysis and the average and standard deviation values regarding the variables are presented in Table 3.

*Table 3 - Mean ( $\mu$ ), standard deviation ( $\sigma$ ), Cronbach’s alpha ( $\alpha$ ) and average variance extracted (AVE) values of the variables used in the study.*

| <b>Factor</b>                           | <b>Item number</b> | <b>Mean (<math>\mu</math>)</b> | <b>Standard deviation (<math>\sigma</math>)</b> | <b>Cronbach’s alpha (<math>\alpha</math>)</b> | <b>AVE</b> |
|---|--------------------|--------------------------------|---|---|------------|
| Soundness of the business and workforce | 7                  | 3.800                          | 0.73945   | 0.880   | 0.497      |
| Planning and control                    | 6                  | 3.916                          | 0.70167   | 0.825   | 0.414      |
| Quality performance                     | 6                  | 3.932                          | 0.72844   | 0.826   | 0.691      |
| Past performance                        | 6                  | 3.950                          | 0.64024   | 0.769   | 0.412      |
| Safety performance                      | 4                  | 4.151                          | 0.82305   | 0.858   | 0.749      |
| Overall project success                 | 4                  | 4.048                          | 0.73593   | 0.796   | 0.412      |

The Cronbach’s alpha ( $\alpha$ ) value is an average of the standard change in weight that is found by the ratio of the sum of the variances stated in the questions in the sample to the overall variance. Whenever the Cronbach’s alpha ( $\alpha$ ) value is 0.70 and above, the questions stated in that group are considered as reliable [48]. The Cronbach’s alpha value of all the variables provided in Table 3 is above 0.70 and therefore the measurement is statistically reliable. As presented in Table 3, all the obtained average variance extracted (AVE) values exceed the recommended value of 0.50 [49]. Eliminated measurement items (SBW2, SBW5, SBW7, PC3, PC6, QP1, QP2, QP5, PP3, PP4, SP4) were not taken into consideration in the evaluation as they weaken the strength of the model when calculating the AVE value.

The structural model recommended for the research method was analyzed using Amos 23.0. The recommended goodness-of-fit (GOF) values obtained from the solution of structural models are stated in Table 3. The recommended level of GOF values was obtained from the studies by Tawalare et al. [50], Durdyev and Ihtiyar [51], Zhao et al. [52] and Civici [53].

The reliability of the results obtained from the model was interpreted using the GOF results given in Table 4. As a result of the analysis of the model, it can be seen that the GOF values are above the recommended threshold values, and this indicates that the B values obtained as a result of the analysis are significant and reliable. In Figure 2, the standardized regression weight values are presented regarding the measurement items related to the variables used in the model.

Table 4 - Results of GOF and the recommended level of GOF measures.

| Goodness-of-fit (GOF) measure                   | Results of GOF | Recommended level of GOF |
|---|----------------|--------------------------|
| $\chi^2$ /degree of freedom                     | 1.137          | $\leq 3.0$               |
| GFI (goodness-of-fit index)                     | 0.863          | $\geq 0.90$              |
| AGFI (adjusted goodness-of-fit index)           | 0.765          | $\geq 0.80$              |
| NFI (normal fit index)                          | 0.897          | $\geq 0.90$              |
| CFI (comparative fit index)                     | 0.986          | $\geq 0.90$              |
| TLI (Tucker–Lewis index)                        | 0.977          | $\geq 0.95$              |
| IFI (incremental fit index)                     | 0.986          | $\geq 0.95$              |
| RFI (relative fit index)                        | 0.839          | $\geq 0.90$              |
| RMSEA (root mean square error of approximation) | 0.039          | $\leq 0.05$              |

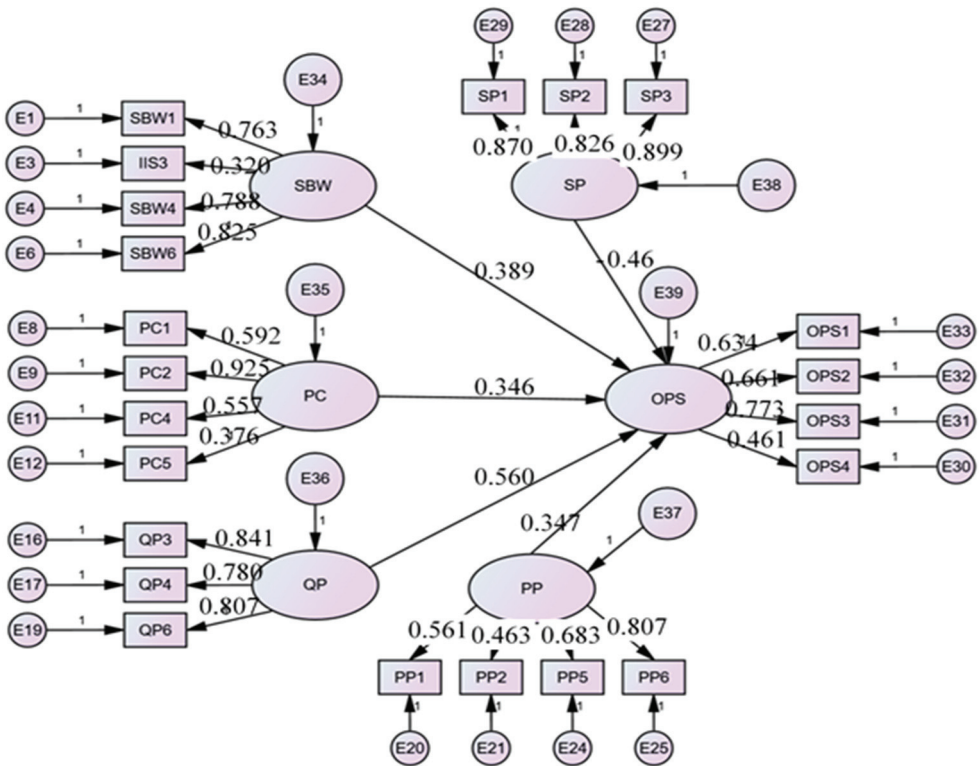


Figure 2 - Measurement model with standardized path coefficients.

The weights for all the measurement items were found to be statistically positive and significant ( $p < 0.05$ ) except for the impact of safety performance (SP) on the overall project success, which was found to be statistically negative and not significant ( $p = 0.617$ ,  $p > 0.05$ ).

## **6. CONCLUSIONS**

The main purpose of the contractor selection process is to reduce the project risk, maximize the quality and ensure timely completion of the project by maintaining a strong relationship between the project parties. The same process applies to the subcontractor selection process. This process is quite important for companies that have a project commitment. In this study, the performance factors of subcontractors used in construction projects were assessed and the impact of the subcontractor performance on the overall project performance was measured. Construction firms that use subcontractors were selected as the target group, and data were collected through the survey method. A reliability analysis was conducted on the data obtained from 93 participants. As in every scientific study, this study was carried out within a certain scope due to resource limitations. These limitations were time, financial resources, human thinking and interpretation capacity.

Four of the five hypotheses proposed in this study were accepted, and only safety performance was rejected. An examination of Figure 2 shows that “quality performance” (QP) is the leading criterion among the subcontractor selection factors. These factors were observed as a situation that was overemphasized by the participants during the face-to-face data collection process. Numerous contractual sanctions and audit frequency regarding quality performance made these factors important for the general contractors’ selections. The soundness of the business and workforce (SBW) was measured as a secondarily important factor. The underlying reason for the importance of the factor is that subcontractors represent general contractors in their work. They continue to work with the subcontractors with which they have previously worked and been satisfied in forthcoming projects. General contractors give importance to the past performance (PP) and the planning and control (PC) of subcontractors. While these two factors show the success of the completed work, they are also a reference for the projects that they will perform. Safety performance puts pressure on overall project success, both at the subcontractor level and at the general contractor level. Since it is the responsibility of the general contractor to ensure work safety in the project, subcontractor employees are often expected to follow only the safety instructions. Therefore, although it is an important factor for general contractors, there is no statistically significant relationship between the overall project success and this situation.

The most important contribution of this study is that four factors that have a direct positive effect on project success and the expressions used in their measurement can be used in the pre-evaluation process of subcontractor selection. Thus, general contractors will realize more successful projects with subcontractors that have a certain prequalification. The most important limitation of this study is the small number of participants. This situation affects the number of measurement factors. In the future, considering the subcontractors’ fields of activity, more research with more measurement factors and more participants is recommended.

## References

- [1] Doloi, H., Iyer, K.C. and Sawhney, A., Structural equation model for assessing impacts of contractor's performance on project success, *International Journal of Project Management*, Vol. 29, pp. 687-695, 2011.
- [2] El-Mashaleh, M. S., A construction subcontractor selection model, *Jordan Journal of Civil Engineering*, Vol. 3., No.4, pp. 375-378, 2009.
- [3] Ng, S. T.; Luu, C. D. T., Modelling subcontractor registration decisions through case-based reasoning approach, *Automation in Construction* Vol. 17, No. 7, pp. 873–881, 2008.
- [4] Benjaoran, V., A cost control system development: A collaborative approach for small and medium-sized contractors, *International Journal of Project Management*, Vol. 27, pp. 270–277, 2009.
- [5] Albino V and Garavelli A.C., A neural network application to subcontractor rating in construction firms, *International Journal of Project Management*, Vol. 16, pp. 9–14, 1998.
- [6] Mbachu, J., Conceptual framework for the assessment of subcontractors' eligibility and performance in the construction industry, *Construction Management and Economics* Vol.26, pp. 471–484, 2008.
- [7] Marzouk M. M., El-Kherbawy A. A. and Khalifa M., Factors influencing sub-contractors selection in construction projects, *HBRC Journal*, Vol. 9, No.2, pp. 150–158, 2013.
- [8] Hinze J. and Tracey A.2 Contractor-subcontractor relationship: the subcontractor's view, *Journal of Construction Engineering and Management*, Vol. 120, No. 2, pp. 274–287, 1994.
- [9] Dainty, A, Briscoe. G, and Millet. O., Subcontractor perspective on supply chain alliances, *Construction management and Economics*, Vol.19, No. 2, pp. 841-848, 2010.
- [10] Eccles,R., Bureaucratic versus craft administration: the relationships of market structure to the construction firm, *Administrative Science Quarterly*, Vol. 26, No. 3, pp. 449-469, 1981.
- [11] Miller,C.; Packham, G. and Thomas, B., Harmonisation between main contractors and subcontractors: prerequisite for lean construction, *Journal of Management in Engineering*, Vol. 16, No. 3, pp. 47-57, 2002.
- [12] Kumaraswamy, M. and Matthews, J., Improved subcontractor selection employing, *Journal of Construction Research Partnering Principles*, Vol. 16, No. 3: pp. 47-57, 2000.
- [13] Brook, M., *Estimating and tendering for construction work*, Oxford: Butterworth Heinemann, 2008.
- [14] Shiau, Y., Tsai, T., Wang, W. and Huang, M., Use questionnaire and AHP techniques to develop subcontractor selection system, *Construction Management and Economics*, Vol. 33, No. 2, pp. 1-6, 2002.

- [15] Ulubeyli, S., Uluslararası inşaat projelerinde alt yüklenici seçimi için bulanık çok ölçütlü karar verme modeli, PhD Thesis (in Turkish), İstanbul University, 2008.
- [16] Arslan, G., Kıvrak, S., Birgönül, M. T. and Dikmen, İ., Improving sub-contractor selection process in construction projects: web-based sub-contractor evaluation system (WEBSES), *Automation in Construction*, Vpl. 17, No. 4, s.480-488, 2008.
- [17] Topcu, İ., A decision model proposal for construction contractor selection in Turkey, *Building and Environment*, vol. 39, no. 4, pp. 469–481, 2004.
- [18] Ulubeyli, S., Kazaz, A., Arslan, V., Decision Criteria for Subcontractor Selection in International Construction Projects. International Conference on Civil and Environmental Engineering (ICOCEE), At Nevsehir, Turkey, 2017.
- [19] Polat G., Kaplan B, Bingol B.N., Subcontractor selection using genetic algorithm, *Procedia Engineering* 123: 432-440, 2015.
- [20] Hatush, Z. and Skitmore, M., Contractor selection using multicriteria utility theory: An additive model, *Building and Environment*, Vol.33, No. 2-3, pp. 105-115, 1998.
- [21] Okoroh, M. I. and Torrance, V. B., A model for subcontractor selection in refurbishment projects, *Construction Management and Economics*, Vol. 17, No. 3, pp. 315-327, 2010.
- [22] Abbasianjahromi H., Rajaie H. and Shakeri E., A framework for subcontractor selection in the construction industry, *Journal of Civil Engineering and Management*, Vol. 19, No. 2, pp. 158-168, 2013.
- [23] Piasny, J. and Paslawski, J., Selection of subcontractors as the quality improvement tool in housing construction, *Procedia Engineering*, Vol. 122, pp. 274-28, 2015.
- [24] Bingöl, B.N., Polat G., Risk analysis in the subcontractor selection process for international construction projects, *International Conference on Construction and Real Estate Management*, pp. 1285-1292, 2017.
- [25] Lew YL, Hassim S, Muniandy R, Hua L.T., Structural equation modelling for subcontracting practice: Malaysia chapter, *Engineering, Construction and Architectural Management*, Vol. 25, No. 7, pp. 835-860, 2018.
- [26] Yu W.D., Chang H.K., Hsu Y.Y., Cheng S.T., Wang K.W., Pretending decision model for contractor selection of public procurement projects, *Journal of Construction Engineering and Management – ASCE*, Vol. 146, Issue 11, 2020.
- [27] Çiftçioğlu, B., Contractor selection by AHP method in construction sector. Application in a housing project. ITU Master Thesis., 2013.
- [28] Acar, Y. (2014). Choosing sub-contractor by ANP (Analytic Network Process) method in construction sector. Osmangazi University Master Thesis., 2014.
- [29] Polat G., Damci A., Subcontracting practices in international construction projects evidence from Turkish contractors, *Creative Construction Conference*, Prague, 2014.

- [30] Aydın, H., Okul, B., Ayvaz, B., Kuşakçı, A. O., Kağıtçıoğlu, S., Çok kriterli karar verme teknikleri ile alt yüklenici seçimi: İnşaat sektöründe bir uygulama, Bartın Üniversitesi İktisadi ve İdari Bilimler Fakültesi Dergisi, 7(14), 29-44, 2016.
- [31] Ulubeyli S., Manisali E., Kazaz A., "Subcontractor selection practices in international construction projects" *Journal of Civil Engineering and Management*, 16, 47-56, 2010.
- [32] Erdoğan, O., Topraklı Y., Türkiye inşaat endüstrisinde risk tabanlı alt yüklenici seçiminde TOPSIS metodolojisi ve değerlendirmesi. *Bayburt Üniversitesi Fen Bilimleri Dergisi*, Cilt 2, Sayı 1, 2019.
- [33] Bagozzi R. P., Fornell C., *Theoretical Concepts, Measurement, and Meaning*, Vol. 2, C. Fornell (Ed.) *A Second Generation of Multivariate Analysis*, Praeger, ss. 5-23, 1982.
- [34] Anderson J. C., Gerbing D. W., *Structural equation modeling in practice: A review and recommended two-step approach*", *Psychological Bulletin*, 103, ss. 411-423, 1988.
- [35] Yin, H.; Wang, Z.; Yu, J.; Ji, Z.; Ni, H., *Application of DEA cross evaluation model in project dynamic alliance subcontractors selection*, *International Workshop on "Intelligent Systems and Applications"*, 23–24 May, Wuhan, 1–4, 2009.
- [36] Wang, D.; Yung, K. L.; Ip, W. H., *A heuristic genetic algorithm for subcontractor selection in a global manufacturing environment*, *IEEE Transactions on Systems, Man and Cybernetics. Part C. Applications and Reviews*, Vol. 31, No. 2, pp. 189–198, 2001.
- [37] Hartmann, A.; Caerteling, J., *Subcontractor procurement in construction: the interplay of price and trust*, *Supply Chain Management: An International Journal of Project Management*, Vol.15, pp. 354–362, 2010.
- [38] Kozlovská, M., and Struková, Z., *Integration of occupational safety to contractors' or subcontractors' performance evaluation in construction projects*, *Journal of Civil Engineering*, Vol. 8, No. 1, pp. 13-24, 2013.
- [39] Subramaniam C., Shamsudin F.M., Alshuaibi, A., *Investigating employee perceptions of workplace safety and safety compliance using pls-sem among technical employees in Malaysia*, *Journal of Applied Structural Equation Modeling*: 1(1), 44-61, 2017.
- [40] Tam, V.W.Y., Shen, L. and Kong, J.S.Y., *Impacts of multi-layer chain subcontracting on project management performance*. *International Journal of Project Management*, 29, 108-116, 2011.
- [41] Kinneer, T.C. and Taylor, J.R., *Marketing research: an applied approach*, fourth edition, McGraw-Hill, Singapore, 2012.
- [42] Kar S., Jha K., *Examining the effect of material management issues on the schedule and cost performance of construction projects based on a structural equation model: survey of indian experiences*. *Journal of Construction Engineering and Management*. 146. 10.1061/(ASCE)CO.1943-7862.0001906, 2020.

- [43] Budayan C., Çelik T., Determination of important building construction nuisances in residential areas on neighbouring community, *Teknik Dergi*, 32 (2), DOI: 10.18400/tekderg.486628, 2021.
- [44] Demirdöğen G., Işık Z., Structural equation model of the factors affecting construction industry innovation success. *Teknik Dergi*, 32 (2), 0-0 . DOI: 10.18400/tekderg.567272, 2021.
- [45] Arbuckle, J.L., *Amos 4.0 Users Guide*, Chicago, Ill: SPSS Inc., 1999.
- [46] Dong, L., Neufeld, D. and Higgins, C., Testing Klein and Sorra's innovation implementation model: An empirical examination, *Academy of management conference*, Vol. 25, No:4, pp. 237-255, 2008.
- [47] Peterson, I., Pick a sample, *Science News*, Vol.140, pp. 56-57, 1991.
- [48] Nunally J. C., *Psychometric theory* (2nd edition). McGraw-Hill, New York, 1978.
- [49] Hair, J. F., Black, W. C., Babin, B. J., & Anderson, R. E., *Multivariate data analysis* (7th edition), New York: Pearson, 2010.
- [50] Tawalare, A., Laishram, B., & Thottathil, F. (2020). "Relational partnership in public construction organizations: front-line employee perspective." *Journal of Construction Engineering and Management*, Vol. 146, No. 1, DOI: 10.1061/(ASCE)CO.1943-7862.0001723.
- [51] Durdyev, S., & Ihtiyar, A. (2019). "Structural equation model of factors influencing students to major in architecture, engineering, and construction." *Journal of Professional Issues in Engineering Education and Practice*, Vol. 145, No. 2, pp. 1-8, DOI: 10.1061/(ASCE)EI.1943-5541.0000402.
- [52] Zhao L., Wang B., Mbachur J. and Liu Z. (2019). "New Zealand building project cost and its influential factors: A structural equation modelling approach." *Advances in Civil Engineering*, Vol. 2019, pp. 1-15, DOI: 10.1155/2019/1362730.
- [53] Çivici, T . (2017). Mimari tasarım firmalarında müşteri yönlülük: Bir yapısal denklem modeli . *Balıkesir Üniversitesi Fen Bilimleri Enstitüsü Dergisi* , 19 (2) , 87-98 . DOI: 10.25092/baunfbed.340543.

# **Multi Agent System Based Risk Allocation Model for Public-Private-Partnership Type Projects (RAMP<sup>3</sup>)**

**Hande ALADAG<sup>1</sup>**

**Zeynep ISIK<sup>2</sup>**

## **ABSTRACT**

The performance of the Public Private Partnership (PPP) projects depends on the efficiency of the risk allocation strategies between the public and private parties. Therefore, a multi agent system-based Risk Allocation Model for PPP projects (RAMP<sup>3</sup>) was developed to determine the proper risk allocation decisions between the public and private parties within the study. The methodology of RAMP<sup>3</sup> involves i) identification of risks by agents, ii) assessment of each risk's importance and impact, iii) communication of agents to negotiate on risk allocation decision and iv) determination of strategies and utility functions to be used in negotiation process. Focus of the study is presenting the steps of negotiation process of agents using economic theory and Zeuthen bargaining strategy. RAMP<sup>3</sup> was validated on two real PPP projects and results show that the higher risk value of an agent gets, agent's utility due to counter agent in that concession round lowers. Preliminary findings also show that risk is allocated to the party that has a higher risk acceptability in negotiation process. The RAMP<sup>3</sup> will enable project parties to determine the appropriate risk allocation strategies by considering the effects of emerging risks in terms of time delay, cost overrun and conflict and provide contract success. The model can also be used as a decision support system by public partner for performing an efficient and accurate risk allocation.

**Keywords:** Construction industry, construction projects, Multi-Agent System (MAS), Public Private Partnership (PPP), risk management.

## **1. INTRODUCTION**

Growing population and urbanization create a need for infrastructure investments along with improvement of the existing ones. Upon considering the increased infrastructure requirements along with the economic growth targets, Public Private Partnership (PPP)

---

Note:

- This paper has been received on May 30, 2020 and accepted for publication by the Editorial Board on March 1, 2021.
- Discussions on this paper will be accepted by September 30, 2022.

• <https://doi.org/10.18400/tekderg.745510>

1 Yildiz Technical University, Department of Civil Engineering, Istanbul, Turkey - [haladag@yildiz.edu.tr](mailto:haladag@yildiz.edu.tr)  
<https://orcid.org/0000-0001-7627-8699>

2 Yildiz Technical University, Department of Civil Engineering, Istanbul, Turkey - [zeynep@yildiz.edu.tr](mailto:zeynep@yildiz.edu.tr)  
<https://orcid.org/0000-0001-8825-0001>

projects has been identified as an important potential by experts in terms of maintaining sustainable performance of the construction industry.

Despite being a financial model developed for establishing the public investments, PPP models are considered as a contract type that determine the rights, responsibilities and privileges between the public and the private sectors. Therefore, contracts between the public and the private sectors are important for ensuring effectiveness and efficiency during the entire lifecycle of the project [1], [2] along with resolving risk allocation problems which has the potential to affect the long term and stable cooperation between stakeholders in PPP projects [3], [4].

Risk management is important in each construction project. However, it plays a more outstanding role in PPP projects, since they are implemented as long-term contracts where the risks are distributed between the public and the private sectors appropriately. The performance of PPP infrastructure projects depends upon the efficiency of the risk distribution strategies adopted between the public and the private sectors and how the risks are balanced on the contracts within this context. Therefore, considering the long-term impacts of risk allocation decisions, the associated risks should be assigned to the stakeholder that is able to manage the risk better via contract [5]. However, it is observed that the principle of assigning the risk to the stakeholder that would manage it better is not practiced in general due to the disagreements between the project stakeholders based on their risk management skills [6], [7]. Thus, risk allocation process in PPP projects is generally implemented based on subjective interpretation of the parties. To overcome this shortcoming, there is a significant need for risk allocation models that determine which stakeholder (public or private sector) should manage the potential risks in PPP projects based on the possible impacts of the risks on the parties and risk allocation attitudes of the parties. However, it is observed that parameters such as risk sharing attitudes, risk management capacities of the stakeholders, contract conditions, etc. are not often addressed by the previous risk management studies related to PPP projects.

Within this background, a multi agent system-based Risk Allocation Model for PPP projects (RAMP<sup>3</sup>) was developed to simulate the risk assessment process for PPP projects. RAMP<sup>3</sup> allows establishing realistic risk assignments by exhibiting how the general risks regarding PPP projects should be shared between the parties based on the different objects, goals, utilities, motivation, and knowledge-skill levels of each parties. The multi agent-based risk sharing system of RAMP<sup>3</sup> ensures inclusion of the decisions regarding the risk assignment in the contract at the end of the negotiations carried for each individual risk between the parties regarding the assignment of the relevant risk in PPP projects. The advantages of RAMP<sup>3</sup> for the construction companies comprise; achieving contractual success in PPP projects and determining appropriate risk allocation strategies based on the assessment of potential time, cost, and disputes. Another important advantage of RAMP<sup>3</sup> is that it can be used as an auxiliary tool for early identification and effective management of potential risk factors in PPP projects.

## **2. MULTI AGENT SYSTEMS (MAS)**

Multi Agent Systems (MAS) consist of multiple autonomous units called agents that interact with each other to increase utility or to achieve a common goal. An agent is a computer

system capable of autonomous action in some environment. Multi agent systems are also considered as a fast-developing information technology, where several intelligent agents, representing the real-world parties, co-operate, negotiate, or compete to reach a common agreement, purpose or plan [8]. Achieving the common goal can be done either by cooperation where knowledge is shared among agents or by competition where knowledge is not shared. The following are the essential characteristics of agents that make them ideal for supporting cooperation, coordination, and negotiation:

- **Autonomy** - agents can operate without the direct intervention of humans or others and have control over their actions and internal state.
- **Reactive** - agents maintain an ongoing interaction with its environment and respond to the changes that occur in the environment.
- **Pro-activeness** - agents do not simply act in response to their environment, they attempt to achieve their goals.
- **Social ability** - agents can interact with other agents via agent communication language such as cooperate, coordinate, and negotiate with others.
- **Ability to learn** - agents can learn and update their information when interacting with the external environment [9].

## 2.1. MAS Use in Construction Management Literature

MAS can solve problems that are difficult or impossible for an individual agent or a monolithic system to solve. Therefore, in recent years, there is an increasing tendency in construction management literature to use MAS due to their ability to provide robustness and efficiency and to solve problems in which data, expertise, or control is distributed [8]. The construction industry requires multiple parties who should work together to execute a construction project (such as employer, designer, contractor, subcontractor etc.). Considering that those parties are mostly geographically diverse and have different perspectives and/or objectives about the project, it becomes crucial to use distributed problem-solving systems with multi agents to simulate the characteristic of construction projects [10]. Thus, multi-agent systems have considerable potential to address some of the fragmentation of the construction industry. In this context, many researchers in construction management area applied MAS in their research for solving distributed problems of the industry. General application of MAS methodology is used for solving construction engineering and management problems that involves a negotiation process between parties. Claim management, supply chain management, and risk management are some of the research fields that MAS is commonly used in construction management area.

## 2.2. MAS Use in Risk Management Literature

Although the studies related to risk management area generally aim to provide conceptual frameworks about risk allocation decisions, there should be more efforts for establishing decision support systems and developing risk management models by using information technologies. Thus, more systematic and realistic risk management models should be established. It is seen that the number of studies adopting MAS in risk management area for construction industry is quite

limited [10]. Chengshuang and Guochang [11] created a MAS based risk management system for construction projects in terms of the analysis of risk characteristics and management process of construction projects. Li and Ren [12] discussed the general procedure, the principles of risk allocation between the public client and the private consortium in a PPP project. They suggest that Bayesian approach, which is considering the responding information from the opponent, is more suitable in dynamic decision making for risk allocation. Karakas et al. [13] also developed MAS that simulates the negotiation process between parties (mainly contractor and client) about risk allocation and sharing of cost overruns in construction projects. Taillandier et al. [14] proposed a multi-agent model coupled with a stochastic approach with the aim of evaluating risk impacts for each stakeholder and for the whole construction project. Proposed model test different risk mitigation strategies to measure their interest and then to support risk management decisions. The main reason for developing this model is that the risks affecting construction projects are varied throughout the different phases of the project and there is more than one interaction between the risks.

In addition, risk management models developed by using MAS frequently used as decision-making processes and focus on risk-cost sharing or resolution of disputes between parties [11], [12], [13], [14], [15], [16], [17]. RAMP<sup>3</sup> model developed within the scope of this study is a decision support system that can be used primarily by decision makers like the existing models in the literature. However, rather than deciding which stakeholder should manage cost increases due to risks, it offers a decision support system for determining risk allocation decisions depending on impact of each risk on the project's success criteria along with the risk attitudes of the parties. In this context, it is possible to simulate the risk sharing process among the project participants and to identify risks that should be assigned to the stakeholder that is able to manage the risk better by the contract between the public and the private sectors. Considering that risk allocation studies for PPP construction project with MAS adaptation is relatively limited, the multi agent-based risk allocation model developed within the scope of this study aims to fill an important gap in the literature. In existing studies related to risk management area, parameters such as risk sharing attitudes, risk management capacities, contract conditions, etc. are often not addressed. However, within the scope of effective risk management, more than one project participant with different utility functions should be identified and the communication rules between them must be determined [16]. In this context, RAMP<sup>3</sup> model can be used as a decision support system for determining the risk allocation strategies of the project parties by evaluating risk factors specific to PPP transport projects according to project parties' objectives, knowledge-ability levels along with the impact of risk factors such as time extension, cost increase and conflict.

### **3. DESIGN OF RAMP<sup>3</sup> MODEL**

RAMP<sup>3</sup> consists of "agents" that are negotiating with each other to undertake or transfer risks depending on criteria such as contract, utility, risk attitudes and stakeholders' knowledge and management skills related to specific risk factor. RAMP<sup>3</sup> ensures the final risk sharing decisions as a result of the negotiation process depending on the risk response of the stakeholders and reflect risk sharing decisions to the contract. Therefore, RAMP<sup>3</sup> consist of stages such as i) identification of risks by agents, ii) assessment of each risk's importance and impact, iii) communication of agents to negotiate on risk allocation decision and iv) determination of strategies and utility functions to be used in negotiation process. Since the focus of this study is presenting negotiation process of agents (and steps it involves) through

the designed RAMP<sup>3</sup> model, detailed information regarding the first two stages were excluded (However, Table 1. shows the overall findings related to identification of risk factors affecting PPP construction projects and their predicted weights).

Within the architectural structure of the RAMP<sup>3</sup>, model constitutes four main agents representing concessionaire (private sector), public institution, contract, and risk factors. The architectural structure of the RAMP<sup>3</sup> is explained in detail below:

- **Risk factor agent:** This agent allows user to display information regarding all the risks and importance level of the risks that may affect the PPP project. Within this context, all risk factors affecting PPP projects through their life cycle were identified initially (Table 1). This agent delivers the relevant information to the agent representing public institution and the concessionaire to be used in the negotiation process.
- **Concessionaire agent:** The main purpose of this agent is to negotiate with the agent representing public institution to finalize the risk assignment result of the relevant risk. This agent obtains information related to the importance of each risk factor and calculates the impact of each risk factor. This agent negotiates with the agent representing public institution depending on criteria such as knowledge, organization, and management skills of the concessionaire. The agent also communicates with the agent representing the project contract to ensure that the risk allocation decision is concluded as a contract clause.
- **Public institution agent:** The main purpose of this agent is to negotiate with the agent representing concessionaire to finalize the risk assignment result of the relevant risk. This agent obtains information related to the importance of each risk factor and calculates the impact of each risk factor. This agent negotiates with the agent representing concessionaire depending on criteria such as knowledge, organization, and management skills of the public institution. The agent also communicates with the agent representing the project contract to ensure that the risk allocation decision is concluded as a contract clause.
- **Project contract agent:** This agent represents the terms of the project contract. User can display all the risk factors and risk allocation decisions related to the project. In addition, this agent coordinates with risk factors agent to find out if there are any risk factors not included in the contract draft. In addition, the contract intermediary provides the materialization of the associated issues if any, not included in the contract draft text but as a result of the information received from the risk factors intermediary. If any risk allocation decisions of the associated risk factors have not been discussed in the contract draft, this agent gives an alert to the user.

Figure 1 shows the overview diagram of the negotiation process in the RAMP<sup>3</sup>. There is only information flow from risk factor agent to the agents representing public institution and concessionaire. The negotiation process only takes place between public institution agent and concessionaire agent. The process ends when the related risk allocation decision is made. The risk allocation decisions given as a result of the negotiation process is conveyed to the contract agent. Thus, the parties responsible for the risk factors are determined in the contract text. Within the RAMP<sup>3</sup> model, the risk factor agent is responsible for identification of the project-specific risks whereas public institution and concessionaire agents are responsible for

initiating the negotiation process by estimating the time and cost increase in case of the occurrence of risk.

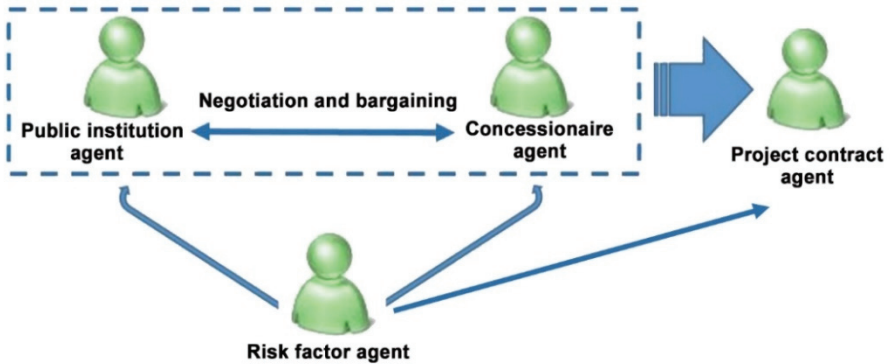


Figure 1 - The overview diagram of the negotiation process in the RAMP<sup>3</sup> model

The architecture of the RAMP<sup>3</sup> model was realized in Python programme. Python is an interpreted, object-oriented, high-level programming language with dynamic semantics. Its high-level built-in data structures, combined with its object-oriented approach help programmers write clear, logical code for small and large-scale projects [18]. An empirical study found that scripting languages, such as Python, are more productive than conventional languages, such as C++ and Java, for programming problems involving string manipulation and determined that memory consumption was often better than Java and not much worse than C++ [19]. The fact that python is commonly preferred to C++ or Java in cases where prototypes of large software have to be produced and tested quickly was effective in selecting this program.

#### 4. SYSTEM IMPLEMENTATION OF RAMP<sup>3</sup> MODEL

The output of multi agent system-based platform is the reflection of risk allocation decisions specific to PPP projects to the contract as a result of the negotiation process between the public and private sector parties. Since negotiation process between agents within the RAMP<sup>3</sup> model is one of the most important factors affecting the results produced by the system, sub-topics such as negotiation process, negotiation theories, concession protocols in negotiations, bargaining strategies, conflict deal and flowchart of negotiation process that will guide the communication and decision-making processes of the agents should be detailed.

##### 4.1. Negotiation Process

One of the critical stages in successful risk mitigation and fairly distribution is the capturing of the dynamics in negotiation process. The basic elements of the negotiation are defined as the interest, social motivates of the participants and their interactions [20]. Through negotiation, parties try to find a settlement point, from several options, that is acceptable for both parties. Risk allocation in a multi-agent environment can also be considered as a form

of negotiation [10]. Each negotiation has a start point (target), an end (agreement or disagreement) and a series of steps (offers) in between. To direct these steps, negotiators should be conscious of its characteristics and steps [17]. The factors influencing the decisions of the agents representing public institution and concessionaire are essential to understand their target values and minimum amounts that they can accept. Concessionaire agent’s target is to compensate almost all his losses, while public institution agent wants to complete the project with minimum additional payments. Negotiation will take place only if there is possible agreement zone between the defined positions (Figure 2).

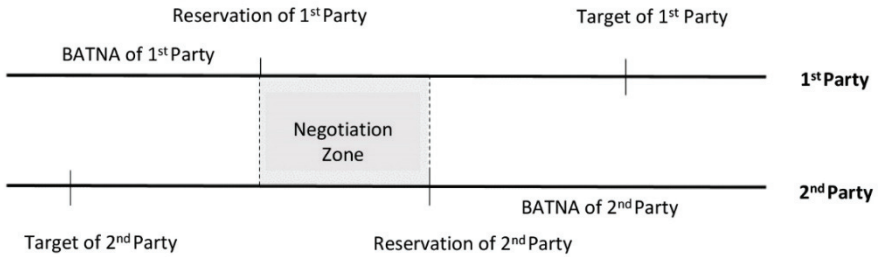


Figure 2 - Negotiation terms [17]

- **Target (Optimum) Value:** The highest amount that a party aimed to take from the negotiation is named as “target” and it will be the initial proposal of the parties. Calculation of initial offer is important, as the parties cannot suggest any more improvement during the negotiation process.
- **Reservation Value:** The minimum value that a party is willing to accept in negotiation is named as reservation value. Reservation value is closely related with Best Alternative to Negotiated Agreement (BATNA). BATNA defines what will happen in case of a conflict in negotiation, therefore parties need to know their BATNA to assess whether the incoming offer is acceptable or not. Defining reservation point before the negotiation is a key factor in successful negotiation. By determining reservation value, parties are protecting themselves from accepting an unfavorable option during negotiation.

In RAMP<sup>3</sup> model, each agent calculates its reservation value considering risk weight of each risk factor and risk impact that can be expressed as the loss if the risk occurs. The reservation value (RV) proposed by each agent at the beginning of the negotiation process, is calculated by using Equation (1) and (2).

$$RV = Risk\ Weight \times Risk\ Impact \tag{1}$$

$$Risk\ Impact = \sqrt[3]{(x_1y_1)(x_2y_2)(x_3y_3)} \tag{2}$$

where  $x_1, x_2, x_3$  indicates risk weight considering time extension, cost increase and claim for the relevant risk respectively;  $y_1, y_2, y_3$  the value of the loss to be incurred in terms of time extension, cost increase and claim respectively.

RAMP<sup>3</sup> was developed to determine the proper risk allocation decisions between the public and private parties for PPP projects. With this aim, all risk factors related to PPP projects were identified through a comprehensive literature review. As the result of comprehensive literature review, total number 99 risk factors were identified under 12 categories. Users can eliminate or add new project-specific risks by using risk factor agent in RAMP<sup>3</sup> model. Determined risk factors were conveyed to the risk factor agent within the RAMP<sup>3</sup> model. The predicted weight of each risk factor was calculated using Fuzzy Analytical Hierarchy Process (FAHP). For the details of FAHP calculations of determined risk factors, please see [29]. The predicted weight of each risk factor is presented to the model user within the RAMP<sup>3</sup> model. However, users can determine risk weight of each project specific risk factor. Table 1 shows Exogenous risk factors affecting PPP construction projects and their predicted weights as an example.

Table 1 - Exogenous risk factors affecting PPP construction projects [29]

|                 | Risk Categories                   | Risk Factors  | Risk Weights |
|-----------------|-----------------------------------|---|--------------|
| Exogenous Risks | <b>1. Political Risks</b>         | 1. Political instability                                  | 0,202        |
|                 |                                   | 2. Lack of national strategies                            | 0,243        |
|                 |                                   | 3. Termination of concessionaire by public institution    | 0,293        |
|                 |                                   | 4. Political opposition                                   | 0,262        |
|                 | <b>2. Legal Risks</b>             | 5. Inadequate legal framework:                            | 0,099        |
|                 |                                   | 6. Lack of law and regulations specific to PPP            | 0,118        |
|                 |                                   | 7. Changes in law and regulations                         | 0,113        |
|                 |                                   | 8. Environmental and Social Impact Assessment             | 0,123        |
|                 |                                   | 9. Failure/delay in obtaining permit/approval             | 0,159        |
|                 |                                   | 10. Ownership assets                                      | 0,119        |
|                 |                                   | 11. Expropriation   | 0,151        |
|                 |                                   | 12. Uncompetitive tender                                  | 0,118        |
|                 | <b>3. Macro-Economic Risks</b>    | 13. Importance for local economy                          | 0,167        |
|                 |                                   | 14. Instability of national economy                       | 0,097        |
|                 |                                   | 15. Fluctuation of the inflation rate                     | 0,071        |
|                 |                                   | 16. Fluctuation of interest rate                          | 0,140        |
|                 |                                   | 17. Currency risk   | 0,187        |
|                 |                                   | 18. Taxation risk   | 0,085        |
|                 |                                   | 19. Loan risk   | 0,159        |
|                 |                                   | 20. Fluctuation of the labor, material, equipment prices  | 0,095        |
|                 | <b>4. Socio-Cultural Risks</b>    | 21. Socio-cultural differences in the host country        | 0,294        |
|                 |                                   | 22. Socio-cultural differences between JV partners        | 0,310        |
|                 |                                   | 23. Social opposition to the project                      | 0,396        |
|                 | <b>5. Industry-Specific Risks</b> | 24. Demand changes  | 0,246        |
|                 |                                   | 25. Level of competition                                  | 0,234        |
|                 |                                   | 26. Market share of the project stakeholder               | 0,268        |
|                 |                                   | 27. Presence of supporting sectors                        | 0,252        |
|                 | <b>6. Natural Risks</b>           | 28. Force Majeure   | 0,272        |
|                 |                                   | 29. Unexpected weather conditions                         | 0,224        |
|                 |                                   | 30. Unexpected geological conditions                      | 0,251        |
|                 |                                   | 31. Unexpected site conditions (archeological finds etc.) | 0,253        |

Table 1 - Exogenous risk factors affecting PPP construction projects (continue) [29]

|                  | Risk Categories                               | Risk Factors   | Risk Weights |
|------------------|---|--|--------------|
| Endogenous Risks | <b>1. Project Management Competence Risks</b> | 1. Project time management                                       | 0,063        |
|                  |   | 2. Project cost management                                       | 0,060        |
|                  |   | 3. Project quality management                                    | 0,061        |
|                  |   | 4. Project human resource management                             | 0,039        |
|                  |   | 5. Project communications management                             | 0,058        |
|                  |   | 6. Project risk management                                       | 0,078        |
|                  |   | 7. Project procurement management                                | 0,056        |
|                  |   | 8. Project stakeholder management                                | 0,069        |
|                  |   | 9. Contract and dispute management                               | 0,074        |
|                  |   | 10. Demand management  | 0,077        |
|                  |   | 11. Process and documentation management                         | 0,063        |
|                  |   | 12. Occupational health and safety management                    | 0,057        |
|                  |   | 13. Waste and energy management                                  | 0,071        |
|                  |   | 14. Innovation management  | 0,067        |
|                  |   | 15. Operational management                                       | 0,106        |
|                  | <b>2. Competency Related Risks</b>            | 16. Organizational expertise and capabilities of the parties     | 0,070        |
|                  |   | 17. Tendering and pricing ability of the parties                 | 0,090        |
|                  |   | 18. PPP experience of public institution                         | 0,021        |
|                  |   | 19. PPP experience of private partners                           | 0,149        |
|                  |   | 20. Skilled workforce  | 0,150        |
|                  |   | 21. Financial adequacy of the partners                           | 0,110        |
|                  |   | 22. Financial adequacy of the subcontractors                     | 0,082        |
|                  |   | 23. Technical competency   | 0,178        |
|                  |   | 24. Know-How based on new technology and innovation applications | 0,151        |
|                  | <b>3. Organization and Coordination Risks</b> | 25. Improper partner selection                                   | 0,098        |
|                  |   | 26. Incompetent contractor selection                             | 0,085        |
|                  |   | 27. Incompetent supplier selection                               | 0,064        |
|                  |   | 28. Lack of cooperation and communication between stakeholders   | 0,078        |
|                  |   | 29. Project objective/purpose differences between stakeholders   | 0,076        |
|                  |   | 30. Improper risk allocation decisions                           | 0,079        |
|                  |   | 31. Lack of commitment between stakeholders                      | 0,079        |
|                  |   | 32. Know-how/working method differences between stakeholders     | 0,067        |
|                  |   | 33. Inadequate relationships with industry (trade unions)        | 0,076        |
|                  |   | 34. Inadequate relationships with employer (public)              | 0,086        |
|                  |   | 35. Inadequate relationships with stakeholders                   | 0,074        |
|                  |   | 36. Inadequate relationships with NGOs                           | 0,075        |
|                  |   | 37. Inadequate relationships with end user (society)             | 0,064        |

Table 1 - Exogenous risk factors affecting PPP construction projects (continue) [29]

|  | Risk Categories                         | Risk Factors   | Risk Weights |
|--|---|--|--------------|
| Endogenous Risks                                       | 4. Financial Risks                      | 38. Purchasing guarantees by public institution                                  | 0,070        |
|  |   | 39. Financial attractiveness of the project                                      | 0,075        |
|  |   | 40. Revenue (income) risk  | 0,071        |
|  |   | 41. Payment mechanisms   | 0,065        |
|  |   | 42. Investment costs   | 0,075        |
|  |   | 43. Unit costs   | 0,068        |
|  |   | 44. Finance issues related to cost increase                                      | 0,062        |
|  |   | 45. Bankruptcy/insolvency of stakeholders  | 0,073        |
|  |   | 46. Additional costs related to fast-track construction                          | 0,069        |
|  |   | 47. High costs (bidding costs, design and construction costs, operational costs) | 0,068        |
|  |   | 48. Residual value   | 0,041        |
|  |   | 49. Instability of financial structure   | 0,067        |
|  | 50. Lack of credibility of stakeholders | 0,064  |              |
|  | 51. Inability of debt service           | 0,063  |              |
|  | 52. Wrong estimation of cost trade-offs | 0,069  |              |
|  | 5. Contractual Risks                    | 53. Redundancy in contract variations  | 0,208        |
|  |   | 54. Contract content   | 0,155        |
|  |   | 55. Different interpretation of the agreement by the parties                     | 0,199        |
|  |   | 56. Insufficient plans and specifications  | 0,239        |
|  |   | 57. Lack of a definitive dispute resolution process                              | 0,199        |
|  | 6. Design and Construction Risks        | 58. Delays, uncertainties and inconsistencies in design and construction phases  | 0,064        |
|  |   | 59. Improper design (deficient and defective design)                             | 0,103        |
|  |   | 60. Excessive design variations  | 0,105        |
|  |   | 61. Occupational accidents   | 0,108        |
|  |   | 62. Improper technology use  | 0,082        |
|  |   | 63. Delays in procurement  | 0,097        |
|  |   | 64. Construction changes   | 0,101        |
|  |   | 65. Lack of supportive facilities  | 0,068        |
| 66. Lack of supportive infrastructural facilities      |   | 0,080  |              |
| 67. Integration between design and construction phases |   | 0,108  |              |
| 68. Technical construction risks                       |   | 0,083  |              |

- First (Initial) Offer:** The first offer is the initial offer given by an agent. This value defines the highest utility for the agent. The concessionaire agent's first-offer value is always higher than its reservation value. For the public institution agent, its reservation value is always higher than its initial value. The initial offer value proposed by each agent at the beginning of the negotiation process, is calculated by using Equation (3) and (4).

$$FO_{Ca} = RV + (RV \times RA) \tag{3}$$

$$FO_{Pla} = RV - (RV \times RA) \tag{4}$$

where  $FO_{Ca} / FO_{Pla}$  = The First Offer given by concessionaire/public institution agent,  $RV$  = Reservation Value of concessionaire/public institution agent;  $RA$  = Risk Attitude of concessionaire/public institution agent. Risk attitude value shows the willingness of each agent for taking the risk over depending on their ability to manage that risk. The numerical values for risk attitude are 0.1 for very low; 0.3 for low; 0.5 for medium; 0.7 for high; 0.9 for too high.

- **Concession:** The range between the target point and reservation point is the concession range. The bargaining tactics should start with the target and make concessions to reach an agreement. Under reservation point, negotiator should not accept any offer and put an end to negotiation.
- **Negotiation zone:** The area between the reservation values of the negotiating parties is called as negotiation zone or bargaining range. The negotiation starts with the target offer from a party and takes places within the negotiation zone. This area will be positive or negative. If it is negative, then there will be no settlement unless one or both the parties change reservation points.
- **Utility:** The objectives of the parties are usually specified as “utility”, or more explicitly “profit”. The utility of a negotiator at his target point is highest, and utility decreases by coming closer to reservation point. Utility functions are the mathematical representations of the user preferences that are useful in development of automated systems. In RAMP<sup>3</sup> model, linear utility curves was used for simplicity [10], [21].

Agents calculate the utility and then make their decision using utility values. The utility of given offers is calculated using the utility curves for each agent. All agents have a utility of 1 for their first offer and a utility of 0.6 for their reservation value. In between these values the utility curve is linear. Using its utility curve at each round, the agent calculates the utility from its previous offer and the utility from its opponent’s offer. Zeuthen’s strategy uses fully informed agents, so each agent can also access its opponent’s reservation value. This information and the first offer received from the opposing agent are used to calculate the other agent’s utility curve and its risk for that round. Then the opponent’s risk is compared with the agent’s own risk, and if the risk for the opponent is greater than the agent’s own risk value, then a concession is made. The value of this concession is the minimum amount that will make the opposing agent’s risk equal to or less than the agent’s own risk. At each round, agents calculate their offers and either make a concession or offer the same amount that was offered in the previous round [10]. Figure 3 shows the general characteristics of utility curves in RAMP<sup>3</sup> model whereas Figure 4 shows the key negotiation features adopted in RAMP<sup>3</sup> model.

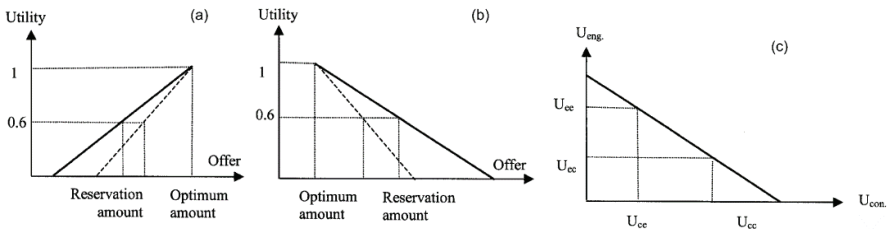


Figure 3 - Utility function of: (a) Concessionaire agent; (b) Public institution agent; (c) The function between the two agents’ utilities [21]

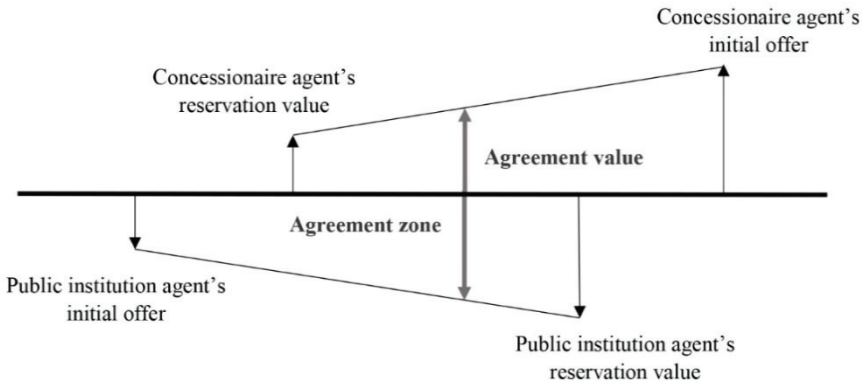


Figure 4 - The key negotiation features in RAMP<sup>3</sup> model (adopted from [21])

- Agent’s Willingness to Risk Conflict (Risk Value):** Zeuthen’s strategy simulates the negotiation process by comparing gains and losses. It measures each agent’s willingness to risk conflict. According to this strategy at each negotiation step, parties evaluate their willingness to take conflict risk, which is calculated by dividing -the loss due to accepting opponents offer- to -the loss due to going into conflict. Agents calculate the utility for various cases and then make their decision using these utility values. In each round an agent determines the loss of its utility due to accepting the opponent’s offer and loss due to rejecting the offer and running into a conflict (conflict is assumed to have a utility of 0). The ratio of these items is the calculated risk for this agent [28]:

$$\text{Risk} = \frac{\text{Utility agent 1 loses by conceding and accepting agent 2's offer}}{\text{Utility agent 1 loses by not conceding and causing a conflict}} \quad (5)$$

Risk is the indication of how much an agent is willing to risk a conflict by sticking to its last offer. As risk grows, the agent has less to lose from a conflict and will be more willing to not concede and risk creating a conflict [28]. According to the negotiation protocol, in each round the concession for an agent is the minimum amount that will make the opponent’s risk less than or equal to the agent’s own risk. Using Equation (5), following risk formulas for each agent are obtained:

$$R_{Ca} = \frac{U^t_{CaCa} - U^t_{CaPIa}}{U^t_{CaCa} - 0} ; R_{PIa} = \frac{U^t_{PIaPIa} - U^t_{PIaCa}}{U^t_{PIaPIa} - 0} \quad (6)$$

where  $R_{Ca} / R_{PIa}$  = calculated risk for concessionaire/public institution agent for round  $t$ ;  $U^t_{CaCa} / U^t_{PIaPIa}$  = utility of concessionaire/public institution agent due to its own offer in round  $t$ ;  $U^t_{CaPIa} / U^t_{PIaCa}$  = utility of concessionaire/public institution agent due to opponent agent’s offer in round  $t$ . The utility of conflict for each agent in the model is assumed to be 0. If the utility of an offer is assumed to be 0 for an agent, then

the risk value should be taken as 1. At each round, agents calculate and compare the risk value of their own and counteragent's risk value. According to the negotiation protocol, if the risk value of the counteragent is greater than the risk value of the agent; counteragent will have fewer losses in case of conflict and will be less prone to reach agreement. Therefore, the agent having the less risk value will make next offer by making concession [10], [21], [22], [23]. In other words, each agent should continue to make concessions until its willingness to risk conflict (risk value) is greater than counteragent [27]. The value of the concession to be made by the agent is the value that makes the counteragent's risk value less than or equal to the agent's own risk value. Otherwise, the agent will repeat the offer value in the previous round. Agents will continue to compromise until the maximum risk of conflict within both parties reaches to "0" [10], [21], [22], [23].

#### **4.2. Negotiation Theories**

In literature, there are three main approaches used to model negotiation in a multi agent environment: game theory, economic theory, and behavior theory [21], [22], [23], [24]. Game theory based studies typically assume that agents are allowed to select the best strategy from the space of all possible strategies by considering all possible interactions. It turns out that the search space of strategies and interactions that needs to be considered has exponential growth, which means that the problem of finding an optimal strategy is in general computationally intractable [24]. Game theory seeks to get at the essentials of decision-making and the associated strategies in situations where two or more parties are interdependent, and where, therefore, the outcome of their conflict and competition must be the product of their joint requirements and the interaction of their separate choices [23]. Although game theory is known to propose an influential mechanism for studying and arranging strategic interaction among agents, its usage in negotiation has negative aspects. In game theory, it is assumed that agents can characterize their preferences by considering all possible outcomes and they have perfect computational rationality [25]. Economic theory seeks to develop dynamic models of process, involving offers and counteroffers and interdependent concession making. In contrast to the classical game theory, there is no concern for the discovery of once-and-for-all strategies, but rather an intention to examine how the bargainers should interact in terms of their expectations of each other. Economic models analyze the processes through which the demands of the participants converge over time toward some specific point on the contract curve. The key element is the development of a specific concession mechanism that permits the positions of the parties to converge in the course of offers and counteroffers [21], [23]. Behavior theory focuses on the complex human factors of negotiation. It attempts to analyze the negotiation processes in which negotiators influence each other's expectations, perceptions, assessments, and decisions during the search for an outcome, thereby affecting the outcome. Much attention is given to the nature of changing expectations and bargainers' tactics, and to the significance of uncertainties of information, perception, and evaluation—all matters that tend to be ignored by game theory and economic theory [21], [23]. Economic theory approach was used in RAMP<sup>3</sup> model since it seeks to develop a dynamic structure by considering the process of making concessions through proposals, counteroffers, and interconnected proposals. This theory examines how the bargainers act according to each other's demands, and according to this theory, each negotiator should only consider its own interests. However, the bargainers

wishing to reach an agreement converge in the course of offers and counteroffers. The reason for choosing the economic theory approach is that game theory is insufficient to reflect the dynamic structure of the bargaining process, whereas behavioral theory is criticized for focusing on the modeling of intermediaries rather than modeling the bargaining process [21], [22], [23].

### **4.3. Concession Protocols in Negotiation**

Concession protocol in negotiations is the base for directing the interaction of parties. These rules cover the number of parties involved in the negotiation, main stages (like accepting the offer or ending it), progresses throughout negotiation (like sending new offer), the acts of parties (like who will make the decision, who will send the message, etc.). In RAMP<sup>3</sup> model, there is a one-to-one interaction between agents to create an interactive negotiation process. Until reaching a settlement, negotiating parties need to make concession over their offers. In case, parties do not have willingness to concede, the negotiation will end with conflict (monotonic concession process) [23]. After the input variables are calculated, the model simulates negotiations using Zeuthen's (complete information) negotiation protocols. Zeuthen's strategy simulates the negotiation process by comparing gains and losses. According to the Zeuthen strategy adopted within the scope of the bargaining process, agents determine their offers for each counter using their utility curves. In each round an agent determines the loss of its utility due to accepting the opponent's offer and loss due to rejecting the offer and running into a conflict (conflict is assumed to have a utility of 0). The ratio of these items is the calculated risk for this agent [10]. Risk is the indication of how much an agent is willing to risk a conflict by sticking to its last offer. As risk grows, the agent has less to lose from a conflict and will be more willing to not concede and risk creating a conflict [28]. According to the Zeuthen's strategy, agents do not try to learn each other's utility curve since they are fully informed about each other's utility curve. Thus, the reserve value of counteragent can be calculated in each round of the negotiation process.

### **4.4. Bargaining Strategies**

The bargaining strategy to be used by the parties is playing an important role in determination of how much compromise a party shall make from his target. In literature, the most widely used strategy is Zeuthen strategy [17]. Thus, RAMP<sup>3</sup> model adapts Zeuthen strategy as bargaining strategy. In Zeuthen bargaining strategy, parties determine the highest possibility of disagreement that they can accept and the party with the less risk acceptance level makes concession [26]. In negotiation process, parties have willingness to give as less concession as possible until reaching the agreement. According to Zeuthen bargaining strategy, an agent makes its decision of concession based on how much it has to lose by running into conflict at that time. If an agent has already made many concessions, it will have less to lose from a conflict, and will be less willing to concede. Thus, it has a high acceptability to risk conflict. Here, risk acceptability is measured by the comparison of an agent's loss caused by accepting the opponent's current offer and its loss caused by a conflict deal. At each step, each agent will compare its risk acceptability with that of its opponent. The agent with smaller risk acceptability will make the next concession, which will be sufficient to make its opponent's risk acceptability smaller than its own [27]. Since risk allocation decisions are mostly affected by the risk attitudes of the parties and the compromises to be made by the parties in the

negotiation process are shaped by the risk attitudes of the parties, risk attitudes of the parties are included in the bargaining process of RAMP<sup>3</sup> model.

**4.5. Conflict Deal**

Generally, if neither agent concedes at the same step, then the negotiation ends with a conflict deal. This restriction is relaxed in RAMP<sup>3</sup> model. Negotiations will not necessarily fall into a conflict deal even if agents stand still for five encounters. If the bargaining cannot be resolved at the end of the relevant rounds, the relevant risk factor will be allocated to the public and private sectors together.

**4.6. Negotiation Phases**

Negotiation process consists three main stages namely: i) Preparation stage (calculation of input variables), ii) Bargaining stage (negotiations between parties) and iii) Closing stage. In preparation stage, public institution agent and concessionaire agent communicate with risk factor agent and determinate risk factors that are going to be allocated between parties on the current project basis as a situation assessment. In this stage, the input variables that are needed to start a negotiation (the reservation value of each agent and first-offer values) are calculated. After these values are calculated, the negotiations start by using negotiation protocols. In bargaining stage, utility determination, making first offer, evaluation of risks taken by agents to decide which should make a concession, determining concession amount and making counteroffer/offer take place, respectively. The entire negotiation process is carried out by the agents without interference of the user. Lastly, in closing stage agents make decision to accept or conflict. Table 2 summarize the general characteristics of negotiation process in RAMP<sup>3</sup> model.

*Table 2 - Characteristics of negotiation process in RAMP<sup>3</sup> model*

|                                     |  |
|-------------------------------------|--|
| Bargaining strategies               | Each agent tries to increase its own benefit in the incoming offer. The loss of the party is accepted as counterparty's profit.  |
| Determination of bargaining values  | Within the negotiation process, parties negotiate based on their reservation and optimum values.   |
| Parties                             | In the context of the monotonous concession protocol, negotiations are only made between the public institution agent and the concessionaire agent.  |
| Parties' approach                   | According to Zeuthen bargaining strategy, the parties make their offers in each encounter by making concessions. In this process, each agent analyzes its loss due to the counterparty's offer. The agent with smaller risk acceptability will make the next concession. |
| Impact of counterparty's strategies | According to Zeuthen bargaining strategy, parties do not try to learn the concession rate of the counterparty in each round of the bargaining process.   |

### 4.7. Flowchart of Negotiation Process

Negotiations take place only between two agents representing concessionaire and public institution. Each agent in the system is independent and carries out the negotiation process on its own. At the end of the negotiations, either a settlement is reached or, if a deadlock is identified, a conflict deal is declared. In RAMP<sup>3</sup> model, a negotiation process is carried out for each risk factor. At the end of negotiation process, the risk allocation decision for the related risk is made. All the negotiation processes mainly depend on reservation value and offer value. In the negotiation process, both agents' goal is to have the maximum utility. In the first step of negotiation process, both agents calculate their reservation value and first (initial) offer primarily. The first offer is the initial offer given by an agent. The reservation value can be described as the highest amount that public institution agent can accept as a result of bargaining and it is the lowest offer that the concessionaire agent can accept. During the negotiation process, public institution and concessionaire agents calculate their first offer and reservation values in the same way. Agents make concessions as much as the difference between their reserve value that have zero concession and their offer values which are their target points. To start the negotiation process, the agents must determine these points. During the negotiation process, the concessionaire agent does not accept offers lower than its own reservation value whereas the public institution agent does not accept offers above its reservation value. The explanations related to the calculation of input variables for each agent are given below.

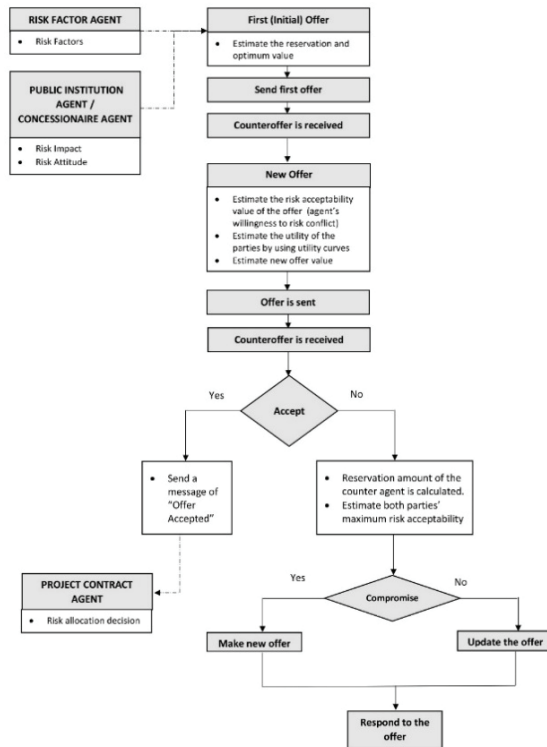


Figure 5 - Flowchart of negotiation process

Negotiation process starts when the message of the concessionaire agent's opening offer is delivered to public institution agent. The public institution agent replies this offer with its own opening offer. When a message is received, agent first decides what to do based on the message type. If the received message is of "Offer Accepted" type, this means that the counterparty has accepted the offer. In this case, agent concludes that an agreement has been made based on the last offer and ends the negotiation process. If the received message is of "Offer Rejected" type, this means that bargaining is dragged into a dilemma. However, considering the concession protocol the negotiation process should be continued without a deadlock. Therefore, agents should continue encounters by making concession over their past offers until they reach to a settlement. If the received message is of "Offer" type, this means that a new offer has been received and agent calculates its new offer amount based on the negotiation protocol. If there is no impasse in the offers, agent compares its own offer with the counterparty's offer. If it is indicated that that counterparty's offer provides more advantages from its own offer, agent would accept this offer and a message of "Offer Accepted" type is sent to the counterparty. The flowchart of the negotiation process for RAMP<sup>3</sup> model is presented in Figure 5.

## 5. TESTING AND VALIDATION

Validation of RAMP<sup>3</sup> model was performed in two stages: 1) Theoretically validation: conceptual model validation that checks if agents are modelled in consistency with accepted theories and 2) Operational validation: that ensures the correspondence between model and reality by determining that the model outputs behavior has sufficient accuracy for its intended purpose and use.

Four major attributes should be included in a negotiation protocol to argue that the multi agent-based model is theoretically valid. These major attributes are distributed model, efficiency, simplicity, and symmetry [16], [21].

- **Distributed Model:** This attribute ensures that there is no central decision-making unit in the model, and hence the freedom of each agent to make its own decisions and to negotiate according to its own priorities.
- **Efficiency:** The efficiency of the model is measured by the fact that the agents can generate results where the sum of earnings is the largest. Zeuthen strategy used within the model ensures that the model meets the efficiency attribute.
- **Simplicity:** Transactions should consume reasonable computing and communication resources. Since the bargaining process occur only between two agents representing concessionaire and public institution, the number of messages sent, and the communication resources used are limited.
- **Symmetry:** This attribute ensures that the model treats each agent equally.

Operational validation of the model was carried out with two real PPP projects. Testing of RAMP<sup>3</sup> model was carried out by conducting interviews with experts from both concessionaire and the public institution. During the operational validation of the model, one main risk group with the most sub-risk factors was selected (financial risk factors) instead of focusing 99 risk parameters belonging to 12 main risk groups. Participants were asked to

enter the data required in the architectural structure of the RAMP<sup>3</sup> model related to selected risk factors. Based on the data obtained, the proposed risk allocation decision of the related risks was determined after the negotiation process carried out by agents. As a next step, an expert with 16 years of experience in risk management in PPP projects was asked to interpret the risk allocation decisions independently generated by the model.

- **First case:** A mega tunnel project which was awarded to private sector using Built-Operate-Transfer (BOT) approach with a total investment of 1.245 billion USD was considered as the first case. The concessionaire won the tender in 2008 and signed the implementation agreement for the BOT model of the project with the public institution in 2011. The construction phase of the tunnel with a 55-month construction period started in 2013 and completed in 2016. The participants were as follows: 1) Concessionaire representative: a project manager with 12 years of experience in PPP project companies with civil engineering background, and 2) Public institution representative: one public representative from General Directorate of Highways. As a result of the evaluations, it is seen that the model accurately predicts the results by 87% (13 out of 15 criteria) which means model estimation results are in agreement with the expert's evaluation (Table 3).

*Table 3 - Trial results of first case*

| <b>Risk Factors</b>  | <b>Risk allocation results according to RAMP<sup>3</sup></b> | <b>Risk allocation results according to expert assessment</b> |
|--|--|---|
| 1. Purchasing guarantees by public institution                                   | Concessionaire + Public institution                          | Concessionaire + Public institution                           |
| 2. Financial attractiveness of the project                                       | Concessionaire   | Concessionaire + Public institution                           |
| 3. Revenue (Income) risk   | Concessionaire   | Concessionaire  |
| 4. Payment mechanisms  | Concessionaire + Public institution                          | Concessionaire + Public institution                           |
| 5. Investment costs  | Concessionaire   | Concessionaire  |
| 6. Unit costs  | Concessionaire   | Concessionaire + Public institution                           |
| 7. Finance issues related to cost increase                                       | Concessionaire   | Concessionaire  |
| 8. Bankruptcy/insolvency of stakeholders   | Concessionaire   | Concessionaire  |
| 9. Additional costs related to fast-track construction                           | Concessionaire   | Concessionaire  |
| 10. High costs (bidding costs, design and construction costs, operational costs) | Concessionaire + Public institution                          | Concessionaire + Public institution                           |

Table 3 - Trial results of first case (continue)

|   |                |                |
|---|----------------|----------------|
| 11. Residual value                      | Concessionaire | Concessionaire |
| 12. Instability of financial structure  | Concessionaire | Concessionaire |
| 13. Lack of credibility of stakeholders | Concessionaire | Concessionaire |
| 14. Inability of debt service           | Concessionaire | Concessionaire |
| 15. Wrong estimation of cost trade-offs | Concessionaire | Concessionaire |

- Second case:** An airport project which was awarded to private sector using BOT approach with a total investment of 38.7 billion USD was considered as the second case. The concessionaire won the tender and signed the implementation agreement for the BOT model of the project with the public institution in 2013. The first construction phase of the airport with a 42-month construction period will be finalized in 2018, whereas all construction phases are going to be completed by the first half of 2025. Operational validation of RAMP<sup>3</sup> in second case was carried out by conducting interviews with both concessionaire and public institution representatives. The participants were as follows: 1) Concessionaire representative: a project manager with 8 years of experience in PPP project companies with civil engineering background, and 2) Public institution representative: one public representative from General Directorate of State Airports Authority. As a result of the evaluations, it is seen that the model accurately predicts the results by 80% (12 out of 15 criteria) which means model estimation results are in agreement with the expert's evaluation (Table 4).

Table 4 - Trial results of second case

| <b>Risk Factors</b>                            | <b>Risk allocation results according to RAMP<sup>3</sup></b> | <b>Risk allocation results according to expert assessment</b> |
|--|--|---|
| 1. Purchasing guarantees by public institution | Concessionaire + Public institution                          | Concessionaire + Public institution                           |
| 2. Financial attractiveness of the project     | Concessionaire + Public institution                          | Concessionaire + Public institution                           |
| 3. Revenue (Income) risk                       | Concessionaire + Public institution                          | Concessionaire  |
| 4. Payment mechanisms                          | Concessionaire   | Concessionaire + Public institution                           |
| 5. Investment costs                            | Concessionaire   | Concessionaire  |
| 6. Unit costs                                  | Concessionaire   | Concessionaire + Public institution                           |
| 7. Finance issues related to cost increase     | Concessionaire   | Concessionaire  |
| 8. Bankruptcy/insolvency of stakeholders       | Concessionaire   | Concessionaire  |

Table 4 - Trial results of second case (continue)

|  |                |                                     |
|--|----------------|-------------------------------------|
| 9. Additional costs related to fast-track construction                           | Concessionaire | Concessionaire                      |
| 10. High costs (bidding costs, design and construction costs, operational costs) | Concessionaire | Concessionaire + Public institution |
| 11. Residual value   | Concessionaire | Concessionaire                      |
| 12. Instability of financial structure   | Concessionaire | Concessionaire                      |
| 13. Lack of credibility of stakeholders  | Concessionaire | Concessionaire                      |
| 14. Inability of debt service  | Concessionaire | Concessionaire                      |
| 15. Wrong estimation of cost trade-offs  | Concessionaire | Concessionaire                      |

## 6. FINDINGS AND DISCUSSION

Results show that RAMP<sup>3</sup> is theoretically valid since i) it does not have any central decision-making unit, ii) it proceeds the negotiation process as each agent maximizes its own utility, iii) transactions consume reasonable computing and communication resources between two agents, iv) model treats intermediaries equally during the bargaining process. This means that RAMP<sup>3</sup> model meets the distributed model, efficiency, simplicity, and symmetry criteria, respectively. On the other hand, the results of operational validation of the model shows that the level of prediction of the model is high since model estimation results are in agreement with the expert’s evaluation for two cases (above %80).

In addition, some lessons learnt from RAMP<sup>3</sup> implementation and recommendations for improving the model can be summarized as follows:

- Results shows that the rule of “allocating risk factor to both public and private sectors if the negotiations do not end in five encounters” prevents deadlocks and accelerates negotiation process.
- Results shows that in concession rounds, the higher risk value of an agent gets, agent’s utility due to counter agent in that concession round lowers.
- In conjunction with that situation, the higher utility gets, offer value of an agent also gets higher.
- Preliminary findings show that it is mainly the reservation value that determines the settlement amount of the negotiation and risk factor is assigned to the party that has a higher risk acceptability in negotiation process.
- Developed RAMP<sup>3</sup> model should be tested on variable case studies and the sensitivity of the model should be analyzed in the light of the data obtained.
- This study presents the architectural structure of RAMP<sup>3</sup> with an aim of predicting the right party who can manage PPP project related risk factors based on each risk’s importance and impact. Interactions of risk factors were neglected. Considering impact or significance of a risk factor can be affected by other risk factor(s), interrelated relationships should be taken account within MAS model.
- Inclusion of learning ability for agents would improve model’s performance.

- The research opens to future evaluations after the integration of a project agent that will transfer information from the designer(s), subcontractor(s) or financiers to the project-specific model in order to improve the performance of the model.

## 7. CONCLUSION

In existing studies related to risk management area, parameters such as risk sharing attitudes, risk management capacities, contract conditions, etc. are often not addressed. However, within the scope of effective risk management, more than one project participant with different utility functions should be identified and the communication rules between them must be determined [16]. Considering that the performance of PPP infrastructure projects depends on the efficiency of the risk allocation strategies adopted between public and private sectors and how the risks between the parties are balanced by the contract [4], [5], risks should be assigned to the party that can better manage them. However, it is observed that this principle is generally not implemented due to the difference in perception among project stakeholders regarding risk management capabilities [6], [7]. Within this context, a multi agent system-based Risk Allocation Model (RAMP<sup>3</sup>) that simulates the risk allocation process for PPP projects was developed to fill this gap in literature. Developed model enables users to determine risk allocation decisions by evaluating project parties' risk attitudes (varies according to their objectives, knowledge-ability levels) along with the impact of risk factors such as time extension, cost increase and conflict. Thus, final risk allocation results generated from this model can be reflected into contract clauses to ensure that risk factors are assigned to the party who can better manage the risks. Therefore, this study differentiates from other risk management studies that adapted MAS since the focus of those studies were the simulation of either cost-sharing process or risk-mitigation decisions under different scenarios regarding the risk-allocation principles.

The methodology of RAMP<sup>3</sup> involves i) identification of risks by agents, ii) assessment of each risk's importance and impact, iii) communication of agents to negotiate on risk allocation decision and iv) determination of strategies and utility functions to be used in negotiation process. The focus of study is presenting the steps of negotiation process of agents using economic theory and Zeuthen bargaining strategy. RAMP<sup>3</sup> developed within the scope of this study consists risk factor agent, concessionaire agent, public institution agent and project contract agent. Within the negotiation process made between the public institution agent and the concessionaire agent, parties negotiate based on their reservation and optimum values. In RAMP<sup>3</sup>, each agent tries to increase its own benefit in the incoming offer using utility curves. According to bargaining strategy, each agent analyzes its loss due to the counterparty's offer and the agent with smaller risk acceptability makes the next concession. RAMP<sup>3</sup> enables users to evaluate risk factors specific to PPP projects according to project parties' objectives, knowledge-ability levels along with the impact of risk factors such as time extension, cost increase and conflict. RAMP<sup>3</sup> was validated on two real PPP projects. Preliminary findings show that the higher risk value of an agent gets, agent's utility due to counter agent in that concession round lowers. Results also show that risk is allocated to the party that has a higher risk acceptability in negotiation process.

Considering the importance of PPP projects for the construction sector, determination of the risk allocation decision in accordance with the competencies of the parties should be prior

step within the framework of an effective risk management. Thus, RAMP<sup>3</sup> that has been developed as a decision support system for determining who should manage the potential risk in PPP transport projects creates sectoral contributions.

The multi agent system-based risk allocation model developed within the scope of this study focuses on the negotiation process between in PPP projects. This study can contribute to the development of other works whose focus is negotiation between parties with multiple perspectives, objectives, and different levels of knowledge. Similarly, the multi agent system-based risk allocation model developed for PPP projects can be subject to the future research related to PPP-typed energy, telecom or water and sewerage projects.

## **Notation**

*The following symbols are used in this paper:*

FAHP = Fuzzy Analytical Hierarchy Process

MAS = Multi Agent System.

PPP = Public-Private-Partnership.

RAMP<sup>3</sup> = Risk Allocation Model for PPP Projects.

## **Acknowledge**

The work was supported by Coordinatorship of Scientific Research Projects of Yildiz Technical University (Project Number: 2014-05-01-DOP03). The RAMP<sup>3</sup> model described in this paper was also registered by Turkish Patent and Trademark Office (Patent Number: TR 2016 20062 B).

## **References**

- [1] Ke, Y., Wang, S., Chan, A. P., Lam, P. T. I., Preferred Risk Allocation in China's Public-Private Partnership (PPP) Projects, *International Journal of Project Management*, 28(5), 482-492, 2010.
- [2] Hwang, B. G., Zhao, X., Gay, M. J.S., Public Private Partnership Projects in Singapore: Factors, Critical Risks and Preferred Risk Allocation from the Perspective of Contractor, *International Journal of Project Management*, 31(3), 424-433, 2013.
- [3] Gross, M. E., *Aligning Public-Private Partnership Contracts with Public Objectives for Transportation Infrastructure*, Doctoral Thesis, Virginia Polytechnic Institute and State University, 2010.
- [4] Yun-na, W. U., Xin-liang, H. U., Ling-shuang, X. U., Ze-zhong, L., Research on Risk Allocation of Public-Private Partnership Projects Based on Rough Set Theory, *Communications in Information Science and Management Engineering*, 2(7), 15-20, 2012.

- [5] Marques, R. C., Berg, S., Risks, Contracts, and Private-Sector Participation in Infrastructure, *Journal of Construction Engineering and Management*, 137(11), 925-932, 2011.
- [6] Thomas, A. V., Kalidindi, S. N., Ananthanarayanan, K., Risk Perception Analysis of BOT Road Project Participants in India, *Construction Management and Economics*, 21(4), 393-407, 2003.
- [7] Lam, K. C., Wang, D., Lee, T. K. P., Tsang, Y. T., Modelling Risk Allocation Decision in Construction Contracts, *International Journal of Project Management*, 25(5), 485-493, 2000.
- [8] Ren, Z., Anumba, C. J., Multi-Agent Systems in Construction-State of The Art and Prospects, *Automation in Construction*, 13(3), 421-434, 2004.
- [9] Zhu, L., Zhao, X., Chua, D. K. H. Agent-Based Debt Terms' Bargaining Model to Improve Negotiation Inefficiency in PPP Projects. *Journal of Computing in Civil Engineering*, 30(6), 04016014, 2016.
- [10] Ke, Y., Wang, S., Chan, A., Cheung, E., Research Trends of PPP in Construction Journal, *Journal of Construction Engineering and Management*, 135(10), 1076-1086, 2009.
- [11] Chengshuang, S., Guochang, Risk Management Framework of Multi-agent System for Construction Projects. *Journal of Northeast Forestry University*, 1-5, 2006.
- [12] Li, B., Ren, Z., Bayesian Technique Framework for Allocating Demand Risk Between The Public and Private Sector in PPP Projects, 6th International Conference on Service Systems and Service Management, China, 2009.
- [13] Karakas, K., Dikmen, I., Birgonul, M.T., Multiagent System to Simulate Risk-Allocation and Cost-Sharing Processes in Construction Projects, *Journal of Computing in Civil Engineering*, 27(3), 307-319, 2013.
- [14] Taillandier, F., Taillandier, P., Tepeli, E., Breysse, D., Mehdizadeh, R., Khartabil, F., A Multi-Agent Model to Manage Risks in Construction Project (SMACC). *Automation in Construction*, 58, 1-18, 2015.
- [15] Karakaş, K., Development of A Multi Agent System for Negotiation of Cost Overrun in International Construction Projects, Master of Science Thesis, Middle East Technical University, 2010.
- [16] Dikmen, İ., Birgönül, M. T., Tanyer, A. M., Alparslan, F. N., Uluslararası İnşaat Projeleri İçin Çok Aracılı Bir Risk Modelleme Platformunun Geliştirilmesi, TÜBİTAK Project Report, Project No: 107M334, 2010.
- [17] Dağkırın, G., A Multi Agent Risk Analysis and Sharing Platform for International Construction Projects Doctoral Thesis, Middle East Technical University, 2015.
- [18] Python, <https://www.python.org/> 29 July 2019.
- [19] Prechelt, L. An empirical Comparison of C, C++, Java, Perl, Python, Rexx And Tcl. *IEEE Computer*, 33(10), 23-29, 2000.

- [20] Sycara, K., Dai, T. Agent Reasoning in Negotiation. In: Kilgour D., Eden C. (eds) Handbook of Group Decision and Negotiation. Advances in Group Decision and Negotiation, vol 4. Springer, Dordrecht, 2010.
- [21] Ren, Z., Anumba, C. J., Ugwu, O. O., Negotiation in a Multi-Agent System for Construction Claims Negotiation, Applied Artificial Intelligence, 16(5), 359-394, 2002.
- [22] Ren, Z., Anumba, C. J., Ugwu, O. O., The Development of a Multi-Agent System for Construction Claims Negotiation, Advances in Engineering Software, 34(11), 683-696, 2003a.
- [23] Ren, Z., Anumba, C. J., Ugwu, O. O., Multiagent System for Construction Claims Negotiation, Journal of Computing in Civil Engineering, 17(3), 80-188, 2003b.
- [24] Jennings, N. R., Faratin, P., Lomuscio, A. R., Parsons, S., Sierra, C., Wooldridge, M., Automated Negotiation: Prospects, Methods and Challenges, International Journal of Group Decision and Negotiation, 10(2), 199–215, 2001.
- [25] Fidan, G., Dikmen, I., Birgonul, M. T., Using Multi Agent Systems in Construction Claim Negotiation, International Conference on Computing in Civil and Building Engineering and XVII Workshop on Intelligent Computing in Engineering, Nottingham-UK, 2010.
- [26] Young, O.R., Bargaining: Formal Theories of Negotiation. University of Illinois Press, Urbana, 1975.
- [27] Ren, Z., Anumba, C.J., Ugwu, O. O., Construction Claims Management: Towards an Agent-Based Approach, Engineering Construction and Architectural Management, 8(3), 185-197, 2001.
- [28] Rosenschein, J. S., Zlotkin, G., Rules of Encounter: Designing Conventions for Automated Negotiation Among Computers, MIT Press, Cambridge, MA, 1994.
- [29] Aladağ, H.. Multi-Agent Risk Allocation Model for Build-Operate-Transfer (BOT) Type Transportation Projects, Doctoral Dissertation, Yildiz Technical University, 2016.

# The High Temperature Performance Evaluation of Polymer/Nanocomposite Modified Asphalt Cement

Mustafa ALAS<sup>1</sup>

Ali Shaban ALBRKA ISMAEL<sup>2</sup>

Hüseyin GÖKÇEKUŞ<sup>3</sup>

## ABSTRACT

The current study focuses on the effect of Acrylate-styrene-acrylonitrile (ASA)/Nanosilica (Si) modified binders on the complex modulus ( $G^*$ ) and rutting resistance parameters ( $G^*/\sin\delta$ ) of Asphalt Cement (AC). Four different blends including the base binder and the polymer nanocomposites which were formed by blending 5% ASA to base binder with the addition of nanosilica at 3, 5 and 7% by the weight were the subject of investigations. Conventional and Dynamic Shear Rheometer (DSR) testing procedures were conducted as well as morphology analysis using Fourier Transform Infrared Spectroscopy (FT-IR). The rheological characteristics of AC were analysed by master curves, isochronal plots and rutting resistance parameter plots. Test results revealed that  $G^*$  and  $G^*/\sin\delta$  of all modified samples were significantly enhanced compared to the base binder. Multiple Stress Creep Recovery Test (MSCRT) conducted at 100 Pa and 3200 Pa showed that, non-recoverable compliance was reduced and elastic recovery of modified binders were improved. Optimum concentration was found to be 5% ASA/Si composite, as further addition of polymer nanocomposite resulted in lower enhancement in the rheological properties of modified AC due to the occurrence of agglomeration between the composite and the base binder.

**Keywords:** Rheological characterization, polymer/nanocomposite, acrylate-styrene-acrylonitrile, nano-silica.

## 1. INTRODUCTION

Asphalt cement (AC) is used as the binding agent in the design and construction of flexible pavement roads. The viscoelastic properties of AC makes it a suitable option as it shows

---

Note:

- This paper was received on June 30, 2020 and accepted for publication by the Editorial Board on December 11, 2020.
- Discussions on this paper will be accepted by September 30, 2022.

• <https://doi.org/10.18400/tekderg.761208>

1 Civil Engineering Department, Near East University, Nicosia, North Cyprus, Turkey - mustafa.alas@neu.edu.tr - <https://orcid.org/0000-0002-8988-2008>

2 Civil Engineering Department, Near East University, Nicosia, North Cyprus, Turkey - shabarofking10@gmail.com - <https://orcid.org/0000-0003-1938-9127>

3 Civil Engineering Department, Near East University, Nicosia, North Cyprus, Turkey - huseyin.gokcekus@neu.edu.tr - <https://orcid.org/0000-0001-5793-4937>

resistance to dynamic vehicular loading and extreme climatic conditions. It is favorable that AC demonstrates stiff behavior at high temperatures and low frequencies to prevent permanent deformation as well as elastic behavior at low temperatures and high frequencies to prevent fatigue cracking failures (1). Additionally, AC is required to be resistant to aging and it should possess strong adhesion properties for achieving more durable AC in order to minimize the maintenance cost and to increase the service life of pavement (2). Virgin asphalt may not always ensure desired performance across the entire service life. Thus, modification of AC has become essential to improve the performance characteristics and durability of pavement roads. On this basis, polymers, nanomaterials, and polymer/nanocomposite materials have previously been utilized to modify AC (3, 4).

Polymer modifiers have proven to be effective in enhancing the physical and rheological properties as well as improving the durability of AC, thus reducing the life cycle costs. Polymer modified asphalt is considered to be cost effective, providing that the cost of modification does not exceed the cost of base asphalt by more than 100% (5). Based on their characteristics, polymers are categorized into different groups. Elastomers and plastomers are the most widely utilized modifiers.

Polyolefin plastomers, such as Polyethylene (PE), polypropylene (PP) and ethylene vinyl acetate (EVA), have been acknowledged in the literature as they improve the high temperature performance of AC in the prevention of rutting failure (6). Ameri et al., and Brovelli et al., (7, 8) studied EVA modified binders by using different penetration grade base asphalt modified at various concentrations. Their findings showed an increase in the rutting parameter ( $G^*/\sin \delta$ ) induced by the enhancement in the stiffness of modified binders. Furthermore, studies investigating the effect of recycled EVA modified binders have demonstrated promising results, which was evidential that reclaimed plastomers also have the potential to improve the performance of modified binders at high service temperatures (9, 10). Research regarding PE and PP modified binders has demonstrated similar findings, such as that increased complex modulus and reduced phase angle generate better resistance to permanent deformation. However, it was also noted in the literature that the addition of plastomeric modifiers commonly leads to more brittle behavior of AC, thus exhibiting poor low temperature performance (11, 12). Consequently, coupling agents have been used with plastomers in order to eliminate the drawbacks related to the chemical and physical properties of plastomeric polymers (13). A study conducted by Yuanita et al., (11) demonstrated that the addition of lignin to PP leads to better compatibility between the base bitumen and the polymer. The findings of Bala et al., (12) also demonstrated that PE/nanosilica modified binders possess better morphological properties as well as improved low temperature performance.

In contrast to the plastomeric polymers, elastomeric polymers can resist permanent deformation and also demonstrate the ability to recover elastically after being loaded and when exposed to low temperatures (14). Elastomers that contain styrenic blocks such as Styrene-butadiene-styrene (SBS), Styrene-butadiene-rubber (SBR) and Acrylate-styrene-acrylonitrile (ASA) were found to be the most suitable modifiers since they extend to improve both the high temperature and low temperature performance characteristics of AC (15-17). According to Airey and Kok et al., (14, 18), styrene block copolymers ensure higher strength and better rutting resistance due to the presence of polystyrene end-blocks, while the formation of polybutadiene mid-blocks is responsible for the better elastic properties. SBS

and SBR copolymers have been investigated extensively by a number of researchers and their findings corroborated their positive influence such as increased aging resistance, prevention of high temperature rutting and low temperature fatigue failures of pavement roads (15, 19, 20). Ali et al., (17) investigated the morphology and rheological properties of ASA modified binders and their findings validated the advancements in the rheological properties. Although polymer-modified bitumen offers promising results, many researchers have noted a major shortcoming of the modification process, which is the compatibility issue between the polymer and bitumen (21, 22) (23). According to Al-Mansob et al., (24) the incompatibility is associated with the occurrence of phase separation due to the differences in density, molecular weight and solubility between the polymer and asphalt. Lu et al., (25) further stated that the phase separation is governed by the chemical composition of the bitumen and the characteristics of the polymer. Due to the shortcomings of the polymer modified bitumen, researchers have gravitated towards the investigation of the potential of nano-materials and nanocomposite materials as modifiers to AC.

Nanomaterials have been rapidly incorporated in pavement engineering and utilized as direct modifiers to base AC or are considered as polymer/nanomaterial composites with the aim of eliminating the drawbacks of virgin asphalt and certain polymeric modifiers (26). The role of nanomaterials in asphalt modification is not only to improve the rheological properties but also to enable better dispersion, improve aging resistance and allow stability and compatibility of modified AC due to the unique properties of nanomaterials, such as increased surface area to volume ratio and the quantum effects resulting from spatial confinement (27, 28). Positive effects of modifying AC with well-known nanomaterials such as carbon nanotubes (CNT), nanoclay and nanosilica have been reported in numerous studies (29-31). Arabani et al., (32) and Ziari et al. (33) conducted research on CNT-modified asphalt binders and mixtures and concluded that the CNT modifiers enhanced the mechanical properties and also improved the aging resistance and self-healing mechanism of binders and hot mix asphalt (HMA). According to Crucho et al., (4) and You et al., (34), nanoclay modified binders enhance the stiffness and elasticity of AC; however, due to the limited enhancement in the elastic behavior of AC, nanoclay is more frequently used as a second modifier to polymer modified AC. Jun et al., (28) stated that the addition of a small amount of nanoclay into SBS modified binders can enhance the thermal properties of AC both at high and low temperatures while also improving the compatibility between the polymer and bitumen. Numerous studies have reported that, based on its cost effectiveness and notable enhancements in physical and rheological properties, nanosilica is considered as one of the most substantial advancements in asphalt modification (26, 28). Studies conducted by You et al., (34) and Yao et al., (35) discovered that 2% to 4% use of nanosilica by the weight of bitumen can reduce the rut depth up to 50%. Additionally, Arabani et al., (36) achieved remarkable enhancement in fatigue resistance of up to 37%. Nanosilica has also been utilized in numerous studies in order to build new polymer nanocomposites that can perform better over a longer life span. The drawbacks of well-known polymers such as SBS, PP and PE were found to be satisfactorily recovered with the addition of nanosilica (37-39).

Polymer/nanocomposite modified AC is considered to be the latest advancement in the field of pavement engineering that facilitates the design of roads with superior performance and increased durability (6). Unlike polymeric modifiers, polymer nanocomposites are relatively new, not readily available and have received limited attention in the literature (3). ASA and nano silica have previously been utilized as sole modifiers to AC. Besides the positive

influence of utilizing these materials, major shortcomings such as the stability problem due to phase separation phenomena with ASA modified asphalt cement has also been reported in a previously conducted study (17). The current research aims to overcome the stability concern by adding nano silica to ASA modified AC and also aims to investigate the effectiveness of the modification process regarding to high temperature performance characteristics under unaged and short-term aged conditions.

## **2. Experimental Procedures**

### **2.1. Materials and Sample Preparation**

Materials used for the modification of the base binder of 80/100 penetration grade were ASA and nanosilica. ASA was in the form of a white powder and was obtained from Shijiazhuang Changhang Import & Export Trading (Shijiazhuang, China). Nanosilica particles were in the form of a white powder, spherical in shape and the average particle size was 30-50 nm.

The hot melting method was used to blend base AC with ASA at 5% concentration and adding nano silica by 3, 5 and 7% by the weight of bitumen to form ASA/Si composite modified binders. ASA is an elastomeric polymer which was previously investigated by Ali et al., (17) as a sole modifier to asphalt cement. According to the findings of their study, the optimum enhancement in physical and rheological properties of asphalt cement was achieved at 5% ASA by the weight of bitumen modification to asphalt cement. Findings of their study formed the foundations to the current study by adding nano silica in the blend to form a different polymer-nanocomposite modified asphalt cement (PNC) to mitigate certain drawbacks of polymer modified asphalt cement (PMAC) and to further improve the performance characteristics. Nano silica particles were added at 3, 5 and 7% by the weight of PMAC as suggested by numerous researchers that adding nanomaterials in small proportions typically between 2%-5% can enhance performance characteristics of asphalt cement significantly (31). The blending process was performed with a Silverson high shear mixer at a shear rate of 1500 rotations per minute (rpm) at a constant temperature of 165 °C±1. In order to ensure fine dispersion of particles and hence the homogeneity of the prepared blends, samples were taken every 30 minutes and investigated by the ring and ball softening point test. Stabilization of the softening point values indicated that the optimum duration for the blending process was 60 minutes.

### **2.2. Temperature Susceptibility**

Asphalt is a thermoplastic material, meaning that its physical properties are time and temperature dependent. As the physical properties of asphalt change at elevated temperatures, its consistency and temperature susceptibility are described by two parameters called the penetration index (PI) and pen-vis number (PVN) (40). The PI was calculated using the penetration value at 25 °C and softening point test results by eq. 1. PVN was calculated by eq. 2 based on the penetration and rotational viscosity test results at reference temperatures of 25°C and 135 °C, respectively (24).

$$PI = \frac{1952 - 500 \log(\text{Pen}25) - 20S.P}{50 \log(\text{Pen}25) - S.P - 120} \quad (1)$$

Where Pen(25) is the penetration test result at 25 °C in one tenths of a millimeter and S. P is the ring and ball softening point test result in °C.

$$PVN = \frac{\text{LogL}-\text{LogX}}{\text{LogL}-\text{LogM}} \times 1.5 \quad (2)$$

Where L is the rotational viscosity value at 135 °C for a PVN of 0.00,

$$L = 4.25800 - 0.79670\text{LogPen} \quad (3)$$

M is the rotational viscosity value at 135 °C for a PVN of -1.50,

$$M = 3.46289 - 0.61094\text{LogPen} \quad (4)$$

X is the rotational viscosity value at 135 °C and LogPen is the logarithmic penetration value for bitumen at 25°C.

### **2.3. Storage Stability**

The storage stability test was conducted using aluminum foil tubes with a diameter of 30 mm and a height of 160 mm. The tubes were filled with bitumen and placed vertically in the oven at 163±5 °C for 48 hours, followed by resting at room temperature to cool down. The top third and bottom thirds of the tube were cut and bitumen was taken to perform the softening point test.

### **2.4. Rotational Viscosity**

The viscosity is used in the determination of the mixing and compaction temperatures for hot mix asphalt (HMA) design (17). The test was performed according to ASTM D4402 in a range of temperatures from 120 °C to 180 °C by 15°C increments in order to observe the variation of viscosity at elevated temperatures for the base and modified binders. The readings were taken when the measurements were stabilized and then the temperature was increased to the next increment. The test was conducted using a Brookfield rotational viscometer with spindle number 4 set to a constant speed of 20 rpm.

### **2.5. FT-IR**

The Fourier Transform Infrared Spectroscopy (FT-IR) for ASA/Nanosilica composite modified bitumens was conducted to evaluate the formation of chemical bonding between the polymer nanocomposite modifier and the base bitumen as well as to identify the formation of functional groups. FT-IR spectroscopy was conducted in the wavenumber range of 4000 cm<sup>-1</sup> to 600 cm<sup>-1</sup> at room temperature.

## 2.6. Simulation of Short-Term Aging

A rolling thin film oven (RTFO) was used to simulate the conditions of short-term ageing that occurs during the production and construction stages of the HMA. The standard test procedure (ASTM D2872) specifies that 35 grams of bitumen should be placed in cylindrical open mouthed bottles and then placed into a preheated carousel equipped oven at 163 °C, which rotates under air blown pressure at 15 rpm for 85 minutes. The samples were then used for the physical and rheological testing of the RTFO-aged bitumen. The significance of the procedure is that it provides an insight into the binder ‘as laid’ properties (41).

## 2.7. Dynamic Shear Rheometer (DSR)

The rheological behavior of asphalt cement was characterized by its viscous and elastic properties at intermediate and high temperatures. DSR was used to conduct frequency sweep and multiple stress creep recovery tests (MSCR) in accordance with AASHTO T315 and ASTM: D7405 – 15, respectively. The tests were conducted with the binder samples that were placed between the two parallel plates of the DSR (25.0 mm in diameter and 1.0 mm spacing between plates). Frequency sweep tests were performed to measure fundamental parameters such as the complex modulus ( $G^*$ ) and the phase angle ( $\delta$ ), which determined the stiffness of the samples. The tests were performed under strain-controlled conditions, while the temperature was shifted from 46 °C to 82 °C with increments of 6 °C. To maintain stable temperature conditions within  $\pm 0.1$  °C as suggested by SHRP, a temperature unit that consisted of a fluid bath system was used. The shearing action was achieved by the movement of upper plate at nine different frequencies for each elevated temperature in the range of 0.159 Hz – 15.92 Hz.  $G^*$  and  $\delta$  outcomes of the frequency sweep tests were used to construct master curves for base and modified asphalt binders. Isochronal plots at varying temperatures for 0.159 Hz and 15.92 Hz and the rutting resistance parameter were further plotted in order to evaluate the effect of the modification process on the performance characteristics of AC.

The multiple stress creep recovery (MSCR) test was utilized to determine the non-recoverable creep compliance ( $J_{nr}$ ) and the percentage of recovery (%R) for the base and modified AC under RTFO aged condition. ASTM: D7405 – 15 procedure was used for MSCR testing. The test was conducted at 64 °C with two different stress levels of 100 Pa and 3200 Pa. DSR with a plate of 25 mm in diameter and 1 mm gap was used to apply a haversine shear load on the sample for a period of 1 second. Then the load is removed and the sample was allowed to recover for a period of 9 seconds in order to complete 1 cycle (3). 10 cycles for each stress level were conducted where the first 10 cycles were performed at 100 Pa and the second 10 cycles were performed at 3200 Pa stress levels. Outcomes of the test were used to compute  $J_{nr}$  and %R using eq 5 and 6, respectively.

$$J_{nr}(\sigma, N) = \frac{\varepsilon_r - \varepsilon_o}{\sigma} \quad (5)$$

Where,  $J_{nr}$  is the non-recoverable creep compliance,  $\varepsilon_r - \varepsilon_o$  is the non-recoverable strain at the end of rest period,  $\sigma$  is the applied stress level and  $N$  is the number of cycles.

$$\%R = \frac{\varepsilon_1 - \varepsilon_{10}}{\varepsilon_1} \times 100\% \quad (6)$$

Where, %R is the percentage recovery,  $\varepsilon_1$  is the strain at the end of 1 second creep phase and  $\varepsilon_{10}$  is the strain at the end of 10 seconds creep phase.

### 3. Results and Discussion

#### 3.1. Physical Properties

The effect of adding ASA/Nanosilica to the base binder was investigated using the penetration, softening point and viscosity test results. The results of the physical tests and the associated parameters evaluated based on the test results are demonstrated in Table 1. Penetration index (PI) and Penetration Viscosity Number (PVN) were the two parameters used in assessing the temperature susceptibility of AC. A PI value for base bitumen ranges from -3 to +7, where lower values indicate a more temperature susceptible AC and higher values represent the opposite. As can be deduced from Table 1, the reduction in the penetration value and increase in the softening point indicated that the AC became stiffer with the addition of ASA/Nanosilica composite at higher concentrations. Furthermore, the increased PI and PVN numbers show that the modification process led to the improved temperature susceptibility of modified AC.

*Table 1 - Physical properties of base and polymer-nano composite modified binders*

|           | Penetration<br>(dmm) | Softening<br>point (°C) | Viscosity @<br>135 °C (cp) | PI       | PVN      |
|-----------|----------------------|-------------------------|----------------------------|----------|----------|
| Base AC   | 89.6                 | 50.5                    | 474.0                      | 0.468604 | -0.09302 |
| ASA/Si 3% | 63.3                 | 54.5                    | 648.0                      | 0.458391 | -0.02429 |
| ASA/Si 5% | 61.1                 | 55.0                    | 888.0                      | 0.478665 | 0.374701 |
| ASA/Si 7% | 53.4                 | 57.0                    | 1050.0                     | 0.571275 | 0.432553 |

#### 3.2. Storage Stability

Storage stability is an important property of modified AC that is used in the evaluation of the integrity and homogeneity of asphalt mixtures during storage and handling of AC in the field. Although polymer-modified AC offers significant improvement in the properties of AC, many researchers' findings have indicated that the phase separation problem due to dissimilarity between the polymer and asphalt chemistry such as solubility and density are the causes of instability and incompatibility in polymer modified AC (42). The phase separation is related to the accumulation of polymer particles in the upper section of the binder at high temperatures, which forms a stationary state. The ring and ball softening point test was used to evaluate the differences in the top and bottom sections of the conditioned samples in the aluminum foil tube, which was split into 3 equal sections. Although a difference of up 4 °C - 4.5 °C in softening point values between the top and bottom sections

was considered within acceptable limits, the common perception among the researchers is that in order to classify AC as storage stable, the difference in softening points should not exceed 2.5 °C (12). A previous study conducted on ASA modified AC by Ali et al., (17) indicated that the differences in softening points between the top and bottom sections were observed to reach up to 12 °C, displaying signs of phase separation between the polymer and bitumen. The results of the addition of nanosilica at 3, 5 and 7% by the weight of ASA modified AC are demonstrated in Figure 1. The storage stabilities of polymer nanocomposite samples improved as the binder to asphalt concentration was increased. Differences in softening points between the top and bottom sections were observed to be less than 2.5 °C for 5% and 7% ASA/Si modified AC, while at 3% ASA/Si concentration, the difference in softening points was 4.5 °C.

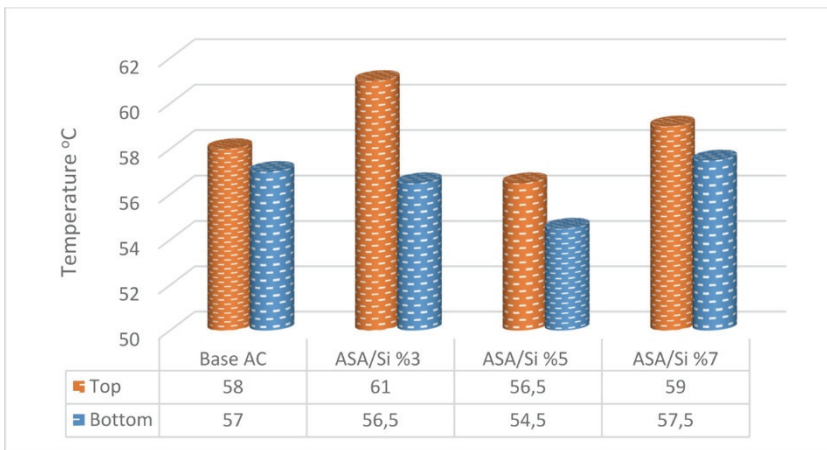


Figure 1 - Difference in softening point between the top and bottom sections

### 3.3. Rotational Viscosity

The rotational viscosity test results for unaged and short-term aged base and polymer nanocomposite modified asphalt binders are illustrated in Figure 2. The viscosity values for all samples were reduced as the test temperature increased regardless of the modifier content. Furthermore, the increase in the modifier content resulted in higher viscosities. It can also be observed that the short-term aged samples demonstrated higher viscosities compared to the unaged samples. Substantially, the RTFO-aged and unaged samples test results for rotational viscosity at 135 °C allowed the computation of Viscosity Aging Index (VAI) using eqn. 7 (43). VAI was used to evaluate the aging resistance of base and modified binders. The results displayed in Table 2 demonstrate that the VAI numbers were successively reduced with the increase in polymer nanocomposite concentration in the AC, indicating an improvement in the aging resistance. It is noteworthy to mention that the rotational viscosity test results are useful in the determination of the physical properties of AC as well as the mixing and compaction temperatures of HMA; however, the results are not indicative of significant rheological properties.

$$VAI = \frac{\text{Viscosity}_{RTFO} - \text{Viscosity}_{unaged}}{\text{Viscosity}_{unaged}} \quad (7)$$

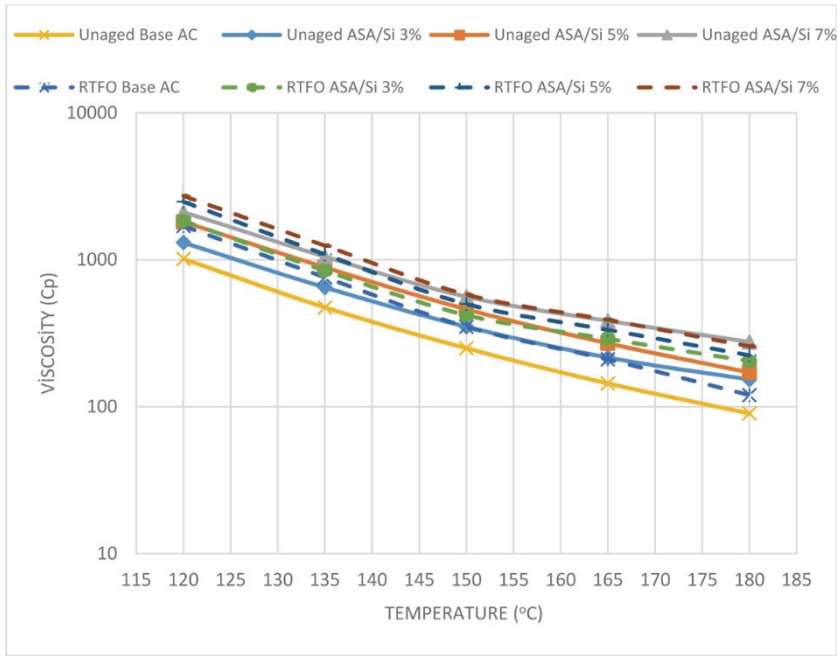


Figure 2 - Rotational viscosities for unaged and RTFO-aged base and ASA/Si modified AC

Table 2 - Viscosity Aging Index

|           | Viscosity of unaged AC @135 (cp) | Viscosity of RTFO aged AC @135 (cp) | Viscosity Aging Index |
|-----------|----------------------------------|-------------------------------------|-----------------------|
| Base AC   | 474                              | 760                                 | 0.603                 |
| ASA/Si 3% | 648                              | 844                                 | 0.302                 |
| ASA/Si 5% | 888                              | 1088                                | 0.225                 |
| ASA/Si 7% | 1050                             | 1248                                | 0.189                 |

### 3.4. FT-IR

The FTIR analysis was employed to observe the presence of specific chemical functional groups and bonding changes that occur when the base and modified binders were subjected to aging conditions. The FTIR investigation was performed in a spectra of wavenumbers from 4000 cm<sup>-1</sup>-600 cm<sup>-1</sup>. The evidence of the formed groups can be found in the spectra along with the reference IR bands as illustrated in Figure 3. During the aging process, the chemical composition of the bitumen may change due to bonding with atmospheric oxygen.

Carbonyl compounds and sulfoxides were formed during the chemical transformations caused by oxidative aging. Additionally, aromatic and aliphatic compounds are related to the aging of asphalt cement and therefore monitored during the aging process. In order to quantitatively analyze the changes of specific functional groups due to the aging effects and the influence of modifiers on the aging effect, the peak areas under the specific bands were measured from valley to valley for each plot at specifically selected wavenumbers of the obtained spectrum. The results of the quantitative analysis were illustrated in Figures 4a, 4b and 4c.

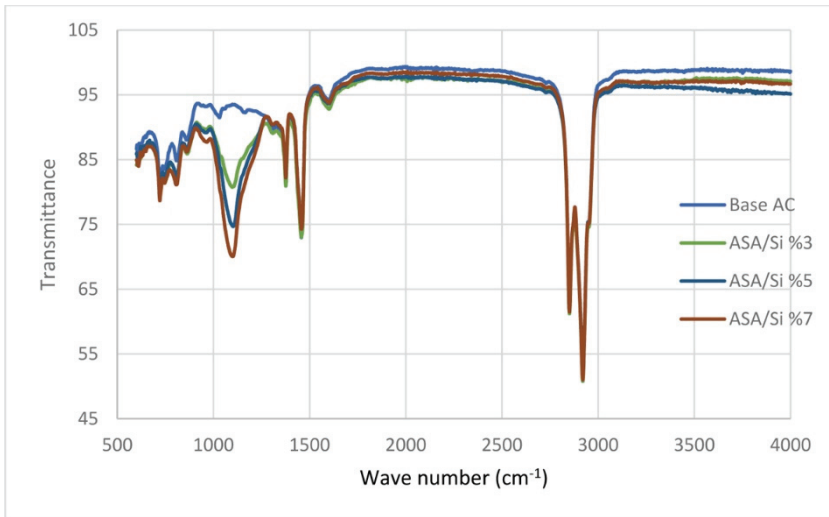


Figure 3 - FT-IR Pattern for base and ASA/Si composite binders

The aliphatic structures exist in the light fractions of bitumen. During the aging process, light components of bitumen volatiles and aliphatic chains form aromatic rings. Hence, a reduction of aliphaticity with aging was observed for all binders as illustrated in Figure 4a. It is also noteworthy to mention that the aliphaticity index of unaged modified binders decrease with the increase of modifier content. This was due to ASA and nano silica absorbing the light fractions of bitumen during the interaction process. As illustrated in Figure 4b, the aromaticity of base bitumen increased after aging for base and ASA/Si 3%, which confirmed that the formation of aromatics was associated with an equivalent reduction of the aliphatic structures. However, for ASA/Si 5% and ASA/Si 7%, a reduction in the aromatics was observed. This was associated to continued interaction between the ASA and nano silica with bitumen to absorb aromatic structures. Sulfoxides and carbonyls are considered to be the main oxidation products of bitumen aging. Sulfoxide peak appears in the FTIR graph around  $1034\text{ cm}^{-1}$ . Although this band was visible for the base binder, it was not apparent for the modified binders due to the overlapping phenomena of the bonds in the spectra since the silica and oxygen bonding was present within the same band wavenumbers. Another group that is associated with the aging index is the carbonyl group which appears around  $1700\text{ cm}^{-1}$  in the FTIR spectrum. It can be observed from Figure 4c that, the carbonyl index increases after aging however, with the addition of modifiers, the gap between the unaged

and aged binders was decreasing which indicated that, by increasing the amount of modifiers in the blend, the aging resistance of the asphalt was increased.

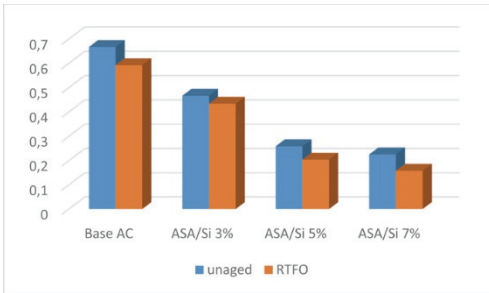


Figure 4a - Aliphatic index

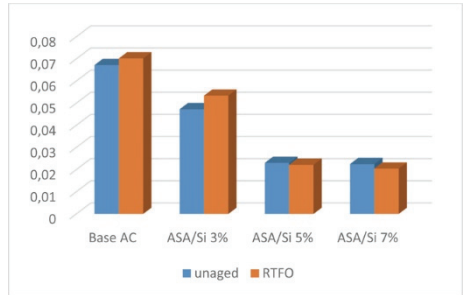


Figure 4b - Aromaticity index

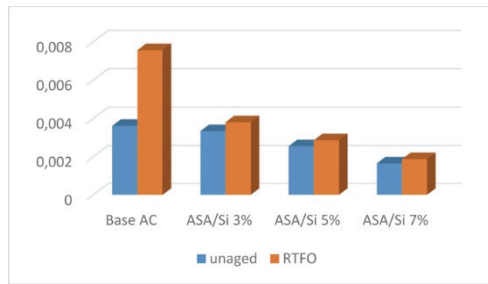


Figure 4c - Carbonyl index

### 3.5. Rheological Properties

#### 3.5.1. Isochronal Plots

Isochronal plots allowed the viscoelastic features of base and modified AC such as  $G^*$  and  $\delta$  versus temperature at certain frequencies to be displayed. The effects of the modification process on the stiffness and temperature susceptibility of AC were visualized in isochronal plots. As illustrated in Figures 5a-5d,  $G^*$  for unaged and RTFO-aged base and polymer nanocomposite modified binders were plotted versus a range of temperatures between 46 °C–82 °C at 0.159 Hz and 15.92 Hz. The increase in the  $G^*$  for up to 5% ASA/Si addition to base binder indicated that the dispersion of nanosilica in the blend led to enhancement in the strength of modified AC. The differences in  $G^*$  at 15.92 Hz for the base and ASA/Si modified binders at 3, 5 and 7% were more remarkable than  $G^*$  at 0.159 Hz, indicating that the influence of nanoparticles is more prominent at low frequencies and high temperatures. The isochronal plots constructed after the short-term aging procedure followed a similar trend for modified and base asphalt; therefore, the increase in the  $G^*$  was attributed to the short-term aging of the asphalt phase rather than the rearrangement of polymer/nanocomposite particles. Furthermore, the relatively small increase in the  $G^*$  of modified binders compared to the base binder was related to improved temperature susceptibility.

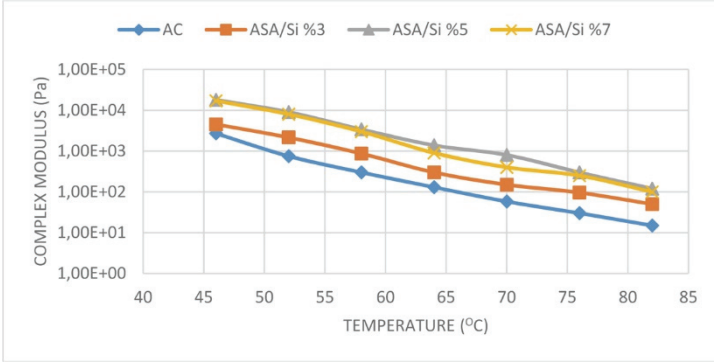


Figure 5a - Isochronal plot of unaged  $G^*$  at 0.159 Hz

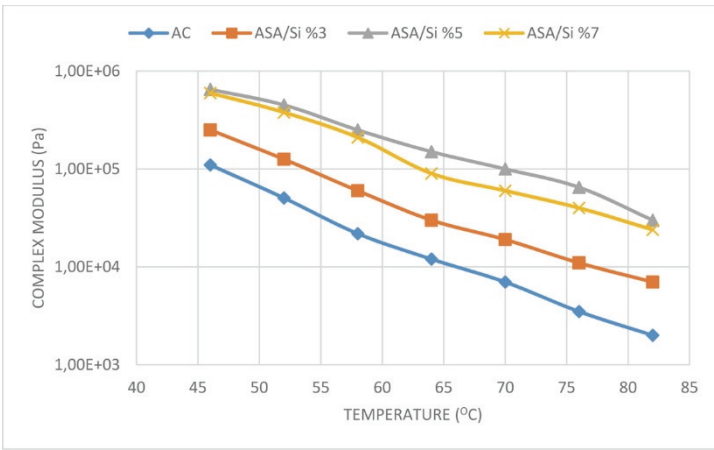


Figure 5b - Isochronal plot of unaged  $G^*$  at 15.92 Hz

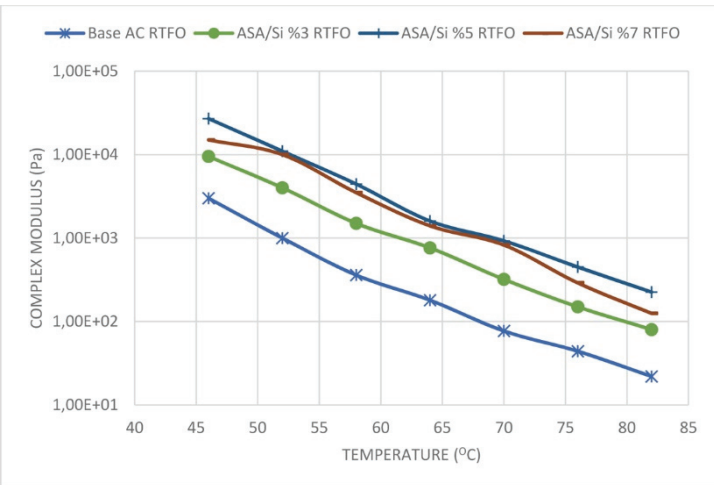


Figure 5c - Isochronal plot of RTFO aged  $G^*$  at 0.159 Hz

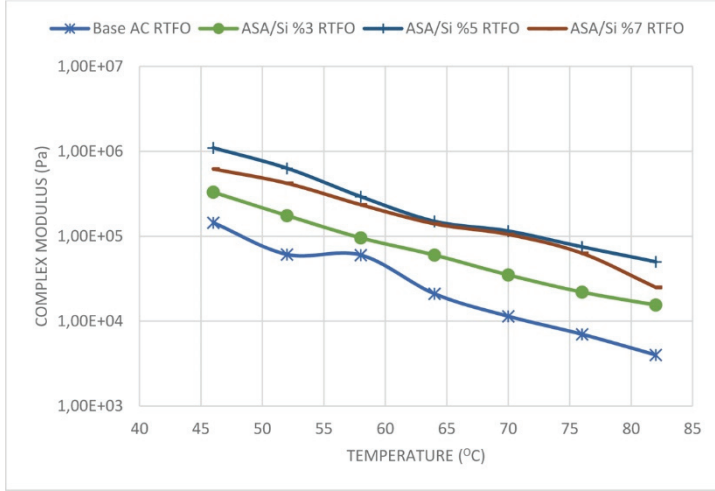


Figure 5d - Isochronal plot of RTFO aged  $G^*$  at 15.92 Hz

### 3.5.2. Master Curves

A master curve reflects the time dependency of binders by representing rheological parameters such as  $G^*$  and  $\delta$  over a range of temperatures and frequencies. Construction of the master curve involved time-temperature superposition. A reference temperature of 64 °C was selected and the rheological data at other temperatures were shifted horizontally with relevant shift factors in order to plot a smooth curve. The master curves for the  $G^*$  of base and polymer nanocomposite modified binders for the unaged and RTFO aged samples are presented in Figures 6a and 6b, respectively. A smooth increase in the  $G^*$  was observed for modified binders up to 5% addition of ASA/Si composites, while at 7% concentration, the behavior was changed resulting in lower stiffness and therefore lower rutting resistance of AC. Similar trends were observed for both samples in unaged and under RTFO-aged conditions with a slight increase in the  $G^*$  for RTFO-aged binders corresponding to an increase in stiffness. It should be noted that previous studies that have utilized ASA and nanosilica as solitary modifiers to base AC reported improvement in  $G^*$ ; however, a similar trend of degradation in  $G^*$  with the addition of modifier at higher concentrations was also observed (17, 44).

### 3.5.3. MSCR Test

The use of the multiple stress creep recovery (MSCR) test is essential in the determination of the rutting potential of the binders. The MSCR test was utilized to measure the amount of permanent deformation during the 9 seconds resting period in the loading-unloading cycle. Non recoverable compliance ( $J_{nr}$ ) and the percentage recovery (%R) were the two parameters revealed by the MSCR test. A higher degree of recovery and lesser  $J_{nr}$  were noted as desirable properties for AC. The MSCR test was conducted at 100 Pa and 3200 Pa in order to evaluate the low stress and high stress level traffic scenarios. Figure 7a and 7b display the creep and

creep recovery schemas for base and 3%, 5% and 7% ASA/Si modified binders at the temperature of 64 °C. From Figure 8, an increase in the elastic recovery of ASA/Si modified asphalt up to 5% concentration was observed while this increase was less for the 7% ASA/Si modifier content AC. At 100 Pa stress level, the percentage increase for the ASA/Si modifiers at 3, 5 and 7% content compared to the base asphalt were 39.5%, 92.8% and 52.0% respectively, while at the 3200 Pa stress level, the percentage increase was 93.4%, 199.0% and 95%. The  $J_{nr}$  results illustrated in Figure 9 also demonstrated that, the non-recoverable creep was reduced after the modification process. The reduction of the  $J_{nr}$  compared to the base asphalt were 22.0%, 43.5% and 17.7% for the ASA/Si 3, 5 and 7% at the 100 Pa stress level and they were 31.9%, 41.30% and 12.9% at the 3200 Pa stress level, respectively.

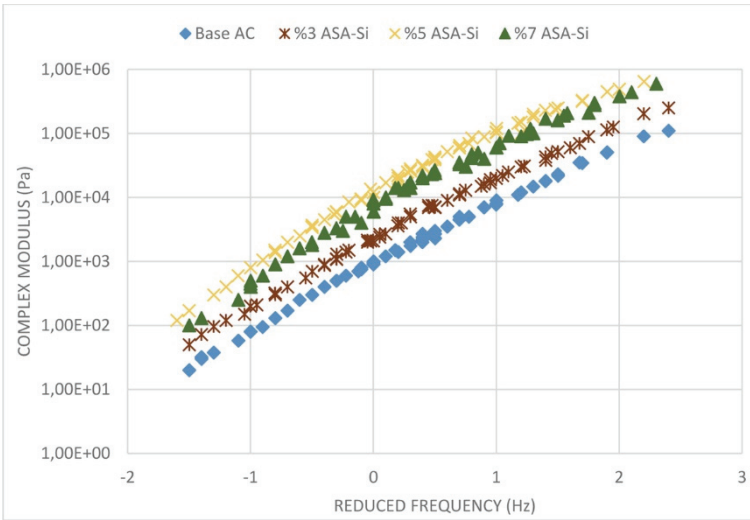


Figure 6a - Complex modulus master curve for unaged base and modified binders

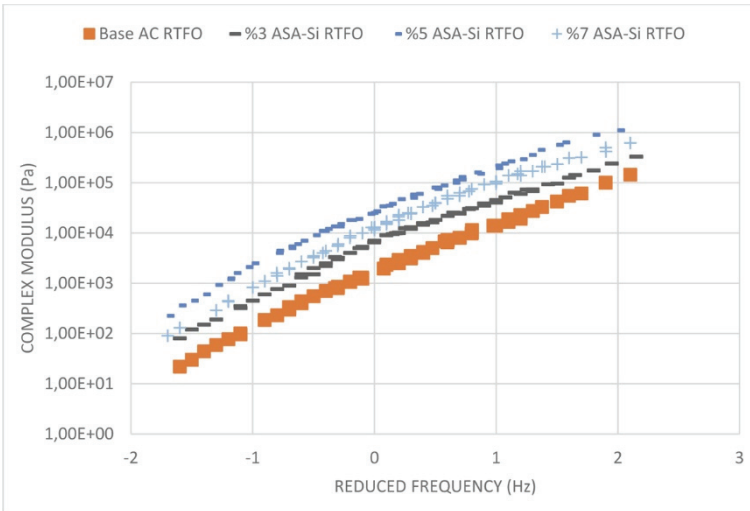


Figure 6b - Complex modulus master curve for RTFO aged base and modified binders

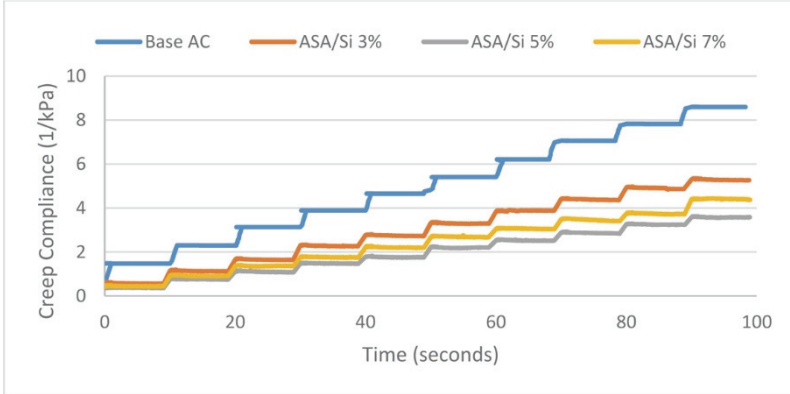


Figure 7a - Creep compliance at 100 Pa

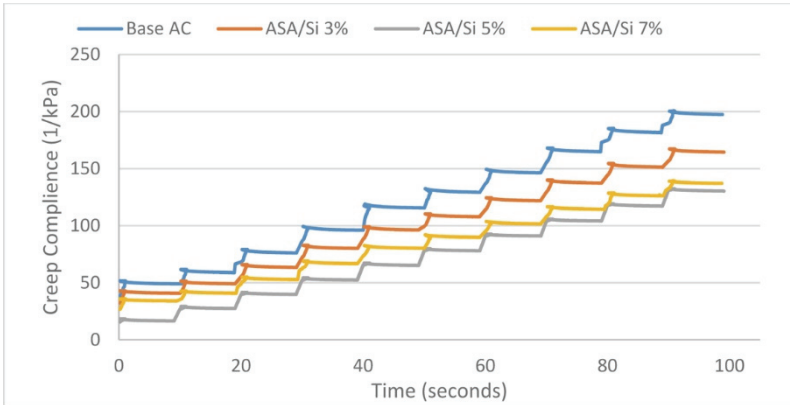


Figure 7b - Creep compliance at 3200 Pa

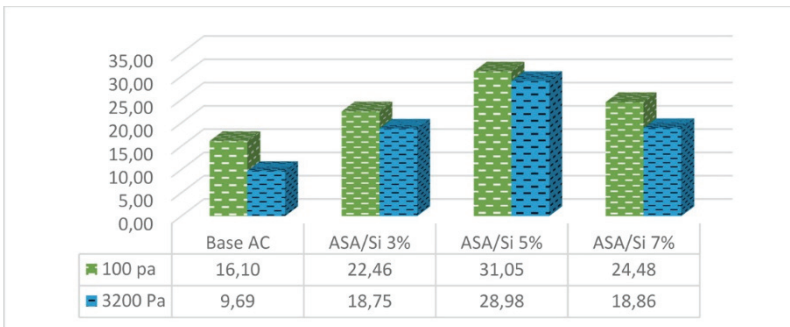


Figure 8 - Elastic recovery of base and modified binders

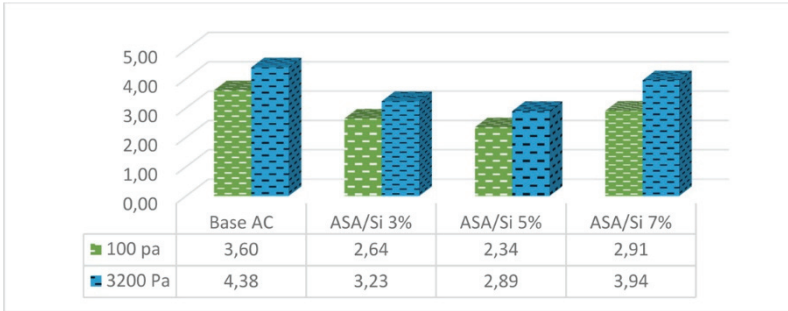


Figure 9 - Non-recoverable compliance of base and modified binders

### 3.5.4. Rutting Resistance Parameter

The formula  $G^*/\sin\delta$  was used to explain the rutting resistance (permanent deformation) of asphalt at high temperatures. Al Mansob et al. (24) stated that the rutting parameter reflects the resistance of AC to permanent deformation when subjected to dynamic loading and the relative amount of energy dissipated into non-recoverable deformation during the loading cycle. According to Superpave standards, at a loading rate of 1.592 Hz, a minimum of 1 kPa is the allowable requirement for an unaged sample of binder. The rutting parameter was evaluated in a range of temperatures between 46 °C-82 °C at 1.592 Hz using the  $G^*$  and  $\delta$  outcomes of the frequency sweep test results. As illustrated in Figure 10,  $G^*/\sin\delta$  was the lowest for base AC. Binders containing ASA/Si composites up to 5% by the weight of bitumen demonstrated the highest  $G^*/\sin\delta$  value, while the addition of polymer nanocomposite above 5% concentration led to reduced  $G^*/\sin\delta$ . The compatibility problem between the polymer nanocomposite and the binder was considered to be the factor leading to the reduction in rutting resistance parameter at 7% ASA/Si concentration. In general, the rutting performance of the modified binders was increased compared to the base binder and satisfied the minimum requirement of 1 kPa at 1.592 Hz and at 64°C.

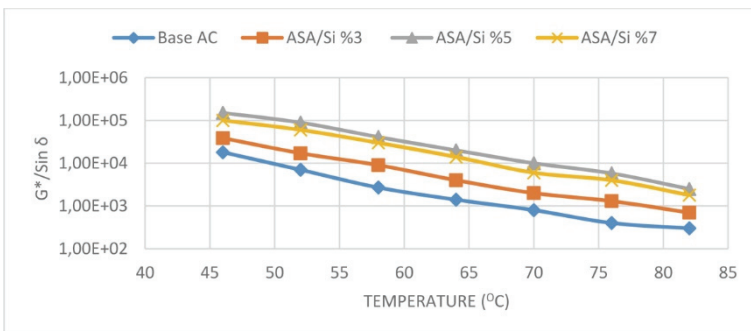


Figure 10 - Effect of temperature on rutting parameter of base and ASA/Si-modified asphalt binders

#### **4. CONCLUSION**

The influence of ASA/Nanosilica polymer nanocomposite modifier were evaluated under unaged and RTFO aged conditions with respect to physical, chemical and rheological properties. ASA was used in 5% concentration whereas, the addition of nanosilica was 3, 5 and 7% by the weight of AC. Based on the results of the study; 1. The physical properties of the PNC were improved and also demonstrated better aging resistance after short term aging. 2. The frequency sweep test results showed that, the stiffness of the PNC was increased leading to higher  $G^*$  and improved rutting resistance. 3. Based on the MSCRT results, higher R% and lesser Jnr indicated that the materials' high temperature characteristics were improved. 4. The performance enhancement at 7% ASA/Si composition was slightly less than that of 5% ASA/Si modified AC which was a sign of agglomeration.

In general, ASA/Si composite modified binders at all concentrations improved temperature susceptibility and rheological properties under intermediate and high temperature conditions. The reduced enhancement at 7% ASA/Si compared to 5% ASA/Si concentration was attributed to the occurrence agglomeration between the particles within the asphalt matrix. The present study demonstrated that ASA/Si composite binders were able to address the rutting failure of asphalt at high temperatures. It is recommended for a future study that the results of the present study be used as foundations to investigate the influence of ASA/Si composite asphalt under different asphalt concrete mixture conditions. This would enable designers and engineers to reach to a better conclusion prior to any field application.

#### **References**

- [1] Ahmed AW, Said SF, Lu X, Carlsson H. Pavement performance follow-up and evaluation of polymer-modified test sections. *International Journal of Pavement Engineering*. 2019;20(12):1474-87.
- [2] Al-Mansob RA, Ismail A, Yusoff NIM, Albrka SI, Azhari CH, Karim MR. Rheological characteristics of unaged and aged epoxidised natural rubber modified asphalt. *Construction and Building Materials*. 2016;102:190-9.
- [3] Mahali I, Sahoo UC. Rheological characterization of Nanocomposite modified asphalt binder. *International Journal of Pavement Research and Technology*. 2019;12(6):589-94.
- [4] Crucho J, Picado-Santos L, Neves J, Capitão S. A Review of Nanomaterials' Effect on Mechanical Performance and Aging of Asphalt Mixtures. *Applied Sciences*. 2019;9(18):3657.
- [5] Ponniah J, Kennepohl G. Polymer-modified asphalt pavements in Ontario: Performance and cost-effectiveness. *Transportation research record*. 1996;1545(1):151-60.
- [6] Porto M, Caputo P, Loise V, Eskandarsefat S, Teltayev B, Oliviero Rossi C. Bitumen and bitumen modification: A review on latest advances. *Applied Sciences*. 2019;9(4):742.

- [7] Ameri M, Mansourian A, Sheikhmotevali AH. Investigating effects of ethylene vinyl acetate and gilsonite modifiers upon performance of base bitumen using Superpave tests methodology. *Construction and Building Materials*. 2012;36:1001-7.
- [8] Brovelli C, Hilliou L, Hemar Y, Pais J, Pereira P, Crispino M. Rheological characteristics of EVA modified bitumen and their correlations with bitumen concrete properties. *Construction and Building Materials*. 2013;48:1202-8.
- [9] Garcia-Morales M, Partal P, Navarro F, Gallegos C. Effect of waste polymer addition on the rheology of modified bitumen. *Fuel*. 2006;85(7-8):936-43.
- [10] García-Morales M, Partal P, Navarro F, Martínez-Boza F, Gallegos C, González N, et al. Viscous properties and microstructure of recycled eva modified bitumen. *Fuel*. 2004;83(1):31-8.
- [11] Yuanita E, Hendrasetyawan B, Firdaus D, Chalid M, editors. Improvement of polypropylene (PP)-modified bitumen through lignin addition. *IOP Conf Ser Mater Sci Eng*; 2017.
- [12] Bala N, Napiyah M, Kamaruddin I, Danlami N. Rheological properties investigation of bitumen modified with nanosilica and polyethylene polymer. *International Journal of Advanced and Applied Sciences*. 2017;4(10):165-74.
- [13] Brasileiro L, Moreno-Navarro F, Tauste-Martínez R, Matos J, Rubio-Gámez MdC. Reclaimed polymers as asphalt binder modifiers for more sustainable roads: A review. *Sustainability*. 2019;11(3):646.
- [14] Kok BV, Yilmaz M, Sengoz B, Sengur A, Avci E. Investigation of complex modulus of base and SBS modified bitumen with artificial neural networks. *Expert Systems with Applications*. 2010;37(12):7775-80.
- [15] Zorn S, Mehta Y, Dahm K, Batten E, Nolan A, Dusseau R. Rheological properties of the polymer modified bitumen with emphasis on SBS polymer and its microstructure. *Road Materials and New Innovations in Pavement Engineering* 2011. p. 41-8.
- [16] Pyshyev S, Gunka V, Grytsenko Y, Bratyshak M. Polymer modified bitumen. *Chemistry & Chemical Technology*. 2016(10,№ 4 (s)):631-6.
- [17] Ali SIA, Ismail A, Yusoff NIM, Karim MR, Al-Mansob RA, Alhamali DI. Physical and rheological properties of acrylate–styrene–acrylonitrile modified asphalt cement. *Construction and Building Materials*. 2015;93:326-34.
- [18] Airey GD. Rheological properties of styrene butadiene styrene polymer modified road bitumens☆. *Fuel*. 2003;82(14):1709-19.
- [19] Fernandes MRS, Forte MMC, Leite LFM. Rheological evaluation of polymer-modified asphalt binders. *Materials research*. 2008;11(3):381-6.
- [20] Rossi CO, Spadafora A, Teltayev B, Izmailova G, Amerbayev Y, Bortolotti V. Polymer modified bitumen: Rheological properties and structural characterization. *Colloids and Surfaces A: Physicochemical and Engineering Aspects*. 2015;480:390-7.

- [21] Galooyak SS, Dabir B, Nazarbeygi AE, Moeini A. Rheological properties and storage stability of bitumen/SBS/montmorillonite composites. *Construction and Building Materials*. 2010;24(3):300-7.
- [22] Polacco G, Filippi S, Merusi F, Stastna G. A review of the fundamentals of polymer-modified asphalts: Asphalt/polymer interactions and principles of compatibility. *Advances in colloid and interface science*. 2015;224:72-112.
- [23] Yildirim Y. Polymer modified asphalt binders. *Construction and Building Materials*. 2007;21(1):66-72.
- [24] Al-Mansob RA, Ismail A, Rahmat RAO, Borhan MN, Alsharef JM, Albrka SI, et al. The performance of epoxidised natural rubber modified asphalt using nano-alumina as additive. *Construction and Building Materials*. 2017;155:680-7.
- [25] Lu X, Isacson U, Ekblad J. Phase separation of SBS polymer modified bitumens. *Journal of Materials in Civil Engineering*. 1999;11(1):51-7.
- [26] Bhargava S, Raghuwanshi AK, Gupta P. Nanomaterial Compatibility and Effect on Properties of Base Bitumen Binder and Polymer Modified Bitumen. *IJSET-International Journal of Innovative Science, Engineering & Technology*. 2016;3(6):276-82.
- [27] de Mello Donegá C. *The Nanoscience Paradigm: "Size Matters!"*. Nanoparticles: Springer; 2014. p. 1-12.
- [28] Yang J, Tighe S. A review of advances of nanotechnology in asphalt mixtures. *Procedia-Social and Behavioral Sciences*. 2013;96:1269-76.
- [29] Ziari H, Farahani H, Goli A, Akbari T. The effect of carbon nano-tube on the fatigue life of asphalt mixtures. *International Journal of Transportation Engineering*. 2014;2(1):81-96.
- [30] Sadeghpour Galooyak S, Palassi M, Goli A, Zanjirani Farahani H. Performance evaluation of nano-silica modified bitumen. *International Journal of Transportation Engineering*. 2015;3(1):55-66.
- [31] Jahromi SG, Khodaii A. Effects of nanoclay on rheological properties of bitumen binder. *Construction and building materials*. 2009;23(8):2894-904.
- [32] Arabani M, Faramarzi M. Characterization of CNTs-modified HMA's mechanical properties. *Construction and Building Materials*. 2015;83:207-15.
- [33] Ziari H, Amini A, Goli A, Mirzaiyan D. Predicting rutting performance of carbon nano tube (CNT) asphalt binders using regression models and neural networks. *Construction and Building Materials*. 2018;160:415-26.
- [34] You Z, Mills-Beale J, Foley JM, Roy S, Odegard GM, Dai Q, et al. Nanoclay-modified asphalt materials: Preparation and characterization. *Construction and Building Materials*. 2011;25(2):1072-8.
- [35] Yao H, You Z, Li L, Lee CH, Wingard D, Yap YK, et al. Rheological properties and chemical bonding of asphalt modified with nanosilica. *Journal of Materials in Civil Engineering*. 2013;25(11):1619-30.

- [36] Arabani M, Haghi A, Tanzadeh R, editors. Laboratory study on the effect of Nano-SiO<sub>2</sub> on improvement fatigue performance of aged asphalt pavement. 4th International Conference on Nanostructures, Kish Island, IR Iran; 2012.
- [37] Bala N, Napiah M, Kamaruddin I. Effect of nanosilica particles on polypropylene polymer modified asphalt mixture performance. *Case studies in construction materials*. 2018;8:447-54.
- [38] Bala N, Kamaruddin I, Napiah M, Danlami N, editors. Rheological and rutting evaluation of composite nanosilica/polyethylene modified bitumen. Proceedings of the 7th International Conference on Key Engineering Materials (ICKEM 2017) held between 11th to 13th March; 2017.
- [39] Rezaei S, Ziari H, Nowbakht S. Low temperature functional analysis of bitumen modified with composite of nano-SiO<sub>2</sub> and styrene butadiene styrene polymer. *Petroleum Science and Technology*. 2016;34(5):415-21.
- [40] Ehinola OA, Falode OA, Jonathan G. Softening point and Penetration Index of bitumen from parts of Southwestern Nigeria. *Nafta*. 2012;63(9-10):319-23.
- [41] Yan C, Huang W, Tang N. Evaluation of the temperature effect on Rolling Thin Film Oven aging for polymer modified asphalt. *Construction and Building Materials*. 2017;137:485-93.
- [42] Yin F, Moraes PR. Storage Stability Testing of Asphalt Binders Containing Recycled Polyethylene Materials. Phase II-A Study Report, Prepared for the Plastics Industry Association; 2018.
- [43] Abutalib N, Fini EH, Aflaki S, Abu-Lebdeh TM. Investigating effects of application of silica fume to reduce asphalt oxidative aging. *American Journal of Engineering and Applied Sciences*. 2015;8(1):176-84.
- [44] Yusoff NIM, Alhamali DI, Ibrahim ANH, Rosyidi SAP, Hassan NA. Engineering characteristics of nanosilica/polymer-modified bitumen and predicting their rheological properties using multilayer perceptron neural network model. *Construction and Building Materials*. 2019;204:781-99.

# **Experimental Study of Hydrodynamic Pressures Acting on a Submerged Gate**

**Sochheat SMOK<sup>1</sup>**

**Mehmet Anil KIZILASLAN<sup>2</sup>**

**Adnan Tolga KURUMUS<sup>3</sup>**

**Ender DEMİREL<sup>4</sup>**

## **ABSTRACT**

Vortical flow formed by a submerged hydraulic jump may produce significant hydrodynamic lift and drag pressures on a gate beneath the hydraulic jump. In this study, an experimental setup equipped with multi-pressure sensors was used to measure fluctuating impact pressures on the submerged gate for different flow conditions characterized by the inlet Froude number and submergence factor (S). Time-averaged and instantaneous pressure coefficients are evaluated based on simultaneous measurements of wall pressures at multiple locations, including those at the lip and downstream face of the gate. In particular, instantaneous lift pressure coefficients are observed to be independent of the submergence ratio for  $S > 0.6$ . It is found that low Froude number flows produce high surface pressure fluctuations and the dominant frequency of pressure fluctuations shifts to higher frequency as the Froude number increases. Pressure measurements for the free hydraulic jump suggest that the power spectra of lift pressure fluctuations are devoid of any significant energy level, whereas the resulting power spectra of the submerged flow exhibits significant energy level in the frequency range of 14-19 Hz. The proposed measurement system can be used for the in situ identification of hydrodynamic pressures acting on the gates in irrigation canals.

**Keywords:** Submerged gate, pressure sensor, hydrodynamic impact, pressure coefficient.

---

## Note:

- This paper has been received on March 23, 2020 and accepted for publication by the Editorial Board on January 18, 2021.
- Discussions on this paper will be accepted by September 30, 2022.
- <https://doi.org/10.18400/tekderg.707668>

1 Civil Engineer (MSc), Cambodia -

smok.sochheat@gmail.com – <https://orcid.org/0000-0001-9662-3517>

2 Çanakkale Onsekiz Mart University, Construction Department, Çanakkale, Turkey -

makizilaslan@comu.edu.tr - <https://orcid.org/0000-0002-0621-4646>

3 Eskişehir Osmangazi University, Civil Engineering Department, Eskişehir, Turkey -

tolgakurumus@gmail.com - <https://orcid.org/0000-0002-2694-067X>

4 Eskişehir Osmangazi University, Civil Engineering Department, Eskişehir, Turkey -

edemirel@ogu.edu.tr - <https://orcid.org/0000-0002-0440-7866>

## 1. INTRODUCTION

Gates are the most common hydraulic structures not only to control the flow but also to measure the flow discharge in streams under free and submerged flow conditions. Submerged hydraulic jump occurs downstream of a vertical gate when the tail water depth exceeds conjugate subcritical depth of the free hydraulic jump.

This results in less air-water interaction and energy dissipation than that in the free jump. Interaction of the backward flow with the mean flow creates spatially and temporally varying vortices in the roller region downstream of the control structure. Prediction of vortex-induced hydrodynamic forces acting on the gate is important in design stage since the interaction of incoming jet with the recirculating flow in the roller region may cause the breakdown of the control structure depending on the flow conditions that develop.

Most of the experimental studies conducted in the literature consist of measuring instantaneous velocity components by using Acoustic Doppler Velocimetry (ADV), Particle Image Velocimetry (PIV) by Amir et al. [1] and Laser Doppler Anemometry (LDA) by Svendsen et al. [2]. Turbulent flow downstream of a submerged gate develops in a three-dimensional flow structure and strong fluctuations occur due to the interaction of mean and recirculating flows. Long et al. [3] experimentally studied flow characteristics in the submerged jump based on the LDA measurements of velocity and turbulence components for various submergence factors and Froude numbers. They reported that the vortical structure near the gate to be the main source of the “climb effect” in velocity components. Dey and Sarkar [4] analysed ADV measurements of mean velocity components, Reynold stresses and turbulence intensity in submerged wall jet associated with the sudden change from smooth to rough bed. Experimental results indicate that the self-preserving feature of the flow appears in the fully developed region for smooth and rough bed conditions. In a latter study by Dey and Sarkar [5], experimental studies were conducted for similar flow characteristics as in the former study to investigate the mean velocity components, Reynold stresses and turbulence intensity components, as well as shear stress distributions along the rough bed. Their experimental studies revealed that the rate of jet decay in the submerged jump increases with an increase in bed roughness and thus the flow structure on rough and smooth beds were not identical. Gümüş et al. [6] conducted experimental and numerical studies to examine water surface profiles under submerged hydraulic jump conditions with different Froude numbers. Results indicated that the RNG turbulence model was in the highest agreement with the experimental results in comparison to other turbulence closure models.

In an open channel flume with smooth and horizontal bed in Figure 1(a), magnitude of the submerged wall jet can be assessed by the Froude number defined underneath the gate as  $F_r = U_1/\sqrt{gy_1}$ , where  $g$  is the gravitational acceleration,  $y_1$  and  $U_1$  are the water depth and average flow velocity under the gate, respectively. Corresponding subcritical conjugate depth can be calculated using Belanger equation  $y_2 = 0.5y_1(\sqrt{1 + 8F_r^2} - 1)$  based on the assumptions of inviscid flow and hydrostatic pressure distribution. The hydraulic jump forms beneath the free surface when the tail water depth  $y_t$  becomes greater than the conjugate depth  $y_2$  and the corresponding submergence ratio can be evaluated with the submergence factor  $S = (y_t - y_2)/y_2$  (e.g., [7]). Interaction of the incident flow with the recirculating flow in this region creates temporally and spatially varying vortices, which may result in significant

hydrodynamic effects such as lift forces at the gate lip and drag forces on the downstream face of the gate.

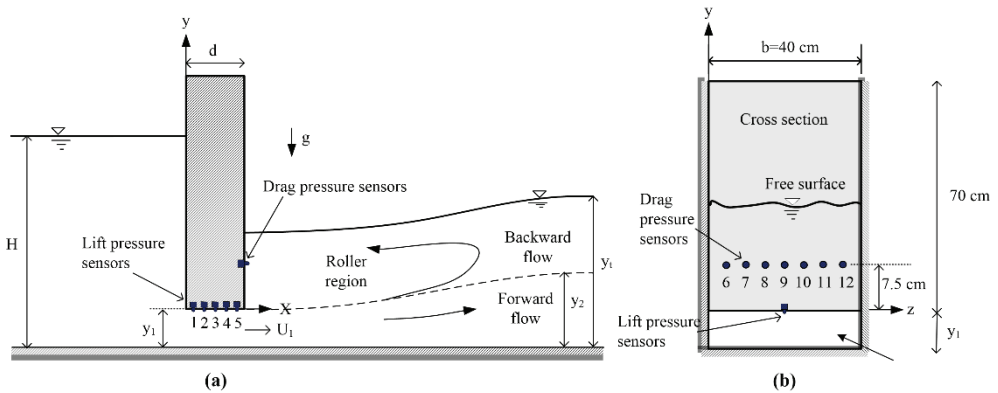


Figure 1 - Schematic representation of the submerged jump downstream of a vertical gate, (a) side view; and, (b) front view of the gate. Pressure sensors were embedded at the gate lip and downstream face of the gate

Several investigators have focused on the characteristics of hydrodynamic effects acting on different hydraulic structures. Thang and Naudascher [8] examined vortex-excited vibration of underflow vertical lift gates. They found that the dynamic interaction between elastic gate and unstable shear layer created a vortex that may force the gate to oscillate. Characteristics of the interaction process were analysed based on the spectral analysis of the hydrodynamic forces and the response of the gate. Bhargava and Narasimhan [9] carried out experimental studies to analyse hydrodynamic effects on the gate lip with various geometries. Time-averaged and fluctuating pressure coefficients were investigated using different Froude numbers and gate openings. They concluded that the gate lip with inclination less than  $45^\circ$  reduced the tendency of flow towards the separation. Geometry of the gate lip having  $45^\circ$  sloping lip with sharp and rounded upstream edges evidently provided the best reduction of total mean and fluctuating pressures. Fiorotto and Rinaldo [10] conducted experimental studies to investigate the pressure fluctuations under hydraulic jumps. They explored that the pressure at the jump location was maximum for  $Fr=0.5$ . Roth and Hager [11] carried out experimental studies to investigate the flow under the gates. Viscosity and surface tension effects, as well as pressure distributions on the channel bottom were discussed in detail. Corner vortices created by the stagnation flow near the gate were successfully suppressed by introducing a novel anti-vortex element mounted on the gate. Billeter and Staubli [12] experimentally studied flow-induced multiple-mode vibration of the submerged sluice gate. They used LDA and miniature pressure transducer to measure velocity and pressure simultaneously. Authors concluded that the self-excited vibration with the range of reduced velocity from 0.8 to 14 and the transition to galloping produced instability-induced excitation. The interaction between two different instability-induced vibrations was strongly dependent on the frequency ratio and the velocity range. Amir et al. [1] studied hydrodynamic effects on the sediment particle in free-surface flows using pressure sensors and PIV. Results showed that spatial and temporal scales in pressure fluctuations were relevant to the flow

depth and bed slope. Erdbrink et al. [13] conducted experimental studies to reduce the cross-flow vibration of underflow gates using resistance-type water level and force meter equipment. Experimental results on the submerged gate with low gate openings showed that the leakage flow approach could significantly reduce vibrations. Kampel et al. [14] experimentally studied the pressure fluctuations on the underflow gate due to the generation of upstream vortices. They concluded that the reduction of mean hydrodynamic pressure and increment in pressure fluctuations depended on the location of the longitudinal corner vortex upstream of the gate. Smok and Demirel [15] carried out experimental studies under different flow conditions of jet Froude number and submergence factor in order to provide how the vortex induced pressure fluctuations affect the gate stability. Results show that the fluctuation components are high at the leading and trailing edges of the gate due to the separation effects below the gate. Also Smok [16] investigated the hydrodynamic characteristic of lift and drag pressures on the submerged sluice gate, performing experimental studies under different flow conditions of Froude number, submergence factor and gate opening. Dios et al. [17] experimentally examined the behaviour of three-dimensional flow structure using ADV and PTV. Various Froude numbers and submergence factors were considered to analyse the mean velocity components and turbulence statistics. Velocity magnitude and turbulent kinetic energy were found to be significantly dependent on the submergence factor and Froude number. Bijankhan et al. [18] investigated velocity profiles downstream of the sluice gate using ADV and electromagnetic flowmeter for high submerged flow conditions. They concluded that the interaction of the energy correction factors and head loss values provided accurate results in head-discharge evaluation.

These studies reveal that the vortical structure around the submerged gate may result in hydrodynamic loads on the gate. The objective of the present study is to address how the gate responds to the vortical flow created by the submerged hydraulic jump under different flow conditions. Experimental studies were conducted in a laboratory flume for various Froude numbers, submergence factors and gate openings. Pressure fluctuations acting on the gate lip and downstream of the gate were measured simultaneously using pressure sensors at multiple locations. The contribution of the vortices to the wall pressures on the gate is examined by means of power spectrum analysis of instantaneous pressure measurements.

### **1.1. Experimental Setup and Pressure Measurement**

Experimental studies were carried out in a rectangular flume of 10 m long, 65 cm high and 40 cm wide with transparent glass sidewalls and stainless-steel bottom. The head tank is used at the inlet of the flume to maintain a constant head at the upstream of the control structure. Water was supplied by a feeding pipe connected to the head tank. The flow discharge in the flume was controlled by using a valve located at the entrance of the head tank and monitored precisely using the ultrasonic flowmeter mounted on the feeding pipe. Tail water depth was controlled using a tilting gate located downstream of the flume.

The vertical rectangular gate was installed at the location 3.5 m away from the inlet section of the flume in order to avoid unsteady effects at the inlet. The sluice gate was designed with 70 cm of height, 12 cm of width and 38 cm of cross section with 1 cm of thickness of the steel bars at the sides. On the sidewalls, the opening between the channel and gate have been secured by silicone to prevent water leakage. Gate model was designed taking into account

laboratory conditions and device features such as gate thickness and minimum distance required for the connection of sensors. As seen in Fig. 2, five lift pressure sensors and seven drag pressure sensors were embedded at the centreline of the gate bottom and downstream side of the gate, respectively. These sensor arrays enabled to evaluate spatial variations of lift and drag pressures acting on the gate. Lift pressure sensors at the bottom of the gate were located at distances of 19, 41, 61, 81 and 101 mm from the upstream corner of the gate. Drag pressure sensors from 6 to 12 were located at horizontal distances of 6, 11, 15.5, 20, 24.5, 29 and 34 cm from the reference coordinate system shown in Figure 1(b). The geometry and dimensions of the gate were selected such that adverse hydrodynamic effects would be prominent. Thus the present experimental setup is not representative of an operating gate. Modelling studies conducted on large gates have been examined in detail in technical reports of USBR and a real scale gate design has been developed applying similarity models. The ratio of  $y_0 / B$  was determined as 1.308 from the dimensional analysis based on 16 physical parameters. Here,  $y_0$  is the upstream water depth and  $B$  is the gate width [19]. This ratio was calculated as 1.71 for the present gate model, which is similar to the previously reported prototype case. Lip extension tests were carried out for 20, 40, 60 and 80% of gate width. It was reported that the lip length could be changed between 7.6 cm and 30.4 cm. Thus, width of the present gate remains in this range.

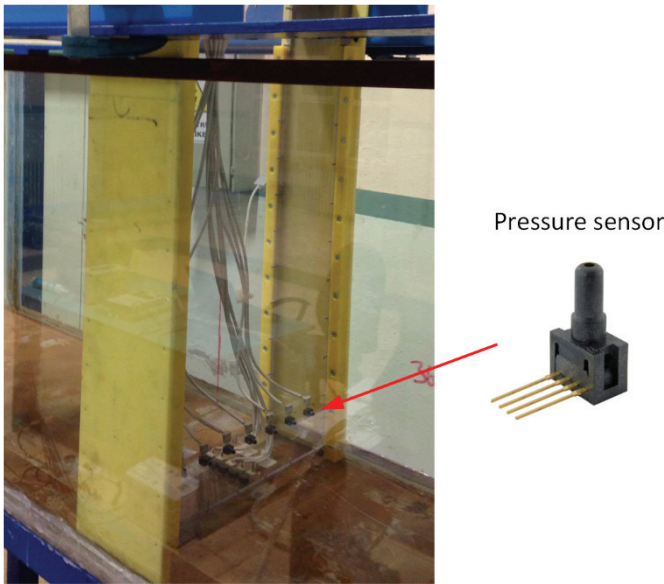


Figure 2 - Vertical gate equipped with multi-pressure sensors

Scale effects may be significant in the laboratory studies of engineering problems such as air-water flows in hydraulic jumps, void fraction, interfacial velocity, bubble count rate, turbulence intensity and bubble chord time [20]. In the present experimental setup, large eddies in the roller region may produce smaller hydrodynamic forces on the gate due to the scale effects.

*Experimental Study of Hydrodynamic Pressures Acting on a Submerged Gate*

The National Instrument data acquisition system (NI USB 6343 series) was used to measure the voltage signal from the stationary pressure sensors. The output voltage signal is collected by connecting the sensor pins to analogue input channels of data logger and to power supply. Measurements of pressure fluctuations were made by using the Honeywell pressure sensors (24PC-EFA6G series) as shown in Figure 2. These gage sensors, made from the fluorosilicone and straight type, have a full-scale range of 0 to 3450 Pa. The response of the pressure variation is typically supplied by 10 V directional current (DC) and the response time of 1 ms is justified by the manufacturer. Pressure sensors measure the pressure with respect to ambient pressure and hydrodynamic pressures cause the differential voltage to change. In order to facilitate stable pressure measurement, the cables connected to the pins of pressure sensors were configured into the side of the gate. The cables wired from sensor pins was then hooked up to the block hole of pre-barrier steel plate of the gate. The voltage signals in each pressure sensors were experimentally measured during 6 minutes in order to acquire adequate data for time averaging. A current regulator was integrated to the experimental setup in order to prevent noise effects originating from the electricity infrastructure network.

Static calibration test for the pressure sensor was conducted in a cubic water tank in order to justify the pressure gradient with the water depth and obtain an equation for the conversion of the voltage output to the pressure. A cubic water tank was designed and manufactured using 40 cm height and 30 cm × 30 cm surface bottom of plexiglass, Fig 3 (a). This test was performed in the range of 2 cm to 30 cm of water height in the calibration device by measuring the output voltage from pressure sensor in LabVIEW configuration. Every sensor has a different starting voltage depending on the manufacturing conditions. Thus, the voltage signals were proportionally and individually converted to the pressure using the best linear fit obtained from the measured data.

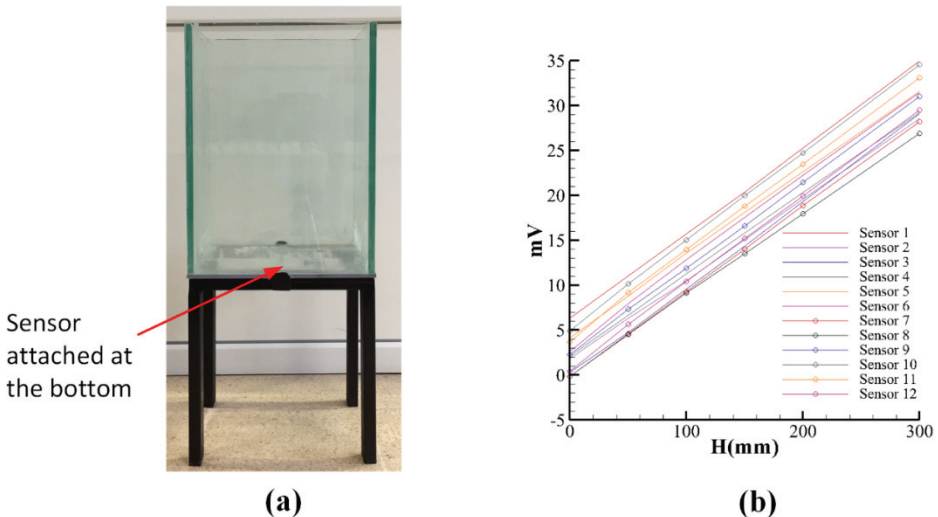


Figure 3 - (a) Static calibration test device; and, (b) variations of the voltage output with water depth for each sensor

Pressure sensor was dynamically calibrated on a draining cubic tank when the water depth in the tank is 30 cm initially. As depicted in Fig. 4, experimental measurements are compared with the available analytical results which were based on the inviscid flow assumption by Streeter et al. [21]. Analytical solution predicts a rapid draining at the early stage due to the neglected viscous effects. As the draining process develops with time, experimental measurements approach to the analytical results. The present dynamic calibration test shows that the present sensors are sensitive to the hydrodynamic conditions.

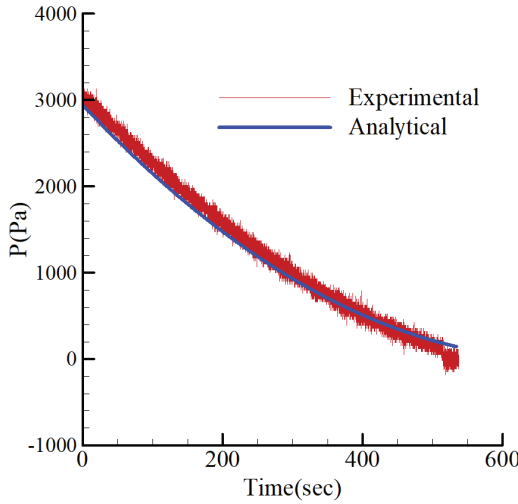


Figure 4 - Comparison of experimental measurements and analytical results during draining of the tank.

## 2. METHODOLOGY

### 2.1. Pressure Coefficients

Time-averaged and instantaneous wall pressures are evaluated using the following dimensionless pressure coefficients suggested by Bhargava and Narasimhan [9]:

$$C_{\bar{p}} = \frac{(H - \frac{\bar{p}}{\gamma})}{\frac{U_1^2}{2g}} \tag{1}$$

$$C_{p'} = \frac{\sqrt{p'^2} y_t}{\frac{1}{2} \rho U_1^2 H} \tag{2}$$

Where  $C_{\bar{p}}$  is mean pressure coefficient,  $C_{p'}$  instantaneous pressure coefficient,  $H$  is the upstream water depth,  $\bar{p}$  is the time-averaged pressure,  $\gamma$  is the specific weight of water ( $= \rho g$ ),  $\rho$  is the density of water,  $U_1$  is the average flow velocity under the gate and  $\sqrt{p'^2}$  is the

root mean square of pressure fluctuations. Bhargava and Narasimhan [9] found that the pressure fluctuations collapsed into a single curve for various values of  $y_t/H$ . Thus, the term  $y_t/H$  is included in Eq. (2).

**2.2. Experimental Conditions**

In order to investigate the hydrodynamic response of the gate to the vortex induced fluctuations, experimental studies were carried out under different flow conditions of gate opening, submergence factor and jet Froude number. The pertinent variables describing the flow conditions are calculated and summarized in three different groups in Table 1 to analyse the effects of key parameters describing the submerged hydraulic jump in a systematic manner. In the first group of experiments, various gate openings are considered for constant submergence factor and incident Froude number. To see the effect of submergence ratio, various submergence factors are adjusted for constant Froude number and gate opening in the second experimental set. In the last set, effect of jet Froude number was investigated for constant gate opening and submergence factor. These experimental conditions are tagged and depicted in the first column of Table 1, showing the first number as the group number and the second number as the run of the experiment in each set. Eleven experimental runs were carried out for the evaluation of mean and instantaneous wall pressures.

*Table 1 - Flow parameters and dimensionless numbers for different experimental runs*

| Run | Q (m <sup>3</sup> /s) | H(m)  | $y_1$ (m) | $V_1$ (m/s) | Fr    | $y_2$ (m) | $y_t$ (m) | S   |
|-----|-----------------------|-------|-----------|-------------|-------|-----------|-----------|-----|
| 1.1 | 0.013                 | 0.279 | 0.025     | 1.3         | 2.625 | 0.081     | 0.146     | 0.8 |
| 1.2 | 0.0171                | 0.336 | 0.03      | 1.425       | 2.627 | 0.097     | 0.175     | 0.8 |
| 1.3 | 0.0215                | 0.415 | 0.035     | 1.536       | 2.626 | 0.114     | 0.205     | 0.8 |
| 1.4 | 0.0263                | 0.495 | 0.04      | 1.644       | 2.624 | 0.13      | 0.234     | 0.8 |
| 2.1 | 0.015                 | 0.33  | 0.025     | 1.5         | 3.029 | 0.095     | 0.152     | 0.6 |
| 2.2 | 0.015                 | 0.35  | 0.025     | 1.5         | 3.029 | 0.095     | 0.172     | 0.8 |
| 2.3 | 0.015                 | 0.38  | 0.025     | 1.5         | 3.029 | 0.095     | 0.19      | 1.0 |
| 3.1 | 0.013                 | 0.279 | 0.025     | 1.3         | 2.625 | 0.081     | 0.146     | 0.8 |
| 3.2 | 0.015                 | 0.35  | 0.025     | 1.5         | 3.029 | 0.095     | 0.172     | 0.8 |
| 3.3 | 0.017                 | 0.441 | 0.025     | 1.7         | 3.433 | 0.110     | 0.197     | 0.8 |
| 3.4 | 0.019                 | 0.516 | 0.025     | 1.9         | 3.837 | 0.123     | 0.223     | 0.8 |

Instantaneous pressure data obtained from the pressure sensors were filtered by using moving-average method. The moving-average method first takes the average of a subset with a specified windows size  $w$ , and then the fixed size of the subset is shifted forward successively to filter the entire raw data using the following equation (e.g., [22]):

$$Y(z) = \frac{b(1) + b(2)z^{-1} + \dots + b(n_b + 1)z^{-n_b}}{1 + a(2)z^{-1} + \dots + a(n_a + 1)z^{-n_a}} X(z) \quad (3)$$

The numerator and denominator coefficients in Eq. (3) are calculated as  $b = \text{ones}(1,w)/w$  and  $a = 1$  in Matlab. The form of the dimensional digital moving average is functionally modified in Matlab programming [23] as  $y = \text{filter}(b, a, x)$ , where  $x$  is the raw pressure data in vector form. In the present study, the window size was selected as  $w = 100$  with respect to the pressure noise condition and a feedback from the autocorrelation procedure. The window size is determined by trying different values and selecting the value at which the data is removed from the noise at the most appropriate level. Time variations of raw and filtered pressures are represented in Fig. 5 (a) and Fig. 5 (b) for sensors 3 and 9, respectively, located in the middle of the gate lip and downstream face.

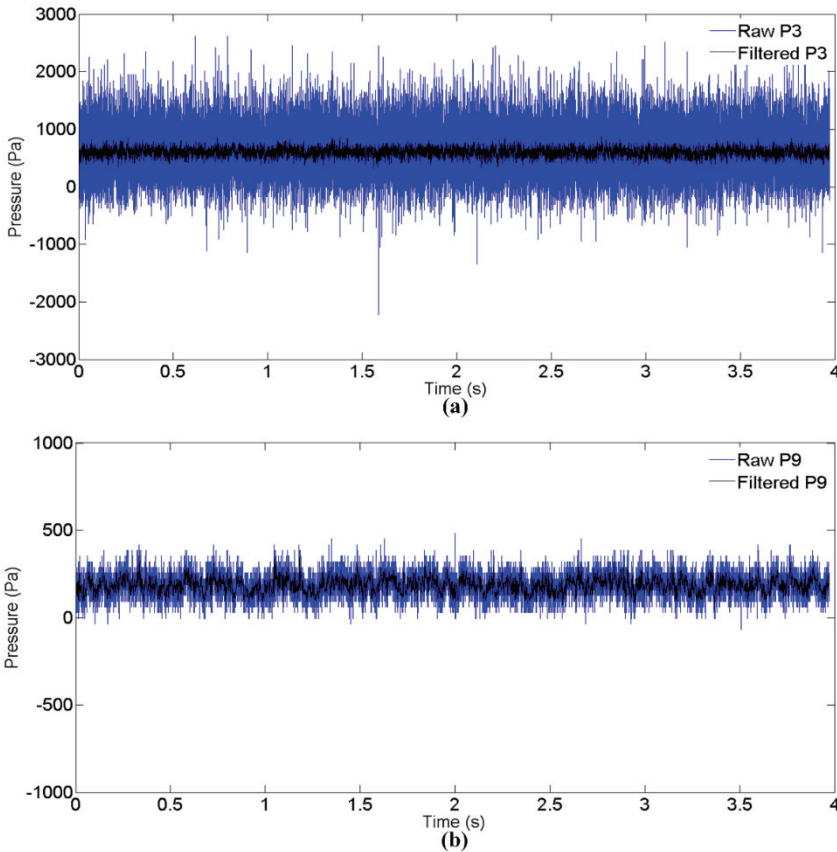


Figure 5 - (a) Comparison of raw and filtered pressure data for: (a) lift; and, (b) drag pressures ( $Fr = 3.029$ )

### 3. RESULTS AND DISCUSSIONS

#### 3.1. Lift Pressures

Instantaneous pressures were measured simultaneously at five different locations on the gate bottom for different flow conditions given in Table 1. It should be noted again that the frequency of each pressure sensor was 1000 Hz during experimental measurements. Gate opening is a critical parameter for the hydrodynamic response of the submerged gate even for constant Froude numbers since the same Froude number can be provided with different gate openings. Fig. 6 depicts the mean pressure variations at the gate lip. It can be observed that the minimum and maximum pressure magnitude ranges increase at relatively greater gate openings and pressures at the trailing edge of the gate decrease constantly due to the decreasing gate opening. The stagnation point is determined at  $x/d=0.667$  for  $y_l=0.03$  and  $y_l=0.025$  (Fig. 1). The positions of the different variables will be defined with the expression  $x/d$ . The effect of the gate opening is observed to be more pronounced at the trailing edge of the gate at low gate openings. This observation suggests that the interaction of incoming jet with the recirculating flow has significantly reduces the pressure at the trailing edge of the gate, even for the same Froude number and submergence factor.

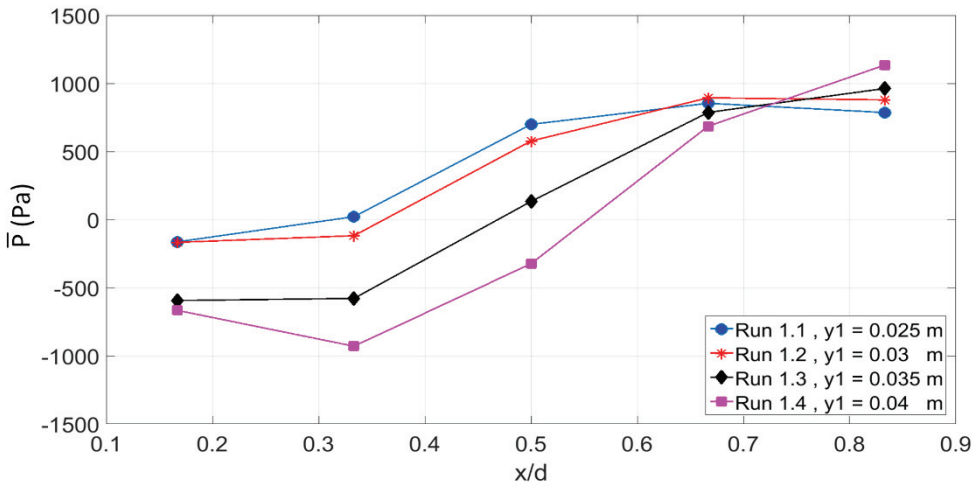


Figure 6 - Comparison of mean pressure variations at different locations on the gate lip for various gate openings ( $Fr = 2.63$  and  $S = 0.8$ )

Spatial variations of time-averaged and instantaneous pressure coefficients at the gate lip are shown in Fig. 7 for different gate openings. Spatial coordinates of the measurement points are non-dimensionalised with the thickness of the gate. The minimum  $C_{\bar{p}}$  occurs at  $x/d=0.667$  for,  $y_l=0.025$  whereas the location of the minimum  $C_{\bar{p}}$  shifts to the downstream edge of the gate as the gate opening increases. Notice that the minimum  $C_{\bar{p}}$  corresponds to the maximum pressure coefficient. The location of the maximum  $C_{p'}$  in Fig. 7(b) apparently depends on the gate opening. The maximum value of  $C_{p'}$  occurs just downstream of the leading corner of

the gate for  $y_l=0.04$ . The starting points of  $C_p'$  values were almost at the same locations for all gate openings. On the contrary, the interaction of the backward flow with the incident flow significantly increased the pressure fluctuations at higher gate openings.

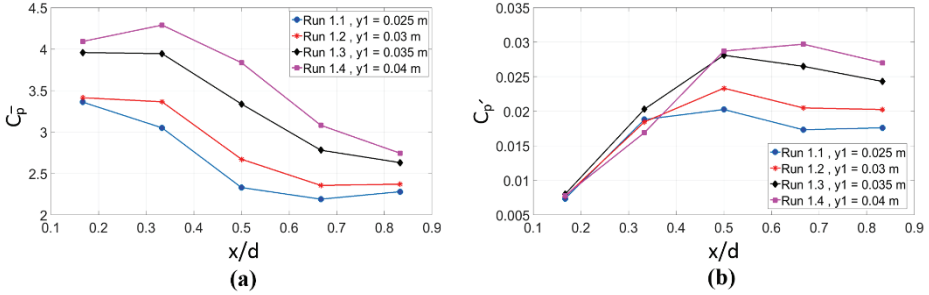


Figure 7 - Spatial variations of (a) mean; and, (b) fluctuating pressure coefficients along the gate bottom for various gate openings ( $Fr = 2.63$  and  $S = 0.8$ )

Fig. 8 shows the mean pressures at different locations on the gate lip for various submergence factors. Froude number and gate opening were kept constant to investigate the effect of downstream conditions on the lift pressures. It can be concluded from the figure that the hydrodynamic pressures are almost proportional to the submergence ratio. Comparison of the pressure magnitudes at each measurement point shows that the separated flow from the upstream leading edge reattaches to the gate bottom to increase the pressure at the downstream edge of the gate. Magnitudes of hydrodynamic pressures at the leading edge are less than that at other measurement points since the accelerating flow at the entrance of the gate opening causes the pressure magnitudes to reduce in this region.

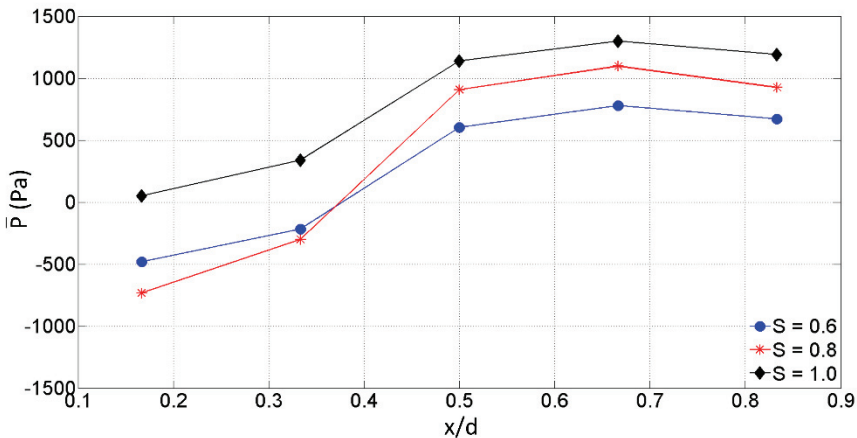


Figure 8 - Comparison of mean pressure variations at different locations on the gate lip for various submergence factors ( $Fr = 3.029$  and  $y_l = 0.025$  m)

Spatial variations of time-averaged and fluctuating pressure coefficients along the gate bottom are shown in Fig. 9 for various submergence factors. The uncertainty in experimental data is customarily represented using error bars. In 10% of cases used the error bar on the 90% confidence interval. Time-averaged pressure coefficients synchronized at similar values with the submergence factor and takes the minimum value at the point  $x/d=0.667$  of the gate bottom. Error bar values of  $S = 0.6$  and  $0.8$  show similar trends along the gate bottom in terms of mean pressure coefficient. When the comparison is made according to the maximum value of the submergence factor 1; it has been observed that varying submergence factors have the greatest effect on the mean pressure coefficient at the upstream and downstream corners of the gate. Scattering of the mean pressure near the leading and trailing edges of the gate lip associated with the separation pocket below the gate, which was also observed by Bhargava and Narasimhan [9] experimentally. The spatial distributions of the  $C_p'$  along the gate bottom in Fig. 9(b) show that the pressure fluctuations increase as the submergence factor decreases. The peak value of the  $C_p'$  is observed at the middle of the gate. The strong interaction of the recirculating flow with the incoming flow at low submergence caused higher pressure fluctuations. As the submergence factor increases, the effect of the downstream flow conditions disappears. It can be observed from Fig. 9(b) that pressure fluctuations depend on the submergence factor between upstream corner and middle of the gate. The uncertainty in  $C_p'$  values were similarly represented using error bars with 90% confidence interval. Here, pressure coefficients along the gate bottom are independent of the submergence ratio and differences converge to a constant value.

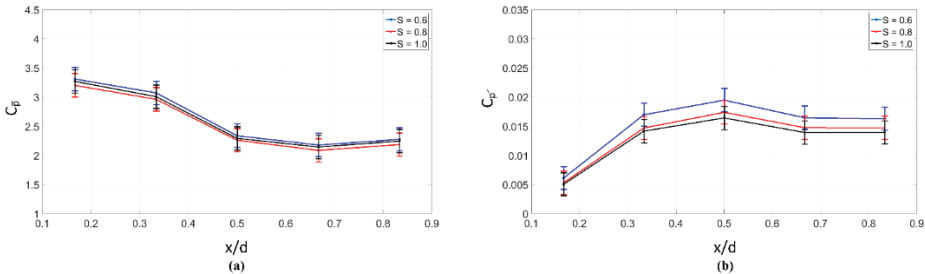


Figure 9 - Spatial variations of (a) mean; and, (b) fluctuating pressure coefficients along the gate bottom for various submergence factors ( $Fr = 3.029$  and  $y_1 = 0.025$  m)

Spatial variations of time-averaged pressure coefficient along the centerline of the gate lip are given in Fig. 10(a) for different Froude numbers. In Eq. (1), the low mean pressure coefficient corresponds to a high mean pressure. It can be seen in Fig. 10(a) that the time-averaged pressure coefficient decreases as the Froude number increases due to the increasing upstream water depth. Moreover, the 90% confidence interval of mean pressure coefficients with Froude number is effective only in the middle of the gate. The uncertainty analysis on the fluctuating pressure coefficient shows that the effect of the Froude number increases along the gate. While the  $C_p'$  values are in the same range, the difference grows near the downstream corner of the gate and varies depending on the Froude number.

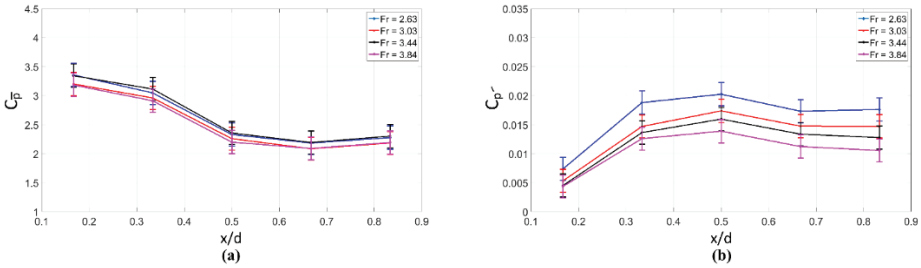


Figure 10 - Spatial variations of (a) mean; and, (b) fluctuating pressure coefficients along the gate bottom for various Froude numbers ( $S = 0.8$  and  $y_1 = 0.025$  m)

The minimum mean pressure coefficient is observed immediately downstream of the center of the gate lip ( $x/d=0.667$ ) due to the impingement of the separated flow from the upstream corner. Therefore, the location of a minimum mean pressure coefficient corresponds to a stagnation point at the gate bottom. High  $C_p$  values downstream of the stagnation point are associated with the accelerating flow in this region. The confidence interval boundary (CIB) values for spatial variations of mean; and, fluctuating pressure coefficients along the gate bottom for various submergence factors are given in Table 2.

Table 2 - The confidence interval boundary values for spatial variations of mean; and, fluctuating pressure coefficients along the gate bottom for various submergence factors

| Run |        | x/d=0.167 |         | x/d=0.333 |         | x/d=0.5 |         | x/d=0.667 |         | x/d=0.833 |         |
|-----|--------|-----------|---------|-----------|---------|---------|---------|-----------|---------|-----------|---------|
|     |        | Up CIB    | Low CIB | Up CIB    | Low CIB | Up CIB  | Low CIB | Up CIB    | Low CIB | Up CIB    | Low CIB |
| 2.1 | $C_p$  | 3.478     | 3.144   | 3.226     | 2.918   | 2.453   | 2.219   | 2.285     | 2.067   | 2.388     | 2.16    |
|     | $C_p'$ | 0.0064    | 0.0058  | 0.0178    | 0.0161  | 0.0204  | 0.0185  | 0.0173    | 0.0156  | 0.0171    | 0.0155  |
| 2.2 | $C_p$  | 3.361     | 3.041   | 3.109     | 2.813   | 2.372   | 2.146   | 2.189     | 1.98    | 2.293     | 2.074   |
|     | $C_p'$ | 0.0055    | 0.005   | 0.0154    | 0.0139  | 0.0182  | 0.0165  | 0.0155    | 0.014   | 0.0154    | 0.0139  |
| 2.3 | $C_p$  | 3.432     | 3.105   | 3.158     | 2.857   | 2.406   | 2.177   | 2.249     | 2.035   | 2.357     | 2.132   |
|     | $C_p'$ | 0.0053    | 0.0047  | 0.0148    | 0.0134  | 0.0172  | 0.0156  | 0.0146    | 0.0132  | 0.0146    | 0.0132  |
| 3.1 | $C_p$  | 3.525     | 3.189   | 3.2       | 2.895   | 2.446   | 2.213   | 2.294     | 2.075   | 2.39      | 2.163   |
|     | $C_p'$ | 0.0077    | 0.0069  | 0.0197    | 0.0178  | 0.0212  | 0.0192  | 0.0182    | 0.0165  | 0.0185    | 0.0167  |
| 3.2 | $C_p$  | 3.361     | 3.041   | 3.109     | 2.813   | 2.372   | 2.146   | 2.189     | 1.98    | 2.293     | 2.075   |
|     | $C_p'$ | 0.0055    | 0.005   | 0.0154    | 0.0139  | 0.0182  | 0.0165  | 0.0155    | 0.014   | 0.0154    | 0.0139  |
| 3.3 | $C_p$  | 3.511     | 3.176   | 3.271     | 2.96    | 2.475   | 2.24    | 2.302     | 2.083   | 2.418     | 2.188   |
|     | $C_p'$ | 0.0047    | 0.0045  | 0.0143    | 0.0136  | 0.0167  | 0.0159  | 0.014     | 0.0133  | 0.0134    | 0.0127  |
| 3.4 | $C_p$  | 3.342     | 3.024   | 3.057     | 2.766   | 2.309   | 2.089   | 2.195     | 1.986   | 2.303     | 2.083   |
|     | $C_p'$ | 0.0045    | 0.0043  | 0.0132    | 0.0126  | 0.0146  | 0.0138  | 0.0118    | 0.0112  | 0.011     | 0.0105  |

### 3.2. Drag Pressure

Instantaneous pressures were measured at different locations on the downstream face of the gate (Fig. 1(b)) during the experimental studies. Spatial variations of the time-averaged and instantaneous pressure coefficients on the downstream face of the gate are shown in Fig. 11

for various Froude numbers. The time-averaged pressure coefficient is slightly higher at the near edges. This suggests that the time variation of the vorticity field downstream of the gate does not result in a symmetrical mean pressure field on the gate. The minimum time-averaged pressure coefficient occurs at the center of the gate. The vortex pair observed downstream of the gate creates a low momentum region at the center of the gate. The same behaviour is observed in the spatial variation of the instantaneous pressure coefficient  $C_p'$  on the gate. Unsteady motion of the vortex pair downstream of the gate created an almost symmetrical behaviour in both mean and instantaneous pressure coefficients. The maximum  $C_p'$  values occur at  $z/b \approx 0.28$  and  $z/b \approx 0.72$  at which location the recirculation effects were found to be significant from the span-wise measurements of velocity profiles downstream of the submerged gate by Long et al. [3]. This suggests that the surface pressure fluctuations on the gate are closely connected with the vortical flow in the roller region downstream of the gate.

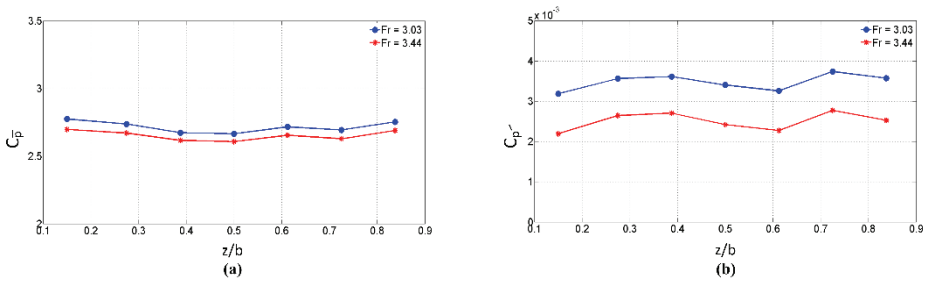


Figure 11 - Spatial variations of (a) mean; and, (b) fluctuating pressure coefficients along the downstream face of the gate for various Froude numbers

Spatial variations of the mean and instantaneous pressure coefficients on the downstream face in Fig. 12 reveal the same non-symmetrical distribution along the span-wise direction for different gate openings. The maximum  $C_p'$  occurs at  $z/b \approx 0.38$  again and the magnitude of the  $C_p'$  increases as the gate opening increases. This again suggests that the fluctuating pressure coefficient strongly depends on the gate opening, as displayed in Fig. 11(b). Vortex induced pressure fluctuations on the downstream face of the gate increased with the gate opening. The position of the peak of the  $C_p'$  is independent of the flow condition.

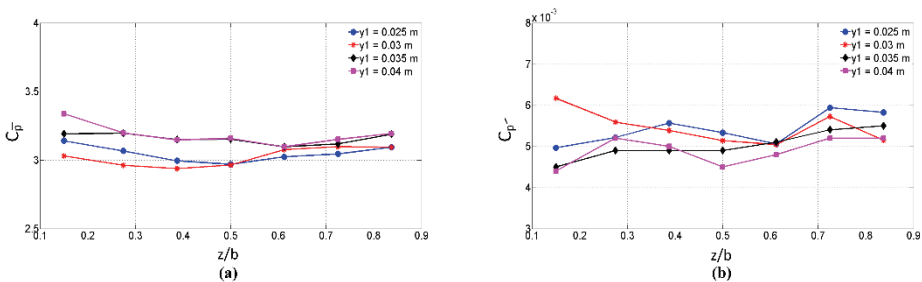


Figure 12 - Spatial variations of (a) mean; and, (b) fluctuating pressure coefficients along the downstream face of the gate for various gate openings

$C_{\bar{p}}$  values pursue a constant magnitude range throughout the gate for different gate openings and same Froude number. According to the complex recirculation flow region,  $C_{p'}$  magnitudes have also fluctuating behaviour along the downstream of the gate. Considering the low extent,  $C_{p'}$  values were not highly differ from each other for different gate openings. Fig. 12 indicates that the changing velocities due to the constant Froude number and different gate openings have a direct relation with the pressure magnitudes.

### 3.3. Frequency Spectra

The power spectrum obtained from the instantaneous pressure measurements were employed in order to examine the contribution of the vortices to the wall pressure fluctuations on the gate. The power spectrum analysis was performed using Welch [24] method. The frequency spectra of lift pressure fluctuations are shown in Fig. 13 for  $Fr = 3.837$  with constant submergence factor and gate opening. The spectral magnitude at P1 which is the closest pressure sensor to the leading edge experiences a peak frequency at 14.65 Hz and then starts to decrease until the high-frequency range of 170 Hz. For the other lift sensors, significant peaks were not observed at a low-frequency range and the magnitude only increases at 200 Hz then decays synchronized with a distinct slope. The low-pressure magnitudes at the leading and trailing edges of the gate lip produce less spectral level due to the accelerating flow in this region. The reliability of the collected data was provided after repeated experiments.

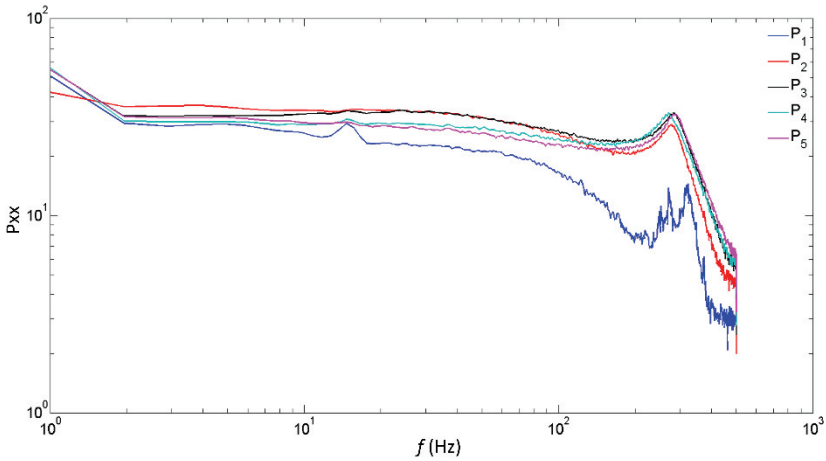


Figure 13 - Spectra of lift pressure fluctuations for  $Fr = 3.837$ ,  $S = 0.8$  and  $y_1 = 0.025$  m

The estimated frequency spectra for lift and drag pressure fluctuations were spatially averaged on the lip and downstream face of the gate, respectively. Fig. 14 shows the averaged power spectrum of lift pressure fluctuations for various Froude numbers in order to see the effect of Froude number on the spectral behaviour. The dominant frequency is observed within the range of 14-19 Hz for all cases, and for the Froude numbers of 2.625 and 3.029

dominant frequencies are also observed at around 40, 55 and 95 Hz. The largest spectral contributions to lift pressures occur at approximately between the frequency of  $f \cong 14$ ,  $f \cong 19$  Hz for various Froude numbers. As the Froude number increases, the dominant frequency shifts to the higher frequencies and the spectral magnitude diminishes with a constant slope in the high-frequency region. This suggests that contributions of the recirculation effects to the lift pressures decreases as the Froude number increases for a constant gate opening and submergence factor since the flow jet with high momentum can suppress recirculation effects. Thus, the low Froude number flow experiences high pressure fluctuations in the low-frequency region. As shown in Fig. 14, the spectral decay follows the Kolmogorov power law as  $f^{-5/3}$  in the high-frequency range.

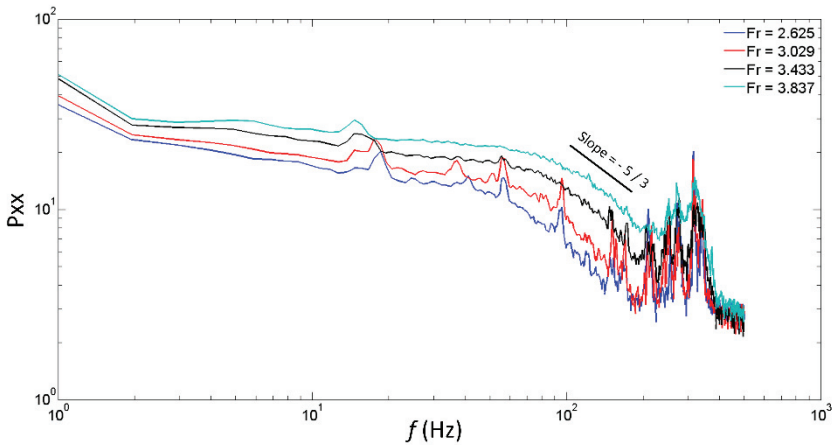


Figure 14 - Spatially averaged spectra of lift pressure fluctuations for various Froude numbers ( $S = 0.8$  and  $y_1 = 0.025$  m)

Spatially averaged lift and drag pressure fluctuations are compared for different Froude numbers in Fig. 15. The spectra of drag pressure fluctuations roll off more sharply compared to the lift pressures in the low-frequency range. The energy level of the lift pressure fluctuations is larger than that of the drag pressure fluctuations. Lift and drag pressure fluctuations contain the peak energy at the same frequency close to 13 Hz for  $Fr = 3.837$ . The power spectra of drag pressure fluctuations in the high-frequency range show unstable behaviour which may be attributed to the high frequency surface wave fluctuations in the vicinity of the gate.

The power spectra of lift pressure fluctuations are compared in Fig. 16 for free and submerged flow conditions. It can be clearly seen in the figure that the interaction of the recirculation flow with the mean flow induces lift pressure fluctuations on the gate lip. However, a significant spectral level is not observed for the free flow conditions. This observation suggests that when the gate is subjected to the submerged hydraulic jump, recirculating flow downstream of the gate may give rise to increase hydrodynamic effects below the gate. It should be noted here that drag pressure fluctuations are not available for free flow conditions.

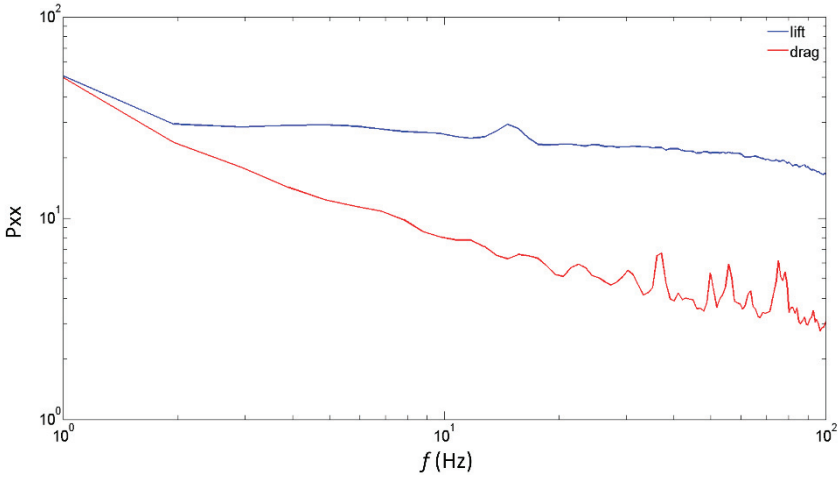


Figure 15 - Comparison of spatially averaged power spectra of pressure fluctuations for  $Fr = 3.837$ ,  $S = 0.8$  and  $y_l = 0.025$  m

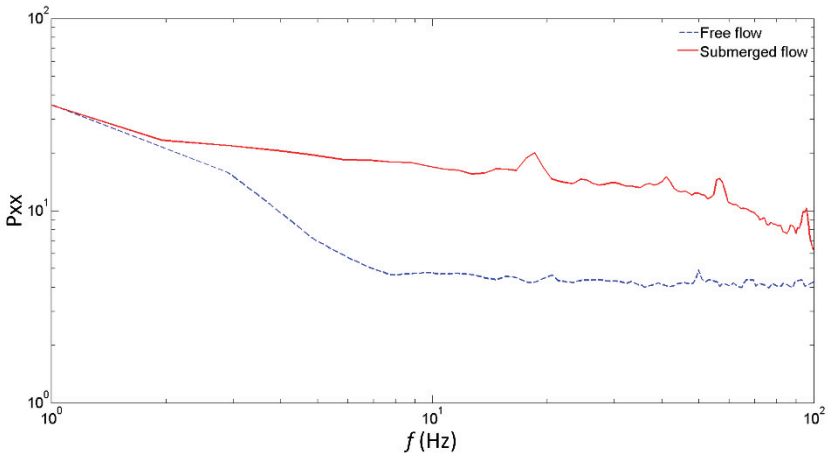


Figure 16 - Comparison of spatially averaged power spectra of lift pressure fluctuations for submerged and free flow conditions ( $Fr = 2.625$  and  $y_l = 0.025$  m.)

#### 4. CONCLUSIONS

Laboratory studies were carried out by means of instantaneous pressure measurements to investigate surface pressure fluctuations on the gate under various flow conditions. Experimental results enabled to gain insights on the contributions of vortices to the pressure fluctuations acting on the control structure. The experimental system used in this study can be classified as a large gate model in terms of model scale.

For low Froude number flows, backward flow downstream of the gate interacts with the separated flow and significantly affects the pressure fluctuations near the upstream corner of the gate bottom. The minimum mean pressure coefficient along the gate lip is observed immediately downstream of the center of the gate lip due to the impingement of the separated flow from the upstream corner. Interaction of the flow jet with the recirculating flow significantly reduces the pressure magnitude near the downstream corner of the gate, even for the same Froude number and submergence factor. On the other hand, the position of the maximum of the instantaneous pressure coefficient occurs at the center of the gate lip independently from the gate opening. The position of the minimum pressure coefficient close to the downstream of the gate attributed to a stagnation point. Stagnation points were observed significantly at relatively narrow gate openings such as 3 cm and 2.5 cm. The vortex pair observed downstream of the gate creates a low momentum region at the center of the gate. Unsteady motion of the vortex pair downstream of the gate shows non-symmetrical distributions of mean and instantaneous drag pressure coefficients. The maximum instantaneous pressure coefficients were observed at the same location where recirculation effects were found significant from the previous span-wise velocity measurements downstream of the submerged gate in the literature. This suggests that the surface pressure fluctuations on the gate are closely connected with the vortical flow in the roller region downstream of the gate.

Experimental results of this study show that the power spectra of drag and lift pressure fluctuations are found to decay with different slopes in the low-frequency range. Results show that different Froude number flows experience the same frequency fluctuations as in the low-frequency region and additional frequency fluctuations occur in the high-frequency region for the low Froude number. The power spectra of lift pressure fluctuations are devoid of any significant spectral level over a wide frequency range for the free flow conditions. Findings from this experimental study suggest that the hydrodynamic features of the control structures in irrigation systems need to be monitored using pressure sensors depending on the seasonal operational and downstream conditions. The experimental analysis described in this study can be used by engineers to increase economic life of hydraulic structures based on the monitoring of hydraulic infrastructures. Hydrodynamic pressure measurements reported in this study can also be used to validate high resolution numerical models, which may be used for the simulation of turbulent flows through real scale submerged gate flows.

## **Symbols**

$C_{\bar{p}}$  : Mean pressure coefficient

$C_{p'}$  : Instantaneous pressure coefficient

$d$  : Gate width

$Fr$  : Froude number

$g$  : Gravitational acceleration

$H$  : Upstream water depth

$\overline{p'^2}$  : Pressure fluctuation

- $\bar{p}$  : Time-averaged pressure  
S : Submergence factor  
 $U_1$  : Average flow velocity  
w : Window size  
 $y_1$  : Upstream water depth  
 $y_2$  : Downstream water depth  
 $y_t$  : Tail water depth  
 $\gamma$  : Specific weight of water

### **Acknowledgements**

This work was supported by the Scientific and Technological Research Council of Turkey (TUBITAK) under Grant no. 216M521.

### **References**

- [1] Amir, M., Nikora, V.I., Stewart, M.T., Pressure forces on sediment particle in turbulent open-channel flow: A laboratory study. *J. Fluid Mech.*, 757, 458-497, 2014.
- [2] Svendsen, I.A., Veeramony J., Bakunin J., Kirby, J.T., The flow in weak turbulent hydraulic jumps. *J. Fluid Mech.*, 418, 25-57, 2000.
- [3] Long, D., Steffler, P.M., Rajaratnam N., LDA study of flow structure in submerged hydraulic jump. *J. Hydraul. Res.*, 28, 437-460, 1990.
- [4] Dey, S., Sarkar, A., Response of velocity and turbulence in submerged wall jets to abrupt changes from smooth to rough beds and its application to scour downstream of an apron. *J. Fluid Mech.*, 556, 387-419, 2006.
- [5] Dey, S., Sarkar, A., Characteristics of turbulent flow in submerged jumps on rough beds. *J. Eng. Mech.*, 134, 49-59, 2008.
- [6] Gümüş, V., Aköz, M.S., Kırkgöz, M.S., Kapak mansabında batmış hidrolik sıçramanın deneysel ve sayısal modellenmesi. *Teknik Dergi*, 24(117), 2013.
- [7] Rajaratnam, N., Advan J. Hydraulic jumps. *Hydro-Sci*, 4, 197-280, 1967.
- [8] Thang, N.D., Naudascher, E., Vortex-excited vibration of underflow gates. *J. Hydraul. Res.* 24, 133-151, 1986.
- [9] Bhargava, V.P., Narasimhan, S., Pressure fluctuation on gates. *J. Hydraul. Res.*, 27, 215-231, 1989.
- [10] Fiorotto, V., Rinaldo, A., Turbulent pressure fluctuations under hydraulic jumps. *J. Hydraul. Res.*, 30, 499-520, 1992.

- [11] Roth, A., Hager, W.H., Underflow of standard sluice gate. *J. Exp. Fluid.*, 27, 339-350, 1999.
- [12] Billeter, P., Staubli, T., Flow-induced multiple-mode vibrations of gates with submerged discharge. *J. Fluids. Struct.*, 14, 323-338, 2000.
- [13] Erdbrink, C.D., Krzhizhanovskaya, V.V., Sloot, P.M.A., Reducing cross-flow vibration of underflow gates: Experiments and numerical studies. *J. Fluid. Struct.*, 50, 25-48, 2014.
- [14] Kampel, I., Prenner, R., Krouzecky, N. Pressure fluctuations on underflow gates of weirs due to upstream vortex generation. *Materials Today: Proceedings.*, 4, 5833-5838, 2017.
- [15] Smok, S., Demirel, E., Pressure Measurements on the Gate Subjected to Submerged Hydraulic Jump. *Advances in Fluid Mechanics*, Ljubljana, Slovenia, 2018.
- [16] Smok, S. Experimental Investigation of Vortex Induced Hydrodynamic Effects Acting on the Submerged Gate and Development of Vortex Breaker Apparatus, Master Thesis, Eskişehir Osmangazi University, 2019.
- [17] Dios, M., Bombardelli, F.A., Garcia, C.M., Liscia, S.O., Lopardo, R.A., Parravicini, J.A., Experimental characterization of three-dimensional flow vortical structures in submerged hydraulic jumps. *J. Hydro-Environ. Res.*, 15, 1-12, 2017.
- [18] Bijankhan, M., Kouchazadeh, S., Belaud, G., Application of the submerged experimental velocity profiles for the sluice gate's stage-discharge relationship. *Flow. Meas. Instrum.*, 54, 97-108, 2017.
- [19] Murray, R.I., Simmons, W.P., Hydraulic Downpull Forces on Large Gates. Bureau of Reclamation, Report Number Research Report No. 4., 1966.
- [20] Murzyn, F., Chanson, H., Experimental assessment of scale effects affecting two-phase flow properties in hydraulic jumps. *Exp. Fluids*, 45, 513-521, 2008.
- [21] Streeter, V. L., Wylie, E. B., Bedford, K. W., *Fluid Mechanics*, 9ed, McGraw-Hill, US, 1998.
- [22] Oppenheim, A.V., Schaffer, R.W., Buck, J.R., *Discrete-time signal processing*, Upper Saddle River, New Jersey, 1999.
- [23] The MathWorks, *Pro-Matlab User's Guide*. South Natick, MA, 1990.
- [24] Welch, P.D., The use of fast Fourier transforms for estimation of power spectra: A method based on time averaging over short, modified periodograms. *IEEE Transactions on Audio and Electroacoustic*, 15, 70-73, 1967.

# **Evaluation of Stripping Problem in Terms of Additive Types and Ratios in Asphalt Pavements**

**Celeleddin Ensar ŞENGÜL<sup>1</sup>**

**Atakan AKSOY<sup>2</sup>**

**Erol İSKENDER<sup>3</sup>**

## **ABSTRACT**

Stripping in asphalt mixtures is the one of foremost distress mechanisms. To prevent stripping, fatty acids (AS) and hydrated lime (HL) additives are often used as anti-stripping additives. The determination of the correct usage ratios of these additives and the storage stability of bitumen constitutes important research topics for anti-stripping additive applications. Three surfactants and hydrated lime were used in three ratios to evaluate the effect of additive ratio and type. Indirect tensile strength (ITS) values obtained from samples with one and three cycle modified Lottman conditioning and indirect tensile strength ratios (ITSRs) were interpreted in the context of water damage. The load-carrying capacity of the conditioned mixtures increased significantly. Even if the degree of damage was considerably increased at the end of three cycles, the integrity of the mixtures was maintained. Both AS and HL significantly increased water damage resistance. Modified Lottman conditioning has an observable level of damage. Additives remained functional and maintain their mechanisms of benefit, especially in the event of a high degree of damage.

**Keywords:** Asphalt pavement, stripping, modified Lottman test, amine surfactants, hydrated lime.

## **1. INTRODUCTION**

The problem of water damage (stripping) in asphalt pavements is one of the most complex pavement problems. Various additives are used to prevent or minimize stripping and a high degree of emphasis is placed on the design phase. Although the subject is evaluated with qualitative and quantitative test methods, there is no internationally accepted method in terms

---

Note:

- This paper was received on September 29, 2020 and accepted for publication by the Editorial Board on January 11, 2022.
- Discussions on this paper will be accepted by September 30, 2022.
- <https://doi.org/10.18400/tekderg.798398>

1 General Directorate of State Hydraulic Works, Fourteenth Regional Directorate, Istanbul, Turkey  
celensen@dsi.gov.tr - <https://orcid.org/0000-0003-0998-028X>

2 Karadeniz Technical University, Civil Engineering Department, Trabzon, Turkey  
aaksoy@ktu.edu.tr - <https://orcid.org/0000-0001-5232-6465>

3 Karadeniz Technical University, Civil Engineering Department, Trabzon, Turkey  
eiskender@ktu.edu.tr - <https://orcid.org/0000-0001-7934-839X>

of evaluating the performance level of the methods used and the long-term performance issues.

Highway institutions express the need for a reliable and practical laboratory method that can simulate moisture damage in the field, even if continuous improvement is made in moisture sensitivity tests to clarify and understand the mechanisms of moisture damage [1]. The most common technique to mitigate moisture damage is the use of additives or modifiers with the asphalt binder or the aggregate, and AASHTO T-283 is a widely-recognized laboratory test method for the evaluation of moisture susceptibility [2]. Developing laboratory moisture damage evaluation tests is challenging and it is hard to simulate field performance because of the high variability of the factors affecting moisture damage and the process of developing new test procedures still continues [3]. Because of the complexity of the moisture damage phenomenon, it is difficult to find a unique test or analytical method that accurately simulates the field behavior and quantifies and predicts moisture damage [4].

At this point, a discussion topic arises in determining the correct contribution rate. At the point of accurate assessment of field long-term performance, the issue of water damage conditioning models and performance approaches depending on the storage stability of the additives is a rather complex problem. New experimental methods are researched and the subject is examined. Under these circumstances, this research was applied as a widely accepted water damage experiment to evaluate and determine the results of the Modified Lottman test under many different alternatives. Determining the damage ratios and determining the relative effectiveness of the additives (anti-strips or other additives with indirect effects) are widely mentioned in the literature as complex topics. As four different additives, both fatty acid anti-stripping and hydrated lime additives were selected and these additives were used in three different rates in order to evaluate the rate effect. In addition, the applied damage system of the selected Modified Lottman damage test was repeated three times on identical briquettes, and an experimental systematic was created and the effect level of the Modified Lottman test was investigated for the very high damage levels and in this sense, the evaluation of the ratio values and additive activities was made. In this regard, although an experimental method was used in the research, a wide parameter change and an experimental framework were created at the point of complexity of the subject.

Moisture sensitivity is an important pavement degradation mechanism faced by most highway agencies. Along with the complex thermodynamic mechanisms, the subject develops due to various factors in the asphalt mixture. Various types of pavement distress trigger breakdown problems and cause billions of dollars in economic damage through maintenance and rehabilitation practices. The most accepted traditional technique to minimize or prevent water damage is to add additives or modifiers to bituminous mixtures. After all, every additive or modifier put in performance distinctively. Using proper additives and modifiers is considered the most cost-effective technique for mitigating moisture damage. If a particular HMA is determined to be moisture susceptible or sensitive, most U.S. transportation agencies add additives or modifiers to binder or aggregate to make the mix more resistant to moisture damage. The ability of numerous additives and modifiers to reduce stripping potential has been evaluated. Liquid anti-strip and polymers are added to asphalt binder while Portland cement, hydrated lime, and fly ash are added to the aggregates. These additives and modifiers are expected to improve the resistance of HMA to moisture damage by improving the adhesion bond between asphalt binder and aggregate surface. Additives

and modifiers follow several mechanisms for improving the adhesion bond such as modifying the aggregate surface, promoting the spread of binder around aggregate particles by reducing binder surface tension, or improving the chemical properties of the binder and aggregate surface at the same time [5].

Water damage is not considered to be a damage mode alone, it can speed up other modes of deterioration and cause serious troubles namely bleeding, rutting, raveling and shoving [6, 7]. Existence of moisture in asphalt mixes disrupts mixture structural integrity. It acts upon as a catalyst in the formation of other pavement problems with water damage [8].

To increase durability of the pavement surfaces, adhesion issues between aggregate and bitumen should be understood [9]. To increase the stripping resistance of the mixtures, in general, changes are made to the internal thermodynamic factors, because changes in external factors such as changing the weather and / or traffic are expensive and, in most cases, even impossible. The most important, effective, efficient method to increase the performance of asphalt mixes towards stripping is to choose material properties, mix design or anti-stripping additives. The idea of replacing materials causes to increased transport distances and consequently increases project total costs. Changing the mixture design with unsuitable materials could have an unimportant effect in increasing the resistance of the asphalt mix to water damage [10]. Due to the mineralogical change of aggregate properties and the heterogeneity of the mixtures, it is important to choose the right additive and apply the usage ratios correctly. Even if the mixture design is changed, the problem of stripping may still be a problem for these reasons. The overall equivalent performance feature of the mixtures should be strengthened.

There is great difficulty in obtaining which physicochemical properties are preponderant for adhesiveness, since the mechanisms that govern this property are still not well-understood. Owing to the difficulty in measuring aggregate-binder adhesiveness reliably, most studies attempt to relate this property to moisture damage, but few studies have attempted to explain how this property affects asphalt pavement distresses such as fatigue cracking [11].

Various experiments are available to evaluate the effectiveness of anti-stripping (surfactants) additives, to question and calculate the water sensitivity of asphalt mixes. Experiments could be performed as loose and compacted mix tests [12].

Amines and amidoamines are used as water damage (stripping) inhibitors [13]. Modified Lottman experiment is the most suitable test method available in the context of these experiments and gives high consistency with field performance results [2, 14]. Although the sensitivity of asphalt mixes to field moisture is estimated correctly, avowable that the Modified Lottman test does not focus on indicating the main characteristics of the respective road making materials. In addition, the proposed index shows asphalt mix resistance to various breaking mechanisms using a number without being interpreted and evaluated. Therefore, the reasons for the proper or poor resistance of an asphalt mix to water damage are unknown until the pavement design engineer redesigned the asphalt mix based on the interpretation of the results [15, 16]. In the tests carried out with the same type of bitumen without any anti-stripping additives after damage conditioning with the modified Lotmann test; the asphalt mixture consisting of limestone aggregate appears to be more resistant to moisture damage. Asphalt mixtures demonstrate the highest indirect tensile strength ratio

(TSR) of 61.7% with limestone aggregate, followed by slate aggregate with 48.6% and granite aggregate with 58.5% [17].

Accordingly, a method is needed to determine the effects of bitumen, aggregate and water system on adhesion based on the basic properties of the materials. A better understanding of the adhesion processes between asphalt and aggregate is necessary to extend the durability and life of the pavement materials [18, 19].

Caltrans also conducted a statewide field investigation and laboratory testing to determine the severity and major factors conjunction with water damage. The field investigation surveyed the condition of 194 pavement sections that includes dense graded asphalt mixture (DGAC) (now known as HMA), and gap graded rubber modified asphalt concrete (RAC-G) (now known as R-HMA) located in California. About 10 percent of the pavement sections showed moderate to severe moisture damage, which recommended that the evaluation of moisture damage must be considered in assessing the performance of asphalt pavements in California. Also, the effect of variables (such as air void and asphalt cement content) on moisture damage was determined by the laboratory testing, and dynamic loading test procedures were also developed for evaluating moisture sensitivity. Also, the effectiveness of the HWTD and the long-term active effectiveness of hydrated lime and liquid anti-strip additives were evaluated. The results of the laboratory tests are: i) if void contents  $\leq 7.0$  percent, dense-graded HMA sections showed little or no moisture damage, but medium or severe moisture damage was observed for void content higher than 7.0 percent, ii) a few R-HMA sections with high air void contents ( $>7\%$ ) showed severe stripping, iii) RHMA sections did not show an advantage in resisting moisture damage over dense-graded HMA, iv) well designed and maintained adequate pavement drainage systems may reduce the moisture damage, and v) HWTD was found to be an effective predictor with a reasonable correlation with field performance. Based on laboratory and field data, hydrated lime and liquid anti-strip agents increased the stripping resistance of asphalt mixtures [20].

The purpose of this research is to investigate the stripping problem, using Modified Lottman tests for different anti-stripping additives (at different rates for fatty acid type and hydrated lime), under different water damage cycling levels, and the effect of their ratios. The problem is questioned under the influence of these parameters.

## **2. MATERIALS AND METHOD**

### **2.1. Materials**

50/70 penetration grade asphalt cement and basalt rock aggregates were used. Specific properties of bituminous binder and general physical properties of used basalt aggregates were given in Table 1 and Table 2 respectively.

Dense graded aggregate combination (Type-1) was used in accordance with the Turkish Highways Technical Specification [21]. Maximum aggregate size was selected as 19 mm. The aggregate gradation and specification limits were given in Table 3.

*Table 1 - Values of used asphalt cement binder*

| Test                       | Method         | Value |
|----------------------------|----------------|-------|
| Specific gravity (25°C)    | ASTM D-70      | 1.014 |
| Softening point (°C)       | TS EN 1427     | 48.4  |
| Cleveland flash point (°C) | TS EN ISO 2592 | 324   |
| Penetration (25°C)         | TS EN 1426     | 53    |
| Retaining penetration (%)  | TS EN 12607-1  | 72    |
| Ductility (25°C)           | ASTM D-113     | 100+  |

*Table 2 - Values of basalt rock aggregates*

| Properties                             | Test Method       | Value |
|--|-------------------|-------|
| Specific gravity (coarse agg.)         | TS EN 1097-6      | 2.696 |
| Specific gravity (fine agg.)           | TS EN 1097-6      | 2.676 |
| Specific gravity (filler)              | TS EN 1097-7      | 2.628 |
| Los Angeles abrasion (%)               | ASTM C-131        | 22    |
| Flakiness (%)                          | BS 812 (Part 105) | 12.3  |
| Stripping resistance (no additive) (%) | ASTM D-1664       | 65-70 |
| Water absorption (%)                   | ASTM C-127        | 0.40  |
| Soundness in MgSO <sub>4</sub> (%)     | ASTM C-88         | 2.0   |

*Table 3 - Grain size distribution and specification limits*

| Sieve size |       | Specification limits |             | Aggregate gradation<br>(% passing) | Aggregate fractions   |
|------------|-------|----------------------|-------------|------------------------------------|-----------------------|
| Inch       | mm    | Lower limit          | Upper limit |                                    |                       |
| 3/4        | 19.0  | 100                  | 100         | 100.0                              |                       |
| 1/2        | 12.5  | 88                   | 100         | 90.7                               | Coarse aggregate, 52% |
| 3/8        | 9.5   | 72                   | 90          | 80.0                               |                       |
| No. 4      | 4.75  | 42                   | 52          | 48.0                               |                       |
| No. 10     | 2.00  | 25                   | 35          | 30.5                               | Fine aggregate, 42.5% |
| No. 40     | 0.425 | 10                   | 20          | 14.9                               |                       |
| No. 80     | 0.18  | 7                    | 14          | 9.3                                |                       |
| No. 200    | 0.075 | 3                    | 8           | 5.5                                | Filler, 5.5%          |

Four different additives were used in the study: hydrated lime, TeraGrip AN (liquid), TeraGrip ANG (solid) and ENEM AP 245 (liquid). TeraGrip AN and TeraGrip ANG are basic form and contain alkylamidopolyamine. Hydrated lime additive contains 84.66% CaO. All additives were used in three addition ratios. Hydrated lime was substituted for filler in 0.5%, 1.0% and 1.5% ratios by weight of total dry aggregate, while other additives were incorporated to the bitumen binder in 0.2%, 0.4% and 0.6% ratios by weight of asphalt cement.

## 2.2. Mixture design

Dense graded asphalt concrete design was done according to the Marshall Design method (ASTM D 1559). Optimum bitumen content was determined using pure bitumen. The optimal asphalt cement content was taken as the percentage of bitumen corresponding to 4% air voids and determined as 4.75%. The mixture properties obtained from the design results and specification limits were presented in Table 4. Optimum bitumen content determined by pure bitumen was used for modified bitumen options.

Table 4 - Asphalt concrete design results

| Design parameters             | Specification limits | Design results |
|-------------------------------|----------------------|----------------|
| Density, gr/cm <sup>3</sup>   |                      | 2.410          |
| Marshall stability, kg        | Min. 900             | 1570           |
| Air voids, %                  | 3-5                  | 4.0            |
| Voids filled with asphalt, %  | 65-75                | 71.0           |
| Flow, mm                      | 2-4                  | 3.65           |
| Bitumen content, %            | 4-7                  | 4.75           |
| Voids in mineral aggregate, % | 14-16                | 14.20          |
| Filler/Bitumen ratio          | Max. 1.5             | 1.2            |

## 2.3. Test methods

In addition to the control mixes, mixtures modified with TeraGrip AN-TeraGrip ANG-ENEM AP 245 fatty acid derived anti-stripping additives and hydrated lime modified mixtures were produced. A large number of standard Marshall briquettes with a diameter of 101.6mm were produced with these control and modified mixtures. The additives were used in three ratios. Asphalt mixtures were evaluated with modified Lottman method for moisture damage resistance. The flow diagram of the study was shown in Figure 1.

Stripping problem or moisture sensitivity is one of the foremost important distress mechanisms in asphalt mixtures. Several tests have been used in the literature to evaluate the stripping problem, but one of the most widely accepted experiments is the Modified Lottman (AASHTO T283) method [22]. In this study Modified Lottman procedure was used for reviewing water sensitivity of the produced asphalt mixture compacted samples.

Samples used for the Modified Lottman tests were separated in two parts, unconditioned and conditioned samples. The compacted samples in conditioned group were saturated with water between 70% and 80% with a vacuum pycnometer. The samples were then covered with a plastic film material and located in a plastic bag containing 10 ml of water. Samples in plastic were kept frozen at -18°C for 20 hours. The samples, which completed the freezing process, were placed in a water bath at 60°C for 24 hours without waiting. After water bath, plastic bag and film were removed and conditioning process completed. After samples in conditioned and unconditioned groups were placed in a water bath at 25°C for 2h, indirect tensile strength (ITS) test was made. Using the peak load recorded by test machine and sample sizes, the tensile strengths are calculated by the Equation 1.

$$S_t = \frac{2000 \cdot P}{\pi \cdot t \cdot D} \tag{1}$$

In equation 1:  $S_t$ : indirect tensile strength, kPa;  $P$ : maximum load recorded by test machine, N;  $t$ : asphalt briquette thickness, mm;  $D$ : asphalt sample diameter, mm.

Moisture susceptibility can be evaluated with tensile strength ratio (TSR). TSR is calculated by dividing the average tensile strength of the samples in the conditioned group by the average tensile strength of the samples in the unconditioned group. Higher TSR means higher resistance to moisture sensitivity. A value of 0.80 can be used as a criterion in the assessment of moisture sensitivity [23].

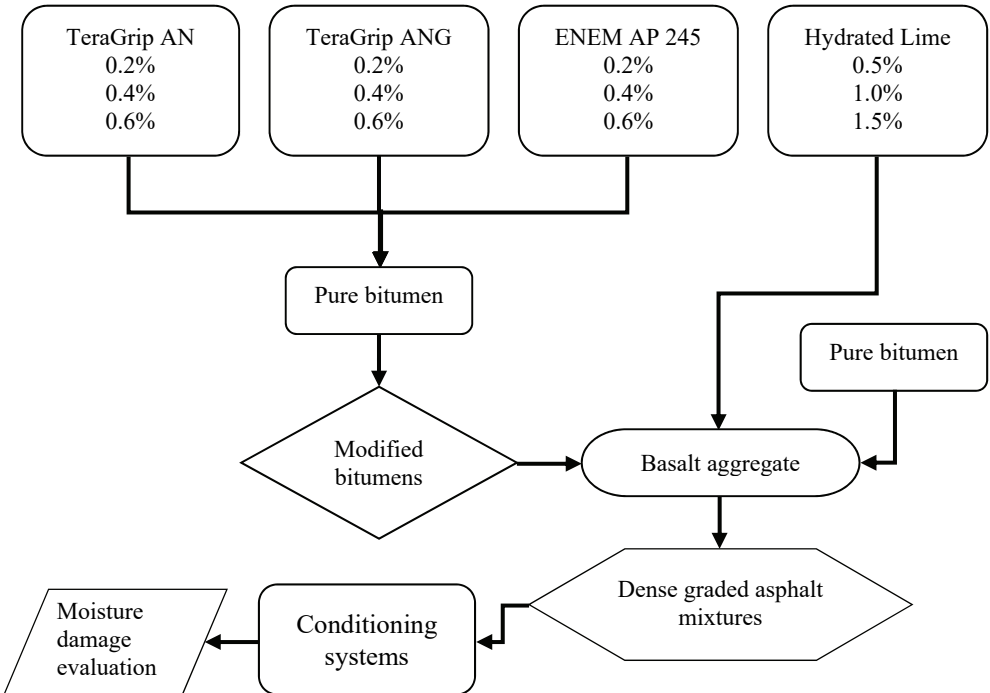


Figure 1 - Flow diagram of the experimental program

### 3. TEST RESULTS AND DISCUSSIONS

In the study, besides control mixture, four different additives namely TeraGrip AN, TeraGrip ANG, ENEM AP 245, and hydrated lime were examined at three rates. Hydrated lime was used at 0.5%, 1% and 1.5%, while the other additives were added to the bitumen in 0.2%, 0.4% and 0.6% ratios. Nine identical samples were produced for each mixture alternative and divided into three groups. The first group was not conditioned; the second group was conditioned with one cycle of modified Lottman procedure and the third group with three cycles of modified Lottman conditioning. The indirect tensile strength test was performed at 25°C and tensile strength of mixtures was determined through three tests. Test results were shown in Figures 2-4.

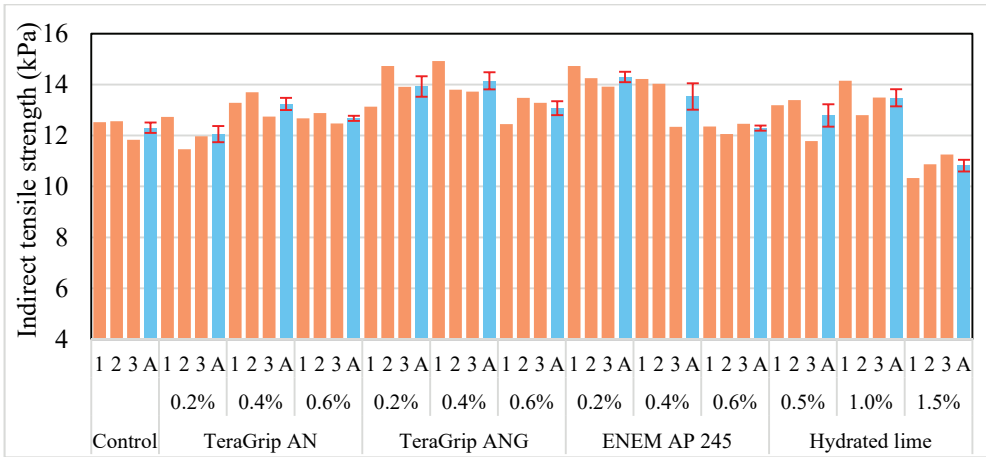


Figure 2 - Tensile strengths of unconditioned mixtures

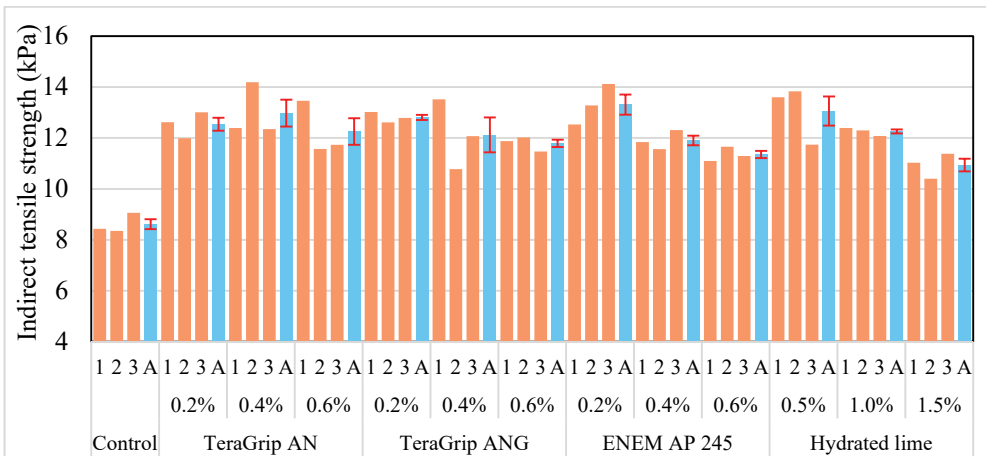


Figure 3 - Tensile strengths of conditioned (1 cycle) mixtures

The following evaluations may be made for unconditioned mixtures. Indirect tensile strength values of 0.2-0.4-0.5% selected for fatty amine acid derived anti-stripping additives are obtained higher than the indirect tensile strength of control mixtures (9 of 10 mixtures). The liquid additive of 0.2% TeraGrip gives almost the same value. Hydrated lime additive provides a higher indirect tensile strength for unconditionally 0.5% and 1% additives. Indirect tensile strength value decreases at 1.5% hydrated lime additive ratio. For normal use rates for fatty acid derived anti-stripping additives, the unconditional case has a substantially higher indirect tensile strength value, while the tendency for 0.5% and 1% for hydrated lime is the same. In service conditions, it is essential to make these comments under conditional modeling for water damage due to the pavement being exposed to water damage under climatic and traffic impacts.

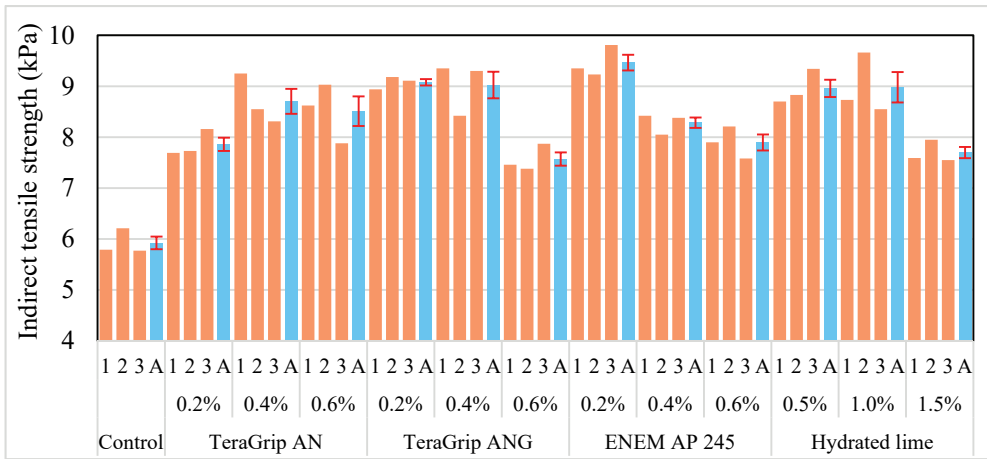


Figure 4 - Tensile strengths of conditioned (3 cycles) mixtures

For single-cycle water damage conditionally, for mixtures; indirect tensile strength values of the control mixture are significantly decreased. This result indicates that there is a significant reduction in the indirect tensile strength of the control mixtures under the single cycle Lottman condition, and that the load spreading capacity of the mixtures is significantly reduced. However, under these single cycle conditions all mixtures with anti-stripping additives (fatty acid amine derived and hydrated lime) exhibit significantly higher strength. Under the water damage model, damaged mixtures with anti-stripping additive clearly indicate their effectiveness, even with unconditional control mixtures, giving high strength values.

Under the three-cycle heavy damage model, strength values continue to decrease. In all cases, however, all anti-stripping additives (modified fatty acid derived and modified lime) produce higher performance improvements. Particularly under active adhesion conditions it is understood that the additives have an important function.

The TSR test has achieved standardization, functioning as a sort of reference and control in a wide variety of countries. This test measures the effect of water on asphalt mixtures by looking at indirect traction; it is suited for dense mixtures made with or without an adhesive

additive, which come in the form of liquids and powdered solids [24]. The TSR results of the mixtures with one and three cycle conditioning were calculated and presented in Figures 5-7.

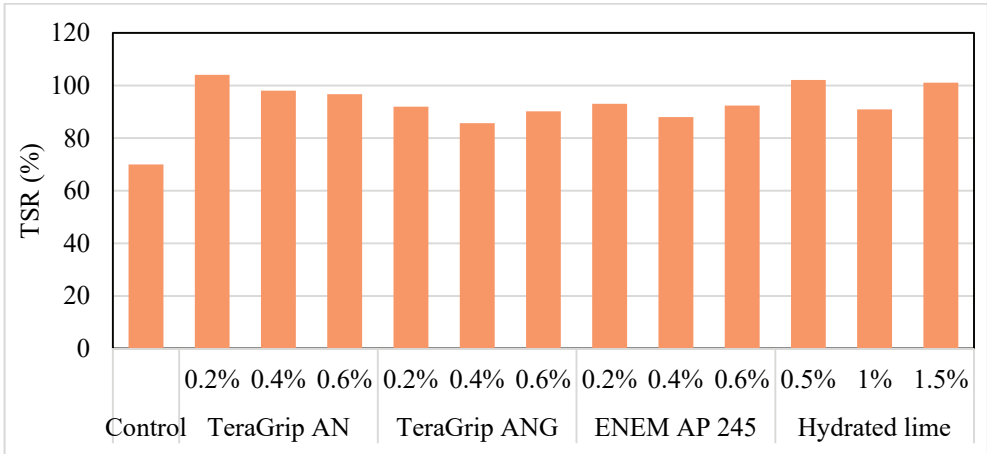


Figure 5 - TSRs (one cycle-conditioned/uncond.) of modified and unmodified mixtures

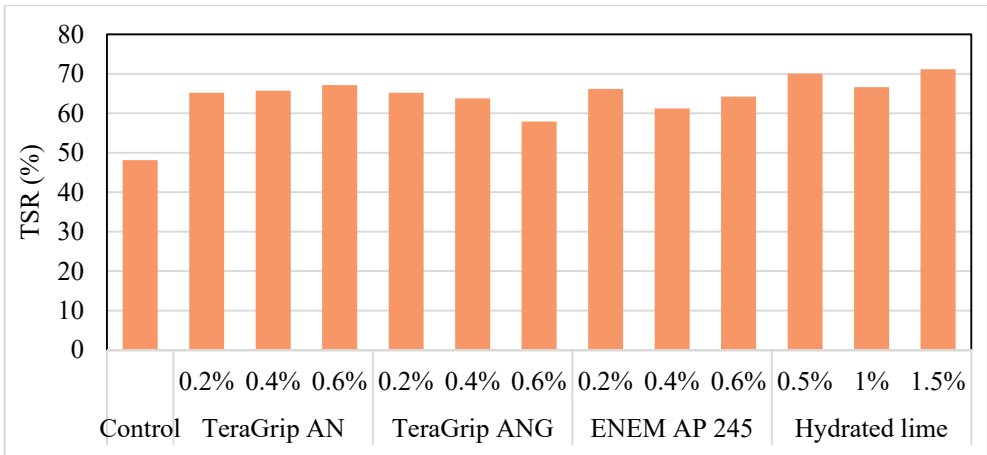


Figure 6 - TSRs (three cycles-conditioned/uncond.) of modified and unmodified mixtures

The proportional changes in tensile strength and TSR values were shown in Table 5 and Table 6 depending on the conditioning systems. Indirect tensile strength values are increased between 30% and 59.9% in three different ratios using both fatty acid derived anti-stripping additives and hydrated lime anti-stripping additives. The fact that the samples give higher indirect tensile strength values under the condition of Lottman water damage is interpreted as meaning that the load spreading capacity of the mixtures increases significantly in the

damaged state. Similarly, the Lottman damage cycle modeling is extended from one cycle to three cycles, resulting in an indirect tensile strength reduction of 1.2% to 12.1%. This issue; it is understood that the integrity of the mixtures is maintained even if the degree of damage increases considerably.

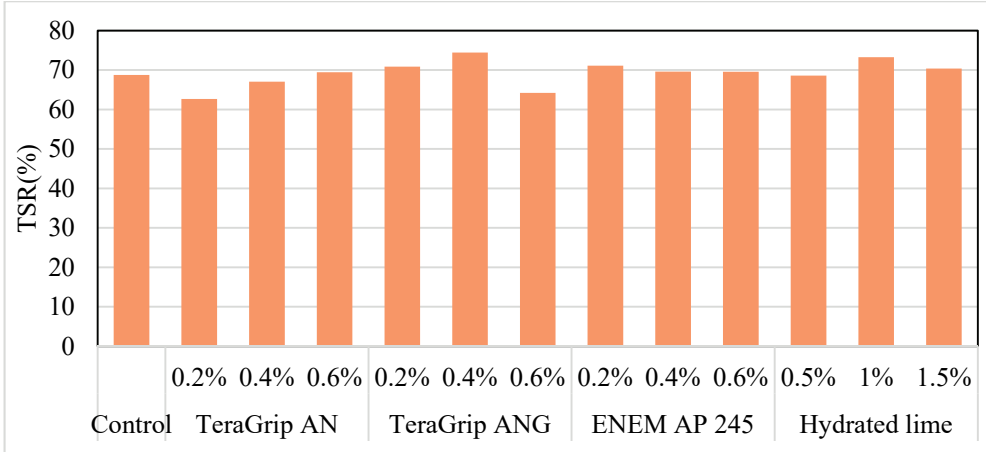


Figure 7 - TSRs (three cycles-conditioned/one cycle-conditioned) of modified and unmodified mixtures

The proportional changes in tensile strength and TSR values were shown in Tables 5 and 6 depending on the conditioning systems. Ratios of tensile strength of modified mixtures due to one cycle damaged modified mixtures to indirect tensile strength of control mixtures can be found greater than 100%, as can be seen in Figure 5. Experiments are carried out on three identical samples. Briquettes are prepared identically with great care. The fact that the indirect tensile strength values given by the additives at certain usage ratios (appropriate usage ratio) can exceed the values of the control mixtures in damaged cases, means that the additives show their function. With the increase in the number of damage cycles, the values decrease below 100%. Another reason for obtaining values higher than 100% in case of a cycle damage is that the experiments are performed on different identical briquettes. Although identical briquettes are prepared under the same conditions (in terms of mixing parameters), depending on the aggregate angularity values, different values can be obtained depending on the aggregate orientation in the mortar.

Indirect tensile strength values are increased between 30% and 59.9% in three different ratios using both fatty acid derived anti-stripping additives and hydrated lime anti-stripping additives. The fact that the samples give higher indirect tensile strength values under the condition of Lottman water damage is interpreted as meaning that the load carrying capacity of the mixtures increases significantly in the damaged state. The indirect tensile strength test is a measure of tensile strength and a good indicator of mixture cohesion. Indirect tensile strength test would provide information on cohesion, specifically asphalt binder stiffness, but not angle of internal friction provided by the aggregates [25].

Similarly, the Lottman damage cycle modeling is extended from one cycle to three cycles, resulting in an indirect tensile strength reduction of 1.2% to 12.1%. This issue; it is understood that the integrity of the mixtures is maintained even if the degree of damage increases considerably.

Table 5 - Variation of tensile strengths depending on the degree of conditioning

|               |      | Uncond. mixtures   | One cycle conditioning |                    | Three cycle conditioning |                    |                     |
|---------------|------|--------------------|------------------------|--------------------|--------------------------|--------------------|---------------------|
|               |      | I% C <sub>um</sub> | I% C <sub>cm1</sub>    | I% C <sub>um</sub> | I% C <sub>cm3</sub>      | I% C <sub>um</sub> | I% C <sub>cm1</sub> |
| Control       |      |                    |                        | -30                |                          | -51.9              | -31.2               |
| TeraGrip AN   | 0.2% | -2.0               | 45.6                   | -96.2              | 32.8                     | -36.1              | -8.8                |
|               | 0.4% | 7.6                | 50.6                   | -95.8              | 47.1                     | -29.3              | 1.0                 |
|               | 0.6% | 3.0                | 42.2                   | -96.5              | 43.8                     | -30.8              | -1.2                |
| TeraGrip ANG  | 0.2% | 13.2               | 48.7                   | -96.0              | 53.4                     | -26.2              | 5.4                 |
|               | 0.4% | 15.0               | 40.7                   | -96.6              | 52.5                     | -26.7              | 4.8                 |
|               | 0.6% | 6.2                | 36.9                   | -97.0              | 27.9                     | -38.5              | -12.1               |
| ENEM AP 245   | 0.2% | 16.2               | 54.5                   | -95.5              | 59.9                     | -23.1              | 9.9                 |
|               | 0.4% | 10.0               | 38.2                   | -96.9              | 40.0                     | -32.7              | -3.8                |
|               | 0.6% | -0.1               | 31.8                   | -97.4              | 33.4                     | -35.8              | -8.3                |
| Hydrated lime | 0.5% | 3.9                | 51.6                   | -95.8              | 51.3                     | -27.2              | 4.0                 |
|               | 1%   | 9.6                | 42.3                   | -96.5              | 51.7                     | -27.0              | 4.2                 |
|               | 1.5% | -12.1              | 27.0                   | -97.8              | 30.0                     | -37.4              | -10.6               |

\*Increase compared to Control Unconditioned Mixture (I% C<sub>um</sub>) \*Increase compared to Control-one cycle conditioned mixture (I% C<sub>cm1</sub>) \*Increase compared to Control-three cycle conditioned mixture (I% C<sub>cm3</sub>)

According to the Lottman damage modeling, fatty acid amine-derived additives significantly increase water damage resistance in the selected combination. However, it is seen from Table 6 that the hydrated lime anti-stripping additive used for three different ratios creates a water damage resistance increase between 29.9% and 45.9% under Lottman damage modeling. As a result, it is seen that both fatty acid amine anti-stripping additives and hydrated lime significantly increase water damage stripping resistance. Lottman conditioning has an observable level of damage, however, the values of the same fit and development are obtained with the approach of indirect tensile strength ratios.

Water damage level has been increased so as to maintain integrity of the anti-stripping surfactant additive materials in the mixture, to maintain their effectiveness and to see the benefit mechanisms. Lottman water damage conditioning was extended from one cycle to three cycles and reapplied on identical samples. Indirect tensile strength tests were performed

to found water damage rates after three damage cycles. After three damage cycles, the doped anti-stripping agents mixtures give a higher water damage resistance value for the selected additive ratios, still higher ratios between 20.3% and 47.8%. This means that the additives remain functional and maintain their mechanisms of benefit, especially in the event of a high degree of damage. While the ratio values of the three damage cycle doped mixtures give a strength reduction of 4.1% to 17.3% compared to the ratio values of one damaged modified mixtures, the ratio values are much higher than the conditioned samples. It is seen that the water damage resistance of the mixtures is maintained and increased as the damage level of the additives increases.

Table 6 - Variation of tensile strength ratios according to degree of conditioning degree

|               | One cycle conditioning |                     | Three cycle conditioning |                     |
|---------------|------------------------|---------------------|--------------------------|---------------------|
|               |                        | I% C <sub>cm1</sub> | I% C <sub>cm3</sub>      | I% C <sub>cm1</sub> |
| Control       |                        |                     |                          | -31.2               |
| TeraGrip AN   | 0.2%                   | 48.6                | 35.4                     | -6.9                |
|               | 0.4%                   | 40.0                | 36.5                     | -6.1                |
|               | 0.6%                   | 38.1                | 39.5                     | -4.1                |
| TeraGrip ANG  | 0.2%                   | 31.4                | 35.4                     | -6.9                |
|               | 0.4%                   | 22.4                | 32.5                     | -8.9                |
|               | 0.6%                   | 28.9                | 20.3                     | -17.3               |
| ENEM AP 245   | 0.2%                   | 33.0                | 37.5                     | -5.5                |
|               | 0.4%                   | 25.7                | 27.2                     | -12.6               |
|               | 0.6%                   | 31.9                | 33.5                     | -8.2                |
| Hydrated lime | 0.5%                   | 45.9                | 45.5                     | 0.1                 |
|               | 1%                     | 29.9                | 38.4                     | -4.8                |
|               | 1.5%                   | 44.4                | 47.8                     | 1.6                 |

\*Increase compared to Control Unconditioned Mixture (I% C<sub>um</sub>) \*Increase compared to Control-one cycle conditioned mixture (I% C<sub>cm1</sub>) \*Increase compared to Control-three cycle conditioned mixture (I% C<sub>cm3</sub>)

For Lottman water damage ratios, it can be said that the Lottman test clearly demonstrates its superiority in this sense, as it can be distinctive in terms of comparing the mixing performances even if the number of damage cycles is increased from one to three.

Also, the addition of an anti-stripping additive will increase the resistance of the asphalt mixture against moisture damage. It can be seen that the TSR value recorded in asphalt mixes created by adding anti-stripping additives such as limestone powder is very high compared to the asphalt mix without anti-stripping additives. With base type bitumen and aggregate,

values are 48% and 60% [26]. This can also be seen in studies showing a high TSR rate of 72 to 95.2% in asphalt mixes, compared to the addition of anti-stripping additives [17], without any additives in the range of 48% to 61.7%.

For asphalt mixtures, when it is formed by adding limestone aggregate, modified bitumen and anti-stripping additives, it is seen that it will be more resistant to moisture damage. This result is similar in other researches [27-29]. Hydrated lime tends to be the most popular among anti-strip additives because it has been shown to be effective in increasing the moisture resistance of the asphalt mixture. While polymer modified bitumen is the most popular in asphalt mix design, it shows more moisture damage resistance than the commonly used asphalt binder. In general, it is emphasized that the Modified Lottman test, Immersion Compression test and Boiling Water test are reliable tests in evaluating the moisture sensitivity of the asphalt mixture [30].

Hydrated lime-doped mixtures were also noteworthy. In particular, when the Lottman damage cycle number is applied in three cycles, when the indirect tensile strength ratios are evaluated, the hydrated lime modified mixtures generally show higher ratio increases, often compared to other admixture and fatty acid amine anti-stripping additives. As a descriptor of water damage and a performance indicator, it has been wondered how the indirect tensile strength values will change with respect to hydrated lime modified mixtures if the damage level increases further. Further research will focus on the topic.

A second common preservative additive is hydrated lime. Hydrated lime works similar to amine-based anti-peel additives, because its primary purpose is to modify the electrical charge of the constituent materials. The difference is that hydrated lime allows to change the surface charge of aggregates from negative to positive and to produce better adhesion with asphalt binders (tendency to be negative). Lime is often mixed in slurry form or directly into moist aggregates, as it needs moisture to activate it. The use of lime has been approved by many organizations and is included as part of the specifications. The added benefit of slaked lime is that it acts as an "active" filler that hardens the bituminous binder and helps to increase friction resistance, especially in hot and wet conditions [31].

The use of solid and liquid anti-stripping additives is one of the effective solutions for strengthening the adhesion between aggregates and asphalt cement and for the wettability of the aggregate. The use of liquid anti-strips dates back to the 1930s, and such materials are not sufficiently sustainable at high temperature exposure [32].

Adding certain anti-stripping surfactants from Evonik and Zycotherm to the mixes creates a stronger adhesion between asphalt cement and aggregates. Dynamic behavior response of modified bituminous mixtures is increased. These nanomaterials form a covalent bond between the bituminous binder and the aggregate and prevent the penetration of moisture at the bitumen aggregate interface through a hydrophobic layer. The resistance of bituminous mixtures to water damage can be increased by using anti-stripping agents. Evonik as a newly introduced additive, Zycotherm as a common nanomaterial and hydrated lime; to evaluate and compare the effects of asphalt mixes on moisture damage and other performance properties. Moisture sensitivity was evaluated using indirect tensile strength (modified Lottman) and Texas Boiling tests. In other respects; Marshall, Resilient Modulus and Dynamic Creep tests were also applied. All three additives increase the moisture resistance of asphalt mixes, and the mixture containing 0.1 percent Zycotherm has the best performance.

Hydrated lime has the best effect to increase the rutting resistance of asphalt mixes due to the hardening effect on the mixtures. Among the considered dosages of nanomaterials, the optimum amounts of Zycotherm and Evonik are 0.1% and 0.3%, respectively, based on the weight of the bitumen binder. The first contributes to a 15% increase in ITS, and the second increases ITS values by 9% [23].

The moisture susceptibility of asphalt mixtures modified with Zycosoil as a nano-organosilane antistripping agent and the hydrated lime in the form of slurry was evaluated. Because the siliceous aggregates are more moisture susceptible than the limestone aggregates, two asphalt mixtures made from these aggregates were sampled to capture the effects of Zycosoil on stripping damage. Siliceous aggregate based asphalt mixtures, the Zycosoil had better performance in enhancing the resistance of the mixture against water damage. Also, in mixtures with limestone aggregates, the limestone filler material had slightly better performance than the Zycosoil [33].

The effects of Zycosoil in moisture susceptibility of glassphalt mixtures were interrogated. It was obtained that mixtures containing 4.5% zycosoil by the weight of the bitumen binder had best performance in mechanical and anti-stripping properties [34].

The moisture susceptibility of asphalt mixtures modified with Wetfix and Tackamin-200 was studied. These additives at 0.0, 0.4, 0.5 and 0.6 percent by the weight of bitumen were added to mixtures. The mixture containing 0.5% of nanoclay had highest resistance against water induced damage [35].

The effects of liquid anti-strip, hydrated lime, SBS, and PPA on HMA stripping susceptibility were evaluated through selected laboratory tests, covering the modified Lottman AASHTO T283-02 test with five FT cycles, wheel track test, and a fracture test using SCB specimens. It was concluded anti-strip additive and hydrated lime are effective in reducing water damage potential [5].

The effect of aggregate gradation, hydrated lime, and Sasobit additive on moisture damage using indirect tensile tests and response surface method was researched. Dry samples had better mixing behavior with bituminous binder than wetted samples. The TSR value of mixture samples with hydrated lime content ranging from 1.1% to 2.5%, Sasobit content from 0.5% to 2.5%, and fine aggregates from 66% to 74% was greater than 80% [36].

Anti-stripping agents of hydrated lime and Zycosoil modified mixtures had nearly similar dry tensile strength but the saturated ITS values were better than control mixtures. The effect of lime and Zycosoil on tensile strength of samples in wet condition was same. adding anti-stripping agents, TSR values for all the mixtures satisfied the standard requirement and the specimens showed favorable behavior against moisture. Zycosoil with concentrations about 5% of hydrated lime had good performance in cutting into the stripping damage of warm mix asphalt (WMA) mixtures [37].

The values of indirect tensile strength test may be used to evaluate the relative quality of bituminous mixtures in conjunction with laboratory mix design testing and for estimating the potential for rutting or cracking. The results can also be used to determine the potential for field pavement moisture damage when results are obtained on both moisture-conditioned and unconditioned specimens [38]. For additive alternatives; indirect tensile strength values

increase between 30 and 59.9%. Therefore, it is understood that the load-spreading capacity of the mixtures in the damaged state increases significantly.

By increasing the damage level to three cycles, indirect tensile strength decreases between 1.2% and 12.1%. This issue; even if the degree of damage is considerably increased, the integrity of the mixtures is maintained.

Indirect tensile strength ratios increase from 20% to 48%. Among the anti-stripping additives of the fatty acid type, the teraGrip AN additive offers higher rates in all three ratio options. Increasing rates means increased resistance to water damage. According to the Lottman damage modeling, fatty acid amine-derived additives significantly increase water damage resistance in the selected combination.

Modified Lottman water damage test with indirect tensile test; if the number of water damage cycle modeling applied is increased from one cycle to three cycles, the ratios of water damage appear to decrease. This topic shows that the Modified Lottman test will be used successfully to predict long-term field performance. It is not possible to evaluate the ratios obtained at different rate levels of the same additive in a linear manner, although in all cases a higher ratios of water damage is obtained compared to additives. It is considered that it will be more beneficial to use the contributions at a low ratio in the context of the economic principle. However, it is considered an imperative that low ratio addition is included in the evaluation of the relative effectiveness of different additives, especially in the long-term performance mix test tests for quality performance.

#### **4. CONCLUSIONS**

It is possible to draw the following conclusions from the research.

- When the indirect tensile strength test results are interpreted as a sign of mixture cohesion, it is considered that the cohesion of all mixtures with additives increases.
- With the application of three cycles of the Modified Lottman conditioning cycle, the admixtures still retain their structural integrity.
- Both fatty acid amine anti-stripping additives and hydrated lime significantly increase water damage resistance.
- The anti-stripping additives remain effective even when the Modified Lottman water damage conditioning is applied repeatedly as three times.
- Modified Lottman test was found to be highly effective in determining stripping behavior. It was distinguished both at its own damage level and at increased damage levels.
- At the economic approach point, it can be proposed as a control mechanism in which low addition ratios can be selected. As the determination of the relative effectiveness of different additives and price analysis, it is considered an imperative to perform field simulated tests, such as the Hamburg wheel tracking test that may reflect long-term performance, for the process of deciding the ratio of use. The anti-stripping additives should be used at low ratios, but long-term performance needs to be checked by wheel track tests.

## **Symbols**

|             |                                   |
|-------------|-----------------------------------|
| <b>AS</b>   | : Fatty amine acid                |
| <b>HL</b>   | : Hydrated lime                   |
| <b>HMA</b>  | : Dense graded asphalt            |
| <b>ITS</b>  | : Indirect tensile strength       |
| <b>ITSR</b> | : Indirect tensile strength ratio |
| <b>RHMA</b> | : Rubber modified asphalt         |
| <b>WMA</b>  | : Warm mix asphalt                |

## **References**

- [1] Diab, A., You, Z. Development of a realistic conditioning and evaluation system to study moisture damage of asphalt materials. In *Airfield and Highway Pavement 2013: Sustainable and Efficient Pavements*, 1008-1017, 2013.
- [2] Solaimanian, M., Harvey, J., Tahmoressi, M., Tandon, V. Test methods to predict moisture sensitivity of hot-mix asphalt pavements. In *Transportation research board national seminar*. San Diego, California, 77-110, 2003.
- [3] Al-Qadi, I.L., Abuawad, I.M., Dhasmana, H., Coenen, A.R., Trepanier, J.S. *Effects of Various Asphalt Binder Additives/Modifiers on Moisture-Susceptible Asphaltic Mixtures Research Report FHWA-ICT-14-004*, University of Illinois, Urbana, 2014.
- [4] Caro, S., Masad, E., Bhasin, A., Little D.N. Moisture susceptibility of asphalt mixtures, Part 2: Characterization and modeling. *Int J Pavement Eng* 9(2), 99–114, 2008.
- [5] Abuawad, I. M., Al-Qadi, I. L., Trepanier, J. S. Mitigation of moisture damage in asphalt concrete: Testing techniques and additives/modifiers effectiveness. *Construction and Building Materials*, 84, 437-443, 2015.
- [6] Sebaaly, P. E., Hitti, E., Weitzel, D. Effectiveness of lime in hot-mix asphalt pavements. *Transportation Research Record*, 1832(1), 34-41, 2003.
- [7] Wasiuddin, N. M., Fogle, C. M., Zaman, M. M., O'Rear, E. A. Effect of antistrip additives on surface free energy characteristics of asphalt binders for moisture-induced damage potential. *Journal of testing and evaluation*, 35(1), 36-44, 2007.
- [8] Airey, G. D., Collop, A. C., Zoorob, S. E., Elliott, R. C. The influence of aggregate, filler and bitumen on asphalt mixture moisture damage. *Construction and building materials*, 22(9), 2015-2024, 2008.

- [9] Cui, S., Blackman, B. R., Kinloch, A. J., Taylor, A. C. Durability of asphalt mixtures: Effect of aggregate type and adhesion promoters. *International Journal of Adhesion and Adhesives*, 54, 100-111, 2014.
- [10] Epps, J., Berger, E., Anagnos, J. N. Moisture Sensitivity of Asphalt Pavements: Treatments. In *A National Seminar, Transportation Research Board, San Diego, California*, 77-177, 2013.
- [11] Júnior, J. L. L., Babadopulos, L. F., Soares, J. B. Moisture-induced damage resistance, stiffness and fatigue life of asphalt mixtures with different aggregate-binder adhesion properties. *Construction and Building Materials*, 216, 166-175, 2019.
- [12] Solaimanian, M., Bonaquist, R. F., Tandon, V. Improved conditioning and testing procedures for HMA moisture susceptibility (Vol. 589). *Transportation Research Board*, 2007.
- [13] Xiao, F., Amirkhanian, S. N. Effects of liquid antistrip additives on rheology and moisture susceptibility of water bearing warm mixtures. *Construction and Building Materials*, 24(9), 1649-1655, 2010.
- [14] Lottman, R., Johnson, D. L. Pressure-induced stripping in asphaltic concrete. *Highway Research Record*, 340, 13-28, 1970.
- [15] Lottman, R. P. Laboratory test methods for predicting moisture-induced damage to asphalt concrete. *Transportation Research Record*, 843, 1982.
- [16] Hamedi, G. H., Moghadas Nejad, F. Evaluating the effect of mix design and thermodynamic parameters on moisture sensitivity of hot mix asphalt. *Journal of Materials in Civil Engineering*, 29(2), 04016207, 2017.
- [17] Khosla, N., Birdsall, B. G., Kawaguchi, S. Evaluation of moisture susceptibility of asphalt mixtures: conventional and new methods. *Transportation Research Record*, 1728(1), 43-51, 2000.
- [18] Blackman, B. R., Cui, S., Kinloch, A. J., Taylor, A. C. The development of a novel test method to assess the durability of asphalt road-pavement materials. *International Journal of Adhesion and Adhesives*, 42, 1-10, 2013.
- [19] Horgnies, M., Darque-Ceretti, E., Fezai, H., Felder, E. Influence of the interfacial composition on the adhesion between aggregates and bitumen: Investigations by EDX, XPS and peel tests. *International Journal of Adhesion and Adhesives*, 31(4), 238-247, 2011.
- [20] California Department of Transportation, California Test Methods, Materials, Engineering and Testing Services, <http://www.dot.ca.gov/hq/esc/ctms>. (Accessed October 31, 2017).
- [21] General Directorate of Highways of Turkey, Highway Technical Specifications, General Directorate of Highways of Turkey, 2013, Ankara, Turkey.
- [22] Mirhosseini, A. F., Tahami, S. A., Hoff, I., Dessouky, S., Ho, C. H. Performance evaluation of asphalt mixtures containing high-RAP binder content and bio-oil rejuvenator. *Construction and Building Materials*, 227, 116465, 2019.

- [23] Ameri, M., Vamegh, M., Naeni, S. F. C., Molayem, M. Moisture susceptibility evaluation of asphalt mixtures containing Evonik, Zycotherm and hydrated lime. *Construction and Building Materials*, 165, 958-965, 2018.
- [24] Figueroa, A.S. and Reyes, F.A. Moisture damage analysis through the TSR and MIST test using water conditioning asphalt, 6th Eurasphalt & Eurobitume Congress 1-3 June 2016, Prague, Czech Republic.
- [25] Srinivasan, G. Evaluation of indirect tensile strength to identify asphalt concrete rutting potential, Graduate Theses, Dissertations, and Problem Reports, 1465, 2004, West Virginia University.
- [26] Abo-Qudais, S. The effects of damage evaluation techniques on the prediction of environmental damage in asphalt mixtures. *Building and Environment*, 42(1), 288-296, 2007.
- [27] Lavin, P. Comparison of liquid antistripping additives and hydrated lime using AASHTO T-283. *Construction chemicals technical director, ARR-MAZ products*, 1999.
- [28] Uddin, W. Viscoelastic characterization of polymer-modified asphalt binders of pavement applications. *Applied Rheology*, 13(4), 191-199, 2003.
- [29] Aman, M. Y., Shahadan, Z., Noh, M., Zaime, M. A Comparative study of anti-stripping additives in porous asphalt mixtures. *Jurnal Teknologi*, 70(7), 139-145, 2014.
- [30] Taib, A., Jakarni, F. M., Rosli, M. F., Yusoff, N. I. M., Aziz, M. A. Comparative study of moisture damage performance test. In *IOP Conference Series: Materials Science and Engineering*, 512 (1), 012008, 2019.
- [31] Dave, E. V. Moisture Susceptibility Testing for Hot Mix Asphalt Pavements in New England. Prepared for The New England Transportation Consortium, August 2018, NETCR109 Project No. 15-3, University of New Hampshire 105 Main Street Durham, NH, 03824, 2018.
- [32] Ford Jr, M. C., Manke, P. G., O'Bannon, C. E. Quantitative evaluation of stripping by the Surface Reaction Test, No. 517, 1974.
- [33] Ameri, M., Kouchaki, S., Roshani, H. Laboratory evaluation of the effect of nano-organosilane anti-stripping additive on the moisture susceptibility of HMA mixtures under freeze-thaw cycles. *Construction and Building Materials*, 48, 1009-1016, 2013.
- [34] Behbahani, H., Ziari, H., Kamboozia, N., Khaki, A. M., Mirabdolazimi, S. M. Evaluation of performance and moisture sensitivity of glassphalt mixtures modified with nanotechnology zycosoil as an anti-stripping additive. *Construction and Building Materials*, 78, 60-68, 2015.
- [35] Imaninasab, R., Joodaki, S. Performance evaluation of polyamine anti-stripping additives. *Proceedings of the Institution of Civil Engineers-Construction Materials*, 172(3), 155-163, 2019.
- [36] Kavussi, A., Qorbani, M., Khodaii, A., Haghshenas, H. F. Moisture susceptibility of warm mix asphalt: a statistical analysis of the laboratory testing results. *Construction and Building Materials*, 52, 511-517, 2014.

- [37] Omrani, H., Ghanizadeh, A. R., Tanakizadeh, A. Effect of SBS Polymer and Anti-stripping Agents on the Moisture Susceptibility of Hot and Warm Mix Asphalt Mixtures. *Civil Engineering Journal*, 3(10), 987-996, 2017.
- [38] ASTM Designation: D6931 – 12. Standard Test Method for Indirect Tensile (IDT) Strength of Bituminous Mixtures, ASTM International, 100 Barr Harbor Drive, PO Box C700, West Conshohocken, PA 19428-2959. United States.

# **Influence of Gravity Framing on the Collapse Probability of Steel Buildings with Special Moment Frames**

**Adem KARASU<sup>1</sup>**

**Cüneyt VATANSEVER<sup>2</sup>**

## **ABSTRACT**

This paper presents the influence of gravity framing on the collapse risk of steel frame buildings with perimeter special moment frames (SMFs) designed in Turkey. For this, four- and eight-story buildings have been designed considering the related current specifications and codes. Header end-plate connections are used for the beam-to-column joints of the gravity frame system. A nonlinear analytical model that simulates the hysteretic behavior of header end-plate connections is calibrated with past experimental data. Nonlinear static pushover analysis (NSPA) and nonlinear response history analyses (NRHAs) were implemented for both four-story and eight-story SMFs with and without the gravity framing to quantify their collapse performance and monitor the system-level seismic response of the building through collapse. The advantage of presence of the gravity framing is investigated and differences in structural responses between the models are also examined. When the models were excited by different ground motions, median responses of the detailed models showed an increase in lateral force carrying capacity and a decrease in first-story drift demand, compared to the nonlinear static pushover analyses results. Furthermore, the results demonstrate that gravity frames in a structure profoundly decrease the possibility of collapse.

**Keywords:** Steel structures, gravity framing, nonlinear dynamic analysis, collapse probability.

## **1. INTRODUCTION**

Before the Northridge earthquake, welded moment resisting frames had been considered to be the most ideal structural system. Following the Northridge Earthquake many steel moment resisting frames experienced fractures in the beam-to-column joints. The damage observed after the earthquake ranged from minor cracking to completely severed members. However, structural collapse was not observed after the Northridge earthquake. The most likely reason

---

Note:

- This paper has been received on October 12, 2020 and accepted for publication by the Editorial Board on January 18, 2021.
- Discussions on this paper will be accepted by September 30, 2022.

• <https://doi.org/10.18400/tekderg.809233>

1 Istanbul Technical University, Department of Civil Engineering, Istanbul, Turkey - [karasuad@itu.edu.tr](mailto:karasuad@itu.edu.tr) - <https://orcid.org/0000-0002-1063-8484>

2 Istanbul Technical University, Department of Civil Engineering, Istanbul, Turkey - [cuneyt.vatansever@itu.edu.tr](mailto:cuneyt.vatansever@itu.edu.tr) - <https://orcid.org/0000-0002-9954-925X>

that the buildings remained standing is that the gravity framing acted as a “backup system” preventing structural collapse (Leon [1]). The damage observed after the Northridge Earthquake exposed weakness of design procedures and led to the development of performance-based guidelines. Furthermore, performance assessment by nonlinear dynamic analyses is increasingly used for the seismic assessment of buildings.

Over decades, various research projects have focused on predicting seismic collapse capacity of structural systems (Huang and Foutch [2], Lignos and Krawinkler [3]). Gupta and Krawinkler [4] affirmed that the gravity system can significantly increase the post-yield stiffness of the structure which in turn reduces the influence of P-Delta effects under high intensity ground motions. According to their study, the gravity frames could be effective in delaying or preventing dynamic instability if the gravity framing increases the post-yield tangent stiffness. Ramos et al. [5] presented a series of hybrid simulations conducted on a four-story steel moment frame to experimentally assess the seismic performance of a steel building from the onset of damage through collapse. MacRae et al. [6] showed that the continuous gravity column in a structure significantly decrease the possibility of large drift concentrations and prevent soft story mechanism for braced frames. Ji et al. [7] demonstrated that gravity columns can contribute to the mitigation of drift concentration by adding lateral stiffness and strength for multi-story concentrically braced frames. Elkady and Lignos [8] showed that when the contribution of the gravity framing is considered, total base shear strength of steel buildings with steel SMFs is on average 50% larger than bare frame and this was primarily attributed to the gravity framing as well as the composite action provided by the concrete slab. Lee and Foutch [9] evaluated performance of the post-Northridge buildings and showed that they have a high confidence level of satisfying collapse prevention and immediate occupancy performance objectives. Flores et al. [10] investigated the influence of the gravity framing system on the seismic performance of SMFs and concluded that continuous stiffness provided by gravity column with no splices helps the structure deform in the first mode and that is why drift concentrations and soft story mechanisms could be prevented. Foutch and Yun [11] showed that when the gravity framing system is considered as a part of the corresponding analytical model, its lateral stiffness and strength are increased and story drift concentrations along the height of a steel frame building can be mitigated. Astaneh-Asl et al. [12] assessed the seismic performance of moment resisting frames damaged during the Northridge earthquake and concluded that, for buildings subjected to Northridge-Newhall records, the roof drift and base shear of the damaged semi-rigid frame is smaller than the roof drift of the undamaged rigid frame. Sizemore et al. [13] performed nonlinear inelastic analysis as well as nonlinear inelastic incremental dynamic analysis for suite of earthquake ground motions. The results showed that the fixity of the bases in the gravity framing system appears to be very effective at providing reserve strength and stiffness to the system, which helps to prevent collapse for concentrically braced frames.

Secondary systems such as the gravity framing system are typically ignored in seismic performance assessment of structures. The simple connections such as header end-plate connections that may be used in gravity frames are assumed to provide minimal lateral resistance to the structure. However, quasi-static experimental tests show that header end-plate connections have some inherent flexural capacity reaching up to 34% of the plastic flexural capacity  $M_p$ , of the gravity beam with increasing strength and stiffness at large displacements (Karasu and Vatansever [14]).

Limited research has been conducted to assess the effect of the gravity framing system on the seismic response of structures near collapse. Considering the large number of beam-to-column joints which are nominally defined as pinned connections such as header end-plate connections, their contribution to its lateral load resistance may be significantly larger than expected. In addition, the considerable flexural capacity of header end-plate connections in conjunction with the gravity column is assumed to behave as a secondary lateral load resisting system. As a result, it could possibly help to share the story shear force which in turn relieve the existing seismic force resisting frames from excessive story shear.

In most of the studies conducted, beam-to-column connections of the interior gravity frames are typically designed with shear tab connections. The motivation for the study presented here was the lack of studies where the header end-plate beam-to-column connections are used as the connections of gravity frames.

In this paper, two types of buildings with four and eight stories were designed in accordance with the Turkish Seismic Code for Buildings 2018 (TSCB 2018, [15]). The influence of the gravity frames on the seismic response of steel buildings that utilize perimeter special moment frames is traced from the onset of damage through collapse. The effect of the gravity frames on the steel building's over-strength and collapse capacity is investigated. Only side-sway collapse mechanisms are considered in the present study, where dynamic instability results from second-order P-Delta effects accelerated by component deterioration fully overcoming the shear resistance of a structure at large lateral deformations.

## **2. BEAM-TO-COLUMN CONNECTIONS IN GRAVITY FRAMES**

Accurate response predictions of steel buildings subjected to earthquake loading involve the use of models which are able to simulate properly the cyclic behavior of the critical regions such as beam-to-column connections. In this study, calibration conducted to better represent the behavior of the header end-plate beam-to-column connections is based on matching the numerical cyclic model and experimental data retrieved from Karasu and Vatansever [14]. Furthermore, the calibrated models should be able to represent hardening and softening, stiffness and strength degradation properties of the moment-rotation curve of the connection. However, according to the main outcome from the study given (Chisari et al. [16]) is that a calibration based on cyclic response only is not robust, because under different loading conditions, its accuracy may deteriorate. Nevertheless, steel gravity framing connection models are required for detailed structural analysis at the macro level.

This section discusses the approach used to explicitly model the cyclic behavior of bare header end-plate connections as a part of gravity frame. The ductile behavior of header end-plate connections generally governed by the flexural behavior of end-plate and eventually connection failure as a result of end-plate tearing at large rotations. Experimental test results for specimens T4-15 and T5-15 (Karasu and Vatansever [14]) showed that symmetric cyclic behavior was observed in both positive and negative moments. Since composite action between the beam and concrete slab was ignored in the tests, the maximum moment was taken 34% of the plastic flexural capacity  $M_p$ , of the gravity beam at both side of the moment-rotation curve. The 'UniaxialMaterial Hysteretic' material model available in OpenSees [17] was employed to simulate the actual behavior of the beam-to-column connections with header end-plates under cyclic loading. The model simulates moment-rotation curve of a

structural component that exhibits degradation in flexural strength and stiffness under cyclic loading. The cyclic deterioration in unloading stiffness is controlled with beta parameter. The pinching of force and deformation, damage due to ductility and energy are controlled with the parameters of pinchY, pinchX, damage1 and damage2, respectively. Table 1 summarizes the cyclic deterioration parameters for header end-plate connections. Figure 1 shows the calibrated examples of hysteretic material models with experimental data (Karasu and Vatansever [14]). The calibrated hysteretic model shown in Fig. 1 is assumed to be acceptable to represent the behavior of the gravity framing connections. Beyond the maximum rotations given in Figure 1, calibrated hysteretic models do not deteriorate further according to program algorithm. This condition is consistent with the behavior of specimen T4-15 in which larger rotations can be maintained without loss of strength.

*Table 1 – Calibrated cyclic deterioration parameters of the hysteretic material model for the specimens of T4-15 and T5-15*

|       | pinchX | pinchY | damage1 | damage2 | beta |
|-------|--------|--------|---------|---------|------|
| T4-15 | 0.55   | 0.60   | 0       | 0       | 0.4  |
| T5-15 |        |        |         |         |      |

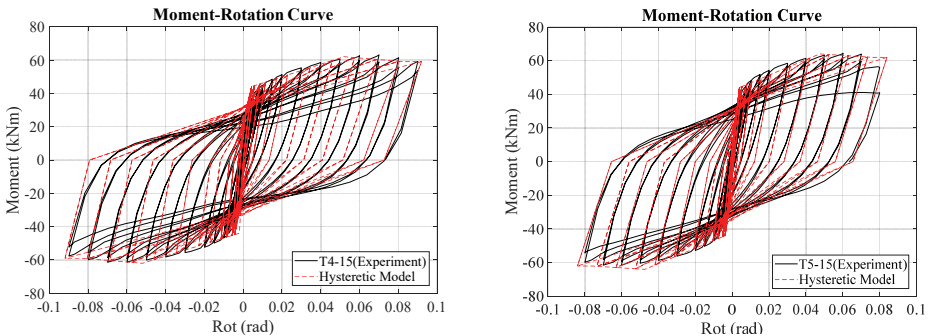


*Figure 1 - Comparison of the hysteretic models and experimental test results*

### **3. BUILDING OVERVIEW**

In this study, to evaluate the effect of the gravity framing on the seismic response of steel buildings with perimeter SMFs, two typical steel buildings with different heights of 4 and 8 stories are designed with current specifications and codes in Turkey such as Turkish Seismic Code for Buildings 2018 (TSCB 2018, [15]) and Turkish Code for Design and Construction of Steel Structures (TCDCSS 2016, [18]). Simple elastic models based on centerline dimensions of beams and columns were used for the design of steel buildings. This method has been found acceptable for design of SMFs (Krawinkler [19]). Direct analysis method was used to obtain the required strengths including second order effects for the structural members. For this, 3D structural model of the buildings has been developed and analyses have been performed by using SAP2000 software [20]. In design, the equivalent lateral force method was employed for the distribution of the seismic base shears on the structural systems. The lateral force resisting system of the buildings consists of special moment frames

with reduced beam section in both principle directions resulting in the response reduction factor of  $R=8$ . Reduced beam section connection model was built by reducing the beam flange area to form plastic hinges away from column face.

Figure 2 and Figure 3 illustrate a typical plan and elevations of the steel buildings including assigned member sections as a result of the analyses, respectively. The plan view of the steel buildings is selected similar to the archetype steel frame buildings described in [8]. This plan view is considered to be feasible in order to better explain and conveniently model the gravity frames. The filled triangle represents moment resisting connections (MC) and hollow circle represents pin connections (PC) for the simple model as shown in Figure 2. The buildings were assumed to locate in Istanbul. Design spectral acceleration at the short period,  $S_{DS}$  and at a period of 1 second  $S_{D1}$  are equal to  $0.873g$  and  $0.451g$  respectively and the soil conditions were assumed to be defined as soil type ZD and this corresponds to seismic design category 1 in Turkish Seismic Code for Buildings 2018 (TSCB 2018, [15]). The buildings have a ground-story height of 4.0 m and a typical story height of 3.0 m. The bay width between columns is 6.0 m. The dead load is  $4.9 \text{ kN/m}^2$  on all floors and  $4.0 \text{ kN/m}^2$  on the roof. The unreduced live load is  $2.0 \text{ kN/m}^2$  uniformly distributed over each floor. Wind load was not considered as a part of the design process. The beams and columns are fabricated from European steel sections with a specified minimum yield stress  $F_y=275 \text{ N/mm}^2$  (S275). The interior gravity framing system of the buildings consists of 16 gravity columns and 40 gravity beams at each floor. The gravity columns are oriented around their strong axis with respect to East-West loading direction and considered as a pin connected at the base. The gravity columns and beams are assigned HE300B and IPE300 sections, respectively. In the gravity frames, the same column section is used to reflect the experimental study [14] through the height of the two buildings. The interior gravity framing connections are designed as header end-plate connections. The column bases were considered as fixed at the base of the SMFs.

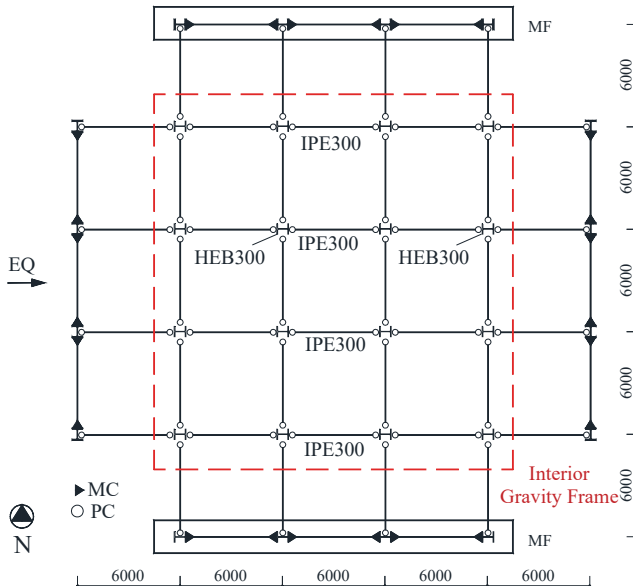


Figure 2 - Plan view of typical steel buildings with SMFs



the inelastic behavior of the plastic hinges located at the reduced beam section and the actual behavior of header end-plate connections for SMFs and equivalent gravity frame, respectively. Column springs represent the potential plastic hinges at the extremes of columns for both SMFs and equivalent gravity frame. These springs are able to capture the cyclic deterioration in flexural strength and stiffness of steel components subjected to cyclic loading. These hysteretic models are called modified Ibarra-Medina-Krawinkler (IMK) deterioration model. The input parameters of the IMK deterioration model can be computed from multivariate regression equations developed by Lignos and Krawinkler [22] and Lignos et al. [23]. The panel zones were explicitly modeled using the parallelogram model (Gupta and Krawinkler [24]). The inelastic behavior of the panel zone is captured with a tri-linear hysteretic model.

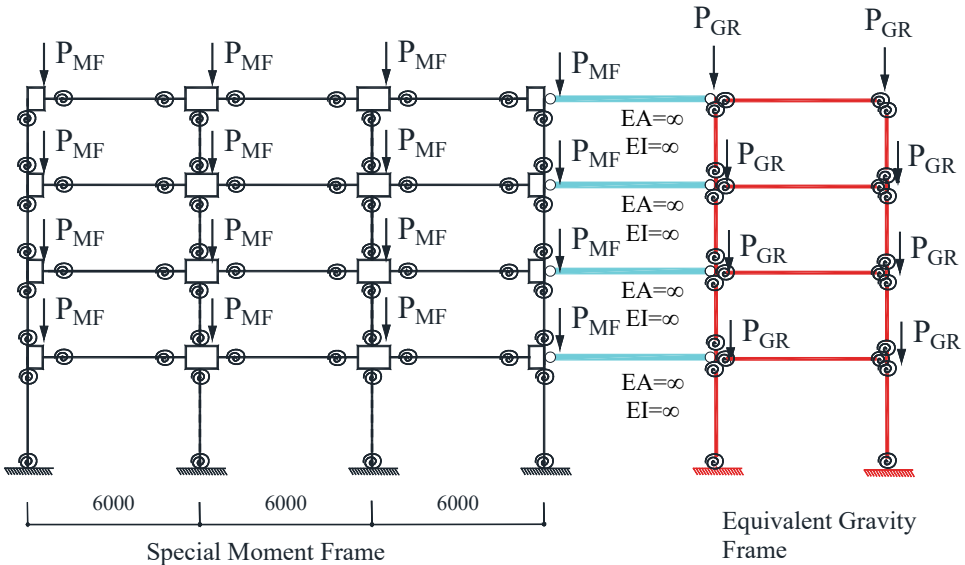


Figure 4 - 2D OpenSees model of the SMFs including equivalent gravity frame

A fictitious single-bay frame is attached to the main SMF using axially rigid trusses, as indicated by Gupta and Krawinkler [24] and Lignos et al. [25] to account for the gravity framing as part of 2D analytical model representations of the same steel building in its East-West loading direction. This frame is called the equivalent gravity frame that may be represented with a single-bay in case of rigid diaphragm assumption. In order to lump together n-bay frames into a single-bay frame with an equivalent beam length  $L_{b,eq}$ , moment of inertia  $I_{b,eq}$ , plastic moment  $M_{p,b,eq}$  and equivalent columns with moment of inertia  $I_{c,eq}$ , and plastic moment  $M_{p,c,eq}$  the following rules apply;

$$\sum_{n=1}^n EI_{b,i} / L_{b,i} = EI_{b,eq} / L_{b,eq}, \quad \sum_{n=1}^n EI_{c,i} = 2EI_{c,eq} \quad (1)$$

$$\sum_{n=1}^n M_{pb,i} = M_{pb,eq}, \quad \sum_{n=1}^n M_{pc,i} = 2M_{pc,eq} \tag{2}$$

In the equations given above, E is the modulus of elasticity of the steel material,  $I_{b,i}$ ,  $L_{b,i}$  and  $M_{pb,i}$  are the moment of inertia, length and plastic moment of i-th beam in a story, respectively,  $I_{c,i}$  and  $M_{pc,i}$  are the moments of inertia and plastic moment of i-th column in a story, respectively. For example, the elastic element of the equivalent gravity frame beam in i-th story is assigned a flexural strength and stiffness equal to half of the sum of those gravity beams (ten gravity beams) in i-th story for the East-West direction.

The P-Delta load equal to half of the gravity load ( $1.05G + 0.25Q$  [26]) of the building minus the tributary load that is assigned to the SMFs columns is divided equally and applied to the columns of the equivalent gravity frame. Geometric nonlinearities are captured using the simplified P-Delta formulation available in OpenSees. Doubler plates were inserted at the panel zones of the interior SMF columns to satisfy the shear requirement. Steel SMFs are designed with strong column/weak beam ratios larger than 1.0. Rayleigh damping is incorporated to in the 2D models. The stiffness-proportional term is assigned to elastic beam and column elements while the mass-proportional term is assigned to all the frame nodes. Two percent Rayleigh damping ratio is assigned at the first and third mode of all buildings according to approach given in the studies ([Zareian and Medina [27] and Chopra [28]). Based on the eigenvalue analysis, the first mode periods of the model BF and Model GF are summarized in Table 2.

*Table 2 - First mode periods of the models*

| T <sub>1</sub> (s)      | 4-Story  |          | 8-Story  |          |
|-------------------------|----------|----------|----------|----------|
|                         | Model BF | Model GF | Model BF | Model GF |
| SAP 2000 3D Model       | 0.92     | -        | 1.50     | -        |
| OpenSees 2D Model       | 0.86     | 0.82     | 1.32     | 1.28     |
| Empirical Equation [15] | 0.767    | 0.767    | 1.25     | 1.25     |

As a result of the eigenvalue analyses, GF Models are stiffer than the bare BF models. This is indicated by the smaller periods of GF models compared to BF models. This difference is attributed to the gravity framing effect. Moreover, while simple 3D models use centerline dimensions and panel zones without doubler plates, 2D models use clear length and stronger panel zone with doubler plates. That leads to differences between the first mode period of the 3D and 2D models. The differences between the first mode period of the 3D and 2D models are minimized when both ignoring the doubler plates inserted at the panel zone of the SMF columns and using centerline dimensions of beams and columns in the 2D models. Therefore, OpenSees models are found to be acceptable to represent the nonlinear behavior of 3D building model in East-West direction.

## 5. NONLINEAR STATIC PUSHOVER ANALYSIS

The nonlinear static pushover analysis (NSPA) has much value in understanding significant characteristics that are not being explored in a nonlinear response history analysis (NRHA). In a pushover analysis, engineers generally focus on the demand/capacity ratio rather than visualization of the building behavior. Therefore, it is proposed to employ a combination of NSPA and NRHAs to understand the seismic performance of steel buildings with SMFs (Lignos et al. [25] and Lignos et al. [29]). In the present study, 2D detailed OpenSees models were adopted to conduct both nonlinear static pushover and nonlinear response history analyses.

The nonlinear static pushover analysis was performed on each building to evaluate gravity framing effect on the static over-strength of the steel buildings. Pushover analysis is conducted using the first-mode lateral load pattern for each steel building in the East-West direction. The force and displacement relationships were plotted in terms of the seismic base shear and roof drift. The roof drift is calculated by dividing the roof displacement by the total height of the building. The over-strength ratio  $D$ , was defined here as the ratio of ultimate strength  $V_{max}$  of the frame to the design strength  $V_{des}$ , given in TSCB 2018, [15]. Table 3 summarizes the over-strength ratio obtained for all of the buildings with steel SMFs. The static over-strength factors ( $D$ ) obtained from analyses are much higher than given in the code ( $D=3$ , Table 4.1) (TSCB 2018, [15]). Because the strict rule on inter-story drift limits based on the equivalent displacement approach makes the structure extremely stiff and that leads to larger member sections. For example, in design, deflection amplifier factor was taken to be equal to  $R/I=8/1=8$  (Response modification factor/Importance factor) according to TSCB 2018 [15], that is larger value comparing to the value of  $C_d/I=5.5/1=5.5$  as specified in ASCE provisions (ASCE/SEI 2017, [30]). In conclusion, drift requirements governed the design for both of the buildings, and demand/capacity ratios in terms of the strength were very low at the end of the analyses.

Table 3 - Over-strength factors ( $D$ ) obtained from NSPA analysis

|                     | 4-Story  |          | 8-Story  |          |
|---------------------|----------|----------|----------|----------|
|                     | Model BF | Model GF | Model BF | Model GF |
| $V_{max}$ (kN)      | 6039.65  | 7158.92  | 8679.40  | 9614.17  |
| $V_{des}$ (kN)      | 1172.45  | 1172.45  | 1466.94  | 1466.94  |
| $D$                 | 5.15     | 6.10     | 5.91     | 6.55     |
| Model GF / Model BF | 1.185    |          | 1.108    |          |

Analysis results, shown in Figure 5, demonstrate the benefits of the interior gravity frames on the secondary stiffness and lateral load carrying capacity. The four-story building experiences more than 18% increase in base shear strength compared with 10.8% for eight-story as a result of the consideration of the gravity framing. The higher effect of P-Delta is noticeable for the eight-story building because pushover curves of the eight story models shows steeper negative tangent slopes at larger drifts due to stiffness and strength deterioration of the structural components.

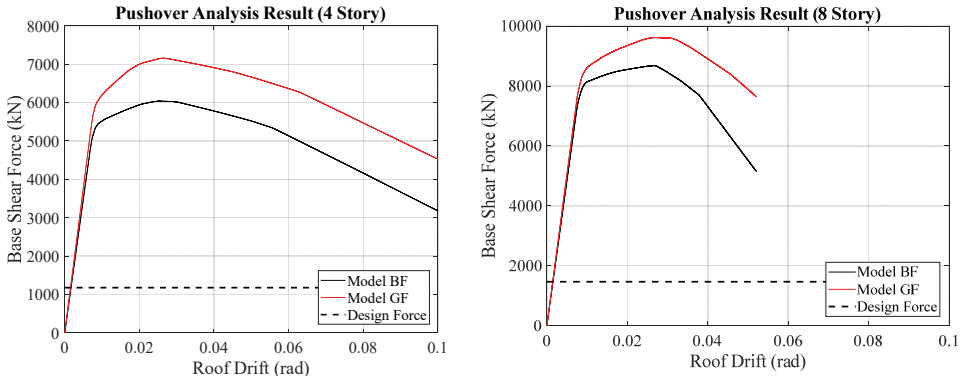


Figure 5 - Pushover curves of steel buildings

Once the global strength deterioration occurs, the period based ductility  $\mu_T$  is indicator of the buildings performance. In FEMA P695 [26], this factor is defined as the ratio of the global roof drift to corresponding to a 20% drop in the maximum base shear to global yield roof drift. As shown in Figure 5, GF models achieve larger  $\mu_T$  values. This is attributed to the smoother post-capping stiffness of the GF models. Because when the gravity framing is considered as a part of the lateral force resisting system of the building; there is less drift concentration in the bottom stories of the steel buildings especially for the eight-story steel building. In general, a four-story collapse mechanism is developed compared to the three-story one of the bare BF model for the eight-story building and more energy is dissipated through the beams of the SMFs that contribute to larger lateral load carrying capability. In Figure 6, red filled circles represent plastic hinge regions.

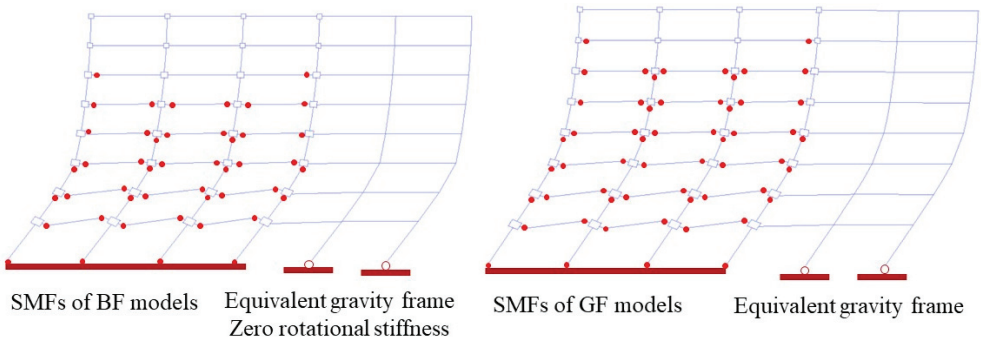


Figure 6 - Collapse mechanisms for the eight story buildings based on different analytical model representations

## 6. NONLINEAR RESPONSE HISTORY ANALYSES AND COLLAPSE RISK

This section quantifies the effect of the gravity framing on the collapse capacity of the steel buildings. The far-field as well as long-distance and strong earthquake ground motion record

sets were selected as defined in FEMA P695 [26] by considering maximum considered earthquake having a 2% probability of being exceeded in 50 years. These sets include 22 component pairs representative of the site and hazard level, for each principal directions (H1, H2) (total of 44 records). Around 2500 nonlinear response history analyses were performed to obtain collapse capacity of the steel buildings through the use of OpenSees software.

The global drift capacity is ultimate building drift capacity against total collapse. Vamvatsikos and Cornell [31] developed incremental dynamic analysis (IDA) procedure to determine global capacity of the building. The ground motions are scaled incrementally based on the IDA. They were also used to capture global trends related to collapse through incremental dynamic analysis.

The procedure that was used to perform IDA is as follows; at first, a linear response history analysis for one of the accelerograms is performed to establish the elastic baseline. The vertical axis of a graph is the 5% damped spectral acceleration at the first mode period of the steel building (calculated in the previous step). Next, a nonlinear response history analysis is performed to obtain maximum inter-story drift value and horizontal axis of the graph is chosen as maximum calculated drift ratio at any story. The slope of the straight line from the origin to this point ( $S_a(T_1, 5\%), \theta_{max}$ ) is referred to elastic slope. Then, the intensity of the ground motion is increased by a scale factor of  $\lambda$  and the analysis is repeated. Note that vertical axis of the IDA curve  $S_a(T_1, 5\%)$  is monotonically increasing with scale factor  $\lambda$ . However, maximum story drift ratio can be deduced from the output of the corresponding detailed non-linear dynamic analysis. The global drift capacity is reached when the building becomes unstable. It occurs when the equivalent stiffness of the building is less than 20% of the slope in the elastic part. This can be thought of as the point at which the inelastic drifts are increasing at 5 times the rate of the elastic drifts. If these conditions do not occur the drift limit of 0.15 is chosen as the global drift capacity. Finally median responses were calculated for the engineering demands calculations. Figure 7 illustrates an example of a single record IDA study of the eight-story steel buildings with SMFs subjected to the North Palm Springs record from the 1992 Landers Earthquake. As seen from the figure, gravity frames could be effective in delaying or preventing dynamic instability.

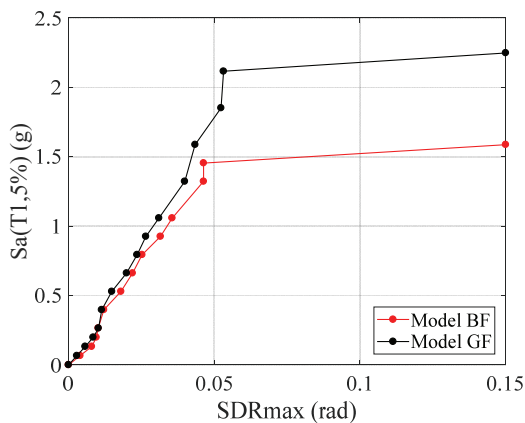
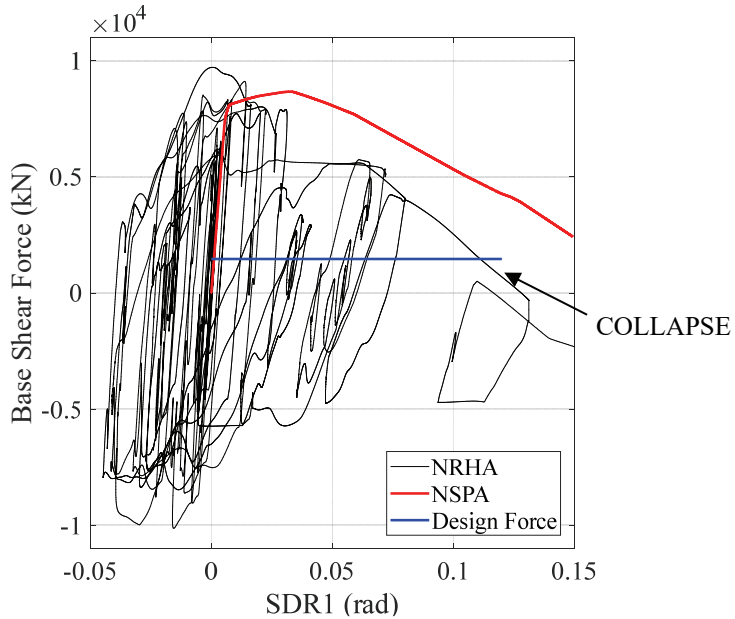


Figure 7 - An example of single record IDA study.

Collapse intensity of the building is defined as the intensity at which a story displaces sufficiently and story shear resistance becomes zero as a result of P-Delta effects accelerated by steel component deterioration in strength and stiffness of the structural components.

Figure 8 illustrates the base shear versus first story drift ratio for the eight story BF model when subjected to the collapse intensity of the North Palm Springs record from the 1992 Landers Earthquake. In the same figure, base shear versus the first story drift ratio from the pushover analysis and base shear design forces have been superimposed. From the figure, it is clear that dynamic over-strength capacity is larger than the static one. This difference is primarily attributed to the dynamic redistribution of story shear forces as a result of higher mode effects. Because NSPA is conducted using the first-mode lateral load pattern only. Therefore, the taller the building, the larger the difference between the static and dynamic base shear. Dynamic over-strength may be noticeable for evaluation of force-sensitive components subjected to earthquake loading.



*Figure 8 - Base shear force versus first story drift ratio curve*

Figure 9 and Figure 10 illustrate the IDA curves including 44 ground motions for the four- and eight-story buildings, respectively in terms of  $S_a(T_1, 5\%)$  versus  $SDR_{max}$ . Each point in the figures corresponds to result of one nonlinear dynamic analysis and each line in the figures connects nonlinear dynamic analysis results from a ground motion record till the collapse of the building.

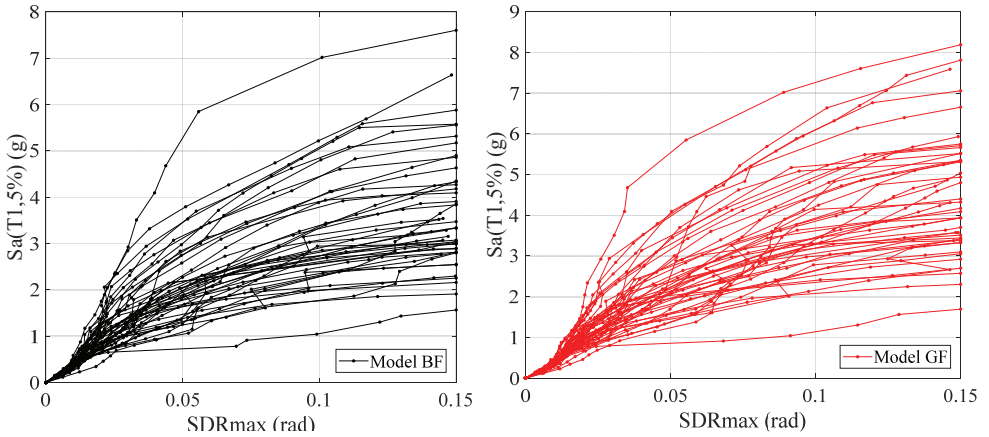


Figure 9 - IDA curves for the four-story buildings

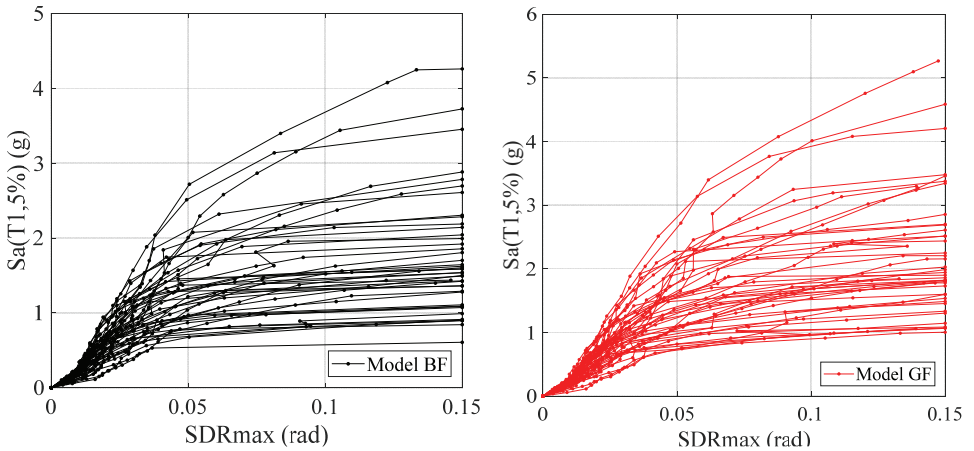


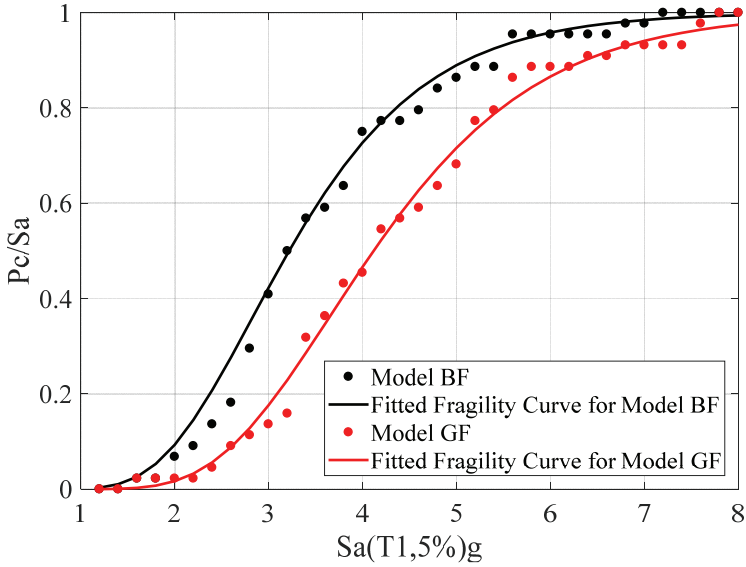
Figure 10 - IDA curves for the eight-story buildings

As seen in these figures, when the gravity framing is considered as a part of the analytical models of the steel buildings, its collapse capacity is larger than the bare BF model. Therefore, collapse probability of the GF model is lower than the bare BF models.

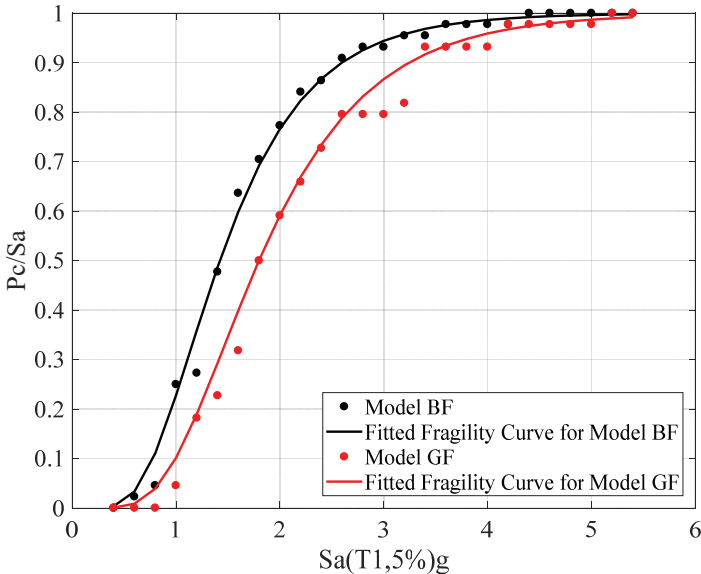
Figure 11 and Figure 12 show the collapse fragility curves for the four-story and eight-story buildings, respectively. The cumulative probabilities of collapse corresponding to 44 collapse intensities obtained from IDAs are calculated and fitted with a lognormal cumulative distribution as shown in the figures.

Table 4 summarizes the median collapse intensity ( $S_{CT}$ ) for the 44 ground motion considered for four-story and eight-story steel buildings. When considering gravity framing, both of the buildings exhibit an average increase about of 27% in the median collapse capacity compared with bare BF models. As a result, according to the FEMA P695 methodology [26], the

collapse margin ratio (CMR), that is the rate of the median collapse intensity of the building to the intensity associated with maximum considered earthquake at the location of the building, is increased.



*Figure 11 - Collapse fragility curves of the four-story steel building*



*Figure 12 - Collapse fragility curves of the eight-story steel building*

Table 4 - Median collapse capacities  $S_{CT}$ , of the four and eight story steel buildings

|                     | $S_{CT}$ (T1, bare 5%) (g) |         | Global drift capacity |         |
|---------------------|----------------------------|---------|-----------------------|---------|
|                     | 4-Story                    | 8-Story | 4-Story               | 8-Story |
| Model BF            | 3.218                      | 1.422   | 0.123                 | 0.083   |
| Model GF            | 4.117                      | 1.799   | 0.129                 | 0.106   |
| Model GF / Model BF | 1.279                      | 1.265   | -                     |         |

Compared to four-story buildings, the global drift capacities of the eight-story buildings were reduced as the P-Delta effects are more severe for the eight-story buildings. In case of considering gravity framing, global drift capacities were increased for both of the steel buildings. Similar to NSPA results, global collapse mechanisms involve more stories compared with BF models.

## 7. CONCLUSIONS

In this study, four-story and eight-story buildings with ductile connections, were designed in accordance with Turkish Seismic Code for Buildings 2018. Beam-to-column connections for the interior gravity framing of the buildings were designed as header end-plate connections. In the analysis of structures and particularly in nonlinear dynamic analysis of semi-rigid steel buildings, the connection models should be modelled as realistically as possible. The study presents calibrated hysteretic models based on the experimental data obtained from [14] to represent the actual behavior of header end-plate connections in the GF models, while in the BF models it is idealized as a pin connection. NSPA and NRHAs were performed on steel buildings with SMFs to investigate the effect of gravity framing on structural demands and collapse probability. OpenSees software simulations were conducted. The following conclusions are drawn from this study.

1. The existing rules in TSCB [15] are found to be very strict for the control of SDRs during the design process, leading to overly rigid buildings. To mitigate the requirements of inter-story drift ratio, these rules should be updated. It is suggested to use smaller deflection amplification factor ( $< R/I$ ) to find inter-story drift demand.
2. Steel frame buildings with SMFs, regardless of contribution of gravity framing to lateral strength, have shown to have greater static over-strength factors than code-specified ( $D=3$ ).
3. The period of vibration of the analysed structures decreases when the gravity frame is considered as a part of the structural system. However, since the steel buildings designed in accordance with TSCB 2018 are very rigid, the decrease in the vibration period is small.
4. Dynamic shaking effects caused the engineering demands to change from the static case. As a result of the higher mode effects, the taller the buildings the larger dynamic amplification of story shear forces of the building. Therefore, it is clear that

quantification of demand parameters from NSPA only is questionable for structures that have considerable higher mode effects.

5. Gravity frames can contribute to the mitigation of drift demands by adding lateral stiffness and strength. When considering gravity framing, the base shear strength is 18.5% and 10.8% larger than that of the bare frame only for the four-story and eight-story buildings, respectively. As a result of incremental dynamic analyses, the median collapse intensity of the buildings was average increased about of 27% compared with bare BF models for both of buildings.
6. Models that include the interior gravity frames had smaller drift demands and greater global drift capacity of the buildings than those without them.
7. Bottom story collapse mechanism that is not a desirable scenario for ductile design is triggered when the gravity framing is not regarded as a part of the building during the nonlinear dynamic analyses.
8. The gravity framing system appears to be effective at providing reserve strength and stiffness to the system which helps to prevent or delay collapse.
9. The probability of collapse decreased significantly when the gravity framing is included in the analysis. Incorporation of the gravity framing improved the collapse capacity based on the FEMA P-695 methodology.

## **Symbols**

|            |   |   |
|------------|---|---|
| $BF$       | : | Bare frame model                                  |
| $C_d$      | : | Deflection amplification factor                   |
| $D$        | : | Static over-strength factor                       |
| $E$        | : | Modulus of Elasticity (N/mm <sup>2</sup> )        |
| $F_y$      | : | Nominal yield stress of structural steel          |
| $G$        | : | Dead load   |
| $GF$       | : | Gravity framing model                             |
| $H1, H2$   | : | Principle horizontal directions for accelerograms |
| $I$        | : | Importance factor                                 |
| $I_{b,eq}$ | : | Equivalent beam moment of inertia                 |
| $I_{b,i}$  | : | Moment of inertia of i-th beam in a story         |
| $I_{c,eq}$ | : | Equivalent column moment of inertia               |
| $I_{c,i}$  | : | Moment of inertia of i-th column in a story       |
| $L_{b,eq}$ | : | Equivalent beam length                            |
| $L_{b,i}$  | : | Length of i-th beam in a story                    |
| $MC$       | : | Moment resisting connection                       |
| $M_p$      | : | Flexural strength capacity of bare gravity beam   |

|                 |  |
|-----------------|--|
| $M_{p,b,eq}$    | : Equivalent beam plastic moment   |
| $M_{pb,i}$      | : Plastic Moment of i-th beam in a story   |
| $M_{p,c,eq}$    | : Equivalent column plastic moment   |
| $M_{pc,i}$      | : Plastic Moment of i-th column in a story                                       |
| $PC$            | : Pin connection   |
| $PC/Sa$         | : Probability of collapse for a given intensity $Sa$                             |
| $P_{GF}$        | : Gravity load for Gravity Frames  |
| $P_{MF}$        | : Gravity load for Moment Frames   |
| $Q$             | : Live load  |
| $R$             | : Response modification factor   |
| $Sa$            | : Spectral acceleration  |
| $Sa (T_1, 5\%)$ | : 5% damped spectral acceleration at the first mode period of the steel building |
| $S_{CT}$        | Median collapse intensity (g)  |
| $SDR_1$         | : First story drift ratio  |
| $SDR_{MAX}$     | : Maximum story drift ratio  |
| $S_{DS}$        | : Design spectral acceleration at the short period                               |
| $S_{D1}$        | : Design spectral acceleration at a period of 1 second                           |
| $V_{des}$       | : Code-based design force of the steel building                                  |
| $V_{max}$       | : Ultimate strength of the steel building  |
| $\theta_{max}$  | : Maximum calculated story drift angle   |
| $\lambda$       | : Scale factor for the ground motion records                                     |
| $\mu_T$         | : Period based ductility   |

## Acknowledgments

This research was financially supported by Research Fund of the Istanbul Technical University. Project Number: 41573

## References

- [1] Leon, R., Composite connections, Structural Engineering Handbook, CRC Press LLC, 1999.
- [2] Huang, Z., and Foutch, D.A., Effect of hysteresis type on drift limit for global collapse of moment frame structures under seismic loads, Journal Earthquake Engineering, 13(7), 939-964, 2009.

- [3] Lignos, D., and Krawinkler, H., Sidesway Collapse of Deteriorating Structural systems under Seismic Excitations, Report No. TB 172, John A. Blume Earthquake Engineering Center, Stanford University, CA, 2012.
- [4] Gupta, A., and Krawinkler, H., Behavior of ductile SMRFs at various seismic hazard levels, *Journal of Structural Engineering*, 126(1), 98–107, 2000.
- [5] Ramos, M.D., Mosqueda, G. and Hashemi, M.J., Large-scale hybrid simulation of a steel moment frame building structure through collapse, *Journal of Structural Engineering*, 142(1), 04015086, 2016.
- [6] MacRae, G.A., Kimura, Y. and Roeder, C., Effect of column stiffness on braced frame seismic behavior, *Journal of Structural Engineering*, 130(3), 381-391, 2004.
- [7] Ji, X., Kato, M., Wang, T., Hitaka, T. and Nakashima, M., Effect of gravity columns on mitigation of drift concentration for braced frames, *Journal of Constructional Steel Research*, 65(12), 2148-2156, 2009.
- [8] Elkady, A. and Lignos, D. G., Effect of gravity framing on the overstrength and collapse capacity of steel frame buildings with perimeter special moment frames, *Earthquake Engineering & Structural Dynamics*, 44, 1289-1307, 2015.
- [9] Lee, K. and Foutch, D. A., Performance evaluation of new steel frame buildings for seismic loads, *Earthquake Engineering and Structural Dynamics*, 31, 653-670, 2002.
- [10] Flores, F.X., Charney, F.A. and Lopez-Garcia, D., Influence of the gravity framing system on the collapse performance of special steel moment frames, *Journal of Constructional Steel Research*, 101, 351-362, 2014.
- [11] Foutch, D. A., and Yun, S., Modeling of steel moment frames for seismic loads, *Journal of Constructional Steel Research*, 58, 529-564, 2002.
- [12] Astaneh-Asl, A., Modjtahedi, D., McMullin, K., Shen, J. and D'Amore, E., Stability of damaged steel moment frames in Los Angeles, *Journal of Constructional Steel Research*, 20, 443-446, 1998.
- [13] Sizemore, J., Davaran, A., Fahnestock, L., Tremblay, R. and Hines, E., Seismic behaviour of low-ductility concentrically-braced frames, *Structures Congress, ASCE Library*, 2014.
- [14] Karasu, A. and Vatansver, C., Experimental Study on the Behavior of Header End - Plate Connections under Cyclic Loading, *Technical Journal of Turkish Chamber of civil engineers*, 32(6), 2021.
- [15] Turkish Seismic Code for Buildings 2018, Specifications for Design of Buildings under Earthquake Action, Disaster and Emergency Management Presidency, Ankara.
- [16] Chisari, C., Francavilla, A.B., Latour, M., Piluso, V., Amadio, C. and Rizzano, G., Critical issues in parameter calibration of cyclic models for steel members, *Engineering Structures*, 132, 123-138, 2017.
- [17] OpenSees, Version 2.0, User Command-Language Manual, 2009.

- [18] Turkish code for design and construction of steel structures 2016, Ministry of Environment and Urbanisation, Ankara, Turkey.
- [19] Krawinkler, H., The state-of-the-art report on system performance of moment resisting steel frames subjected to earthquake ground shaking, FEMA 355c, Washington, DC: Federal Emergency Management Agency, 2000.
- [20] CSI. SAP2000 v18 integrated finite element analysis and design of structures, Berkeley: Computers and Structures; 2016.
- [21] Ibarra, L.F., Medina, R.A., and Krawinkler, H., Hysteretic models that incorporate strength and stiffness deterioration, *Earthquake Engineering Structural Dynamic*, 34(12), 1489-1511, 2005.
- [22] Lignos, D. G. and Krawinkler, H., Deterioration Modeling of Steel Components in Support of Collapse Prediction of Steel Moment Frames under Earthquake Loading, *Journal of Structural Engineering*, 137 (11), 1291-1302, 2011.
- [23] Lignos, D. G., Hartloper, R.H., Elkady, A., Deierlein, G.G. and Hamburger, R., Proposed Updates to the ASCE 41 Nonlinear modeling parameters for wide-flange steel columns in support of performance-based seismic engineering, *Journal of Structural Engineering*, 145 (9), 04019083, 2019.
- [24] Gupta, A. and Krawinkler, H., Seismic demands for the performance evaluation of steel moment resisting frame structures, Report No. 132, The John A. Blume Earthquake Engineering Center, Stanford University, CA, 1999.
- [25] Lignos, D.G., Putman, C., Krawinkler, H., Seismic assessment of steel moment frames using simplified nonlinear models, *Computational Methods in Earthquake Engineering*, 30(0), 91–109, 2013.
- [26] FEMA, Quantification of building seismic performance factors, Report FEMA-P695, Federal Emergency Management Agency, Washington, DC, 2009.
- [27] Zareian, F., Medina, R.A., A practical method for proper modeling of structural damping in inelastic plane structural systems, *Computers & Structures*, 88(1), 45–53, 2010.
- [28] Chopra, A.K., *Dynamics of structures theory and applications to earthquake engineering*, Fourth edition, Prentice Hall, U.S.A, 2013.
- [29] Lignos, D.G., Putman, C., Krawinkler, H., Application of simplified analysis procedures for performance-based earthquake evaluation of steel special moment frames, *Earthquake Spectra*, 31(4), 2015.
- [30] ASCE/SEI 7-16, Minimum design loads for buildings and other structures, Reston, VA: ASCE, 2017.
- [31] Vamvatsikos, D., Cornell, C.A., Incremental dynamic analysis, *Earthquake Engineering & Structural Dynamics*, 31(3), 491–514, 2002.



# **Meteorological Drought Analysis for Helmand River Basin, Afghanistan**

**Mohammad Musa ALAMI<sup>1</sup>**

**Gokmen TAYFUR<sup>2</sup>**

## **ABSTRACT**

This study evaluates drought at Lashkargah, Farah, Adraskan, and Gardandiwal stations in Helmand River Basin (HRB) in Afghanistan to determine appropriate drought indices for the basin. Thirty seven years of monthly recorded precipitation data from 1979 to 2015 are employed with different drought index (DI) methods which include the Standardized Precipitation Index (Normal-SPI, Log-SPI, and Gamma-SPI), the Percent of Normal (PN), and the Deciles. All the methods are applied to the annual long term precipitation data. The log-SPI and the gamma-SPI predict extreme drought conditions, whereas, the normal-SPI determines wet and less dry conditions. The results emphasize that the PN and the Deciles methods predict more drought years in comparison to the SPI methods. The Deciles method shows longer period of extreme and severe drought than other methods. The five methods indicate various drought intensities in 1985, 1987, 1994, 1997, 1999, 2000, 2001, 2002, 2003, and 2004 at all the stations. The extreme drought condition in 2001 at all the stations confirms to the recorded drought reports for the same region. It is noted that since the log-SPI and the gamma-SPI capture the historical extreme and severe drought periods successfully, these are recommended as the drought monitoring indices for Helmand River Basin.

**Keywords:** Afghanistan, deciles, drought indices, Helmand River Basin, PN, SPI.

## **1. INTRODUCTION**

Drought is a natural phenomenon that adversely affects environment, agriculture, humans, wildlife, economic and social life [1, 2]. Various drought indices have been developed as the drought monitoring and assessment tools in different parts of the world. Drought indices are quantitative measurements that determine drought level and intensity by integrating one or more variables of data such as precipitation and evapotranspiration into a single numerical value [3]. The widely employed drought indices are the Standardized Precipitation Index

---

Note:

- This paper was received on January 26, 2021 and accepted for publication by the Editorial Board on January 11, 2022.
- Discussions on this paper will be accepted by September 30, 2022.
- <https://doi.org/10.18400/tekderg.868595>

1 Helmand University, Department of Civil Engineering, Helmand, Afghanistan  
musa\_afghanistan@yahoo.com - <https://orcid.org/0000-0002-1478-9482>

2 Izmir Institute of Technology, Department of Civil Engineering, Izmir, Turkey  
gokmentayfur@iyte.edu.tr - <https://orcid.org/0000-0001-9712-4031>

(SPI) which is used worldwide, the Palmer Drought Severity Index (PDSI) used in the United States, the Deciles Index widely used in Australia, the China-Z Index (CZ) used in China, and the Percent of Normal (PN).

There are many new indices that have been developed since early 2000s using not only precipitation but also soil moisture, snow, and evaporation effects, such as the RDI (Reconnaissance Drought Index developed by [4]), the Non-Stationary RDI [5]), the SPEI (the standardized precipitation evapotranspiration index, [6]), among many. Mishra and Singh [7] and Eslamian et al. [8] have reviewed the mostly employed drought indices, together with their advantages and limitations. Bulut and Yılmaz [9] have carried out drought analysis for Turkey using the remote sensing hydrological and vegetation cover data. Keskiner et al [10] have investigated drought effects on ponds in Seyhan River Basin. Dikici and Aksel [11] have employed two different drought indices (Normalized Difference Vegetation Index (NDVI) and Vegetation Condition Index (VCI)) to assess drought at Asi River Basin. Mehr et al [12] have employed the wavelet-packet-genetic programming meteorological drought tool and performed application at two stations in Ankara province. Dikbas and Bacanlı [13] have used the SPI for the assessment of drought at 13 stations in the central Anatolia. In Afghanistan, other than precipitation, there are no available data on other hydrological variables such as evaporation, snow, soil moisture etc. Therefore, this study has employed drought indices requiring only precipitation data.

Although Afghanistan has suffered drought for the last three decades, there is no substantial scientific research that has evaluated the drought conditions due to lack of meteorological data. Nevertheless, there are some reports that mention historical drought conditions in Afghanistan. The World Bank Working Paper by Ahmad and Wasiq [14] indicates four consecutive years of drought from 1998 to 2001 in Afghanistan. Mayan [15] cites the unusual droughts in 1995-2001 in Afghanistan until heavy snow in 2002-2003 winter season. Another scientific project report by the Asia-Pacific Network for Global Change Research [16] states the worst drought in 2001 in its recorded history of Afghanistan.

There are also some articles that have investigated drought conditions in neighboring countries of Iran and Pakistan. Ashraf and Routray [17] point out the most severe drought years of 2000, 2001, 2002, and 2004 in province of Balochistan province of Pakistan. A study by Zarei *et al.* [1] in bordering city of Saravan, Iran, indicates extreme droughts in 1987, 1998, 2010, and 2001. Morid *et al.* [18] have states that the most recent drought of 1998-2001 in Iran has been the worst for the last three decades.

This study aims to evaluate the performance of several drought indices to find the most appropriate one(s) for monitoring droughts in Helmand River Basin of Afghanistan. The Normal-SPI, the log-SPI, the gamma-SPI, PN, and the Deciles are employed since they require only precipitation data.

## **2. STUDY AREA AND DATA**

### **2.1. Study Area**

Afghanistan is a land-locked country with a total area of 652000 km<sup>2</sup> in the south central Asia with geographic location of 33 00 N, 65 00 E. The climate is arid to semi-arid with cold winters and hot summers [19]. Afghanistan is divided into five major river basins as Amu

Darya River Basin, Harirud-Murghab River Basin, Helmand River Basin, and Kabul River Basin (Figure 1).

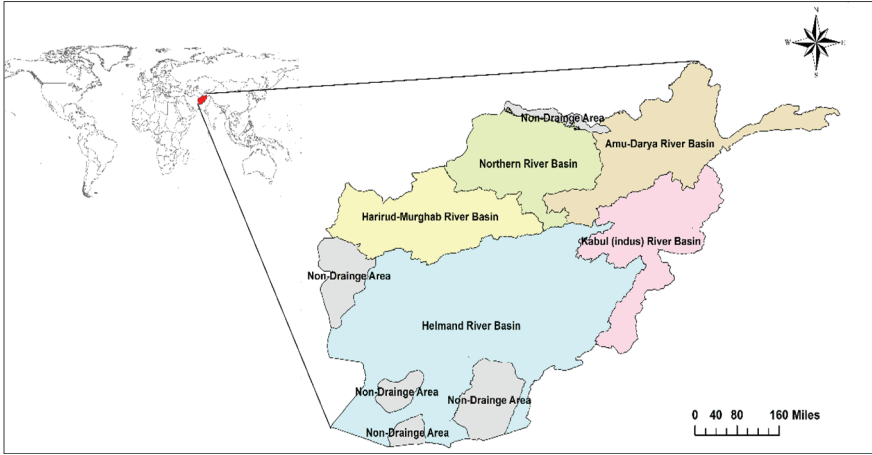


Figure 1 - Five major river basins of Afghanistan

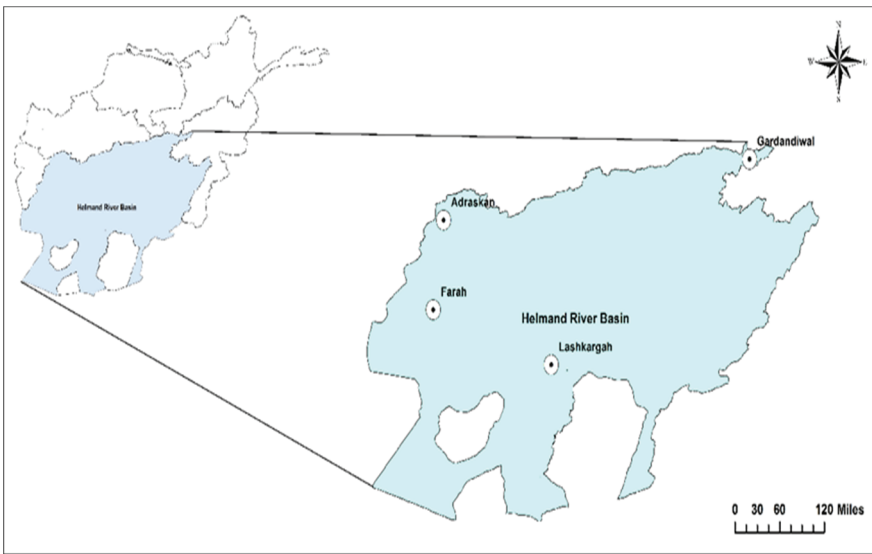


Figure 2 - Helmand River Basin and four precipitation stations

The study area is Helmand River Basin (HRB) which is also known as Hirmand River Basin. It is the largest basin among the five basins in Afghanistan (Figure 2) and has a total area of 345200 km<sup>2</sup>, of which 82.2 % is located in Afghanistan [20]. The basin covers the catchment area for Helmand River, which is the longest river in Afghanistan with 1300 km length [21].

Helmand River originates from Hindu Kush Mountains in the north-east of Afghanistan and drains into Sistan Depression near to the Afghan-Iranian border in the south-east of Afghanistan. The annual mean precipitation varies from about 50 mm in the southwest to almost 300 mm in the northwest part of the basin [22]. Precipitation mostly happens in winter months (December, January, February, and March) and falls as snow in the upper basin.

## 2.2. Data

Due to four decades of war and conflict in Afghanistan, there have been gaps in the meteorological data. Recently, the missing precipitation data have been completed for the meteorological stations of Afghanistan by the Ministry of Energy and Water of Afghanistan (MEW). The data used in this study are obtained from the MEW for the four stations of Helmand River Basin, namely Lashkargah (31°34'58.36"N-64°21'17.12"E), Farah

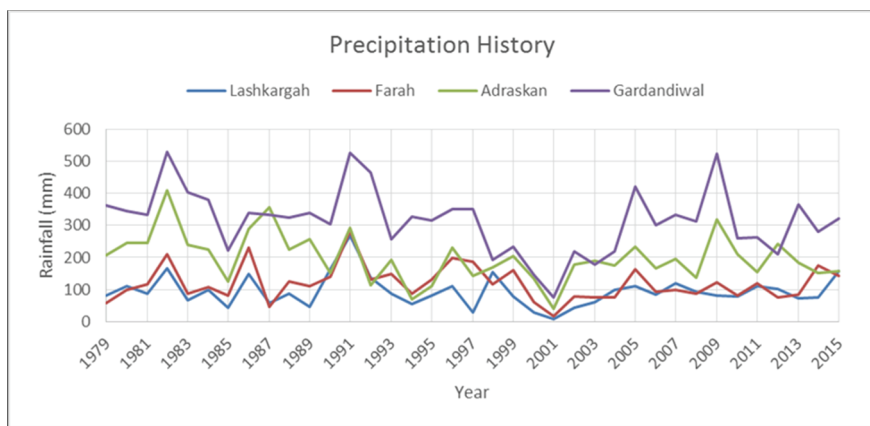


Figure 3 - Monthly recorded precipitation data for the stations

Table 1 - Rainfall characteristics at the meteorological stations

| Rainfall characteristics | Lashkargah | Farah | Adraskan | Gardandiwal |
|--------------------------|------------|-------|----------|-------------|
| Mean (mm)                | 94         | 119   | 199      | 315         |
| Standard deviation (mm)  | 59         | 66    | 78       | 91          |
| Variance (mm)            | 3481       | 4356  | 6084     | 8281        |
| Kurtosis                 | -0.85      | -0.43 | -0.012   | -0.0098     |
| Skewness                 | 0.65       | 0.59  | 0.46     | 0.24        |
| Range (mm)               | 287.3      | 307.1 | 365.7    | 466.2       |
| Minimum (mm)             | 21.6       | 30.7  | 38.5     | 66.4        |
| Maximum (mm)             | 308.9      | 337.8 | 404.2    | 532.6       |

(32°21'52.15"N-62°3'42.48"E), Adraskan (33°38'13.44"N-62°15'45.6"E), and Gardandiwal (34°30'1.35"N-68°12'45.56"E), as shown in Figure 2. Thirty seven years (1979-2015) annual precipitation data used for the analysis are shown in Figure 3. The annual mean precipitation for Lashkargah, Farah, Adraskan, and Gardandiwal stations are 94 mm, 119 mm, 199 mm, and 315 mm, respectively. Table 1 summarizes the rainfall characteristics for each station.

### 3. METHODOLOGY

In this study, the normal-SPI, the log-SPI, the gamma-SPI, the PN, and the Deciles methods are applied to evaluate the meteorological drought at the four stations in Helmand River Basin in Afghanistan to find the appropriate one(s) for the basin.

#### 3.1. Standardized Precipitation Index

The SPI method is developed by McKee *et al.* [23]. Precipitation is the only input parameter for the SPI and it requires transformation of original data to the normal distribution. The mean of the transformed data series becomes zero with a standard deviation of 1. The drought classification by the z-score index for the normal-SPI, the log-SPI and the gamma-SPI is shown in Table 2. Positive SPI values indicate wet periods, conversely negative SPI values indicate dry periods. This study has employed the normal-SPI, the log-SPI and the gamma-SPI [24].

Table 2 - Drought classification for SPI values [25]

| SPI value(z-score) | Drought Classification |
|--------------------|------------------------|
| 2.00 or more       | Extremely wet          |
| 1.50 to 1.99       | Very wet               |
| 1.00 to 1.49       | Moderately wet         |
| 0.99 to -0.99      | Near normal            |
| -1.00 to -1.49     | Moderate drought       |
| -1.50 to -1.99     | Severe drought         |
| -2.00 or less      | Extreme drought        |

##### 3.1.1. Normal-SPI

The normal-SPI method uses the normal probability distribution instead of the gamma distribution [26]. It is mathematically easier to calculate. In this case, the SPI index simply becomes:

$$SPI = z = \frac{x-\mu}{\sigma} \tag{1}$$

where;  $z$  is the standardized value (the SPI value),  $x$  is a value in the data series,  $\mu$  is the mean of the data series, and  $\sigma$  is the standard deviation of the data series.

**3.1.2. Log-SPI**

The log-SPI distribution is non-negative and positively skewed. It is simple and just a logarithmic transformation of data. By applying the log-normal distribution with the sample mean of logarithmic transformed data, the SPI becomes:

$$SPI = z = \frac{\ln(x)-\mu}{\sigma} \tag{2}$$

Note that  $\mu$  and  $\sigma$  are the mean and the standard deviation of the log-data series, respectively.

**3.1.3. Gamma-SPI**

The gamma-SPI is the most widely applied observational method for precipitation data. It involves fitting of a gamma probability density function to a given time series of precipitation data [26]. It is defined by its probability density function as [26]:

$$g(x, \alpha, \beta) = \frac{1}{\beta^\alpha \Gamma(\alpha)} x^{\alpha-1} e^{-\frac{x}{\beta}} \tag{3}$$

where  $\alpha$  is a shape parameter greater than zero,  $\beta$  is a scale parameter greater than zero, and  $x$  is the amount of precipitation greater than zero.  $\Gamma(\alpha)$  is the gamma function, which is defined as follows [26]:

$$\Gamma(\alpha) = \int_0^\infty x^{\alpha-1} e^{-x} dx \tag{4}$$

$\alpha$  and  $\beta$  parameters can be estimated as follows [27]:

$$\alpha = \frac{1}{4A} \left( 1 + \sqrt{1 + \frac{4A}{3}} \right) \tag{5}$$

$$\beta = \frac{\bar{x}}{\alpha} \tag{6}$$

$$A = \ln(\bar{x}) - \frac{\sum \ln(x)}{n} \tag{7}$$

In Eq. (7),  $n$  is the number of observations.  $\bar{x}$  is the mean value of the precipitation data. After estimating  $\alpha$  and  $\beta$  coefficients, the probability density function is integrated with

respect to  $x$ , which yields the following expression  $G(x)$  for the cumulative probability distribution function [26]:

$$G(x) = \int_0^x g(x)dx = \frac{1}{\beta^\alpha \Gamma(\alpha)} \int_0^x x^{\alpha-1} e^{-x/\beta} dx \tag{8}$$

Substituting  $t$  for  $x/\beta$  in Eq. (8) yields to [26]:

$$G(x) = \frac{1}{\Gamma(\alpha)} \int_0^x t^{\alpha-1} e^{-t} dt \tag{9}$$

As the gamma function is not defined for  $x = 0$ , for possibility of zero values, the cumulative probability function becomes [26]:

$$H(x) = q + (1 - q)G(x) \tag{10}$$

where  $q$  is the probability of zero precipitation. This cumulative probability distribution is then transformed into the standard normal distribution to yield the SPI. The approximate conversion provided by Abramowitz and Stegun [28] is given as follows:

for  $0 < H(x) < 0.5$

$$z = SPI = - \left( t - \frac{c_0 + c_1 t + c_2 t^2}{1 + d_1 t + d_2 t^2 + d_3 t^3} \right), t = \sqrt{\ln \left( \frac{1}{(H(x))^2} \right)} \tag{11}$$

for  $0.5 < H(x) < 1.0$

$$z = SPI = + \left( t - \frac{c_0 + c_1 t + c_2 t^2}{1 + d_1 t + d_2 t^2 + d_3 t^3} \right), t = \sqrt{\ln \left( \frac{1}{(1.0 - H(x))^2} \right)} \tag{12}$$

where  $c_0 = 2.515517$ ,  $c_1 = 0.802853$ ,  $c_2 = 0.010328$ ,  $d_1 = 1.432788$ ,  $d_2 = 0.189269$ , and  $d_3 = 0.001308$

### 3.2. Percent of Normal

The PN method is a drought index for the evaluation of meteorological data as the percent actual precipitation percent of the normal precipitation. It is generally applied to long-term mean precipitation data where at least a 30-year mean is considered [18, 21]. PN values of 80%-120% indicate normal conditions while values less than 80% indicate dry periods. Drought index classification for the PN values is shown in Table 3. Note that the literature recommends to employ the PN method together with other drought indices for healthy predictions [29].

*Table 3 - Drought index classification for PN [21]*

| <b>NP values</b> | <b>Drought Classification</b> |
|------------------|-------------------------------|
| 180% or more     | Extremely wet                 |
| 161% to 180%     | Very wet                      |
| 121% to 160%     | Moderately wet                |
| 81% to 120%      | Near normal                   |
| 41% to 80%       | Moderate drought              |
| 21% to 40%       | Severe drought                |
| 20% or less      | Extreme drought               |

### **3.3. Deciles**

The Deciles approach is developed by Gibbs and Maher [30]. By this method, long-term monthly precipitation is ranked from the highest to the lowest to construct a cumulative frequency distribution. The distribution is divided into ten parts (Deciles) on the basis of equal probabilities [26]. The first Decile is the precipitation value not exceeded by the lowest 10% of all the precipitation values in a record. The second Decile is in between the lowest 10% and 20%, etc. The Deciles are grouped into five classes as two Deciles per class. If a precipitation falls into the lowest 20% (Deciles 1 and 2), it is classified as the much below normal, corresponding to the extreme drought condition. Deciles 3 to 4 (20 to 40%) indicate the below normal precipitation, corresponding to the severe drought. Deciles 5 to 6 (40 to 60%) indicate the near normal precipitation (normal condition), Deciles 7 and 8 (60 to 80%) indicate the above normal precipitation (very wet condition) and Deciles 9 and 10 (80 to 100%) indicate the much above normal precipitation (extremely wet condition) Morid et al. [18]. The Deciles values and the drought ranking classifications are given in Table 4. As seen, the Deciles ranking indicates two drought intensities as the below normal (severe drought) and the much below normal (extreme drought).

*Table 4 - Deciles drought ranking classification*

| <b>Deciles values</b>          | <b>Drought Classification</b>       |
|--------------------------------|-------------------------------------|
| Deciles 1-2 (lowest 20%)       | Much below normal (extreme drought) |
| Deciles 3-4 (next lowest 20%)  | Below normal (severe drought)       |
| Deciles 5-6 (middle 20%)       | Near normal                         |
| Deciles 7-8 (next highest 20%) | Above normal (very wet)             |
| Deciles 9-10 (highest 20%)     | Much above normal (extremely wet)   |

### 4. RESULTS

The SPI (Normal-SPI, Log-SPI, and Gamma-SPI), the PN, and the Deciles values are computed for Lashkargahm, Farah, Adraskan, and Gardandiwal stations of Helmand River Basin in Afghanistan.

#### 4.1. Lashkargah Station

According the SPI results for Lashkargah station (Figure 4), all the methods provide almost the same results except for years 1991 and 2001. The normal-SPI makes higher wet prediction for 1991 while it underestimates the drought in 2001. The log-SPI and the gamma-SPI methods predict the extreme drought in 2001 which is the worst drought in its recorded history of Afghanistan [14, 15, 16]. The extreme and severe drought conditions happened in 1997 and 2000 are also predicted by all the methods, except the normal-SPI. Moderate drought years include 1985, 1989 and 2002 while the extreme wet periods are 1990, 1991 and 1992. The severe and moderate wet years include 1982, 1986 and 1998.

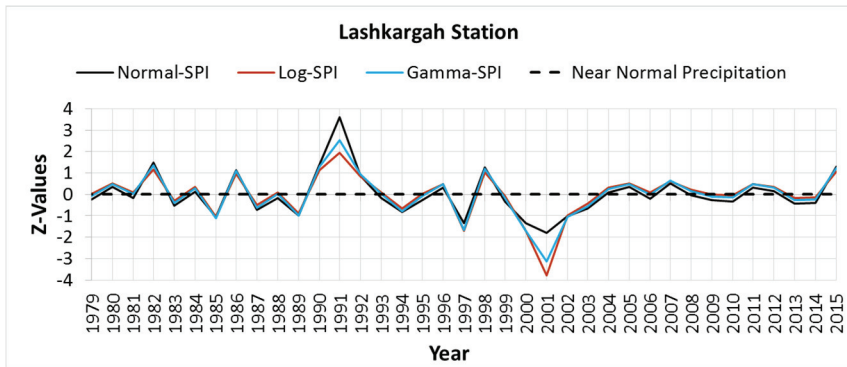


Figure 4 - SPI results for Lashkargah station

Table 5 - Deciles result for all the stations

| Annual Rianfall Values (mm/year) |                 |                 |                 | Classification                      |
|----------------------------------|-----------------|-----------------|-----------------|-------------------------------------|
| Lashkargah                       | Farah           | Adraskan        | Grandandiwal    |                                     |
| 44.22 - 60.19                    | 69.45 - 79.59   | 121.72 - 144.59 | 203.97 - 224.95 | Much below normal (extreme drought) |
| 74.68 - 81.59                    | 87.65 - 94.68   | 157.44 - 176.56 | 262.23 - 306.81 | Below normal (severe drought)       |
| 86.53 - 95.53                    | 109.72 - 120.78 | 192.19 - 209.74 | 323.25 - 333.39 | Near normal                         |
| 110.42 - 118.01                  | 133.75 - 158.37 | 232.01 - 243.67 | 346.92 - 365.74 | Above normal (very wet)             |
| 155.85 - 168.83                  | 191.64 - 282.39 | 290.78 - 409.71 | 438.74 - 527.82 | Much above normal (extremely wet)   |

The Deciles results and threshold ranges for Lashkargah Station are given in Table 5. When precipitation is less than 81.6 mm/year and 60.2 mm/year, the severe and extreme droughts occur, respectively. Figure 5 shows the Deciles ranking for Lashkargah station. As compared to the SPI results, the Deciles ranking indicates long extreme and severe drought conditions. Extreme drought years are 1985, 1987, 1989, 1994, 1997, 2000, 2001 and 2002. The severe drought years are 1983, 1999, 2003, 2009, 2010, 2013 and 2014. According to the Deciles method, the extreme wet conditions include 1982, 1986, 1990, 1991, 1992, 1998 and 2007.

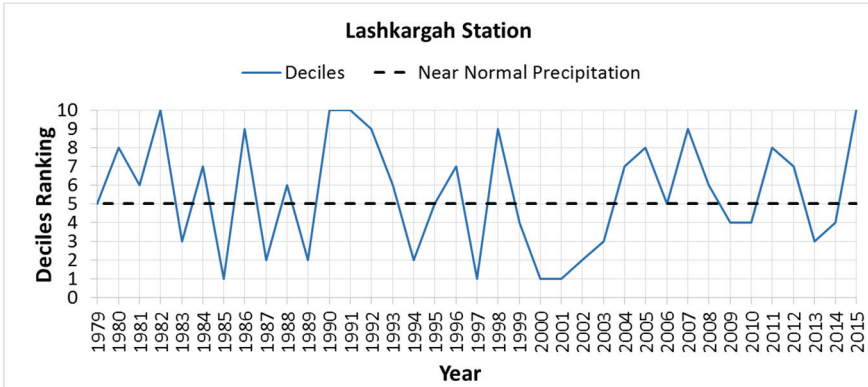


Figure 5 - Deciles ranking for Lashkargah station

Figure 6 presents the results for the PN method for Lashkargah station. This method indicates the extreme and severe droughts in 1997, 2000 and 2001. The moderate droughts include 1983, 1985, 1987, 1989, 1994, 2010, 2013 and 2014. According to this index, the extreme wet periods are 1990, 1991 and 1992. The severe and moderate wet years are 1982, 1986, 1998 and 2007.

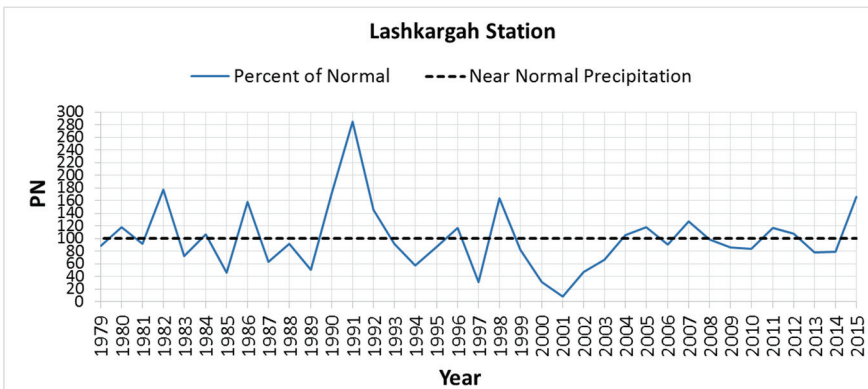


Figure 6 - PN results for Lashkargah station

**4.2. Farah Station**

As presented in Figure 7, all the methods provide almost the same results except for the years of 1991 and 2001. The normal-SPI makes slightly higher wet prediction for 1991 while it underestimates the drought condition in 2001. The log-SPI and the gamma-SPI methods make the extreme drought prediction for 2001 while the normal SPI makes this prediction as the severe drought. The extreme wet conditions include 1986, and 1991 while the moderate and severe wet years are 1982, 1996 and 1997.

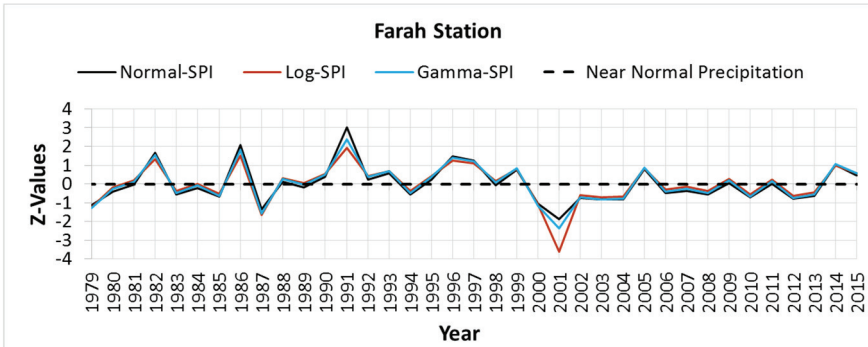


Figure 7 - SPI results for Farah station

The Deciles results and threshold ranges for Farah station are given in Table 5. When the precipitation is less than 94.6 mm/year and 79.6 mm/year, the severe and extreme drought conditions occur, respectively. Figure 8 shows the deciles ranking for this station. As compared to the SPI results, the Deciles make more extreme and severe drought predictions. The extreme drought years include 1979, 1987, 2000, 2001, 2002, 2003, 2004 and 2012. The severe drought years are 1983, 1985, 1994, 2006, 2008, 2010 and 2013. According the Deciles index, the extreme wet conditions are 1982, 1986, 1991, 1996, 1997, 1999 and 2014.

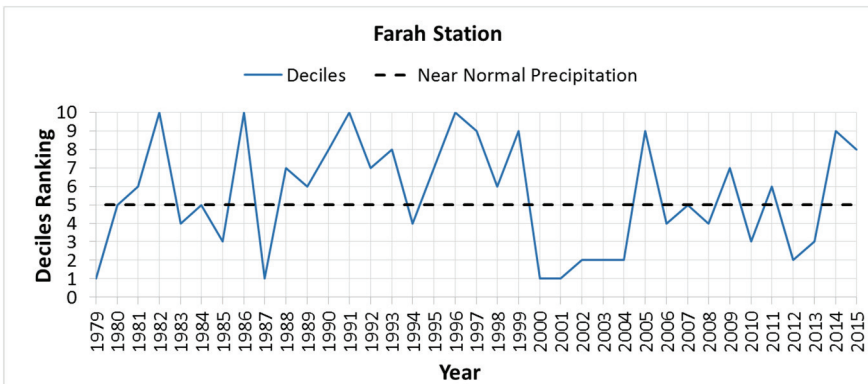


Figure 8 - Deciles ranking for Farah station

Figure 9 shows the results for the PN method for Farah station. This method indicates the extreme drought in 2001 and severe drought in 1987. The moderate drought years are 1979, 1980, 1983, 1985, 1994, 2000, 2002, 2003 and 2014. This method specifies the extreme wet periods as 1986 and 1991. The severe and moderate wet years are 1982, 1993, 1996, 1997, 1999, 2005 and 2014.

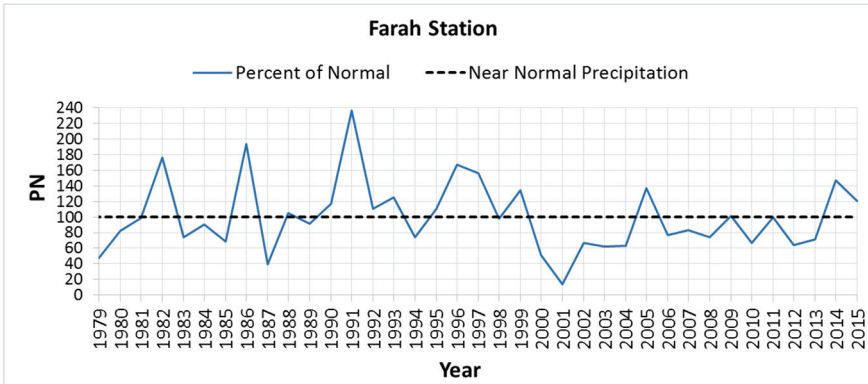


Figure 9 - PN results for Farah station

### 4.3. Adraskan Station

Figure 10 shows that the normal-SPI and the gamma-SPI indicate almost the same results for Adraskan station and the log-SPI predicts the extreme drought condition in 2011. According the SPI results at Adraskan station, the extreme and severe drought years are 1994 and 2001. Moderate drought years include 1985, 1992, 1995 and 2000. The extreme wet periods are 1982 and 1987 while the severe and moderate wet years include 1986 and 2009.

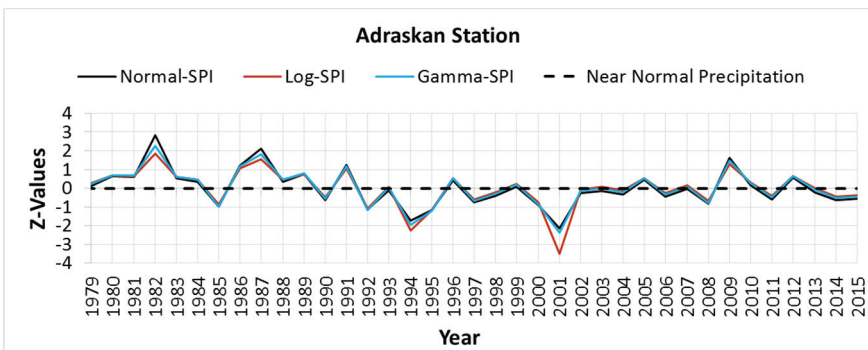


Figure 10 - SPI results for Adraskan station

The Deciles results and threshold ranges for this station are given in Table 5. When precipitation is less than 176.6 mm/year and 144.6 mm/year the severe and extreme droughts occur, respectively. Figure 11 shows the Deciles ranking for Adraskan station. The comparison of the Deciles results against those of the SPI indicates more extreme and severe drought conditions. Extreme drought years are 1985, 1992, 1989, 1994, 1995, 1997, 2000, 2001 and 2008. The severe drought years are 1990, 1998, 2004, 2006, 2011, 2014 and 2015. According to the Deciles method, the extreme wet condition years are 1980, 1981, 1982, 1986, 1987, 1991 and 2009.

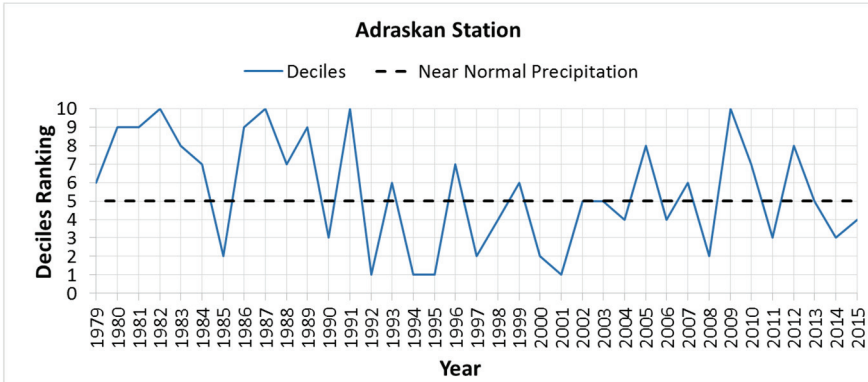


Figure 11 - Deciles ranking for Adraskan station

The results for the PN method are given in Figure 12 for Adraskan station. The PN method indicates the extreme drought condition in 2001 and severe drought in 1994. The moderate drought conditions are 1985, 1990, 1992, 1994, 1995, 1997, 2000, 2006, 2008, 2011 and 2014. This method specifies the extreme and severe wet periods in 1982 and 1987. The moderate wet years are 1980, 1981, 1986, 1989, 1991, 2009 and 2012.

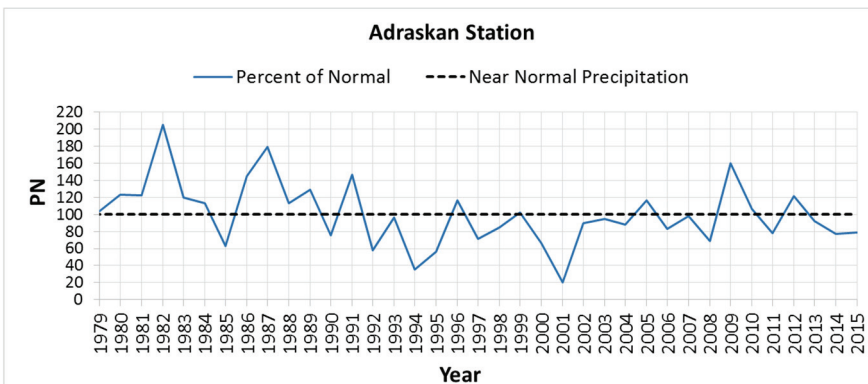


Figure 12 - PN results for Adraskan station

**4.4. Gardandiwal Station**

Figure 13 shows the results of the SPI method for Gardandiwal station. According to the results, the normal-SPI tends to show the wet and less drought conditions. Conversely, the log-SPI and the gamma-SPI predict the extreme drought conditions. The log-SPI and the gamma-SPI results in this station indicate the extreme drought conditions in years 2000 and 2001, but the normal-SPI shows the extreme drought condition only in 2001 and the severe drought in 2000. All the SPI methods show the same moderate drought conditions at this station in 1985, 1998, 1999, 2002, 2003, 2004 and 2012. The extreme wet years are 1982, 1991 and 2009 while the moderate and severe wet years include 1992 and 2005.

The Deciles results and the threshold ranges for Gardandiwal station are given in Table 5. When precipitation is less than 306.8 mm/year and 224.9 mm/year the severe and extreme drought conditions have occurred, respectively. Figure 14 shows the Deciles ranking for this station. The comparison of the Deciles ranking with the SPI results indicates more extreme and severe drought conditions. The extreme drought conditions include 1985, 1998, 2000, 2001, 2002, 2003, 2004 and 2012. The severe drought years are 1990, 1993, 1999, 2006, 2010, 2011 and 2014. Based on the results of the Deciles, the extreme wet conditions include 1982, 1983, 1984, 1991, 1992, 2005, 2009 and 2013.

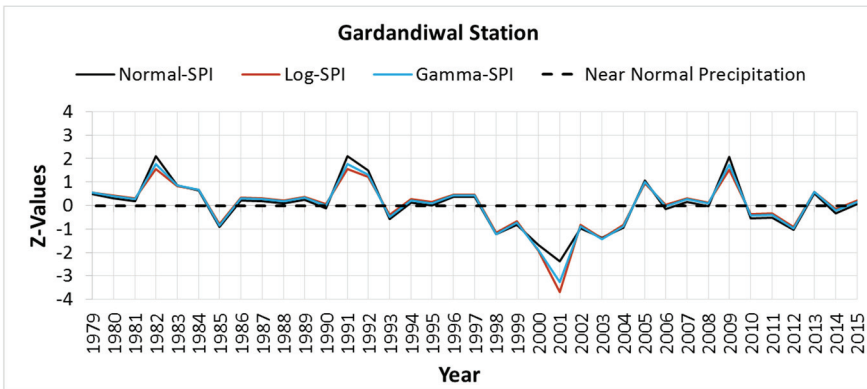


Figure 13 - SPI results for Gardandiwal station

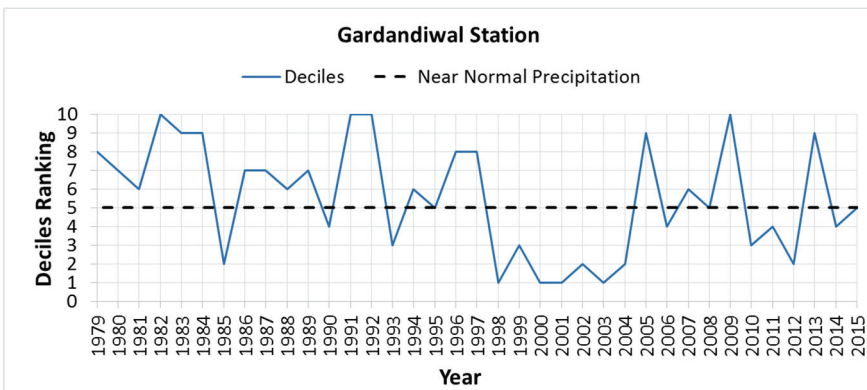


Figure 14 - Deciles ranking for Gardandiwal station

The results for the PN method are given in Figure 15 for Gardandiwal station. The PN does not indicate the extreme drought condition for this station. The PN shows the severe drought in 2001. The moderate drought years are 1985, 1993, 1998, 1999, 2000, 2002, 2003, 2004 and 2012. This method specifies the very wet period as 1982, 1991 and 2009 while the moderate wet years include 1983, 1984, 1992 and 2005.

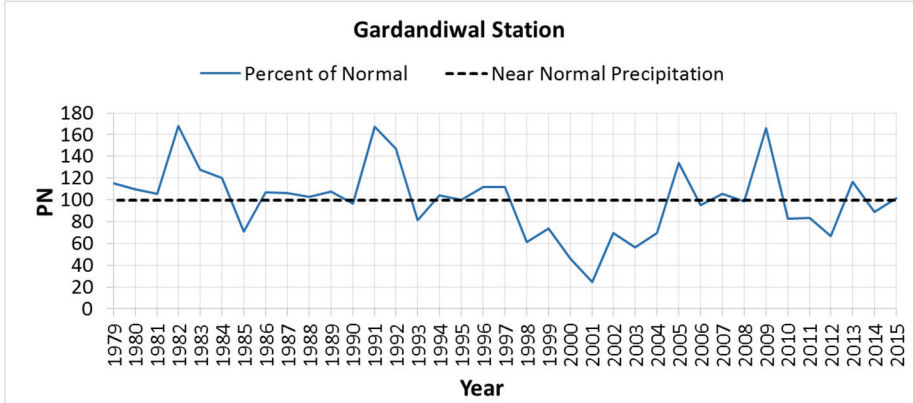


Figure 15 - PN results for Gardandiwal station

## 5. DISCUSSIONS ON THE RESULTS

Table 6 summarizes the drought intensities for the stations. The extreme, severe, and moderate drought intensities are listed for the normal-SPI, the log-SPI, the gamma-SPI, and the PN methods. The moderate drought intensity is not listed for the Deciles method because this method just indicates the extreme and severe droughts.

According to the results of all the methods, the common extreme drought year is found to be 2001 for all the stations. Year 2000 is also generally predicted as the extreme drought year for Gardandiwal station and 1994 for Adraskan station. Years 1997 and 2000 are predicted as the severe drought years for Lashkargah station and 1987 for Farah station. The common moderate drought conditions are observed as 1985 and 2002. As discussed before in Figures 4-15, the extreme wet conditions are also generally common for all the stations in 1982, 1991, and 1992. Therefore, all the stations seem to have experienced almost the same occurrences of the drought and wet conditions. The results indicate that the PN method overpredicts the number of moderate drought years as opposed to the SPI methods. Since the Deciles ranking indicates two drought intensities as the severe, and the extreme, this method predicts more years of the extreme and severe droughts than the other methods (see Table 6).

These results confirm the reports ([14, 15, 16]) about Afghanistan's droughts during the last three decades. As discussed earlier, the extreme droughts in the central and southwestern parts of Afghanistan and neighboring regions of the study area in Iran and Pakistan, occurred mostly in between 1998 and 2002 with the peak in 2001, are reported elsewhere [15, 17, 18].

Table 6 - Summary of the indicated historical droughts by the five DI methods

| Stations    | Methods           |        |  |              |              |  |              |              |  |                   |              |  |  |  |
|-------------|-------------------|--------|--|--------------|--------------|--|--------------|--------------|--|-------------------|--------------|--|--|--|
|             | Normal-SPI        |        |  | Log-SPI      |              |  | Gamma-SPI    |              |  | Percent of Normal |              |  | Deciles  |  |
|             | Drought Intensity |        |  |              |              |  |              |              |  |                   |              |  |  |  |
|             | Extreme           | Severe | Moderate   | Extreme      | Severe       | Moderate   | Extreme      | Severe       | Moderate   | Extreme           | Severe       | Moderate   | Extreme  | Severe   |
| Lashkargah  | —                 | 2001   | 1985<br>1989<br>1997<br>2000<br>2002                 | 2001         | 1997<br>2000 | 1985<br>1989<br>2002                                 | 2001         | 1997<br>2000 | 1985<br>1989<br>2002                                 | 2001              | 1997<br>2000 | 1983<br>1985<br>1987<br>1989<br>1994<br>1997<br>2000<br>2010<br>2013<br>2014         | 1985<br>1987<br>1989<br>1994<br>1997<br>2000<br>2002                         | 1983<br>1999<br>2003<br>2009<br>2010<br>2013<br>2014 |
| Farah       | —                 | 2001   | 1979<br>1987<br>2000                                 | 2001         | 1987         | 1979<br>2000   | 2001         | 1987         | 1979<br>2000   | 2001              | 1987         | 1979<br>1980<br>1983<br>1985<br>1987<br>1994<br>2000<br>2002<br>2003<br>2004         | 1979<br>1987<br>1985<br>2000<br>2001<br>2002<br>2006<br>2008<br>2010<br>2013 | 1983<br>1985<br>1994<br>2006<br>2008<br>2010<br>2013 |
| Adraskan    | 2001              | 1994   | 1985<br>1992<br>1995<br>2000                         | 1994<br>2001 | —            | 1985<br>1992<br>1995                                 | 1994<br>2001 | —            | 1985<br>1992<br>1995<br>2000                         | 2001              | 1994         | 1985<br>1990<br>1992<br>1994<br>1995<br>1997<br>2000<br>2006<br>2008<br>2011<br>2014 | 1985<br>1992<br>1994<br>1995<br>1995<br>1997<br>2000<br>2001<br>2008         | 1990<br>1998<br>2004<br>2006<br>2011<br>2014<br>2015 |
| Gardandiwal | 2001              | 2000   | 1985<br>1998<br>1999<br>2002<br>2003<br>2004<br>2012 | 2000<br>2001 | —            | 1985<br>1998<br>1999<br>2002<br>2003<br>2004<br>2012 | 2000<br>2001 | —            | 1985<br>1998<br>1999<br>2002<br>2003<br>2004<br>2012 | —                 | 2001         | 1985<br>1993<br>1998<br>1999<br>2000<br>2002<br>2003<br>2004<br>2012                 | 1985<br>1998<br>2000<br>2001<br>2002<br>2003<br>2004<br>2012                 | 1990<br>1993<br>1999<br>2006<br>2010<br>2011<br>2014 |

According to Table 6, the log-SPI and the gamma-SPI produce almost the same drought predictions while the normal-SPI predicts the extreme drought year of 2001 as the severe drought at Lashkargah and Farah stations. At Gardandiwal station, all the methods predict drought years from 1998 to 2004 (Table 6). The PN method predicts the extreme drought year of 2001 as the severe drought only at Gardandiwal station. The Asia-Pacific Network for Global Change Research [16] states the worst drought year in its recorded history of Afghanistan as 2001, which is predicted by the log-SPI and the gamma-SPI for all the stations.

As opposed to the SPI methods, the PN produces more moderate drought years in 1980s and early 2010s at Laskargah, 1980s and early 2000s at Farah, 1990s, 2000s and 2010s at Adraskan and 1990s and early 2000s at Gardandiwal stations. As opposed to the other methods, the Deciles index predicts many extreme and severe drought years at the four stations (Table 6). The PN and Deciles indices predict, in general, more drought years. For example; for Adraskan station, while each SPI method, in total, makes 6 drought predictions, this number is 13 for the PN and 15 for the Deciles (Table 6).

## 6. CONCLUSIONS

This study explores the performances of five widely employed drought indices (the normal-SPI, the log-SPI, the gamma-SPI, the PN, and the Deciles) at four stations of Helmand River Basin in Afghanistan to find the appropriate indices for monitoring the drought in the basin.

The following conclusions can be drawn from the Helmand River Basin drought analysis:

- 1) Although the five DI methods provide almost the same results for Lashkargah, Farah, Adraskan, and Gardandiwal stations of Helmand River Basin, the normal-SPI could not predict the extreme drought year of 2001 ([14, 15, 16]) at two stations and the PN at one station.
- 2) More droughts are experienced at the stations from late 1990s to early 2000s with the extreme drought condition in 2001, confirming the reported worst drought in the region ([14, 15, 16]).
- 3) According to the Deciles drought index, when precipitation is less than 60.2 mm/year, 79.6 mm/year, 144.6 mm/year, and 224.9 mm/year the extreme drought occurs in Lashkargah, Farah, Adraskan, and Gardandiwal stations, respectively.
- 4) The Deciles method produces too many extreme and severe droughts, most of which are not predicted by the other four indices.
- 5) The historical extreme year of 2001 at all the stations is captured by the log-SPI and the gamma-SPI methods.
- 6) The PN and Deciles indices, in general, predict more drought occurrences as opposed to the SPI methods (almost twice of the SPI methods).
- 7) Based upon above conclusions, the log-SPI and the gamma-SPI can be recommended as the drought monitoring and assessment methods for Helmand River Basin in Afghanistan.

## Acknowledgments

The authors thank the Ministry of Energy and Water of Afghanistan for providing the meteorological and hydrological data used in this study.

## **Declarations**

**Funding** Not applicable

**Conflicts of interest** None

## **Availability of data and material**

The data that support the findings of this study may be available from the Ministry of Energy and Water of Afghanistan, upon request.

**Code availability** Not applicable

**Ethical Approval** Not applicable

**Consent to Participate** Not applicable

## **Authors' contributions**

M.Musa Alami: Carried out all the data collections and model applications and contributed on the writing of the paper.

Gokmen Tayfur: Discussed the application problems and modelling tools, advised the student during the research, and wrote the paper.

## **References**

- [1] Zarei A. R., Moghime M. M, and Mahmodi M. R, 2015. Parametric and Non-Parametric Trend of Drought in Arid and Semi-Arid Regions Using RDI Index, *Water Resource and Management*, 30, 5479-5500.
- [2] Sirdas S., and Sen Z., 2003. Spatio-temporal drought analysis in the Tarakya region, Turkey, *Hydrological Sciences Journal*, 48(5), 809-819.
- [3] Yacoub E., and Tayfur G., 2017. Evaluation and Assessment of Meteorological Drought by Different Methods in Tazara Region, Mauritania, *Water Resource and Management*, DOI: 10.1007/s11269-016-1510-8.
- [4] Tsakiris, G., & Vangelis, H., 2005. 'Establishing a drought index incorporating evapotranspiration.' *European Water*, 9(10), 3-11.
- [5] Bazrahshan, J. and Hejabi, S. (2018). 'A Non-Stationary Reconnaissance Drought Index (NRDI) for Drought Monitoring in a Changing Climate.' *Water Resources Management*, 32:2611–2624, <https://doi.org/10.1007/s11269-018-1947-z>
- [6] Wang, L., Yua, H., Yang, M., Yang, R., Gao, R. and Wang, Y. (2019). 'A drought index: The standardized precipitation evapotranspiration runoff index.' *Journal of Hydrology*, JH 2019, 651-668.
- [7] Mishra, A.K. and Singh, V.P. (2010). 'Drought modelling- A review.' *Journal of Hydrology*, 403, 157-175.

- [8] Eslamian, S. Askari, KOA, Singh, VP, Dalezios, NR, GHane, M., Yihdego, Y. and Matouq, M. (2017). 'A Review of Drought Indices.' *International Journal of Constructive Research in Civil Engineering (IJCRCE)*, Volume 3, Issue 4, 2017, PP 48-66
- [9] Bulut, M. and Yilmaz, T. 2016. 'Türkiye'deki 2007 ve 2013 yılı kuraklıklarının NOAH hidrolojik Modeli ile incelenmesi.' *Teknik Dergi*, 27(4), 7619 – 7634.
- [10] Keskiner, A.D., Cetin, M., Simsek, M. and Akin, S. 2020. 'Kuraklık riski altındaki havzalarda gölet haznelerinin tasarımı: Seyhan Havzasında Bir Uygulama.' *Teknik Dergi*, 31(5), 10189 – 10210.
- [11] Dikici, M. and Aksel, M. 2021. 'Evaluation of two vegetation indices (NDVI and VCI) over Asi Basin in Turkey.' *Teknik Dergi*, 32(4) (in press).
- [12] Mehr, A.D., Safari, M.J.S. and Nourani, V. 2021. 'Wavelet packet-genetic programming: A new model for meteorological drought hindcasting.' *Teknik Dergi*, 32(4) (in press).
- [13] Dikbas, F. and Bacanlı, U.G. 2021. 'Detecting drought variability by using two-dimensional correlation analysis.' *Teknik Dergi*, 32(4), (in press).
- [14] Ahmad, M., and Wasıq, M., 2004. *Water resources development in Northern Afghanistan and its implications for Amu Darya Basin* (No. 36). World Bank Publications.
- [15] Miyan, M. A., 2015. *Droughts in Asian Least Developed Countries: Vulnerability and sustainability*. *Weather and Climate Extremes*, 7, 8-23.
- [16] APN, 2015. *An International Geosphere-Biosphere Programme Synthesis Theme on Global Environment Change and Sustainable Development: Needs of Least Developed Countries*. A project report by Asia-Pacific Network for Global Change Research, 16-17.
- [17] Ashraf M., and Routray J. K., 2015. *Spatio-Temporal Characteristics of Precipitation and Drought in Balochistan Province, Pakistan*, *Nat Hazards*, 77, 229-254.
- [18] Morid S., Smakhtin V., and Moghaddasi M., 2006. *Comparison of Seven Meteorological Indices for Drought Monitoring in Iran*, *International Journal of Climatology*, 26, 971-985.
- [19] Broshears, R.E., Akbari, M.A., Chornack, M.P., Mueller, D.K., and Ruddy, B.C., 2005. *Inventory of ground-water resources in the Kabul Basin, Afghanistan: U.S. Geological Survey Scientific Investigations Report 2005-5090*.
- [20] Wolf, A. T., Natharius, J. A., Danielson, J. J., Ward, B. S., and Pender, J. K., 1999. *International River Basins of the World*. *International Journal of Water Resources Development*, 15(4), 387-427.
- [21] Thomas, V., Azizi, M. A., and Behzad, K., 2016. *Developing transboundary water resources: What perspectives for cooperation between Afghanistan, Iran and Pakistan?* *Afghanistan Research and Evaluation Unit, Case Study*.

- [22] Goes, B. J. M., Howarth, S. E., Wardlaw, R. B., Hancock, I. R., and Parajuli, U. N., 2015. Integrated water resources management in an insecure river basin: a case study of Helmand River Basin, Afghanistan. *International Journal of Water Resources Development*, 32(1), 3-25.
- [23] Mckee TB., Doesken NJ., and Kleist J., 1993. The relationship of drought frequency and duration to time scales. *Proceedings of the 8th Conference on Applied Climatology*, 1993. American Meteorological Society Boston, MA, USA, 179–18.
- [24] Cacciamani C., Morgillo A., Marchesi S., and Pavan V., 2007. Monitoring and forecasting drought on a regional scale: Emilia-Romagna region, *Methods and Tools for Drought Analysis and Management*, Springer, 29-48.
- [25] Barua S., Ng A., Perera B., 2010. Comparative Evaluation of Drought Indexes: Case Study on the Yarra River Catchment in Australia, *Water Resour Plan Manag*, 137, 215-226.
- [26] Angelidis P., Maris F., Kotsovinos N., Hrisanthou V., 2012. Computation of Drought Index SPI with Alternative Distribution Functions, *Water Resources Management*, 26(9), 2453-2473.
- [27] Thom HCS., 1958. A note on the gamma distribution, *Mon Weather Rev* 86:117–122.
- [28] Abramowitz M., and Stegun A., eds 1965. *Handbook of mathematical formulas, graphs and mathematical tables*, Dover Publications Inc, New York.
- [29] Hayes M. J., 2006 *Drought Indices*, Willy Online Library Center. (Online). < <https://drought.unl.edu/whatis/indices.htm>
- [30] Gibbs, W. J., and Maaher, J. V., 1967. Rainfall deciles as drought indicators. Bureau of Meteorology, Bulletin No. 48, Commonwealth of Australia, Melbourne, Australia.

# **The Effect of Hydrated Lime Mixing Forms and Ratios on Performance in Asphalt Pavements**

**Celaleddin Ensar ŞENGÜL<sup>1</sup>**

**Dündar AYYILDIZ<sup>2</sup>**

**Erol İSKENDER<sup>3</sup>**

**Atakan AKSOY<sup>4</sup>**

## **ABSTRACT**

In this study; the water damage problem and indirect tensile strengths (ITS) were investigated for different hydrated lime (HL) additive ratios and adding methods. In this regard, identical briquettes modified with hydrated lime have been produced. HL was used both in the bituminous binder (wet method) and as part of the filler aggregate. The hydrated lime was added in two different ways to form the defined equivalent ratios. By producing nine identical briquettes in each option, the values of water damage and ITS in both unconditioned and modified mixtures were compared, and the level of significance differences between the identical briquettes and mixtures was questioned. Increasing the HL content increases the standard deviation between identical samples in terms of ITS. The workability of the mixture is adversely affected by the increase in the hydrated lime ratio. When HL is mixed into the asphalt cement (AC), the standard deviations of ITS values among identical samples remain lower due to the increase in mixing rates. Increasing the ratio of adding HL to the asphalt cement reduces the ITS ratios compared to the option of adding filler to aggregate. If HL is added to the mixture in low HL content, the water damage ratios show, on average, higher water damage resistance (15% higher) than the HL being added to the AC. However, if the HL content is increased to medium and high levels, mixing HL to AC creates higher water damage resistance than adding it as filler.

**Keywords:** Asphalt pavements, hydrated lime, HL mixing forms, mechanical tests.

---

## Note:

- This paper has been received on March 29, 2021 and accepted for publication by the Editorial Board on April 8, 2022.
- Discussions on this paper will be accepted by September 30, 2022.
- <https://doi.org/10.18400/tekderg.902668>

1 General Directorate of State Hydraulic Works, Fourteenth Regional Directorate, İstanbul, Turkey  
celensen@dsi.gov.tr - <https://orcid.org/0000-0003-0998-028X>

2 Ayyıldızlar Construction and Engineering Services Limited Company, Trabzon, Turkey  
dundarayyildiz@hotmail.com - <https://orcid.org/0000-0002-6851-6914>

3 Karadeniz Technical University, Civil Engineering Department, Trabzon, Turkey  
eiskender@ktu.edu.tr - <https://orcid.org/0000-0001-7934-839X>

4 Karadeniz Technical University, Civil Engineering Department, Trabzon, Turkey  
aaksoy@ktu.edu.tr - <https://orcid.org/0000-0001-5232-6465>

## **1. INTRODUCTION**

During the past 40 years, researchers from all over the world have focused their attention on the effects of hydrated lime as an active filler in the asphalt mixtures, finding that hydrated lime (HL) can actually provide many other benefits to asphalt mixtures in addition to the reduction of moisture sensitivity and to the mitigation of stripping [1].

In the United States, the use of lime as a filler in asphalt pavements is a common practice for more than hundred years. In Europe, hydrated lime is commonly used as a filler in porous asphalt pavements to decrease water damage susceptibility of mixtures. In Netherlands, for example, 90% of the highways are paved with open-graded friction course asphalt mixtures that contain hydrated lime from 1% to 2% by weight of dry aggregates [2].

The presence of HL in the filler (20% of the total filler weight), increases deformability and tensile resistance of both mastics and asphalt mixtures and decreases the creep compliance when both unmodified and modified binders are used [3]. Since lime is an effective asphalt modifier for improving the moisture resistance of asphalt pavements, it is often used as a mineral filler in asphalt concrete mixtures. Addition of lime can also improve pavement performance and durability. Hydrated lime added to asphalt can increase penetration and on the other hand can lower the viscosity of asphalt cements [4-6].

Hydrated lime is known to be an effective moisture damage additive, and it can also reduce the chemical ageing of the AC and stiffen the mastic. However, the optimum content and fineness of hydrated lime used in asphalt have been rarely studied [7].

Different laboratory testing methods and field studies have shown that HL is equal to or better than chemical anti-stripping agents and additives such as cement. However, the differences between the effects of the additives was not equally demonstrated by the different test methods. For example, the difference between additives is not remarkable when the retained Marshall stability approach is used. However, multiple freeze-thaw methods, e.g. the repeated Lottman and Texas freeze-thaw method are more differentiated test methods in addition to the Hamburg rutting tests. The use of HL in asphalt mixtures revealed long-term improvement in the mechanical properties of asphalt mixtures such as stiffness, resistance to cracking, rutting and aging [8-10].

It has been found that about 4-6% of the asphalt absorbed on the surface of the HL particles cannot be recovered and the addition of HL can significantly reduce the formation of anhydride, ketone and most carboxylic acids, thereby slowing the aging process of asphalt. It is stated that HL collects calcium ions on the aggregate surface, making the aggregate and asphalt bond closer. Using HL reduces the difference between the surface free energies of asphalt-aggregate and water-aggregate, indicating that more energy is required for stripping to occur and the rate of moisture damage is reduced. HL was used instead of mineral powder, and the test results showed that the retaining Marshall Stability (MS0) and Indirect Tensile Strength Ratio (ITSR) of the mixed material after adding HL could fully meet the specification requirement [11].

For more than four decades, hydrated lime has been a well-known material for improving the resistance against moisture and frost damage of asphaltic mixtures. The decrease of asphalt quality, as a result of the oil crisis in 1970s, made the mixtures prone to moisture and frost damage, and the modification of asphaltic mixtures by HL improved the

performance of the mixtures. HL is composed of calcium hydroxide [Ca(OH)<sub>2</sub>] which is produced from quicklime by slaking it with water using a hydrator as a specific equipment.

HL was added to the mixtures by two different methods. The method of adding lime as filler, a method widely used by many institutions, has been applied. Second, HL is blended with asphalt cement. The second method is used by few researchers and even less in practice [12]. State agencies in North America estimate that by using HL at the usual range of 1–2%, the durability of asphalt mixtures in highways increases by 25–50% [13]. For lime modified mixes, ITSR and dynamic modulus  $|E^*|$ , good resistance to moisture damage with the data has been established [14].

In this study; modified Lottman water damage model and indirect tensile strength test were used as an important indicator of load-spreading capacity as a widely accepted test method in evaluating water damage performance. The aim of the research is to determine how the application of hydrated lime affects the water damage and indirect tensile strength performance approaches. For this purpose, hydrated lime mixing ratios were chosen as an option and also hydrated lime was mixed with mixtures of these amounts in two different methods. Three different mixing ratios in the form of low-medium-high usage rates for hydrated lime were used as two different alternatives, both by mixing hydrated lime into filler aggregate and directly mixing into the bituminous binder. However, experimental study results are examined by using nine identical samples in each option due to the sensitivity of the study and the interpretation of the subject at the point of change of identical samples.

The use of HL in asphalt pavements showed that the performance properties of asphalt mixes such as rigidity, cracking resistance, rutting and aging were improved [8-10]. HL was used instead of mineral filler powder. According to the experimental results, it showed that the retaining Marshall Stability and Indirect Tensile Strength Ratio (ITSR) with the HL modification could fully meet the specification requirements [15]. By using HL for modification purposes normally in the range of 1-2%, it is evaluated that the durability of asphalt mixes on roads is increased by 25–50% [13]. The HL-containing samples have greater resistance to deformation at nanoscale in the mastic and matrix phases. The resistance is more pronounced in the mastic phase. There is also strong evidence suggesting that HL has the most potent effect on the mastic phase, with significant increase in elastic modulus and hardness [16]. HL is typically used as an additive to enhance the anti-stripping resistance of asphalt mixtures. As a result, HL has received the greatest share of academic attention, and its other long-term effects such as the resulting resistance against fatigue cracks have been relatively neglected. Effects of different quantities of HL (by weight of aggregate) on the fatigue properties of asphalt mixtures was investigated by four-point bending fatigue testing of unaged and aged specimens. Laboratory long-term aging procedure was carried out in accordance with AASHTO PP2 (120 h of treatment at 85 °C). Fatigue tests were conducted in strain-controlled mode with a sinusoidal load applied with frequency of 10 Hz (without rest) at 20 °C. Fatigue life was evaluated with the stiffness reduction and dissipated energy methods. Test results showed that fatigue life of asphalt mixtures is sensitive to their HL content. Addition of 1%, 1.5% and 2% of HL to mix design was found to improve the fatigue life of unaged asphalt specimens. For the aged specimens, adding of 1% and 1.5% HL increased the fatigue life by 25% and 50%, respectively, but use of 2% HL led to 40% reduction. For all asphalt mixtures, the best improvement in the fatigue life was achieved by mixes containing 1.5 of HL [17]. The addition of HL enhances the mechanical properties and

durability of asphalt mixture in terms of the resilient modulus, rutting resistance, moisture susceptibility under freeze-thaw conditions, and fatigue life. HL can be used not only for anti-strip aims in the mixtures for wearing course but also in the mixtures for other structural courses to produce an integration of the improvements in mechanical and durability behaviour of pavement structures. The improvement of the mechanical properties works in a relatively wide range of weather temperatures. A high HL content does not mean a definite improvement of the durability of mixtures, because extra HL reduces the effective amount of asphalt cement, the active binder. In general, an optimum maximum of 2.5% HL content by total weight of aggregate to replace the same weight of conventional mineral filler is suggested for all practices in terms of both mechanical behaviour and durability improvement [18].

The aim of this research is to evaluate the performance of hydrated lime for low-medium-high usage rate options, depending on the method of adding it to asphalt mixtures. The use of HL as a filler aggregate in AC at different rates and its direct relationship with the AC chemistry, as well as the interaction performance between the aggregate granule and asphalt, by adding the filler to the aggregate, are important variables. It was aimed to question the hydrated lime in terms of mixing practice by considering the field plant conditions. Indirect tensile strength tests and water damage assessment methods were chosen as performance tests. Depending on the addition ratio of hydrated lime; it is considered important to investigate the homogeneity of dispersion in the mixture, the degree of dispersion, the degree of effectiveness, and its ability to fulfil its expected function. In this respect, it is planned to increase the sensitivity of the study by working on nine identical samples with the same options for the determined multiple additive options. The water damage and indirect tensile strengths of the mixtures with and without additives in the selected options are examined in the context of the benefit mechanisms of HL.

## **2. MATERIALS AND METHOD**

In this study, asphalt cement as bituminous binder and basalt rock aggregates were used. Specific properties of bituminous binder and general physical properties of aggregates were given in Table 1 and Table 2, respectively.

*Table 1 - Properties of used asphalt cement*

| Test                      | Test Method    | Value |
|---------------------------|----------------|-------|
| Specific gravity (25°C)   | ASTM D-70      | 1.014 |
| Softening point (°C)      | TS EN 1427     | 48.4  |
| Flash point (Cleveland)   | TS EN ISO 2592 | 324   |
| Penetration (25°C)        | TS EN 1426     | 53    |
| Retaining penetration (%) | TS EN 12607-1  | 72    |
| Ductility (25°C)          | ASTM D-113     | 100+  |

Dense graded aggregate combination was used in accordance with the Turkish Highways Technical Specification. Aggregate gradation used and specification limits were given in Table 3.

*Table 2 - Engineering properties of basalt rock aggregates*

| Properties                             | Test Method       | Value |
|--|-------------------|-------|
| Specific gravity (coarse agg.)         | TS EN 1097-6      | 2.696 |
| Specific gravity (fine agg.)           | TS EN 1097-6      | 2.676 |
| Specific gravity (filler)              | TS EN 1097-7      | 2.628 |
| Los Angeles abrasion (%)               | ASTM C-131        | 22    |
| Flakiness (%)                          | BS 812 (Part 105) | 12.3  |
| Stripping resistance (no additive) (%) | ASTM D-1664       | 65-70 |
| Water absorption (%)                   | ASTM C-127        | 0.40  |
| Soundness in MgSO <sub>4</sub> (%)     | ASTM C-88         | 2.0   |

*Table 3 - Aggregate gradation and specification limits*

| Sieve size (mm) | Specification limits (%) [19] |             | Aggregate gradation (%) | Aggregate fractions   |
|-----------------|-------------------------------|-------------|-------------------------|-----------------------|
|                 | Lower limit                   | Upper limit |                         |                       |
| 19.0            | 100                           | 100         | 100.0                   | Coarse aggregate, 52% |
| 12.5            | 88                            | 100         | 90.7                    |                       |
| 9.5             | 72                            | 90          | 80.0                    |                       |
| 4.75            | 42                            | 52          | 48.0                    | Fine aggregate, 42.5% |
| 2.00            | 25                            | 35          | 30.5                    |                       |
| 0.425           | 10                            | 20          | 14.9                    |                       |
| 0.18            | 7                             | 14          | 9.3                     |                       |
| 0.075           | 3                             | 8           | 5.5                     | Filler, 5.5%          |

In the study, the effect of adding hydrated lime (HL) additive to asphalt mixtures was investigated in terms of water damage with different additive ratios. HL can be added to the asphalt cement (AC) or aggregate mixture. Dry method; It is generally preferred because it is simpler and more economical. In the dry method, HL is added to the dry aggregate mixture (mostly filler material) at the rate of total aggregate weight. In the wet method, HL is added to the moistened aggregate mixture. In the third method, known as the slurry method, a mortar is formed by adding water to the HL and this mortar is mixed with the aggregate mixture. In

the wet method and the slurry method, the moisture in the mixture is dried. Afterwards, the asphalt mixture is prepared by adding AC.

In this study, two participation methods were used for HL. In the first method, HL was added to AC with a high shear mixer. The modification process was applied at 160°C temperature and at 5000 rpm mixing speed for 30 minutes. In this method, 10%, 20% and 30% of HL by weight of AC is used. These rates are expressed as HL10, HL20 and HL30 in the article, respectively. Modification parameters were decided in the light of previous experience and similar studies in the literature [20]. In the second method, HL was added to the dry aggregate mixture at the rates of 0.5%, 1% and 1.5%. These options were expressed as HL0.5, HL1.0 and HL1.5 respectively. The total amount of HL used for a Marshall briquette in both methods is shown in Table 4.

*Table 4 - Amount of hydrated lime per briquette (gr)*

| Lime adding method           | L10  | L20   | L30   | L0.5 | L1.0  | L1.5  |
|------------------------------|------|-------|-------|------|-------|-------|
| Amount of HL for a briquette | 5.46 | 10.93 | 16.38 | 5.75 | 11.50 | 17.25 |

The important point here is the hydrated lime. It was used in three different rates of additions, which can be described as low, medium and high. In case of hydrated lime as part of filler or in AC; in the context of the selected ratios, (L10-L0.5), (L20-L1.0) and (L30-L1.5) mixtures are compared as equivalent mixtures.

Dense graded asphalt concrete design was done according to the Marshall design method. Optimum AC content was determined using base AC. The optimum AC content was taken as the percentage of AC corresponding to 4% air voids and determined as 4.75%. Optimum AC content determined by base AC was used for modified AC options. There are similar studies in the literature in which the content of base asphalt cement is used for modified mixtures or AC [21-22]. Many briquettes were produced and the mixtures were evaluated according to the Modified Lottman (AASHTO T283) method in terms of water damage resistance. Nine conditioned and three unconditioned briquettes were used for each type of mixture.

### **3. TEST RESULTS AND DISCUSSIONS**

#### **3.1. Indirect Tensile Strength (ITS) Test**

Control and modified mixtures were evaluated by indirect tensile strength test. The test results were given in Table 5, Figure 1 and 2 for conditioned and unconditioned mixtures.

In performance analysis processes of asphalt mixtures, the sensitivity of producing identical samples is extremely important. Even when identical samples are produced under the same conditions such as the same compaction energy, the same mixture temperature, the same gradation, performance differences between identical samples may be occur. For this reason, it is important to determine the change interval between identical briquettes. The strength

differences between identical samples produced for conventional mixtures may be higher than the strength differences between conventional and modified ones for some additive types and mixture designs. Here, when mixing parameters are used the same, aggregate individual properties and angularity can come to the fore. For these reasons, the production of many identical briquettes has been planned as the main subject of the study. Although gradation works were carried out in a controlled manner, differences may occur between identical samples due to the angularity parameters and various variables (such as the dispersion of the additive in the mixture, and the individual mineral characteristics of the aggregate) in the selected aggregates. In various studies, it has been observed that the performance criteria emerging between the additive and control options may be greater than the performance difference between the samples with or without additives. Therefore, it is important that the samples produced in this context are excessive and they should be evaluated with these aspects among themselves. Especially, the issue becomes more important when filler additives, such as hydrated lime, can make the mixture more rigid, as in this study.

*Table 5 - Indirect tensile strength test results*

| Unconditioned mixtures |         |         |         |         |         |         |         |
|------------------------|---------|---------|---------|---------|---------|---------|---------|
| Mixture                | L10     | L20     | L30     | L0.5    | L1.0    | L1.5    | Control |
| Sample 1               | 1049.67 | 1111.83 | 1120.85 | 1560.97 | 1230.13 | 1162.96 | 828.14  |
| Sample 2               | 1068.72 | 1081.75 | 1156.94 | 1456.71 | 1329.38 | 1089.77 | 841.32  |
| Sample 3               | 1041.65 | 1154.94 | 1186.02 | 1548.94 | 1365.47 | 1138.90 | 881.12  |
| Conditioned mixtures   |         |         |         |         |         |         |         |
| Mixture                | L10     | L20     | L30     | L0.5    | L1.0    | L1.5    |         |
| Sample 1               | 1018.59 | 1031.63 | 1046.66 | 1309.33 | 1182.01 | 1259.20 |         |
| Sample 2               | 1033.63 | 948.41  | 919.34  | 1242.16 | 1289.28 | 1083.76 |         |
| Sample 3               | 977.49  | 1030.62 | 1099.80 | 1270.23 | 1231.13 | 1075.74 |         |
| Sample 4               | 1017.59 | 1085.76 | 1004.56 | 1276.25 | 1229.13 | 1107.82 |         |
| Sample 5               | 985.51  | 1071.73 | 1064.71 | 1225.12 | 1226.12 | 1134.89 |         |
| Sample 6               | 1051.68 | 1032.63 | 1061.70 | 1318.35 | 1276.25 | 1131.88 |         |
| Sample 7               | 977.49  | 994.53  | 1054.68 | 1283.27 | 1233.14 | 1118.85 |         |
| Sample 8               | 1017.59 | 1053.68 | 978.49  | 1197.05 | 1301.31 | 1086.77 |         |
| Sample 9               | 1047.67 | 1055.69 | 1032.63 | 1341.41 | 1154.94 | 1185.02 |         |

Experimental research was carried out on briquettes produced according to Marshall Design. Nine identical samples were prepared at each addition rate. Standard deviations between identical samples were examined. Mixtures without additives are considered as control

mixtures. Many identical Marshall briquettes were produced for different additive ratios and different additive options. The performance variation between the briquettes with and without additives was questioned, and the mixtures with and without additives were compared in terms of average values. This comparison is considered important in terms of questioning the consistency of the results of the experiments and interpreting the additive performance correctly. The preparation of a large number of identical samples in terms of the selected mixture design parameters was aimed at this point. After all, two different types of lime adding; in each addition process, three different addition rates and nine identical samples were studied at each addition rate. In case HL is used both in AC and as filler, the degree of homogeneous mixture is considered important due to the increase in the additive ratio. With the increase in HL ratio, the issue of mixing especially in AC becomes more difficult. It is considered that the hydrated lime additive that is sufficient for the chemical modification of the asphalt cement reacts, but more of it remains in its present form in the mixture. Therefore, mixing time is considered important and special attention should be paid to uniform mixing time.

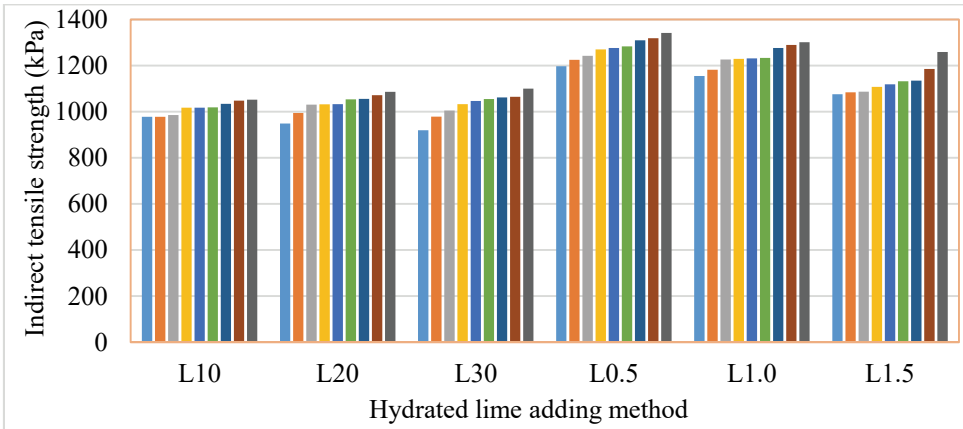


Figure 1 - Relationship between HL adding method and tensile strength for conditioned mixtures

The results obtained from the indirect tensile strength tests performed on conditioned briquettes are shown in Figure 1. ITS values of nine samples were given for each mixing ratio and type. As clearly seen from the figure, if hydrated lime is used as filler (L0.5-L1.0-L1.5), it shows higher indirect tensile strength compared to lime incorporation in the AC (L10-L20-L30).

In the method where hydrated lime is added to the asphalt cement (it is described as the wet method), the indirect tensile strength values offer similar values. This trend is valid for all three selected additive rates. Similar strength values are obtained for the selected incremental additive ratio values. In case lime is added to AC, the indirect tensile strength values seem independent of the lime ratio.

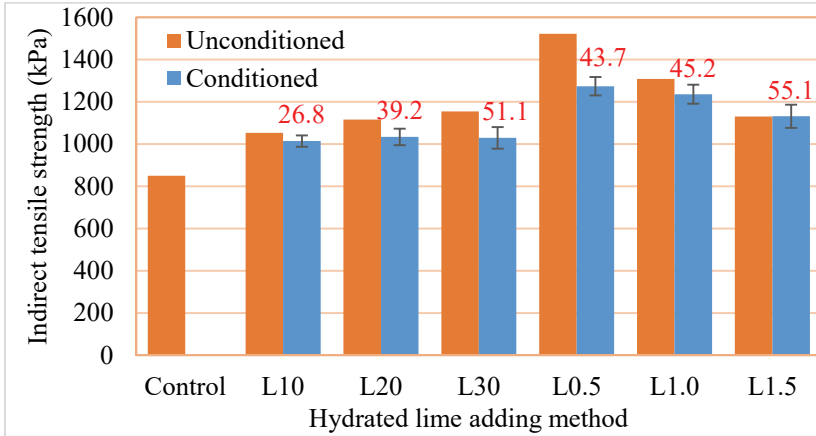


Figure 2 - Average strength of HL modified conditioned and unconditioned mixtures

The ITS values of the unconditioned and water damage conditioned briquettes are presented in Figure 2. Water damage reduces the ITS of identical samples for all mix options. HL when mixed to the filler in the low usage rate option (L0.5), it gives higher ITS values in the unconditioned and conditioned conditions. Questioning the mix performance in the conditioned situation is important to determine the water damaged performance in the field. Modified Lottman test results of conditioned briquettes have similar values when HL is added to AC (L10-L20-L30). When HL is added to the filler, the ITS values decrease with the increase of the HL content. ITS tests were carried out by keeping the same briquettes in a 25°C temperature cabinet. When ITS conditioned values are interpreted in medium temperature condition; it is recommended to add HL to the filler material at a low rate. In cases where HL may need to be used at a high rate for design; it is considered more appropriate to include fillers as part of the aggregate.

Depending on the HL adding method and the rate of HL for unconditioned samples, the standard deviation values of the tensile strengths were shown in Figure 2. With the increase of HL content, the standard deviation between identical samples increases. Asphalt mixtures are produced under the same conditions in terms of production technique. Although they are known as heterogeneous mixtures, they are produced under the same conditions as homogeneous mixtures to obtain the desired performance levels in terms of production logic. Due to the wide variety of material properties, they are seen as heterogeneous mixtures. This heterogeneity approach is in question in terms of changes in aggregate angularity values, distribution of additives in the mixture, individual properties of aggregates and especially rock mineralogy. Current studies on the application of mixtures more homogeneously both in plant conditions and in laying conditions come to the fore. Increasing standard deviation with increasing HL content reveals that due to the lime usage rate, much more attention should be paid to mixing, field laying and compaction conditions in terms of quality control because the raveling problems which may also develop in a limited amount, can trigger different damage conditions that can affect the entire pavement together.

The interpretation that the homogeneity of the mixtures was negatively affected was expressed based on the following point. While preparing identical briquettes, all mixing parameters were selected the same. Although the gradation is controlled, depending on the effect of the angularity of the aggregate and the placement of the aggregates in the mixture mortar, identical samples may reveal different results in performance approaches. For example; in questioning the performance of an additive, the difference between identical samples for the same mixtures can sometimes be greater than the average difference between conventional and modified mixtures. Various efforts are also being made to homogenize the holistic performance levels that the mixture will give, that is, to create similar mixing conditions (in the mortar structure) at the point of quality control processes. Trying to reflect the angularity issue, preferring the same mineralogical rocks, and other compatibilizing additives is considered as a situation where it is desired to give similar results at every point of the mixtures. Here, the increase in the standard deviation between samples is interpreted as differentiating the mixing conditions. The workability of the mixture is adversely affected by the increase in the hydrated lime ratio.

ITS values were performed on nine identical samples. Standard deviation between the strength values of these identical samples; for low and medium usage rates, it is smaller if the hydrated lime is mixed with AC. If the hydrated lime is mixed into AC at a low rate, the standard deviation between identical samples decreases, that is, the opportunity to produce a more homogeneous mixture. When the hydrated lime additive is used at high rates, the standard deviation value between samples exceeds 50kPa. This change (50 kPa) is valid for both addition types of hydrated lime. This result shows that asphalt mix mixing conditions are getting difficult.

The ITS values of nine samples in each option were examined. If HL is added to the fillers, higher ITS values are obtained for both unconditioned and conditioned samples. L0.5-L1.0-L1.5 mixtures, which express the incorporation of HL into the filler aggregate, and the L10-L20-L30 mixtures, which express the addition of AC (wet method) (one-to-one mixtures in terms of mixing ratio) were compared for nine samples. The range of variation of sample results was examined. These differences show that the load distribution capacity of the mixture changes. ITS values obtained for equivalent mixtures with different additive ratios were compared in terms of determining the highest and lowest variation range. Table 6-9 presents the highest and lowest limits.

The most important conclusions that can be drawn from the interpretation of the Table 9 are; in terms of indirect tensile strengths, it is more appropriate to use hydrated lime at low rates and as filler material. If hydrated lime is intended to be used at high rates as part of design analysis processes, it may be advisable to use lime in filler. Use as a high percentage of filler may be an alternative to use with a low rate of AC. However, this benchmark appears as an important issue for future research that requires research as a long-term performance problem. The method of adding to filler, according to the method of adding AC, is between 13% and 37% in the low rate of use of hydrated lime; it shows higher indirect tensile strength between 6%- 37% in medium usage rate and (- 2)% - 37% in high usage ratio. Low-medium rate in filler and low-rate use options in AC can be specified as a more accurate choice in terms of quality control. In cases where hydrated lime is compulsory or preferred for mixing into the AC in terms of central plant conditions, it is more reasonable to use it in AC in order to achieve the level of added value to filler.

*Table 6 - Tensile strength ratios according to hydrated lime addition method (L10)*

| L10             |       |       |       |       |       |       |       |       |       |  |
|-----------------|-------|-------|-------|-------|-------|-------|-------|-------|-------|--|
| <b>L0.5/L10</b> | S. 1  | S. 2  | S. 3  | S. 4  | S. 5  | S. 6  | S. 7  | S. 8  | S. 9  |  |
| S. 1            | 1.225 | 1.225 | 1.215 | 1.176 | 1.176 | 1.175 | 1.158 | 1.143 | 1.138 |  |
| S. 2            | 1.253 | 1.253 | 1.243 | 1.204 | 1.204 | 1.203 | 1.185 | 1.169 | 1.165 |  |
| S. 3            | 1.271 | 1.271 | 1.260 | 1.221 | 1.221 | 1.219 | 1.202 | 1.186 | 1.181 |  |
| S. 4            | 1.299 | 1.299 | 1.289 | 1.248 | 1.248 | 1.247 | 1.229 | 1.212 | 1.208 |  |
| L0.5 S. 5       | 1.306 | 1.306 | 1.295 | 1.254 | 1.254 | 1.253 | 1.235 | 1.218 | 1.214 |  |
| S. 6            | 1.313 | 1.313 | 1.302 | 1.261 | 1.261 | 1.260 | 1.242 | 1.225 | 1.220 |  |
| S. 7            | 1.339 | 1.339 | 1.329 | 1.287 | 1.287 | 1.285 | 1.267 | 1.250 | 1.245 |  |
| S. 8            | 1.349 | 1.349 | 1.338 | 1.296 | 1.296 | 1.294 | 1.275 | 1.258 | 1.254 |  |
| S. 9            | 1.372 | 1.372 | 1.361 | 1.318 | 1.318 | 1.317 | 1.298 | 1.280 | 1.276 |  |
| L10             |       |       |       |       |       |       |       |       |       |  |
| <b>L1.0/L10</b> | S. 1  | S. 2  | S. 3  | S. 4  | S. 5  | S. 6  | S. 7  | S. 8  | S. 9  |  |
| S. 1            | 1.182 | 1.182 | 1.172 | 1.135 | 1.135 | 1.134 | 1.117 | 1.102 | 1.098 |  |
| S. 2            | 1.209 | 1.209 | 1.199 | 1.162 | 1.162 | 1.160 | 1.144 | 1.128 | 1.124 |  |
| S. 3            | 1.254 | 1.254 | 1.244 | 1.205 | 1.205 | 1.204 | 1.186 | 1.170 | 1.166 |  |
| S. 4            | 1.257 | 1.257 | 1.247 | 1.208 | 1.208 | 1.207 | 1.189 | 1.173 | 1.169 |  |
| L1.0 S. 5       | 1.259 | 1.259 | 1.249 | 1.210 | 1.210 | 1.209 | 1.191 | 1.175 | 1.171 |  |
| S. 6            | 1.262 | 1.262 | 1.251 | 1.212 | 1.212 | 1.211 | 1.193 | 1.177 | 1.173 |  |
| S. 7            | 1.306 | 1.306 | 1.295 | 1.254 | 1.254 | 1.253 | 1.235 | 1.218 | 1.214 |  |
| S. 8            | 1.319 | 1.319 | 1.308 | 1.267 | 1.267 | 1.266 | 1.247 | 1.231 | 1.226 |  |
| S. 9            | 1.331 | 1.331 | 1.320 | 1.279 | 1.279 | 1.278 | 1.259 | 1.242 | 1.237 |  |
| L10             |       |       |       |       |       |       |       |       |       |  |
| <b>L1.5/L10</b> | S. 1  | S. 2  | S. 3  | S. 4  | S. 5  | S. 6  | S. 7  | S. 8  | S. 9  |  |
| S. 1            | 1.101 | 1.101 | 1.092 | 1.057 | 1.057 | 1.056 | 1.041 | 1.027 | 1.023 |  |
| S. 2            | 1.109 | 1.109 | 1.100 | 1.065 | 1.065 | 1.064 | 1.048 | 1.034 | 1.031 |  |
| S. 3            | 1.112 | 1.112 | 1.103 | 1.068 | 1.068 | 1.067 | 1.051 | 1.037 | 1.033 |  |
| S. 4            | 1.133 | 1.133 | 1.124 | 1.089 | 1.089 | 1.088 | 1.072 | 1.057 | 1.053 |  |
| L1.5 S. 5       | 1.145 | 1.145 | 1.135 | 1.100 | 1.100 | 1.098 | 1.082 | 1.068 | 1.064 |  |
| S. 6            | 1.158 | 1.158 | 1.149 | 1.112 | 1.112 | 1.111 | 1.095 | 1.080 | 1.076 |  |
| S. 7            | 1.161 | 1.161 | 1.152 | 1.115 | 1.115 | 1.114 | 1.098 | 1.083 | 1.079 |  |
| S. 8            | 1.212 | 1.212 | 1.202 | 1.165 | 1.165 | 1.163 | 1.146 | 1.131 | 1.127 |  |
| S. 9            | 1.288 | 1.288 | 1.278 | 1.237 | 1.237 | 1.236 | 1.218 | 1.202 | 1.197 |  |

Table 7 - Strength ratios according to hydrated lime addition method (L20)

| L20  |                 |       |       |       |       |       |       |       |       |       |
|------|-----------------|-------|-------|-------|-------|-------|-------|-------|-------|-------|
|      | <b>L0.5/L20</b> | S. 1  | S. 2  | S. 3  | S. 4  | S. 5  | S. 6  | S. 7  | S. 8  | S. 9  |
|      | S. 1            | 1.262 | 1.204 | 1.161 | 1.160 | 1.159 | 1.136 | 1.134 | 1.117 | 1.102 |
|      | S. 2            | 1.292 | 1.232 | 1.189 | 1.188 | 1.186 | 1.163 | 1.160 | 1.143 | 1.128 |
|      | S. 3            | 1.310 | 1.249 | 1.205 | 1.204 | 1.203 | 1.179 | 1.177 | 1.159 | 1.144 |
|      | S. 4            | 1.339 | 1.277 | 1.232 | 1.231 | 1.230 | 1.206 | 1.203 | 1.185 | 1.170 |
| L0.5 | S. 5            | 1.346 | 1.283 | 1.238 | 1.237 | 1.236 | 1.211 | 1.209 | 1.191 | 1.175 |
|      | S. 6            | 1.353 | 1.290 | 1.245 | 1.244 | 1.243 | 1.218 | 1.216 | 1.197 | 1.182 |
|      | S. 7            | 1.381 | 1.317 | 1.270 | 1.269 | 1.268 | 1.243 | 1.240 | 1.222 | 1.206 |
|      | S. 8            | 1.390 | 1.326 | 1.279 | 1.278 | 1.277 | 1.251 | 1.249 | 1.230 | 1.214 |
|      | S. 9            | 1.414 | 1.349 | 1.302 | 1.300 | 1.299 | 1.273 | 1.271 | 1.252 | 1.235 |
| L20  |                 |       |       |       |       |       |       |       |       |       |
|      | <b>L1.0/L20</b> | S. 1  | S. 2  | S. 3  | S. 4  | S. 5  | S. 6  | S. 7  | S. 8  | S. 9  |
|      | S. 1            | 1.218 | 1.161 | 1.121 | 1.120 | 1.118 | 1.096 | 1.094 | 1.078 | 1.064 |
|      | S. 2            | 1.246 | 1.189 | 1.147 | 1.146 | 1.145 | 1.122 | 1.120 | 1.103 | 1.089 |
|      | S. 3            | 1.293 | 1.233 | 1.190 | 1.189 | 1.187 | 1.164 | 1.161 | 1.144 | 1.129 |
|      | S. 4            | 1.296 | 1.236 | 1.193 | 1.191 | 1.190 | 1.167 | 1.164 | 1.147 | 1.132 |
| L1.0 | S. 5            | 1.298 | 1.238 | 1.195 | 1.193 | 1.192 | 1.168 | 1.166 | 1.149 | 1.134 |
|      | S. 6            | 1.300 | 1.240 | 1.196 | 1.195 | 1.194 | 1.170 | 1.168 | 1.151 | 1.136 |
|      | S. 7            | 1.346 | 1.283 | 1.238 | 1.237 | 1.236 | 1.211 | 1.209 | 1.191 | 1.175 |
|      | S. 8            | 1.359 | 1.296 | 1.251 | 1.250 | 1.249 | 1.224 | 1.221 | 1.203 | 1.187 |
|      | S. 9            | 1.372 | 1.308 | 1.263 | 1.261 | 1.260 | 1.235 | 1.233 | 1.214 | 1.199 |
| L20  |                 |       |       |       |       |       |       |       |       |       |
|      | <b>L1.5/L20</b> | S. 1  | S. 2  | S. 3  | S. 4  | S. 5  | S. 6  | S. 7  | S. 8  | S. 9  |
|      | S. 1            | 1.134 | 1.082 | 1.044 | 1.043 | 1.042 | 1.021 | 1.019 | 1.004 | 0.991 |
|      | S. 2            | 1.143 | 1.090 | 1.052 | 1.051 | 1.050 | 1.029 | 1.027 | 1.011 | 0.998 |
|      | S. 3            | 1.146 | 1.093 | 1.054 | 1.053 | 1.052 | 1.031 | 1.029 | 1.014 | 1.001 |
|      | S. 4            | 1.168 | 1.114 | 1.075 | 1.074 | 1.073 | 1.051 | 1.049 | 1.034 | 1.020 |
| L1.5 | S. 5            | 1.180 | 1.125 | 1.086 | 1.085 | 1.083 | 1.062 | 1.060 | 1.044 | 1.030 |
|      | S. 6            | 1.193 | 1.138 | 1.098 | 1.097 | 1.096 | 1.074 | 1.072 | 1.056 | 1.042 |
|      | S. 7            | 1.197 | 1.141 | 1.101 | 1.100 | 1.099 | 1.077 | 1.075 | 1.059 | 1.045 |
|      | S. 8            | 1.249 | 1.192 | 1.150 | 1.149 | 1.148 | 1.125 | 1.123 | 1.106 | 1.091 |
|      | S. 9            | 1.328 | 1.266 | 1.222 | 1.221 | 1.219 | 1.195 | 1.193 | 1.175 | 1.160 |

*Table 8 - Strength ratios according to hydrated lime addition method (L30)*

| L30  |                 |       |       |       |       |       |       |       |       |       |
|------|-----------------|-------|-------|-------|-------|-------|-------|-------|-------|-------|
|      | <b>L0.5/L30</b> | S. 1  | S. 2  | S. 3  | S. 4  | S. 5  | S. 6  | S. 7  | S. 8  | S. 9  |
|      | S. 1            | 1.302 | 1.223 | 1.192 | 1.159 | 1.144 | 1.135 | 1.127 | 1.124 | 1.088 |
|      | S. 2            | 1.333 | 1.252 | 1.220 | 1.186 | 1.170 | 1.162 | 1.154 | 1.151 | 1.114 |
|      | S. 3            | 1.351 | 1.269 | 1.237 | 1.203 | 1.187 | 1.178 | 1.170 | 1.167 | 1.129 |
|      | S. 4            | 1.382 | 1.298 | 1.264 | 1.230 | 1.214 | 1.204 | 1.196 | 1.193 | 1.155 |
| L0.5 | S. 5            | 1.388 | 1.304 | 1.270 | 1.236 | 1.219 | 1.210 | 1.202 | 1.199 | 1.160 |
|      | S. 6            | 1.396 | 1.311 | 1.277 | 1.243 | 1.226 | 1.217 | 1.209 | 1.205 | 1.167 |
|      | S. 7            | 1.424 | 1.338 | 1.303 | 1.268 | 1.251 | 1.241 | 1.233 | 1.230 | 1.191 |
|      | S. 8            | 1.434 | 1.347 | 1.312 | 1.277 | 1.260 | 1.250 | 1.242 | 1.238 | 1.199 |
|      | S. 9            | 1.459 | 1.371 | 1.335 | 1.299 | 1.282 | 1.272 | 1.263 | 1.260 | 1.220 |
| L30  |                 |       |       |       |       |       |       |       |       |       |
|      | <b>L1.0/L30</b> | S. 1  | S. 2  | S. 3  | S. 4  | S. 5  | S. 6  | S. 7  | S. 8  | S. 9  |
|      | S. 1            | 1.256 | 1.180 | 1.150 | 1.118 | 1.103 | 1.095 | 1.088 | 1.085 | 1.050 |
|      | S. 2            | 1.286 | 1.208 | 1.177 | 1.145 | 1.129 | 1.121 | 1.113 | 1.110 | 1.075 |
|      | S. 3            | 1.334 | 1.253 | 1.221 | 1.187 | 1.171 | 1.163 | 1.155 | 1.152 | 1.115 |
|      | S. 4            | 1.337 | 1.256 | 1.224 | 1.190 | 1.174 | 1.165 | 1.158 | 1.154 | 1.118 |
| L1.0 | S. 5            | 1.339 | 1.258 | 1.226 | 1.192 | 1.176 | 1.167 | 1.160 | 1.156 | 1.119 |
|      | S. 6            | 1.341 | 1.260 | 1.228 | 1.194 | 1.178 | 1.169 | 1.161 | 1.158 | 1.121 |
|      | S. 7            | 1.388 | 1.304 | 1.270 | 1.236 | 1.219 | 1.210 | 1.202 | 1.199 | 1.160 |
|      | S. 8            | 1.402 | 1.318 | 1.283 | 1.249 | 1.232 | 1.222 | 1.214 | 1.211 | 1.172 |
|      | S. 9            | 1.415 | 1.330 | 1.295 | 1.260 | 1.243 | 1.234 | 1.226 | 1.222 | 1.183 |
| L30  |                 |       |       |       |       |       |       |       |       |       |
|      | <b>L1.5/L30</b> | S. 1  | S. 2  | S. 3  | S. 4  | S. 5  | S. 6  | S. 7  | S. 8  | S. 9  |
|      | S. 1            | 1.170 | 1.099 | 1.071 | 1.042 | 1.028 | 1.020 | 1.013 | 1.010 | 0.978 |
|      | S. 2            | 1.179 | 1.108 | 1.079 | 1.050 | 1.035 | 1.028 | 1.021 | 1.018 | 0.985 |
|      | S. 3            | 1.182 | 1.111 | 1.082 | 1.052 | 1.038 | 1.030 | 1.024 | 1.021 | 0.988 |
|      | S. 4            | 1.205 | 1.132 | 1.103 | 1.073 | 1.058 | 1.050 | 1.043 | 1.040 | 1.007 |
| L1.5 | S. 5            | 1.217 | 1.143 | 1.114 | 1.083 | 1.069 | 1.061 | 1.054 | 1.051 | 1.017 |
|      | S. 6            | 1.231 | 1.157 | 1.127 | 1.096 | 1.081 | 1.073 | 1.066 | 1.063 | 1.029 |
|      | S. 7            | 1.234 | 1.160 | 1.130 | 1.099 | 1.084 | 1.076 | 1.069 | 1.066 | 1.032 |
|      | S. 8            | 1.289 | 1.211 | 1.180 | 1.148 | 1.132 | 1.124 | 1.116 | 1.113 | 1.077 |
|      | S. 9            | 1.370 | 1.287 | 1.253 | 1.219 | 1.203 | 1.194 | 1.186 | 1.183 | 1.145 |

Table 9 - Min. & max. strength increase rates according to hydrated lime addition method

|          | Min. strength increase ratio | Max. strength increase ratio | Difference |
|----------|------------------------------|------------------------------|------------|
| L0.5/L10 | 1.138                        | 1.372                        | 0.234      |
| L0.5/L20 | 1.102                        | 1.414                        | 0.312      |
| L0.5/L30 | 1.088                        | 1.459                        | 0.371      |
| L1.0/L10 | 1.098                        | 1.331                        | 0.233      |
| L1.0/L20 | 1.064                        | 1.372                        | 0.308      |
| L1.0/L30 | 1.050                        | 1.415                        | 0.365      |
| L1.5/L10 | 1.023                        | 1.288                        | 0.265      |
| L1.5/L20 | 0.991                        | 1.328                        | 0.337      |
| L1.5/L30 | 0.978                        | 1.370                        | 0.392      |

### 3.2. Moisture Damage Evaluation

The tensile strength ratios of the modified mixtures were calculated by proportioning the conditioned tensile strength to the unconditioned. The ratios calculated using the average tensile strengths were given in Figure 3.

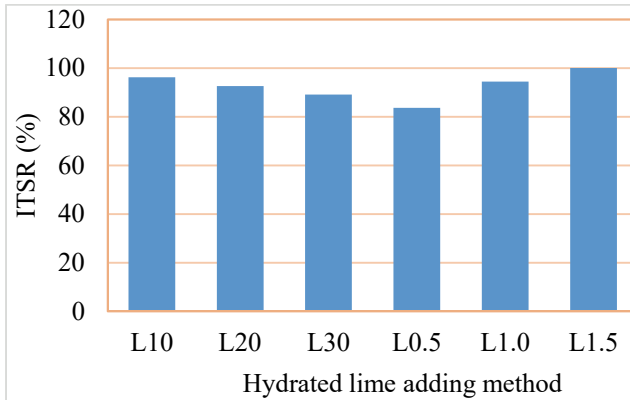


Figure 3 - ITSR – lime adding method interaction (conditioned/unconditioned)

When acceptable limit that the mixture shows sufficient resistance against water damage was taken as 80%; it can be stated that all mixtures show sufficient resistance to stripping (Figure 3). At the point of interpretation of stripping damage, if the hydrated lime is added to the AC, the resistance to water damage partially decreases with the increase in the rate of use. In terms of water damage performance, it is considered a more correct approach to add hydrated lime to AC at lower rate. But; in case the hydrated lime is added to the filler aggregate, the water damage resistance increases with the increase in usage rate. In terms of water damage resistance, it is more accurate to use hydrated lime with low AC, medium and high filler.

When used at low rates in AC, the capacity of binding and wetting the aggregate is increased, and when used with filler, it is understood that the aggregate harmonizes the surface energy and creates better binding.

In terms of average stripping resistance; with low hydrated lime content, if lime is added to the mixture (as filler), it shows higher water damage resistance (12% more) than adding the AC. However, if the hydrated lime content is increased to medium and high levels, mixing lime to AC creates lower water damage resistance than adding it as filler. It is known that hydrated lime shows its effect in the presence of water. The reactions occur with the entry of water into the mortar and reach the stability to function under the damage systems that occur over time. With the applied Lottman water damage modeling, ITR values of all mixtures (conditional/unconditional) are given. In case the hydrated lime is added directly to the bituminous binder, according to the fillers' aggregation system, 1% higher water damage resistance at moderate rate and 11% higher water damage resistance is obtained in the upper usage rate.

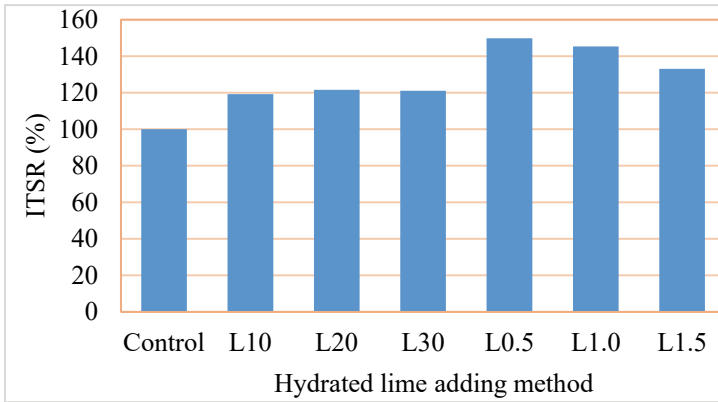


Figure 4 - Average ITR values for all mixtures (conditioned/control-conditioned)

At the point of active and passive adhesion, the indirect tensile strength of conditioned averages of each mixture type were divided by the average of unconditioned strength values of the same mixture and stripping damage ratios were obtained. Figure 4 shows these conditioned/unconditioned ratio values. It is understood that the selected Modified Lottman water damage conditioning model creates an observable damage in all mixtures.

An evaluation was made by proportioning the conditioned strength averages of each modified mixture to the average control-unconditioned strength values of the no additive mixtures. All modified mixtures show 20% to 40% higher water damage resistance than base mixtures, as seen in Figure 5. However, if the hydrated lime is mixed with filler, there are higher water damage resistance values compared to AC, which means that there is approximately 20% more resistance.

In Figure 5, there are basic ratios expressing the interpretation of stripping damage: The hydrated lime increases the resistance of water damage in all cases, creates similar water damage resistance for all usage rates when added to the AC, and its low rate is considered

sufficient, higher water damage resistances are obtained in case of addition to filler. It can be emphasized that the water damage resistance decreases as the addition rate to filler increases, and it is more logical to use it in low AC in terms of water damage resistance.

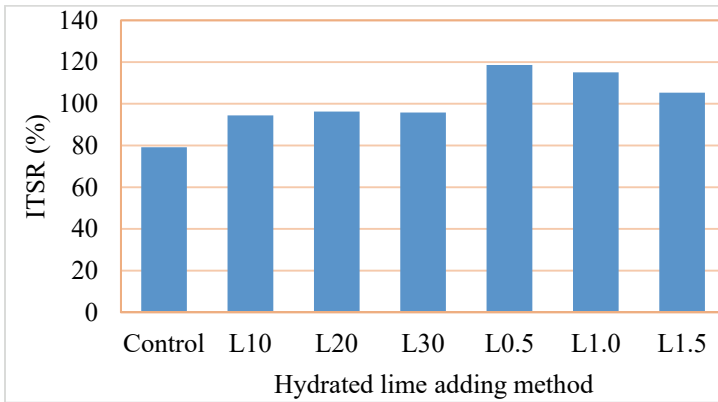


Figure 5 - Average ITSR values for asphalt mixtures (conditioned/control-unconditioned)

In low lime content, if lime is added to the mixture (filler), water damage ratios show, on average, higher water damage resistance (15% more) than lime being added to the AC. However, if the lime content is increased to medium and high levels, mixing lime to AC creates higher water damage resistance than adding it as filler. Participation in AC creates a 6% water resistance in medium use and 12% in high use. In terms of interpretation of water damage, in this study, the Modified Lottman test was used and the average of 27 values was used in each mixture; if the hydrated lime is used at a low rate, it is seen that higher values are obtained in terms of both water damage and indirect tensile strength. It is considered more reasonable to add hydrated lime to filler at a low rate under these conditions.

Asphalt mixtures modified with HL using wet method showed better performance properties as compared to mixtures modified with HL using dry or slurry method ones. This could be attributed to the best coverage of aggregate surfaces with HL in the case of wet method. Overall description aids that the wet method is better than dry or slurry methods in spite of the little effect on Marshall and water susceptibility test results when comparing all the test result and seems to provide better performance for pavement courses. Application of HL decreased the Marshall Stability values of asphalt mixtures by a little effect but increased Indirect Tensile strength by more than 10%. Wet method gave the highest ITS values with respect to method of HL application in increasing fatigue properties of asphalt. ITS ratios show that the samples have resistance against water susceptibility. Therefore, the addition of HL in all three methods improve the water susceptibility properties [21].

HL has been added to asphalt pavements for many years. HL rehabilitates asphalt pavement mixes in many ways and improves performance. It has been observed that the use of HL in asphalt mixtures is beneficial. There is still confusion as to the appropriate method for obtaining the criteria of the optimum modification of HL. Methods are discussed. HL modification is done in different ways. Mixture modifications can be made by adding dry HL to dry or wet aggregates or by adding lime mortar to dry aggregates. The mechanical and

fatigue properties of asphalt mixes were evaluated using different application methods. Mechanical and simulative tests, namely ITS test, elastic modulus test and controlled stress fatigue test were applied. The overall results showed that regardless of the method of adding HL to the mixtures, the mechanical and fatigue properties were generally improved by adding HL. Mechanical test results were sensitive to the method of adding HL to mixtures, unlike fatigue tests. Mixtures modified with HL added in the form of mortar showed the best results compared to mixtures modified with HL using the dry and wet methods [23].

The performance of hot mix asphalts modified with rubber with HL additive was investigated. HL was added in three different ways: dry-wet method and mortar method. The performance of the defined mixtures was examined according to ITS, modulus of elasticity, fracture resistance, fatigue life and creep compliance. Fracture strength and fatigue life were determined using the semi-circular bending test and split tension-controlled stress fatigue test, respectively. A power law model was used to characterize the creep compliance behaviour of the studied asphalt mixtures. The crumb rubber content of 15% by weight of the bituminous binder and the HL content of 3% by weight of the total mixture were included for all samples tested. The test temperature was kept constant as 35°C. HL treatment increased ITS, hardness, fatigue strength, fracture resistance and permanent deformation properties of rubber modified HMA blends. The mixtures contain HL added using the wet method, meeting the highest ITS, modulus of elasticity, fracture resistance and lowest creep compatibility. The fatigue life of the mixtures tested showed less dependence on the HL application method [24].

One of the common anti-stripping additives, HL, is considered to improve the properties of asphalt mixture in resisting water damage. The HL application process can be introduced to asphalt mixture by either adding dry HL to wet aggregates or adding HL slurry to dry aggregates. This study goals to evaluate the laboratory performance-based properties of asphalt mixtures using two different HL application processes as well as to compare between HL-modified and polymer modified asphalt mixture. Results showed that the performance of HL modified asphalt mixture in moisture damage and rutting resistance is related to the HL application processes. Adding HL to asphalt binder is an effective and economical method to improve performance of asphalt mixture in moisture damage and rutting resistance [25].

HL has traditional been preferred in asphalt mixtures primarily for increasing the water damage resistance of bituminous mixtures. Most available literature is about studies realized on mixes in which HL was added as filler material. It was explored that the effect of different proportions of HL added by two different methods (wet and dry methods) on the rutting performance of bituminous mixes. The rutting characteristics of unmodified and HL modified binders were evaluated in terms of superpave binder rutting parameter ( $G^*/\sin\delta$ ) and non-recoverable creep compliance. Mix rutting performance was measured in terms of  $E^*$ ,  $E^*/\sin\phi$ , flow number and accumulated strain measured in dynamic creep test. Rutting performance of mixes improved significantly by HL modification. Wet method of addition of HL has significantly higher beneficial effect than the dry method. Flow number determined at 60°C showed the beneficial effect of HL more distinctly compared with the dynamic creep test conducted at 40°C. The beneficial effect of HL addition in reducing rutting was realized more at higher mix temperatures [26].

The use of both HL addition methods exhibited a good resistance against the moisture damage, an increase in ITSR is achieved by 4.2%, 5.3%, 5.9% 10.9%, 12% and 9.0% for dry

HL replacement method and 3.4%, 6%, 18.8%, 20.8% and 19.8% for wet HL replacement method corresponding to 1.0, 1.5, 2.0 and 3.0 HL contents, respectively. The wet addition method was more effective than the dry method in improving the resistance to moisture induced damage of asphalt concrete pavement modified with HL. The permanent deformation parameters, slope and intercept, was significantly affected using dry and wet HL addition methods employing different percentages of HL and this effects are more pronounced at high testing temperatures. The HL modified mixed with 2.5 percent in dry method and wet method result in a decrease in permanent deformation slope at higher temperature of 40°C and 60°C as compared to control mixture with no HL [27].

Depending on the methods of adding hydrated lime to asphalt mixtures and different addition rates in different adding methods; in the point of evaluating of proportional water damage based on indirect tensile strength test and Lottman water damage conditioning, the discrimination of the selected methodologies was found to be superior.

The effectiveness of hydrated lime additive, which is a performance enhancer in asphalt pavements, is directly related to the degree of performance, the method of adding the mixes and the ratio of addition. Hydrated lime reveals different performance levels according to the method of addition.

In terms of average water damage rates; When lime is added to the mixture at low lime content, it shows higher water damage resistance (15% more) than AC. However, if the lime content is increased to medium and high levels, mixing lime into AC creates higher water damage resistance than adding lime as filler. Inclusion in AC, according to filler joining aggregate; it creates 6% higher water damage resistance in medium use and 12% higher in high use. It is considered more logical to add hydrated lime to the filler at a low rate under these conditions. It appears that the Lottman water damage conditioning model chosen causes observable damage to all mixtures. Hydrated lime increases the resistance to water damage in all cases, creates similar water damage resistance for all usage rates in case of AC addition, and its low rate is sufficient, higher water damage resistance is obtained in the case of adding to filler, water damage resistance decreases with the increase of the added ratio to filler, water damage, it can be emphasized that it is more logical to use it in low AC in terms of resistance.

Depending on the methods of joining hydrated lime into asphalt mixtures and different additive rates in different addition methods; The discrimination of the selected methodologies was found to be superior at the point of interpretation of proportional water damage based on the indirect tensile strength test and Lottman water damage conditioning. The efficiency of the hydrated lime additive used, which is a performance enhancer in asphalt pavements, is directly related to the degree of performance, the method of addition to the mixtures and the rate of addition. Hydrated lime reveals different performance levels according to the addition method.

#### **4. CONCLUSIONS**

With this research, it is possible to reach the following conclusions.

The use of HL as a part of the AC gives higher ITS values. HL increases ITS values. If HL is used as part of the fillers, ITS values decrease for HL ratios increasing from low to high. It is considered appropriate to use HL as a part of filler at a low rate.

The increase in the standard deviation in terms of performance between identical samples with the increase of the HL rate requires attention to the quality control process in terms of field conditions. HL should be used at a low rate in AC.

Although low use of AC seems to be equivalent to high use in fillers, the issue should be examined in terms of long-term performance, for example, fatigue strength.

Increasing use of HL in AC reduces water damage resistance. Increasing use with filler increases water damage resistance. It is recommended to use with AC at a low rate and with filler for medium-high rates. Using with AC at a low rate creates a more homogeneous mixture.

Modified Lottman water damage conditioning reduces ITS values and gives distinctive results.

### **Symbols**

**AC** : Asphalt cement

**HL** : Hydrated lime

**HMA** : Hot mix asphalt

**ITS** : Indirect tensile strength

**ITSR** : Indirect tensile strength ratio

### **References**

- [1] Preti, F., Accardo, C., Gouveia, B. C. S., Romeo, E., Tebaldi, G. (2020). Influence of high-surface-area hydrated lime on cracking performance of open-graded asphalt mixtures. *Road Materials and Pavement Design*, 1-7.
- [2] Lesueur, D., Denayer, C., Ritter, H.-J., Kunesch, C., Gasiorowski, S., d'Alto, A. (2016). The use of hydrated lime in the formulation of asphalt mixtures: European case studies. *E&E Congress 2016, 6th Eurasphalt & Eurobitume Congress, Prague, Czech Republic*
- [3] Roberto, A., Romeo, E., Montepara, A., & Roncella, R. (2020). Effect of fillers and their fractional voids on fundamental fracture properties of asphalt mixtures and mastics. *Road Materials and Pavement Design*, 21(1), 25-41.
- [4] Peterson, J.C. (1998). Lime-treated pavements offer increased durability. *Roads and Bridges Journal* 26(1), 85-87.
- [5] Wang, H., Al-Qadi, I. L., Faheem, A. F., Bahia, H. U., Yang, S. H., Reinke, G. H. (2011). Effect of mineral filler characteristics on asphalt mastic and mixture rutting potential. *Transportation Research Record*, 2208(1), 33-39.
- [6] Rashwan, N.K. (2016). Hot Mix Asphalt (HMA) performance as affected by limestone powder filler content. *World Applied Sciences Journal* 34 (2), 237-244.

- [7] Han, S., Dong, S., Yin, Y., Liu, M., Liu, Y. (2020). Study on the effect of hydrated lime content and fineness on asphalt properties, *Construction and Building Materials*, 244, 118379.
- [8] Sebaaly, P. E., Little, D. N., Epps, J. A. (2006). The benefits of hydrated lime in hot mix asphalt. Prepared for the National Lime Association, April 2006
- [9] Lesueur, D. (2010). Hydrated lime: A proven additive for durable asphalt pavements–Critical literature review. Brussels: European Lime Association (EuLA) Ed. 2010.
- [10] Little, D. N., Petersen, J. C. (2005). Unique effects of hydrated lime filler on the performance-related properties of asphalt cements: Physical and chemical interactions revisited. *Journal of Materials in Civil Engineering*, 17(2), 207-218.
- [11] Han, S., Dong, S., Liu, M., Han, X., Liu, Y. (2019). Study on improvement of asphalt adhesion by hydrated lime based on surface free energy method. *Construction and Building Materials*, 227, 116794.
- [12] Huang, S. C., Robertson, R. E., Branthaver, J. F., Petersen, J. C. (2005). Impact of lime modification of asphalt and freeze–thaw cycling on the asphalt–aggregate interaction and moisture resistance to moisture damage. *Journal of Materials in Civil Engineering*, 17(6), 711–718.
- [13] Hicks, R. G., Scholz, T. V. (2003). Life Cycle Costs for Lime in Hot Mix Asphalt, Report & Software for National Lime Association
- [14] Souliman, M. I., Piratheepan, M., Hjj, E. Y., Sebaaly, P. E., Sequeira, W. (2015). Impact of lime on the mechanical and mechanistic performance of hot mix asphalt mixtures. *Journal of Road Materials and Pavement Design*, 16(2), 421–444.
- [15] Guo, N. S., Wang, C., Zhao, Y. H. (2014). Pavement performance of asphalt mixtures containing silica. *Journal of Dalian Maritime University*, (2), 29.
- [16] Barbhuiya, S., & Caracciolo, B. (2019). Effects of hydrated lime on mechanical behaviour of asphalt concrete at nanoscale. *Proceedings of the Institution of Civil Engineers-Construction Materials*, 172(2), 116-122.
- [17] Rasouli, A., Kavussi, A., Qazizadeh, M. J., & Taghikhani, A. H. (2018). Evaluating the effect of laboratory aging on fatigue behavior of asphalt mixtures containing hydrated lime. *Construction and Building Materials*, 164, 655-662.
- [18] Al-Tameemi, A. F., Wang, Y., Albatyati, A., & Haynes, J. (2019). Moisture Susceptibility and Fatigue Performance of Hydrated Lime–Modified Asphalt Concrete: Experiment and Design Application Case Study. *Journal of Materials in Civil Engineering*, 31(4), 04019019.
- [19] General Directorate of Highways of Turkey (2013), Highway Technical Specifications, General Directorate of Highways of Turkey, Ankara, Turkey.
- [20] İskender, E., Sayın, A., Aksoy, A., İskender, C. (2020). Evaluation of the Effect of Glass Granule Size on Water Damage Performance of Asphalt Mixtures. *Teknik Dergi*, 31 (6), 10399-10411.

- [21] Dan-Ali, F. M., Tuncan, A., Onur, M. İ., Evirgen, B., Tuncan, M. (2015). Investigation of Hydrated Lime Effect in Asphalt Pavements. *Bilecik Őeyh Edebalı Üniversitesi Fen Bilimleri Dergisi*, 2(2), 25-34.
- [22] Varlı Bingöl, B. (2019). Investigation of the effect of hydrated lime on low temperature cracking of asphalt concrete. Doctorate Thesis, Middle East Technical University, Ankara.
- [23] Diab, A., You, Z., Othman, A. M., Ahmed, H. Y. (2012). Effect of hydrated lime application method on mechanical and fatigue properties of HMA. *Multimodal Transportation Systems-Convenient, Safe, Cost-Effective, Efficient*, 3327-3334.
- [24] Othman, A. M. (2011). Evaluation of hydrated lime effect on the performance of rubber-modified HMA mixtures. *Journal of Elastomers & Plastics*, 43(3), 221-237.
- [25] Atud, T. J., Kanitpong, K., & Martono, W. (2007). Laboratory evaluation of hydrated lime application process in asphalt mixture for moisture damage and rutting resistance. *Transportation Research Board 86th annual meeting*, Washington, DC.
- [26] Kakade, V. B., Reddy, M. A., & Reddy, K. S. (2018). Rutting performance of hydrated lime modified bituminous mixes. *Construction and Building Materials*, 186, 1-10.
- [27] Albayati, A. H. K., & Mohammed, A. M. (2016). Effect of Lime Addition Methods on Performance Related Properties of Asphalt Concrete Mixture. *Journal of Engineering*, 22(9), 1-20.



# **Fully Implicit Form of Differential Quadrature Method for Multi-Species Solute Transport in Porous Media**

**Amin GHAREHBAGHI<sup>1</sup>**

## **ABSTRACT**

Solute transport problems, including sequential multi-species transport phenomena, frequently occur in soil systems. The goal of this paper is to present a novel one-dimensional numerical model with a fully implicit form of differential quadrature method for solving multi-species solute transport equations. The analytical results of three multi-species solute dispersion problems with three- and four-chain members are used to analyse the developed model. Simultaneously, the outcomes of the developed model are compared with the performance of the fully implicit fourth-order finite difference method. Finally, the accuracy of the established model is discussed and evaluated. According to the numerical experiments, the derived model is very useful and widely applicable.

**Keywords:** Multi-species, solute transport, porous media, Fully Implicit Differential Quadrature Method, Fully Implicit Fourth-Order Finite Difference Method.

## **1. INTRODUCTION**

To manage groundwater and surface water resources, the estimation of the solute and contaminant transport phenomena is significant. Due to the impact of this issue in human life, numerous experimental studies carried out in this field, and various numerical and analytical models have been developed by researchers. Nevertheless, most of the analytical and numerical models developed only for describing single-member transport of various contaminants (Kumar et al., 2010; Savovic and Djordjevich 2012; Singh et al., 2012; Gharehbaghi 2016 & 2017; Ciftci, 2017; Das et al., 2018; among many). But, the transport processes of some dangerous contaminants, e.g., pesticides and their degradation products, generally include a more complicated series of first-order or pseudo-first-order decay. Accordingly, single-member transport models cannot calculate the process of degradable contaminants transformation from the parent species to the daughter species. In other respects, mostly analytical solutions have specific and restricted enforcements. Therefore, one-, two-, or three-dimensional (1D, 2D, 3D) analytical solutions in this field (e.g., Van Genuchten 1985, Sun 1999 et al., Chaudhary and Singh 2020) have their limitations. To the

---

Note:

- This paper has been received on July 28, 2021 and accepted for publication by the Editorial Board on November 29, 2021.
- Discussions on this paper will be accepted by September 30, 2022.
- <https://doi.org/10.18400/tekderg.975457>

<sup>1</sup> Hasan Kalyoncu University, Civil Engineering Department, Gaziantep, Turkey  
amin.gharehbaghi@hku.edu.tr - <https://orcid.org/0000-0002-2898-3681>

best of author's knowledge, in numerical modeling, most scientists prefer to employ one of the conventional methods such as finite difference method (FDM), finite element method (FEM), or finite volume method (FVM). (Gharehbaghi et al., 2017). However, new numerical techniques such as the differential quadrature method (DQM), have many advantages over the traditional methods. One of the advantages of DQM is that it could calculate more accurate outcomes by using a small number of nodes in space and time. Moreover, DQM normally prevents confusion and linearization to obtain more accurate solutions of given nonlinear equations. As a global numerical method, DQM employs more points in the model domain to estimate the functional value of a certain point. Therefore, it provides rapidly converging and more reliable results than FEM or FDM, particularly in nonlinear problems (Chen and Zhong, 1997). The traditional numerical techniques are developed on relatively complicated mathematical derivations and require sophisticated mathematical calculations; more struggle in the discretization process. "The DQM is capable of producing solutions at high accuracy, with fewer grid points, comparatively little computational effort and less storage requirements" (Ciftci 2017). According to the study carried out by Gharehbaghi (2016), the fully implicit form of the solution with DQM (IDQM) obtained more accurate outcomes than the explicit form. Consequently, in this paper, the author employed IDQM. The summaries of several studies, related to this paper in 1D form, are presented as follows:

Konikow and Bredehoeft (1978) developed a 2D numerical model, called MOC, by employing an implicit form of FDM to determine the average linear flow velocities. Subsequently, these calculated values are employed to solve the transport equation by applying the method of characteristics. Later, Essaid and Bekins (1997) improved the MOC and named it BIOMOC. They announced that the BIOMOC model simulated the 2D transport and biotransformation of multiple reacting solutes. Massoudieh and Ginn (2007) presented an integrated unsaturated flow and colloid-facilitated contaminant transport model for multiple species with competitive sorption. They announced that the unsaturated flow part of the model and colloid-facilitated transport part of the model solved employing a semi-implicit FDM with Crank–Nicholson time weighing scheme, and fully coupled implicit FDM with dynamic blocking function  $B$  evaluated explicitly from the previous time step, respectively. Chen-Charpentier et al., (2009) presented a numerical model for the flow, the transport of nutrients and contaminants, and the growth of two types of microorganisms in porous media to gain a better understanding of the interactions between two microbial species as part of a single biofilm capable of performing multiple functions (bioremediation, biofilm formation, etc.). They solved the coupled system of equations by using mixed-finite elements for the flow and a non-standard method for the transport equations. Natarajan and Kumar (2010) proposed an alternative approach to the decomposition method for solving multispecies transport in porous media coupled with first-order reactions. They developed the numerical solution based on the implicit FDM. Ramos et al., (2011) carried out several experimental studies and employed HYDRUS-1D software package based on the Galerkin-type linear finite element schemes to assess soil salinization and sodification risks. Torlapati (2013) established a multi-component reactive transport model to simulate the fate and transport of biochemical and geochemical reactive transport problems in 1D conditions. He employed explicit forms of backward difference FDM and total variation diminishing schemes and fully implicit approaches for solving the governing equations. Bagalkot and Kumar (2015) carried out a 1D numerical analysis on multispecies radionuclide transport in

a single-horizontal coupled fracture-matrix system by FDM. They considered Linear, Langmuir, and Freundlich adsorption isotherms and the results from each were compared. Sharma et al., (2016) by using constant, linear, and exponential dispersivity functions investigated the influence of distance-dependent dispersion on the multispecies solute transport process. They used implicit FDM and discretized the governing equations with upwind and central difference schemes. Engdahl and Aquino (2018) studied the possibility of backward-in-time simulations on nonlinear reactive transport systems in an operational sense. They simulated a steady-state flow field employing a second-order, cell-centered implicit FDM. Zhang et al., (2018) suggested a 1D model based on the Maxwell-Stefan diffusion theory and the MCL equation. Moreover, numerical simulation was carried out using the finite element software COMSOL Multiphysics. Pathania et al., (2020) suggested a numerical model based on the meshless element-free Galerkin method to predict the groundwater flow and multispecies reactive transport coupled with sequential decay reactions in unconfined aquifers. They compared the results of the developed model with FDM, FEM, and MODFLOW-RT3D.

The motive for this research is to provide a powerful and effective mathematical model based on the fully implicit form of the DQM for the first time for solving the multi-species solute transport phenomenon in 1D form with advection-dispersion equation (ADE). Unlike other researchers, who generally deal with the problem explicitly, in this research, I have considered the fully implicit form of the solution. In this paper, three analytical solutions are extracted from the studies of Bauer et al., (2001) and Pérez Guerrero et al., (2009) to assess the outcomes of the derived model. Likewise, the fully implicit fourth-order finite difference method (IFOFDM) is developed and employed to examine the performance of the enforced scheme in the established model.

## 2. PROBLEM FORMULATION

A series of chemical intermediates or radionuclides coupled with first-order decay processes form a decay chain. From the mathematical point of view, for reactive multi-species solute transport that is subject to linear equilibrium sorption and includes a sequential first-order decay chain, the governing equations are written as follows: (Bauer et al. 2001; Pérez Guerrero et al. 2009):

$$R_m \frac{\partial c_m}{\partial t} = D \frac{\partial^2 c_m}{\partial x^2} - v \frac{\partial c_m}{\partial x} - R_m \lambda_m c_m + R_{m-1} \lambda_{m-1} c_{m-1}; \quad m = 1, \dots, M; \quad \lambda_0 = 0; \quad 0 < x < \infty; \quad t > 0; \quad (1)$$

where  $c_m$ ,  $R_m$ ,  $D$ ,  $v$ ,  $\lambda_m$ ,  $x$ , and  $t$  are the concentration of the  $m^{\text{th}}$  member of the decay chain formed by  $M$  species, the retardation coefficient for the  $m^{\text{th}}$  species, the dispersion coefficient, the constant pore water velocity, the first-order decay constant for the  $m^{\text{th}}$  species, the longitudinal axis, and time, respectively. To simplify in Eq. (1), instead of  $R_m \lambda_m$ , the symbol of  $k_m$  is used.

### 3. NUMERICAL INVESTIGATION

As underlined earlier, in this paper, a fully implicit form of solution for two different numerical methods (i.e., IDQM and IFOFDM) is employed to solve the governing equations. The chief idea behind DQM is based on the Gauss Quadrature method. “Extending Gauss quadrature to finding the derivatives of various orders of a differentiable function gives rise to differential quadrature” (Bellman and Casti, 1971). For the first time, Bellman introduced this method. Afterward, other researchers such as Shu (2000), Civalek (2004), Kaya (2010), Kaya and Arisoy (2011), Gharehbaghi (2016) tried to improve and apply this technique to the various fields of engineering. About this study, even though the suggested model has no restrictions on the number of multi-species since the analytical solutions applied were developed for a maximum of four species, solutions for four species are presented in this paper. In this step, the numerical solution of IDQM for the first member by substituting the value of  $m$  as one in Eq. (1) (i.e.,  $m=1$ ) is given as follows:

$$R_1 \frac{\partial C_1}{\partial t} = D \frac{\partial^2 C_1}{\partial x^2} - v \frac{\partial C_1}{\partial x} - k_1 C_1 \quad 0 < x < \infty, \quad t > 0 \tag{2}$$

Based on the DQM, the first- and second-order derivatives for each node are arranged as follows:

$$\frac{\partial C_1}{\partial x} = \sum_{j=1}^N a_{ij} C_{1j} = (a_{i1} C_{11} + a_{i2} C_{12} + a_{i3} C_{13} + \dots + a_{iN} C_{1N}) \tag{3}$$

$$\frac{\partial^2 C_1}{\partial x^2} = \sum_{j=1}^N b_{ij} C_{1j} = (b_{i1} C_{11} + b_{i2} C_{12} + b_{i3} C_{13} + \dots + b_{iN} C_{1N}) \tag{4}$$

where  $a_{ij}$  and  $b_{ij}$  are the weighting coefficients of the first- and second-order derivatives, respectively. With respect to the notations of the DQM, Eq. (5) is rewritten as follows

$$R_1 \frac{\partial C_1}{\partial t} = D \sum_{j=1}^N b_{ij} C_{1j} - v \sum_{j=1}^N a_{ij} C_{1j} - k_1 C_1 \tag{5}$$

The values of weighting coefficients are calculated by the following relations (Zong and Zhang, 2009):

$$a_{ij} = \frac{1}{(x_j - x_i)} \prod_{\substack{k=1 \\ k \neq i, j}}^N \frac{x_i - x_k}{x_j - x_k} \quad i, j = 1, 2, \dots, N; \quad i \neq j \tag{6}$$

$$a_{ii} = - \sum_{\substack{j=1 \\ j \neq i}}^N a_{ij} \quad i, j = 1, 2, \dots, N \tag{7}$$

$$b_{ij} = 2 \left[ a_{ij} \cdot a_{ii} - \frac{a_{ij}}{(x_j - x_i)} \right] \quad i, j = 1, 2, \dots, N; \quad i \neq j \tag{8}$$

$$b_{ii} = - \sum_{\substack{j=1 \\ j \neq i}}^N b_{ij} \quad i, j = 1, 2, \dots, N \tag{9}$$

where  $\Pi$  denotes the product sign. To calculate the node distributions several approaches were proposed by the experts. “It can be selected with equal intervals, or non-equal intervals like Chebyshev–Gauss–Lobatto grid points, or with the normalization of the routes of Legendre polynomials” (Shu, 2000). According to the results of previous researches, including the author’s, the approaches proposed by Chebyshev-Gauss-Lobatto for grid points provided the most suitable node distributions in DQM. Therefore, in the present study, this approach is used as follows:

$$x_i = x_1 + \frac{1}{2} \left( 1 - \cos \frac{i-1}{N-1} \pi \right) (x_n - x_1) \quad i = 1, 2, \dots, N \tag{10}$$

And the derivative of the time for the first-order for point  $i$  is substituted by the following relation:

$$\frac{\partial c_{1i}}{\partial t} = \frac{c_{1i}^t - c_{1i}^{t-\Delta t}}{\Delta t} \tag{11}$$

where  $c_{1i}^t$  and  $c_{1i}^{t-\Delta t}$  are the values at time level  $t$  (new-time) and time level  $t-\Delta t$  (old-time), respectively. By using this expression, Eq. (5) is re-written as follows:

$$R_1 \frac{c_{1i}^t - c_{1i}^{t-\Delta t}}{\Delta t} = D \sum_{j=1}^N b_{ij} c_{1j} - v \sum_{j=1}^N a_{ij} c_{1j} - k_1 c_{1i} \tag{12}$$

By selecting the values of the right-hand side of Eq. (12) as  $t$ , it means that the solution is calculated in fully implicit form. Thus, by employing some manipulations, the ultimate form of fully implicit solution is given as follows:

$$c_{1i}^t + \frac{\Delta t \cdot v}{R_1} \sum_{j=1}^N a_{ij} c_{1j}^t - \frac{\Delta t \cdot D}{R_1} \sum_{j=1}^N b_{ij} c_{1j}^t = c_{1i}^{t-\Delta t} - \frac{\Delta t k_1}{R_1} c_{1i}^{t-\Delta t} \tag{13}$$

And by using the following coefficients  $Y_{i1} = \frac{\Delta t \cdot v}{R_1}$ ,  $G_{i1} = \frac{\Delta t \cdot D}{R_1}$ , and  $K_1 = \frac{\Delta t k_1}{R_1}$  the matrix form of the solution is given as:

$$S = \begin{bmatrix} 1 + Y_{11} a_{11} - G_{11} b_{11} & Y_{11} a_{12} - G_{11} b_{12} & \dots & Y_{11} a_{1N} - G_{11} b_{1N} \\ Y_{21} a_{21} - G_{21} b_{21} & 1 + Y_{21} a_{22} - G_{21} b_{22} & \dots & Y_{21} a_{2N} - G_{21} b_{2N} \\ \vdots & \vdots & \ddots & \vdots \\ Y_{N1} a_{N1} - G_{N1} b_{N1} & Y_{N1} a_{N2} - G_{N1} b_{N2} & \dots & 1 + Y_{N1} a_{NN} - G_{N1} b_{NN} \end{bmatrix}$$

$$C = \begin{bmatrix} c_{11}^t \\ c_{12}^t \\ \vdots \\ c_{1N}^t \end{bmatrix} \quad R = \begin{bmatrix} c_{11}^{t-\Delta t} - K_1 c_{11}^{t-1} \\ c_{12}^{t-\Delta t} - K_1 c_{12}^{t-1} \\ \vdots \\ c_{1N}^{t-\Delta t} - K_1 c_{1N}^{t-1} \end{bmatrix} \quad C \cdot S = R \tag{14}$$

It is worth noting that the solution process of both numerical methods applied here, should be solved in matrix form since the numerical models are provided in fully implicit form. By

enforcing the similar process for other species, the final forms of solution for the second-, third- and fourth-species are extracted as follows:

$$C_{2i}^t + \frac{\Delta t.v}{R_2} \sum_{j=1}^N a_{ij} C_{2j}^t - \frac{\Delta t.D}{R_2} \sum_{j=1}^N b_{ij} C_{2j}^t = C_{2i}^{t-\Delta t} - \frac{\Delta tk_2}{R_2} C_{2i}^{t-\Delta t} + \frac{\Delta tk_1}{R_2} C_{1i}^{t-\Delta t} \quad (15)$$

$$C_{3i}^t + \frac{\Delta t.v}{R_3} \sum_{j=1}^N a_{ij} C_{3j}^t - \frac{\Delta t.D}{R_3} \sum_{j=1}^N b_{ij} C_{3j}^t = C_{3i}^{t-\Delta t} - \frac{\Delta tk_3}{R_3} C_{3i}^{t-\Delta t} + \frac{\Delta tk_2}{R_3} C_{2i}^{t-\Delta t} \quad (16)$$

$$C_{4i}^t + \frac{\Delta t.v}{R_4} \sum_{j=1}^N a_{ij} C_{4j}^t - \frac{\Delta t.D}{R_4} \sum_{j=1}^N b_{ij} C_{4j}^t = C_{4i}^{t-\Delta t} - \frac{\Delta tk_4}{R_4} C_{4i}^{t-\Delta t} + \frac{\Delta tk_3}{R_4} C_{3i}^{t-\Delta t} \quad (17)$$

As noted previously, to compare the outcomes of the suggested model with IDQM, the governing equations were solved with IFOFDM, too. In this step of the numerical experiment, to derive the appropriate form of the discretization, the relations for first- and second-order derivatives in time and spaces are written as follows (Kaya and Gharehbaghi, 2014):

$$\frac{\partial C_1}{\partial t} = \frac{c_{1i}^t - c_{1i}^{t-\Delta t}}{\Delta t} \quad (18)$$

$$\frac{\partial C_1}{\partial x} = \frac{C_{1i-2} - 8C_{1i-1} + 8C_{1i+1} - C_{1i+2}}{12\Delta x} + o(\Delta x^4) \quad (19)$$

$$\frac{\partial^2 C_1}{\partial x^2} = \frac{-C_{1i-2} + 16C_{1i-1} - 30C_{1i} + 16C_{1i+1} - C_{1i+2}}{12\Delta x^2} + o(\Delta x^4) \quad (20)$$

"The key idea of finite difference method relies on the conversation of continuous functions to their discretely sampled counterparts. To obtain these discrete sample points, the whole problem domain is decomposed into the regular grid" (Verma, and Wille (2021)). In this study, the equal interval node distribution approach for IFOFDM is used to determine grid points. By replacing Eq.'s (18–20) into Eq. (1), the solution of IFOFDM for the first-member is given as follows:

$$R_1 \frac{c_{1i}^t - c_{1i}^{t-\Delta t}}{\Delta t} = D \frac{-C_{1i-2}^t + 16C_{1i-1}^t - 30C_{1i}^t + 16C_{1i+1}^t - C_{1i+2}^t}{12\Delta x^2} - v \frac{C_{1i-2}^t - 8C_{1i-1}^t + 8C_{1i+1}^t - C_{1i+2}^t}{12\Delta x} - k_1 C_{1i}^t \quad (21)$$

And by some manipulation, the final form of the solution is obtained as:

$$C_{1i-2}^t \left( \frac{\Delta t D}{12\Delta x^2 R_1} + \frac{\Delta t v}{12\Delta x R_1} \right) + C_{1i-1}^t \left( -\frac{16\Delta t D}{12\Delta x^2 R_1} - \frac{8\Delta t v}{12\Delta x R_1} \right) + C_{1i}^t \left( 1 + \frac{30\Delta t D}{12\Delta x^2 R_1} + \frac{\Delta t}{R_1} k_1 \right) + C_{1i+1}^t \left( -\frac{16\Delta t D}{12\Delta x^2 R_1} + \frac{8\Delta t v}{12\Delta x R_1} \right) + C_{1i+2}^t \left( \frac{\Delta t D}{12\Delta x^2 R_1} - \frac{\Delta t v}{12\Delta x R_1} \right) = C_{1i}^{t-\Delta t} \quad (22)$$

To present the final form of the solution (i.e., Eq. 22) in a simpler form,  $ka_m$  and  $kb_m$  coefficients are used as follows:

$$ka_m = \frac{\Delta t D}{12\Delta x^2 R_m} \quad m = 1, \dots, M; \tag{23}$$

$$kb_m = \frac{\Delta t v}{12\Delta x R_m} \quad m = 1, \dots, M; \tag{24}$$

And by replacing these coefficients Eq. (22) can rearrange as follows:

$$C_{1i-2}^t(ka_1 + kb_1) + C_{1i-1}^t(-16ka_1 - 8kb_1) + C_{1i}^t\left(1 + 30ka_1 + \frac{\Delta t}{R_1}k_1\right) + C_{1i+1}^t(kb_1 + 8kb_1) + C_{1i+2}^t(ka_1 - kb_1) = c_{1i}^{t-\Delta t} \tag{25}$$

By applying the same steps for other species, the last forms of solution of IFOFDM for second-, third- and fourth-species are written as follows:

$$C_{2i-2}^t(ka_2 + kb_2) + C_{2i-1}^t(-16ka_2 - 8kb_2) + C_{2i}^t\left(1 + 30ka_2 + \frac{\Delta t k_2}{R_2}\right) + C_{2i+1}^t(-16ka_2 + 8kb_2) + C_{2i+2}^t(ka_2 - kb_2) - \frac{\Delta t k_1}{R_2} C_{1i}^t = C_{2i}^{t-\Delta t} \tag{26}$$

$$C_{3i-2}^t(ka_3 + kb_3) + C_{3i-1}^t(-16ka_3 - 8kb_3) + C_{3i}^t\left(1 + \frac{30\Delta t D}{12\Delta x^2 R_3} + \frac{\Delta t k_3}{R_3}\right) + C_{3i+1}^t(-16ka_3 + 8kb_3) + C_{3i+2}^t(ka_3 - kb_3) - \frac{\Delta t k_2}{R_3} C_{2i}^t = C_{3i}^{t-\Delta t} \tag{27}$$

$$C_{4i-2}^t(ka_4 + kb_4) + C_{4i-1}^t(-16ka_4 - 8kb_4) + C_{4i}^t\left(1 + \frac{30\Delta t D}{12\Delta x^2 R_4} + \frac{\Delta t k_4}{R_4}\right) + C_{4i+1}^t(-16ka_4 + 8kb_4) + C_{4i+2}^t(ka_4 - kb_4) - \frac{\Delta t k_3}{R_4} C_{3i}^t = C_{4i}^{t-\Delta t} \tag{28}$$

#### 4. NUMERICAL EXPERIMENTS AND RESULTS

In this section, the analytical results of three well-established multi-species solute transport problems introduced by Pérez Guerrero et al., (2009) and Bauer et al., (2001) are employed to assess the accuracy and efficiency of the presented numerical model with IDQM. Furthermore, the outcomes of the suggested model are compared with the numerical results of the IFOFDM approach. The code of the proposed model has been generated in MATLAB.

In the first and second case studies, the analytical results of dimensionless concentration for a three-species nitrification chain ( $NH_4^+ \rightarrow NO_2^- \rightarrow NO_3^-$ ) are employed. For the first case study, the length of the domain and duration were selected as 220cm and 200h, respectively. For benchmark purposes, in the second case study, the domain length and duration were applied as 110cm and 50h (much smaller time), respectively. The linear interpolation method has been used to access the required point values of reported analytical results.

Details of the problems for the first and second cases, including retardation coefficient ( $R_m$ ), decay coefficient ( $\lambda_m$ ), initial and boundary conditions, etc., are described in Table (1). It is worthwhile to mention that in tables and figures below, the first and second case studies are referred to as the analytical results of dimensionless concentration for the three-species nitrification chain ( $NH_4^+ \rightarrow NO_2^- \rightarrow NO_3^-$ ) introduced by Pérez Guerrero et al., (2009) for 220cm, 200h, and 110cm, 50h, respectively, and case three is referred to the analytical results of four-member decay chain solute transport problems introduced by Bauer et al., (2001). Meanwhile, in all of the figures and tables below, the x, c, curve\_1, curve\_2, and curve\_3 are the abbreviations of distance (cm), concentration (mM), results of analytical expressions introduced by Pérez Guerrero et al., (2009), for  $NH_4^+$ ,  $NO_2^-$ , and  $NO_3^-$ , respectively. Moreover, IFOFDM\_C1, IFOFDM\_C2, IFOFDM\_C3 are the abbreviations of numerical results of the developed model with IFOFDM (i.e., calculated dimensionless concentration) for  $NH_4^+$ ,  $NO_2^-$ , and  $NO_3^-$ , respectively, and IDQM\_C1, IDQM\_C2, and IDQM\_C3 are the abbreviations of numerical results of the developed model with IDQM (i.e., calculated dimensionless concentration) for  $NH_4^+$ ,  $NO_2^-$ , and  $NO_3^-$ , respectively.

Table 1 - Parameter values for the nitrification chain problem

| Description                       | $NH_4^+$ (m=1)  | $NO_2^-$ (m=2)  | $NO_3^-$ (m=3)                        |
|-----------------------------------|-----------------|-----------------|---------------------------------------|
| Retardation coefficient ( $R_m$ ) | 2               | 1               | 1                                     |
| Decay coefficient, $\lambda_m$    | 0               | 0.1             | 0                                     |
| First case $\rightarrow C(x, 1)$  | 0               | 0               | 0                                     |
| First case $\rightarrow C(1, t)$  | 0.9982064510    | 0.001731801827  | 0.00006174718691                      |
| First case $\rightarrow C(N, t)$  | 1.199389159E-89 | 1.255589051E-12 | 0.0002545665546                       |
| Second case $\rightarrow C(x, 1)$ | 0               | 0               | 0                                     |
| Second case $\rightarrow C(1, t)$ | 0.9982064510    | 0.001731801827  | 0.00006174718691                      |
| Second case $\rightarrow C(N, t)$ | 5.1438380E-177  | 1.622019705E-50 | 2.260630087E-48                       |
| Pore velocity=1 cmh <sup>-1</sup> | Dispersion      | coefficient     | D=0.18cm <sup>2</sup> h <sup>-1</sup> |

The results of numerical experiments for the first and second test cases are summarized in figures (1) and (2) and Tables (2-4). These cases are solved with two different space and time intervals. The first case is solved with ( $N_x=221, N_t=5001$ ) and ( $N_x=441, N_t= 8001$ ) number of nodes in space ( $N_x$ ) and time ( $N_t$ ), and the second case is employed ( $N_x=221, N_t=1001$ ) and ( $N_x=331, N_t=5001$ ) numbers of nodes in space ( $N_x$ ) and time ( $N_t$ ) to run the calculation. The numerical outcomes of the first case in domain length and at the duration equal to 200h for all the nitrogen species are illustrated in figure (1). Similarly, the numerical results of the second case in domain length and at the duration equal to 50h for all the nitrogen species are demonstrated in figure (2). It is crucial to remember that the Chebyshev-Gauss-Lobatto formula provides a non-uniform distribution of nodes. Hence, it is pointless to talk about the distance between adjacent nodes. Consequently, in distance sections of the tables below regarding the DQM and IDQM approximations,  $\Delta x$  has been replaced with (...). According to the numerical results provided in the figures, it is evident that both the IDQM and IFOFDM are gained very close results to the analytical results. For this reason, to make a better

evaluation result, the total mean square error (TMSE),  $L_2$ - and  $L_\infty$ -norms are determined by the following relations. The results of the comparisons are given in Tables (2-4).

$$TMSE = \frac{\sum(c_{Numerical\ solution} - c_{analytical\ results})^2}{N} \tag{29}$$

$$\|x\|_2 = \sqrt{x_1^2 + x_2^2 + \dots + x_{N-1}^2 + x_N^2} \tag{30}$$

$$\|x\|_\infty = \max[|x_1|, |x_2|, \dots, |x_N|] \tag{31}$$

"Although only radioactive decay is a true first-order process, also chemical and biological transformations can be often described approximately in terms of first-order decay"; Bauer et al., (2001). Consequently, the numerical solutions for convey of a decay chain in porous media are widely applicable. According to the outcomes presented in the tables below, it can be revealed that both IDQM and IFOFDM approaches can estimate reliable outcomes and show good agreements with the results of analytical values. Based on the table of TMSE, in both first- and second-case studies, in the first- ( $NH_4^+$ ) and third-members ( $NO_3^-$ ) the numerical results of the IDQM are slightly better and in the second-member ( $NO_2^-$ ), the IFOFDM have calculated slightly better results than IDQM. Nevertheless, by considering the numerical outcomes of  $L_2$ - and  $L_\infty$ -norms are given in tables 3 and 4, in the first-member ( $NH_4^+$ ) the numerical results of the IDQM are slightly better, and in the second- ( $NO_2^-$ ) and third- member ( $NO_3^-$ ) the IFOFDM has computed slightly better results than IDQM. Moreover, with regard to the execution time, IDQM is required more execution time to obtain the outcomes than IFOFDM. These two test cases conclude that although numerical results of both of the methods are close to each other the results of IDQM are more reliable.

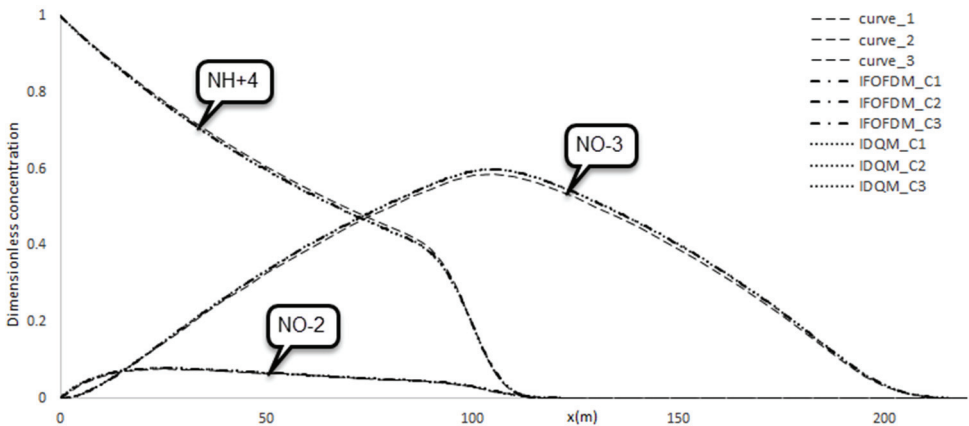


Fig. 1 - Illustration of results of first case for 1D transient concentration distribution for all the nitrogen species (220cm and 200h) and ( $N_x=441, N_t=8001$ ).

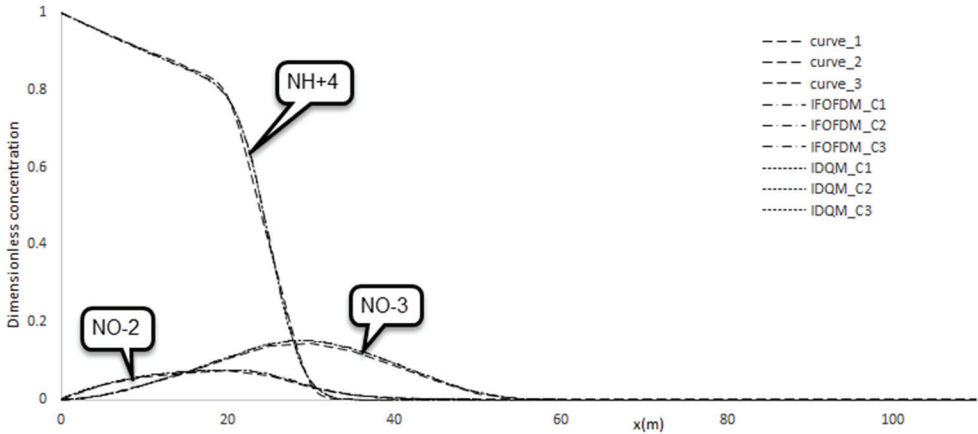


Fig. 2 - Illustration of results of second case for 1D transient concentration distribution for all the nitrogen species (110cm and 50h) and ( $N_x=221, N_t=1001$ ).

Table 2 - Table of TMSE for the first and second cases

| Description        | $N_x(\Delta x); N_t(\Delta t)$ | $NH_4^+$ (m=1) | $NO_2^-$ (m=2) | $NO_3^-$ (m=3) | Execution time(s) |
|--------------------|--------------------------------|----------------|----------------|----------------|-------------------|
| First case→IDQM    | 221(..);5001(0.04)             | 2.23187E-05    | 1.5288E-06     | 5.72399E-05    | 126.378909        |
| First case→IFOFDM  | 221(1);5001(0.04)              | 2.43501E-05    | 9.72845E-07    | 8.08827E-05    | 61.511134         |
| First case→IDQM    | 441(..);8001(0.025)            | 2.22319E-05    | 1.53588E-06    | 5.68567E-05    | 851.121429        |
| First case→IFOFDM  | 441(0.5);8001(0.025)           | 2.68109E-05    | 1.05194E-06    | 8.05886E-05    | 371.228101        |
| Second case→IDQM   | 221(..);1001(0.05)             | 9.15407E-05    | 2.51205E-06    | 8.01173E-06    | 31.272120         |
| Second case→IFOFDM | 221(0.5);1001(0.05)            | 0.000124512    | 2.31983E-06    | 1.07669E-05    | 17.430015         |
| Second case→IDQM   | 331(..);5001(0.01)             | 0.000111603    | 2.58196E-06    | 7.94743E-06    | 248.877210        |
| Second case→IFOFDM | 331(0.3333);5001(0.01)         | 0.000148968    | 2.46452E-06    | 1.1026E-05     | 106.136469        |

Table 3 - Table of  $L_2$ -norms for the first and second cases

| $L_2$ -    | Description  | $N_x(\Delta x); N_t(\Delta t)$ | $NH_4^+$ (m=1) | $NO_2^-$ (m=2) | $NO_3^-$ (m=3) |
|------------|--|--------------------------------|----------------|----------------|----------------|
| First case | Values of analytical results for Chebyshev–Gauss–Lobatto node distribution | 221(..);5001(0.04)             | 7.714794599    | 0.577455       | 4.441281364    |
|            | IDQM   | 221(..);5001(0.04)             | 7.667190368    | 0.592854       | 4.55057        |
|            | Values of analytical results for equal interval node distribution          | 221(1);5001(0.04)              | 6.570121269    | 0.607462       | 5.401541442    |
|            | IFOFDM   | 221(1);5001(0.04)              | 6.514591873    | 0.62115        | 5.530701       |
|            | Values of analytical results for Chebyshev–Gauss–Lobatto node distribution | 441(..);8001(0.025)            | 10.88757454    | 0.816626       | 6.280916403    |
|            | IDQM   | 441(..);8001(0.025)            | 10.82030731    | 0.838446       | 6.43531        |
|            | Values of analytical results for equal interval node distribution          | 441(0.5);8001(0.025)           | 9.264546037    | 0.859011       | 7.638814144    |
|            | IFOFDM   | 441(0.5);8001(0.025)           | 9.17891276     | 0.87859        | 7.822758       |

Table 3 - Table of  $L_2$ -norms for the first and second cases (continue)

| $L_2$ -     | Description  | $N_x(\Delta x); N_t(\Delta t)$ | $NH_4^+ (m=1)$ | $NO_2^- (m=2)$ | $NO_3^- (m=3)$ |
|-------------|--|--------------------------------|----------------|----------------|----------------|
| Second case | Values of analytical results for Chebyshev–Gauss–Lobatto node distribution | 221(..);1001(0.05)             | 7.587391907    | 0.433717       | 0.788799473    |
|             | IDQM   | 221(..);1001(0.05)             | 7.601745166    | 0.455104       | 0.827535       |
|             | Values of analytical results for equal interval node distribution          | 221(0.5);1001(0.05)            | 6.104308005    | 0.449497       | 0.912087457    |
|             | IFOFDM   | 221(0.5);1001(0.05)            | 6.140133425    | 0.470554       | 0.957084       |
|             | Values of analytical results for Chebyshev–Gauss–Lobatto node distribution | 331(..);5001(0.01)             | 9.279202108    | 0.531191       | 0.966017155    |
|             | IDQM   | 331(..);5001(0.01)             | 9.300437483    | 0.557605       | 1.01355        |
| Second case | Values of analytical results for equal interval node distribution          | 331(0.3333);5001(0.01)         | 7.459270646    | 0.550474       | 1.117018559    |
|             | IFOFDM   | 331(0.3333);5001(0.01)         | 7.50537397     | 0.576871       | 1.173536       |

Table 4 - Table of  $L_\infty$ -norms for the first and second cases

| $L_\infty$ -   | Description  | $N_x(\Delta x); N_t(\Delta t)$   | $NH_4^+ (m=1)$     | $NO_2^- (m=2)$ | $NO_3^- (m=3)$ |
|--|--|--|--------------------|----------------|----------------|
| First case   | Values of analytical results for Chebyshev–Gauss–Lobatto node distribution | 221(..);5001(0.04)   | 0.998097           | 0.07701        | 0.586774641    |
|  | IDQM   | 221(..);5001(0.04)   | 0.998091           | 0.079031       | 0.598597       |
|  | Values of analytical results for equal interval node distribution          | 221(1);5001(0.04)  | 0.988487           | 0.077057       | 0.587139464    |
|  | IFOFDM   | 221(1);5001(0.04)  | 0.989172           | 0.079023       | 0.598491       |
|  | Values of analytical results for Chebyshev–Gauss–Lobatto node distribution | 441(..);8001(0.025)  | 0.998179           | 0.077017       | 0.586774641    |
|  | IDQM   | 441(..);8001(0.025)  | 0.998178           | 0.079036       | 0.598795       |
| First case   | Values of analytical results for equal interval node distribution          | 441(0.5);8001(0.025)   | 0.993347           | 0.077057       | 0.587139464    |
|  | IFOFDM   | 441(0.5);8001(0.025)   | 0.993638           | 0.079035       | 0.598705       |
|  | Second case  | Values of analytical results for Chebyshev–Gauss–Lobatto node distribution | 221(..);1001(0.05) | 0.998152       | 0.074356       |
| IDQM   |  | 221(..);1001(0.05)   | 0.998149           | 0.076721       | 0.152878       |
| Values of analytical results for equal interval node distribution          |  | 221(0.5);1001(0.05)  | 0.993347           | 0.074712       | 0.146364487    |
| IFOFDM   |  | 221(0.5);1001(0.05)  | 0.993638           | 0.076723       | 0.152725       |
| Values of analytical results for Chebyshev–Gauss–Lobatto node distribution |  | 331(..);5001(0.01)   | 0.998182           | 0.074526       | 0.146065318    |
| IDQM   |  | 331(..);5001(0.01)   | 0.998180849        | 0.076808       | 0.153172       |
| Second case  | Values of analytical results for equal interval node distribution          | 331(0.3333);5001(0.01)   | 0.994967           | 0.074712       | 0.146364487    |
|  | IFOFDM   | 331(0.3333);5001(0.01)   | 0.995139634        | 0.076811       | 0.153123       |

The third case study is used an arbitrary decay chain with four species in an arbitrary complex porosity medium in the 3000 m and 3000 days. The implementation of these domain lengths and durations shows that the developed model can solve semi-infinite and long-term problems. The details of the problem for the third case study are presented in Table (5). Besides, in all of the figures and tables below related to the third case, the  $x$ ,  $c$ ,  $C_1$ ,  $C_2$ ,  $C_3$ ,  $C_4$ ,  $IDQM\_C_1$ ,  $IDQM\_C_2$ ,  $IDQM\_C_3$ ,  $IDQM\_C_4$ ,  $IFOFDM\_C_1$ ,  $IFOFDM\_C_2$ ,  $IFOFDM\_C_3$ , and  $IFOFDM\_C_4$  are the abbreviations of distance (cm), concentration (mM), outcomes of analytical expressions for the concentration introduced by Bauer et al., (2001) for four species, numerical results of the concentration with the suggested model for IDQM for four species, and numerical results of the concentration with the suggested model for IFOFDM for four species, respectively. This case study is solved for six different space and time intervals, including  $N_x=101, N_t=3001$ ;  $N_x=101, N_t=10001$ ;  $N_x=301, N_t=3001$ ;  $N_x=301, N_t=10001$ ;  $N_x=501, N_t=1501$ ; and  $N_x=501, N_t=10001$ . Similar to the two earlier cases to make a better evaluation result, the TMSE,  $L_2$ - and  $L_\infty$ -norms are determined, too. The outcomes of the comparisons have given in Tables (6-8). The numerical results of concentration distributions for the four-member decay chain for this case study for  $N_x=501, N_t=1501$  are presented in figure (3). The numerical results presented in Tables (6-8) show that for all of the implemented space and time intervals, the numerical results of the IDQM are more accurate than the IFOFDM. But according to the values given in the tables below, with fewer numbers of space and time node points, the IDQM has obtained more reliable results than IFOFDM. Furthermore, based on these results, the IDQM requires more execution time than IFOFDM.

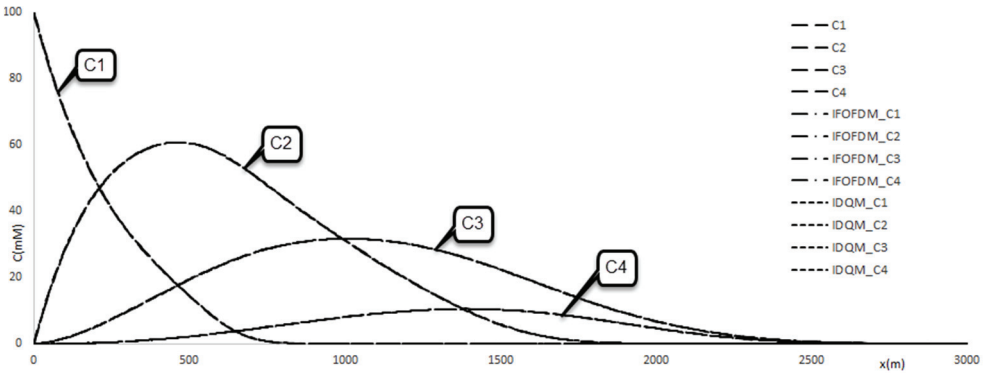


Fig. 3 - 1D transient concentration distribution for constant boundary condition (3000m and 3000day) in ( $N_x=501, N_t=1501$ ).

Table 5 - Parameter values for the third case

| Description  | $C_1$ (m=1) | $C_2$ (m=2) | $C_3$ (m=3)                          | $C_4$ (m=4) |
|--|-------------|-------------|--------------------------------------|-------------|
| Retardation coefficient ( $R_m$ )                                  | 5.3         | 1.9         | 1.2                                  | 1.3         |
| Decay coefficient, $\lambda_m \times 10^{-4}$ (day <sup>-1</sup> ) | 7           | 5           | 4.5                                  | 3.8         |
| Third case $\rightarrow C(x, 1)$ (mM)                              | 0           | 0           | 0                                    | 0           |
| Third case $\rightarrow C(1, t)$ (mM)                              | 100         | 0           | 0                                    | 0           |
| Third case $\rightarrow C(N, t)$ (mM)                              | 0           | 0           | 0                                    | 0           |
| Pore velocity=1 mday <sup>-1</sup>                                 | Dispersoin  | coefficient | D=10m <sup>2</sup> day <sup>-1</sup> |             |

Table 6 - Table of TMSE for the third case

| Description      | Nx( $\Delta x$ ); Nt( $\Delta t$ ) | C <sub>1</sub> (m=1) | C <sub>2</sub> (m=2) | C <sub>3</sub> (m=3) | C <sub>4</sub> (m=4) | Execution time(s) |
|------------------|------------------------------------|----------------------|----------------------|----------------------|----------------------|-------------------|
| Third case→IDQM  | 101(.,.);3001(1)                   | 0.02303187           | 0.015139854          | 0.001525551          | 0.001407             | 66.787963         |
| Third ase→IFOFDM | 101(30);3001(1)                    | 0.106788638          | 0.104846677          | 0.010803551          | 0.00228              | 12.547559         |
| Third case→IDQM  | 101(.,.);10001(0.3)                | 0.027600203          | 0.014447211          | 0.001497311          | 0.001468             | 110.461599        |
| Third ase→IFOFDM | 101(30);10001(0.3)                 | 0.10734477           | 0.106451881          | 0.0103502            | 0.002098             | 38.984924         |
| Third case→IDQM  | 301(.,.);3001(1)                   | 0.02303187           | 0.015139854          | 0.001525551          | 0.001407             | 190.529084        |
| Third ase→IFOFDM | 301(10);3001(1)                    | 0.013655793          | 0.01813048           | 0.002349908          | 0.001684             | 66.787963         |
| Third case→IDQM  | 301(.,.);10001(0.3)                | 0.023034354          | 0.01507317           | 0.001487377          | 0.001532             | 560.674821        |
| Third ase→IFOFDM | 301(10);10001(0.3)                 | 0.01373847           | 0.018717975          | 0.002112538          | 0.001659             | 187.716471        |
| Third case→IDQM  | 501(.,.);1501(2)                   | 0.023435438          | 0.015701183          | 0.002425594          | 0.001617             | 221.940376        |
| Third ase→IFOFDM | 501(6);1501(2)                     | 0.007617517          | 0.009957415          | 0.002738082          | 0.001915             | 97.215048         |
| Third case→IDQM  | 501(.,.);10001(0.3)                | 0.023374174          | 0.015127306          | 0.001491743          | 0.001537             | 1561.336216       |
| Third ase→IFOFDM | 501(6);10001(0.3)                  | 0.007640485          | 0.010622715          | 0.001749389          | 0.001684             | 641.655791        |

Table 7 - Table of L<sub>2</sub>-norms for the third case

| L <sub>2</sub> - | Description  | Nx( $\Delta x$ ); Nt( $\Delta t$ ) | C <sub>1</sub> (m=1) | C <sub>2</sub> (m=2) | C <sub>3</sub> (m=3) | C <sub>4</sub> (m=4) |
|------------------|--|------------------------------------|----------------------|----------------------|----------------------|----------------------|
|                  | Values of analytical results for Chebyshev–Gauss–Lobatto node distribution | 101(.,.);3001(1)                   | 355.846              | 273.52               | 149.7069             | 46.23924             |
|                  | IDQM   | 101(.,.);3001(1)                   | 356.8835             | 273.4465             | 149.6668             | 46.1735              |
|                  | Values of analytical results for equal interval node distribution          | 101(30);10001(1)                   | 224.8856             | 287.7221             | 179.0449             | 56.97991             |
|                  | IFOFDM   | 101(30);10001(1)                   | 227.6443             | 287.4638             | 178.8244             | 56.80733             |
| Third case       | Values of analytical results for Chebyshev–Gauss–Lobatto node distribution | 101(.,.);10001(0.3)                | 355.846              | 273.52               | 149.7069             | 46.23924             |
|                  | IDQM   | 101(.,.);10001(0.3)                | 356.8847             | 273.4378             | 149.6295             | 46.14533             |
|                  | Values of analytical results for equal interval node distribution          | 101(30);10001(0.3)                 | 224.8856             | 287.7221             | 179.0449             | 56.97991             |
|                  | IFOFDM   | 101(30);10001(0.3)                 | 227.6506             | 287.5197             | 178.8753             | 56.82232             |
|                  | Values of analytical results for Chebyshev–Gauss–Lobatto node distribution | 301(.,.);3001(1)                   | 608.5267             | 473.7572             | 259.2994             | 80.10468             |
|                  | IDQM   | 301(.,.);3001(1)                   | 609.9979             | 473.6232             | 259.2306             | 79.97485             |
|                  | Values of analytical results for equal interval node distribution          | 301(10);3001(1)                    | 375.774              | 498.2827             | 310.115              | 98.69671             |
|                  | IFOFDM   | 301(10);3001(1)                    | 377.5027             | 498.1249             | 309.7794             | 98.40844             |
|                  | Values of analytical results for Chebyshev–Gauss–Lobatto node distribution | 301(.,.);10001(0.3)                | 608.5267             | 473.7572             | 259.2994             | 80.10468             |
|                  | IDQM   | 301(.,.);10001(0.3)                | 610                  | 473.6082             | 259.1658             | 79.92606             |
|                  | Values of analytical results for equal interval node distribution          | 301(10);10001(0.3)                 | 375.774              | 498.2827             | 310.115              | 98.69671             |
|                  | IFOFDM   | 301(10);10001(0.3)                 | 377.5141             | 498.2218             | 309.8675             | 98.43445             |
|                  | Values of analytical results for Chebyshev–Gauss–Lobatto node distribution | 501(.,.);1501(2)                   | 783.485              | 611.647              | 334.7578             | 103.4202             |

Table 7 - Table of  $L_2$ -norms for the third case (continue)

| $L_2$ - | Description  | $N_x(\Delta x); N_t(\Delta t)$ | $C_1 (m=1)$ | $C_2 (m=2)$ | $C_3 (m=3)$ | $C_4 (m=4)$ |
|---------|--|--------------------------------|-------------|-------------|-------------|-------------|
|         | IDQM   | 501(..);1501(2)                | 785.3808    | 611.4726    | 334.785     | 103.3376    |
|         | Values of analytical results for equal interval node distribution          | 501(6);1501(2)                 | 481.6137    | 643.2655    | 400.3579    | 127.4187    |
|         | IFOFDM   | 501(6);1501(2)                 | 483.0585    | 642.916     | 399.7652    | 126.9986    |
|         | Values of analytical results for Chebyshev–Gauss–Lobatto node distribution | 501(..);10001(0.3)             | 783.485     | 611.647     | 334.7578    | 103.4202    |
|         | IDQM   | 501(..);10001(0.3)             | 785.3874    | 611.4256    | 334.5817    | 103.1841    |
|         | Values of analytical results for equal interval node distribution          | 501(6);10001(0.3)              | 481.6137    | 643.2655    | 400.3579    | 127.4187    |
|         | IFOFDM   | 501(6);10001(0.3)              | 483.0947    | 643.2195    | 400.041     | 127.0796    |

Table 8 - Table of  $L_\infty$ -norms for the third case

| $L_\infty$ - | Description  | $N_x(\Delta x); N_t(\Delta t)$ | $C_1 (m=1)$ | $C_2 (m=2)$ | $C_3 (m=3)$ | $C_4 (m=4)$ |
|--------------|--|--------------------------------|-------------|-------------|-------------|-------------|
|              | Values of analytical results for Chebyshev–Gauss–Lobatto node distribution | 101(..);3001(1)                | 98.72462    | 60.67081    | 31.68947    | 10.47882    |
|              | IDQM   | 101(..);3001(1)                | 99.7352472  | 60.7669     | 31.66417    | 10.43484    |
|              | Values of analytical results for equal interval node distribution          | 101(30);10001(1)               | 89.75127    | 60.70631    | 31.69296    | 10.48347    |
|              | IFOFDM   | 101(30);10001(1)               | 90.9395646  | 60.72168    | 31.64842    | 10.42173    |
| Third case   | Values of analytical results for Chebyshev–Gauss–Lobatto node distribution | 101(..);10001(0.3)             | 98.72462    | 60.67081    | 31.68947    | 10.47882    |
|              | IDQM   | 101(..);10001(0.3)             | 99.7352472  | 60.77122    | 31.664      | 10.43486    |
|              | Values of analytical results for equal interval node distribution          | 101(30);10001(0.3)             | 89.75127    | 60.70631    | 31.69296    | 10.48347    |
|              | IFOFDM   | 101(30);10001(0.3)             | 90.9395646  | 60.72967    | 31.66032    | 10.42911    |
|              | Values of analytical results for Chebyshev–Gauss–Lobatto node distribution | 301(..);3001(1)                | 99.7783     | 60.75209    | 31.69223    | 10.485      |
|              | IDQM   | 301(..);3001(1)                | 99.9705462  | 60.78502    | 31.67563    | 10.43887    |
|              | Values of analytical results for equal interval node distribution          | 301(10);3001(1)                | 96.30834    | 60.76353    | 31.69298    | 10.485      |
|              | IFOFDM   | 301(10);3001(1)                | 96.8136065  | 60.77551    | 31.65793    | 10.42804    |
|              | Values of analytical results for Chebyshev–Gauss–Lobatto node distribution | 301(..);10001(0.3)             | 99.7783     | 60.75209    | 31.69223    | 10.485      |
|              | IDQM   | 301(..);10001(0.3)             | 99.97055    | 60.78889    | 31.67536    | 10.43902    |
|              | Values of analytical results for equal interval node distribution          | 301(10);10001(0.3)             | 375.774     | 498.2827    | 310.115     | 98.69671    |
|              | IFOFDM   | 301(10);10001(0.3)             | 377.5141    | 498.2218    | 309.8675    | 98.43445    |
|              | Values of analytical results for Chebyshev–Gauss–Lobatto node distribution | 501(..);1501(2)                | 99.92019    | 60.76635    | 31.70456    | 10.485      |
|              | IDQM   | 501(..);1501(2)                | 99.9894     | 60.778      | 31.676      | 10.43835    |
|              | Values of analytical results for equal interval node distribution          | 501(6);1501(2)                 | 97.53872    | 60.78184    | 31.69583    | 10.485      |

Table 8 - Table of  $L_\infty$ -norms for the third case (continue)

| $L_\infty$ - | Description  | $N_x(\Delta x); N_t(\Delta t)$ | $C_1$ (m=1) | $C_2$ (m=2) | $C_3$ (m=3) | $C_4$ (m=4) |
|--------------|--|--------------------------------|-------------|-------------|-------------|-------------|
|              | IFOFD  | 501(6);1501(2)                 | 98.0604     | 60.77047    | 31.64168    | 10.41751    |
|              | Values of analytical results for Chebyshev–Gauss–Lobatto node distribution | 501(.);10001(0.3)              | 99.92019    | 60.76635    | 31.70456    | 10.485      |
|              | IDQM   | 501(.);10001(0.3)              | 99.9894     | 60.78784013 | 31.6753     | 10.43872    |
|              | Values of analytical results for equal interval node distribution          | 501(6);10001(0.3)              | 97.53872    | 60.78184    | 31.69583    | 10.485      |
|              | IFOFD  | 501(6);10001(0.3)              | 98.0603959  | 60.78666    | 31.67011    | 10.43577    |

## 5. CONCLUSION

In the present study, for the first time, a novel numerical model for multi-species solute transport phenomenon based on the IDQM is established and effectively analysed. Furthermore, the IFOFD is used to compare the performance of the suggested model. Although there is no restriction in the number of multi-species, the analytical results of three different three-species ( $NH_4^+ \rightarrow NO_2^- \rightarrow NO_3^-$ ) and four-species problems reported in the literature are employed for numerical interpretation of the developed model. Presented results proved that both numerical models with IDQM and IFOFD for each species converged to previously reported literature values, and a good agreement is found between both the numerical solutions for all of the three-species and four-species problems. TMSE,  $L_2$ - and  $L_\infty$ -norms have been applied for in-depth evaluation of numerical results. All case studies were simulated with at least two different space and time intervals. In all cases, the numerical results of IDQM are better than the numerical results of IFOFD. In the first two case studies, the numerical results of IDQM for the ( $NH_4^+$ ) and ( $NO_3^-$ ) members are more accurate. In the last case study based on the numerical results of six numerical experiments, it is obviously clear that the numerical outcomes of the IDQM are more accurate and reliable than the IFOFD. The third case study demonstrated that the established model is able to predict long-term problems in the semi-infinite domain. Moreover, despite the high accuracy, the application of the IDQM needs less computational effort compared to other implemented numerical methods, and the application process is not complicated. In addition, low memory storage requirement is another advantage of this method. The only weak point of the IDQM is related to the execution time for integration, which increases due to the structure of the coefficient matrix. Consequently, it can be stated that although the IDQM provides better results, by considering the execution time may be IFOFD is more economical to use.

## Acknowledgements

This research did not receive any specific grant from funding agencies in the public, commercial, or not-for-profit sectors.

## References

- [1] Bagalkot, N., Kumar, G.S., 2015. Effect of nonlinear sorption on multispecies radionuclide transport in a coupled fracture-matrix system with variable fracture aperture: a numerical study. *ISH Journal of Hydraulic Engineering*. 21(3) 242–254, <http://dx.doi.org/10.1080/09715010.2015.1016125>
- [2] Bauer, P., Attinger, S., Kinzelbach, W., 2001. Transport of a decay chain in homogenous porous media: analytical solutions, *Journal of Contaminant Hydrology*. 49, 217–239.
- [3] Bellman, R., Casti, J., 1971. Differential quadrature and long-term integration. *J. Math. Anal. Appl.* 34 (2), 235–238.
- [4] Chaudhary, M., Singh, M.K. 2020, Study of multispecies convection-dispersion transport equation with variable parameters, *Journal of Hydrology* 591 (2020), <https://doi.org/10.1016/j.jhydrol.2020.125562>
- [5] Chen, W. and Zhong, T., 1997, The study on the nonlinear computations of the DQ and DC methods. *Numerical Methods for Partial Differential Equations*, 13, 57–75
- [6] Chen-Charpentier, B.M., Dimitrov, D.T., Kojouharov H.V., 2009. Numerical simulation of multi-species biofilms in porous media for different kinetics, *Mathematics and Computers in Simulation*, 79, 1846–1861.
- [7] Ciftci, E., 2017. Modelling coupled density-dependent flow and solute transport with the differential quadrature method, *Geosciences Journal*, 21(5), 807–817, <http://dx.doi.org/10.1007/s12303-017-0009-5>
- [8] Konikow, L.F., and Bredehoeft, J.D., 1978, Computer model of two-dimensional solute transport and dispersion in ground water: U.S. Geological Survey, *Techniques of Water-Resources Investigations*, Book 7, Chap. C2.
- [9] Civalek, O. 2004, Application of differential quadrature (DQ) and harmonic differential quadrature (HDQ) for buckling analysis of thin isotropic plates and elastic columns, *Engineering Structures*, 26,171–186.
- [10] Das, P., Akhter, A., Singh, M.K., 2018. Solute transport modelling with the variable temporally dependent boundary, *Sadhana*, 43, 1-12, <https://doi.org/10.1007/s12046-017-0778-6>
- [11] Essaid, H.I. and Bekins, B.A., 1997, BIOMOC, A Multispecies Solute-Transport Model with Biodegradation, U.S. GEOLOGICAL SURVEY, *Water-Resources Investigations Report 97-4022*.
- [12] Gharehbaghi, A., 2016. Explicit and implicit forms of differential quadrature method for advection–diffusion equation with variable coefficients in semi-infinite domain, *J. Hydrol.* 541 (1), 935–940, <http://dx.doi.org/10.1016/j.jhydrol.2016.08.002>
- [13] Gharehbaghi, A., 2017. Third- and fifth-order finite volume schemes for advection–diffusion equation with variable coefficients in semi-infinite domain. *Water and Environment Journal*. 31 (2), 184–193. doi:10.1111/wej.12233

- [14] Gharehbaghi, A., Kaya, B., Saadatnejadgharahassanlou, H., 2017. Two-dimensional bed variation models under nonequilibrium conditions in turbulent streams. *Arabian Journal for Science and Engineering*. 42 (3), 999–1011.
- [15] Kaya, B., 2010. Solution of the advection-diffusion equation using the differential quadrature method. *KSCE J. Civil Eng.* 14 (1), 69–75.
- [16] Kaya, B., Arisoy, Y., 2011. Differential quadrature solution for one-dimensional aquifer flow, *Mathematical and Computational Applications*, 16(2), 524-534.
- [17] Kaya, B., Gharehbaghi, A., 2014. Implicit Solutions of Advection Diffusion Equation by Various Numerical Methods. *Aust. J. Basic & Appl. Sci.*, 8(1): 381-391.
- [18] Kumar, A., Kumar, D., Kumar, J.N., 2010. Analytical solutions to one-dimensional advection–diffusion equation with variable coefficients in semi-infinite media. *J. Hydrol.* 380, 330–337.
- [19] Massoudieh, A., Ginn, T.R., 2007, Modeling colloid-facilitated transport of multi-species contaminants in unsaturated porous media, *Journal of Contaminant Hydrology* 92, 162–183, doi:10.1016/j.jconhyd.2007.01.005
- [20] Engdahl N.B., Aquino, T., 2018, Considering the utility of backward-in-time simulations of multi-component reactive transport in porous media, *Advances in Water Resources*, 119, 17–27. <https://doi.org/10.1016/j.advwatres.2018.06.003>
- [21] Natarajan N., Kumar S.G., 2010. Finite difference approach for modeling multispecies transport in porous media, *International Journal of Engineering Science and Technology*. 2(8), 3344-3350.
- [22] Pathania, T., Eldho, T.I., Bottacin-Busolin, A. 2020. Coupled simulation of groundwater flow and multispecies reactive transport in an unconfined aquifer using the element-free Galerkin method. *Engineering Analysis with Boundary Elements*. 121, 31–49.
- [23] Pérez Guerrero, J.S., Skaggs, T.H., van Genuchten, M.Th., 2009. Analytical Solution for Multi-Species Contaminant Transport Subject to Sequential First-Order Decay Reactions in Finite Media. *Transp Porous Med.* 80, 373–387, DOI 10.1007/s11242-009-9368-3
- [24] Ramos, T.B., Šimůnek, J., Gonçalves, M.C., Martins, J.C., Prazeres, A., Castanheira, N.L., Pereira, L.S., 2011, Field evaluation of a multicomponent solute transport model in soils irrigated with saline waters, *Journal of Hydrology*, 407(1–4), 129-144, <https://doi.org/10.1016/j.jhydrol.2011.07.016>.
- [25] Savovic, S., Djordjevich, A., 2012. Finite difference solution of the one-dimensional advection–diffusion equation with variable coefficients in semi-infinite media. *Int. J. Heat Mass Transf.* 55, 4291–4294. <http://dx.doi.org/10.1016/j.ijheatmasstransfer.2012.03.073>
- [26] Sharma A., Guleria, A., Swami D., 2016. Numerical modelling of multispecies solute transport in porous media. *Hydro 2016 international conference*. 159-169.

- [27] Shu, C., 2000. *Differential Quadrature and its Application in Engineering*. first ed. Springer-Verlag, London Limited.
- [28] Šimůnek, J., Šejna, M., Saito, H., Sakai, M., and van Genuchten, M. Th., 2012, *The HYDRUS-1D Software Package for Simulating the One-Dimensional Movement of Water, Heat, and Multiple Solutes in Variably-Saturated Media*, university of california riverside riverside, California
- [29] Singh, M.K., Ahamad S., and Singh, V.P., 2012. Analytical Solution for One-Dimensional Solute Dispersion with Time-Dependent Source Concentration along Uniform Groundwater Flow in a Homogeneous Porous Formation. *Journal of Engineering Mechanics*. 138(8).
- [30] Sun, Y., Petersen, J. N., Clement, T. P., and Skeen, R. S., 1999, Development of analytical solutions for multispecies transport with serial and parallel reactions, *water resources research*, 35(1), 185-190.
- [31] Torlapati, J., 2013. *Development and Application of One Dimensional Multi-component Reactive Transport Models*. Phd dissertation, Auburn, Alabama, USA, May 4, 2013
- [32] Van Genuchten, M.Th., 1985, Convective-dispersive transport of solutes involved in sequential first-order decay reactions, *Computers & Geosciences*, 11(2), 129-147, [https://doi.org/10.1016/0098-3004\(85\)90003-2](https://doi.org/10.1016/0098-3004(85)90003-2).
- [33] Verma, K., Wille, R., *High Performance Simulation for Industrial Paint Shop Applications*, Springer Nature, 2021
- [34] Zhang, Z., Zhang, J., Ju, Z. Zhu, M. 2018, A one-dimensional transport model for multi-component solute in saturated soil, *Water Science and Engineering*, 11(3), 236-242, <https://doi.org/10.1016/j.wse.2018.09.007>.
- [35] Zong, Z., Zhang, Y., 2009. *Advanced Differential Quadrature Methods*, first ed. CRC Press, Taylor and Francis Group, New York.

# **An Investigation on Force Modification Factors in Cold-Formed Steel Structures**

**Macit YURTSEVER<sup>1</sup>**

**Serdar SOYÖZ<sup>2</sup>**

## **ABSTRACT**

The Force Modification Factors defined in the Turkish Seismic Code (2018) for cold-formed steel structures are examined within the scope of this paper. Experimental and analytical studies are carried out on a real-life structure to investigate if the defined coefficients are practically applicable. An Ambient Vibration Survey is implemented to obtain the characteristic modal periods of the building, which is then modelled in computing environment through modal calibration. Additional laboratory experiments are carried out to determine a mathematical relationship for the connections between the bracing and the frame members of the building. Performance analysis is conducted to analyze the nonlinear behavior of the structure, and the force modification factors are evaluated. It is observed that the computed values from the analyses are generally within the range of what is defined in the Code, if not greater. Several suggestions as to where the Code content could be improvised are also included.

**Keywords:** Cold-formed steel, performance analysis, force modification factors, real-life building, Turkish Seismic Code 2018.

## **1. INTRODUCTION**

Construction industry has only become familiar with cold-formed steel (CFS) structures for a couple of decades, but thanks to technological improvements and development of sophisticated testing facilities, there are already plenty of available data (codes, recommendations and other written sources) to be used in the design of such structures. There are already numerous projects in Turkey, as well where cold-formed steel is utilized. Considering that Turkey frequently falls prone to earthquakes with mild to severe intensities, this growing construction sector has recently seen an increasing interest, and the newest Turkish Seismic Code (TSC 2018) (1) provides some very helpful and elaborate design

---

Note:

- This paper has been received on August 4, 2021 and accepted for publication by the Editorial Board on February 18, 2022.
- Discussions on this paper will be accepted by September 30, 2022.
- <https://doi.org/10.18400/tekderg.977677>

1 Sur Yapi A.S., Istanbul, Turkey

macityurtsever@gmail.com - <https://orcid.org/0000-0002-3402-3847>

2 Department of Civil Engineering, Boğaziçi University, Istanbul, Turkey

serdar.soyoz@boun.edu.tr - <https://orcid.org/0000-0002-5502-6545>

methodologies on CFS structures. Yet some of the aspects that have entered the Code still require more research to be finalized, and force modification factors are among those aspects. This paper will specifically focus on the ductility-related modification factor (described as the Structural Behavior Factor in the Code), which are defined as  $R=4$  for structural systems with high ductility, and  $R=3$  for structural systems with limited ductility.

Plenty of valuable reference is available covering both experimental and analytical research previously done by academics and other professionals. Della Corte *et al.* (2) provided and discussed the results of a numerical study on seismic deformation demand to sheathed CFS structures. It is part of a wider research, also involving calibration of the numerical model against data from physical tests, which were conducted by Landolfo *et al.* (3) through an extensive experimental study on the seismic behavior of cold-formed steel stud shear walls. Dubina (4) provided an extensive examination that summarizes the results and findings of monotonic and cyclic tests performed on full-scale shear panels, tests on various connection details, and in-situ ambient vibration tests on a house under construction. Velchev *et al.* (5) evaluated typical strap braced wall configurations with respect to their strength and inelastic behavior. Nithyadharan and Kalyanaraman (6) presented the results of an experimental study on the behavior and strength of the CFS shear wall panel, when subjected to monotonically increasing and reversed cyclic in-plane shear deformation. Their paper also proposes a 'simplified method' for evaluating the shear strength of the wall panel as governed by the sheathing-to-frame screw connections' strength. Shamim and Rogers (7) described the numerical modelling using OpenSees for shear walls constructed of cold-formed steel framing and flat steel sheathing. The paper also includes an analytical example of a two-story office building modelled in OpenSees. Sato and Uang (8) verified the adequacy of the proposed seismic performance factors for the newly developed Cold-Formed Steel Special Bolted Moment Frames in the AISI S110 Seismic Standard using the FEMA P695 methodology. Within the scope of an Italian research project called RELUIS-DPC 2010-2013, undertaken at the University of Naples, Iuorio *et al.* (9) investigated the seismic behavior of strap-braced stud walls. Bian *et al.* (10) combined two types of analytical modelling techniques to provide a highly versatile shear wall model capable of capturing both fastener-based and member-based limit states in the shear wall. Senkardesler *et al.* (11) presented the results of dynamic and cyclic experiments conducted on two different 3-D and 2-storey models, which were two CFS structures with and without infill materials. Borzoo *et al.* (12) investigated the stiffness, strength and failure modes of CFS shear panels under monotonic loading, using ABAQUS software. Madsen *et al.* (13) provided guidelines for NEHRP Seismic Design Technical Brief No.12, which is an extensive document specialized for cold-formed steel structures, including basic construction outlines as well as seismic design guidelines and experimental literature. Karabulut (14) performed cyclic tests on a number of specimens using various configurations in order to observe the effects of board type, steel thickness, screw spacing and axial loads on structural performance of CFS shear panels. Leng *et al.* (15) performed shake table tests on a two-story CFS-framed building with OSB sheathed shear walls. FE models of the building during its various test phases were also developed in OpenSees. Riahi *et al.* (16) evaluated the seismic performance factor of CFS frames with K-shaped bracings in accordance with Iranian seismic code, again by utilizing the OpenSees software. Most recently, Haghpanah and Schafer (17) provided fragility functions for various configurations of CFS-framed shear walls, after investigating as to which displacement levels they could be subjected before a probability of failure occurs.

The motivation of this study is to investigate if the force modification factors defined in TSC 2018 for cold-formed steel structures are reliable. In this regard, it may be fair to assume it mostly differs from the aforementioned literature. However, there are minor links to the work of Karabulut (14), and it overlap with the work of Riahi *et al.* (16). At this point, it must be said that it does not aim to fully challenge the specifications provided in TSC 2018. The sole intent is to get an insight on how the computational values fare against the Code recommendations, and to provide a starting point for further studies of similar focus. Although this study only considers the factors given in TSC 2018, the subjects covered within may as well be interpreted and made available for use with other codes and specifications.

In order to have a reliable basis for verification of the factors, an ambient vibration survey is performed on a real-life CFS structure, and a faithful representation of the structure is generated through an analytical model. Then the model is used for performance assessment and other required computations related to the objective. Also, cyclic tests are performed on typical specimens to calibrate various structural parameters.

## 2. AMBIENT VIBRATION TEST ON A REAL-LIFE STRUCTURE

### 2.1. General Information

A two-story CFS building was provided by courtesy of Akkon Celik Yapi Sistemleri A.S., builders of the building, and has been monitored through ambient vibration tests. The equipment used in this test is manufactured by Kinemetrics, which is essentially a 12-channel substation with a sampling rate of 200 Hz and is provided by the Structures Laboratory of Boğaziçi University.



*Figure 1 - Some images of the typical mirror-villa used for AVT*

The building is situated in one of the resorts close to the Enez Harbour in Trapez district of Enez (Edirne). This resort consists of monotype two-story mirror-villas and is one of many similarly constructed groups of villas that can be observed around in the district. The building considered in this study was presumably built in the early 2000s, and is understandably not compliant with the TSC 2018. It has approximately a 12.0 m by 6.7 m footprint (see Figure 1). Sensors of the monitoring device were all installed on the second floor (slab or ceiling) in the left-half of the building since the other half was not available for testing purposes because of its residents at the time.

For this test, a total of 10 sensors were installed. The only sensors that were placed on the wall close to the ceiling are #9 and #10, and the rest of the sensors were all placed on the second story floor, as demonstrated in Figures 2(a)-(b). More detailed information regarding the ambient vibration test and the subsequent results is provided by Yurtsever (18), only the Power Spectral Density (PSD) is covered here for the sake of simplicity.



(a) Upper floor slab

(b) Upper floor ceiling

Figure 2 - Sensor layouts on the upper floor of the test building

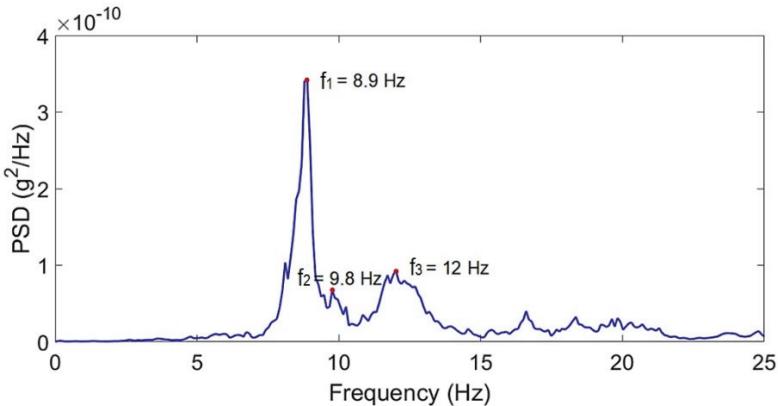


Figure 3 - Windowed and filtered results of the Fast Fourier Transformation

Power Spectral Density was obtained by ‘windowing’ the total length data, for which the length was assumed as 2048 data-points. The sampling rate of the data was 200 Hz, the same

as obtained from the test. Cut-off frequency of 50 Hz and an overlap (averaging rate) of 50% was used in the analysis. Also, a high-pass filter (0.15~0.50 Hz) was applied to all acceleration records.

As can be traced from Figure 3, the first natural frequency of the building appears to be 8.9 Hz ( $T_1 = 0.112$  sec) in X-direction (along the longer dimension of the building), and the second natural frequency is 9.8 Hz ( $T_2 = 0.102$  sec) in Y-direction (along the shorter dimension). The third natural frequency is about 12 Hz ( $T_3 \approx 0.08$  sec).

## 2.2. Finite Element Modelling

In order to carry on with the performance assessment phase, a 3-dimensional analysis model was prepared using the software SAP2000 (19) in line with the information provided by Akkon Celik Yapi Sistemleri A.S. The walls of the structure incorporate double layers of OSB panels, with a thickness of 12.5 mm each. The dimensions of the panels are 1220 mm (width) by 2440 mm (height), with a stud spacing of 610 mm on average. The screw distance is reported to be 150 mm on the exterior studs (of each panel) and 300 mm on the interior studs. The same panel and screw configuration is also used for the slabs. All panels and slabs are modelled as 4-node shell elements, rigorously meshed at appropriate sizes. It was observed that floor diaphragms caused numerical difficulties and unrealistic/unreliable FE behavior during the analyses. Thus, the floor members of the building (i.e. slabs and beams alike) were explicitly modelled and no diaphragms were assigned at floor levels.

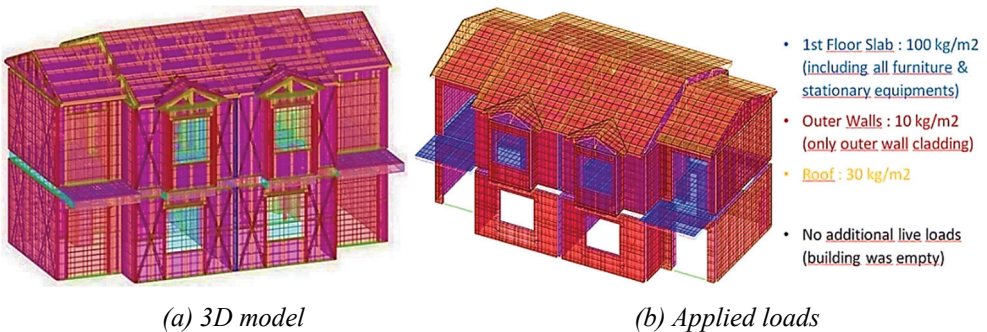


Figure 4 - Graphical representation of the analytical model

Apart from the project drawings, the mechanical properties of the panels and screws are defined similar to those provided by Karabulut (14). Suspended ceiling is not included in the model, and minor dimensional differences between the real-life structure and the analytical model, especially around the staircase, are ignored. The entire FE model of the building rests on simple supports, located at each frame intersection at the base level. Considering that the site was mostly uninhabited at the time of the visit, and that the present layout of the household consisted of limited furniture, a cautious approach was adopted for load definitions. Figures 4(a)-(b) illustrate the 3-D analysis model, along with the external loads applied on the structure.

The calibration of the analytical model is done through modal analysis. More detailed information about the modal calibration is provided by Yurtsever (18), and the modal results are obtained as given in Table 1. As the analyses progressed, there occurred a necessity to improve the analytical model, since the obtained results were far from being satisfactory (i.e. low modal participating mass ratios). Modifications yielded more stable results, as demonstrated in the table. Improvements to the model include updating the stiffness of the link elements, and the introduction of some rigid elements in order to counter unrealistic FE behavior, which are thoroughly explained by Yurtsever (20).

*Table 1 - Structural modal periods after updated link properties*

| Comparison of Natural Vibration Modes                 | 1st Natural Vibration Mode | Dir. | Modal Participating Mass Ratio | 2nd Natural Vibration Mode | Dir. | Modal Participating Mass Ratio | 3rd Natural Vibration Mode | Dir.  | Modal Participating Mass Ratio |
|---|----------------------------|------|--------------------------------|----------------------------|------|--------------------------------|----------------------------|-------|--------------------------------|
| Experimental Results                                  | 0.115 sec.                 | X    | N.A.                           | 0.107 sec.                 | Y    | N.A.                           | 0.080 sec.                 | X / Y | N.A.                           |
| Analytical Results                                    |                            |      |                                |                            |      |                                |                            |       |                                |
| W/O Links - Rigid Connections                         | 0.072 sec.                 | X    | 44%                            | 0.060 sec.                 | Y    | 66.6%                          | 0.043 sec.                 | X     | 20%                            |
| W/ Links (Elastic Stiffness) No Doors & Windows       | 0.130 sec.                 | X    | 37.7%                          | 0.117 sec.                 | Y    | 32.3%                          | 0.079 sec.                 | Y     | 27.5%                          |
| W/ Links (Elastic Stiffness) External Doors & Windows | 0.116 sec.                 | X    | 36.5%                          | 0.115 sec.                 | Y    | 39.9%                          | 0.074 sec.                 | Y     | 19.2%                          |
| W/ Links (Updated Stiffness) External Doors & Windows | 0.121 sec.                 | X    | 75.2%                          | 0.114 sec.                 | Y    | 82.7%                          | 0.094 sec.                 | X     | 8.7%                           |

### **2.3. Additional Improvements to the FE Model**

In order to verify and improve the link properties of the brace-to-frame connections used in the analytical model, two additional experiments were carried out in the Structures Laboratory of Boğaziçi University. The test specimens were prepared by combining two 1200x2400 mm CFS frames and assembling 70x1.5 mm strips as braces on both sides. Figures 5(a)-(b) illustrate both the general dimensions, and the sensor and/or strain gauge layout of the specimens, whereas Figures 6(a)-(b) provide the relevant analytical model details.

The first specimen was equipped with 11 mm gypsum, and the second was equipped with 11 mm OSB panels on both sides. Screw spacing on both specimens is 150 mm on the outer studs and girders, including the middle stud. The spacing on the interior studs and girders is 300 mm. From the three loading protocols proposed by ASTM E2126-11 (21), Test Method C (CUREE Basic Loading Protocol) was applied, using a push-pull type actuator with a maximum stroke of 200 mm. The resultant force-displacement curves for each specimen are given in Figures 7(a)-(b), respectively.

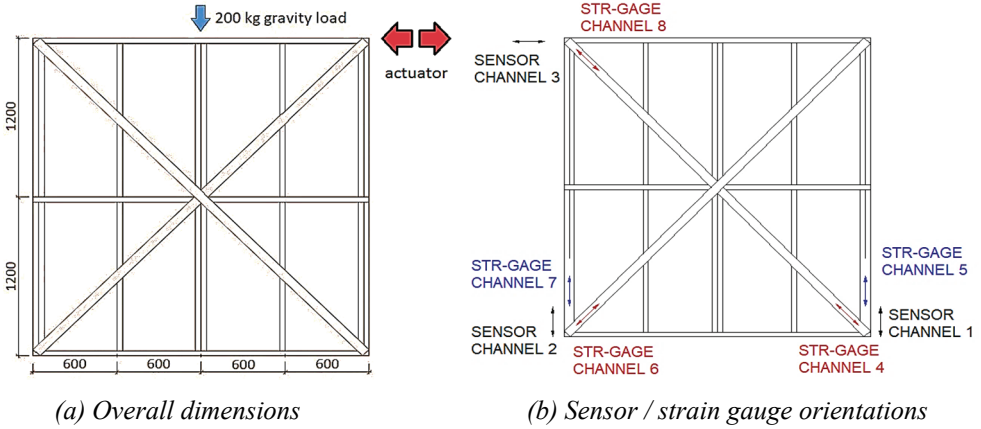


Figure 5 - General layout of the test specimens

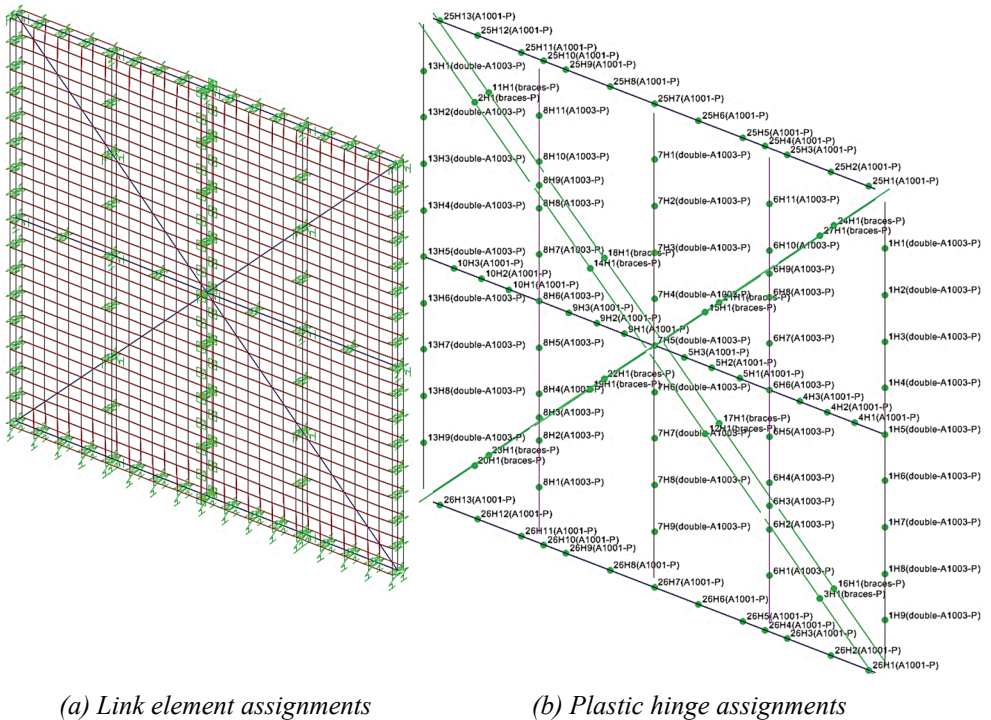
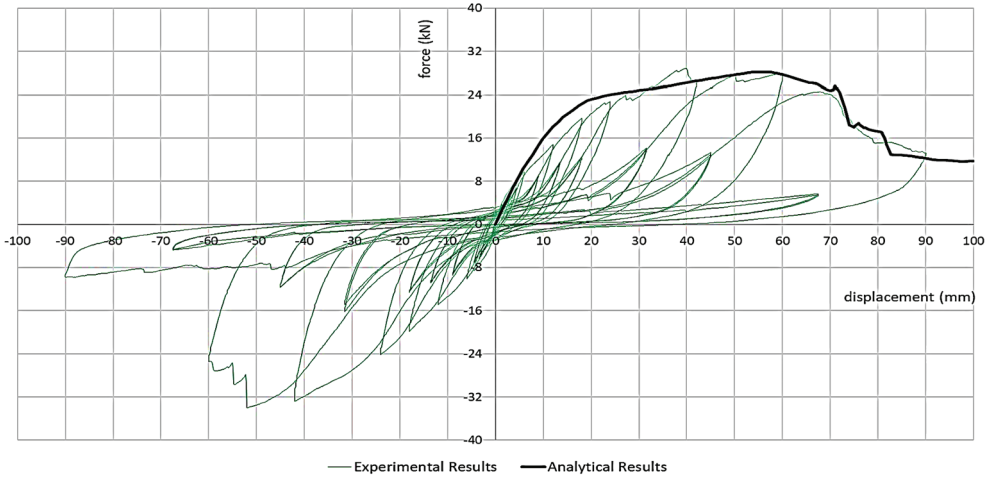
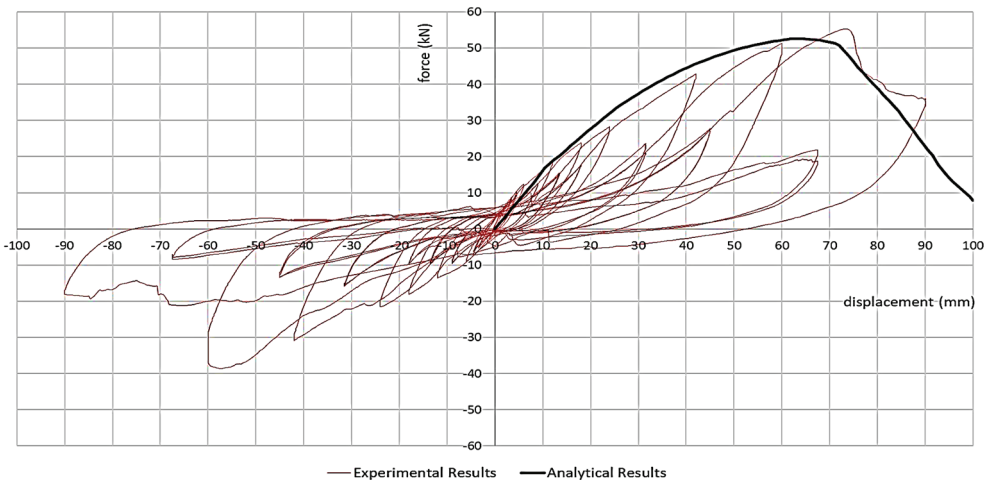


Figure 6 - A detailed representation of the analysis model

As stated previously, these experiments are aimed at generating a reliable force-displacement relationship for the brace-to-frame connections. Using two different panel types within the specimens helps to verify that the proposed relationship works for both panel types. An updated link property is defined (see Figure 8) and is verified in accordance with the test results. Additional nonlinearity is considered in the analysis in the form of plastic hinges in the studs, girders and braces, which are extensively covered in the following chapter.



*(a) Actuator force vs. panel top displacement for CFS frame with gypsum panels*



*(b) Actuator force vs. panel top displacement for CFS frame with OSB panels*

*Figure 7 - Cyclic test results of the braced CFS frames, superimposed with analysis results*

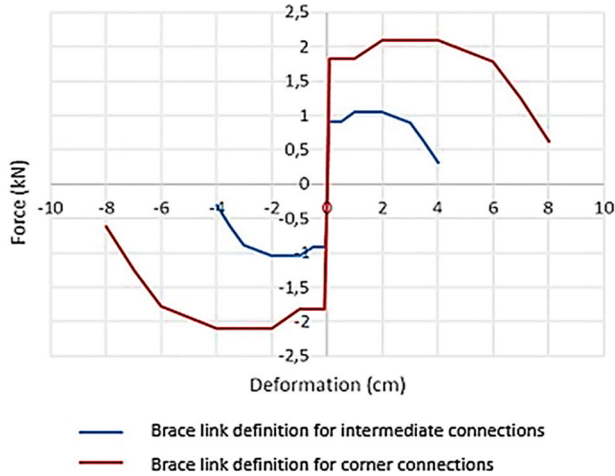


Figure 8 - The proposed force-deformation curves for the brace connections

### 3. PERFORMANCE ASSESSMENT OF THE FINALIZED FE MODEL

#### 3.1. Performance-Based Analyses: Introduction

In line with the assumptions and revisions made during experimental analyses, all braces in the analytical model of the Enez building have been redefined as two separate frame elements, connected to the CFS frame via additional two-joint links. Force-displacement behavior of the said links has been demonstrated in Figure 8. Table 2 displays the structural modes of the analytical model after these final improvements.

Table 2 - modal periods after updating the link properties of the brace connections

| Comparison of Natural Vibration Modes                 | 1st Natural Vibration Mode | Dir. | Modal Participating Mass Ratio | 2nd Natural Vibration Mode | Dir. | Modal Participating Mass Ratio | 3rd Natural Vibration Mode | Dir.  | Modal Participating Mass Ratio |
|---|----------------------------|------|--------------------------------|----------------------------|------|--------------------------------|----------------------------|-------|--------------------------------|
| Experimental Results                                  | 0.115 sec.                 | X    | N.A.                           | 0.107 sec.                 | Y    | N.A.                           | 0.080 sec.                 | X / Y | N.A.                           |
| Analytical Results                                    |                            |      |                                |                            |      |                                |                            |       |                                |
| W/ Links (Updated Stiffness) External Doors & Windows | 0.121 sec.                 | X    | 75.2%                          | 0.114 sec.                 | Y    | 82.7%                          | 0.094 sec.                 | X     | 8.7%                           |
| W/ Links (Updated Brace Links) No Doors & Windows     | 0.120 sec.                 | Y    | 43%                            | 0.117 sec.                 | X    | 54.1%                          | 0.099 sec.                 | Y     | 32.9%                          |

Regarding the pushover analyses, hinge definitions and assignments have also been modified. In studs for example, deformation controlled axial hinges are assigned along every one-tenth of the stud length. Similarly for girders around the door and window openings, deformation controlled axial hinges are defined along every one-fifth, one-fourth, one-third or half length

of the girder (depending on the girder length). Hinge interval is selected so that a sufficient level of nonlinearity is covered through a single frame element. After thoroughly examining the initial (pushover) analysis results and observing that some of the upper girders of the first-floor walls experience high compressive forces at the later stages of the analysis, it is acknowledged that these members, too, sustain significant nonlinear deformations. Thus, additional hinge definitions are made for girders at story levels in a similar manner. Formation of any shear-induced plastic hinges are ignored since there is no evident and reliable data in recent literature regarding this concept. For braces, deformation controlled axial hinges are considered and assigned at the mid-span of the braces, for which a small compression limit is defined to account for buckling. Hinges in all elements at rooftop level are also ignored.

A sample definition for stud hinges is given in Figure 9. As can be noticed, the value of applicable compressive stress immediately drops to 5% of the assumed buckling stress level, just after the yield strain is attained (point C [yellow dots] and point D [orange dots]). A typical stress-strain relationship is utilized to define controlling parameters, in order to keep the calculations as simple as possible. Hinge length is taken as approximately the half-depth of the section. Positive stress limit is taken as the yield stress, and the corresponding strain limit is obtained by simply dividing the yield stress by the modulus of elasticity (of steel). Negative stress and strain limits are calculated using the software GBTUL (22), CUFSM (23) and CUTWP (24), which have been specifically designed for evaluating the buckling modes of CFS sections. Their respective results are compared, and the lowest value is assigned as the buckling load of the member and divided by the cross-section area to obtain the relevant stress values.

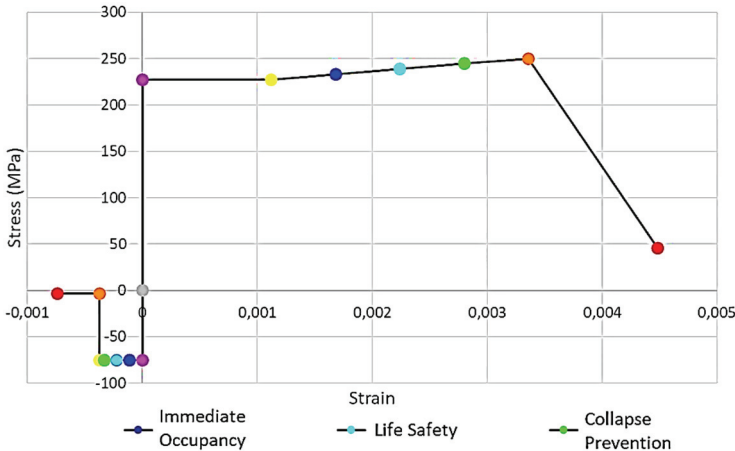


Figure 9 - Typical hinge definition (example given for studs)

For buckling mode calculations, braces are assumed to be clamped at both ends, considering that adjacent portions of the brace would both have to buckle towards the inside of a shear wall, and the rotations where they are fixed to the frame would then be practically zero. Studs are assumed to be free at one end and clamped at the other. Also, only half-length of the

member is considered since it was observed during laboratory tests that specimens showed no deformations around the mid-height of the studs (hence the clamped-end assumption). Girders are again assumed to be free at one end and clamped at the other. Member length is taken as the unrestrained distance between each stud (600 mm).

Post-buckling response of the elements (if there could be any) is neglected since their reliability is not verified for this specific model and/or requires extensive and time-consuming research. Instead, plastic hinges in compressive members are defined such that their load carrying capacity is diminished as soon as the buckling load limit is reached. A detailed interpretation for the post-buckling option is provided in Chapter 3.3, and it was eventually concluded that post-buckling need not be taken into consideration.

### 3.2. Performance-Based Analyses: Results

The resultant pushover curves are illustrated in Figures 10(a)-(b). There is a notable kink at the beginning of each curve, corresponding to the majority of the braces buckling at the initial stages of the analysis, which will be covered in detail in the following sections. It is also worth mentioning that pushover curves are only plotted up to the point where the analysis results are found to be reliable.

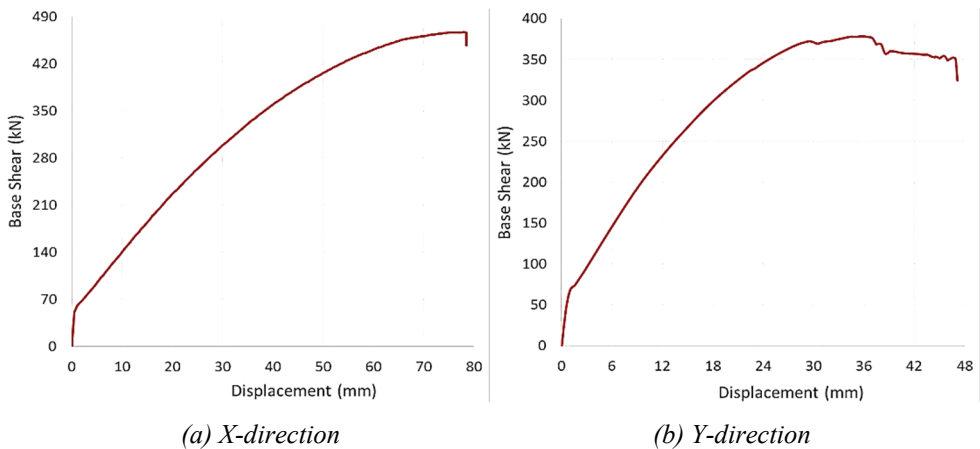


Figure 10 - The resultant pushover curves

A general representation for the resultant deformed shapes of the building after the pushover analyses in X-direction and Y-direction are given in Figures 11(a)-(b), respectively. Note the damage concentration in the structural elements around the stairs and back doors. There is also a slight damage propagation around the first-floor windows. Also, some damage appears to be concentrated in the structural elements on the central walls and around the first-floor windows, especially for the pushover analysis in Y-direction.

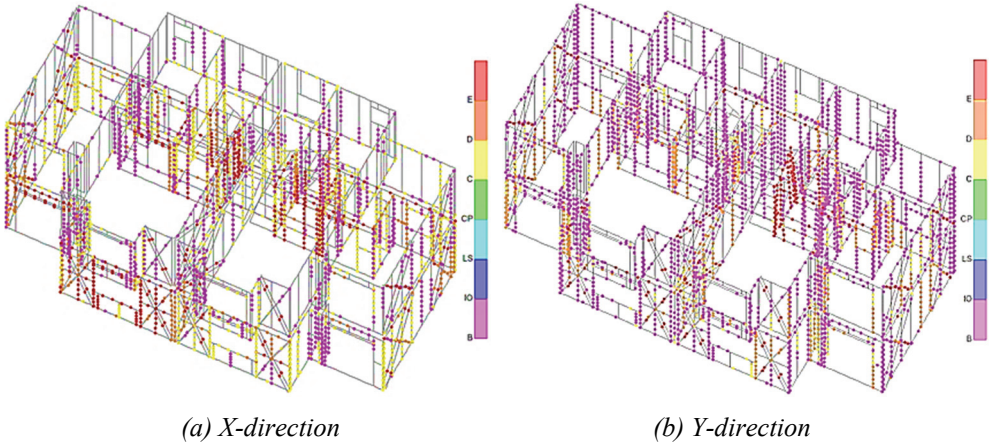


Figure 11 - Deformed shapes of the model after pushover analyses

The progression of the important events during the analysis is illustrated on the pushover curve in Figure 12, and it can easily be seen that the structure attains its base shear capacity at about 35 mm structural sway, when the structure nears to an unstable state where the number of failing elements increases unpredictably. Considering these results, *Immediate Occupancy* damage level has been selected as the stage where the first buckling members occur back at the staircase, and not the stage where the first hinge in a stud is observed. This assumption aims at prioritizing the importance of the stairwell rather than just any studs. It may be argued that prioritizing the staircase above all other structural components sounds more like a *life safety* condition. However, it should be noted that the proposed IO damage level only corresponds to the *first* plastic hinge in the staircase, which occurs at a reasonable displacement level of about 2.0 cm. Defining the same displacement as a life safety limit could as well be considered as over-design.

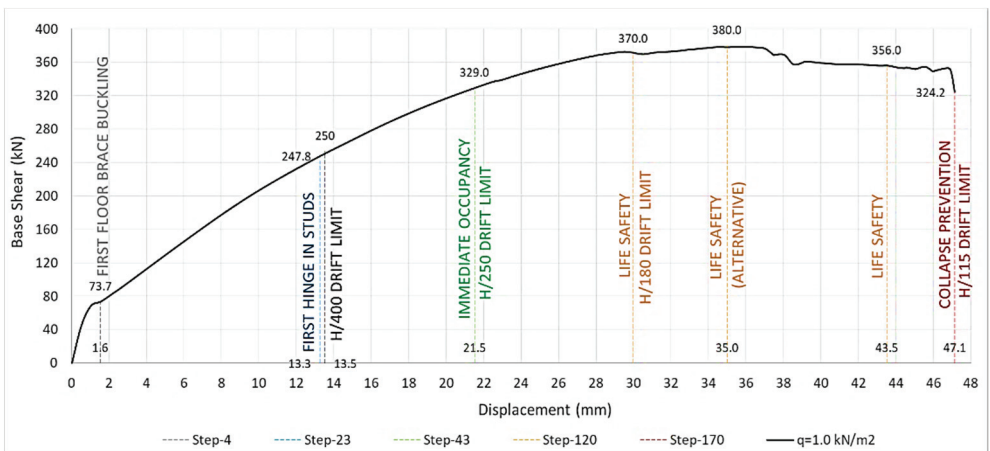


Figure 12 - Significant event progression and the proposed structural damage levels

*Life Safety* damage level, on the other hand, has been selected as the penultimate stage just before a multiple failure progression starts in any member. Understandably, *Collapse Prevention* damage level has been selected as the final point on the curve. Obviously, LS and CP damage levels appear too close for comfort, thus it is fair to say that LS damage level could as well be taken as the reference point in the design process. It may also be logical to shift LS damage level to the stage where the ultimate base shear is attained, which in this case corresponds to about 30-35 mm structural sway. While it is feasible according to the curve, it should be noted that this displacement level does not appear to physically represent a milestone in the performance history of the building. There are on-going hinge formations in the panels, yet it is difficult to ascertain which of the failing elements at this stage should define the ‘life safety’ limits.

A structural drift limit of  $H/400$ , where  $H$  is the height of the building, has also been considered. Excluding the rooftop, the effective height of this building is 5.40 m, and thus the allowable drift limit corresponds to 13.5 mm of structural sway. It has been demonstrated that this sway level corresponds to the very first plastic hinge occurring in a stud. In a similar way, it can be said that the proposed IO damage level corresponds to a structural drift limit of  $H/250$ . Similarly, CP damage level is attained at a structural drift of about  $H/115$ . Therefore, it can be surmised that LS damage level should bracket these limits, such as  $H/180$ . This translates to a 30 mm displacement, which in this case roughly corresponds to the stage where the base shear capacity is reached. It is important to note that the use of  $H/400$  limit here can be considered as a second method for determining the conventional elastic limit of the pushover curve. It is known that there are two methods available for determining the elastic limit of force-displacement relationships. One of them considers that the initial stiffness can be taken as the secant stiffness to the load level of  $0.4 \times F_{max}$ , as demonstrated and outlined in AISI S213 (25). In the other method proposed by Kawai et al. (26), the initial stiffness is considered as the secant stiffness to the drift level of  $H/400$ . A detailed interpretation for both methods is provided in the following section.

### 3.3. Evaluation of the Force Modification Factors

An additional analysis option was examined which also considered post-buckling in the structural elements. A post-buckling strength of 5-10% higher (depending on the section properties) was defined for CFS members, and their respective hinge behavior characteristics were adjusted. This method was attempted to see if the analysis results could be any different. In the end, it was observed that the results yielded only minor discrepancies, as illustrated in Figure 13.

These results must have been expected, because it was shown that the progression of plastic hinges in the studs appeared very late, yet very rapidly. The nonlinear behavior of the structure remained almost indifferent, since the only elements in the structure that would be in their ‘post-buckling’ state (before any stud reached the buckling load limit) would have been braces. In contrast, their failures appear earlier, and since their load carrying capacity is relatively very low, any post-buckling strength they would acquire would not change the overall nonlinear behavior of the structure. In other words, the post-buckling strength of the braces is very low (due to inherent small capacity) and therefore could be neglected. The post-buckling strength of the studs could also be neglected, since any hinge formation in the studs begin much later, so it does not have a considerable effect on the structural behavior

before the state of collapse. Therefore, the analysis results obtained without post-buckling option were retained.

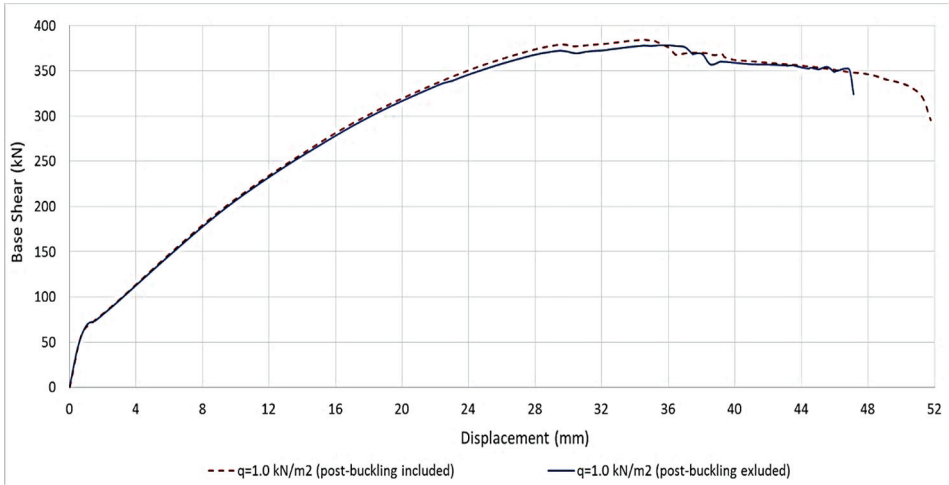


Figure 13 - Pushover analysis results with and without post-buckling effect

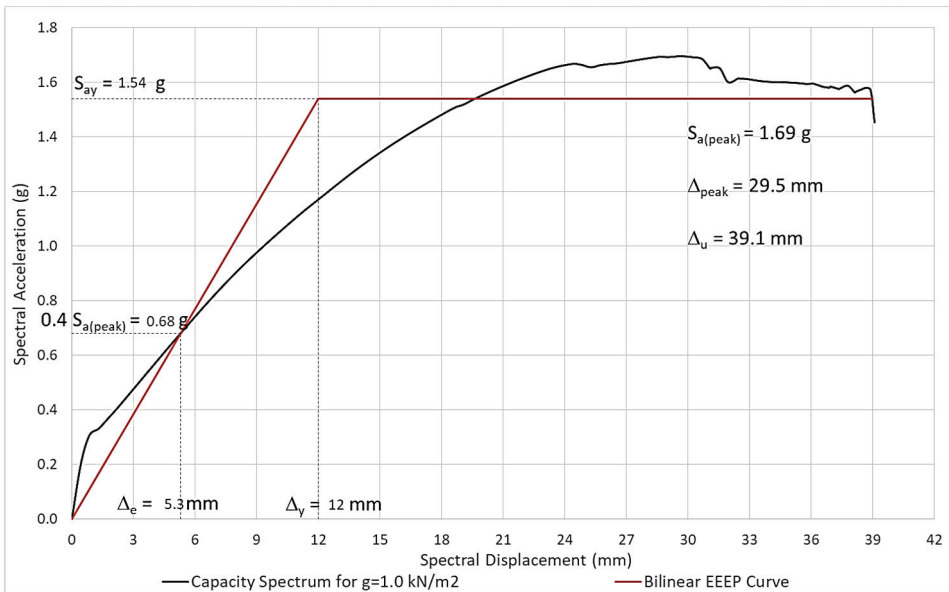


Figure 14 - Performance assessment in Y-direction

Other than that, it may be proper to add a few comments regarding the structural stiffness abruptly decreasing in the initial stages of the analysis. Obviously, this breaking point on the capacity curve does not predominantly represent the general structural behavior. This portion

of the curve may always be approximated to a smoother transition. However, the structure does behave in a linear fashion at the very beginning of the analysis. It should be fair to consider that if all structural elements (links, frames, etc.) could retain their elasticity, the structural response would have remained completely linear, and would follow up on the slope of this very steep initial portion of the curve. Thus, it is concluded that this initial portion must remain as it is in the related figures.

Evaluation of the seismic force modification factors is described in the Appendix 4A of the latest Turkish Seismic Code. Having converted the pushover curves for both X- and Y-directions into ADRS format (Acceleration-Displacement Response Spectra), performance assessment of the building starts with generating a bilinear EEEP (Equivalent Energy Elastic Plastic) approximation of the capacity curve. Figure 14 illustrates the determination of the bilinear EEEP curve for the pushover analysis in Y-direction, which is covered here for the sake of simplicity. The yield displacement is calculated to be  $\Delta_y = 27.7$  mm, and the ultimate displacement is  $\Delta_u = 65.2$  mm, which denotes the collapse point.

According to the Code, this specific building can be categorized as a structural system with limited ductility, for which the Structural Behavior Factor is defined as  $R = 3$  and the Overstrength Factor is given as  $D = 2$ . These values correspond to a ductility ratio of  $\mu_k = 1.5$ , as given in Equation 1, which is provided by the Code in Appendix 4A.3.1.

$$\frac{R}{I} = \mu_k * D \quad \rightarrow \quad \mu_k = \frac{R}{I * D} = \frac{3}{1 * 2} = 1.5 \quad [1]$$

where  $I$  is the Importance Factor, which is  $I = 1$ . However, the bilinear EEEP curve indicates that the real ductility ratio must be,

$$\mu_k = \frac{\Delta_u}{\Delta_y} = \frac{39.1}{12} = 3.26 \quad [2]$$

By substituting this value in Equation (1), the Structural Behavior Factor is computed as,

$$R = I * \mu_k * D = 1 * 3.26 * 2 = 6.5 \quad [3]$$

which is more than twice the value defined in the Code. For comparison, the values of the Force Modification Factors ( $R_a$ ) computed by using the default values in the Code and by using the ductility ratio obtained from the pushover analysis are given in Equations (4)-(5). It may be concluded from these results that the seismic force reduction factors tend to increase compared to those calculated with the default Code values, i.e. the seismic forces could have been reduced further.

$$R_a = D + \left(\frac{R}{I} - D\right) \frac{T}{T_B} = 2 + (3 - 2) \frac{0.1}{0.52} = 2.19 \quad (TSC 2018) \quad [4]$$

$$R_a = D + \left(\frac{R}{I} - D\right) \frac{T}{T_B} = 2 + (6.5 - 2) \frac{0.1}{0.52} = 2.86 \quad (Pushover analysis) \quad [5]$$

It is interesting to note that using the drift limit  $H/400$  here for determining the elastic limit is impractical, since the drift value of 13.5 mm corresponds to a spectral displacement of

about 11.0 mm. This value is just too large to be the elastic limit for the capacity curve in Y-direction and using this drift limit can only yield to unreliable calculations.

A brief interpretation of the Overstrength Factor should be made at this point. The value provided in TSC 2018 is intentionally preserved for above calculations since the computation of the factor varies from code to code. In TSC 2018 it is defined as the yield force value obtained from the EEEP approximation by the force value at which the first yielding in the structure takes place. Since there are very slender members such as braces in the structure, it can be claimed that buckling occurs at very early stages, which is testified by the analysis results. However, this may not always be considered as ‘yielding’, and it may be feasible to investigate for other structural members which undergo higher levels of deformations: positive elongations, for example. Identifying such members may not always be an easy task, and the obtained results may always be debatable, which may lead to unreasonably low or high overstrength values. Hence, the default value provided in the Code is utilized in order to eliminate any disputable results.

There is also another interesting aspect that needs to be pointed out at this stage. An elaborate observation of the hysteresis curves obtained from laboratory experiments (see Figure 7) hints that the envelopes of the curves appear to break slightly at a load level of about  $0.3 \times F_{max}$ . This point may also be considered as the yielding point since a significant decrease in stiffness takes place. However, the same trend does not persist in the force-displacement curves of the building model, apart from the obvious breaking in the initial portion. This may be attributed to the fact that component-based behavior may not always represent the full-scale structural response. In this specific case, for example, taking the  $0.3 \times P_{peak}$  value as the conventional elastic limit results in a smaller yield displacement, and consecutively a larger ductility ratio, which then only exaggerates the already higher force modification factors. Thus, it can be concluded that the existing assumption of  $0.4 \times P_{peak}$  for the elastic limit is reasonable.

#### **4. ADDITIONAL ANALYSES WITH VARIABLE PROPERTIES**

The variation of  $R$  values with regards to changeable design parameters is investigated through additional numerical studies. Again, it should be noted that only the capacity spectra in Y-direction are considered for the sake of simplicity, and that the pushover curves are only plotted up to the point where the analysis results are considered to be reliable.

##### **4.1. Gravity Loading Variations**

The results indicate that both base shear and deformation capacity of the structure tend to decrease with higher gravity loads (as expected). It was also observed that the gravity load levels and their distribution along the building influence the capacity spectrum (see Figure 15). Load distribution mainly dominates the first mode shape, resulting in varying capacity spectra with increasing gravity loads. It must be noted that the natural vibration period of the building changes as well. It can be concluded that Structural Behavior Factor varies with respect to the magnitude and distribution of the gravity loads. Performance-wise, it is observed that ductility ratios fluctuate between 3.08 and 3.70, where values generally tend to decrease with higher gravity load levels.

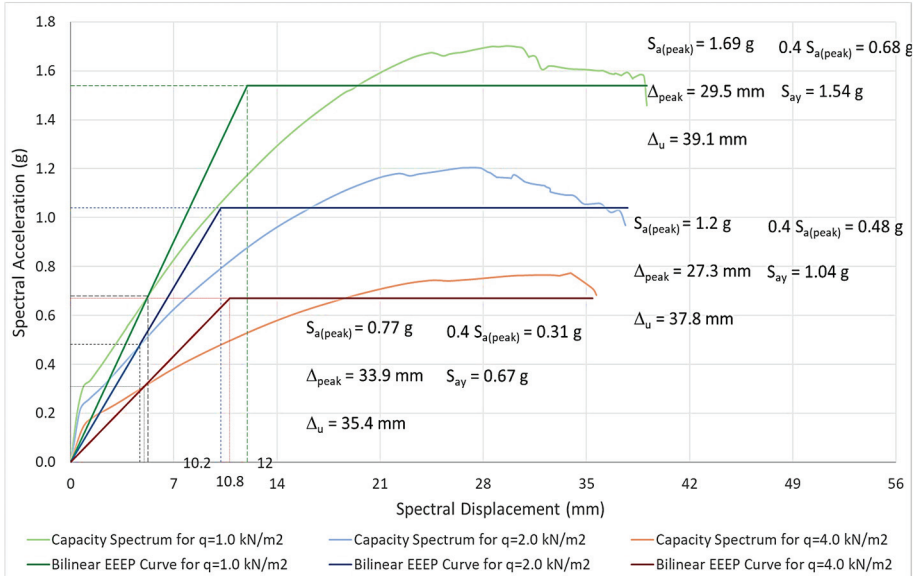


Figure 15 - Performance-based computations for analysis models with varying gravity loads

#### 4.2. OSB Shear Panel Variations

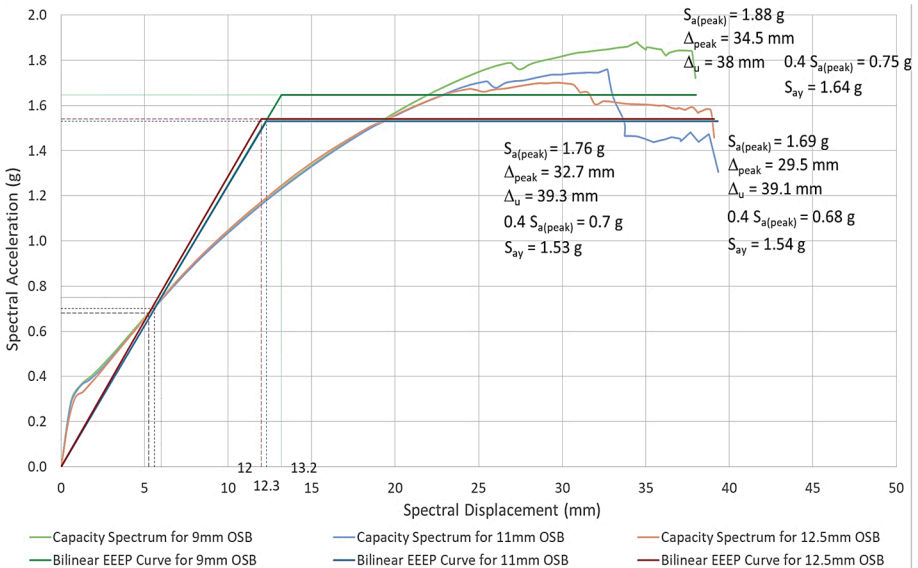


Figure 16 - Performance-based computations for analysis models with varying OSB panel thickness

For this investigation, gravity load levels are taken as 1.0 kN/m<sup>2</sup> live loads in addition to 1.0 kN/m<sup>2</sup> superimposed dead loads. It was observed that the natural vibration period of the

building did not change by much, thus the original value is used in the calculations. It can be concluded from the results (see Figure 16) that both base shear and structural deformation capacities do not vary greatly with respect to panel thickness. Here, it is observed that ductility ratios fluctuate between 2.90 and 3.26, where values tend to increase with panel thickness.

### 4.3. Gypsum Shear Panel Variations

Similar to the previous investigation, a live load level of 1.0 kN/m<sup>2</sup> in addition to 1.0 kN/m<sup>2</sup> superimposed dead loads is taken as gravity loads. Again, it was observed that the natural vibration period of the building did not change by much, thus the original value is used in the calculations. By looking at the results (see Figure 17), it can be concluded that both base shear and structural deformation capacities do not change by much with respect to panel thickness, in fact they look almost identical. Ductility ratios fluctuate between 6.25 and 7.30, where values tend to increase with respect to panel thickness.

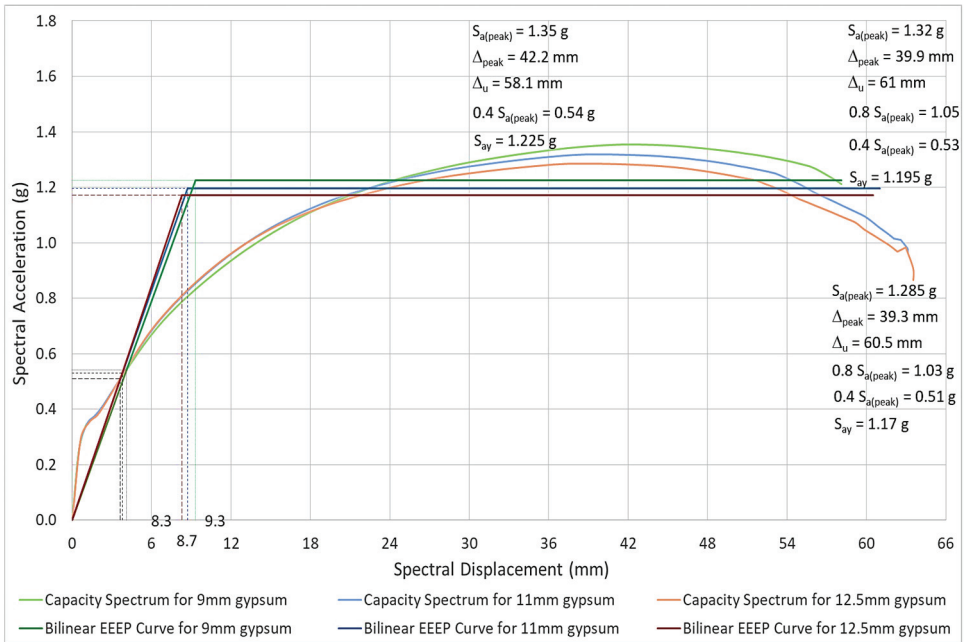


Figure 17 - Performance-based computations for analysis models with varying gypsum panel thickness

### 4.4. Connection Rigidity Variations

The original screw spacing is kept unaltered for all analyses for the sake of simplicity. Thus, varying levels of robustness is taken into consideration for singular connections. ‘Mild connection’ corresponds to one-half  $F-d$  values, and ‘stiff connection’ means twice as much  $F-d$  values than those given for the original set of connections.

It can be concluded from the results that using a stiffer connection type increases both the base shear and the structural deformation capacities (see Figure 18). It is also observed that ductility ratios range between 2.55 and 5.00, where values decrease with higher robustness. It should be noted that the applied gravity loads are 1.0 kN/m<sup>2</sup> live loads in addition to 1.0 kN/m<sup>2</sup> superimposed dead loads, and that the natural vibration period of the building does not change by much.

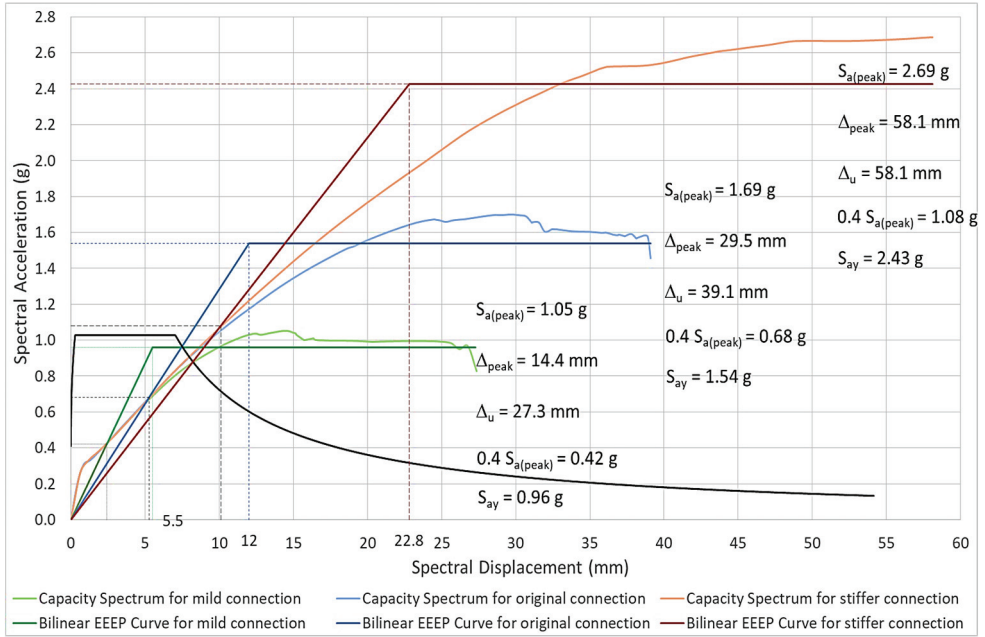


Figure 18 - Performance-based computations for analysis models with varying connection stiffness

## 5. RESULTS AND OTHER CONSIDERATIONS

It is certain that results obtained from only one building are not sufficient to draw a precise picture. In this specific study, it was shown that the Structural Behavior Factors calculated from the pushover analysis results were generally higher than those defined in TSC 2018. In some cases, calculated values appeared to go up by as much as three times, which is in fact higher than they normally should be. There is always an inevitable possibility of numerical errors in such sensitive analyses, therefore it is essential that these results are backed by further studies. The Structural Behavior Factor definition of the Code may as well be interpreted as having a decent margin for safety. Some other conclusions that can be drawn from this study are outlined below.

1. Both base shear capacity and deformation capacity of the structure tend to decrease with higher gravity loads. Also, the applied gravity loads and their distribution along the building greatly effects the structural capacity spectrum. Load distribution mainly dominates the first mode shape, i.e. the natural vibration period(s) of the building changes

with increasing load levels. In conclusion, Structural Behavior Factor varies with respect to the magnitude and distribution of the gravity loads.

Although not perfectly fit, the proposed approximate trend-line (see Figure 19) suggests that the ductility ratio (hence the Structural Behavior Factor) should decrease with increasing amount of dead and live loads, which sounds meaningful to some degree. The notation ‘seismic weight ratio’ in the figure corresponds to the total seismic weight computed in compliance with the Code, divided by the dead weight of the building, rooftop and sidewall claddings included. For example, the self-weight of the building is 165 kN according to analysis results, while the seismic weight of the building is calculated as 267.1 kN for the gravity loading case where dead loads are 1.0 kN/m<sup>2</sup> and live loads are 1.0 kN/m<sup>2</sup>. This gives the ratio of 1.62, which is the lowest value on the figure. For higher levels of the gravity loading, higher seismic weight ratios are obtained, which are subsequently indicated on the figure. When there are absolutely no loads acting on the structure, i.e. the very initial case where the structure has just been constructed, the seismic weight ratio of the structure is 1.0, according to the above definition. In this case, trend-line suggests that the ductility ratio could be just about 3.5.

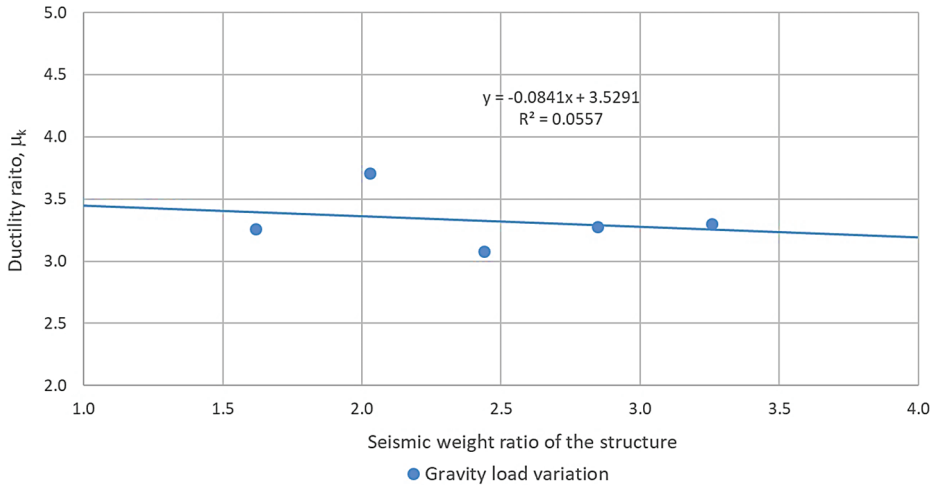


Figure 19 - The variation of the ductility ratio with respect to varying gravity load levels

2. For a predefined level of the gravity loads, OSB or gypsum thickness is nearly ineffectual on either the resultant base shear capacity or the resultant structural deformation capacity. The calculated values of the ductility ratio for both panel types are illustrated in Figure 20, along with their trend-lines. It should be noted that the Structural Behavior Factors are simply twice their respective ductility values, according to the assumptions  $D = 2$  and  $I = 1$ .

It is evident that the ductility appears to be higher in buildings with gypsum-sheathed CFS shear walls. Also, the variation of the ductility ratio with respect to panel thickness is greater with gypsum panels. The proposed trend-lines suggest that, while an average

value could be applied for the Structural Behavior Factor in buildings with OSB-sheathed CFS shear walls,  $R$  values should be increased along with greater values of board thickness in buildings with gypsum-sheathed CFS shear walls. It is fair to say that TSC 2018 lacks necessary guidelines in this aspect and should be modified.

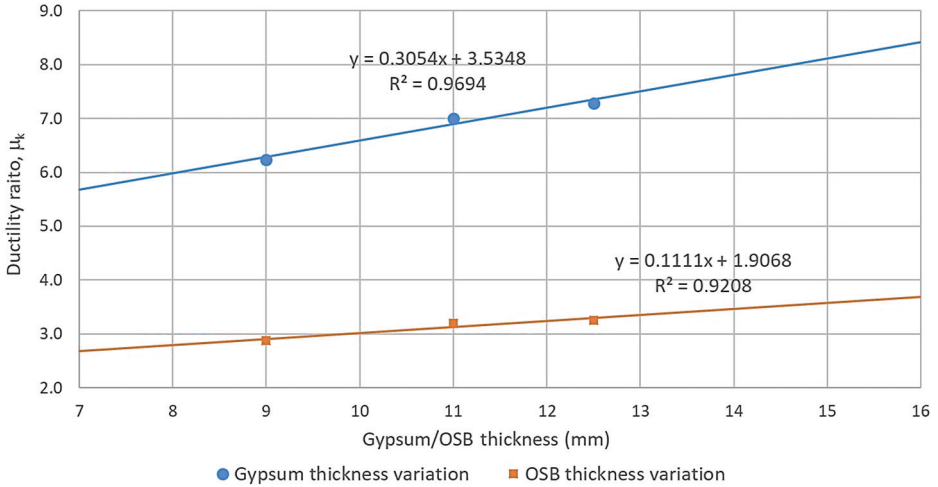


Figure 20 - The variation of the ductility ratio with respect to gypsum & OSB thickness

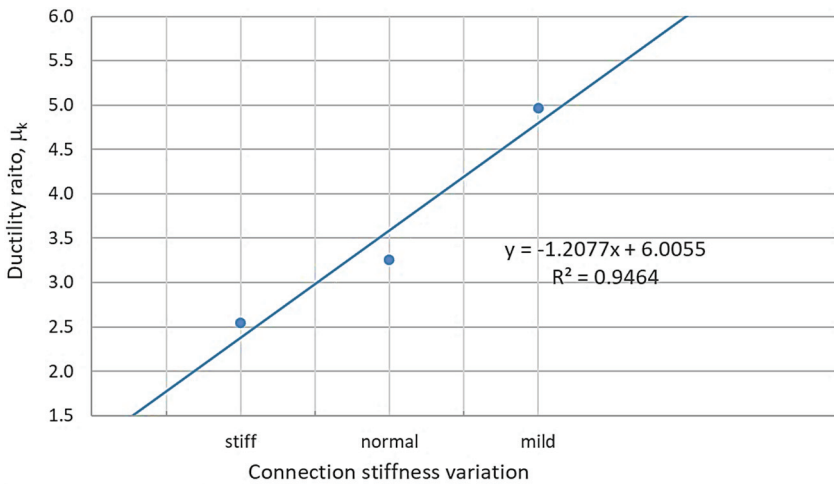


Figure 21 - The variation of the ductility ratio with respect to connection stiffness

3. Regarding the rigidity level of a single frame-to-frame or frame-to-panel connection, it was shown that using a stiffer connection type greatly increases both the base shear capacity and the structural deformation capacity. However, the proposed trend-line (see Figure 21) suggests that the stiffer they are, the smaller is the Structural Behavior Factor.

While this is somewhat addressed in TSC 2018 by defining a lower  $R$  value for structural systems with limited ductility, there is no exact definition of a structural system with limited ductility, other than the referral to utilizing braces and/or gypsum panels within the structure. There is no example of what ductility level should be considered for buildings where OSB panels *and* braces are used together, for example. In this specific study, it was shown that in such systems the ductility ratio could be as much as 5.0 or even greater.

## 6. CONCLUSIONS

Although this construction material can be regarded as one of the most reliable, it may still contain imperfections. Moreover, a cold-formed steel section is arguably more sensitive to faulty workmanship during the construction phase: even the slightest tilting or bending of the member may cause significant second-order stress concentrations within the cross-section. Thus, it may be helpful to introduce a safety factor ( $\gamma_m$ ) as caution. Taking this into account, the formulations given in Chapter 5 can be rewritten as below.

for considering the effect of gravity loading:

$$R = \frac{I^*D}{\gamma_m} \left( 3.5 - \frac{W_E}{12W} \right) \quad [6]$$

(where  $W_E$  is the total seismic weight, and  $W$  is the dead weight of the structure)

for OSB-sheathed CFS buildings with double-X strap braces:

$$R = \frac{I^*D}{\gamma_m} \left( \frac{t}{9} + 1.9 \right) \quad (\text{where } t \text{ is panel thickness}) \quad [7]$$

for gypsum-sheathed CFS buildings with double-X strap braces:

$$R = \frac{I^*D}{\gamma_m} \left( \frac{t}{3.3} + 3.5 \right) \quad (\text{where } t \text{ is panel thickness}) \quad [8]$$

While it is obvious that stiffer connections are less ductile, it is difficult to formulate this relationship. As already stated, many factors contribute to the connection rigidity, and should be separately analyzed. Here for this case study, only the screw cross-section is considered for the sake of simplicity. Thus, an equation can be formulated as in Eq. (9).

$$R = \frac{I^*D}{\gamma_m} \left( 6 - \frac{1.2A}{A_{ref}} \right) \quad [9]$$

where  $A$  is the area of the screw cross-section, and  $A_{ref}$  is a reference screw section. Instead of area proportioning, the term  $d/d_{ref}$  may also be preferred since the diameter of the screw can be more of a meaningful criterion in design. Here it is important to determine a reference screw section ( $d_{ref}$  or  $A_{ref}$ ), and a benchmark experiment may be required to define a standard ductility level. The screws used in this experiment may be accepted as  $A_{ref}$  or  $d_{ref}$  for example,

and the effect of different screw sections on the structural behavior factor can be put into numbers with the above formula.

It was shown in this specific example that the ductility ratio, hence the Structural Behavior Factor generally decreases with increasing gravity loads. The reason for this was based on the load distribution within the building, thus affecting the structural mode shapes. Load distributions may not always be similar in different types of buildings. However, if additional studies on the same subject support this trend, i.e.  $R$  values decrease with gravity loads, it may be convenient to associate the values in the Code with the design loads of a structure. In practice, this could mean that the Structural Behavior Factors of a CFS-framed residential building and a CFS-framed school or hospital, for instance, would not be the same.

It is also worthwhile to recall for the sake of simplicity that, the analytical the analytical studies within this study only included the investigation of the structural performance with respect to the rigidity of a singular connection,. The rigidity of a single connection may as well originate from the thickness of the screws, the thickness of the frame cross-section, the thickness of the panels, or a combination of all of these. It was shown that the increasing connection stiffness yields a higher base shear capacity and a higher deformational capacity. Yet, the exact manner by which the connection stiffness is doubled or tripled is open to discussion. Thus, it may also be interesting to see if structural performance is anyhow affected by varying screw spacing, which is a more meaningful interpretation of connection rigidity.

## Symbols

|            |   |
|------------|---|
| $A$        | Area of the screws  |
| $A_{ref}$  | Area of a reference set of screws                                   |
| $d$        | Displacement (or deformation); screw diameter                       |
| $d_{ref}$  | Diameter of a reference set of screws                               |
| $D$        | Overstrength factor, as defined in TSC 2018                         |
| $F$        | Force   |
| $F_{max}$  | Peak value of the force   |
| $g$        | Gravitational acceleration; gravity loads (superimposed dead loads) |
| $H$        | Height of the structure   |
| $I$        | Earthquake importance factor of the structure                       |
| $P_{peak}$ | The peak value of base shear (or force)                             |
| $q$        | Live loads  |
| $R$        | Response modification factor; structural behavior factor            |
| $R^2$      | Proportion of variance  |
| $R_a$      | Seismic force reduction factor                                      |

|                 |  |
|-----------------|--|
| $S_{a(peak)}$   | The peak value of spectral (response) acceleration                   |
| $S_{ay}$        | Spectral (response) acceleration at yield                            |
| $t$             | Panel thickness  |
| $T$             | Period; the fundamental period of the building                       |
| $T_B$           | Upper corner period of the elastic design acceleration spectrum      |
| $T_i$           | The natural vibration period related to the $i^{th}$ structural mode |
| $W$             | Dead weight of the structure   |
| $W_E$           | Total seismic weight (computed in accordance with TSC 2018)          |
| $\Delta_e$      | Elastic displacement   |
| $\Delta_{peak}$ | The displacement value at peak response acceleration level           |
| $\Delta_u$      | Ultimate displacement  |
| $\Delta_y$      | Yield displacement   |
| $\gamma_m$      | Factor of safety   |
| $\mu_k$         | Ductility ratio  |

### **Acknowledgements**

The authors acknowledge the Department of Civil Engineering of Boğaziçi University for the technical support to the research activity, and Akkon Celik Yapi Sistemleri A.Ş. for the procurement of the steel strap-braces for laboratory experiments, and the real-life building for ambient vibration tests. The authors would also like to thank the anonymous reviewer for the precious comments and suggestions to improve the quality of the paper.

### **References**

- [1] Türkiye Bina Deprem Yönetmeliği, Deprem Etkisi Altında Binaların Tasarımı İçin Esaslar, T.C. İçişleri Bakanlığı Afet ve Acil Durum Yönetimi Başkanlığı, Ankara, Türkiye, 2018.
- [2] Della Corte, G., Fiorino, L., Landolfo, R., “Seismic behavior of sheathed cold-formed structures: numerical study”, *Journal of Structural Engineering*, 132(4), 558-569, 2006.
- [3] Landolfo, R., Fiorino, L., Della Corte, G., “Seismic behavior of sheathed cold-formed structures: physical tests”, *Journal of Structural Engineering*, 132(4), 570-581, 2006.
- [4] Dubina, D., “Behavior and performance of cold-formed steel-framed houses under seismic action”, *Journal of Constructional Steel Research*, 64, 896-913, 2008.

- [5] Velchev, K., Comeau, G., Balh, N., Rogers, C.A., “Evaluation of the AISI S213 seismic design procedures through testing of strap braced cold-formed steel walls”, *Thin-Walled Structures*, 48, 846-856, 2010.
- [6] Nithyadharan, M., Kalyanaraman, V., “Behavior of cold-formed steel shear wall panels under monotonic and reversed cyclic loading”, *Thin-Walled Structures*, 60, 12-23, 2012.
- [7] Shamim, I., Rogers, C.A., “Steel sheathed/CFS framed shear walls under dynamic loading: numerical modelling and calibration”, *Thin-Walled Structures*, 71, 57-71, 2013.
- [8] Sato, A., Uang, C.M., “A FEMA P695 study for the proposed seismic performance factors for cold-formed steel special bolted moment frames”, *Earthquake Spectra*, 29(1), 259-282, 2013.
- [9] Iuorio, O., Macillo, V., Terracciano, M.T., Pali, T., Fiorino, L., Landolfo, R., “Seismic response of CFS strap-braced stud walls: experimental investigation”, *Thin-Walled Structures*, 85, 466-480, 2014.
- [10] Bian, G., Padilla-Llano, D.A., Buonopane, S.G., Moen, C.D., Schafer, B.W., “OpenSees modeling of a wood-sheathed cold-formed steel-framed shear walls”, *Proceedings of the Annual Stability Conference*, Structural Stability Research Council, Nashville, Tennessee, March, 2015.
- [11] Senkardesler, O., Goler, G., Soyoz, S., “Dynamic and cyclic response of a full-scale 2-story cold-formed steel structure with and without infill materials”, *Bulletin of Earthquake Engineering*, 15(8), 3207-3326, 2016.
- [12] Borzoo, S., Mir Ghaderi, S.R., Mohebi, S., Rahimzadeh, A., “Nonlinear finite element modeling of steel-sheathed cold-formed steel shear walls”, *Steel and Composite Structures*, 22(1), 79-89, 2016.
- [13] Madsen, R.L., Castle, T.A., Schafer, B.W., “Seismic design of cold-formed steel lateral load-resisting systems: a guide for practicing engineers”, *NEHRP Seismic Design Technical Brief No.12*, Engineering Laboratory, National Institute of Standards and Technology, Gaithersburg, Maryland, August, 2016.
- [14] Karabulut, B., Soyoz, S., "Experimental and Analytical Studies on Different Configurations of Cold-Formed Steel Structures", *Journal of Constructional Steel Research*, 133, 535-546, 2017.
- [15] Leng, J., Peterman, K.D., Bian, G., Buonopane, S.G., Schafer, B.W., “Modeling seismic response of a full-scale cold-formed steel-framed building”, *Engineering Structures*, 153, 146-165, 2017.
- [16] Riahi, H.T., Zeynalian, M., Rabiei, A., Ferdosi, E., “Seismic collapse assessment of K-shaped bracings in cold-formed steel frames”, *Structures*, 25, 256-267, 2020.
- [17] Haghpanah, F., Schafer, B.W., “Updated seismic fragility functions for cold-formed steel framed shear walls per FEMA P-58 methodology”, *Engineering Structures*, 244:112753, 2021.

- [18] Yurtsever, M., “Ortamsal titreşim deneyleriyle hafif-çelik yapılarda titreşim periyotlarının belirlenmesi ve doğrulanması”, *Çelik Yapılar*, 55, 38-45, 2018.
- [19] CSI SAP2000 v20.2.0, *Integrated Finite Element Analysis and Design of Structures*, Computers and Structures Incorporated, Berkeley, California, 2019.
- [20] Yurtsever, M., “An investigation on force modification factors in cold-formed steel structures”, Ph.D. Dissertation, Boğaziçi University, Istanbul.
- [21] ASTM E2126, *Standard Test Methods for Cyclic (Reversed) Load Test for Shear Resistance of Vertical Elements of the Lateral Force Resisting Systems for Buildings*, American Society for Testing and Materials International, West Conshohocken, Pennsylvania, USA, 2011.
- [22] GBTUL 2.06, *Generalized Beam Theory at the University of Lisbon*, Generalised Beam Theory Research Group, Instituto Superior Técnico, University of Lisbon, 2016.
- [23] CUFSM 5.01, *Constrained and Unconstrained Finite Strip Method*, Thin-Walled Structures Group, Department of Civil and Systems Engineering, Johns Hopkins University, Baltimore, 2019.
- [24] CUTWP, *Cornell University Thin-Walled (Section) Properties*, Cold-Formed Steel Structures Research Group, School of Civil and Environmental Engineering, Cornell University, Ithaca, New York, 2003.
- [25] AISI S213-07 w/S1-09, *North American Standard for Cold-Formed Steel Framing – Lateral Design*, American Iron and Steel Institute, Washington D.C., USA, 2012.
- [26] Kawai Y., Kanno R., and Hanya K., “Cyclic shear resistance of light-gauge steel framed walls”, *ASCE Structures Congress*, Poland, USA, 433-437, 1997.

# **Determination of Finite Element Modelling Errors for Box Culverts Using Field Load Tests**

**Tuna ULGER<sup>1</sup>**

## **ABSTRACT**

Buried culverts have been in service more than half a century and their age raises questions about their reliable serviceability for the new standard vehicles. The gross weight and axle spacing of these trucks play an important role on the performance of the buried culverts where the culvert is covered with shallow fill heights. Field live load tests were conducted by driving a loaded truck over some culverts at slow speed while recording data at the critical locations of these culvert. Finite element (FE) models were developed and calibrated using field load test results. Live load distribution formulations were adopted from AASHTO LRFD Bridge Design Specifications for different fill heights. Two- and three-dimensional FE models were modelled and loaded separately to compare the critical section forces. The results showed that the error using two different FE modelling approach yields more than 100% error for the maximum section forces when fill heights is between 60 cm and 120 cm. This study is aimed to highlighting the inherent error in numerical modelling of buried reinforced box culverts for design or rating purposes.

**Keywords:** Box culvert, field test, fill height, load distribution, finite element modelling.

## **1. INTRODUCTION**

The importance of the load distribution on the buried structures remains an important research topic. Either using classical or alternative filling materials, researchers have studied the accurate load distribution methods of these materials [1–9] with others. These studies showed that the correct live load distribution is an important parameter in FE modelling either using traditional or any material as filler material. Generally, the rapid and alternative construction techniques proposed for an engineering solution to minimize the construction costs. One typical example of catastrophic reconstruction collapse of the I-88 crossing of Carrs Creek in Sydney, New York showed that the correct numerical modelling is an important tool for actual load rating and service life estimation of the existing culverts before dealing with an expensive and extensive construction works [7].

---

Note:

- This paper has been received on December 22, 2021 and accepted for publication by the Editorial Board on May 17, 2022.
- Discussions on this paper will be accepted by September 30, 2022.
- <https://doi.org/10.18400/tekderg.1039744>

1 Department of Civil Engineering, Zonguldak Bulent Ecevit University, Zonguldak, Turkey  
tunaulger@beun.edu.tr - <https://orcid.org/0000-0002-1758-8299>

The age of buried culverts in soil has raised questions about their structural performance for transportation activities. Louisiana State required the Transportation Department of the state to rate their culverts to continue their service or post a tonnage limit if the culvert is low load rated in federal program. Early studies showed that the research was concentrated on the steel culvert performances, mainly their corrosive resistance and durability were investigated for different steel pipe culverts [10,11]. In general, their study highlighted and categorized protective measures for metallic culverts. Similar studies today showed that the performance of these metallic culvert's and load rating test have been investigated in recent years [12–14]. Even though the number of transportation alternatives varies, these culverts continue to carry the increased gross weight of heavy vehicles. In addition to these updated axle loads with varying axle spacing, the old detailing of these culverts raises questions about their strength and serviceability. Different modelling approaches and assumptions have been studied to create an accurate approach for the load rating of the culverts including the experimental field load tests [1–5]. The results showed that these culverts do not show any structural deficiency when they are visually inspected; however, the load rating factors were calculated below the threshold after performing finite element analysis [15]. In one study, the wheel loads over 60 cm to 365 cm fill heights were extracted using pressure cells buried in soil during the field tests to define the wheel load distribution on culverts [1]. In a similar investigation, it was determined that when the fill height is less than 60 cm live load distribution defined in AASHTO LRFD method gives conservative results [2]. Another suggestion was that the section forces due to live load can be neglected when the fill height is above 180 cm after the investigation of relation between the fill depth and culvert performances for different fill heights [6]. In other experimentally tested culverts, flexure dominated failures governed the failure of tested box culverts and their load capacities were obtained either above the calculated capacity [3] or similar to the calculated load capacity [16–18] using AASHTO LRFD load distribution. . The shear failure of the box culverts could not be observed until the applied shear force reached 2 times the designed shear capacity of the tested culverts [19]. Another performance defining parameter is found to be the pavements on road surfaces [20]. The pavement redistributes the wheel load before transferring to the soil; therefore, it helps to increase the performance and load rating of the culverts.

The study here investigates the modelling differences for the reinforced concrete box culverts filled with traditional earth fill. The experimental field tests, culvert details, concrete properties, and surveyed fill heights of the four culverts are provided. All of these culverts cross the traffic perpendicularly. Section forces at the critical locations were collected when the culverts are subjected to the three axle tandem truck loads. This study was repeated with two-dimensional (2D) and three-dimensional (3D) finite element (FE) models. AASHTO LRFD live load distribution method [21] was applied to the culverts having different fill heights. The critical section forces were obtained from the parametric studies of the culvert models, and the modelling errors for different barrel sizes having different fill heights were investigated.

## 2. INSPECTED CULVERTS

### 2.1. Loads and FE Modelling

The fill height of each culvert was initially surveyed so that the truck axle load can be distributed following the AASHTO LRFD live load distribution method. The fill heights vary at the centre and the curb of the pavement, so an average fill height was calculated after multiple fill height measurements on the road surfaces. It should be noted that the FE results can vary due to averaging of the fill heights which will overestimates along the center of the pavement path forces and underestimates the pavement edge forces because the load pressure is highly dependent on the AASHTO equations and fill height depth. The tire contact area was given 250 mm x 510 mm according to the AASHTO equations, and the axle pressured area is formulated depending on the fill height as given in Equation (1). After the fill height exceeds 60 cm, a new loaded area can be defined using Equation (2). The axle load pressures at different fill heights can overlap with neighbour axle's the loaded areas depending on the axle spacing. Load pressure at the overlapped area is normally higher than the non-overlapped areas; which intensify the pressure at those overlapped zones; therefore, when the loaded areas were overlapped, the cumulative load pressure was uniformly redistributed to the total loaded area.

The axle loads were calculated as the uniform axle load pressures for the 3D FE element models where the shell elements were assigned to the culverts' sections. The axle load pressure is converted to uniform line load by multiplying the unit width for the beam elements that the influence lines are defined in 2D and 3D FE models.

$$FH \leq 600mm$$

$$W_{perp} = 2440 + 0.12xLS \quad (1)$$

$$W_{span} = 250 + 1.15x FH$$

$$FH > 600mm$$

$$W_{perp} = 250 + 1.15x FH \quad (2)$$

$$W_{span} = 510 + 1.15x FH$$

The notations are; FH = Fill height of the culvert (mm), LS = Clear span length (mm),  $W_{perp}$  = Equivalent distribution width perpendicular to span (mm), and  $W_{span}$  = Equivalent distribution length parallel to span (mm) in Equations (1) and (2)

In 3D FE model, thin shell elements are utilized for modelling the slab and wall sections in SAP2000 commercial structural analysis program [22]. The mid-plane geometry of the culvert sections given in Figure 1(b) was drawn for the 2D culvert model as shown in Figure 1(a). Exact clear width and the height of the barrels are redefined with the rigid end offset option in FE models. The foundation soil can be assumed rigid and the variation of the section forces can be neglected where the previous study showed that the soil springs has about 5% effect on the section forces [23]. In 3D FE models, axle load distribution can be defined with two different approaches. The first one can be step by step loading which is the summation

of loaded area groups which represents all of the axle loads and positions moving from start to the end of the culvert. For example, a typical loaded area group for single truck position is shown as the shaded rectangular elements in Figure 2(a). Axle positions were moved one element length at every step to obtain a continuous data similar to the field experiment. This approach can simulate every truck position and corresponding sensor data readings on the culvert, and it is the best technique to obtain the accurate field results continuously to compute the section forces [23]. In the second method, multiple influence lines were introduced in 3D FE models as shown in Figure 2(b) to form an influence surface along the travelling path. The load pressured area was divided into about 100 mm element size to define each influence line on the path, then the load pressure was converted to line load on each influence line. This method can provide much faster results than the previous method at the specific locations. The drawback of this method however is that, the results can be obtained as the maxima and minima of that location along the truck path; therefore, sub-step results cannot be saved with the second method. These two methods were validated by using the field test results, and the latter 3D FE model, which utilized the multiple influence lines, then used for the parametric studies.

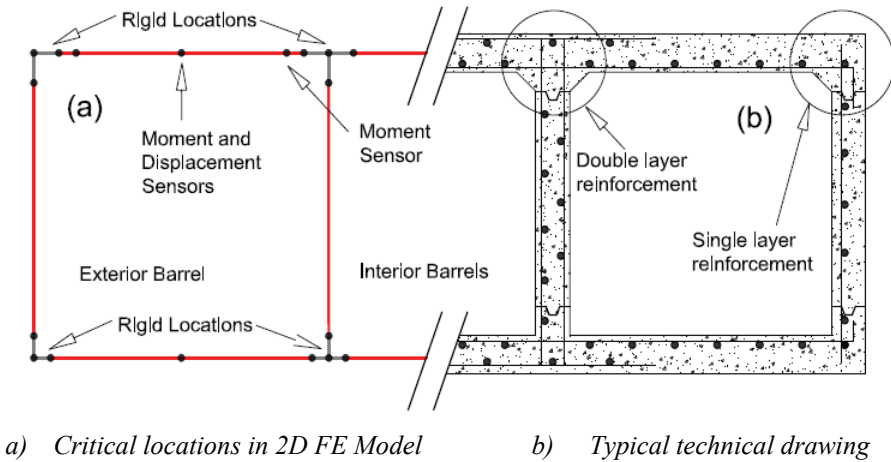


*Figure 1 - Culvert section through a barrel*

On the other hand, two dimensional models are more favourable than three dimensional models in structural analysis due to less detailed model preparation and computational effort. These culvert sections are modelled as unit wide beam elements. Single path is defined on the top slab of the culverts to construct the influence line of the 2D FE models in order to obtain the section forces at the critical locations as shown in Figure 1(a); therefore, the results are obtained as the maxima and minima of the section forces. All the culvert properties and the boundary conditions were adopted from the 3D FE model for the 2D FE culvert model. Loads are applied uniformly distributed line loads using the AASHTO load distribution method. The truck load pressures were applied on a single influence line along the culvert length in 2D FE models. The section forces at critical locations were extracted for different culvert properties and the ratio of these section forces were calculated using 2D and 3D FE model results.

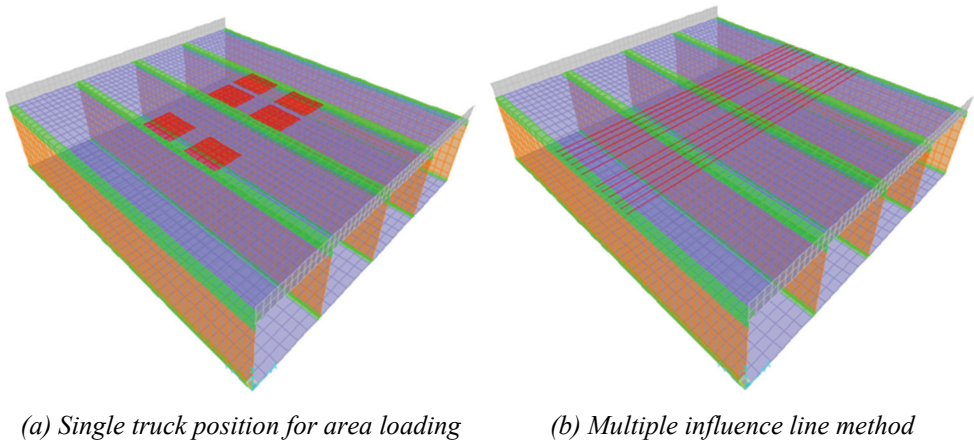


Figure 2 - Equivalent soil pressure loads on culvert slabs

## 2.2. Experimental Load Tests

The load ratings of the culverts modelled with frame elements using 2D FE models showed unrealistic performances [23]. The unexpected load rating of these culverts cannot be attributed to the structural deficiencies of the culverts due to their long service life without major failures. This study addressed the effect of the modelling techniques in multi opening buried box culverts using AAHTO LRFD live load distribution method. The standard details of the aged culverts are shown in Figure 1(b). The most important detail is the reinforcement in the top and bottom slabs. The single layer bars are continuously placed at the bottom layer of top slab. Only the second layer of reinforcing bars are placed for the negative moments on the interior walls. At the corners where the exterior wall joins to slab double layer bars were not placed; therefore, the wall – slab connections at those corner joints can behave like a hinged connection, therefore, the negative moments cannot develop at those corners. The constructed FE models include the hinged joints at both ends of the slabs. This assumption made due to technical details provided in Figure 1(b); however, the cracked sections due to single layer reinforcement cannot be verified by the field inspection due to pavement and earth cover. It should be noted that the haunch at the top wall – slab connections provide partial rigidity to the slab, and this was accounted by adding two thirds of the haunch length to wall thickness in FE models.

Three concrete core specimens from the walls of each tested culverts were obtained and tested under compression to calculate the compressive strength and elastic modulus of those tested culverts following the ASTM standard equations [24]. The field measured properties and calculated elastic modulus of the concrete specimens are given in Table 1.

Tandem three axle dump trucks, one of which is shown in Figure 3(a), were arbitrarily loaded before the test of each culvert. Strain and displacement sensors were placed on the culverts at their critical locations, which are shown in Figure 3(b) inside the opening of the tested culverts. These critical locations are defined as the middle of the exterior opening for displacement and positive strain (moment) and at the ends of the barrel width (30 cm from

the wall surfaces) for the negative strain. The loaded truck passed the culverts about 1 or 2 minutes while the data acquisition system was collecting the sensor data continuously. The truck position and corresponding sensor readings were presented based on the truck positions. Finally, each truck was weighed after the test of the culvert, and axle loads were recorded and axle positions were measured on site. The recorded axle weights of these trucks are given in Table 2. The trucks have typically standard axle spacing; 3.70 m and 1.40 m from front to middle and middle to rear axles, respectively. The recorded rear axle loads were not exactly equal, but the total rear axle loads redistributed equally to all four wheels.

*Table 1 - Experimentally tested culvert properties*

| <b>Culvert ID / number. of barrels</b> | <b>Fill height. (cm)</b> | <b>Barrel size (m x m)</b> | <b>Wall / slab thickness. (cm/cm)</b> | <b>Elastic modulus (MPa)</b> |
|--|--------------------------|----------------------------|---------------------------------------|------------------------------|
| C1 / 5                                 | 65                       | 1.8x1.8                    | 20/15                                 | 31260                        |
| C2 / 4                                 | 210                      | 2.1x2.1                    | 21/18                                 | 32150                        |
| C3 / 4                                 | 70                       | 2.4x2.4                    | 23/20                                 | 37224                        |
| C4 / 2                                 | 50                       | 3.7x3.7                    | 30/30                                 | 33246                        |

*Table 2 - Trucks of the field tests*

| <b>Culvert</b> | <b>Front Axle (kN)</b> | <b>Middle Axle (kN)</b> | <b>Rear Axle (kN)</b> | <b>Gross Weight (kN)</b> |
|----------------|------------------------|-------------------------|-----------------------|--------------------------|
| C1             | 49                     | 83                      | 83                    | 215                      |
| C2             | 56                     | 99                      | 99                    | 254                      |
| C3             | 58                     | 86                      | 86                    | 230                      |
| C4             | 42                     | 73                      | 73                    | 188                      |



*(a) Test Truck*



*(b) Sensor locations*

*Figure 3 - Typical three axle test truck on a travelling path with sensor locations*

### 2.3. Parametric Load Tests

Three different multi opening culverts (2, 3 and 4 barrels) are considered in this study. Each of these culverts is assigned with 1.50 m, 2.50 m and 3.65 m wide width, and these culverts are called CP1, CP2 and CP3, respectively,. These culverts are considered square box culverts so the height to width ratio was selected as one for all the analysis which correspond to the majority of the culverts in the state. The slab and wall thickness of these culverts are taken from archived technical drawings. Their considered properties are given in Table 3. The average of the experimentally obtained concrete properties was assigned to all tested culverts. Single test truck is redefined for the parametric cases using the average axle loads and spacing of the test trucks given in Table 2; therefore, the results are presented for the three-axle tandem dump truck in this section. However, these results can be used to estimate the modelling errors for the various axle numbers, positions, soil properties, and gross weight of the trucks because the parametric results are presented as the ratio of the two different FE analyses where the influence line of the critical sections is unique for each culvert.

The fill height of the analysed culverts was varied from 0 to 60 cm by using Equation (1), and 60 cm to 210 cm by using Equation (2) for the live load distribution given in the previous section. Typically, about 15 -20 cm fill height intervals were investigated from 0 to 210 cm fill height. Therefore, the analysis was repeated 11 times for one culvert and that led to 99 parametric culverts, each studied with 3D FE model. The culvert properties and load cases were kept identical for 2D FE model analysis and the study repeated independently for another same set of 99 culverts.

The ratio of the critical section forces between FE culvert models was investigated in the first part of this section. The critical locations for the strain readings and displacement during field tests were also considered the critical locations for the parametric studies. Instead of presenting the ratio of the maximum strains at the critical location, the positive moment at the mid span, and negative moment at the wall face of the exterior barrel were used to calculate the positive and negative moment ratios between models.

*Table 3 - Parametric properties of the studied culverts*

| <b>Culvert</b> | <b>Barrel size (mxm)</b> | <b>Number of barrels</b> | <b>Slab &amp; wall thickness (cm)</b> | <b>Elastic modulus (MPa)</b> |
|----------------|--------------------------|--------------------------|---------------------------------------|------------------------------|
| CP1            | 1.50 x 1.50              | 2                        | 18.5                                  | 33470                        |
|                |                          | 3                        |                                       |                              |
|                |                          | 4                        |                                       |                              |
| CP2            | 2.50 x 2.50              | 2                        | 20.0                                  |                              |
|                |                          | 3                        |                                       |                              |
|                |                          | 4                        |                                       |                              |
| CP3            | 3.65 x 3.65              | 2                        | 30.5                                  |                              |
|                |                          | 3                        |                                       |                              |
|                |                          | 4                        |                                       |                              |

In the second part of the parametric study, the ratio of the moments obtained in the previous study were used to calculate 3D envelope moments along the culverts. Only the envelope moments of the culvert CP3 with 4 barrels (CP3-4) are presented here for the multi opening culverts. Different sizes of trucks that have varying total gross weights, axle loads and axle positions were crossed the culvert CP3-4, and the variation of the maximum and minimum moments at the critical locations, mid-length and interior wall face of the exterior barrels, were calculated using their influence lines extracted from the 2D dimensional FE models. The simulation of each truck pass was modelled by inputting the influence lines extracted from the SAP2000, axle load coordinates, and axle load pressures to the coded script. Cumulative trapezoidal numerical integration of the influence lines between the predefined two axle load coordinates were calculated and it was repeated for each axle load. Therefore, the section moment variation at the critical location are obtained from the 2D FE models for consecutive load positions. AASHTO HL93 and HL93 tandem design trucks and other standard legal trucks given in Figure 4 are selected to investigate the effect of axle positions on positive and negative moment ratios.

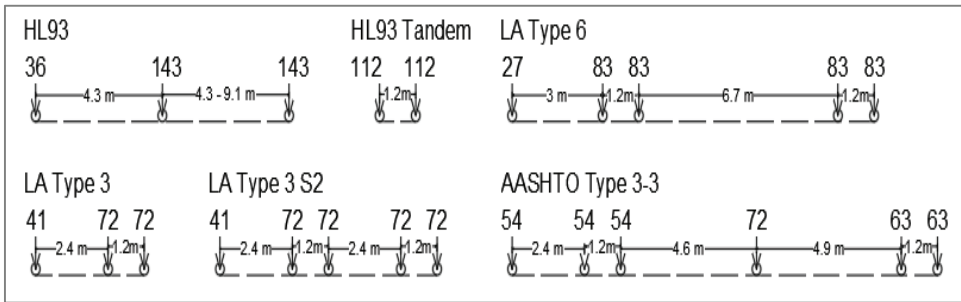


Figure 4 - Selected truck axle positions (m) and loads (kN)

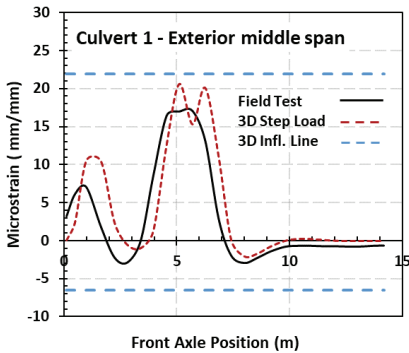
### 3. RESULTS AND DISCUSSIONS

#### 3.1. Experimental Test Results

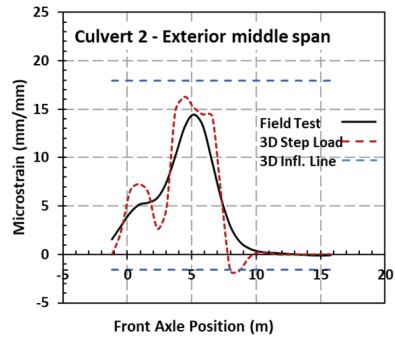
The field test results were investigated for four different culverts, and their 3D FE modelling results are verified in this study, but only first two of them, Culvert 1 and Culvert 2 are presented graphically in this section. Typical results of the 3D FE modelling approaches using step by step area loading and multiple influence line methods results are plotted from Figure 5 to 7. The solid black line represents the field test results, the continuous red dashed line represents the step-by-step area loading results, and constant blue dashed line shows the maximum and minimum peak strain results at the critical location using the multiple influence line method for Culverts 1 and 2 from Figure 5 to 7. Positive strain changes are calculated from the moment forces at the critical location and they are plotted in Figure 5(a) and 5(b). The first positive peak strain recorded when the front axle loads positioned at the middle of the exterior opening, and the trailing rear axle loads caused the maximum strain in the culverts. When the multiple influence line method was used, sensor data at any specific load position diminished and only positive and negative minimum peaks can be obtained; therefore, the second approach concludes an upper and a lower bound of maximum peaks. It can be said the second approach over estimates the positive maximum peaks. The average

error in Figure 5(a) and 5(b) is about 15% and 24% for the positive moments using the area and influence line loading methods, respectively.

The second sensor location was selected near the wall face to capture negative moments at the slab section. All the negative maximum peaks are plotted in Figure 6(a) and 6(b) for Culverts 1 and 2, respectively. It can be concluded that the multiple influence line method predicted the negative maximum peaks moment less than the maximum peaks of the field and step-by-step area loading results. It should be noted that the absolute intensity of the straining action near wall face is smaller when compared to the positive strain results. The area loading and influence line loading methods predict the negative peak strains by 21 % and 15% error, respectively.

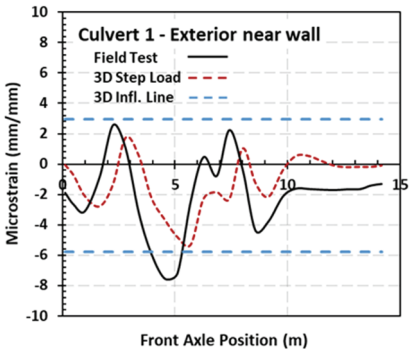


(a) Culvert 1 – Fill height = 65 cm

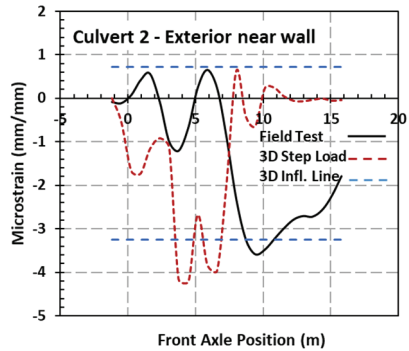


(b) Culvert 2 – Fill height = 210 cm

Figure 5 - Positive strains at the mid-span of the exterior opening



(a) Culvert 1 – Fill height = 65 cm

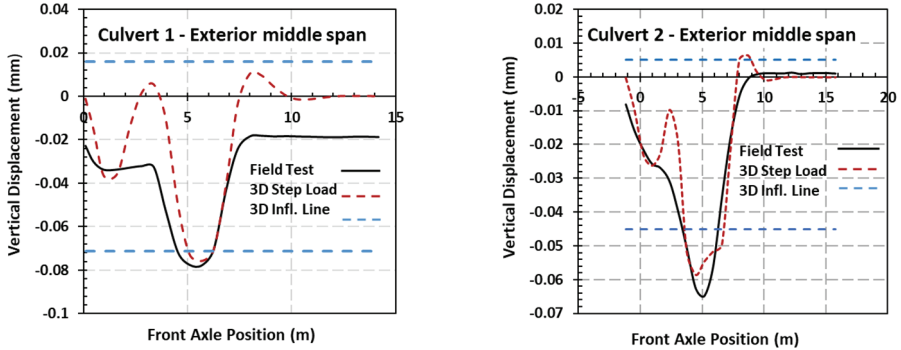


(b) Culvert 2 – Fill height = 210 cm

Figure 6 - Negative strains at the wall face of the exterior opening

Finally, the peak positive moment and the peak vertical displacement were obtained at the same location during the field tests, and the displacement readings are shown in Figure 7(a) and 7(b). The area loading and multiple influence line methods predicted the displacements

by 7.5% and 19% error, respectively. These results showed that the average overall error is about 17% for both culverts. The relative error between the two loading methods is about 5% and 12% for Culvert 1 and 2 respectively. It can be concluded that the influence line method provided an average of about 10% error for all four culvert. Considering computational cost of area loading method, the expected error due to use of multiple influence line method can be disregarded in culvert design or load ratings.



(a) Culvert 1 – Fill height = 65 cm

(b) Culvert 2 – Fill height = 210 cm

Figure 7 - Maximum displacement at the mid-span of the exterior opening

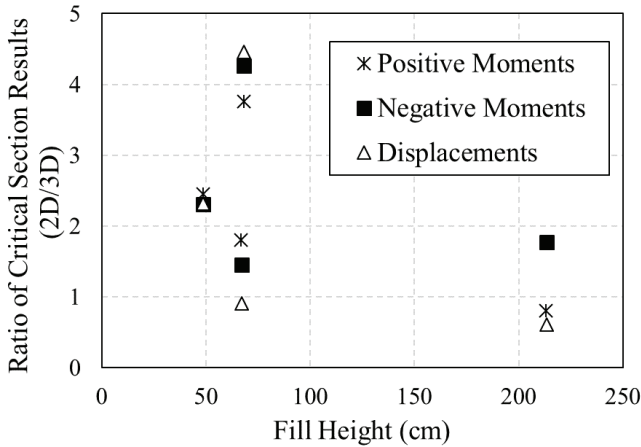


Figure 8 - FE model ratios for the experimentally tested culverts

All four culverts were then modelled using 2D frame elements and they were similarly loaded with the test trucks using single influence line method. The section forces were obtained and compared to the section results of the 3D FE, and the ratio of the section forces are plotted in Figure 8. It was found that the section forces from the 2D FE models can yield up to four times the validated section forces of the 3D FE models. This preliminary study showed that

the modelling approach is an important design consideration specifically for the shallow fill heights when the AASHTO LRFD live load distribution is used. The results in Figure 8 did not show a good correlation for the ratios of the shallow fill height culverts. This implies that the other factors are still effective in the calculation of the section forces, which is not in the scope of this study. Nevertheless, the use of single influence line method using the 2D FE modelling approach cannot accurately represent any of the 3D FE modelling accuracy.

### 3.2. Parametric Test Results

The parametric test results are presented as the ratio of the maximum peak moments and displacement at the critical locations. It should be noted that the critical location of these parametric results can be slightly different from the critical locations shown in Figure 1(a). Therefore, the ratio between two FE models was calculated for their peak results, not the results of one specific location. Fill heights of these culverts was varied from 0 to 210 cm (0, 15, 30, 45, 60, 61, 75, 90, 105, 120, and 210 cm), where the live load pressure is negligible after 240 cm according to AASHTO design manual [25]. The axle load pressures were calculated using the Equations (1) and (2) depending on the selected fill heights. The number of barrels in this study was limited with 2, 3 and 4 for each culvert, and parametric culverts will be called as CP1, CP2 and CP3 as described earlier. The detailed graphic presentation of the calculated ratios for all the culverts are provided from Figure 9 to 10 as the fill height increased from 0 to 210 cm and discussed in details next.

The modelling error in these culverts increased parallel to the culvert sizes, meaning that the flexure dominant culvert, CP3, produced larger model errors. When the fill height is less than 60 cm as shown in Figure 9, for example, the error ratio is about 1.10 and 1.48 for the CP1 and CP3, respectively. The error ratio showed sharp jump at around 60 for the positive moments when the load distribution equation changed from Equations (1) to (2). It was found that the modelling error can reach a ratio of about 2 for CP3 culvert after 60 cm fill height has been exceeded, then that ratio gradually reduces to 1.22 for the CP3 with 210 cm fill height. Therefore, the variation of the ratios at different fill heights can be attributed to the error of the load distribution method. The critical fill height for the load distribution method is found between the 60 cm and 120 cm using the Equation (2) for all the culverts. The span length effect is clearly seen in Figure 9 where the longer span, CP3, produces the larger error for all the fill heights. Therefore, the span length effect should be included in the considered live load distribution formulations when the fill height exceeds 60 cm. Another important result in Figure 9 is that when the culverts have multi openings, CP1-2-3-4, CP2-2-3-4, or CP3-2-3-4, the error ratio between the 2D and 3D FE models does not change much, and it is well correlated when the fill height exceeds 60 cm. The variation of the error ratio is negligible when the fill height exceeds 60 cm which produces maximum 1.73% standard deviation of the mean value of positive moment ratios between the CP1 culverts. The standard variation is slightly larger when the fill height is less than 60 cm, 6.83%, between the CP1 culverts. The other culvert groups, CP2 and CP3, correlated well when compared to the CP1 culverts. Therefore, the variation of the positive moments between the multi opening culverts did not cause a major modelling errors.

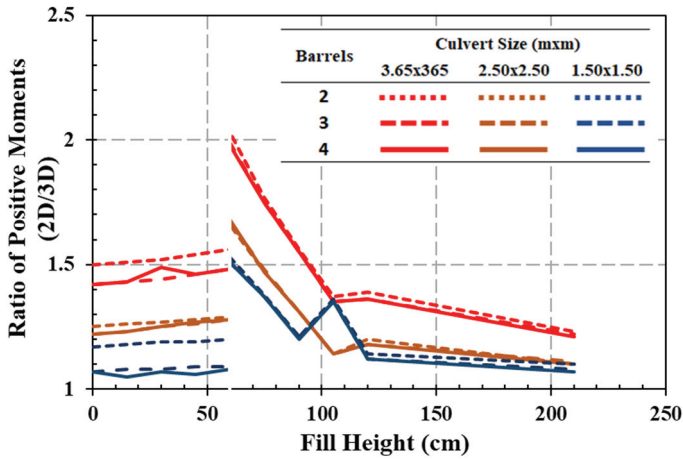


Figure 9 - Positive moment ratios between 2D and 3D FE model analysis

The maximum negative moments are recorded at the interior wall face of the exterior barrels as the minimum peak readings in FE models, and their ratios are shown in Figure 10. Similar to the ratio of positive moments shown in Figure 9, the critical fill height can be located between 60 cm and 120 cm fill heights. The modelling error in this region reaches the average of 1.39 and 1.74 for the CP1 and CP3 culverts, respectively. These ratios between critical fill heights are below the ratio of positive moments, so the modelling error becomes smaller for the calculated negative moments. After the fill height exceeds 120 cm, the average error gradually drops to 1.03 and 1.12 for the CP1 and CP3 culverts, respectively. Some of the ratios of the negative moments on the other hand is calculated less than 1 when the fill height is below 60 cm for culverts CP1-2 and CP1-3. This showed that the FE modelling error is also depend on the location and section forces. The increased barrel width increases the modelling error for the negative moments as well. The number of barrels in a multi opening culvert has similarly negligible effect on the ratios, and error between the culvert groups is strongly correlated. The maximum standard deviation of the mean negative moments can be calculated as 4.04% between the culvert group of CP1.

The maximum span displacement at the mid span of the exterior barrel is recorded in both FE models. The calculated displacement ratios of culvert models are plotted in Figure 11. The adopted load distribution method increased the modelling error between 60 cm and 120 cm fill heights significantly for the maximum displacements. The modelling error between these fill height reaches the average ratio of 1.71 and 2.27 for the CP1 and CP3 culverts, respectively. The variation of the errors between the section forces and displacements on the same culvert showed that one type of live load distribution method cannot represent a valid load distribution for the section forces. The load distribution for the positive moment for example can be different than the load distribution for the negative moments. The same can be said for the maximum displacement.

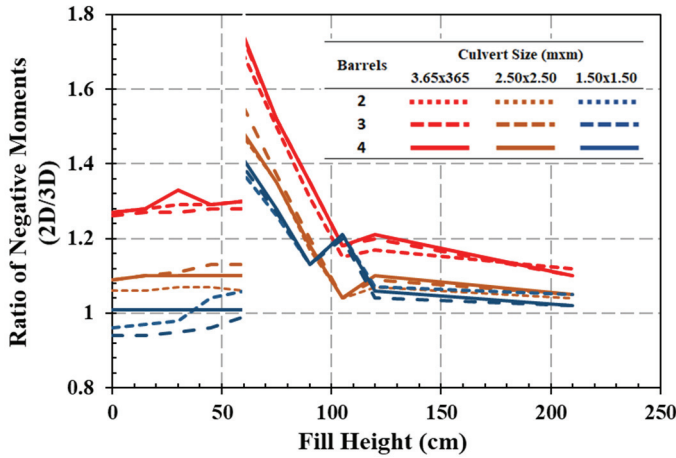


Figure 10 - Negative moment ratios between 2D and 3D FE model analysis

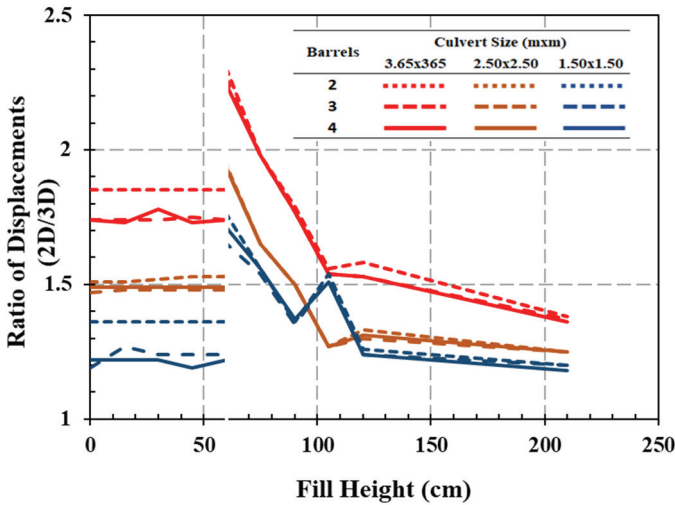


Figure 11 - Displacement ratios between 2D and 3D FE model analysis

The maximum and minimum design or load rating moment envelopes can be created for any culvert properties simply by creating the culvert's corresponding influence line and actual fill height. The resultant moment envelopes will not fit this paper, therefore, only one selected culvert with three different fill heights, 0, 60 cm and 210 cm, are presented in this section. The design envelopes are actually produced from the 2D FE analysis and then multiplied by their corresponding moment ratios described in the aforementioned paragraphs. The positive and negative moments are plotted in the same figure by following the sign conventions from Figure 12 to 14. HL93 with varied axle spacing and HL93 Tandem trucks are the design trucks and dominating the peak maximum and minimum moments for both fill heights. In

Figure 12, the positive and negative moment ratios are 1.42 and 1.26, respectively when there is no fill height was considered. The maximum and minimum moments are divided by their calculated positive and negative moment ratios, 1.48 and 1.30, respectively, which can be found in Figure 9 and 10 when the fill height is at 60 cm. In Figure 14, the positive and the negative moment ratios are 1.22 and 1.10, respectively when the fill height is 210 cm. These three figures show that the maximum envelope depends to the axle weights and positions. Fill height distributes the load more uniformly along the culvert length and section force intensities are also reduces when the fill height is increased due to distribution of the truck loads according to the AASHTO live load distributions. Finally, the section moments depend highly on the axle number and positions instead of the gross weight of the trucks. For example, LA Type 3 has 185 kN gross weight, which is less than AASHTO Type 3 truck at 297 kN; however, they produce almost identical positive and negative moments at the critical sections. Therefore, the variation of the trucks and their axle positions and axle loads needs to be studied independently.

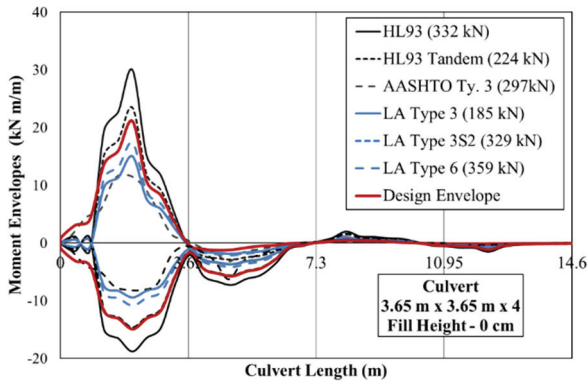


Figure 12 - Moment envelopes for 0 fill height

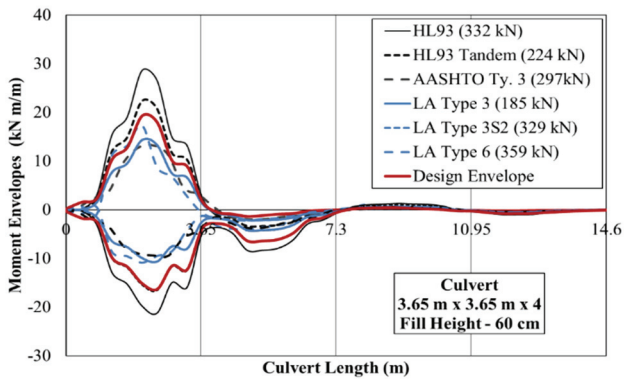


Figure 13 - Moment envelopes for 60 cm fill height

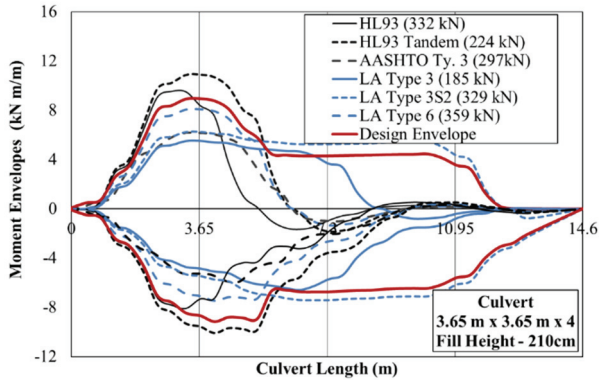


Figure 14 - Moment envelopes for 210 cm fill height

Table 4 - Ratio between 2D and 3D FE Model Results for Culvert CP1

| Culvert<br>x Barrel | Fill Height (FH), cm |      |      |      |      |      |      |      |      |      |      | Location |
|---------------------|----------------------|------|------|------|------|------|------|------|------|------|------|----------|
|                     | 0                    | 15   | 30   | 45   | 60   | 60   | 75   | 90   | 105  | 120  | 210  |          |
| CP1<br>x2           | 1.17                 | 1.18 | 1.19 | 1.19 | 1.2  | 1.53 | 1.38 | 1.21 | 1.36 | 1.14 | 1.1  | M+       |
|                     | 0.96                 | 0.97 | 0.98 | 1.04 | 1.06 | 1.37 | 1.26 | 1.13 | 1.21 | 1.07 | 1.05 | M-       |
|                     | 1.36                 | 1.36 | 1.36 | 1.36 | 1.36 | 1.76 | 1.56 | 1.36 | 1.54 | 1.26 | 1.2  | D        |
| CP1<br>x3           | 1.07                 | 1.08 | 1.08 | 1.09 | 1.09 | 1.51 | 1.37 | 1.21 | 1.35 | 1.12 | 1.08 | M+       |
|                     | 0.94                 | 0.94 | 0.95 | 0.96 | 0.99 | 1.39 | 1.27 | 1.13 | 1.2  | 1.04 | 1.02 | M-       |
|                     | 1.19                 | 1.27 | 1.24 | 1.24 | 1.24 | 1.65 | 1.54 | 1.35 | 1.52 | 1.24 | 1.2  | D        |
| CP1<br>x4           | 1.07                 | 1.05 | 1.07 | 1.06 | 1.08 | 1.51 | 1.37 | 1.2  | 1.35 | 1.12 | 1.07 | M+       |
|                     | 1.01                 | 1.01 | 1.01 | 1.01 | 1.01 | 1.41 | 1.28 | 1.13 | 1.21 | 1.06 | 1.02 | M-       |
|                     | 1.22                 | 1.22 | 1.22 | 1.19 | 1.22 | 1.71 | 1.56 | 1.37 | 1.51 | 1.24 | 1.18 | D        |
| $\mu$               | 1.1                  | 1.1  | 1.11 | 1.11 | 1.12 | 1.52 | 1.37 | 1.21 | 1.35 | 1.13 | 1.08 | M+       |
| $\sigma$ (%)        | 5.77                 | 6.81 | 6.66 | 6.81 | 6.66 | 1.15 | 0.58 | 0.58 | 0.58 | 1.15 | 1.53 |          |
| $\mu$               | 0.97                 | 0.97 | 0.98 | 1    | 1.02 | 1.39 | 1.27 | 1.13 | 1.21 | 1.06 | 1.03 | M-       |
| $\sigma$ (%)        | 3.61                 | 3.51 | 3    | 4.04 | 3.61 | 2    | 1    | 0    | 0.58 | 1.53 | 1.73 |          |
| $\mu$               | 1.26                 | 1.28 | 1.27 | 1.26 | 1.27 | 1.71 | 1.55 | 1.36 | 1.52 | 1.25 | 1.19 | D        |
| $\sigma$ (%)        | 9.07                 | 7.09 | 7.57 | 8.74 | 7.57 | 5.51 | 1.15 | 1    | 1.53 | 1.15 | 1.15 |          |

Table 5 - Ratio between 2D and 3D FE Model Results for Culvert CP2

| Culvert<br>x Barrel | Fill Height (FH), cm |      |      |      |      |      |      |      |      |      |      | Location |
|---------------------|----------------------|------|------|------|------|------|------|------|------|------|------|----------|
|                     | 0                    | 15   | 30   | 45   | 60   | 60   | 75   | 90   | 105  | 120  | 210  |          |
| CP2<br>x2           | 1.25                 | 1.26 | 1.27 | 1.28 | 1.29 | 1.66 | 1.47 | 1.31 | 1.14 | 1.2  | 1.1  | M+       |
|                     | 1.06                 | 1.06 | 1.07 | 1.07 | 1.06 | 1.47 | 1.35 | 1.17 | 1.04 | 1.07 | 1.04 | M-       |
|                     | 1.51                 | 1.51 | 1.52 | 1.53 | 1.53 | 1.94 | 1.65 | 1.5  | 1.27 | 1.33 | 1.25 | D        |

Table 5 - Ratio between 2D and 3D FE Model Results for Culvert CP2 (continue)

| Culvert<br>x Barrel | Fill Height (FH), cm |      |      |      |      |      |      |      |      |      |      | Location |
|---------------------|----------------------|------|------|------|------|------|------|------|------|------|------|----------|
|                     | 0                    | 15   | 30   | 45   | 60   | 60   | 75   | 90   | 105  | 120  | 210  |          |
| CP2<br>x3           | 1.22                 | 1.23 | 1.25 | 1.26 | 1.28 | 1.67 | 1.48 | 1.31 | 1.14 | 1.18 | 1.11 | M+       |
|                     | 1.09                 | 1.1  | 1.11 | 1.13 | 1.13 | 1.55 | 1.37 | 1.2  | 1.04 | 1.09 | 1.05 | M-       |
|                     | 1.47                 | 1.48 | 1.48 | 1.48 | 1.48 | 1.93 | 1.65 | 1.5  | 1.27 | 1.3  | 1.25 | D        |
| CP2<br>x4           | 1.22                 | 1.23 | 1.25 | 1.27 | 1.28 | 1.68 | 1.47 | 1.31 | 1.14 | 1.18 | 1.1  | M+       |
|                     | 1.09                 | 1.1  | 1.1  | 1.1  | 1.1  | 1.48 | 1.35 | 1.18 | 1.04 | 1.1  | 1.05 | M-       |
|                     | 1.49                 | 1.49 | 1.49 | 1.49 | 1.49 | 1.93 | 1.65 | 1.5  | 1.27 | 1.31 | 1.25 | D        |
| $\mu$               | 1.23                 | 1.24 | 1.26 | 1.27 | 1.28 | 1.67 | 1.47 | 1.31 | 1.14 | 1.19 | 1.1  | M+       |
| $\sigma$ (%)        | 1.73                 | 1.73 | 1.15 | 1    | 0.58 | 1    | 0.58 | 0    | 0    | 1.15 | 0.58 |          |
| $\mu$               | 1.08                 | 1.09 | 1.09 | 1.1  | 1.1  | 1.5  | 1.36 | 1.18 | 1.04 | 1.09 | 1.05 | M-       |
| $\sigma$ (%)        | 1.73                 | 2.31 | 2.08 | 3    | 3.51 | 4.36 | 1.15 | 1.53 | 0    | 1.53 | 0.58 |          |
| $\mu$               | 1.49                 | 1.49 | 1.5  | 1.5  | 1.5  | 1.93 | 1.65 | 1.5  | 1.27 | 1.31 | 1.25 | D        |
| $\sigma$ (%)        | 2                    | 1.53 | 2.08 | 2.65 | 2.65 | 0.58 | 0    | 0    | 0    | 1.53 | 0    |          |

Table 6 - Ratio between 2D and 3D FE Model Results for Culvert CP3

| Culvert<br>x Barrel | Fill Height (FH), cm |      |      |      |      |      |      |      |      |      |      | Location |
|---------------------|----------------------|------|------|------|------|------|------|------|------|------|------|----------|
|                     | 0                    | 15   | 30   | 45   | 60   | 60   | 75   | 90   | 105  | 120  | 210  |          |
| CP3<br>x2           | 1.50                 | 1.51 | 1.52 | 1.54 | 1.56 | 2.03 | 1.77 | 1.56 | 1.37 | 1.39 | 1.23 | M+       |
|                     | 1.27                 | 1.28 | 1.29 | 1.29 | 1.30 | 1.69 | 1.50 | 1.31 | 1.15 | 1.17 | 1.20 | M-       |
|                     | 1.85                 | 1.85 | 1.85 | 1.85 | 1.85 | 2.30 | 1.98 | 1.79 | 1.56 | 1.58 | 1.38 | D        |
| CP3<br>x3           | 1.42                 | 1.43 | 1.44 | 1.46 | 1.48 | 1.99 | 1.75 | 1.55 | 1.35 | 1.36 | 1.22 | M+       |
|                     | 1.26                 | 1.27 | 1.27 | 1.28 | 1.28 | 1.73 | 1.52 | 1.35 | 1.18 | 1.20 | 1.10 | M-       |
|                     | 1.74                 | 1.74 | 1.74 | 1.75 | 1.74 | 2.26 | 1.98 | 1.77 | 1.54 | 1.53 | 1.37 | D        |
| CP3<br>x4           | 1.42                 | 1.43 | 1.49 | 1.46 | 1.48 | 1.98 | 1.75 | 1.55 | 1.35 | 1.36 | 1.21 | M+       |
|                     | 1.27                 | 1.28 | 1.33 | 1.29 | 1.30 | 1.74 | 1.52 | 1.35 | 1.18 | 1.21 | 1.10 | M-       |
|                     | 1.74                 | 1.73 | 1.78 | 1.73 | 1.74 | 2.24 | 1.98 | 1.77 | 1.54 | 1.53 | 1.36 | D        |
| $\mu$               | 1.45                 | 1.46 | 1.48 | 1.49 | 1.51 | 2.00 | 1.76 | 1.55 | 1.36 | 1.37 | 1.22 | M+       |
| $\sigma$ (%)        | 4.62                 | 4.62 | 4.04 | 4.62 | 4.62 | 2.65 | 1.15 | 0.58 | 1.15 | 1.73 | 1.00 |          |
| $\mu$               | 1.27                 | 1.28 | 1.30 | 1.29 | 1.29 | 1.72 | 1.51 | 1.34 | 1.17 | 1.19 | 1.13 | M-       |
| $\sigma$ (%)        | 0.58                 | 0.58 | 3.06 | 0.58 | 1.15 | 2.65 | 1.15 | 2.31 | 1.73 | 2.08 | 5.77 |          |
| $\mu$               | 1.78                 | 1.77 | 1.79 | 1.78 | 1.78 | 2.27 | 1.98 | 1.78 | 1.55 | 1.55 | 1.37 | D        |
| $\sigma$ (%)        | 6.35                 | 6.66 | 5.57 | 6.43 | 6.35 | 3.06 | 0.00 | 1.15 | 1.15 | 2.89 | 1.00 |          |

M+: Positive moment, M-: Negative moment, D: Displacement,  
 $\mu$ : Mean,  $\sigma$ : Standard deviation

#### 4. CONCLUSIONS

The experimental field tests on the selected four culverts were conducted and the critical section forces were extracted using the data acquisition system. The cored concrete specimens were tested to obtain the material properties of the tested culverts. Two different 3D FE modelling approaches, namely area loading method, and multiple influence line method were utilized to apply the soil pressure on the culverts using AASHTO live load distribution method. Computationally the least time consuming procedure, multiple influence line method, was verified and adopted for the parametric studies. 2D FE model using frame elements which share identical geometrical, material, load properties of the experimentally tested culverts were developed to obtain the section forces at the critical locations using the influence line method. Maximum positive and negative moments, and displacements were extracted, and the ratio of the 2D to 3D FE model results were investigated as the modelling error. Finally, the study concluded that;

- The construction of 3D FE model with area loading is more cumbersome than the multiple influence line loading method. However, the data is only available for each load position with area loading method. Multiple influence line method only provides envelope of the maximum and minimum results.
- The field tests showed that the exterior barrel of the multi opening box culverts is typically the controlling section for the peak section forces. The maximum positive moments and displacements were recorded at around the mid span of this barrel, and the maximum negative moments on the other hand could be obtained near the wall face of the interior wall of this barrels.
- The difference between the 2D and 3D FE model results are presented as the ratio of peak moments and displacements and the modelling error can reach 2.00 and 2.27 for the peak moments and displacements, respectively.
- AASHTO live load distribution method increases the modelling error when the fill height is between 60 cm and 120 cm. Therefore, it is important to validate FE models when AASHTO live load distribution method is used between these fill heights. Different modelling approaches including the soil properties and load distribution behaviour in FE analysis can be further studied using 3D full section properties.
- The modelling errors show sharp jump at 60 cm fill height for all the culverts. Then the error decreases linearly with a sharp slope until 120 cm fill height. After the fill height exceeds 120 cm, the modelling errors remain constant for narrow barrel widths or gradually reduce for wider barrel widths up to the 240 cm fill height.
- The modelling error is dependent on the barrel width. The increase in barrel width increases the modelling error ratio between the FE models. The modelling error is more dominant for the shallow fill heights. Multi-opening culverts having either 2 or 4 barrels produced similar modelling errors.
- The modelling error and field calibration of 3D FE results showed that one typical load distribution method cannot represent the actual axle loads and its effects on the different section forces. Therefore, different live load distribution method should be considered for the calculation of the critical section forces.

- The study here showed that the modelling approach with 2D FE modelling did not reflect the field performance of the buried box culverts. The validated 3D FE modelling approach showed that simple 2D FE frame models produce very conservative results without considering any load factors. One should remember that the inherent error in 3D FE models adds to the error of 2D FE models without verification of the results. Therefore, the modelling error can be eliminated by validated 2D FE models otherwise inherent errors produce incorrect results and predictions for the design and load rating of the reinforced box culverts.
- The axle loads and positions are important parameters to construct the moment envelopes for the design or load rating purposes. The modelling error ratios can be used for the construction of the corrected section forces.

### **Notations**

$\mu$ : Mean value

$\sigma$ : Standard deviation

D: Displacement

FH: Fill height of the culvert (mm)

LS: Clear span length (mm)

M+: Positive moment

M -: Negative moment

$W_{\text{perp}}$  : Equivalent distribution width perpendicular to span (mm)

$W_{\text{span}}$  : Equivalent distribution length parallel to span (mm)

### **Acknowledgments**

This study is originally funded by Louisiana Transportation Research Center, and Louisiana Department of Transportation. Technical assistant of Louisiana State University and Bridge Diagnostics, Inc. during the field tests is acknowledged. The results presented here are only the author's independent study and does not reflect any other parties interest or views.

### **References**

- [1] Abdel-Karim, A.M., Tadros, M.K. and Benak, J.V., Live Load Distribution on Concrete Box Culverts, Record No.1288; Transportation Research Board of the National Academy of Sciences, Washington, D.C., USA, 1990.
- [2] McGrath, T., Liepins, A. and Beaver, J., Live load distribution widths for reinforced concrete box sections, 6th International Bridge Engineering Conference: Reliability, Security, and Sustainability in Bridge Engineering, Boston, MA, USA, July, 2005.

- [3] Abolmaali, A., and Garg, A.K., Effect of wheel live load on shear behavior of precast reinforced concrete box culverts, *Journal of Bridge Engineering*, 13(1), 93–99, 2008.
- [4] Wood, T.A., Lawson, W.D., Jayawickrama, P.W. and Newhouse, C., Evaluation of production models for load rating reinforced concrete box culverts, *Journal of Bridge Engineering*, 20(1), 4014057, 2015.
- [5] Wood, T.A., Lawson, W.D., Surlis, J.G., Jayawickrama, P.W. and Seo, H., Improved load rating of reinforced-concrete box culverts using depth-calibrated live-load attenuation”, *Journal of Bridge Engineering*, 21(12), 4016095, 2016.
- [6] Orton, S.L., Loehr, J.E., Boeckmann, A. and Havens, G., Live-load effect in reinforced concrete box culverts under soil fill, *Journal of Bridge Engineering*, 20(11), 04015003, 2015.
- [7] Negussey, D., Andrews, L., Singh, S. and Liu, C., Forensic investigation of a wide culvert reconstruction failure, *Journal of Pipeline Systems Engineering and Practice*, 10(3), 2019.
- [8] Puppala, A.J., Ruttanaporamakul, P. and Congress, S.S.C., Design and construction of lightweight EPS geofam embedded geomaterial embankment system for control of settlements, *Geotextiles and Geomembranes*, 47(3), 295–305, 2019.
- [9] Wysokowski, A. (2021), Influence of single-layer geotextile reinforcement on load capacity of buried steel box structure based on laboratory full-scale tests, *Thin-Walled Structures*, 159, 107312, 2021.
- [10] Kinchen, R.W., Temple, W.H., Lacinak, H.W. and Gueho, B.J., Evaluation of drainage pipe by field experimentation and supplemental laboratory experimentation, Report No. FHWA/LA-78/115; Louisiana Department of Transportation & Development, 1978.
- [11] Garber, J.D., Lin, J.H. and Smith, L.G., Feasibility of Applying Cathodic Protection to Underground Culverts, Report No. FWWA/LA-91; Louisiana Department of Transportation & Development, Baton Rouge, LA, USA, 1991.
- [12] Wadi, A., Pettersson, L. and Karoumi, R., FEM simulation of a full-scale loading-to-failure test of a corrugated steel culvert, *Steel and Composite Structures*, 27(2), 217–27, 2018.
- [13] Xu, C., Peiris, A. and Harik, I. (2019), Analysis and load rating of corrugated steel arch culverts”, *Ce/Papers*, 3(3-4), 85–90, 2019.
- [14] Liu, Y., Hoult, N.A. and Moore, I.D., Structural performance of in-service corrugated steel culvert under vehicle loading, *Journal of Bridge Engineering*, 25(3), 4019142, 2020.
- [15] Okeil, A., Ulger, T. and Elshoura, A., Live Load Rating of Cast-in-Place Concrete Box Culverts, Report No. FHWA/LA.17/593; Department of Civil and Environmental Engineering, Louisiana State University, Baton Rouge, LA, USA, 2018.
- [16] Acharya, R., Han, J., Parsons, R.L. and Brennan, J., Field testing and numerical modeling of a low-fill box culvert under a flexible pavement subjected to traffic loading, *Geomechanics and Engineering*, 11(5), 625–38, 2016.

- [17] Beben, D., and Wrzeciono, M., Numerical analysis of steel-soil composite (SSC) culvert under static loads, *Steel and Composite Structures*, 23(6), 715–26, 2017.
- [18] Sun, Q., Peng, D. and Dias, D., Seismic performances of three- and four-sided box culverts: a comparative study, *Geomechanics and Engineering*, 22(1), 49–63, 2020.
- [19] Garg, A. and Abolmaali, A., Finite-element modeling and analysis of reinforced concrete box culverts”, *Journal of Transportation Engineering*, 135(3), 121–28, 2009.
- [20] Acharya, R., Han, J. and Parsons, R.L., Numerical analysis of low-fill box culvert under rigid pavement subjected to static traffic loading, *International Journal of Geomechanics* 16(5), 4016016, 2016.
- [21] AASHTO LRFD Bridge Design Specifications 8th. Ed., American Association of State Highway and Transportation Officials; Washington, DC, USA, 2017.
- [22] SAP2000, Integrated Software for Structural Analysis and Design, Berkeley, California: Computers and Structures Inc, 2014.
- [23] Ulger, T., Okeil, A.M. and Elshoura, A., Load testing and rating of cast-in-place concrete box culverts, *Journal of Performance of Constructed Facilities*, 34(2), 4020008, 2020.
- [24] ASTM C42, Standard method of test for obtaining and testing drilled cores and sawed beams of concrete, ASTM International, West Conshohocken, PA, USA, 2013.
- [25] AASHTO The Manual for Bridge Evaluation 2<sup>nd</sup>. Ed., American Association of State Highway and Transportation Officials; Washington, DC, USA, 2011.

***TECHNICAL NOTE***



# Sliding and Rollover on Highways - Subtleties to Note

Banihan GÜNAY<sup>1</sup>

## ABSTRACT

While the horizontal curves have a duty to protect all types of road vehicles against sliding as well as rollover, the fact that different vehicle types lose their stability for competing criteria makes this task difficult and vital. In relation to the sliding and rollover of a vehicle undergoing centripetal acceleration, this technical note discusses a number of unclear interpretations of some statements seen in reference books and how their better understanding should be. This note has been prepared to observe such benefits as accident investigations, determination of pavement rehabilitation frequencies, and most importantly, ensuring the correct student learning.

**Keywords:** Static stability factor, rollover threshold, tripped rollover.

## 1. INTRODUCTION

Whereas sliding is adequately discussed in many highway engineering books [1-18], it is prominent that the topic of rollover (also known as overturning) has found no mention in these sources. Yet, rollover type accidents are the second most fatal accidents after head-on collisions [19]. It has been proven that a loaded truck rolls over at a speed of 25 km/h on a 20 m radius curve [20] and at only 5 km/h above the design speed on a minimum radius curve [21]. More interestingly, even if the trailer of a truck begins to roll over, the driver in the front cabin, which has a lower centre of gravity, may not be able to feel the danger [22]. Certain statements in a limited number of books containing discussions on rollover however, are sometimes misinterpreted (Section 2). These details may be overlooked in newly prepared textbooks or lecture notes and erroneous interpretations may have been repeated to date. Before commencing the discussion of the topic, the dynamics of sliding and rollover with point mass [23] simplification<sup>†</sup> will be summarised here.

On a level surface, the forces acting on a vehicle (Figure 1) moving in a circular motion in the plan view are its weight ( $mg$ ), the centrifugal reaction ( $mv^2/R$ ), and the frictional force ( $\mu mg$ ). In order for this vehicle (with rigid wheels and body) not to slide laterally, the

---

Note:

- This paper has been received on July 9, 2020 and accepted for publication by the Editorial Board on March 1, 2021.
- Discussions on this paper will be accepted by September 30, 2022.

• <https://doi.org/10.18400/tekderg.766631>

<sup>1</sup> Metropolitan University of Tirana (UMT), Department. of Civil Engineering, Tirana, Albania  
bgunay@umt.edu.al - <https://orcid.org/0000-0002-4640-417X>

<sup>†</sup> With increasing number of wheels of the vehicle, the point mass simplification becomes rather cumbersome.

frictional force must be greater than the centrifugal reaction ( $\mu mg > mv^2/R$ ). Hence, the critical speed for sliding will be

$$v = (\mu g R)^{1/2} \tag{1}$$

The critical speed for rollover on the other hand, by equating the overturning and restoring moments about point *A*, from  $h(mv^2/R) = (e/2)mg$ , will be

$$v = (egR/2h)^{1/2} \tag{2}$$

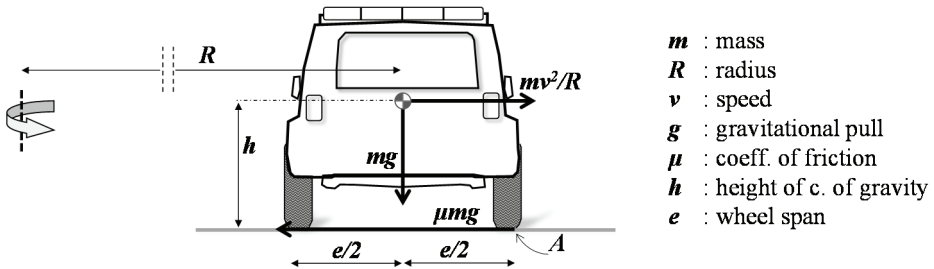


Figure 1 - Forces acting on a vehicle, rotating in the horizontal plane (lateral slope = 0)

From (1) and (2),  $\mu = e/2h$  and  $h = e/2\mu$  are obtained (since  $\mu = v^2/gR$  from physics) and called the static stability factor [24] and the rollover threshold [25], respectively. If the vehicle moves along a horizontal curve with a superelevation of  $\alpha^\circ$ , (1) and (2) become

$$V_s = 11.3 \sqrt{\frac{R(\mu + \tan \alpha)}{1 - \mu \tan \alpha}} \text{ and } V_r = 11.3 \sqrt{\frac{R(h \tan \alpha + e/2)}{h - (e/2) \tan \alpha}}, \text{ respectively. Here, } V_s \text{ and } V_r \text{ are the critical}$$

speeds in km/h for sliding and overturning. The case of  $\alpha = 0^\circ$  (without superelevation) is a special form of these two equations which produces the same outcomes as (1) and (2). The basic assumption of rigid wheels and body is common [26] but if wheel and suspension flexibilities are to be taken into account, the dynamic stability factor [27] should be used instead.

## 2. INTERPRETATION DETAILS AND CLARIFICATION

At certain academic platforms like thesis defence or promotion exams, such lacking or erroneous interpretations as “ $V_r$  is always greater than  $V_s$ ”, “if the speed of the vehicle is between  $V_s$  and  $V_r$ , it will slide, and if it is greater than  $V_r$ , the vehicle will roll over”, or “if the speed of a sliding vehicle increases to  $V_r$ , it will also roll over” have sometimes been noted. In this context, when sources are referred to for the subject of rollover, the following statements appear: “... the majority of the accidents occurred at horizontal curves are due to sliding rather than overturning” [28], although no reference is cited to support this claim; “... vehicles first slide then overturn” [29]; “... on a wet pavement, a truck will roll over before it skids at design speeds of 64 to 80 km/h and below; above that speed, a truck will skid before it rolls over” [30]; “Cars rarely overturn without sliding first” [31]; “in the real

world the critical speed for overturning is greater than that of sliding”, “... it shows that sliding occurs at horizontal curves more easily” [32], although this holds only for vehicles with a low level of centre of gravity; “... the relative danger of lateral skidding and overturning depends on whether  $\mu$  is lower or higher than  $e/2h$ ” [33]; “a vehicle on a (horizontal) curve will overturn ... about the point  $m$  if it exceeds a certain speed value”, “... while the weight of the vehicle plays no role in its sliding or overturning, rather,  $h$  and  $e$  do have an effect” [34], although  $h$  and  $e$  have no effect on sliding. Therefore it is very important that the issue is appropriately explained.

It should be remembered that Equation (2) was derived by taking moments about point  $A$  (Figure 1). As known from physics, in order to be able to take moments, the pivot must be a fixed point<sup>‡</sup>. In other words, since the vehicle will start to slide in a straight line tangential to the circular arc as a result of  $V_s$ , theoretically, this moment will never be taken and the overturning will never happen. In more engineering terms, the lever arm of the system will escape under the loading. As long as the lateral friction demand ( $v^2/gR$ ) due to centripetal acceleration does not reach the threshold level ( $\mu$ ) to give rise to a slide, point  $A$  will act as a fixed support. Hence the vehicle will roll over only if a sufficient moment builds up as a result of the centrifugal reaction. That is to say, in order for a rollover to take place, (in basic terms) the vehicle must not be in a sliding fashion. However much the longitudinal speed of the vehicle increases, in theory, as long as  $\mu$  remains constant, the (sliding) vehicle will not roll over. In this case, the question of how the rollover accidents, initiated by a slide, take place comes to mind. Possible answers are as follows:

*a*-As known, surface roughness is not homogenous and surface wetness varies quite often [35]. Moreover, modern cars on dry pavements can generate friction values as high as 0.9 [36]. As the coefficient of friction changes, in the direction of lateral travel, to a much higher value than that of used in design, the rollover, rather than sliding, will suddenly become critical. For instance, while a passenger car with a roof rack luggage ( $e = 1.6$  m,  $h = 0.95$  m,  $R = 100$  m,  $V = 110$  km/h,  $\alpha = 2.86^\circ$  (5%),  $\mu = 0.2$ ) is sliding, it will roll over as a result of a sudden change of  $\mu$  to a value of 0.85 or higher. If the moment caused by a shock effect of a sudden slowing down is taken into account (see the numerical example below), the rollover can take place even if the coefficient of friction falls short of 0.85.

*b*-Similarly, road surface defects such as corrugation, potholes or roadside obstacles, may behave as hinge points and can bring lateral sliding to a stop by a great deal of deceleration. This time the speed of sliding drops to a complete zero and the momentum caused by the inertia and the already existing centrifugal reaction ( $mv^2/R$ ) together transfer sliding to roll over. For example, while a car ( $m = 1300$  kg,  $h = 0.7$  m,  $e = 1.7$  m,  $V = 100$  km/h,  $R = 100$  m,  $\alpha = 2.86^\circ$  (5%),  $\mu = 0.6$ ) is sliding with a ‘sliding speed’ of 4 m/s, as a result of tripping (hitting a low level fixed obstacle at right angle), with an assumption that the sliding comes to a complete stop within a quarter of a second, the car will eventually roll over (perhaps more than once), since  $m\{(v^2/R) \cos\alpha + (4/0.25)\} h > m\{g \cos\alpha (e/2) + g \sin\alpha h + (v^2/R) \sin\alpha (e/2)\}$ . When the values are substituted,  $(7.7+16) 0.7 > 8.33 + 0.34 + 0.33$ . In the

---

<sup>‡</sup> In case of both the pivot and the force move together in the same direction (if the replacement speed of the application point of the force is greater than that of the pivot), it is still possible to take moments. But because Equation (2) was derived, this detail had not been taken into consideration, only the case of a fixed pivot (point  $A$  does not shift laterally) will be dealt with in the present note.

literature this phenomenon is called a ‘tripped rollover’ [27]. Obviously, questioning the roadway design criteria is outside the scope of this note, but these numerical examples rather demonstrates that, at least mathematically, rollover can suddenly become critical and the shock effects may possess considerable contribution.

*c*-As a matter of fact, like sliding, rollover too takes place over a certain period of time. A vehicle which is in rollover state, as a result of lateral inertia, may first slide for a short period of time.

*d*-Although, in theory, it seems that a sliding vehicle will continue to slide until it exhausts its kinetic energy, in practice, sliding is limited by the width of the roadway. Therefore, when this width comes to an end, the vehicle will roll over as a result of either tripping, undergoing a higher  $\mu$  of a soft shoulder, or suffering from an adverse ditch slope.

*e*-Other than these, though out of scope, a sliding vehicle will also roll over as a result of severe braking, oversteering, cross wind, hydroplane effect, bouncing, and so on.

Although propositions like “whichever of (1) or (2) is smaller, that speed is the critical speed” and “for passenger cars with no roof rack luggage (1) is always smaller than (2)” are mathematically correct, it is risky to generalise the statements above [28, 34], implying that “sliding is always more critical than overturning for passenger cars”. This claim only holds for critical  $\mu$  (or below) where point *A* cannot undertake the role of being a fixed hinge for the entirety of the sliding area.

### 3. CONCLUSION

For increasing values of coefficient of friction, it is a handicap for the same road to become safe against sliding, and, at the same time, less safe against rollover. In design, the friction factor against sliding is chosen low with some margin of safety (for example, according to AASHTO recommendations, on a horizontal curve the value is taken as 0.12 for 100 km/h design speed corresponding to 4%-8% of superelevation) [37, 38], assuming that some of the friction demand is compensated by superelevation. However, real friction values could easily be much higher as discussed above, making rollover potentially critical. This therefore means that whereas a road which is thought to be safe against rollover, as a matter of fact, turns out to be risky especially during dry weather due to sudden roughness changes. Because of this, very importantly, curved freeway exit ramps, where design speeds are likely to be exceeded, possesses high rollover potential. Besides, the rigid wheel/body assumption leads to less conservative results and wheel deflections and body rolls may need to be taken into consideration for safe design and good practice.

#### Symbols

*e* : lateral wheel span (m)

*g* : gravitational acceleration (9.81 m/s<sup>2</sup>)

*h* : height of centre of gravity from road surface (m)

*m* : vehicle mass (kg)

|          |   |
|----------|---|
| $R$      | : radius of circular motion (m)                           |
| $v$      | : longitudinal speed of vehicle (m/s)                     |
| $V$      | : longitudinal speed of vehicle (km/h)                    |
| $\alpha$ | : angle of lateral slope (superelevation)                 |
| $\mu$    | : coefficient of friction between road surface and wheels |

### References

- [1] IHT, Roads and Traffic in Urban Areas, London: HMSO, 1987.
- [2] Macpherson, G., Highway and Transportation Engineering and Planning, Harlow: Longman Scientific & Technical, 1993.
- [3] Lamm, R., Psarianos, B., Mailaender, T., Highway Design and Traffic Safety Engineering Handbook, New York: McGraw-Hill, 1999.
- [4] Rogers, M., Highway Engineering, Oxford: Blackwell, 2003.
- [5] Roess, R., Prassas, E., McShane, W., Traffic Engineering, London: Pearson Prentice Hall, 2004.
- [6] Tunç, A., Yol Güvenlik ve Mühendisliği Uygulamaları, Ankara: Asil Yayın, 2004.
- [7] Wright, P., Dixon, K., Highway Engineering, Wiley, 2004.
- [8] KGM, Karayolu Tasarımı El Kitabı, Ankara: KGM, 2005.
- [9] Fwa, T., The Handbook of Highway Engineering, Boca Raton: Taylor & Francis, 2006.
- [10] Jha, M., Schonfeld, P., Jong, J., Kim, E., Intelligent Road Design, Southampton: WIT Press, 2006.
- [11] Brockenbrough, R., Highway Engineering Handbook, New York: McGraw Hill, 2009.
- [12] Hoel, L., Garber, N, Sadek, A., Transportation Infrastructure Engineering, Stamford: Cengage Learning, 2011.
- [13] Chakroborty, P., Das, A., Principles of Transportation Engineering, New Delhi: PHI Learning, 2012.
- [14] Mannering, F., Washburn, S., Principles of Highway Engineering and Traffic Analysis, Hoboken: Wiley, 2013.
- [15] Robinson, R., Thagesen, B., Road Engineering for Development, London: Spon Press, 2004.
- [16] Kutz, M., Handbook of Transportation Engineering, New York: McGraw-Hill, 2004.
- [17] Fricker, J., Whitford, R., Fundamentals of Transportation Engineering: A Multimodal Systems Approach, New Jersey: Prentice Hall, 2004.

- [18] Findley, D., Schroeder, B., Cunningham, C., Brown, T., Highway Engineering, Amsterdam: Elsevier, 2016.
- [19] NHTSA, Rating System for Rollover Resistance-265, National Academy of Sciences, Washington, DC, 2002.
- [20] Elvik, R., Høye, A., Vaa, T., Sørensen, M., The Handbook of Road Safety Measures, Bingley: Emerald Group Publishing, 2009.
- [21] Wolhuter, K., Geometric Design of Roads Handbook, Boca Raton: Taylor & Francis, 2015.
- [22] Lay, M., Handbook of Road Technology, New York: Spon Press, 2009.
- [23] Günay, B., Enine İvme ve Sademe Formülleri Üzerine Bir Eleştiri, SDÜ Fen Bilimleri Enstitüsü Dergisi, cilt 15, pp. 56-59, 2011.
- [24] O'Flaherty, C., Highways; Traffic Planning and Engineering, Victoria: Arnold, 1986.
- [25] Gillespie, T., Fundamentals of Vehicle Dynamics, Warrendale: Society of Automotive Engineers, Inc., 1992.
- [26] Günay, B., Fişekçioğlu, Y., Yatay Kurp Tahkiklerinde Ball-bank Tekniğinin Kullanımı, Teknik Dergi, cilt 26, no. 3, pp. 7167-7182, 2015.
- [27] Jin, Z., Li, B., Li, J., Dynamic Stability and Control of Tripped and Untripped Vehicle Rollover, Morgan & Claypool, 2019.
- [28] Umar, F., Yol İnşaatı Dersleri, İstanbul: İTÜ Yayınları, 1970.
- [29] Süttaş, İ., Öztaş, G., Karayolu İnşaatında Uygulama ve Projelendirme, İstanbul: TKY, 1986.
- [30] NCHRP, Review of Truck Characteristics as Factors in Roadway Design-505, TRB, Washington DC, 2003.
- [31] Transit, State Highway Geometric Design Manual Section 4: Horizontal Alignment, New Zealand, 2005.
- [32] Yayla, N., Karayolu Mühendisliği, İstanbul: Birsen Yayınevi, 2009.
- [33] Khanna, S., Justo, C., Highway Engineering, Roorkee: Nem Chand & Bros., 2011.
- [34] Kök, B., Karayolu Mühendisliği ve Tasarımı, Ankara: Nobel, 2019.
- [35] Cebon, D., Handbook of Vehicle-Road Interaction, Lisse: Taylor & Francis, 2000.
- [36] Chowdhury et al, Are the criteria for setting advisory speeds on curves still relevant? ITE Journal Feb., 1998
- [37] AASHTO, A Policy on Geometric Design of Highways and Streets, 7<sup>th</sup> Ed. 2018.
- [38] Donnell, E., Wood, J., Himes, S., & Torbic, D. Use of Side Friction in Horizontal Curve Design: A Margin of Safety Assessment. Transp. Research Record, 2588(1), 61-70, 2016.

# Evaluation of Field Shear Wave Velocity in Deep Soil Mixing Based on Laboratory Studies

Mojtaba ASLMAND<sup>1</sup>  
Mehmet Cemal GENES<sup>2</sup>

## ABSTRACT

One of the reasons behind the stabilization of soft and problematic soil by deep soil mixing is to reduce the amplification of seismic waves which arrive to the ground surface and foundation of buildings. Therefore, it is important to correctly predict the dynamic properties of the improved ground. To address the dynamic properties of deep soil mixing, this paper evaluates the in-situ shear wave velocity of deep soil mixing ( $V_{s-field}$ ) based on laboratory investigation ( $V_{s-lab}$ ). The conversion factors, relating to the shear wave velocities of laboratory and field, have been obtained based on a variety of tests including bender element, pulse velocity, and low-amplitude dynamic tests in the resonance column. In this study, the effect of confinement and vertical stress on the dynamic properties of the base stabilized using deep soil mixing technology was evaluated. These effects were combined with the known disturbance and aging influence which is available in the literature.

The research has shown that the most significant factors affecting the shear wave velocity are confinement stress and additional vertical load, which lead to 43% and 17.5% increase respectively.

**Keywords:** Deep soil mixing, shear wave velocity, conversion factor, bender element, resonant column

## 1. INTRODUCTION

Deep soil mixing (DSM) is used broadly to improve the geotechnical properties of soft and problematic soils. It can be applied to most types of soils, including sandy and clayey soil. The main objectives of DSM are increasing the bearing capacity, reducing total and differential settlements, and enhancing the dynamic and cyclic properties of the ground in seismic regions.

---

Note:

- This paper has been received on March 18, 2021 and accepted for publication by the Editorial Board on April 8, 2022.
  - Discussions on this paper will be accepted by September 30, 2022.
- <https://doi.org/10.18400/tekderg.899339>

1 Islamic Azad University, Faculty of Civil and Earth Resources Engineering, Tehran, Iran  
m.aslmand@iauctb.ac.ir - <https://orcid.org/0000-0003-1241-094X>

2 Eastern Mediterranean University, Civil Engineering Department, Famagusta, North Cyprus, Turkey  
cemal.genes@emu.edu.tr - <https://orcid.org/0000-0002-9052-7361>

With DSM, cementitious material is mechanically mixed with the in-situ soil by using a hollow stem auger and paddle arrangement. Mixing can be done using a single auger or a gang of two to eight augers. As the mixing auger advances, the cementitious materials are pumped and mixed with the soil. After the target depth is achieved, augers are withdrawn while the mixing continues. The improvement can be done employing individual improved soil columns in some cases or the entire soil volume underlying the foundation (mass stabilization or block type treatment).

An essential step in the design of earthquake-resisting structures is to correctly predict the characteristics of the ground motion that comes to the structure base. The subsurface soil properties may amplify or de-amplify the level of ground surface shaking while propagating from the bedrock surface through the overlying soil layers. One of the key subsurface information for dynamic soil and rock properties that determines the soil amplification or de-amplification is the shear wave velocity ( $V_s$ ). For earthquake engineering design purposes, many codes and standards- such as AASHTO [1], ASCE 7-16 [2], Eurocode 8 [3], and the International Building Code [4] - classify subsurface soil profiles using the average shear wave velocity ( $V_{s,30}$ ) measured for the top 30 m of soil.

Despite of many laboratory studies on the deep soil mixing, including bender element tests [5,6], the ultrasonic pulse [7] and seismic downhole test [8], there are little information regarding the dynamic and cyclic deformation properties of deep mixing treated soil in the geotechnical literature. For the in-situ strength and deformation properties of clayey soil, there are some tests like falling cone or vane shear test [9]. These tests can be indirectly correlated to shear wave velocity. However, the seismic downhole test could directly determine the dynamic in-situ properties according to ASTM D7400 [10]. Furthermore, it is necessary to perform a laboratory investigation to predict the dynamic properties of the stabilized soil at the initiation phase and before the commencement in the building process. The goal of this paper, therefore, is to conduct lab studies that forecast the change of the improved soil dynamic properties due to the loading of soil improvement with the weight of the building and the increase of wave velocities because of aging of soil-concrete. It is worth mentioning that after the building construction, the stabilized bedding is not easily accessible for in-situ field tests, so finding the relation between field and laboratory shear wave velocity is highly important. The considered type of DSM is mass stabilization in clayey soil which will be accomplished by employing overlapping columns. In the single fluid technique, neat binder slurry is injected into the ground and it creates a stabilized soil column with a diameter of about 1 to 2 m. [11].

## 2. TEST PROCEDURES

The soil layer classification mostly consists of CL, SM, and CL-ML. Tests conducted on soil-cement mixes include bender element testing [12] and sonic testing for measurement of shear wave velocity. For the sample preparation, first, water and cement were mixed, and cement slurry was formed. Then, the cement slurry is mixed with the soil, and cured until testing. The total water-to-cement ratio ( $w_l : c$ ) is 1.7. Then the bender element, pulse velocity, and low-amplitude dynamic tests in the resonance column test were performed on the samples.

Bender elements were piezoelectric bimorphs utilized in pairs to measure the shear wave velocity in a soil specimen. This includes inserting each element near the top and base of a specimen, then applying an excitation voltage to one element to generate a shear wave in the soil. The other elements were used to grab the shear wave that had propagated through the specimen, with its displacement owing to the wave inducing voltage, which was then read by a data acquisition unit. Having the distance between the two elements and monitoring the time needed for the shear wave velocity to propagate, a value of shear wave velocity was acquired.

Bender element tests were conducted for the soil-cement mixtures under no-confinement conditions and confinement condition. Tests were conducted on cured samples which were often cured for 7, 14, 28, and 56 days [13], as shown in Figure 1. Laboratory shear wave velocities were obtained for approximately 28 days of aging. However, the design seismic performance of the improved soil-cement columns was required after the completion of the construction. Piezoelectric elements were carefully inserted into the specimen to ensure full contact. The input signal frequency was varied to determine the strongest output signal, which corresponded to the natural frequency of the sample. Several tests were conducted upon the determination of the input signal frequency. It is preferred to use sin waves as the input frequency, as long as the output can be obtained without significant noise for this wave type. Alternatively, a step function can be considered.

An alternative test can be used to measure wave velocities in the pulse velocity test in accordance with ASTM D2845 [14]. This test can also be carried on selected samples as a check on the Bender test data.

The low-amplitude dynamic tests in the resonance column were conducted on cored elements after the installation of DSM under the building, and they were described in the following sections.

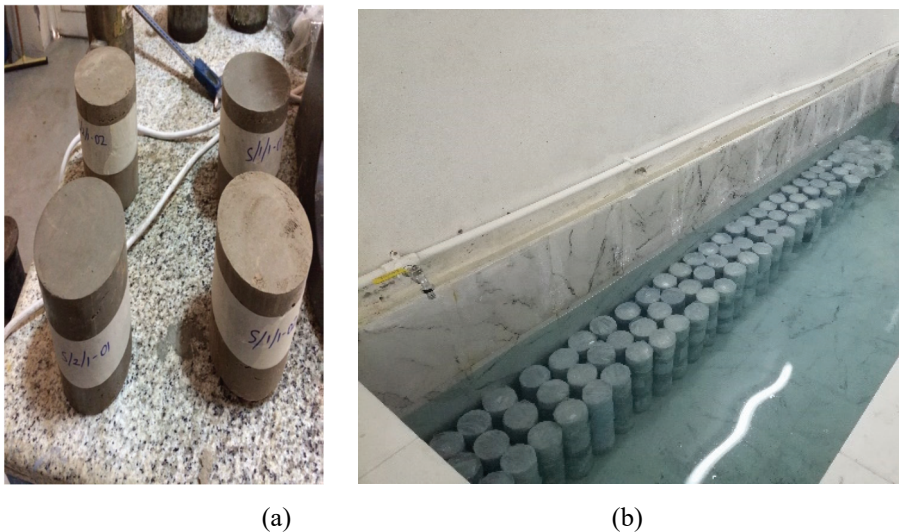


Figure 1 - a. Demolded cylindrical specimens, b. Samples storage in pools for curing

### 3. BENDER ELEMENT AND PULSE VELOCITY TESTS

Shear wave velocity measurements were performed on the samples prepared in the same 5-cm diameter and 10 cm length used for the unconfined compression tests based on ASTM D2166 [15]. These tests involve very low strain excitations. Both bender element tests [16] and sonic pulse velocity tests [14] were conducted. Five sonic pulse velocity tests were used to verify the results from the bender element tests.

*Table 1 - Bender Element results for unconfined testing of cement Type II samples*

| Sample ID. | Age (days) | $\rho$ (kg/m <sup>3</sup> ) | $V_{s0}$ (m/s) |
|------------|------------|-----------------------------|----------------|
| 1.1        | 31         | 1,786                       | 671            |
| 1.2        | 33         | 1,824                       | 639            |
| 1.3        | 28         | 1,743                       | 822            |
| 1.4        | 28         | 1,778                       | 671            |
| 1.5        | 28         | 1,761                       | 637            |
| 1.6        | 28         | 1,849                       | 696            |
| 1.7        | 28         | 1,863                       | 565            |
| 1.8        | 30         | 1,878                       | 530            |
| 1.9        | 31         | 1,684                       | 600            |
| 1.10       | 31         | 1,692                       | 641            |
| 1.11       | 31         | 1,691                       | 548            |
| 1.12       | 29         | 1,720                       | 523            |
| 1.13       | 29         | 1,692                       | 515            |
| 1.14       | 29         | 1,732                       | 499            |
| 1.15       | 29         | 1,599                       | 637            |
| 1.16       | 29         | 1,605                       | 658            |
| 1.17       | 29         | 1,602                       | 713            |
| 1.18       | 32         | 1,639                       | 561            |
| 1.19       | 32         | 1,633                       | 618            |
| 1.20       | 32         | 1,601                       | 630            |
| 1.21       | 29         | 1,613                       | 712            |
| 1.22       | 29         | 1,601                       | 667            |
| 1.23       | 32         | 1,675                       | 467            |
| 1.24       | 32         | 1,677                       | 493            |
| 1.25       | 29         | 1,802                       | 697            |
| 1.26       | 29         | 1,816                       | 673            |
| 1.27       | 29         | 2,005                       | 659            |
| 1.28       | 29         | 1,851                       | 581            |
| 1.29       | 29         | 1,850                       | 772            |
| 1.30       | 29         | 1,844                       | 698            |

Table 1 - Bender Element results for unconfined testing of cement Type II samples  
(continue)

| Sample ID. | Age (days) | $\rho$ (kg/m <sup>3</sup> ) | $V_{so}$ (m/s) |
|------------|------------|-----------------------------|----------------|
| 1.31       | 28         | 1,826                       | 566            |
| 1.32       | 28         | 1,906                       | 665            |
| 1.33       | 28         | 1,826                       | 832            |
| 1.34       | 28         | 1,762                       | 714            |
| 1.35       | 28         | 1,858                       | 577            |

### 3.1. Factors Considered in Bender Element Tests

The list of samples tested and the corresponding shear wave velocity test, for unconfined conditions ( $V_{so}$ ), were given in Table 1 and Table 2 for cement Type II and Type V samples respectively. The last five results (sample ID: 1.31-1.35) presented in Table 1 correspond to the pulse velocity test method. For the primary testing method of bender element tests, the study addressed the effect of loading frequency, effect of bonding between the piezoelectric element and the sample, effect of confinement, effect of sample quality, and effect of natural frequency.

Table 2 - Bender Element results for unconfined testing of cement Type V samples

| Sample ID. | Age (days) | $\rho$ (kg/m <sup>3</sup> ) | $V_{so}$ (m/s) |
|------------|------------|-----------------------------|----------------|
| 2.1        | 33         | 1,751                       | 589            |
| 2.2        | 33         | 1,735                       | 580            |
| 2.3        | 33         | 1,733                       | 630            |
| 2.4        | 32         | 1,782                       | 605            |
| 2.5        | 32         | 1,732                       | 572            |
| 2.6        | 33         | 1,738                       | 658            |
| 2.7        | 32         | 1,702                       | 529            |
| 2.8        | 32         | 1,700                       | 591            |
| 2.9        | 34         | 1,776                       | 614            |
| 2.10       | 32         | 1,677                       | 529            |
| 2.11       | 32         | 1,680                       | 495            |
| 2.12       | 32         | 1,971                       | 814            |
| 2.13       | 31         | 1,950                       | 695            |
| 2.14       | 31         | 1,912                       | 761            |
| 2.15       | 33         | 1,897                       | 787            |
| 2.16       | 32         | 1,909                       | 759            |
| 2.17       | 33         | 1,729                       | 631            |
| 2.18       | 32         | 1,745                       | 513            |

Table 2 - Bender Element results for unconfined testing of cement Type V samples (continue)

| Sample ID. | Age (days) | $\rho$ (kg/m <sup>3</sup> ) | $V_{so}$ (m/s) |
|------------|------------|-----------------------------|----------------|
| 2.19       | 32         | 1,772                       | 483            |
| 2.20       | 32         | 1,755                       | 523            |
| 2.21       | 30         | 1,743                       | 804            |
| 2.22       | 30         | 1,795                       | 630            |
| 2.23       | 30         | 1,791                       | 518            |
| 2.24       | 28         | 1,986                       | 794            |
| 2.25       | 33         | 1,862                       | 847            |
| 2.26       | 32         | 1,893                       | 741            |
| 2.27       | 32         | 1,881                       | 690            |
| 2.28       | 26         | 1,742                       | 708            |
| 2.29       | 31         | 1,900                       | 751            |
| 2.30       | 31         | 1,881                       | 723            |
| 2.31       | 31         | 1,893                       | 688            |
| 2.32       | 27         | 1,770                       | 616            |
| 2.33       | 27         | 1,781                       | 539            |
| 2.34       | 27         | 1,737                       | 572            |
| 2.35       | 27         | 1,697                       | 614            |
| 2.36       | 27         | 1,689                       | 660            |

The measured output signal depends on the input loading frequency. At certain frequencies, secondary and tertiary wave arrivals may be recorded with greater amplitudes that do not correspond to true shear wave velocity measurements. Therefore, multiple methods of data interpretation techniques were used to identify false peaks such that the correct shear wave velocity pick is made. Three data interpolation techniques were used during data analysis: Time Domain-Peak Arrival Time, Cross-Correlation method, and Power Spectrum Comparison method. The final velocity was obtained as the average of two methods when any of them above provide velocities that were within 10% of each other. If all three methods produce velocities within 10%, then, the velocity is calculated as the average of velocities obtained from all three methods.

Since the samples were too stiff to insert the piezoelectric elements, a small groove was opened in the sample to fit the bender elements. The gap between the piezoelectric element and the sample was filled with natural clay, and different types of materials and conditions were tested to get the best output signal response. The natural moist clay fill provided the best output signal quality.

The shear wave velocity varies as a function of confinement in the field. Therefore, 20 tests were conducted with confinement to assess the functional relationship between the shear wave velocity and the confinement pressure. Table 3 shows typical normalized  $V_s$  values for different confinement pressures for cement type V samples.

Table 3 - Normalized shear wave velocity ( $V_s/V_{s0}$ ) results for different confinement pressure for cement type V (sample ID: 2-1)

| psi | kPa | Sample ID: 2.1 |
|-----|-----|----------------|
| 0   | 0   | 1.00           |
| 5   | 34  | 1.38           |
| 10  | 69  | 1.41           |
| 15  | 103 | 1.41           |
| 20  | 138 | 1.47           |
| 25  | 172 | 1.47           |

Since the samples were prepared in relatively small molds compared to the size of field-installed columns (1.6 m vs. 5 cm), small imperfections in the mixing process produced a greater impact on the measured velocity. Therefore, samples were ranked in terms of their quality during testing to obtain a reliable velocity. The sample rating system is qualitatively based on sample external appearance. The rating scale runs from 1 to 5, where 1 is the lowest quality and 5 is the best quality. Only samples with a quality rating of at least 3 were tested. The results showed that sample quality had a noticeable influence on the  $V_s$  value. This is observed when comparing quality 3 to quality 5.

For the fundamental mode of vibration, the natural frequency of the sample was approximated using Eq. (1) [17]:

$$f_n = V_s / 4H \quad (1)$$

Where  $f_n$  = natural frequency in kHz,  $V_s$ = expected shear wave velocity (m/s),  $H$ = sample height (mm)

One test at the natural frequency is conducted to check if the maximum response is obtained.

If the resonance is not obtained with the maximum response, the frequency is increased by 10 Hz interval until the maximum response is obtained (first peak response).

### 3.2. Conversion Factors

The measured shear wave velocities in the laboratory under unconfined conditions were lower than the in-situ shear wave velocity in the field for the following two reasons:

- a) **Confinement level:** Confinement level in the field increases the shear wave velocity. Since structural loads increase the confinement, they are also expected to increase the shear wave velocity.
- b) **Disturbance or imperfections:** The small laboratory samples with a diameter of 5 cm are more likely to cause a decrease in velocity than for large improved soil columns in the field with a diameter of 1.6 m. Besides, extrusion, cutting, and preparation of the laboratory samples in the laboratory introduce more disturbances to the laboratory samples. These disturbance sources do not exist during the field mixing conditions. The

effect of disturbance is more pronounced for shear wave velocity as the small-strain measurements are more prone to disturbance compared to, for example, large-strain unconfined compressive strength.

**3.2.1. Confinement Level**

Bender element tests were conducted for soil sampled from the site and mixed with cement in the laboratory to determine the conversion factor depending on the confinement level. The tests were conducted at 0 psi, 5 psi, 10 psi, 15 psi, 20 psi, and 25 psi (0, 34, 69, 103, 138, and 172 kPa) confinement levels to measure the effect of confinement. These confinement levels correspond to the confinement levels anticipated for the 20 m deep soil-cement columns. The effect of structural loads was not considered here as a conservative approach. For each test, the shear wave velocity at each confinement level was normalized with respect to the no-confinement shear wave velocity, and they were all plotted on the same normalized shear wave velocity vs. confinement plot (Figure 2). A conversion factor was then obtained to account for confinement,  $C_{conf}$ , which means an increase in shear wave velocity compared to the shear wave velocity measured for unconfined conditions. An average conversion factor interpreted of 43%, i.e.,  $C_{conf}=1.43$  was interpreted for all depths in the field. This means an increase in shear wave velocity by 43% compared to the shear wave velocity measured in the laboratory for unconfined conditions.

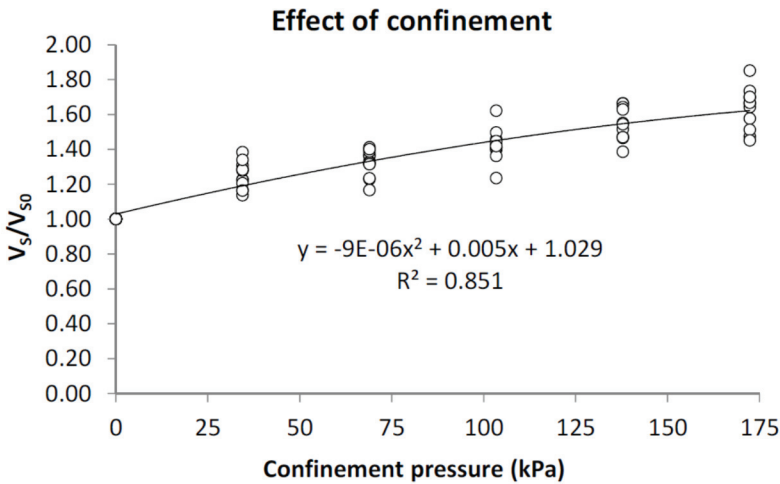


Figure 2 - Normalized Shear Wave Velocity vs. Confinement Pressure Plot

**3.2.2. Disturbance Effects**

Disturbance effects were quantified by Chiara and Stokoe [18] as shown in Figure 3 for soil samples. Field measured shear wave velocities shown in Figure 3 are consistently higher than laboratory-measured shear wave velocities. If the mean-one standard deviation curve on Figure 3 is considered, the conversion factor from the laboratory to the field is around 20%, i.e.,  $C_{dist}=1.20$ . This factor corresponds to the average shear wave velocity measured in the

laboratory for unconfined conditions, and it is conservative since it is based on the mean-one standard deviation curve and not the mean curve.

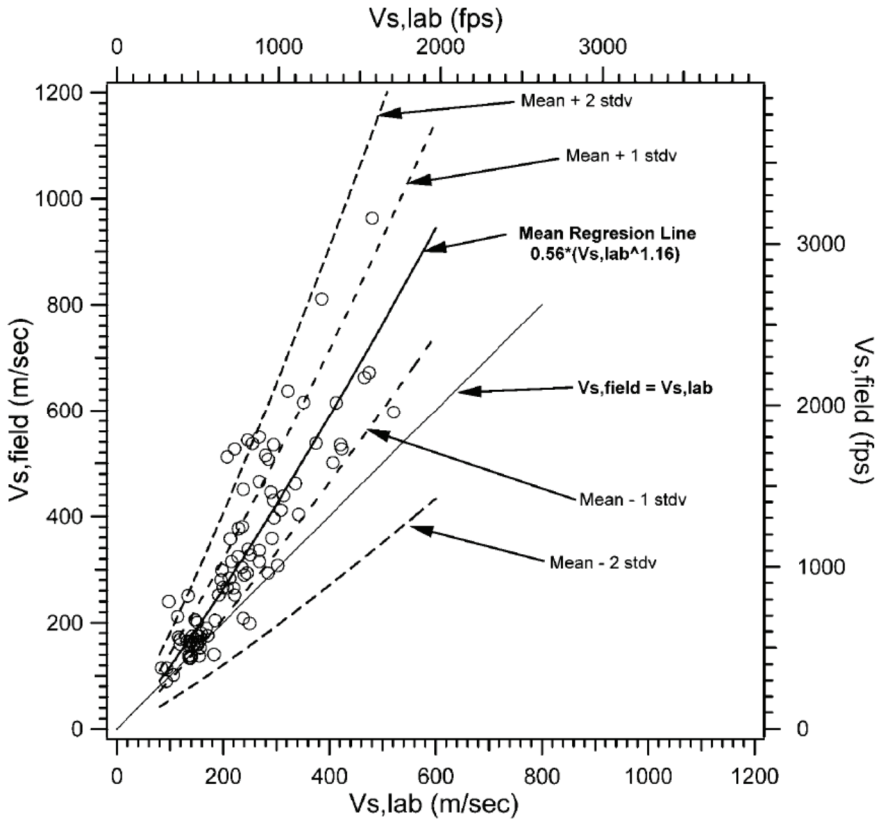


Figure 3 - Disturbance Effects, Field Shear Wave Velocity vs. Laboratory Shear Wave Velocity [18]

#### 4. RESONANCE COLUMN TESTS

The objective of the resonance column test is to determine the elastic shear wave velocity  $V_s$  of the soil-cement specimens cored under the building and its dependence upon the values of confining and axial loads.

In this study, the laboratory testing was conducted by the method of low-amplitude dynamic tests in the resonance column within the approximate shear deformation range of  $10^{-4}$ - $10^{-2}$  %.

The soil-cement specimens prepared in the form of a solid cylinder were placed into the triaxial compression chamber. After preliminary consolidation, these specimens were put through the action of dynamic loading by application of variable frequency torsional vibrations to the upper free-end face of the specimen. The soil-cement experiences a simple

shear deformation during vibrations. The shear deformation amplitude is determined at each frequency of the specified range, which allows obtaining the amplitude response spectrum of the soil-cement and determines the resonance frequency of the specimen. Using the first natural frequency of the specimen, it is possible to calculate the shear wave velocity ( $V_s$ ) and then the dynamic shear modulus ( $G$ ).

The dynamic tests of soil-cements, using the resonance column method, were conducted as per the consolidated-undrained scheme. The reason behind that is any change of the shape or weight of the specimen in the course of testing may change its moment of inertia and distort the final result.

The research was performed using the resonance column with an electromagnetic system for torsional vibration generation, which was drowned inside the triaxial compression chamber. The accelerometers were used as devices for measuring small angular movements (rotations). The loading system supplied the excitation of torsional vibrations within the range from 0 to 200 Hz. The general view of the test facility is shown in Figure 4.



Figure 4 - General View of the Resonance Column

Data processing consists of the calculation of dynamic loading concerning the shear deformations  $\gamma$  for all steps, the determination of its value  $\tau_{\max}$  at the resonance frequency  $\omega$ , and the calculation of the shear wave velocity  $V_s$  for this frequency with subsequent determination of the dynamic shear modulus  $G$ .

The relative shear deformation was calculated at each excitation frequency spacing by the angular displacements measured as the tangent of the azimuth angle  $\theta$  at the point moved away from the specimen center by  $0.78r$  for solid specimens with radius  $r$ . Following the results of the calculation, the resonance curve was plotted, from which the resonance vibration frequency value  $\omega$  is taken at  $\gamma=\gamma_{\max}$ .

The shear wave velocity  $V_s$  (m/s) can be computed from the following formula:

$$V_s = \omega h \left( \frac{J}{J_0} \right)^{\frac{1}{2}} \quad (2)$$

where  $J$  is the moment of inertia of the specimen (to be determined from the weight and geometric dimensions of the specimen according to the known physical relations at the moment of completion of consolidation); for a solid cylindrical specimen with the weight  $m$  and radius  $r$  ( $\text{kg.m}^2$ );

$J_0$  is the moment of inertia of the power drive of the test facility (to be specified by the manufacturer in the device documentation) ( $\text{kg.m}^2$ );  $h$  is the specimen height (m);  $\omega$  is the resonance frequency (rad/s).

Having determined the shear wave velocity  $V_s$  from Eq. 2, the dynamic shear modulus  $G$  (Pa) was calculated from the following formula:

$$G = \rho V_s^2 \quad (3)$$

where  $\rho$  is the specimen density ( $\text{kg/m}^3$ ).

Laboratory tests were performed on samples of improved soil drilled out from the building's footing with a diameter of at least 80 mm and a height of at least 160 mm.

The tests were performed on 3 samples, where number of  $V_s$  determination is 9. The load combinations are provided in Table 4.

*Table 4 - Load combinations for wave velocity measurements*

| Load No | $\sigma_3$ , kPa | $\sigma_1$ , kPa |
|---------|------------------|------------------|
| 1       | 100              | 100              |
| 2       | 100              | 400              |
| 3       | 100              | 700              |

The study obtained the results of the tests showing the impact of the vertical load on the S-wave velocity and confirming the growth of S-wave velocity  $V_s$  in the soil-cement footing of the building.

The results of the tests identified the dependence of the S-wave velocity upon the vertical load. Figure 5 shows the S-wave values normalized to the velocity during isotropic compression at 100 kPa for the same specimen.

The expected velocity gain from the direct action of the vertical load can be equal to 15-20 % (average 17.5%) with an increase in the vertical stress  $\sigma_1$  from 100 kPa to 700 kPa. The

obtained weight conversion factor  $C_{wr}$  based on the logarithmic regression analysis is as follows:

$$C_{wr} = V_s / V_{s0} = 0.0966 \ln(\sigma_1) + 0.5603 \tag{4}$$

The research results were presented in graphical form in Figure 5, on which trend lines were grouped according to each borehole and vertical loads  $\sigma_1$ . The highest approximation confidence coefficient  $R^2 = 0.7565$  was obtained for the second trend line which was given in Figure 5. An average conversion factor of 17% (i.e.  $C_{wr} = 1.17$ ) is interpreted for the impact of vertical load.

Figure 5 shows that when the vertical load increases, the shear wave velocity increases according to weight conversion factor function given in Eq. (4). Depending on higher shear wave velocity of approaching wave, the frequency of the soil beneath the building will be higher which results in less vibration period on the superstructure. Based on the less vibration period of the structure, the top displacement can be kept within the acceptable range for more safe and economical design.

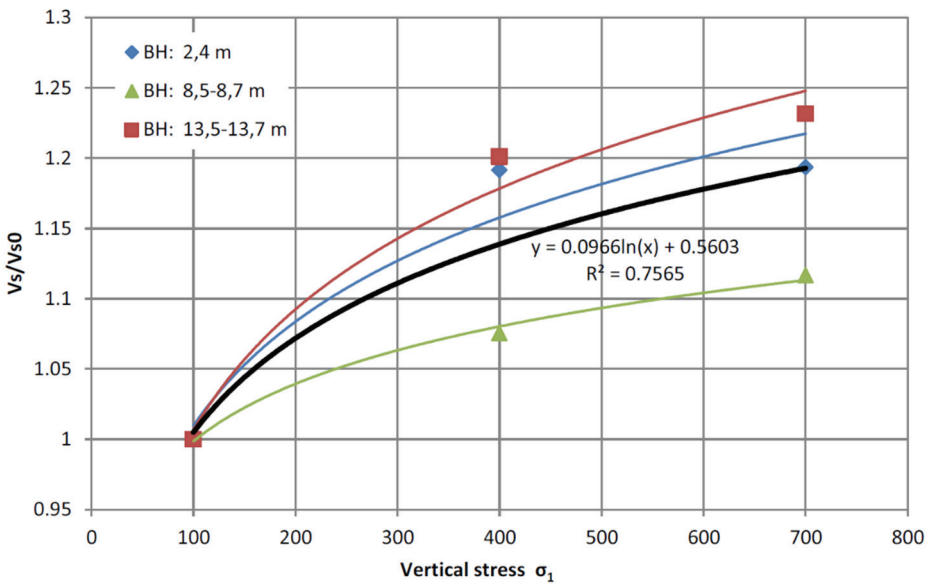


Figure 5 - S-wave velocity increasing ratio vs. vertical load;  $V_{s0}$  is the S-wave velocity during isotropic compression at 100 kPa

### 5. ESTIMATION OF AGING EFFECTS ON THE SHEAR WAVE VELOCITY

According to the FHWA Deep Soil Mixing Manual [13], the effect of aging due to curing can be incorporated using the following equation:

$$f(t) = 0.187 \ln(t) + 0.375 \tag{5}$$

Where  $t$  is the curing time in days;  $f(t)$  is the ratio of unconfined compressive strength at time  $t$  to the unconfined compressive strength at 28 days.

The shear wave velocity can be correlated to the unconfined compressive strength through the general equation [19].

$$V_s = b f_c^\phi \tag{6}$$

where  $f_c$  is the unconfined compressive strength.

The ratio of the S-wave velocity before aging and after aging can be used to cancel out the coefficient  $b$

$$\frac{(V_s)_t}{(V_s)_0} = \left( \frac{(f_c)_t}{(f_c)_0} \right)^\phi = (f(t))^\phi \tag{7}$$

For a curing period of 10 years, the ratio  $f(t)$ , as calculated by Eq. (5), was equal to 1.9. Using the power of 0.2 and 0.25, the range of the shear wave velocity ratio after 10 years varied between 1.13 to 1.17.

Figure 6 shows the values of the aging conversion factor  $C_{age} = (f(t))^\phi$  for a period of 10 years using the power of 0.25. For example, the  $C_{age}$  coefficient value corresponding to the S-wave velocity, gained in the soil improvement foundation from the age of 1 year to the age of 5.5 years, is equal to 1.05.

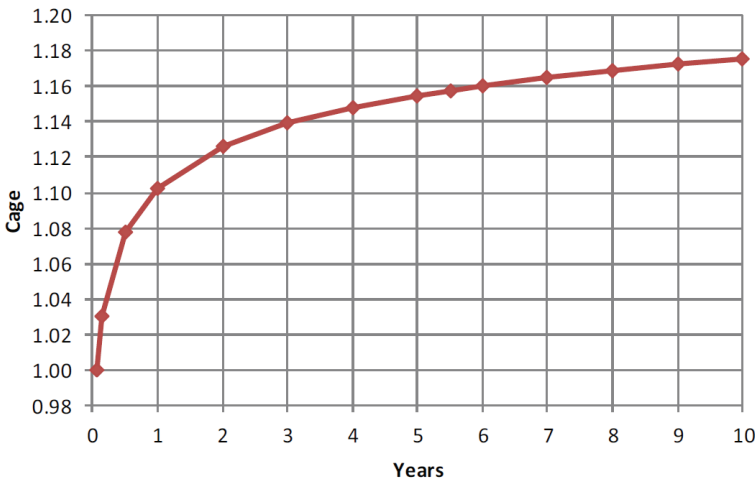


Figure 6 - Conversion Factor  $C_{age}$  vs. Age

Considering all the conversion factors,  $C_{conf}$ ,  $C_{dist}$ ,  $C_{age}$ , and  $C_{wt}$  the resulting shear wave velocity was obtained using Eq. (8) for each test.

$$V_{s-field} = V_{s-lab-unconfined} \cdot C_{conf} \cdot C_{dist} \cdot C_{age} \cdot C_{wt} \quad (8)$$

Eq. 8 represents the field shear wave velocity of Deep Soil Mixed Block after accounting for in-situ confinement effect ( $C_{conf}=1.43$ ), laboratory sample disturbance ( $C_{dist}=1.20$ ), aging and long-term curing ( $C_{age}=1.05$ ), and the weight of building ( $C_{wt}=1.17$ ). The cumulative conversion factor considering all four mechanisms was 2.1. The latter states the importance of conversion factors as the actual shear wave velocity could be more than twice of the laboratory measured ones.

## 6. CONCLUSION

This study performed the laboratory studies (bender element, sonic pulse velocity, and resonance column test) to forecast the change of shear wave velocity of deep soil mixing due to confinement, disturbance, aging, and weight of the structure over the improved base. The following main conclusion in accordance with the obtained test results can be drawn as follows:

1. The influence of confinement and vertical stress (load) from the designed structure on the soil-cement base on the propagation wave velocity was revealed and expressed by a logarithmic formulation. During the test, with the increase of confinement and vertical stress on soil-cement samples, an increase in the shear wave propagation velocity was obtained, which is expected to provide more safe and economical design of structures.
2. The current study also specified the conversion factors related to the shear wave velocity of the laboratory and field. These factors can predict the dynamic properties of deep soil mixing from the preliminary design stage of the project especially accounting for disturbance, confinement, aging, and vertical load on the deep soil mixing elements.

## Symbols

|               |                                  |
|---------------|----------------------------------|
| $V_s$         | : Shear Wave Velocity            |
| $V_{s-field}$ | : Field Shear Wave Velocity      |
| $V_{s-lab}$   | : Laboratory Shear Wave Velocity |
| $w_t$         | : Total Water                    |
| $c$           | : Cement                         |
| $V_{s0}$      | : Unconfined Shear Wave Velocity |
| $\rho$        | : Density                        |
| $f_n$         | : Natural Frequency              |

|            |  |
|------------|--|
| $H$        | : Sample Height  |
| $C_{conf}$ | : Confinement Conversion Factor  |
| $C_{dist}$ | : Disturbance Confinement Factor   |
| $t$        | : curing time  |
| $f(t)$     | : Ratio of Unconfined Compressive Strength at a time to the Unconfined Compressive Strength at 28 days |
| $f(c)$     | : Unconfined Compressive Strength  |
| $C_{age}$  | : Aging Conversion Factor  |
| $C_{wt}$   | : Weight Conversion Factor   |
| $\sigma_1$ | : Vertical Stress  |
| $\sigma_3$ | : Confinement Stress   |
| $G$        | : Shear modulus  |
| $\omega$   | : Resonance Frequency  |
| $\tau$     | : Shear Stress   |
| $\gamma$   | : Shear Deformation  |
| $\Theta$   | : Azimuth Angle  |
| $J$        | : Moment of Inertia  |
| $J_0$      | : Moment of Inertia of the Power Drive of the Test Facility  |
| $h$        | : Specimen height  |
| $m$        | : Specimen weight  |
| $r$        | : Specimen radius  |

### References

- [1] AASHTO. "AASHTO LRFD bridge design specifications", Washington, DC, 2012.
- [2] ASCE. "Minimum Design Loads for Buildings and Other Structures", ASCE/SEI 7-16. Reston, VA, 2016.
- [3] CEN (European Committee for Standardization). "Design of Structures for Earthquake Resistance. Part 1—General rules, seismic actions and rules for buildings", EN 1998-1 Eurocode 8. Brussels, Belgium, 2004.
- [4] ICC (International Code Council). "International building code", Country Club Hills, IL: ICC, 2018.

- [5] Bate B, Cao J, Zhang C, Hao N, Wang S. Monitoring lime and cement improvement using spectral induced polarization and bender element techniques. *Journal of Rock Mechanics and Geotechnical Engineering*. 13(1):202-11, 2021.
- [6] Piriyaikul K, Iamchaturapatr J. Deep soil mixing method for the bio-cement by means of bender element test. In *Advances in Laboratory Testing and Modelling of Soils and Shales 2017* Jan 18 (pp. 375-381). Springer, Cham.
- [7] Canakci H, Güllü H, Dwle MI. Effect of glass powder added grout for deep mixing of marginal sand with clay. *Arabian Journal for Science and Engineering*. 43(4):1583-95, 2018.
- [8] Madhyannapu RS, Puppala AJ, Nazarian S, Yuan D. Quality assessment and quality control of deep soil mixing construction for stabilizing expansive subsoils. *Journal of geotechnical and geo-environmental engineering*. 136(1):119-28, 2010.
- [9] Gulen M., Kılıç H., “Determination of strength and deformation parameters of remolded clays by falling cone and veyn tests”, *Teknik Dergi*, 31(3): 9987-10012, 2020
- [10] ASTM D 7400-14. "Standard Test Methods for Downhole Seismic Testing", 2014.
- [11] Kitazume, Masaki, and Masaaki Terashi, “The deep mixing method”, CRC Press, 2013.
- [12] Viggiani, G. and Atkinson, J.H., “Interpretation of bender element tests”, *Géotechnique*: 45(1), 149–154, 1995.
- [13] Federal Highway Administration (FHWA). “Design Manual: Deep Mixing for Embankment and Foundation Support”, United States Department of Transportation, Publication No. FHWA-HRT-13-046, 2013.
- [14] ASTM D2845-08, “Standard Test Method for Laboratory Determination of Pulse Velocities and Ultrasonic Elastic Constants of Rock (Withdrawn 2017)”, DOI: 10.1520/D2845-08 ASTM International, West Conshohocken, PA, 2008.
- [15] ASTM D2166, “Standard Specification for Unconfined Compressive Strength of Cohesive Soil”, West Conshohocken, PA, USA, 2006.
- [16] ASTM D8295-19, “Standard Test Method for Determination of Shear Wave Velocity and Initial Shear Modulus in Soil Specimens Using Bender Elements”, ASTM International, West Conshohocken, PA, 2019.
- [17] Kramer, S. L., “Geotechnical Earthquake Engineering”, Prentice Hall, Upper Saddle River, NJ, 1996.
- [18] Chiara, N., Stokoe, K.H., “Sample Disturbance in Resonant Column Test Measurement of Small-Strain Shear Wave Velocity, Soil Stress-Strain Behavior: Measurement, Modeling and Analysis”, *Geotechnical Symposium in Roma*, March 16&17, 2006.
- [19] Boone, Darrel, S., “A Comparison Between the Compressive Strength and the Dynamic Properties of Concrete as a Function of Time”, Master's Thesis, University of Tennessee, 2005.

# TEKNİK DERGİ MANUSCRIPT DRAFTING RULES

1. The whole manuscript (text, charts, equations, drawings etc.) should be arranged in Word and submitted in ready to print format. The article should be typed on A4 (210 x 297 mm) size paper using 10 pt (main title 15 pt) Times New Roman font, single spacing. Margins should be 40 mm on the left and right sides and 52.5 mm at the top and bottom of the page.
2. Including drawings and tables, articles should not exceed 25 pages, technical notes 10 pages.
3. Your contributed manuscript must be sent over the DergiPark system. (<http://dergipark.gov.tr/tekderg>)
4. The text must be written in a clear and understandable language, conform to the grammar rules. Third singular person and passive tense must be used, and no inverted sentences should be contained.
5. Title must be short (10 words maximum) and clear, and reflect the content of the paper.
6. Sections should be arranged as: (i) abstract and keywords, (ii) title, abstract and keywords in the other language, (iii) main text, (iv) symbols, (v) acknowledgements (if required) and (vi) references.
7. Both abstracts should briefly describe the object, scope, method and conclusions of the work and should not exceed 100 words. If necessary, abstracts may be re-written without consulting the author. At least three keywords must be given. Titles, abstracts and keywords must be fitted in the first page leaving ten line space at the bottom of the first page and the main text must start in the second page.
8. Section and sub-section titles must be numbered complying with the standard TS1212.
9. Symbols must conform to the international rules; each symbol must be defined where it appears first, additionally, a list of symbols must be given in alphabetic order (first Latin, then Greek alphabets) at the end of the text (before References).
10. Equations must be numbered and these numbers must be shown in brackets at the end of the line.
11. Tables, drawings and photographs must be placed inside the text, each one should have a number and title and titles should be written above the tables and below the drawings and photographs.
12. Only SI units must be used in the manuscripts.
13. Quotes must be given in inverted commas and the source must be indicated with a reference number.
14. Acknowledgement must be short and mention the people/ institutions contributed or assisted the study.
15. References must be numbered (in brackets) in the text referring to the reference list arranged in the order of appearance in the text. References must include the following information:  
If the reference is an article: Author's surname, his/her initials, other authors, full title of the article, name of the journal, volume, issue, starting and ending pages, year of publication.  
Example : Naghdi, P. M., Kalnins, A., On Vibrations of Elastic Spherical Shells. J. Appl. Mech., 29, 65-72, 1962.  
If the reference is a book: Author's surname, his/her initials, other authors, title of the book, volume number, editor if available, place of publication, year of publication.  
Example : Kraus. H., Thin Elastic Shells, New York. Wiley, 1967.  
If the reference is a conference paper: Author's surname, his/her initials, other authors, title of the paper, title of the conference, location and year.  
If the source is a thesis: Author's surname, his/her initials, thesis title, level, university, year.  
If the source is a report: Author's surname, his/her initials, other authors, title of the report, type, number, institution it is submitted to, publication place, year.
16. Discussions to an article published in Teknik Dergi should not exceed two pages, must briefly express the addressed points, must criticize the content, not the author and must be written in a polite language. Authors' closing remarks must also follow the above rules.
17. A separate note should accompany the manuscript. The note should include, (i) authors' names, business and home addresses and phone numbers, (ii) brief resumes of the authors and (iii) a statement "I declare in honesty that this article is the product of a genuinely original study and that a similar version of the article has not been previously published anywhere else" signed by all authors.
18. Copyright has to be transferred to UCTEA Turkish Chamber of Civil Engineers. The standard copyright form signed by the authorised author should therefore be submitted together with the manuscript.

# CONTENTS

## A Foreword by the Retiring Editor

A New and Promising Editor for Teknik Dergi

## Foreword

Thanks to Our Founding Editor, Milestones and Future Targets of Teknik Dergi

Critical Inclination of Failure Surface and Seismic Active Earth Thrust for a Broken Slope Backfill ..... 12027  
**Umit CALIK**

Investigations of Exterior Wind Flow and Aerodynamic Coefficient around Y-Plan Shape Tall Building . 12045  
**Vigneshwaran RAJENDRAN, Prabavathy SHANMUGASUNDARAM**

Entropy Based Regional Precipitation Prediction in the Case of Gediz River Basin ..... 12067  
**Özgür BOZOĞLU, Türkiye BARAN, Filiz BARBAROS**

Rainfall Intensity-Duration-Frequency Analysis in Turkey, with the Emphasis of Eastern Black Sea Basin ..... 12087  
**Ömer YÜKSEK, Tuğçe ANILAN, Fatih SAKA, Emrah ÖRGÜN**

Effect of Sub-Contractor Selection on Construction Project Success in Turkey ..... 12105  
**Ali Erkan KARAMAN, Koray SANDAL**

Multi Agent System Based Risk Allocation Model for Public-Private-Partnership Type Projects (RAMP3) ..... 12119  
**Hande ALADAG, Zeynep ISIK**

The High Temperature Performance Evaluation of Polymer/Nanocomposite Modified Asphalt Cement . 12143  
**Mustafa ALAS, Ali Shaban ALBRKA ISMAEL, Hüseyin GÖKÇEKUŞ**

Experimental Study of Hydrodynamic Pressures Acting on a Submerged Gate ..... 12163  
**Sochheat SMOK, Mehmet Anil KIZILASLAN, Adnan Tolga KURUMUS, Ender DEMİREL**

Evaluation of Stripping Problem in Terms of Additive Types and Ratios in Asphalt Pavements ..... 12183  
**Celeleddin Ensar ŞENGÜL, Atakan AKSOY, Erol İSKENDER**

Influence of Gravity Framing on the Collapse Probability of Steel Buildings with Special Moment Frames ..... 12203  
**Adem KARASU, Cüneyt VATANSEVER**

Meteorological Drought Analysis for Helmand River Basin, Afghanistan ..... 12223  
**Mohammad Musa ALAMI, Gokmen TAYFUR**

The Effect of Hydrated Lime Mixing Forms and Ratios on Performance in Asphalt Pavements ..... 12243  
**Celeleddin Ensar ŞENGÜL, Dündar AYYILDIZ, Erol İSKENDER, Atakan AKSOY**

Fully Implicit Form of Differential Quadrature Method for Multi-Species Solute Transport in Porous Media ..... 12265  
**Amin GHAREHBAGHI**

An Investigation on Force Modification Factors in Cold-Formed Steel Structures ..... 12283  
**Macit YURTSEVER, Serdar SOYÖZ**

Determination of Finite Element Modelling Errors for Box Culverts Using Field Load Tests ..... 12309  
**Tuna ULGER**

## TECHNICAL NOTE

Sliding and Rollover on Highways - Subtleties to Note ..... 12329  
**Banihan GÜNAY**

Evaluation of Field Shear Wave Velocity in Deep Soil Mixing Based on Laboratory Studies ..... 12335  
**Mojtaba ASLMAND, Mehmet Cemal GENES**